

Self assembling cluster crystals from DNA based dendritic nanostructures

Emmanuel Stiakakis ^{1✉}, Niklas Jung², Nataša Adžić ³, Taras Balandin ⁴, Emmanuel Kentzinger ⁵, Ulrich Rücker ⁵, Ralf Biehl ⁶, Jan K. G. Dhont^{1,7}, Ulrich Jonas² & Christos N. Likos ^{3✉}

Cluster crystals are periodic structures with lattice sites occupied by several, overlapping building blocks, featuring fluctuating site occupancy, whose expectation value depends on thermodynamic conditions. Their assembly from atomic or mesoscopic units is long-sought-after, but its experimental realization still remains elusive. Here, we show the existence of well-controlled soft matter cluster crystals. We fabricate dendritic-linear-dendritic triblock composed of a thermosensitive water-soluble polymer and nanometer-scale all-DNA dendrons of the first and second generation. Conclusive small-angle X-ray scattering (SAXS) evidence reveals that solutions of these triblock at sufficiently high concentrations undergo a reversible phase transition from a cluster fluid to a body-centered cubic (BCC) cluster crystal with density-independent lattice spacing, through alteration of temperature. Moreover, a rich concentration-temperature phase diagram demonstrates the emergence of various ordered nanostructures, including BCC cluster crystals, birefringent cluster crystals, as well as hexagonal phases and cluster glass-like kinetically arrested states at high densities.

¹Biomacromolecular Systems and Processes, Institute of Biological Information Processing (IBI-4), Forschungszentrum Jülich, D-52425 Jülich, Germany.

²Macromolecular Chemistry, Department of Chemistry-Biology, University of Siegen, D-57076 Siegen, Germany. ³Faculty of Physics, University of Vienna, Boltzmannngasse 5, A-1090 Vienna, Austria. ⁴Structural Biochemistry, Institute of Biological Information Processing (IBI-7), Forschungszentrum Jülich, D-52425 Jülich, Germany. ⁵Jülich Centre for Neutron Science JCNS and Peter Grünberg Institut PGI, JARA-FIT, Forschungszentrum Jülich, D-52425 Jülich, Germany. ⁶Neutron Scattering and Biological Matter (JCNS-1/IBI-8), Forschungszentrum Jülich, D-52425 Jülich, Germany. ⁷Heinrich-Heine-

Universität Düsseldorf, Universitätsstraße 1, D-40225 Düsseldorf, Germany. ✉email: e.stiakakis@fz-juelich.de; christos.likos@univie.ac.at

Crystals are orderly states of matter in which particles with sizes ranging from sub-nanometer to micron are arranged in a periodic lattice. Crystalline solids epitomize the notion of rigidity, lying at the antipode of fluidity that is embodied by liquids. Accordingly, hybrid, exotic phases that combine crystallinity with (super-)fluidity have fascinated researchers both in the classical realm of soft matter physics^{1–5} and in the quantum domain^{6–10}. In usual crystals, the lattice constant a and the particle concentration c obey the proportionality $a \propto c^{-1/3}$, dictated by the condition that the (conventional) unit cell be populated by a fixed number of particles determined by the lattice geometry. Cluster crystals, a newer concept, are unconventional states of matter whose lattice sites are occupied by clusters of fully or partially overlapping particles rather than single ones^{1–3,6–8,11,12}. In these states, the number of overlapping particles within a cluster, the lattice-site occupancy N_{occ} , is a fluctuating quantity, with its expectation value scaling with concentration as $N_{\text{occ}} \propto c$ and thus resulting in a concentration-independent lattice constant, the latter being the salient structural characteristic of both cluster crystals^{1–3} and cluster quasicrystals^{13,14}.

Cluster crystals were first discovered in a simple model of penetrable spheres¹¹ and thereafter it was established that they are stabilized in general in any system of classical particles interacting by means of soft, bounded potentials whose Fourier transform has negative parts^{1,3}. The interaction can be purely repulsive, leading thereby to the counterintuitive result of clustering in the absence of attractions^{5,15}. This is a physical mechanism distinct to the one that leads to cluster formation in colloidal systems with diverging interactions combined with a strong, short-range attraction and a weak, long-range repulsion^{16–19}. The clustering criterion has since then been generalized also to interactions featuring a hard core²⁰, and clustering phenomena have been experimentally observed in quasi-two-dimensional systems of core-softened magnetic colloids²¹, whereas similar phenomenology has been observed in simulations of cell colonies²². Concrete suggestions for realizing cluster-forming building blocks in the soft matter have been made in computer simulation models on the basis of effective potentials²³, and for concentrated solutions in full, monomer-resolved simulations^{6,24,25}.

Soft matter cluster crystals bear striking analogies with the supersolid state of matter in the quantum regime^{8–10}. Scientific breakthroughs in atomic physics have made it possible to create artificial interatomic potentials by exploiting collective matter-light interactions in cavities^{26,27} or by weakly coupling a Rydberg state to the ground state using laser light^{28–32}. Theoretical investigations have demonstrated that the resulting core-softened, repulsive interactions stabilize cluster- and supersolid phases with remarkable similarities to soft matter cluster crystals^{29,30,33–38}. There has been growing experimental evidence for the existence of (metastable) quantum cluster- or supersolids in the last few years^{39–41} but no experimental realization of the soft matter cluster crystals has been reported thus far. Here, we show theory-informed, suitably designed DNA-based dendritic triblock are appropriate soft-matter building blocks unambiguously leading to the formation of stable cluster crystals whose properties conform to earlier theoretical predictions.

Results and discussion

Building blocks design. We synthesized and studied the self-assembly of DNA-based dendritic-linear-dendritic triblock. Neutral bifunctional Poly(2-oxazoline)-based copolymers (Poxa) chains that possess lower critical solution temperature behavior ($T_{\text{LCST}} \cong 33^\circ\text{C}$ in 150 mM NaCl aqueous salt solutions) were

end-capped with all-DNA charged stiff dendrons^{42,43} of first and second generation (Fig. 1). Poxa is a thermoresponsive polymer that exhibits a reversible and sharp coil-to-globule phase transition in water by increasing the temperature above the T_{LCST} ⁴⁴. The conformational change of the individual Poxa chains is accompanied by partial dehydration, suggesting that Poxa alters hydrophilicity and hydrophobicity abruptly in the vicinity of T_{LCST} (see measurements of the cloud point of Poxa in Supplementary Method 3). The dendrons' free-ends were terminated by a non-sticky single-stranded DNA (ssDNA) dangling tail in order to ensure that possible intermolecular base-stacking interaction between blunt-ended DNA helices is prohibited⁴⁵. We refer to the DNA-based triblock build up from first and second-generation dendrons as the G1-P-G1 (Fig. 1a) and G2-P-G2 (Fig. 1b), respectively. Non-denaturing gel electrophoresis was employed to confirm the successful assembly of the DNA-polymer architectures which are schematically depicted in Fig. 1a–c (see Fig. 1d). The gyration radii R_g are 6.4 nm and 9.8 nm for G1-P-G1 and G2-P-G2, respectively. More details regarding the synthesis and the molecular characterization are given in the Methods, Supplementary Methods 1–3, and Supplementary Note 1.

Our choice of the experimental building blocks is guided by computer-based design ideas for dendritic-type molecules whose effective interactions satisfy the prerequisites for cluster crystal formation^{6,23,25}. The (electrostatically) repulsive dendrimer coronae give rise to a repulsive interaction, which increases as the separation between the dendrimers' centers of mass diminishes. This trend is tempered by the effective mutual attraction between the thermosensitive polymers in the core of the molecule. In this way, a core-softened repulsion results^{6,23,25}. Due to the decreasing solubility of bare Poxa at higher temperatures, we expect that the propensity to cluster formation will become stronger as the temperature increases²³. Similarly, since the electrostatic repulsion between the terminal DNA-dendrons is enhanced at higher generations, the clustering ability of the G2-P-G2 blocks is anticipated to be weaker than that of their G1-P-G1 counterparts. The key structural features of the proposed dendritic-like building blocks are their open structure and the chemical dissimilarity between the flexible Poxa chains

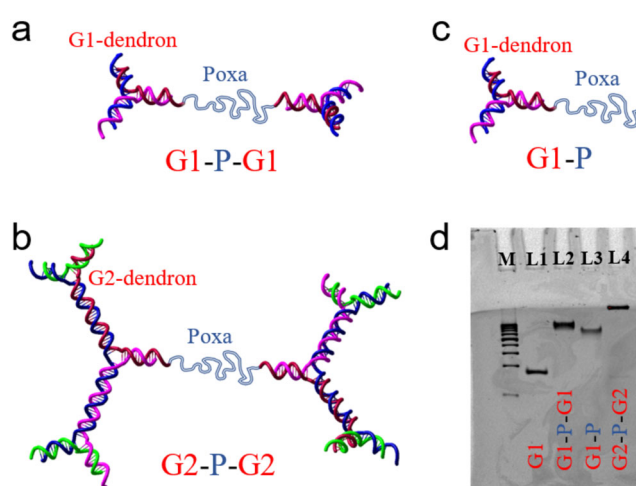


Fig. 1 Schematics and characterization of the tethered all-DNA dendrons.

a First generation of dendritic-linear-dendritic triblock (G1-P-G1). **b** Second generation of dendritic-linear-dendritic triblock (G2-P-G2). **c** First generation of dendritic-linear diblock (G1-P). **d** Non-denaturing polyacrylamide gel electrophoresis (PAGE) analysis. 10% PAGE: Lane M contains 50 base-pair (bp) DNA markers. Lanes 1–4 contain G1, G1-P-G1, G1-P, and G2-P-G2, respectively.

and the stiff all-DNA dendrons. By linking together two stiff and highly charged dendritic blocks (all-DNA dendrons) through a long and flexible polymer chain (Poxa), in combination with the microphase separation mechanism driven by the immiscibility between the DNA and polymeric blocks⁴⁶, we allow the centers of masses of different DNA-based constructs to coincide, without significant interpenetration of the dendrons. We shall demonstrate that the degree of segregation between all-DNA dendron and Poxa blocks can be temperature-controlled within the weak limit⁴⁷, owing to Poxa's LCST and triblock's macromolecular architecture. The beneficial effect of this is reflected by the emergence of stimuli-responsive cluster crystals by altering the temperature, leading to intriguing phase transition pathways. All experiments were carried out in 1xTris/Na buffer (10 mM Tris, pH: 8.0, 150 mM NaCl).

Absence of a micellization mechanism in DNA dendritic-based triblock. The tendency of particles to form stable clusters in the absence of attractions is a phenomenon clearly distinct from micellization, which is common for block copolymers in selective solvents^{48–50}, polymeric amphiphiles^{51–57}, and small molecule amphiphile surfactant systems⁵⁸. A conventional block-copolymer amphiphilie, a system most relevant to our DNA dendritic-based triblock, is commonly composed of a hydrophilic and a hydrophobic segment that are covalently linked. The hydrophobic part can be a synthetic polymeric block^{51,52,54,59} or different types of moieties (such as long-carbon alkyl chains, lipid molecule and fluorescent dyes)^{53,55,57}. These amphiphiles can be assembled into micelles (aggregates) with rich morphological and size diversity at room temperature at low critical micelle concentration (*cmc*); with the latter obtained at extremely low concentrations, and in particular many orders of magnitude below the overlap concentration (c^*) of amphiphiles in solution. In addition, temperature-dependent hydrophobic blocks, similar to the Poxa employed in this study, can result in a thermoresponsive *cmc*, allowing micelle assembly and disassembly upon a change in temperature. This means that the segregation strength between the blocks forming this type of polymeric amphiphiles can be externally controlled, allowing access from the weak- to strong-segregation regime⁴⁷.

However, the segregation strength of the above-mentioned system and consequent its *cmc* behavior is strongly dependent on the position of the thermoresponsive block relative to the hydrophilic block in the block-copolymer amphiphilie. By comparing the dilute self-assembly behavior of the dendritic-based triblock (G1-P-G1) and diblock (G1-P), we show that the encapsulation of the Poxa block in an effective shell of two all-DNA dendrons results in the absence of micellar aggregates at temperatures well above the T_{LCST} of Poxa. Static light scattering (SLS) and dynamic light scattering (DLS) measurements were employed to determine the presence and hydrodynamic radius (R_H) of aggregates. Figure 2 presents the temperature-dependent self-assembly behavior of the G1-P-G1 and its linear-dendritic analog (G1-P, Fig. 1c) in dilute aqueous solutions at a NaCl concentration of 150 mM containing buffer (Methods and Supplementary Note 1). For the G1-P system (red-symbols in Fig. 2), the temperature dependence of R_H and the SLS intensity I (at fixed scattering angle $\theta = 90^\circ$, $q = 0.0187 \text{ nm}^{-1}$) indicate the formation of large aggregates with a narrow distribution in size at a temperature slightly above the Poxa's T_{LCST} ($R_H = 175.3 \text{ nm}$, see Supplementary Fig. 1a). Such a molecular aggregation is clearly absent in the case of G1-P-G1, as illustrated in Fig. 2 (black-symbols); with the scattering intensity and hydrodynamic radius to be virtually unaffected within the range of 15 °C to 50 °C (see also DLS data for the G2-P-G2 at temperature well-above the

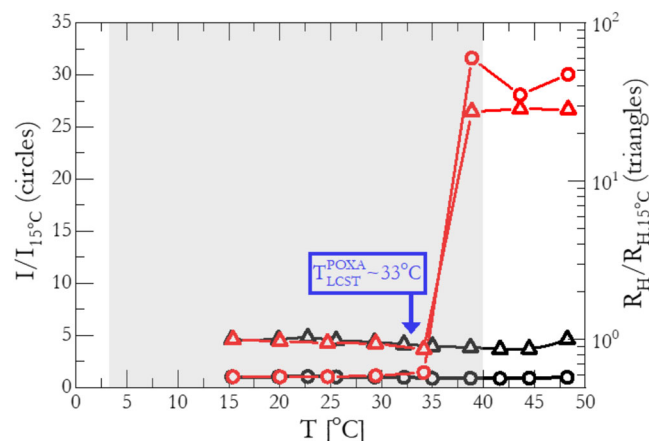


Fig. 2 Dilute solution properties of G1-P-G1 and G1-P. Temperature-dependent static light scattering (SLS) intensity (left-axis, circles) at a scattering angle of $\theta = 90^\circ$, and hydrodynamic radius (R_H , right-axis, triangles), normalized with respect to their values at $T = 15^\circ\text{C}$, of dilute G1-P-G1 (black curves) and G1-P (red curves) aqueous solutions (with DNA concentration c equal to 5.0 mg/ml and 3.0 mg/ml, respectively) using 1xTris/Na buffer (10 mM Tris-HCl, pH: 8.0, 150 mM NaCl). The gray-zone indicates the temperature window where the concentrated G1-P-G1 and G2-P-G2 self-assembled phase behavior is investigated.

T_{LCST} in Supplementary Fig. 1a). In full agreement with the LS data, the G1-P-G1 and G2-P-G2 form-factors, as probed by small-angle X-ray scattering (SAXS) experiments reveal that their global size (radius of gyration, R_g) and internal structure is temperature-insensitive (see Supplementary Fig. 1b, c). The R_g and R_H values of the G1-P-G1 and G2-P-G2 systems are listed in the Methods, (“System parameters” section).

From the above results, it becomes evident that the temperature-dependent solvophobicity of the Poxa-block does not act as an effective short-range attraction in the interaction potential of our DNA-based triblock that could initiate their aggregation into stable clusters. The lack of a critical concentration and/or temperature for the G1-P-G1 and G2-P-G2 micellization is intimately related to the absence of enthalpically driven aggregation processes. However, the change of temperature allows the external steering of the microphase separation between the two chemically incompatible blocks forming the proposed DNA dendritic-based triblock, but only within the weak-segregation limit. We shall demonstrate that this property will emerge as a key factor for the rich phase behavior of G1-P-G1 and G2-P-G2 which is encountered at DNA concentrations above their overlap values c^* (see methods, “system parameters” section).

In the present case, the building blocks have a repulsive effective interaction with one another and the formation of clusters occurs at concentrations close to their overlap value, in agreement with theoretical predictions¹¹. The normal liquid thus crosses over gradually to a cluster liquid^{15,24} as the overlap density is approached, and at even higher concentrations the cluster fluid undergoes a first-order phase transition to the cluster crystal^{2,3}. This self-assembly pathway is sketched in Fig. 3a–c by depicting representative simulation snapshots from the model of Ref. 2. Together, in Fig. 3d–f, the corresponding concentration-dependent cluster-forming scenario for the G1-P-G1 system is depicted.

Phase diagrams of cluster-forming dendrimers. SAXS measurements served as the basis for determining the phase behavior of the dendritic-like constructs presented in Fig. 1a–b. A

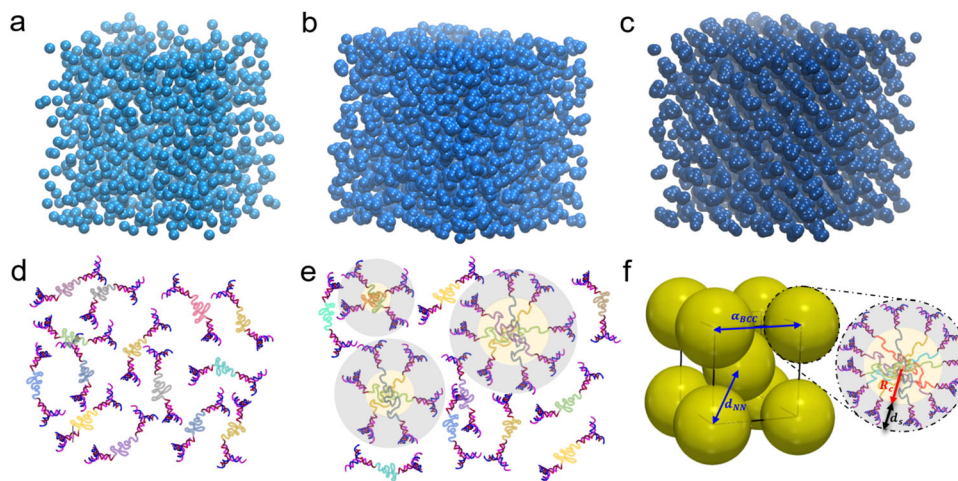


Fig. 3 Simulation snapshots and schematic representations of cluster-forming particles at different concentrations. Top panel: the snapshots were produced by performing Monte Carlo simulations of point particles interacting by the model, cluster-forming potential $v(r) = \varepsilon \exp[-(r/\sigma)^4]$ at temperature $k_B T/\varepsilon = 0.6$, and densities $\rho\sigma^3$ as follows: **a** $\rho\sigma^3 = 1.0$, where a normal fluid is stable; **b** $\rho\sigma^3 = 3.8$, where a cluster fluid forms; **c** $\rho\sigma^3 = 4.1$, resulting into a cluster body-centered cubic (BCC) crystal. Each sphere represents a single building block. Bottom panel: schematic representation of the proposed concentration-dependent mechanism for the G1-P-G1 clustering in the absence of attractions, and, finally, the G1-P-G1 clusters crystallization into a BCC cluster crystal structure: **d** G1-P-G1 fluid; **e** polydisperse G1-P-G1 clusters with a core-shell architecture, in coexistence with non-aggregated species; **f** BCC crystal formed by monodisperse G1-P-G1 clusters. The characteristic lengths are also illustrated (R_c : cluster core radius; d_s : cluster shell thickness; a_{BCC} : BCC lattice constant; d_{NN} : the nearest neighbor distance along with the room diagonal). Different colors for the Poxa block are added to assist in identifying individual G1-P-G1 molecules.

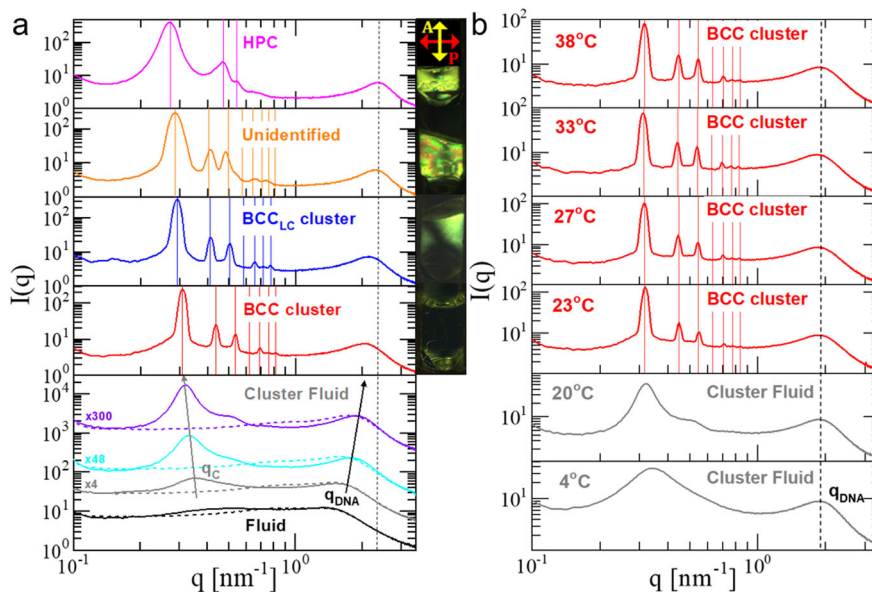


Fig. 4 Self-assembly of G1-P-G1. **a** 1D-SAXS profiles at 20 °C for the G1-P-G1, with DNA concentrations from the bottom to the top panel (solid-lines): 156.5 (black), 188.2 (gray), 216.9 (cyan), 255.7 (violet), 287.7 (red), 322.9 (blue), 337.7 (orange) and 356.2 (magenta) mg/ml. The corresponding image of the sample between cross-polarizers is also illustrated for selected concentrations at the right side of the panels. In the bottom panel, the 1D-SAXS profiles for the G1 system (dashed-lines) are included, at the same total DNA concentration as for the G1-P-G1. Also, selected profiles are shifted along the intensity axis for clarity. The intensity shift factors are presented on the left side of the profiles. In the second panel from the top, the expected reflections for a BCC lattice based on the position of the first intense peak in the 1D-SAXS profile are shown. **b** Temperature-dependent SAXS profiles of the G1-P-G1 at concentration $c = 255.7$ mg/ml. For each 1D-SAXS profile, the corresponding type of phase behavior is indicated (BCC: Body-Centered Cubic with $Im\bar{3}m$ space group symmetry, BCC_{LC} cluster: Liquid Crystalline BCC-like cluster crystal, HPC ($P6/mm$): Hexagonally Packed Cylinders with $P6/mm$ space group symmetry). The vertical solid-lines indicate the positions of the first seven possible reflections for the stated morphologies. The most right black dashed-line is guide for the temperature- and concentration-dependence of the q_{DNA} -peak.

representative series of one-dimensional (1D)-SAXS patterns at 20 °C, a temperature well below the Poxa's LCST, is shown in Fig. 4a for various concentrations of aqueous solutions of G1-P-G1 containing 150 mM NaCl. By increasing the DNA concentration, a rich phase transition pathway from disordered to

various ordered phases is observed. Over the concentration range $156.5 \text{ mg/ml} \leq c \leq 255.7 \text{ mg/ml}$ (bottom panel of Fig. 4a), the SAXS patterns indicate that the G1-P-G1 solution undergoes gradually a transition from a usual fluid to a disordered state of clusters with strong positional correlations between the dendritic-

based building blocks. The latter is evidenced by the presence of a pronounced peak with the maximum of the scattered intensity located around the scattering wave vector value $q_c \cong 0.33 \text{ nm}^{-1}$, which corresponds to a spatial correlation value $d_c = 2\pi/q_c \cong 19.0 \text{ nm}$ and represents the average inter-cluster separation. The prediction from simulation^{24,25} is $d_c \cong 3R_g$; using the value $R_g = 6.4 \text{ nm}$ for the G1-P-G1 blocks at hand (Methods and Supplementary Note 1), we obtain $d_c = 19.2 \text{ nm}$, in excellent agreement with the experiment. The SAXS profile in the fluid phase (Fig. 4a, bottom panel, black solid-line, $c = 156.5 \text{ mg/ml}$) displays a weak and broad Bragg reflection at $q > 1.0 \text{ nm}^{-1}$. The position of this correlation peak, q_{DNA} , is related to the average distance between neighboring DNA helices^{60,61}. Above the fluid phase, at DNA concentration $c = 188.2 \text{ mg/ml}$ (Fig. 4a, bottom panel, gray solid-line), the SAXS pattern shows the existence of an additional broad peak q_c , which becomes progressively more intense and narrow with increasing G1-P-G1 concentration (Fig. 4a, bottom panel, cyan and purple solid-lines); simultaneously the peak moves to noticeable lower q -values.

These observations evidence the presence of stable clusters consisting of finite aggregates of G1-P-G1 molecules, as their concentration approaches its overlap value, $c^* \cong 196.0 \text{ mg/ml}$ (see Methods, “System parameters” section). The existence of such a cluster fluid phase is further corroborated by the SAXS patterns obtained from the G1 system, at the same total DNA concentrations as for the G1-P-G1 system (Fig. 4a bottom panel, dashed-line profiles), which reveal the absence of such cluster-induced interference peak. This allows us to assign the q_c peak to cluster-cluster correlations mediated by electrostatic interactions between the charged clusters, whereas the q_{DNA} -peak, contrary to the fluid phase, corresponds to positional correlations of the DNA segments within a single cluster. Such a peak interpretation can offer a plausible explanation for the opposite concentration dependence of the q_{DNA} - and q_c -peak shifts within the cluster fluid regime (bottom panel, black and gray arrows, Fig. 4a). The very open structure of our dendritic-based macromolecules allows the centers of masses of different G1-P-G1 to lie on top of each other, thus forming spherical aggregates with a core-shell architecture, with the DNA dendrons (G1) located within the shell region (see Fig. 3e). On increasing the DNA concentration, clusters with such an internal structure can progressively grow by further aggregation, however, with a slight change in their overall size avoiding significant overlapping of the charged dendrons. The above intra-cluster packing scenario implies a simultaneous increase of the cluster’s shell DNA density and charge. Both effects are reflected in the q_c - and q_{DNA} -peak shifts with increasing concentration (see arrows at the bottom panel of Fig. 4a), respectively. The stability of the cluster fluid phase is in agreement with theoretical predictions^{2,15,24}.

At the vicinity of the G1-P-G1’s overlap density, the above clustering-forming mechanism is spontaneously triggered to counter high levels of packing frustration owing to excluded-volume constraints at the molecular level^{6,25}. A complete overlap and penetration of a dendritic-linear-dendritic triblock with a few others becomes energetically preferable over partial overlaps with many neighbors as a consequence of its open-internal structure. Additionally, the entropic penalty that the Poxa chains experience as they possibly overstretch in an attempt to increase the aggregation number inside the cluster is effectively counter-balanced by the inherent tendency of the flexible Poxa and the stiff all-DNA dendrons to minimize their unfavorable contacts at the inter-cluster level, similar to classical block copolymers⁶².

The cluster fluid phase persists up to a DNA concentration of 255.7 mg/ml (Fig. 4a, violet solid-line), however, with the q_c -peak accompanied by an emerging, broad peak at slightly higher q -values. This indicates that the cluster fluid phase becomes more

structured, signaling the onset of a disorder-to-order transition by increasing the G1-P-G1 density. Indeed, strikingly different is the appearance of small-angle ($q < 1.0 \text{ nm}^{-1}$) scattering peaks for a DNA concentration of 287.7 mg/ml , as can be seen from the second panel from the bottom in Fig. 4a. An intense and sharp principal peak, at a scattering wave vector value $q^* \cong 0.31 \text{ nm}^{-1}$, slightly below the q_c -peak, and several higher-order reflections appear, offering an unambiguous determination of the lattice structure and lattice constant based solely on the location of these Bragg peaks. The finding $q^* \lesssim q_c$ is consistent with the predictions from simulations^{2,6,25} that upon ordering on a crystalline arrangement, the clusters become less polydisperse and more compact, thereby slightly increasing their inter-cluster separation. The corresponding SAXS profile displays six distinguishable peaks centered at $q/q^* = 1 : \sqrt{2} : \sqrt{3} : \sqrt{5} : \sqrt{6} : \sqrt{7}$ (vertical red lines), providing conclusive evidence that the G1-P-G1 clusters have self-assembled into a body-centered cubic (BCC) crystal (space-group $Im\bar{3}m$) with significant long-range order and a conventional unit cell of size $a_{\text{BCC}} = \sqrt{2}(2\pi/q^*) = 28.7 \text{ nm}$ (see lattice topology in the right cartoon of the bottom panel in Fig. 3c). The faint presence of the fourth reflection at $q/q^* = \sqrt{4}$ is due to the minimum in the cluster’s form-factor (blue curve in Supplementary Fig. 2a and discussion in Supplementary Notes 2.2–2.3). The reported cubic phase is also attested by the absence of optical birefringence, as clearly illustrated in the corresponding depolarized image of Fig. 4a (second panel from the bottom, right image). Upon further compression ($c = 322.9 \text{ mg/ml}$, third panel from the bottom in Fig. 4a), the 1D-SAXS profile shows that all the reflections are preserved and shifted to lower q -values. The blue vertical lines above the intensity profile indicate the locations of Bragg peaks with a BCC lattice constant of 30.7 nm . However, surprisingly, the corresponding depolarized image of the sample reveals a counter-intuitive uniform birefringence (Fig. 4a liquid crystalline BCC-like, BCC_{LC}), since one would expect that a cubic phase will be optically isotropic.

Ultimately, increasing the G1-P-G1 concentration leads to a number of significant changes in the scattering and birefringence patterns. At DNA concentration $c = 337.7 \text{ mg/ml}$, the sample under crossed polarizers shows a vivid colorful birefringence, with the principal q^* -peak becoming noticeably wider; it also shifts to lower q -values (second panel from the top, Fig. 4a). In contrast, the shape of the higher order reflections is distorted, with their positions being concentration-independent. The above observations, in combination with the clear disagreement between the observed peaks and the allowed reflections (orange vertical lines) for a BCC crystal based on the primary and most intense reflection at q^* , are indicative for a mechanically unstable crystal phase. Eventually, upon further increase of the DNA concentration to $c = 356.2 \text{ mg/ml}$, (top panel of Fig. 4a), the G1-P-G1 solution undergoes a structural phase transition to a hexagonal packed cylinders morphology (HPC with P6/mm space-group symmetry), as evidenced by the three clear reflections at ratios $q/q^* = 1 : \sqrt{3} : \sqrt{4}$ (magenta vertical lines). From the primary peak, the inter-column distance $d_{\text{HPC}} = 4\pi/(\sqrt{3}q^*)$ is calculated to be 26.8 nm .

The spontaneous cluster crystallization is clearly demonstrated by the temperature-dependent 1D-SAXS profiles of the G1-P-G1 at DNA concentration $c = 255.7 \text{ mg/ml}$, which are presented in Fig. 4b. By increasing the temperature, a phase transition from (cluster) fluid to BCC crystal with $a_{\text{BCC}} = 28.2 \text{ nm}$ is observed, similar to the concentration-dependent manner presented in the two bottom panels of Fig. 4a (a more detailed discussion regarding the SAXS profiles of Fig. 4b is presented in Supplementary Note 3). It is particularly important to emphasize

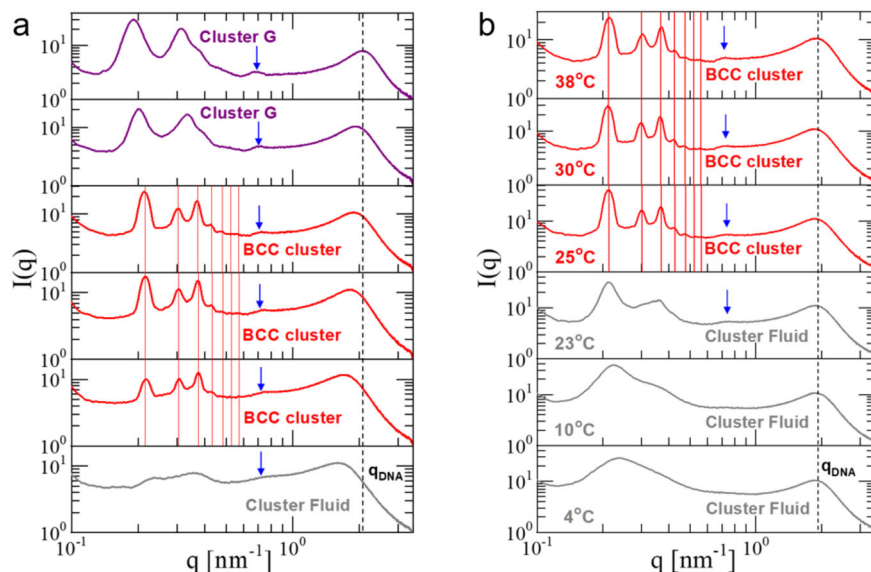


Fig. 5 Self-assembly of G2-P-G2. **a** 1D-SAXS profiles at 38 °C for the G2-P-G2, with DNA concentrations from the bottom to the top panel: 177.2 mg/ml (gray); 190.8, 204.7, 220.5 mg/ml (red); 234.08, 250.6 mg/ml (purple). **b** Temperature-dependent SAXS profiles of the G2-P-G2 at a concentration $c = 220.5$ mg/ml. The blue arrows denote the presence of the cluster form-factor feature in the corresponding 1D-SAXS profiles (see also Supplementary Fig. 2). For each 1D-SAXS profile, the corresponding type of phase behavior is indicated (BCC: body-centered cubic with $Im\bar{3}m$ space group symmetry and Cluster G: Non-birefringent Glass-like). The vertical solid-lines indicate the positions of the first seven possible reflections for the stated morphologies. The most right black dashed-line is guide for the temperature- and concentration-dependence of the q_{DNA} -peak.

that this fluid-to-crystal transition occurs within a narrow temperature range (between 20 and 23 °C) which is noticeably lower than the LCST of Poxa. Interestingly, heating the sample up to 38 °C, a temperature well above the LCST of Poxa, produces identical scattering patterns compare to those at 23 °C. The latter is in accordance with the temperature-independent behavior of G1-P-G1 in dilute conditions. Therefore, the results in Fig. 4b undoubtedly supports our claim for the absence of a micellization mechanism in the reported DNA-based dendritic building blocks.

The influence of dendron generation on the clustering ability of these DNA-based dendritic-linear-dendritic triblock and their subsequent self-assembly to cluster crystals is demonstrated in Fig. 5, where the concentration- and temperature-dependent phase behavior of G2-P-G2 (Fig. 1b) are presented. Both encompass the same type of cluster fluid-to-crystal transition, with the increase of dendron size to be consistently reflected in the measured BCC lattice constant, $a_{\text{BCC}} = 42.0$ nm at DNA concentration $c = 220.5$ mg/ml (fourth panel from the bottom of Fig. 5a and, at for temperatures above 23 °C, Fig. 5b). Also, the BCC crystal shows temperature- and concentration-independent lattice constants, as witnessed by the Bragg peaks positions over a relatively broad range of DNA densities (190.8 $\leq c \leq 220.5$ mg/ml at $T = 38$ °C, Fig. 5a) and temperatures (25 °C $\leq T \leq 38$ °C at $c = 220.5$ mg/ml, Fig. 5b). However, contrary to the G1-P-G1 where the concentration increase revealed a rich phase transition pathway from cluster fluid to various crystalline phases, the G2-P-G2 BCC cluster crystal becomes unstable at high DNA densities, leading to a disordered solid. This is illustrated in the scattering profiles of the two top panels of Fig. 5a, both of which demonstrate that the sharp principal peak and higher orders reflections are replaced by two broad peaks which systematically move toward lower q -values with increasing concentration. These intensity profiles demonstrate an intriguing similarity with the one obtained from the cluster fluid phase (Fig. 5b, $T = 23$ °C), suggesting that the observed disordered phases are reminiscent of cluster glass-like structures (Cluster G). These findings are in agreement with simulation results based on monomer-resolved

models^{6,25}. Indeed, in contrast to simplified models based on pairwise additive effective interactions³, for real dendrimers the cluster population cannot grow indefinitely with concentration and thus the clean theoretical prediction $N_{\text{occ}} \propto c$ eventually breaks down at some system-specific crossover concentration c_x . For values $c \gtrsim c_x$, distortions of the lattice constants, anisotropic phases and even glassy behavior have also been seen in simulations of such systems^{6,25}. Interestingly, the cluster-forming SAXS signature can be easily detected in the 1D-SAXS profiles of Fig. 5a as indicated by the blue arrows, suggesting that clusters persist over the concentration-dependent phase transition pathway from cluster fluid to cluster BCC crystal and finally to a disordered solid. Finally, it is important to underline that the disorder-to-order cluster transition is fully reversible with temperature (Supplementary Fig. 3), and therefore it reflects thermodynamic equilibrium morphologies.

Further analysis of the 1D-SAXS profiles corresponding to the G1-P-G1 (Supplementary Fig. 2a) and G2-P-G2 (Supplementary Fig. 2b) BCC cluster crystals show that the global cluster size of the G1-P-G1 and G2-P-G2 is noticeably larger than the radius of gyration of a single particle, implying the formation of clusters with moderate occupancy (details on the fitting procedure of 1-D SAXS profiles are given in Supplementary Notes 2.1–2.2). A schematic of the cluster model is depicted in Fig. 3c (bottom panel, right cartoon). Indeed, from the total DNA concentration and BCC lattice constant, absolute values of an average cluster occupancy number N_{occ} can be estimated (see Methods, “System parameters” section), leading to $N_{\text{occ}} = 29$ for both G1-P-G1 and G2-P-G2. In addition, the fitting values for the nearest neighbor distance d_{NN} along the body diagonal of the formed BCC crystals (left cartoon in Fig. 4f) indicate that the dendritic-based cluster crystals almost reach the close-packed configuration (see table for the fitting parameters in Supplementary Note 2.1 and relevant analysis in the Supplementary Note 2.2). The lattice constants correspond to a ratio $a_{\text{BCC}}/R_g \cong 4.3$ (27.9 nm/6.4 nm and 42.0 nm/9.8 nm for G1-P-G1 and the G2-P-G2, respectively), in excellent agreement with simulations of generic similar models²⁵,

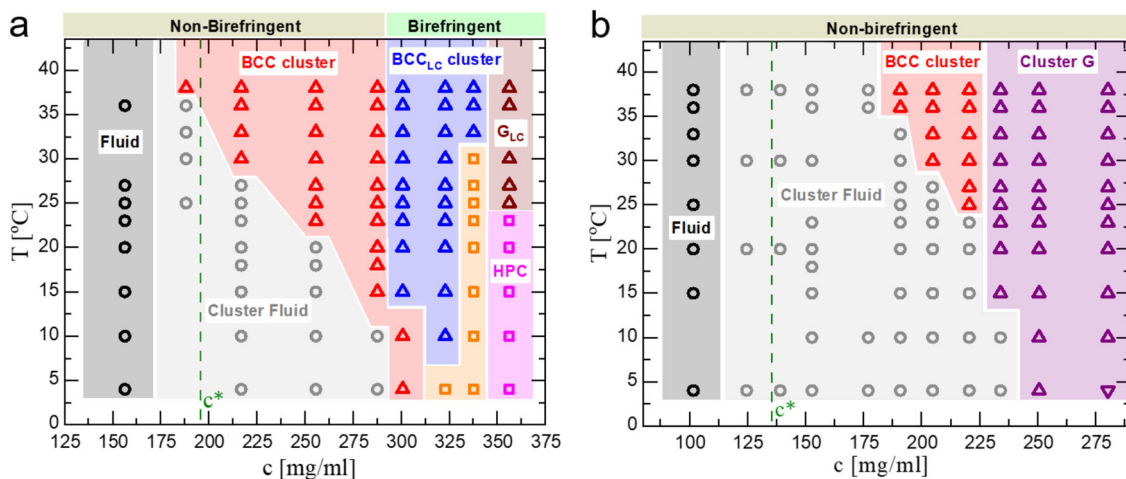


Fig. 6 Phase diagrams of G1-P-G1 and G2-P-G2. A concentration-temperature phase diagram of aqueous solutions of G1-P-G1 (a) and G2-P-G2 (b). The following phases are indicated: Fluid (black circles), cluster fluid (gray circles), BCC cluster crystal (red triangles), liquid crystalline BCC-like cluster crystal (BCC_{LC} cluster, blue triangles), liquid crystalline glass-like (G_{LC}, brown triangles), non-birefringent glass-like (Cluster G, purple triangles) and hexagonal packed cylinder (HPC, magenta squares). The corresponding background colors are added to assist in identifying the various phases. The structural assignment of the orange region in the G1-P-G1 phase diagram based solely on the SAXS data was not possible. The green-dashed lines indicate the DNA overlap concentration c^* of G1-P-G1 and G2-P-G2 (see Methods, “System parameters” section).

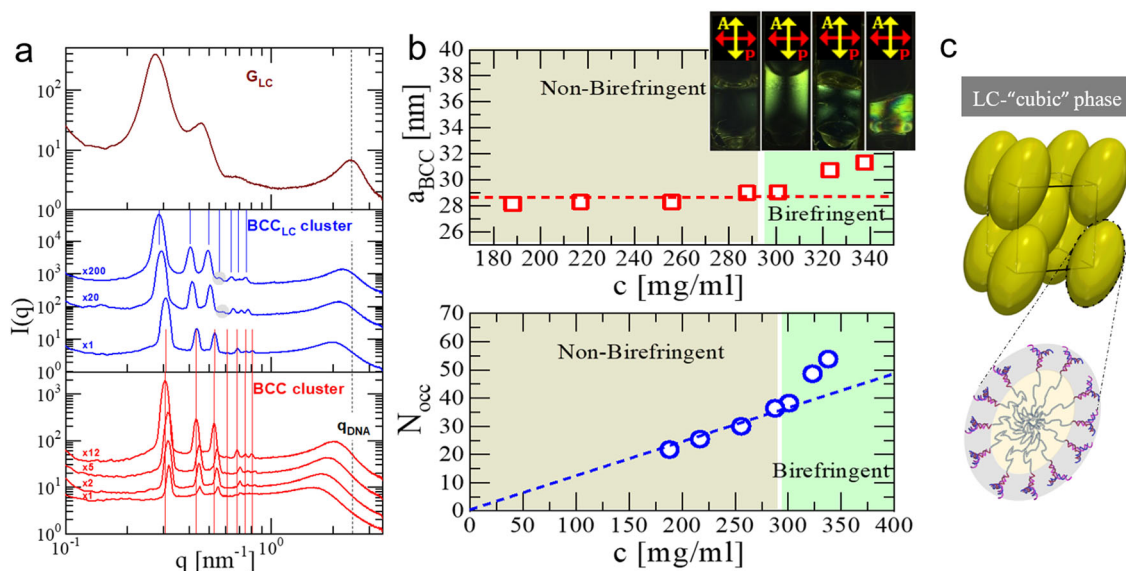


Fig. 7 Cluster phases and extracted lattice parameters at various concentrations. **a** 1D-SAXS profiles at 38 °C for the G1-P-G1, with DNA concentrations from the bottom to the top panel: 188.2, 216.9, 255.7, 287.7 (red profiles), 300.8, 322.9, 337.7 (blue profiles) and 356.2 (brown profile) mg/ml. The vertical solid-lines indicate the positions of the first seven allowed reflections for a BCC crystal. In the middle panel, the gray circles indicate the appearance of the fourth diffraction peak. The black dashed-line is guide for the concentration-dependence of the q_{DNA} peak. The profiles presented in the bottom and middle panels are shifted along the intensity axis for clarity. The intensity shift factors are presented on the left side of the profiles. **b** The BCC lattice constant a_{BCC} (top panel) and the cluster occupancy N_{occ} (bottom panel) against G1-P-G1 concentration at 38 °C. The dashed lines are guides for the concentration-dependence of a_{BCC} (red-line) and N_{occ} (blue-line) within the non-birefringent regime. Top panel inset: Depolarized images of selected G1-P-G1 samples at 38 °C. DNA concentration from the left to the right: 287.7, 300.8, 322.9 and 337.7 mg/ml. **c** Schematic of the proposed arrangement and deformation of the G1-P-G1 clusters within the optically anisotropic BCC-like phase (Liquid Crystalline (LC)-“cubic” phase).

in which the ratio $a_{BCC}/R_g \cong 4.1$ was found for broad density ranges.

The phase diagrams of G1-P-G1 and G2-P-G2 as a function of the temperature and the total DNA concentration are presented in Fig. 6. A combination of the above-mentioned SAXS measurements and depolarized images of the samples allow us to identify most of the formed phases. Both systems, at sufficiently high densities, form stable clusters in the fluid phase, which upon further compression self-organize into cluster BCC

crystals in a temperature-dependent manner. The independence of the peak positions on concentration, the bottom panel of Fig. 7a, points to the density-independent lattice constant, top panel of Fig. 7b. In contrast to the G1-P-G1 case, the phase diagram of G2-P-G2 displays one type of crystal phase (BCC cluster) with its thermodynamic stability restricted in a noticeable narrower region in the plane of temperature versus concentration (red areas in Fig. 6a-b), as previously anticipated. While G2-P-G2 exhibits only an optically isotropic glass-like (Cluster G, purple

area in Fig. 6b and SAXS profiles in Fig. 5a) behavior at higher DNA densities, the G1-P-G1 demonstrates a rich structural polymorphism involving birefringent crystals and birefringent glass-like phases (G_{LC} , brown region in Fig. 6a, and SAXS profile in the top panel of Fig. 7a). This is not surprising given the increased dendron size which is employed for the fabrication of the G2-P-G2 triblock. Although the underlying physical mechanism that drives the emergence of clustering is identical for G1-P-G1 and G2-P-G2, the latter encounters higher levels of dendron packing frustration since the length of the polymeric tether (Poxa chain) has remained unchanged. The correct length of the Poxa chain can lead to not only a widening of the region where the BCC cluster crystal is stable but also allow liquid crystalline morphologies (BCC_{LC} and HPC in Fig. 6a) to become stable. Therefore, the G2-P-G2 phase diagram highlights the key role of the open architecture of the building blocks for the stabilization of cluster crystals with an intriguing structural diversity.

In the phase diagram of G1-P-G1 (Fig. 6a), a stable phase (blue region), which retains the diffraction features of a BCC structure and shows unexpected optical anisotropy (BCC_{LC}), is observed at DNA densities above the ones where the cluster BCC crystal phase (red region) occurs. This birefringent phase is stable over a remarkable wide range of concentrations and temperatures. In addition, the phase transition from BCC-to- BCC_{LC} can also be reversibly driven through the alteration of temperature (at DNA concentration $c = 300.8$ mg/ml in Fig. 6a, see also Supplementary Fig. 4), in accordance with the thermodynamic stability of this phase. The concentration-dependent series of SAXS profiles acquired at 38 °C (Fig. 7a), together with the corresponding depolarized images of the samples (top panel inset of Fig. 7b) offer a qualitative insight into the possible molecular origin of the BCC_{LC} and its clustering character (a more detailed discussion is presented in Supplementary Note 4). A molecular packing scenario for the BCC_{LC} phase based on orientationally ordered ellipsoidal-like clusters occupying the sites of the BCC lattice is schematically shown in Fig. 7c.

Taken together, our work on self-assembly of purely repulsive all-DNA dendritic-based triblock unambiguously demonstrate the experimental realization of the long-anticipated equilibrium cluster crystal structure at high densities. The experimental discovery of this unconventional crystalline state of matter is based on five pillars which constitute the key and unique identifying properties of cluster crystals, namely: the absence of micellar aggregates in dilute conditions; the emergence of clusters in the fluid phase at $c \lesssim c^*$; the stability of the clusters in the absence of attractions; the crystallization of the cluster fluid into a cluster crystal; and finally the crystal's remarkable adaptability in crowded conditions, as reflected by the density-independent lattice constants (top panel of Fig. 7b) and the scaling $N_{occ} \propto c$ (bottom panel of Fig. 7b), that holds over a broad concentration range. The latter is the most prominent hallmarks of cluster crystals predicted by theory^{1–4} and hereby experimentally confirmed.

An intriguing aspect of this study is that the building block design, reliant on the block copolymer paradigm, confers our DNA-based triblock with temperature-responsiveness, resulting to cluster crystal structures with unexpected optical anisotropy and self-assembly transition pathways that can readily be controlled by altering the temperature. This confluence of self-assembly approaches from block copolymers⁶² and DNA nanotechnology⁶³ has already been shown to be capable of furnishing temperature-regulated nanoscale structures with high levels of self-assembled structural complexity⁴⁶. Given its versatile and robust character, the synthetic scheme reported here can easily be applied to any kind of all-DNA nanoscale architecture. We foresee that the present developments in the design and

construction of DNA nanostructures with arbitrary complexity in the research field of structural DNA nanotechnology can provide unprecedented freedom in cluster crystal engineering through careful design of the tethered all-DNA geometry, and therefore opens up the possibility of steering the macroscopic properties of the system in a predictive manner.

Methods

Synthesis of DNA-polymer hybrids. Custom, phosphorylated and dibenzylcyclooctyne (DBCO)-modified oligonucleotides were purchased from Biomers and purified by HPLC. The DNA sequences used for the fabrication of all-DNA dendrons of first (G1) and second (G2) generation were adapted from previous work with a slight modification in order to suppress the base-stacking attraction between the dendrons' blunt-ends⁴³. To assemble the reported DNA-based dendritic nanostructures, a strain-promoted alkyne-azide cycloaddition (SPAAC, copper-free click chemistry) reaction was employed⁴⁶. To construct G1-P and G1-P-G1, a three-arm DNA junction (G1) having one arm terminated with a DBCO and a mono- or di-azide (N_3) end-functionalized Poly(2-oxazoline)-based copolymer Poxa were dissolved in 1xTris/Na buffer (10 mM Tris-HCl, pH 8.0, 150 mM NaCl) and homogenized, respectively. The optimal ratio of reacting compounds (DBCO/ N_3) was found to be close to 4:1. The reactions are carried out at room temperature overnight. A detailed description of the azide-functionalized Poxa polymer synthesis procedure and its characterization is provided in Supplementary Methods 2–3.

For the fabrication of G2-P-G2, a core G1-P-G1 with its free-ends terminated with a phosphorylated non-palindromic 4-base single-stranded overhang (sticky end) is employed. This tetra-functional dendritic-polymer core was hybridized with four other G1 molecules with sticky-ends complementary to the G1-P-G1 in order to finally assemble the G2-P-G2. The post-assembly ligation of the G2-P-G2 is performed by the T4 DNA ligase (Promega). The three-arm DNA junctions involved in the construction of the G1-P, G1-P-G1 and G2-P-G2 were formed by hybridizing three partially complementary to each other synthetic ssDNA strands in a 1:1:1 stoichiometric ratio in 1xTE/Na buffer (10 mM Tris-HCl, pH 7.5, 0.1 mM EDTA and 150 mM NaCl)⁴². The final concentration was 15 μ M for each strand. The DNA concentration was determined by measuring the absorbance at 260 nm with a micro-volume spectrometer (NanoDrop 2000). The oligo mixtures were cooled slowly from 90 °C to room temperature in 10 L water placed in a styrofoam box over 48 h to facilitate strand hybridization. The detailed construction scheme and sequence of DNA oligos used to assemble G1-P, G1-P-G1 and G2-P-G2 systems are listed in Supplementary Method 1. Nondenaturing polyacrylamide gel electrophoresis (PAGE) experiments were employed to confirm the successful assembly of G1, G1-P, G1-P-G1, and G2-P-G2. As shown in Fig. 1, the desired all-DNA and DNA-based dendritic constructs migrate as single sharp bands, with the dendritic-linear-dendritic triblock to demonstrate decreasing mobility with increasing generation.

System parameters. The radius of gyration (R_g) is obtained from small-angle X-ray scattering (SAXS) and hydrodynamic radius, (R_H) is obtained from DLS. The corresponding values for the G1-P-G1 and G2-P-G2 are 6.4 nm and 9.8 nm for R_g ; 4.9 nm and 7.9 nm for R_H , respectively (more details in Supplementary Note 1). The DNA overlap concentration (c^*) of the employed dendritic-linear-dendritic triblock (G1-P-G1 and G2-P-G2) was estimated using the equation $c^* = M_w / (\frac{4}{3} \pi R_H^3 N_A)$, where M_w represents the DNA molecular weight of the triblock ($M_w^{G1-P-G1} = 58.09$ KDa, $M_w^{G2-P-G2} = 170.36$ KDa), R_H the hydrodynamic radius at $T = 38$ °C, and N_A Avogadro's number. The average cluster occupancy N_{occ} is calculated using the relationship $N_{occ} = c N_A a_{BCC}^3 / (M_w f)$, where c is the total DNA concentration, a_{BCC} the edge length of the BCC conventional unit cell, and f is the number of clusters per unit cell ($f = 2$ for a BCC lattice). The molecular weight of the Poxa chains is 15.9 KDa for the G1-P-G1, G2-P-G2, and 19.6 KDa for the G1-P. The concentrated DNA solutions were prepared using 1xTris/Na buffer.

Purification of G1-P-G1 and G2-P-G2. To purify desired dendritic-linear-dendritic structures, reactions products were separated by size-exclusion chromatography (SEC) on Superdex 200 Increase 10/300 GL. The column was developed at the flow rate of 0.2 mL/min in 1xTris/Na buffer. The reaction mixture was diluted in the same buffer to the final concentration of 2.0–4.0 mg/mL and injected into the column by 0.3–0.4 mL portions per run. Two major peaks were collected and the corresponding fractions were analyzed by PAGE. The first peak corresponded to the DNA-based dendritic triblock and the second one to not react to three-arm DNA junctions. Fractions eluted from 10.0–11.0 mL were pooled together and concentrated by ultrafiltration (Amicon-Ultra 15 mL centrifugal filters). For the purification of G1-P, an anion exchange chromatography column HiPrep DEAE Fast Flow16/10 (GE Healthcare) was used⁴⁶.

Light scattering (LS) experiments. DLS and static light scattering (SLS) experiments were performed by employing an ALV goniometer setup equipped with a Helium-Neon laser operating at $\lambda = 632.8$ nm. The Brownian motion of the G1-P-

G1, G2-P-G2 and G1-P was recorded in terms of the time autocorrelation function of the polarized light scattering intensity, $G(q, t)$, employing an ALV-5000 multi-tau digital correlator. In DLS experiments, the intermediate scattering (field) function $C(q, t) = \sqrt{(G(q, t) - 1)/\beta}$ at several scattering wave vectors $q = (4\pi n/\lambda) \sin(\theta/2)$ is obtained, where β is an instrumental factor related to the spatial coherence constant and depends only on the detection optics, n the refractive index of the solvent, and θ the scattering angle. To analyze $C(q, t)$, an inverse Laplace transformation using the CONTIN algorithm was applied. The average relaxation time was determined from the peak of the distribution of relaxation times $L(\ln \tau)^{43}$ (see Supplementary Fig. 1a).

Small-angle X-ray scattering (SAXS). SAXS experiments were carried out at the high brilliance Gallium Anode Low Angle X-ray Instrument (GALAXI) of the Jülich Center for Neutron Science (JCNS, Germany)⁶⁴. A Dectris-Pilatus 1M detector with a resolution of 981×1043 pixels and a pixel size of $172 \times 172 \mu\text{m}^2$ was employed to record the 2D SAXS scattering patterns. The 2D SAXS patterns were integrated using FIT2D software. Bragg peaks indexing in 1D SAXS profiles was performed using the Scatter computer program⁶⁵. 1D SAXS profiles fitting was done using Jscatter⁶⁶ (more details on the fitting procedure are given in Supplementary Note 2). The DNA solution was thoroughly homogenized (up to 3 days for the more viscous samples) ensuring the absence of spatial concentrations gradients before loading into capillaries (2 mm thickness borosilicate, Hilgenberg) for SAXS experiments. The capillaries were sealed and stored at 4 °C for at least 1 month before being used for X-ray experiments. Long term stability and reproducibility were confirmed by repeating SAXS measurements on selected samples almost 6 months later (G1-P-G1 system, Supplementary Fig. 5).

Data availability

The relevant data sets generated during and/or analyzed during the current study are available from the corresponding authors on reasonable request.

Received: 16 April 2021; Accepted: 11 November 2021;

Published online: 09 December 2021

References

- Likos, C. N., Lang, A., Watzlawek, M. & Löwen, H. Criterion for determining clustering versus reentrant melting behavior for bounded interaction potentials. *Phys. Rev. E* **63**, 031206 (2001).
- Mladek, B. M., Gottwald, D., Kahl, G., Neumann, M. & Likos, C. N. Formation of polymorphic cluster phases for a class of models of purely repulsive soft spheres. *Phys. Rev. Lett.* **96**, 045701 (2006).
- Likos, C. N., Mladek, B. M., Gottwald, D. & Kahl, G. Why do ultrasoft repulsive particles cluster and crystallize? Analytical results from density-functional theory. *J. Chem. Phys.* **126**, 224502 (2007).
- Mladek, B. M., Charbonneau, P. & Frenkel, D. Phase coexistence of cluster crystals: beyond the Gibbs phase rule. *Phys. Rev. Lett.* **99**, 235702 (2007).
- Moreno, A. J. & Likos, C. N. Diffusion and relaxation dynamics in cluster crystals. *Phys. Rev. Lett.* **99**, 107801 (2007).
- Lenz, D. A., Blaak, R., Likos, C. N. & Mladek, B. M. Microscopically resolved simulations prove the existence of soft cluster crystals. *Phys. Rev. Lett.* **109**, 228301 (2012).
- Sciortino, F. & Zaccarelli, E. Soft heaps and clumpy crystals. *Nature* **493**, 30–31 (2013).
- Balibar, S. The enigma of supersolidity. *Nature* **464**, 176–182 (2010).
- Boninsegni, M. & Prokofev, N. V. Colloquium: Supersolids: What and where are they? *Rev. Mod. Phys.* **84**, 759–776 (2012).
- Ritsch, H., Domokos, P., Brennecke, F. & Esslinger, T. Cold atoms in cavity-generated dynamical optical potentials. *Rev. Mod. Phys.* **85**, 553–601 (2013).
- Likos, C. N., Watzlawek, M. & Löwen, H. Freezing and clustering transitions for penetrable spheres. *Phys. Rev. E* **58**, 3135–3144 (1998).
- Haering, J. M., Walz, C., Szamel, G. & Fuchs, M. Coarse-grained density and compressibility of nonideal crystals: general theory and an application to cluster crystals. *Phys. Rev. B* **92**, 184103 (2015).
- Archer, A. J., Rucklidge, A. M. & Knobloch, E. Quasicrystalline order and a crystal-liquid state in a soft-core fluid. *Phys. Rev. Lett.* **111**, 165501 (2013).
- Barkan, K., Engel, M. & Lifshitz, R. Controlled self-assembly of periodic and aperiodic cluster crystals. *Phys. Rev. Lett.* **113**, 098304 (2014).
- Mladek, B. M., Gottwald, D., Kahl, G., Neumann, M. & Likos, C. N. Clustering in the absence of attractions: density functional theory and computer simulations. *J. Phys. Chem. B* **111**, 12799–12808 (2007).
- Stradner, A. et al. Equilibrium cluster formation in concentrated protein solutions and colloids. *Nature* **432**, 492–495 (2004).
- Sciortino, F., Mossa, S., Zaccarelli, E. & Tartaglia, P. Equilibrium cluster phases and low-density arrested disordered states: the role of short-range attraction and long-range repulsion. *Phys. Rev. Lett.* **93**, 055701 (2004).
- Campbell, A., Anderson, V., van Duijneveldt, J. & Bartlett, P. Dynamical arrest in attractive colloids: the effect of long-range repulsion. *Phys. Rev. Lett.* **94**, 208301 (2005).
- Zaccarelli, E. Colloidal gels: equilibrium and non-equilibrium routes. *J. Phys.: Condens. Matter* **19**, 323101 (2007).
- Glaser, M. A. et al. Soft spheres make more mesophases. *EPL* **78**, 46004 (2007).
- Osterman, N., Babic, D., Poberaj, I., Dobnikar, J. & Ziherl, P. Observation of condensed phases of quasiplanar core-softened colloids. *Phys. Rev. Lett.* **99**, 248301 (2007).
- Smeets, B. et al. Emergent structures and dynamics of cell colonies by contact inhibition of locomotion. *Proc. Nat. Acad. Sci. U.S.A.* **113**, 14621–14626 (2016).
- Mladek, B. M., Kahl, G. & Likos, C. N. Computer assembly of cluster-forming amphiphilic dendrimers. *Phys. Rev. Lett.* **100**, 028301 (2008).
- Lenz, D. A., Mladek, B. M., Likos, C. N., Kahl, G. & Blaak, R. Monomer-resolved simulations of cluster-forming dendrimers. *J. Phys. Chem. B* **115**, 7218 (2011).
- Lenz, D. A., Mladek, B. M., Likos, C. N. & Blaak, R. Thermodynamic stability and structural properties of cluster crystals formed by amphiphilic dendrimers. *J. Chem. Phys.* **144**, 204901 (2016).
- Baumann, K., Guerlin, C., Brennecke, F. & Esslinger, T. Dicke quantum phase transition with a superfluid gas in an optical cavity. *Nature* **464**, 1301–1306 (2010).
- Léonard, J., Morales, A., Zupancic, P., Esslinger, T. & Donner, T. Supersolid formation in a quantum gas breaking a continuous translational symmetry. *Nature* **543**, 87–90 (2017).
- Henkel, N., Nath, R. & Pohl, T. Three-dimensional roton excitations and supersolid formation in rydberg-excited bose-einstein condensates. *Phys. Rev. Lett.* **104**, 195302 (2010).
- Cinti, F. et al. Supersolid droplet crystal in a dipole-blockaded gas. *Phys. Rev. Lett.* **105**, 135301 (2010).
- Pupillo, G., Micheli, A., Boninsegni, M., Lesanovsky, I. & Zoller, P. Strongly correlated gases of rydberg-dressed atoms: quantum and classical dynamics. *Phys. Rev. Lett.* **104**, 223002 (2010).
- Jau, Y.-Y., Hankin, A. M., Keating, T., Deutsch, I. H. & Biedermann, G. W. Entangling atomic spins with a Rydberg-dressed spin-flip blockade. *Nat. Phys.* **12**, 71–74 (2016).
- Zeher, J. et al. Many-body interferometry of a Rydberg-dressed spin lattice. *Nat. Phys.* **12**, 1095–1099 (2016).
- Honer, J., Weimer, H., Pfau, T. & Büchler, H. P. Collective many-body interaction in Rydberg dressed atoms. *Phys. Rev. Lett.* **105**, 160404 (2010).
- Saccani, S., Moroni, S. & Boninsegni, M. Excitation spectrum of a supersolid. *Phys. Rev. Lett.* **108**, 175301 (2012).
- Mattioli, M., Dalmonte, M., Lechner, W. & Pupillo, G. Cluster luttinger liquids of rydberg-dressed atoms in optical lattices. *Phys. Rev. Lett.* **111**, 165302 (2013).
- Cinti, F., Macri, T., Lechner, W., Pupillo, G. & Pohl, T. Defect-induced supersolidity with soft-core bosons. *Nat. Commun.* **5**, 3235 (2014).
- Angelone, A., Mezzacapo, F. & Pupillo, G. Superglass phase of interaction-blockaded gases on a triangular lattice. *Phys. Rev. Lett.* **116**, 135303 (2016).
- Masella, G., Angelone, A., Mezzacapo, F., Pupillo, G. & Prokofev, V. N. Supersolid stripe crystal from finite-range interactions on a lattice. *Phys. Rev. Lett.* **123**, 045301 (2019).
- Mottl, R. et al. Roton-type mode softening in a quantum gas with cavity-mediated long-range interactions. *Science* **336**, 1570–1573 (2012).
- Strauß, P. et al. Observation of spatially ordered structures in a two-dimensional Rydberg gas. *Nature* **491**, 87–91 (2012).
- Böttcher, F. et al. Transient supersolid properties in an array of dipolar quantum droplets. *Phys. Rev. X* **9**, 011051 (2019).
- Li, Y. et al. Controlled assembly of dendrimer-like DNA. *Nat. Mater.* **3**, 38–42 (2004).
- Jochum, C. et al. Structure and stimuli-responsiveness of all-DNA dendrimers: theory and experiment. *Nanoscale* **11**, 1604–1617 (2019).
- Park, J.-S. & Kataoka, K. Comprehensive and accurate control of thermosensitivity of poly(2-alkyl-2-oxazoline)s via well-defined gradient or random copolymerization. *Macromolecules* **40**, 3599–3609 (2007).
- Nakata, M. et al. End-to-end stacking and liquid crystal condensation of 6 to 20 base pair DNA duplexes. *Science* **318**, 1276–1279 (2007).
- Novak, S. et al. DNA self-assembly mediated by programmable soft-patchy interactions. *ACS Nano* **14**, 13524–13535 (2020).
- Matsen, M. W. & Bates, F. S. Unifying weak- and strong-segregation block copolymer theories. *Macromolecules* **29**, 1091–1098 (1996).
- McConnell, G. A., Gast, A. P., Huang, J. S. & Smith, S. D. Disorder-order transitions in soft sphere polymer micelles. *Phys. Rev. Lett.* **71**, 2102–2105 (1993).

49. Lodge, T. P. & Bang, J. Origin of the thermoreversible fcc-bcc transition in block copolymer solutions. *Phys. Rev. Lett.* **92**, 145501 (2004).
50. Hamley, I. W., Pople, J. A. & Diat, O. A thermally induced transition from a body-centred to a face-centred cubic lattice in a diblock copolymer gel. *Colloid Polym. Sci.* **276**, 446 (1998).
51. Li, Z., Zhang, Y., Fullhart, P. & Mirkin, C. A. Reversible and chemically programmable micelle assembly with DNA block-copolymer amphiphiles. *Nano Lett.* **4**, 1055–1058 (2004).
52. Kwak, M. & Herrmann, A. Nucleic acid amphiphiles: synthesis and self-assembled nanostructures. *Chem. Soc. Rev.* **40**, 5745–5755 (2011).
53. Roh, Y. H. et al. DNAsomes: multifunctional DNA-based nanocarriers. *Small* **7**, 74–78 (2011).
54. Pan, P. et al. Thermoresponsive micellization and micellar stability of poly(nisopropylacrylamide)-bDNA diblock and miktoarm star polymers. *Langmuir* **28**, 14347–14356 (2012).
55. Edwardson, T. G. W., Carneiro, K. M. M., Serpell, C. J. & Sleiman, H. F. An efficient and modular route to sequence-defined polymers appended to DNA. *Angew. Chem. Int. Ed.* **53**, 4567–4571 (2014).
56. Dong, Y. et al. DNA functional materials assembled from branched DNA: Design, synthesis, and applications. *Chem. Rev.* **120**, 9420–9481 (2020).
57. Walczak, M. et al. Responsive core-shell DNA particles trigger lipid membrane disruption and bacteria entrapment. *Nat. Commun.* **12**, 4743 (2021).
58. Seddon, J. M. Structure of the inverted hexagonal (HII) phase, and non-lamellar phase transitions of lipids. *Biochim. Biophys. Acta* **1031**, 1–69 (1990).
59. Wilks, T. R. et al. “Giant Surfactants” created by the fast and efficient functionalization of a DNA tetrahedron with a temperature-responsive polymer. *ACS Nano* **7**, 8561–8572 (2013).
60. Durand, D., Doucet, J. & Livolant, F. A study of the structure of highly concentrated phases of DNA by X-ray diffraction. *J. Phys. II Fr.* **2**, 1769–1783 (1992).
61. Salamonczyk, M. et al. Smectic phase in suspensions of gapped DNA duplexes. *Nat. Commun.* **7**, 13358 (2016).
62. Bates, F. S. & Fredrickson, G. H. Block copolymers—designer soft materials. *Phys. Today* **52**, 32–38 (1999).
63. Seeman, N. C. & Sleiman, H. F. DNA nanotechnology. *Nat. Rev. Mater.* **3**, 17068 (2017).
64. Jülich Centre for Neutron Science. GALAXI: Gallium anode low-angle x-ray instrument. *J. Large Scale Res. Facil.* **2**, A61 (2016).
65. Förster, S., Apostol, L. & Bras, W. Scatter: software for the analysis of nano- and mesoscale small-angle scattering. *J. Appl. Cryst.* **43**, 639–646 (2010).
66. Biehl, R. Jscatter, a program for evaluation and analysis of experimental data. *PLoS ONE* **14**, e0218789 (2019).

Acknowledgements

We thank Prof. Valentin Gordeliy for providing the purification facilities. This work has been supported by the Deutsche Forschungsgemeinschaft (DFG) under grants STI

664/4-1; E.S. and JO 370/5-1; U.J. and by the Austrian Science Fund (FWF) under grant I 2866-N36; C.N.L.

Author contributions

E.S. and C.N.L. conceived the project and designed research; E.S. synthesized the DNA-based dendritic nanostructures; N.J. and U.J. performed the polymer synthesis and characterization; T.B. performed the preparative SEC for the G1-P-G1 and G2-P-G2 purification; N.A. performed the Monte Carlo simulations; E.S. performed the experiments and purification of G1-P; E.K. and U.R. operated the SAXS beamline; R.B. performed the fittings in the 1D-SAXS profiles; J.K. G.D. contributed to initiating the project and data interpretation; E.S. and C.N.L. interpreted the data and wrote the manuscript. All co-authors commented on the manuscript.

Competing interests

The authors declare no competing interests.

Additional information

Supplementary information The online version contains supplementary material available at <https://doi.org/10.1038/s41467-021-27412-3>.

Correspondence and requests for materials should be addressed to Emmanuel Stiakakis or Christos N. Likos.

Peer review information *Nature Communications* thanks the anonymous reviewers for their contribution to the peer review of this work. Peer reviewer reports are available.

Reprints and permission information is available at <http://www.nature.com/reprints>

Publisher's note Springer Nature remains neutral with regard to jurisdictional claims in published maps and institutional affiliations.



Open Access This article is licensed under a Creative Commons Attribution 4.0 International License, which permits use, sharing, adaptation, distribution and reproduction in any medium or format, as long as you give appropriate credit to the original author(s) and the source, provide a link to the Creative Commons license, and indicate if changes were made. The images or other third party material in this article are included in the article's Creative Commons license, unless indicated otherwise in a credit line to the material. If material is not included in the article's Creative Commons license and your intended use is not permitted by statutory regulation or exceeds the permitted use, you will need to obtain permission directly from the copyright holder. To view a copy of this license, visit <http://creativecommons.org/licenses/by/4.0/>.

© The Author(s) 2021

Blunt-End Driven Re-entrant Ordering in Quasi Two-Dimensional Dispersions of Spherical DNA Brushes

Ivany Romero-Sanchez,[#] Ilian Pihlajamaa,[#] Natasa Adžić, Laura E. Castellano, Emmanuel Stiakakis, Christos N. Likos,^{*} and Marco Laurati^{*}

Cite This: <https://doi.org/10.1021/acsnano.1c07799>

Read Online

ACCESS |

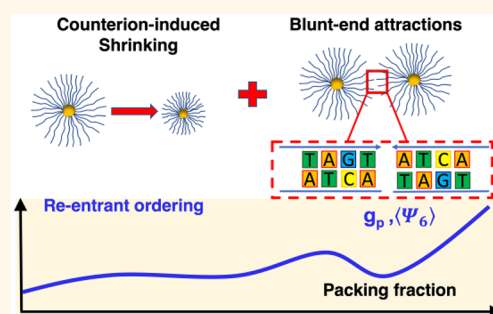
Metrics & More

Article Recommendations

Supporting Information

ABSTRACT: We investigate the effects of crowding on the conformations and assembly of confined, highly charged, and thick polyelectrolyte brushes in the osmotic regime. Particle tracking experiments on increasingly dense suspensions of colloids coated with ultralong double-stranded DNA (dsDNA) fragments reveal nonmonotonic particle shrinking, aggregation, and re-entrant ordering. Theory and simulations show that aggregation and re-entrant ordering arise from the combined effect of shrinking, which is induced by the osmotic pressure exerted by the counterions absorbed in neighbor brushes and of a short-range attractive interaction competing with electrostatic repulsion. An unconventional mechanism gives origin to the short-range attraction: blunt-end interactions between stretched dsDNA fragments of neighboring brushes, which become sufficiently intense for dense and packed brushes. The attraction can be tuned by inducing free-end backfolding through the addition of monovalent salt. Our results show that base stacking is a mode parallel to hybridization to steer colloidal assembly in which attractions can be fine-tuned through salinity and, potentially, grafting density and temperature.

KEYWORDS: blunt-ends, colloids, dna, polyelectrolytes, order transitions



Polyelectrolyte brushes, which consist of charged polymer chains grafted to a planar or curved surface, have found key applications due to their unique properties.^{1,2} Among their applications are the ability to prevent protein adsorption, called an antibiofouling effect^{3,4} and exploited in biomedical applications and tissue engineering.⁵ Conversely, at low ionic strength the opposite effect is observed, i.e., strong protein adsorption.⁶ The two effects can be combined to obtain a protein delivery mechanism.⁷ In addition, spherical polyelectrolyte brushes (SPBs) can be used as nanoreactors for the synthesis of metallic nanoparticles with strong catalytic activity.⁸ Polyelectrolyte brushes also present an exceptionally low mutual friction,^{9,10} which arises from the huge osmotic pressure generated by counterions absorbed within the brush in low ionic strength environments and can be controlled through the addition of multivalent ions.^{11,12} The ultralow friction of polyelectrolyte brushes is essential in biolubrication, for example, for the correct operation of synovial joints¹³ and the production of coatings for medical implants.¹⁴ In the context of polyelectrolyte-mediated lubrication effects, the interactions between contacting brushes and the resulting polymer conformations play a fundamental role: compression or interpenetration can change friction by

orders of magnitude.¹¹ Such interactions and conformations are decisively influenced by the packing of brushes, in particular, in crowded conditions, an aspect which is especially relevant in biological systems. These deformations under crowding, which constitute one of the main issues of the present work, have not been fully explored to date.

DNA is a highly charged polyelectrolyte whose properties have been used to develop nanotechnologies such as electrochemical sensors,¹⁵ field-effect transistors,¹⁶ and smart surfaces.¹⁷ Being highly customizable with molecular precision, DNA is thus the ideal building block for the systematic investigation of polyelectrolyte brush interactions in crowded systems. In addition, the specificity of DNA interactions can be exploited to precisely control assembly. Complex DNA structures can be assembled through Watson–Crick base

Received: September 6, 2021

Accepted: February 2, 2022

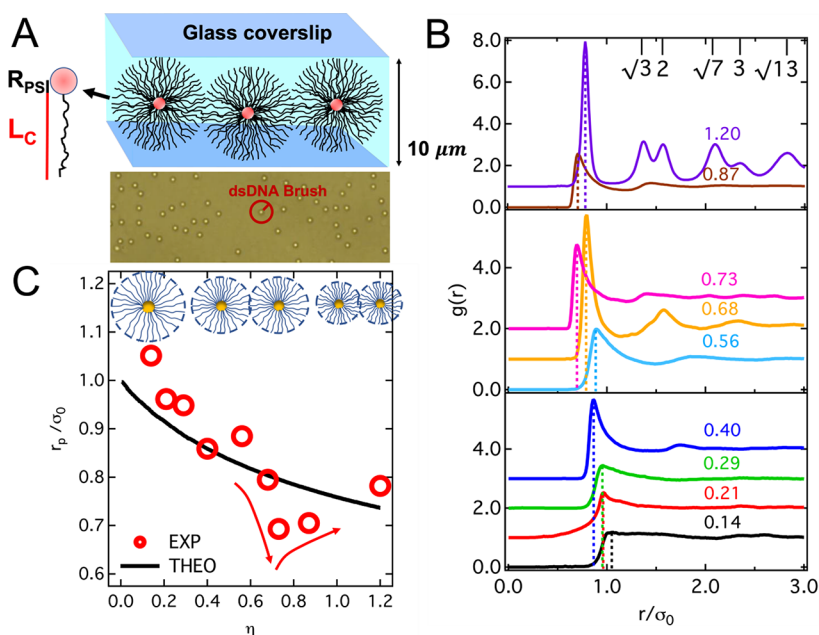


Figure 1. Experimental setup and analysis of the radial distribution function. (A) (Top) Sketch of the experimental setup showing dsDNA-coated particles confined between two microscope coverslips separated by $10\ \mu\text{m}$ spacers. The relative sizes of the core (R_{PS}) and brush (L_C) are represented in the zoomed image on the left side of the sketch, where for clarity a single dsDNA fragment is shown. The coverslips were coated with a hydrophobic material to avoid particles sticking to the glass. (Bottom) Exemplary portion of a bright field microscopy image of a dispersion of dsDNA-coated colloids with packing fraction $\eta = 0.14$. The PS cores are visible. The overall size of the particles is indicated by the red circle. (B) Radial distribution functions $g(r)$ of dispersions with different packing fractions η , as indicated. In each panel curves with larger packing fractions have been shifted vertically by 1 with respect to the previous curve for clarity. Dashed lines indicate the position of the first peak for each curve. In the top panel, the expected positions of the peaks and the corresponding values of the ratios r_i/r_1 for a 2D hexagonal lattice are reported, with r_i and r_1 the positions of peak i and 1, respectively. (C) Position of the first peak of $g(r)$ in units of the particle diameter in dilute conditions, as a function of packing fraction. Symbols: experiments, solid line: theory. Red arrows highlight the nonmonotonic behavior of the experimental data. The progressive size reduction as a function of packing fraction is represented in the cartoon.

pairing of sticky ends,¹⁸ the programmable folding of long single strands (DNA Origami and “brick” assembly),¹⁹ or supramolecular interactions,²⁰ including blunt-end base stacking.^{21–23} DNA can be also used to direct the assembly of colloidal micro- and nanoparticles, which can confer to materials desired optical, electrical, or mechanical properties.^{24,25} For colloidal systems, base-pairing interactions between sticky ends have been the main tool used to construct the desired structural arrangements.^{26,27} Blunt-end interactions, while scarcely considered,²⁸ provide a parallel route to colloidal assembly that exploits base stacking instead of base-pairing. The effective interaction between a collection of blunt-end of dsDNA fragments grafted onto two facing colloidal particles can be fine-tuned through ionic strength and ion type and, potentially, grafting density and temperature.

In this work, we demonstrate that the combination of strong osmotic forces from the neighboring SPBs and the blunt-end DNA attractions leads to unconventional re-entrant ordering phenomena and to the emergence of stringlike patterns in concentrated DNA-brush solutions. To this end, we combined microscopy experiments, theory, and simulations to systematically investigate the interactions and correlations between thick, densely packed SPBs in quasi-2D confinement. In these experiments, the structural organization and the dynamics of thick spherical dsDNA brushes grafted onto latex beads were determined. Two main effects of the brush–brush interactions were found: a progressive reduction of the interparticle effective interaction range (distance of closest approach) with increasing packing and a complex, unusual aggregation

behavior, with a re-entrant ordering as a function of packing fraction. By developing a detailed microscopic model of the effective interactions, which incorporates electrostatic, entropic, and osmotic free energy contributions, as well as the concentration-dependent blunt-end attractions, we determined the conformations of single and contacting SPBs. Moreover, we established that the decrease of the interparticle distance is associated with a size reduction that originates from the pressure exerted on a brush by the absorbed, noncondensed counterions of neighbor brushes. This mechanism significantly differs from that of charged microgels, in which the free counterions surrounding the particles are controlling the deswelling behavior.^{29,30} The size reduction is accompanied by a very limited particle interdigitation. The experimentally observed aggregation phenomena were reproduced in simulations of particles interacting with a short-range attraction in addition to the mild, long-range repulsion associated with electrostatics. The origin of the attractive interaction, which is atypical for polyelectrolyte brushes, could be attributed to base stacking interactions. These become significant in the osmotic regime where dsDNA fragments are stretched, and the blunt-ends of neighbor brushes face each other at a short distance. These blunt-end interactions could be tuned by acting on chain conformations through the addition of monovalent salt.

RESULTS AND DISCUSSION

Experiments: Effect of Packing on the Brush Size. We present in this section the evolution of the conformation and interactions of increasingly packed SPBs extracted from the

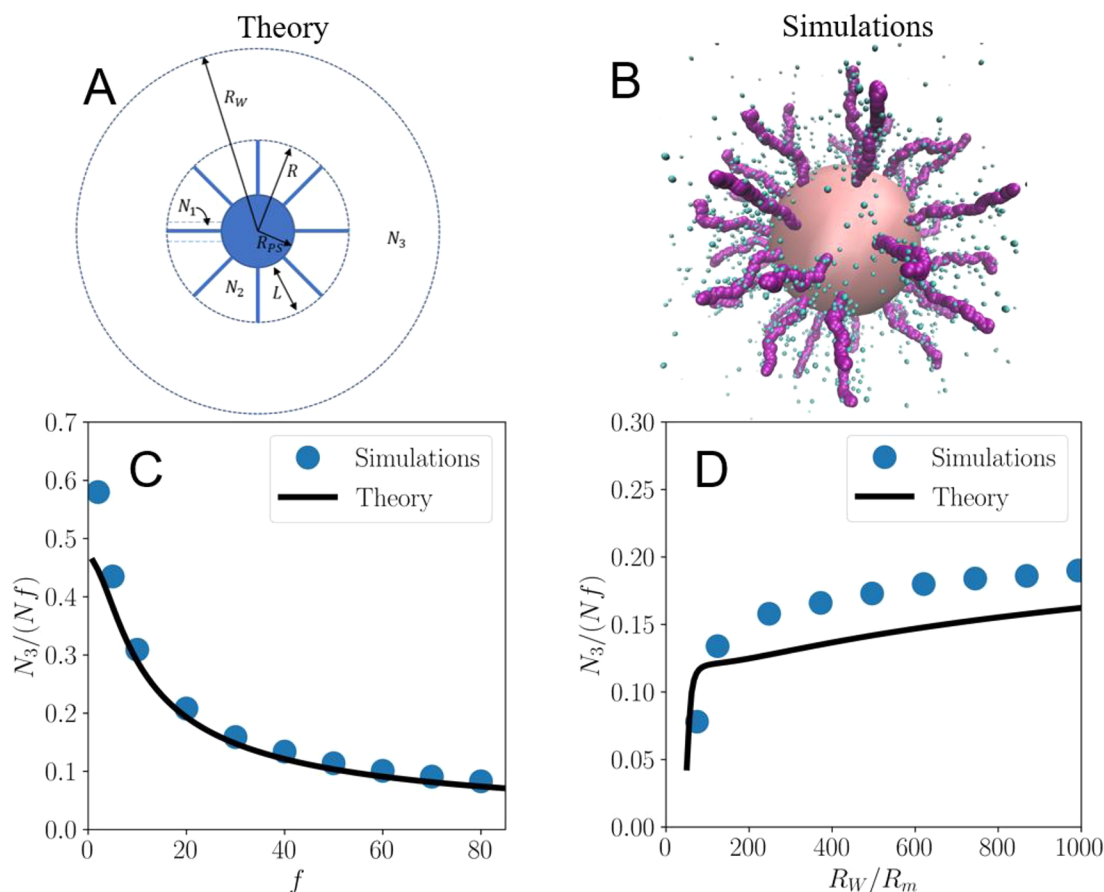


Figure 2. Theoretical and simulation models, fraction of noncondensed counterions. (A) Schematic model of a SPB of total radius $R = R_{PS} + L$, enclosed in a spherical Wigner-Seitz cell of radius R_W . N_1 , N_2 , and N_3 are the numbers of condensed, noncondensed, and free counterions, respectively. (B) Snapshot of coarse-grained MD simulation of miniature SPB ($N = 40$, $R_{PS} = 10$ nm), which presents the same grafting density as the experimental system. (C, D) Fraction of counterions N_3/Nf that escape the SPB, where f is the functionality and N is the chain length. This fraction as a function of functionality f (C) and as a function of Wigner-Seitz radius R_W scaled with the radius R_m of a chain monomer (D). For more information on the simulations of the miniature brushes, see the [Supporting Information](#).

analysis of the radial distribution function $g(r)$ of quasi-2D dispersions of dsDNA-coated polystyrene (PS) particles. A sketch illustrating the quasi-2D confinement is shown in [Figure 1A](#): particle dispersions are contained in a channel formed by a microscope slide and a glass coverslip, separated by $10 \mu\text{m}$ using spacers. The radial distribution function $g(r) = N(r)/(2\pi nr\Delta r)$, with $N(r)$ being the number of particles in a thin shell of thickness Δr at distance r from a selected particle and $n = \langle N_p/A \rangle$ the average particle number surface-density, was determined from particle coordinates extracted from bright-field microscopy experiments. This contrast technique was chosen to avoid possible damages of the DNA fragments due to prolonged exposure to intense laser irradiation in fluorescence-based techniques using labeled DNA.³¹ In addition, fluorescent labeling of the dsDNA chain ends can alter their interactions.³² In bright field contrast only the PS cores are visible. Dense dsDNA brushes were formed by grafting $f \approx 10^5$ dsDNA fragments of length equal to 10 kilobase-pairs (kbp) on PS particles with radius $R_{PS} = 0.49 \mu\text{m}$. In what follows, we will also employ the term *functionality* to denote the number f of grafted dsDNA fragments. As shown in previous work,^{33,34} in water solution without any added salt the dsDNA chains assume a fully stretched configuration resulting in a brush thickness equal to the contour length $L_C = 3.4 \mu\text{m}$, corresponding to a brush-core size ratio $L_C/R_{PS} \approx 6.9$, i.e., a

starlike architecture.³⁵ [Figure 1A](#) shows an exemplary portion of an image of a dispersion, with indication of the overall size of the particles. Details of the synthesis, the preparation of dispersions, and the quasi-2D confinement of the system are reported in the [Methods](#). The $g(r)$ functions of systems with increasing packing fraction $\eta = n\pi\sigma_0^2/4$, shown in [Figure 1B](#), evidence significant structural variations, indicated by changes in the number of the observed peaks, their height, and their position. Note that η is calculated using the particle diameter in dilute solution $\sigma_0 = R_{PS} + L_C$ and thus reflects the increase in particle number density without accounting for the particle shrinking discussed later. A clear nonmonotonic variation of the height of the first peak with increasing η is evident and will be discussed later together with variations of the local order parameter. Here, we focus instead on the variations of the position of the first peak of the $g(r)$, r_p , indicated by the dashed lines in [Figure 1B](#), which represents the shortest interparticle distance. For monodisperse hard spheres, this quantity presents a minimum value equal to the particle diameter when particles are in contact.

For dense dispersions of soft particles, r_p can be smaller than the particle diameter measured in dilute solution due to particle interpenetration, compression (shrinking), or deformation (and combinations of them). It can be therefore used to measure morphological changes of the particles with

increasing crowding. Starting from $r_p \approx 1.05\sigma_0$ for $\eta = 0.14$, when the packing fraction is increased the interparticle distance decreases monotonically until $\eta = 0.40$, for which $r_p \approx 0.88\sigma_0$. Interestingly, for $\eta = 0.56$ the position moves back to a slightly larger value, indicating a re-entrant behavior. For $\eta = 0.68$, the value of r_p decreases again. Note that for this sample also the position of the second peak shifts to significantly smaller values compared to the previous sample, indicating a sudden compaction of the particle neighborhood. The minimum value of r_p is registered for $\eta = 0.73$, while for $\eta = 0.87$ it increases slightly and significantly more for $\eta = 1.20$. For this value of η , the system crystallizes into a 2D hexagonal lattice, as demonstrated by the position of the peaks of the $g(r)$ (Figure 1B). The trend of r_p as a function of η is reported separately in Figure 1C. The nonmonotonic trend discussed in detail above can be observed for packing fractions η around 0.7, even if not particularly pronounced. Overall, the values of r_p lie between $1.05\sigma_0$ and $0.7\sigma_0$. The fact that r_p values are, for the majority of samples, smaller than the particle diameter and decreasing with increasing η indicates that the dsDNA brushes were shrinking, interpenetrating, and/or mechanically deforming. Interpenetration could be excluded in this case according to experimental evidence provided in previous work³³ through confocal fluorescence microscopy images of packed, free-end labeled brushes. The absence of interpenetration was attributed to the large osmotic pressure generated by the absorbed counterions. In the next section, we present a theoretical model that confirms this speculation and explains the physical origin of the observed decrease of r_p in terms of particle shrinking which results from the osmotic pressure generated by absorbed, noncondensed counterions. We will also show in the last section that the particle dynamics even at large packing fractions never fully stop. This finding further supports shrinking as the origin of the reduction of r_p : if an increasingly large number of particles would be able to pack through deformation, particle movements should be strongly suppressed. This finding marks a clear difference with the results of previous work³³ in which particle deformation was observed at high packings: the distinct response can be attributed to the significantly different conditions of the experiments in the two studies. In this work, the packing fraction of the whole macroscopic sample was progressively increased, while in the work of Zhang et al. only a fraction of particles of a dilute suspension was concentrated in a limited portion of space using magnetic forces. Shrinking, deformation, and interpenetration due to crowding have been intensively studied in microgel suspensions.^{30,36–42} For neutral microgels three regimes were recognized: A first regime, below space filling, where no significant shrinking, interpenetration, or deformation are observed; a second, above space filling, in which particle deformation and interpenetration occur; a third at even larger packing fractions in which deformation and interpenetration saturate and particles shrink (deswell).^{39,41} Instead, for ionic microgels shrinking was found to be the main mechanism acting above space filling.⁴² Note that the behavior of the system investigated here is clearly different from the two cases just discussed: a significant shrinking is observed well before space filling and interpenetration is negligible also at large packing fractions.

Theory: Modeling the dsDNA Brush Configurations as a Function of Packing. The primary dependence of the interaction diameter σ of SPBs on their packing fraction η is a monotonic decrease, represented, roughly, by the solid line in

Figure 1C. Since the SPBs are complex macromolecular aggregates, their conformations and interactions depend crucially on a diverse variety of physical parameters, bringing forward their hybrid polymer/colloid character. An understanding of the effective interactions between SPBs requires analysis of their conformations, which result from a minimization of a suitable free energy F , as we elaborate below.

We build a cell model of a SPB of which the geometry is schematically illustrated in Figure 2A. The brush consists of a hard core having a radius R_{PS} , surrounded by a brush of thickness L , which consists of f PE chains comprising N monomers each. Correspondingly, for each chain there are N monovalent counterions, which are contained in a Wigner-Seitz cell with radius R_{W} , related to the overall packing fraction η by the requirement that a single SPB is contained within the volume of one cell. Since the experiment has shown that the size of SPBs can be highly density dependent, we explicitly differentiate between the density dependent brush size $R = R_{PS} + L$, and the brush size in unperturbed dilute conditions $R_0 = \sigma_0/2 = R_{PS} + L_C$, where L_C stands for the brush height at infinite dilution. We assume that the SPB is dissolved in a solvent with electric permittivity ϵ at temperature T . Because of the high bare charge of the DNA fragments, many of the counterions will be condensed along them, the number of which, N_1 , can be approximated with the Manning parameter ξ , which we define as the ratio of the Bjerrum length, $\lambda_B = e^2/4\pi\epsilon k_B T$, and the distance b between each charge, giving $\xi = \lambda_B/b$, with k_B being Boltzmann's constant. Using this parameter, we estimate that the number of condensed counterions is $N_1 = \left\lfloor \frac{Q_{\text{bare}}}{e} \left(1 - \frac{1}{\xi}\right) \right\rfloor$, where $Q_{\text{bare}} = -efN$ is the total bare charge of a brush.⁴³ With this estimation we presume that the counterions condense in such a way that there remains only one net charge per Bjerrum length. Here, we neglect the effect other nearby chains exert because their electrostatic interactions are screened by the counterions in the brush. The remaining $fN - N_1$ counterions are subdivided into two populations N_2 and N_3 , representing those that are free to move within the brush and those that are free outside of the brush. In order to find the number of free counterions within the brush (N_2) and outside of the brush (N_3), as well as the brush thickness L , we set up a variational free energy $F(N_3, L)$ and minimize it to find the equilibrium values of N_3 and L . The remaining population is now easily calculated with the charge-neutrality condition $N_1 + N_2 + N_3 = Nf$. We explicitly minimize for the brush thickness L as well to qualitatively capture the significant decrease of the location of the first peak of the radial distribution function $g(r)$ that was found in the experimental system as shown in Figure 1C.

In this free energy F , we include six contributions and express F as

$$F = U_H + F_{el} + F_{fl} + S_2 + S_3 + F_p \quad (1)$$

We present more information and explicit calculations in the Supporting Information, limiting ourselves to a more concise description in what follows.

The first contribution (U_H) approximates the electrostatic energy modeling the Coulombic interactions between all the charged PE-monomers and counterions. We use a Hartree type expression

$$U_H = \frac{1}{8\pi\epsilon} \iint dr dr' \frac{\rho(r)\rho(r')}{|r - r'|} \quad (2)$$

where $\rho(r)$ is the expectation value of the total charge density resulting from the sum of the counterion charges and the charges on the PE chains and where the integrations run over the entire Wigner–Seitz cell. Theory, simulation, and experiments agree that the chains of isolated, dense PE brushes in a salt-free environment are completely stretched, meaning that the charged monomer density falls off as r^{-2} inside the brush.^{33,44,45} Because counterions are inclined to neutralize the charged monomers, we assume that the distribution of counterions within the brush also has this functional form. Furthermore, we model the free counterions outside the brush as homogeneously dispersed. The charge density resulting from the sum of the counterion and the monomer density is now given by

$$\rho(r) = \begin{cases} 0 & r < R_{PS} \\ \frac{-eN_3}{4\pi Lr^2} & R_{PS} \leq r \leq R \\ \frac{3eN_3}{4\pi(R_W^3 - R^3)} & R < r < R_W \end{cases} \quad (3)$$

in which the prefactors ensure charge neutrality.

The second term (F_{el}) in the free energy models the entropic elasticity of the PE chains, which adds a penalty for a highly stretched chain configuration⁴⁵

$$\frac{F_{el}}{k_B T} = \frac{3fL^2}{2Nb^2} \quad (4)$$

Here, b is the equilibrium length of the bonds between chain monomers.

The third (F_{Fl}) is a Flory self-avoidance term that models the excluded-volume interactions between the chain monomers. We choose to set the excluded volume equal to the volume of a monomer with radius R_m and obtain⁴⁴

$$\frac{F_{Fl}}{k_B T} = \frac{f^2 N^2 R_m^3}{2L^3} \quad (5)$$

The form of this contribution to the free energy is strictly only applicable if the radius of the central colloid is much smaller than the total brush radius $R_{PS} \ll R$. Similarly, we implicitly assume that the chain monomer density within the brush is homogeneous, meaning that the PE chains can fully explore the volume of the brush and are not attached to the central colloid. However, because we are mainly interested in predicting the way in which the brush size L changes with a change in the relevant parameters, we expect that these simplifications do not disqualify our findings.

The next two terms model the entropic free energy S_2 of the noncondensed counterions within the brush and that of the free counterions outside the brush, S_3 . We leave out the entropy of the condensed counterions as it will drop out in the minimization since the number of these counterions is kept constant. However, we do take into account that the presence of the PE chains limits the available free volume to the counterions in the brush. Defining the local number densities $n_i(r)$, $i \in \{2,3\}$, and the counterion diameter d , we can estimate the entropic contributions to the free energy with

$$S_i = k_B T \int_{V_i} dr n_i(r) \ln(n_i(r)d^3) \quad (6)$$

in which we omit the usual characteristic length-scale term as it will yield a constant contribution to the free energy.⁴⁵

The final contribution (F_p) to the free energy takes into account the effects of the surrounding SPBs in a concentrated solution on the size of any given SPB. Following the arguments put forward for the related case of star polymers,⁴⁶ we introduce F_p as the free energy cost of insertion of a SPB of radius R in a concentrated solution of the same. Such an insertion results into the expulsion of the remaining SPBs from a region of size R and the associated free energy cost can be estimated as the product between the volume taken up by the SPB, R^3 , and the osmotic pressure $\Pi(R_W)$ of the remaining solution at packing fraction η , parametrized through the Wigner–Seitz radius R_W . This osmotic pressure, in turn, is dominated by the trapped counterions⁴⁶ and is estimated by the product of the number of entropically active counterions N_2 in each brush, the thermal energy $k_B T$, and the number density of the brushes $\propto R_W^{-3}$. Summarizing, we obtain

$$\frac{F_p}{k_B T} = \frac{N_2 R^3}{R_W^3} \quad (7)$$

and can only be considered in the limit that $N_2 \gg N_3$, which we justify later in this section.

The role of the various terms is antagonistic: some of them favor large SPB sizes whereas others would favor the shrinking of the same; thus, their competition leads to a value that minimizes the total free energy. The sum of these contributions is numerically minimized with respect to L and N_3 . In Figure 2C,D, we show for miniature brushes ($N = 40$, $R_{PS} = 10$ nm) the effect of varying the functionality f and the SPB density on the osmotic power of the brushes, i.e., on the fraction of counterions the brush absorbs. The name miniature is used to indicate that the simulated brushes are a scaled version of the experimental system presenting the same grafting density (but smaller fragment length, see Figure 2B). We validate the results of this procedure with coarse-grained molecular dynamics simulations of these small brushes (see the Supporting Information), finding excellent quantitative agreement between the theoretical cell model and simulations for the fraction of the nonabsorbed counterions (Figure 2C,D). We show that as the functionality increases, a decreasing fraction of counterions manages to escape the brush (Figure 2C). This is due to the increased relative influence of the electrostatic energy.

Since the functionality f , i.e., the number of grafted dsDNA fragments of an experimental brush, is rather large ($f \sim 10^5$), we expect these to be highly osmotic, releasing very few counterions. Indeed, using the geometric parameters of the large experimental brushes, our cell model predicts that the fraction of released counterions is of the order of 10^{-5} , indicating that virtually all available counterions are being absorbed. On the other hand, we see that an increase in the cell size R_W , related to the volume fraction by $\eta = R_0^3/R_W^3$, tends to decrease the osmotic power of the brushes. This is to be expected, of course, since an increase in the available volume for each brush increases the entropy of released counterions.

Applying the model to brushes with the same geometry as that from the experiments results in a concentration-dependent size given by the solid line in Figure 1C, which describes very well the progressive reduction of the position of the first peak of the experimental $g(r)$. For the large experimental brushes, we find that especially the contribution F_p has a very significant

influence on the density dependence of the brush size. Even though the model captures well the experimentally observed density-driven shrinkage of the brushes, it does not manage to accurately predict the absolute size of the experimental brushes, underestimating it by roughly 40%. On the other hand, such deviations are not unusual in scaling-type theories that seek to establish general trends and regimes and do not aim at detailed quantitative accuracy. We remark that an experimental verification of the theoretically predicted particle shrinking presented in this work, which is also related to previous contributions,⁴⁵ was not presented to date.

Even though the SPBs shrink as the local colloid density increases, at constant density the effective interactions between two such particles can be expected to be very strongly repulsive as they start overlapping. In particular, Jusufi et al. showed that the effective interactions between colloidal particles similar to SPBs scale linearly with the number of adsorbed counterions.⁴⁵ To confirm that these findings extend to our system as well, we perform a similar analysis for miniature SPBs of which we present the results in the [Supporting Information](#). Since the number of adsorbed counterions in the experimental brushes must be of the order of $Nf \approx 10^9$, we conclude that even small brush overlaps are penalized with energies orders of magnitude higher than those available for thermal fluctuations. In short, our model prohibits highly osmotic SPBs from (significantly) interdigitating, in agreement with experimental findings in previous work.³³

Experiments: Aggregation and Re-entrant Ordering.

While the theory developed in the previous section identifies the physical origin of the progressive size reduction of the brushes, the experimental data show an additional, non-monotonic trend of the position of the first peak, with significant deviations from the theoretical predictions in the interval $0.7 < \eta < 0.8$. This discrepancy suggests that the monotonic size reduction predicted by theory as an effect of the osmotic pressure of the adsorbed, noncondensed counterions is not sufficient to capture the entire experimental phenomenology, at least when only repulsive interactions between the brushes are considered. To better understand the physical origin of the nonmonotonic experimental trend, we report in [Figure 3](#) the packing fraction dependence of two additional structural parameters, the height of the first peak of the $g(r)$, g_p , and the average 6-fold order parameter, $\langle \Psi_6 \rangle = \langle 1/N \sum_{i=1}^N \Psi_6^i \rangle$, with N the total number of particles in one image of the sample, where $\Psi_6^i = 1/N_b \sum_{j=1}^{N_b} e^{i6\vartheta_{ij}}$ is the 6-fold order parameter of particle i with ϑ_{ij} the relative orientation angle between particles i and j and N_b the number of neighbors of particle i . The brackets $\langle \rangle$ indicate an average over all images of the sample.

Two particles were considered neighbors when the distance between their particle centers was smaller than the diameter plus half the distance between the first maximum and the first minimum of the $g(r)$. Both g_p and $\langle \Psi_6 \rangle$ show a similar trend which, on top of a progressive increase as a function of η , presents a nonmonotonic behavior and the presence of two local maxima. One is observed for $\eta \approx 0.40$ and the second for $\eta \approx 0.68$. These peaks indicate for the corresponding samples the presence of structures with a larger degree of local order and are visualized in the representative renderings of the samples shown in [Figure 3](#), which were obtained using particle coordinates from particle-tracking (representative renderings of all samples can be found in the [Supporting Information](#), [Figure S1](#)). For the sample with $\eta \approx 0.40$ one can see that

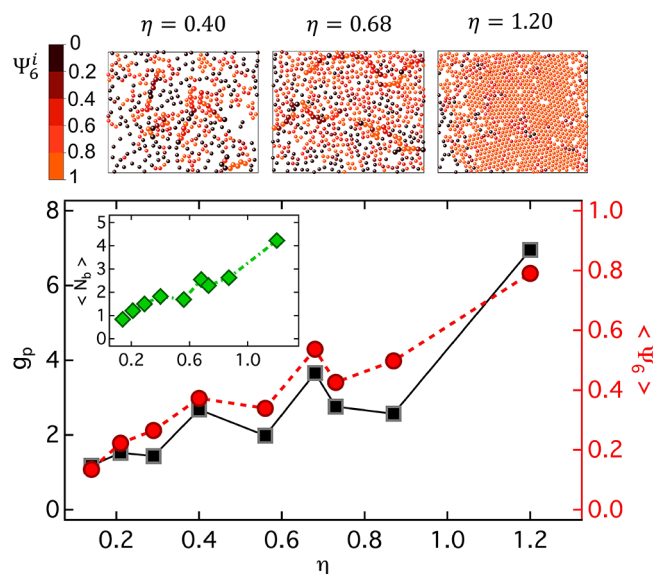


Figure 3. Structural parameters to investigate the degree of ordering. (Bottom) Height of the first peak of the $g(r)$, g_p (squares), and average 6-fold order parameter $\langle \Psi_6 \rangle$ (circles) as a function of packing fraction η . Inset: Average number of neighbors per particle, $\langle N_b \rangle$, as a function of packing fraction η , same x -axis as the main plot. (Top) Images corresponding to exemplary renderings were obtained from coordinates for the samples indicated by the arrows. Particles are colored according to their individual value of Ψ_6^i (see scale-bar). In the snapshots for samples with $\eta = 0.40$ and 0.68 selected particles have been represented with an artificially larger size to highlight the presence of chainlike structures.

chainlike structures are present with a simultaneous emergence of density inhomogeneities (crowded regions and voids), indicating the presence of attractions in the effective brush–brush interaction potential. These attractions, however, are neither broad nor deep enough to bring about macroscopic phase separation (liquid–gas) in the SPB solution, leading rather to the formation of finite-size clusters only. The linear geometry of the structures is also confirmed by the average number of neighbors for each particle which is $\langle N_b \rangle \approx 2$ ([Figure 3](#), inset). The length of the chains presents a broad distribution, and also isolated particles are present. For the sample with $\eta \approx 0.68$, the aforementioned features persist, albeit with suppressed density inhomogeneities with respect to $\eta \approx 0.40$, and the average number of neighbors increases to $\langle N_b \rangle \approx 3$ ([Figure 3](#), inset). The degree of local order within the aggregates is pronounced, as confirmed by the value of the average 6-fold order parameter, $\langle \Psi_6 \rangle \approx 0.54$. Interestingly, for $\eta > 0.68$ g_p and $\langle \Psi_6 \rangle$ (and also $\langle N_b \rangle$) decrease first and then increase again, indicating a re-entrant order–disorder transition. The trends of $\langle \Psi_6 \rangle$ and g_p (and $\langle N_b \rangle$) are all consistent with the trend of r_p , which is also nonmonotonic and presents a minimum value for a comparable value of $\eta = 0.73$. The minimum of r_p indicates the strongest size reduction, which is followed by an increase for larger values of η , indicating reswelling. We speculate then that the sudden disordering indicated by the structural parameters $\langle \Psi_6 \rangle$, g_p , and $\langle N_b \rangle$, i.e., the reduction observed for $\eta > 0.68$, can be associated with the size reduction, and the successive increase of order (increase of the parameters) with the reswelling.

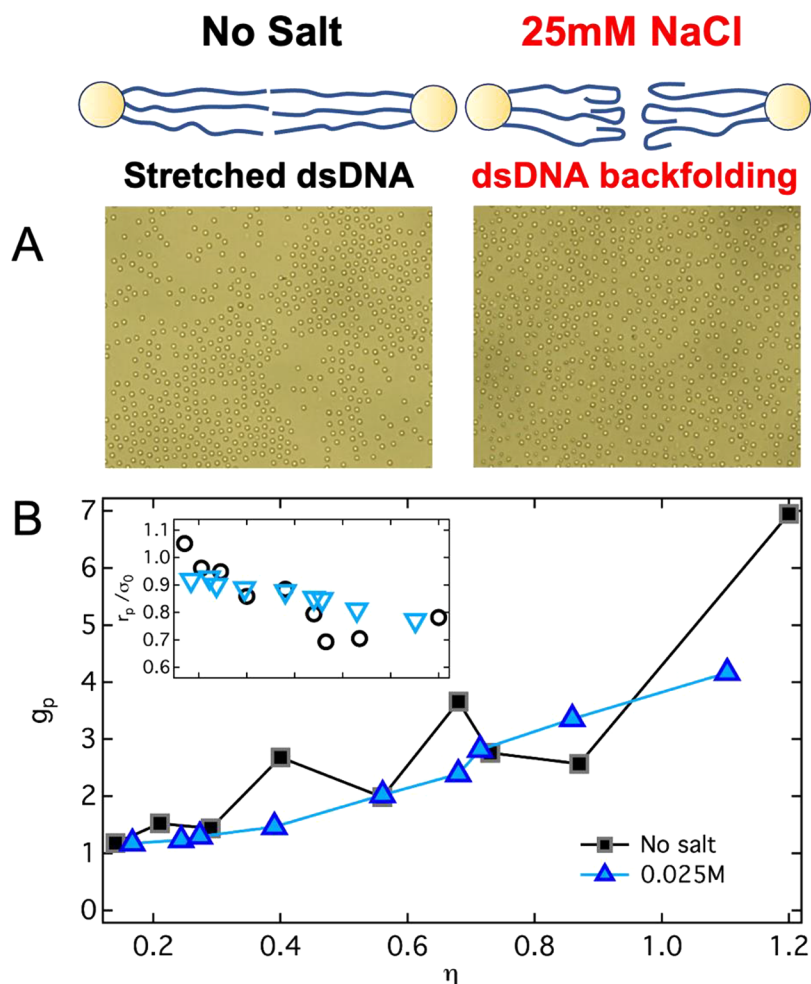


Figure 4. Changes in the dsDNA configuration lead to the disappearance of reentrant ordering. (A) Images of samples with $\eta \approx 0.68$ for systems without any added salt (left) and with 25 mM NaCl (right). (B) Height of the first peak of the $g(r)$, g_p , as a function of packing fraction η for the system without any added salt (same data as in Figure 3) and for the system with 25 mM salt content, as indicated. Inset: Corresponding peak position r_p as a function of η , same range as in the main plot. At the top of the figure, we show a schematic representation of the changes in the configuration of a few exemplary dsDNA fragments for the system with and without added salt.

We already commented on the fact that the size reduction registered for these samples deviates from the monotonic trend predicted by assuming purely repulsive interactions, and we additionally noted that pronounced aggregation is observed for these packing fractions. This leads us to conclude that the pronounced particle shrinking responsible for the reentrant transition might be associated with the strong local packing induced by aggregation. These aggregation phenomena can be explained if an attractive interaction between the brushes is present. We will demonstrate that introducing a model short-range attraction between particles/brushes the experimental reentrant ordering can be qualitatively reproduced; the origin of this attraction can be attributed to blunt DNA ends, and its effect can be suppressed by salinity. Note, finally, that the formation of a hexagonal lattice for the highest packing fraction $\eta = 1.20$ is confirmed by the large value of $\langle \Psi_6 \rangle \approx 0.8$.

Experiments: Testing the Origin of the Short-Range Attraction by Acting on DNA Conformation. The experimental observation of finite-size clusters and density inhomogeneities discussed in the previous section indicates the presence of a short-range attraction of moderate intensity between the dsDNA brushes. We speculate that DNA blunt-end base stacking is the origin of this effective attractive

interaction. Our interpretation is based on the following arguments: Previous experiments³³ and findings in this work indicate the absence of significant interdigitation at large packing fractions and a stretched configuration of the dsDNA fragments within the brushes in the absence of added salt. We can therefore foresee that when two neighbor brushes are in contact and the DNA fragments are stretched, a large number of blunt ends on the two sides will face each other and will be separated by a short distance. Recent experimental and theoretical work on the assembly of DNA nanostructures^{21–23,47,48} showed that when a large number of complementary DNA blunt ends lie at sufficiently small distance from each other, stacking assembly is observed. We propose that this mechanism could be at the origin of the attractive interactions between compressed and densely packed DNA brushes. It was found that the attractive interaction per base contact amounts to a few $k_B T$.²² Upon the SPBs approaching contact, blunt-end-pairs are exposed to such an attraction while at the same time experiencing a weak electrostatic repulsion from the other brush, which is of the order of a few $k_B T$ itself.⁴⁶ The resulting effective interaction between two SPBs could be thus estimated to be of the order of the thermal energy. A fundamental assumption of our

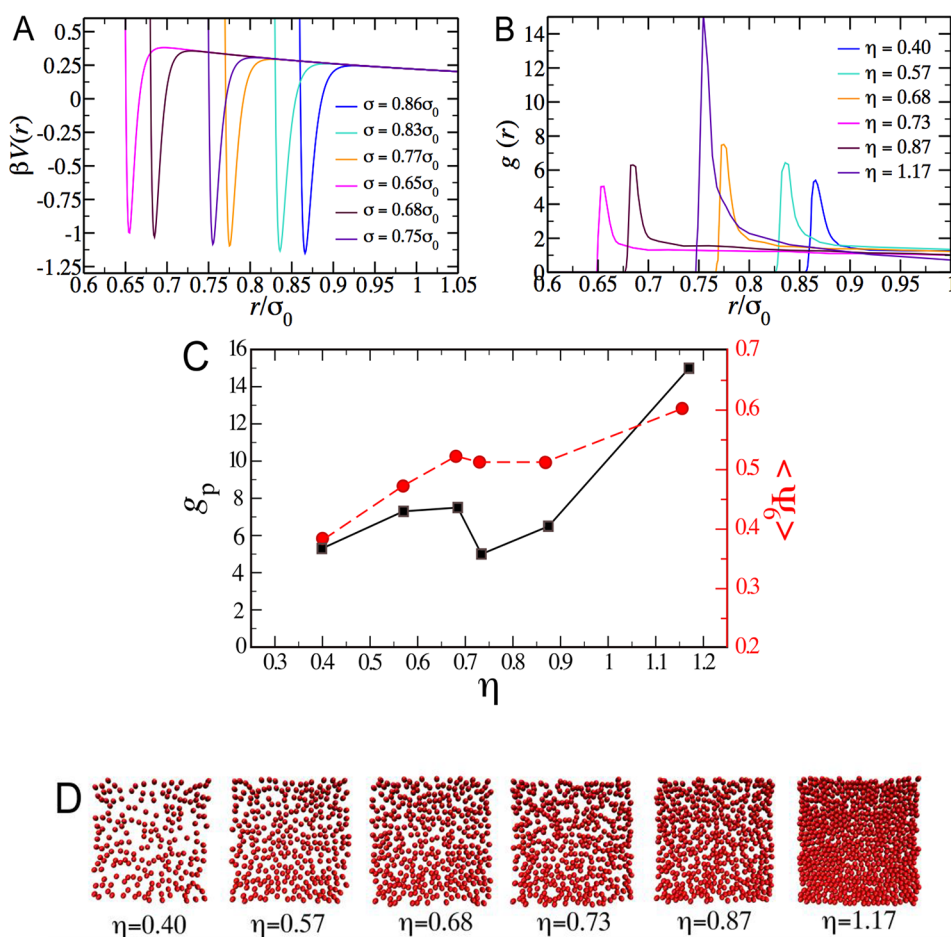


Figure 5. MC simulations of a system with competing attractive and repulsive interactions confirm reentrant ordering. (A) Interaction potential with parameters: $V_1/k_B T = 1.43$; $V_2/k_B T = 0.28$; $\lambda/\sigma_0 = 1.5$, and variable σ as indicated in the legend. (B) Simulated $g(r)$ for various packing fractions, where the color code matches the scheme in (A). (C) Trend of the height of the first peak (black symbols) and the order parameter (red symbols) as a function of packing fraction. (D) Corresponding simulation snapshots.

hypothesis is the stretched configuration of dsDNA fragments due to the presence of a large fraction of counterions adsorbed within the brush in the absence of salt. To test our hypothesis, we performed a similar analysis of the structural evolution of the dsDNA brushes adding 25 mM of NaCl to the dispersions. We report in Figure 4A exemplary images of samples with comparable particle number density for the system in deionized water and with addition of 25 mM NaCl. For the sample in deionized water, which corresponds to $\eta \approx 0.68$, in selected regions like the one reported in Figure 4A (left) one observes a pronounced heterogeneous structure with aggregates and local ordering within the aggregates. For the sample with 25 mM NaCl we did not find instead heterogeneous regions and the structure is generally homogeneous (Figure 4A, right). This suggests an important change of the effective interactions in the sample with 25 mM salt. This pronounced difference is confirmed by the comparison of the trend of g_p as a function of η for the two systems (Figure 4B): No peaks are visible for the system with added salt (the corresponding $g(r)$ are reported in the Supporting Information, Figure S2).

Additionally, also the position of the first peak decreases in this case smoothly, different from the case without added salt (Figure 4B, inset). We speculate that while addition of monovalent salt should increase the strength of blunt-end interactions,^{22,47} at the same time it strongly affects the spatial configuration of the dsDNA fragments: Previous work in ref 33

showed that a significant backfolding (sketch in Figure 4) of the ends of the fragments occurs. This implies that the probability that blunt ends from neighbor brushes face each other drastically reduces and, thus, the effective attraction between brushes decreases. This finding supports the interpretation that the unconventional origin of the effective attraction between brushes is blunt-end interactions.

Simulations: Aggregation and Re-entrant Ordering in a System with Competing Short-Range Attraction and Midrange Repulsion. Based on the experimental evidence on the presence of additional, short-range attractions originated by blunt-end interactions, we postulated an effective repulsive potential that includes additional such attractions and confirm that it brings about the experimentally observed features. In particular, we performed Monte Carlo simulations of colloidal particles in two dimensions, interacting with the following generic pair interaction:

$$V(r) = 4V_1 \left[\left(\frac{\sigma}{r} \right)^{200} - \left(\frac{\sigma}{r} \right)^{100} \right] + V_2 \frac{e^{-r/\lambda}}{r/\lambda} \quad (8)$$

The first term is the Lennard-Jones 100–200 potential, modeling a strong repulsion of hard-core-like spheres of diameter σ , followed by a short-range attraction.

The justification for such strong repulsion which prohibits particles from interdigitation is found in the work of Jusufi et

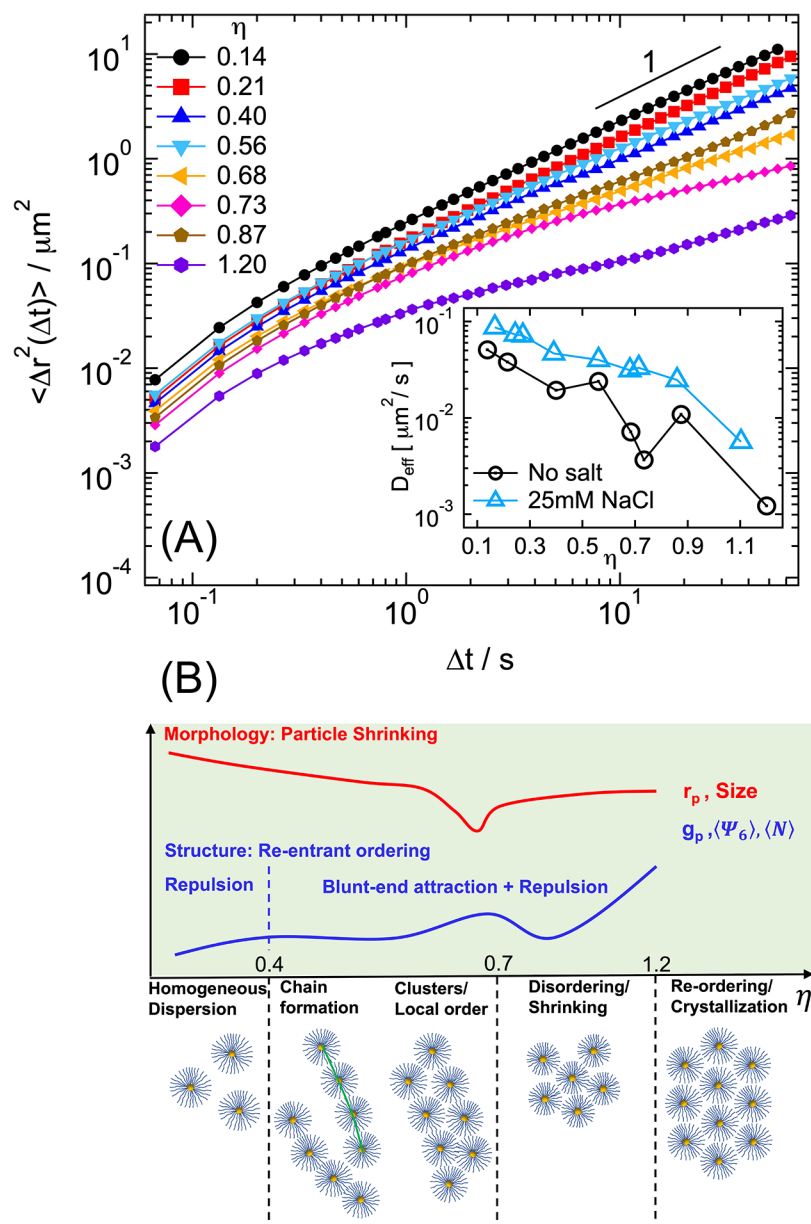


Figure 6. (A) Experimental mean squared displacements for samples with different packing fractions. Average mean squared displacement $\langle \Delta r^2(\Delta t) \rangle$ of dispersions of dsDNA-coated colloids with different packing fraction η , as indicated. Inset: Effective diffusion coefficient D_{eff} extracted from the mean squared displacements as a function of η for the samples in the main panel and for the system with 25 mM NaCl, as indicated. (B) Schematic diagram illustrating the morphological and structural evolution of samples as a function of increasing η , highlighting the combined effect of particle shrinking (red curve, representing the schematic evolution of the particle size) and blunt-end induced attractive interactions in determining the state diagram (sketches at the bottom) and in particular aggregation and re-entrant ordering of the structure (blue curve, representing the evolution of the structural parameters).

al., who showed that the effective interactions between colloidal particles similar to SPBs scale linearly with the number of absorbed counterions.⁴⁵ Since the number of the absorbed counterions in the experimental brushes must be of the order of $Nf \approx 10^9$, we conclude that even small brush overlaps are penalized with energies that are orders of magnitude larger than thermal fluctuations. Note that for the described conditions the interaction can be conveniently modeled by any steeply diverging potential. This assumption is corroborated by the experimental findings of ref 33 where it was shown that dsDNA-coated colloids densely packed on a 2D lattice are resilient to mutual interpenetration of their charged coronas. Moreover, the Lennard-Jones term in eq 7

features an attractive well with a range corresponding to a fraction of σ . This short-ranged attraction is used to model interactions between dsDNA fragments when particles approach each other to close proximity, caused by the blunt DNA-end, as discussed in the previous section. The second term in eq 7 is of a repulsive Yukawa form that models a weak residual electrostatic repulsion between the almost fully neutralized SPBs.

The potential of eq 7 has been used to investigate aggregation phenomena in 3D colloidal systems, showing that the competition between short-range attraction and midrange repulsion drives the formation of aggregates. Similar interactions have been also used to study the phase behavior of

2D colloidal systems.⁴⁹ The choice of the potential parameters, V_1 , V_2 , and λ , determines the morphology of the aggregates.^{50,51} In the simulations based on the potential of eq 7, the experimentally observed size reduction of the particles was included by using the values of the experimental particle diameter as a function of the packing fraction η in Figure 1C. Potentials with different sets of V_1 , V_2 , and λ values were generated. The potential generating the $g(r)$ that shows reasonable, semiquantitative agreement with experiments was chosen as the most representative of the interactions in the experimental system.

The pair potential is reported in Figure 5A and was obtained for $V_1/(k_B T) = 1.43$; $V_2/(k_B T) = 0.28$; $\lambda/\sigma_0 = 1.5$. Although we have not attempted a microscopic derivation for the values of the parameters used, it is possible to offer plausibility arguments for the resulting values on the basis of physical argumentation. The parameter $V_1/(k_B T)$ sets the scale of the attraction, which, as suggested in the previous section, is caused by end-to-end stacking of the dsDNA blunt ends and is expected to be of the order of the thermal energy. The obtained value of $1.43k_B T$ is in very good agreement with this expectation and supports our interpretation about the origin of the attractive interaction. On the other hand, the value of the parameter V_2 is set by the overall SPB charge, which is very low for osmotic brushes and thus a small value results. Finally, the screening length λ is set by the radius of the Wigner–Seitz cell, which is somewhat larger than the brush size in the concentrations under consideration.

The obtained particle configurations were used to determine the corresponding $g(r)$ which are presented in Figure 5B for the investigated values of η . A nonmonotonic behavior of the height of the first peak, g_p , for packing fractions in the range $0.7 < \eta < 0.8$, Figure 5B, is observed, in qualitative agreement with the experimental findings. The re-entrance is also reflected in the nonmonotonicity of the 6-fold order parameter $\langle \Psi_6 \rangle$, Figure 5C. Finally, the snapshots of the simulated systems (Figure 5D) show the presence of chainlike structures and aggregates comparable to those found in experiments. The simulations thus confirm that attractions, which induce aggregation, are a key ingredient to explain the re-entrant ordering phenomenon. Therefore, we conclude that re-entrant ordering is determined by two mechanisms: The formation of aggregates and size reduction due to deswelling. At larger packing fractions, particles get more ordered and progressively shrink; at the same time, attraction induces formation of aggregates. When the aggregates become locally denser than the average packing fraction, a pronounced shrinking occurs, which leads to a sudden disordering. Aggregates are disrupted and the local packing decreases, allowing the particles to rearrange configurations and partially reswell. Further increasing the packing fraction, the order increases again until crystallization occurs. It is interesting to note that a nonmonotonic variation of g_p at packing fractions in the range $0.7 < \eta < 0.9$ can also be found in Monte Carlo simulations in which a monotonic decrease of particle size similar to that predicted by theory is assumed, even though the agreement with experiments is poorer (results not shown). This suggests that there is a critical packing fraction, which depends on the degree of deswelling, at which a restructuring into a more disordered structure is needed to be able to pack additional particles. We remark also that the re-entrant behavior is only found in a very narrow range of potential parameters. Finally, the re-entrant behavior observed for the

investigated family of interaction potentials is in qualitative agreement with previous work on 2D colloidal dispersions with competing interactions.^{52,53}

Experiments: Dynamics as a Function of Packing Fraction. The structural variations observed with increasing packing fraction, and in particular the aggregation phenomena assigned to the interactions between dsDNA fragments of contacting brushes, should also affect the dynamical behavior of suspensions. In particular, the presence of particle aggregates should induce a slowdown of the average single-particle dynamics. To test our expectations, we determined the mean-squared displacement (MSD) of samples with different packing fractions, $\langle \Delta r^2(\Delta t) \rangle = \langle (r_i(\Delta t + t_0) - r_i(t_0))^2 \rangle_{t_0}$, where r_i is the position of particle i , Δt is the delay time, t_0 is the time during the particle trajectory, and $\langle \rangle_{t_0}$ indicates an average over all times t_0 and all particles i . We show the resulting MSD for several packing fractions in Figure 6A. All trajectories were corrected for the possible presence of drift due to stage instabilities: despite this correction, the apparent superdiffusive behavior at very short times might be the result of residual drift contributions.

Samples with $\eta \leq 0.56$ show approximately diffusive dynamics at long times, as indicated by the almost linear dependence of the MSD on t . Aggregation in the form of chainlike structures observed for $\eta = 0.40$ leads to a significant slowdown of the dynamics and smaller values of the MSD, while a slightly larger MSD is obtained for $\eta = 0.56$. This corresponds to the transition to a more uniform spatial distribution of particles with less aggregates. Similarly, a considerably smaller MSD is observed at $\eta = 0.68$ and 0.73 : in particular, the MSDs become subdiffusive, in agreement with the formation of a large number of aggregates in which particle movements are suppressed. The MSD presents a larger value and a time dependence approaching that expected for diffusion for $\eta = 0.87$, while a significantly smaller and subdiffusive MSD is obtained for $\eta = 1.20$. For the latter, the presence of a large number of crystalline regions is at the origin of the slow dynamics. The inset of Figure 6A reports an effective diffusion coefficient calculated as $D_{\text{eff}} = \Delta r^2(\Delta t \approx 55s)/4\Delta t$, which summarizes the behavior illustrated above for the MSD, and which confirms the correspondence between the structural variations and the evolution of the dynamics. The MSDs of samples with 25 mM NaCl are reported in Figure S3. Similar to what was discussed for the $g(r)$, also the dynamics of the system with salt show a smoother slowdown with increasing η , as shown in the inset of Figure 6A. The data of Figure 6A also confirm what was anticipated when discussing the possibility of brush shrinking and/or deformation with increasing packing fraction: For all samples, except the crystalline state for $\eta = 1.20$, the MSD shows a diffusive or moderately subdiffusive behavior, indicating that dynamical arrest is not occurring even at large packing fractions. This supports the scenario of progressive shrinking of the brushes rather than deformation.

CONCLUSIONS

We report unconventional effects of packing on the morphology and interactions of thick, dense spherical dsDNA brushes in planar confinement. These are schematically summarized in Figure 6B. Combining experiments and theory we showed that the large number of free (entropically active) counterions absorbed within a dense brush in the osmotic regime produces a huge entropic pressure which leads

to the progressive shrinking of neighbor brushes with increasing packing fraction. Interestingly, shrinking occurs without significant interdigitation of the brushes and starts well below space filling. Moreover, the absence of dynamical arrest, even for large packing fractions, suggests that shrinking prevents jamming and significant particle deformation. These findings mark a pronounced difference with the behavior of uncharged hairy colloids, where interdigitation is especially relevant,⁵⁴ but also of neutral and charged microgel particles, in which deswelling occurs above space filling or even at larger packings.⁵⁵ As demonstrated in previous experimental and theoretical studies on planar polyelectrolyte brushes, a small degree of interdigitation plays a fundamental role in maintaining the lubrication between contacting brushes under high loads. SPBs find application as lubrication additives in biological environments.^{56,57} Our study, indicating shrinking in the absence of interdigitation of SPBs with increasing packing, suggests that low friction is expected between highly crowded brushes, a condition which is relevant for the applications mentioned above, in which SPBs dispersions are typically strongly confined. The lubrication between brushes is also supported by the dynamics of the system, which do not fully arrest even for highly crowded conditions.

The isotropic repulsive interactions derived in the theory for generic polyelectrolyte brushes do not entirely explain the structural evolution of the increasingly packed spherical dsDNA brushes. Aggregation phenomena in the form of chainlike structures and nonmonotonic shrinking are observed experimentally and were reproduced in simulations by considering an additional short-range attractive interaction, in competition with electrostatic repulsion. We explained the origin of this attraction in terms of base stacking forces between blunt ends of dsDNA fragments, which become particularly important when osmotic brushes are densely packed. In these conditions a large number of blunt ends from neighboring brushes lie at short distance and can attract each other, leading to an effective additional short-range attraction between the particles that drives assembly. This effective attraction induced by blunt-end interactions can be tuned by addition of salt, as demonstrated here, and potentially by temperature, grafting density and the type of free-end modification of the DNA brushes.⁵⁸ Colloidal assembly exploiting DNA hybridization of single-stranded DNA or sticky ends has been largely investigated during the last years,²⁶ mainly for assembling crystals^{59,60} but also nonequilibrium gels.⁶¹ However, it was found that assembling structures with a higher degree of complexity than those also obtained with more conventional colloids, and with a programmable approach similar to that used in DNA nanotechnology, is an extremely demanding task. As mentioned in the introduction, blunt-end base stacking has been shown to be especially powerful in DNA nanotechnology in combination with shape design^{62,63} but is almost unexploited in colloidal assembly. We can foresee that engineering the DNA blunt-ends through careful design of the PCR primers and control over their spatial distribution can allow the orthogonal programming of the directionality and strength of the interactions between dsDNA grafted colloids. The experimental realization of such patchy spherical DNA-based brushes will provide the basis for the development of innovative self-assembly platforms that combine directionality and sequence complementarity of DNA fragments. This may be used to guide the organization of colloidal materials with unique plasmonic^{64,65} and photonic

properties,⁶⁶ thanks also to the possibility of easily changing the material and shape of the colloidal core,^{67,68} and thus the responsiveness to external fields.

METHODS

Synthesis of DNA Star Polyelectrolyte Colloids and Dispersions' Preparation. The procedure to obtain DNA star polyelectrolyte colloids was described in detail before.³³ Here, the main steps of the procedure are recalled. They can be summarized as follows: (i) synthesis of 10 kbp double-stranded DNA through the amplification of end-biotinylated fragments using the polymerase chain reaction (PCR) and (ii) grafting of DNA chains to the streptavidin functionalized surface of polystyrene beads ($R_{PS} = 0.49 \mu\text{m}$). In step (i) we amplified the end-biotinylated dsDNA fragments using a λ -DNA template (New England Biolabs) and a DNA polymerase enzyme contained in the Go Taq Long PCR Master Mix (Promega) and following the detailed PCR protocols accompanied by this product. End-functionalization of the dsDNA strands was achieved by the PCR using commercially synthesized and HPLC purified forward and reverse primers, modified at their 5'-ends (IDT). More specifically, for the aforementioned linear dsDNA fragments the forward primer was 5'-biotinylated, including an extended 15-atom spacer TEG (tetra-ethylene-glycol) in order to reduce steric hindrance and therefore increase the binding efficiency of the long dsDNA to the streptavidin coated PS beads (Bangs Laboratories). The reverse primers were unmodified. Grafting was obtained using a binding buffer (Dynabeads Kilobase binder Kit, Invitrogen). Biotin end-modified dsDNA fragments were mixed in a picomole range with the PS bead suspension in appropriate amounts to obtain a final volume of about 35 μL and incubated at room temperature under gentle rotation for 12 h in order to avoid sedimentation. The unreacted dsDNA fragments were removed using sequential washes with Milli-Q water. This can be easily achieved by centrifuging the suspension and by carefully pipetting off the supernatant and by finally resuspending the DNA coated beads to 40 μL Milli-Q water. This procedure was repeated three times. The number of attached dsDNA chains per bead (functionality f) was quantified, knowing the number of the beads (value that can be determined by the concentration of the stock bead solution) and the number of DNA chains in the reaction vial before the cleaning procedure. The DNA concentration was determined by measuring the absorbance at 260 nm employing a microvolume spectrometer (MicroDrop, ThermoScientific). Grafted particles were then dispersed in deionized water or a saline buffer solution containing 2.5×10^{-2} M of NaCl. Dispersions with different particle concentrations were obtained by diluting a sediment obtained by centrifugation. The average area packing fraction η of the confined dispersions was determined through the analysis of sample images by particle tracking. For each dispersion the results of the analysis of 1000 images were averaged.

Microscopy Experiments. Quasi-2D samples were obtained by confining the dispersions between a microscope slide and a #1 coverslip: The distance between slide and coverslip was controlled by means of a PET-based double-sided tape with thickness $h = 10 \mu\text{m}$ (No. 5601, Nitto). Glass surfaces were made hydrophobic by cleaning with Rain X solution (ITW Krafft) to avoid particle sticking to the glass. After depositing a 1.2 μL droplet of sample onto the microscope slide, the coverslip was uniformly pressed against the slide until the desired separation was reached and then successively glued on the sides using epoxy resin. Microscopy experiments were performed on a Nikon Ti-S inverted microscope using a Nikon 50x LWD objective (N.A. 0.9). For each sample, about 50 series of 1000 images of 1280 \times 1024 pixels were acquired at different locations in the sample using a 2.2Mp Pixelink M2 camera at a frame rate of 15fps. Particle coordinates were extracted from images using the Mosaic Suite for Fiji⁶⁹ while particle trajectories were determined using TrackMate.⁷⁰ Dedrifting procedures available in TrackMate were applied to sample trajectories before calculating the MSDs. In order to avoid sample degradation, experiments were run shortly after sample loading.

Monte Carlo Simulations. Monte Carlo (MC) simulations employing the standard Metropolis algorithm were performed for soft discs in two dimensions interacting with the pair potential of eq 7, cut off at a distance $r_c = 3.5\sigma$, at constant temperature. The parameters of the potential determining the strength of the short-ranged attraction and the long-ranged repulsion as well as its range are reported in Figure 5. The particles are contained in a box of dimensions $L_x = L_y = 20\sigma_0$. The number of particles is $N = \{196, 289, 342, 380, 441, 600\}$ in the systems with packing fraction $\eta = \{0.40, 0.57, 0.68, 0.73, 0.87, 1.17\}$, respectively. Data were gathered for simulation runs of 10^5 MC steps for packing fractions $\eta = 0.40$ and 0.57 ; 10^6 MC steps for $\eta = 0.68, 0.73$, and 0.87 ; and 2×10^6 MC steps for the system with $\eta = 1.17$. Equilibration is achieved after 20–50% of the given MC runs. The steric interaction diameter σ as a function of packing fraction is reported in the legend of Figure 5A.

ASSOCIATED CONTENT

Supporting Information

The Supporting Information is available free of charge at <https://pubs.acs.org/doi/10.1021/acsnano.1c07799>.

Additional renderings of experimental samples (Figure.S1), radial distribution functions and mean squared displacements for the system with 25 mM NaCl (Figures S2 and S3), theoretical details on the derivation of the free energy model, additional information and results of molecular dynamics simulations of the miniature brush (Figures S4 and S5) (PDF)

AUTHOR INFORMATION

Corresponding Authors

Marco Laurati – Dipartimento di Chimica & CSGI, Università di Firenze, 50019 Sesto Fiorentino, Italy; orcid.org/0000-0003-1334-5940; Email: marco.laurati@unifi.it

Christos N. Likos – Faculty of Physics, University of Vienna, A-1090 Vienna, Austria; orcid.org/0000-0003-3550-4834; Email: christos.likos@univie.ac.at

Authors

Ivany Romero-Sanchez – Dipartimento di Chimica & CSGI, Università di Firenze, 50019 Sesto Fiorentino, Italy; División de Ciencias e Ingenierías, Universidad de Guanajuato, 37150 León, Mexico

Ilian Pihlajamaa – Faculty of Physics, University of Vienna, A-1090 Vienna, Austria; Eindhoven University of Technology, Department of Applied Physics, Soft Matter and Biological Physics, NL-5600 MB Eindhoven, The Netherlands

Natasa Adžić – Faculty of Physics, University of Vienna, A-1090 Vienna, Austria; orcid.org/0000-0003-4189-4410

Laura E. Castellano – División de Ciencias e Ingenierías, Universidad de Guanajuato, 37150 León, Mexico; orcid.org/0000-0002-0969-3128

Emmanuel Stiakakis – Biomacromolecular Systems and Processes, Institute of Biological Information Processing (IBI-4), 4 Forschungszentrum Jülich, D-52425 Jülich, Germany; orcid.org/0000-0002-3845-3684

Complete contact information is available at: <https://pubs.acs.org/doi/10.1021/acsnano.1c07799>

Author Contributions

[#]I.R.-S. and I.P. contributed equally. I.R.-S. prepared samples, performed experiments, and analyzed the data. M.L., E.S., and L.-E.C. instructed sample preparation and experimental techniques and provided materials. I.P. and C.N.L. developed

the theoretical model of the PE-brush. I.P. performed the theoretical calculations and the single-brush MD simulations. N.A. performed the MC simulations of the effective model. All authors interpreted the results and wrote the paper. M.L. and C.N.L. designed the research. The manuscript was written through contributions of all authors. All authors have given approval to the final version of the manuscript.

Funding

Conacyt, “Consorzio per lo Sviluppo dei Sistemi a Grande Interfase” (CSGI), Austrian Science Fund (FWF), Deutsche Forschungsgemeinschaft (DFG).

Notes

The authors declare no competing financial interest.

ACKNOWLEDGMENTS

We thank R. Castañeda-Priego, R. Moctezuma-Martíñon, E. Zaccarelli, and P. van der Schoot for fruitful discussions. I.R.-S., L.-E.C. and M.L. acknowledge Conacyt for funding through grant A1-S-9098. M.L. and I.R.-S. acknowledge financial support from “Consorzio per lo Sviluppo dei Sistemi a Grande Interfase” (CSGI). N.A. and C.N.L. acknowledge support by the Austrian Science Fund (FWF) under Grant No. I 2866-N36. E.S. acknowledges financial support by the Deutsche Forschungsgemeinschaft (DFG) under grant STI 664/4-1.

REFERENCES

- (1) Ballauff, M.; Borisov, O. Polyelectrolyte Brushes. *Curr. Opin. Colloid Interface Sci.* **2006**, *11* (6), 316–323.
- (2) Das, S.; Banik, M.; Chen, G.; Sinha, S.; Mukherjee, R. Polyelectrolyte Brushes: Theory, Modelling, Synthesis and Applications. *Soft Matter* **2015**, *11* (44), 8550–8583.
- (3) Yang, W.; Zhou, F. Polymer Brushes for Antibiofouling and Lubrication. *Biosurface and Biotribology* **2017**, *3* (3), 97–114.
- (4) Wong, S. Y.; Han, L.; Timachova, K.; Veselinovic, J.; Hyder, M. N.; Ortiz, C.; Klibanov, A. M.; Hammond, P. T. Drastically Lowered Protein Adsorption on Microbicidal Hydrophobic/Hydrophilic Polyelectrolyte Multilayers. *Biomacromolecules* **2012**, *13* (3), 719–726.
- (5) Krishnamoorthy, M.; Hakobyan, S.; Ramstedt, M.; Gautrot, J. E. Surface-Initiated Polymer Brushes in the Biomedical Field: Applications in Membrane Science, Biosensing, Cell Culture, Regenerative Medicine and Antibacterial Coatings. *Chem. Rev.* **2014**, *114* (21), 10976–11026.
- (6) Wittemann, A.; Ballauff, M. Interaction of Proteins with Linear Polyelectrolytes and Spherical Polyelectrolyte Brushes in Aqueous Solution. *Phys. Chem. Chem. Phys.* **2006**, *8* (45), 5269–5275.
- (7) Wittemann, A.; Haupt, B.; Ballauff, M. Adsorption of Proteins on Spherical Polyelectrolyte Brushes in Aqueous Solution. *Phys. Chem. Chem. Phys.* **2003**, *5* (8), 1671–1677.
- (8) Lu, Y.; Ballauff, M. Spherical Polyelectrolyte Brushes as Nanoreactors for the Generation of Metallic and Oxidic Nanoparticles: Synthesis and Application in Catalysis. *Prog. Polym. Sci.* **2016**, *59*, 86–104.
- (9) Zhulina, E. B.; Rubinstein, M. Lubrication by Polyelectrolyte Brushes. *Macromolecules* **2014**, *47* (16), 5825–5838.
- (10) Raviv, U.; Giasson, S.; Kampf, N.; Gohy, J.-F.; Jérôme, R.; Klein, J. Lubrication by Charged Polymers. *Nature* **2003**, *425* (6954), 163–165.
- (11) Yu, J.; Jackson, N. E.; Xu, X.; Morgenstern, Y.; Kaufman, Y.; Ruths, M.; de Pablo, J. J.; Tirrell, M. Multivalent Counterions Diminish the Lubricity of Polyelectrolyte Brushes. *Science* **2018**, *360* (6396), 1434–1438.
- (12) Ballauff, M. More Friction for Polyelectrolyte Brushes. *Science* **2018**, *360* (6396), 1399–1400.

- (13) Seror, J.; Zhu, L.; Goldberg, R.; Day, A. J.; Klein, J. Supramolecular Synergy in the Boundary Lubrication of Synovial Joints. *Nat. Commun.* **2015**, *6* (1), 6497.
- (14) Macdonald, M. L.; Samuel, R. E.; Shah, N. J.; Padera, R. F.; Beben, Y. M.; Hammond, P. T. Tissue Integration of Growth Factor-Eluting Layer-by-Layer Polyelectrolyte Multilayer Coated Implants. *Biomaterials* **2011**, *32* (5), 1446–1453.
- (15) Drummond, T. G.; Hill, M. G.; Barton, J. K. Electrochemical DNA Sensors. *Nat. Biotechnol.* **2003**, *21* (10), 1192–1199.
- (16) Maune, H. T.; Han, S.; Barish, R. D.; Bockrath, M.; Goddard, W. A., III; Rothmund, P. W. K.; Winfree, E. Self-Assembly of Carbon Nanotubes into Two-Dimensional Geometries Using DNA Origami Templates. *Nat. Nanotechnol.* **2010**, *5* (1), 61–66.
- (17) Tjong, V.; Tang, L.; Zauscher, S.; Chilkoti, A. Smart² DNA Interfaces. *Chem. Soc. Rev.* **2014**, *43* (5), 1612–1626.
- (18) Seeman, N. C.; Sleiman, H. F. DNA Nanotechnology. *Nat. Rev. Mater.* **2018**, *3* (1), 17068.
- (19) Rothmund, P. W. K. Folding DNA to Create Nanoscale Shapes and Patterns. *Nature* **2006**, *440* (7082), 297–302.
- (20) Chidchob, P.; Sleiman, H. F. Recent Advances in DNA Nanotechnology. *Curr. Opin. Chem. Biol.* **2018**, *46*, 63–70.
- (21) Nakata, M.; Zanchetta, G.; Chapman, B. D.; Jones, C. D.; Cross, J. O.; Pindak, R.; Bellini, T.; Clark, N. A. End-to-End Stacking and Liquid Crystal Condensation of 6- to 20-Base Pair DNA Duplexes. *Science* **2007**, *318* (5854), 1276–1279.
- (22) Kilchherr, F.; Wachauf, C.; Pelz, B.; Rief, M.; Zacharias, M.; Dietz, H. Single-Molecule Dissection of Stacking Forces in DNA. *Science* **2016**, *353* (6304), aaf5508.
- (23) Salamonczyk, M.; Zhang, J.; Portale, G.; Zhu, C.; Kentzinger, E.; Gleeson, J. T.; Jakli, A.; De Michele, C.; Dhont, J. K. G.; Sprunt, S.; Stiakakis, E. Smectic Phase in Suspensions of Gapped DNA Duplexes. *Nat. Commun.* **2016**, *7* (1), 13358.
- (24) Jones, M. R.; Mirkin, C. A. Self-Assembly Gets New Direction. *Nature* **2012**, *491* (7422), 42–43.
- (25) Zhang, X.; Wang, R.; Xue, G. Programming Macro-Materials from DNA-Directed Self-Assembly. *Soft Matter* **2015**, *11* (10), 1862–1870.
- (26) Rogers, W. B.; Shih, W. M.; Manoharan, V. N. Using DNA to Program the Self-Assembly of Colloidal Nanoparticles and Microparticles. *Nat. Rev. Mater.* **2016**, *1* (3), 16008.
- (27) Michele, L. Di; Eiser, E. Developments in Understanding and Controlling Self Assembly of DNA-Functionalized Colloids. *Phys. Chem. Chem. Phys.* **2013**, *15* (9), 3115–3129.
- (28) Tan, S. J.; Kahn, J. S.; Derrien, T. L.; Campolongo, M. J.; Zhao, M.; Smilgies, D.-M.; Luo, D. Crystallization of DNA-Capped Gold Nanoparticles in High-Concentration, Divalent Salt Environments. *Angew. Chemie Int. Ed.* **2014**, *53* (5), 1316–1319.
- (29) Pelaez-Fernandez, M.; Souslov, A.; Lyon, L. A.; Goldbart, P. M.; Fernandez-Nieves, A. Impact of Single-Particle Compressibility on the Fluid-Solid Phase Transition for Ionic Microgel Suspensions. *Phys. Rev. Lett.* **2015**, *114* (9), 98303.
- (30) Scotti, A.; Gasser, U.; Herman, E. S.; Pelaez-Fernandez, M.; Han, J.; Menzel, A.; Lyon, L. A.; Fernández-Nieves, A. The Role of Ions in the Self-Healing Behavior of Soft Particle Suspensions. *Proc. Natl. Acad. Sci. U. S. A.* **2016**, *113* (20), 5576–5581.
- (31) de With, A.; Greulich, K. O. Wavelength Dependence of Laser-Induced DNA Damage in Lymphocytes Observed by Single-Cell Gel Electrophoresis. *J. Photochem. Photobiol., B* **1995**, *30* (1), 71–76.
- (32) Repula, A.; Oshima Menegon, M.; Wu, C.; van der Schoot, P.; Grelet, E. Directing Liquid Crystalline Self-Organization of Rodlike Particles through Tunable Attractive Single Tips. *Phys. Rev. Lett.* **2019**, *122* (12), 128008.
- (33) Zhang, J.; Lettinga, P. M.; Dhont, J. K. G.; Stiakakis, E. Direct Visualization of Conformation and Dense Packing of DNA-Based Soft Colloids. *Phys. Rev. Lett.* **2014**, *113* (26), 268303.
- (34) Moreno-Guerra, J. A.; Romero-Sánchez, I. C.; Martínez-Borquez, A.; Tassieri, M.; Stiakakis, E.; Laurati, M. Model-Free Rheo-AFM Probes the Viscoelasticity of Tunable DNA Soft Colloids. *Small* **2019**, *15* (42), 1904136.
- (35) Likos, C. N. Effective Interactions in Soft Condensed Matter Physics. *Phys. Rep.* **2001**, *348* (4), 267–439.
- (36) Seth, J. R.; Mohan, L.; Locatelli-Champagne, C.; Cloitre, M.; Bonnecaze, R. T. A Micromechanical Model to Predict the Flow of Soft Particle Glasses. *Nat. Mater.* **2011**, *10* (11), 838–843.
- (37) Bouhid de Aguiar, I.; van de Laar, T.; Meireles, M.; Bouchoux, A.; Sprakel, J.; Schroën, K. Deswelling and Deformation of Microgels in Concentrated Packings. *Sci. Rep.* **2017**, *7* (1), 10223.
- (38) Gasser, U.; Hyatt, J. S.; Lieter-Santos, J.-J.; Herman, E. S.; Lyon, L. A.; Fernandez-Nieves, A. Form Factor of PNIPAM Microgels in Overpacked States. *J. Chem. Phys.* **2014**, *141* (3), 34901.
- (39) Conley, G. M.; Aebischer, P.; Nöjd, S.; Schurtenberger, P.; Scheffold, F. Jamming and Overpacking Fuzzy Microgels: Deformation, Interpenetration, and Compression. *Sci. Adv.* **2017**, *3* (10), e1700969.
- (40) Conley, G. M.; Zhang, C.; Aebischer, P.; Harden, J. L.; Scheffold, F. Relationship between Rheology and Structure of Interpenetrating, Deforming and Compressing Microgels. *Nat. Commun.* **2019**, *10* (1), 2436.
- (41) Nikolov, S. V.; Fernandez-Nieves, A.; Alexeev, A. Behavior and Mechanics of Dense Microgel Suspensions. *Proc. Natl. Acad. Sci. U. S. A.* **2020**, *117* (44), 27096–27103.
- (42) Nöjd, S.; Holmqvist, P.; Boon, N.; Obiols-Rabasa, M.; Mohanty, P. S.; Schweins, R.; Schurtenberger, P. Deswelling Behaviour of Ionic Microgel Particles from Low to Ultra-High Densities. *Soft Matter* **2018**, *14* (20), 4150–4159.
- (43) Manning, G. S. Limiting Laws and Counterion Condensation in Polyelectrolyte Solutions I. Colligative Properties. *J. Chem. Phys.* **1969**, *51* (3), 924–933.
- (44) Rubinstein, M.; Colby, R. H. *Polymer Physics*; OUP: Oxford, 2003.
- (45) Jusufi, A.; Likos, C. N.; Ballauff, M. Counterion Distributions and Effective Interactions of Spherical Polyelectrolyte Brushes. *Colloid Polym. Sci.* **2004**, *282* (8), 910–917.
- (46) Wilk, A.; Huißmann, S.; Stiakakis, E.; Kohlbrecher, J.; Vlassopoulos, D.; Likos, C. N.; Meier, G.; Dhont, J. K. G.; Petekidis, G.; Vavrin, R. Osmotic Shrinkage in Star/Linear Polymer Mixtures. *Eur. Phys. J. E* **2010**, *32* (2), 127–134.
- (47) Maffeo, C.; Luan, B.; Aksimentiev, A. End-to-End Attraction of Duplex DNA. *Nucleic Acids Res.* **2012**, *40* (9), 3812–3821.
- (48) De Michele, C. Theory of Self-Assembly-Driven Nematic Liquid Crystals Revised. *Liq. Cryst.* **2019**, *46* (13–14), 2003–2012.
- (49) Chacko, B.; Chalmers, C.; Archer, A. J. Two-Dimensional Colloidal Fluids Exhibiting Pattern Formation. *J. Chem. Phys.* **2015**, *143* (24), 244904.
- (50) Mossa, S.; Sciortino, F.; Tartaglia, P.; Zaccarelli, E. Ground-State Clusters for Short-Range Attractive and Long-Range Repulsive Potentials. *Langmuir* **2004**, *20* (24), 10756–10763.
- (51) Sciortino, F.; Mossa, S.; Zaccarelli, E.; Tartaglia, P. Equilibrium Cluster Phases and Low-Density Arrested Disordered States: The Role of Short-Range Attraction and Long-Range Repulsion. *Phys. Rev. Lett.* **2004**, *93* (5), 55701.
- (52) Reinhardt, A.; Williamson, A. J.; Doye, J. P. K.; Carrete, J.; Varela, L. M.; Louis, A. A. Re-Entrant Phase Behavior for Systems with Competition between Phase Separation and Self-Assembly. *J. Chem. Phys.* **2011**, *134* (10), 104905.
- (53) Almaraz, N. G.; Pękalski, J.; Ciach, A. Periodic Ordering of Clusters and Stripes in a Two-Dimensional Lattice Model. II. Results of Monte Carlo Simulation. *J. Chem. Phys.* **2014**, *140* (16), 164708.
- (54) Vlassopoulos, D. Colloidal Star Polymers: Models for Studying Dynamically Arrested States in Soft Matter. *J. Polym. Sci., Part B: Polym. Phys.* **2004**, *42* (16), 2931–2941.
- (55) Scheffold, F. Pathways and Challenges towards a Complete Characterization of Microgels. *Nat. Commun.* **2020**, *11* (1), 4315.
- (56) Ma, S.; Zhang, X.; Yu, B.; Zhou, F. Brushing up Functional Materials. *NPG Asia Mater.* **2019**, *11* (1), 24.
- (57) Liu, G.; Cai, M.; Zhou, F.; Liu, W. Charged Polymer Brushes-Grafted Hollow Silica Nanoparticles as a Novel Promising Material

for Simultaneous Joint Lubrication and Treatment. *J. Phys. Chem. B* **2014**, *118* (18), 4920–4931.

(58) Gvozden, K.; Novak Ratajczak, S.; Orellana, A. G.; Kentzinger, E.; Rücker, U.; Dhont, J. K. G.; De Michele, C.; Stiakakis, E. Self-Assembly of All-DNA Rods with Controlled Patchiness. *Small* **2022**, *18*, 2104510.

(59) Nykypanchuk, D.; Maye, M. M.; van der Lelie, D.; Gang, O. DNA-Guided Crystallization of Colloidal Nanoparticles. *Nature* **2008**, *451* (7178), 549–552.

(60) Macfarlane, R. J.; Lee, B.; Jones, M. R.; Harris, N.; Schatz, G. C.; Mirkin, C. A. Nanoparticle Superlattice Engineering with DNA. *Science* **2011**, *334* (6053), 204–208.

(61) Di Michele, L.; Varrato, F.; Kotar, J.; Nathan, S. H.; Foffi, G.; Eiser, E. Multistep Kinetic Self-Assembly of DNA-Coated Colloids. *Nat. Commun.* **2013**, *4* (1), 2007.

(62) Woo, S.; Rothmund, P. W. K. Programmable Molecular Recognition Based on the Geometry of DNA Nanostructures. *Nat. Chem.* **2011**, *3* (8), 620–627.

(63) Gerling, T.; Wagenbauer, K. F.; Neuner, A. M.; Dietz, H. Dynamic DNA Devices and Assemblies Formed by Shape-Complementary, Non-Base Pairing 3D Components. *Science* **2015**, *347* (6229), 1446–1452.

(64) Fan, J. A.; Wu, C.; Bao, K.; Bao, J.; Bardhan, R.; Halas, N. J.; Manoharan, V. N.; Nordlander, P.; Shvets, G.; Capasso, F. Self-Assembled Plasmonic Nanoparticle Clusters. *Science* **2010**, *328* (5982), 1135–1138.

(65) Kuzyk, A.; Schreiber, R.; Zhang, H.; Govorov, A. O.; Liedl, T.; Liu, N. Reconfigurable 3D Plasmonic Metamolecules. *Nat. Mater.* **2014**, *13* (9), 862–866.

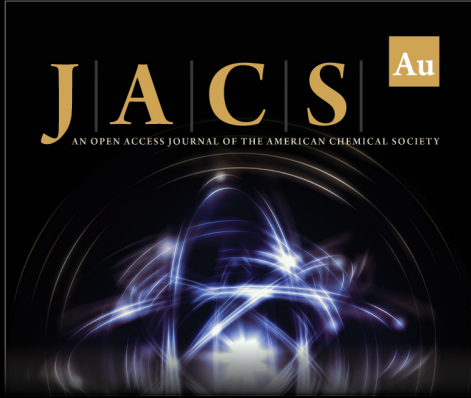
(66) Sun, D.; Tian, Y.; Zhang, Y.; Xu, Z.; Sfeir, M. Y.; Cotlet, M.; Gang, O. Light-Harvesting Nanoparticle Core-Shell Clusters with Controllable Optical Output. *ACS Nano* **2015**, *9* (6), 5657–5665.

(67) Grzelczak, M.; Pérez-Juste, J.; Mulvaney, P.; Liz-Marzán, L. M. Shape Control in Gold Nanoparticle Synthesis. *Chem. Soc. Rev.* **2008**, *37* (9), 1783–1791.

(68) Sacanna, S.; Korpics, M.; Rodriguez, K.; Colón-Meléndez, L.; Kim, S.-H.; Pine, D. J.; Yi, G.-R. Shaping Colloids for Self-Assembly. *Nat. Commun.* **2013**, *4* (1), 1688.


(69) Sbalzarini, I. F.; Koumoutsakos, P. Feature Point Tracking and Trajectory Analysis for Video Imaging in Cell Biology. *J. Struct. Biol.* **2005**, *151* (2), 182–195.


(70) Tinevez, J.-Y.; Perry, N.; Schindelin, J.; Hoopes, G. M.; Reynolds, G. D.; Laplantine, E.; Bednarek, S. Y.; Shorte, S. L.; Eliceiri, K. W. TrackMate: An Open and Extensible Platform for Single-Particle Tracking. *Methods* **2017**, *115*, 80–90.



JACS Au
AN OPEN ACCESS JOURNAL OF THE AMERICAN CHEMICAL SOCIETY

Editor-in-Chief
Prof. Christopher W. Jones
Georgia Institute of Technology, USA

Open for Submissions 

pubs.acs.org/jacsau  ACS Publications
Most Trusted. Most Cited. Most Read.

Charge regulation in ionic solutions: Thermal fluctuations and Kirkwood-Schumaker interactionsNataša Adžić^{1,*} and Rudolf Podgornik^{1,2}¹*Department of Theoretical Physics, J. Stefan Institute, 1000 Ljubljana, Slovenia*²*Department of Physics, Faculty of Mathematics and Physics, University of Ljubljana, 1000 Ljubljana, Slovenia*

(Received 21 December 2014; published 24 February 2015)

We study the behavior of two macroions with dissociable charge groups, regulated by local variables such as pH and electrostatic potential, immersed in a monovalent salt solution, considering cases where the net charge can either change sign or remain of the same sign depending on these local parameters. The charge regulation in both cases is described by the proper free-energy function for each of the macroions, while the coupling between the charges is evaluated on the approximate Debye-Hückel level. The charge correlation functions and the ensuing charge fluctuation forces are calculated analytically and numerically. Strong attraction between like-charged macroions is found close to the point of zero charge, specifically due to asymmetric, anticorrelated charge fluctuations of the macroion charges. The general theory is then implemented for a system of two proteinlike macroions, generalizing the form and magnitude of the Kirkwood-Schumaker interaction.

DOI: [10.1103/PhysRevE.91.022715](https://doi.org/10.1103/PhysRevE.91.022715)

PACS number(s): 87.15.km, 78.30.cd

I. INTRODUCTION

From the point of view of electrostatic interactions, proteins, such as ampholytes, are challenging objects since they carry a nonconstant charge, dependent on dissociation of chargeable molecular moieties such as N and C terminals as well as the (de)protonation of amino acid side groups [1–3]. Consequently, their behavior cannot be analyzed with the assumption of a constant charge [4], otherwise applicable for many (bio)colloidal systems [5], since it misses the crucial contribution of charge regulation and charge fluctuations to the interactions between macroions [6]. In fact, it has been known for some time that extremely-long-ranged attractive interactions occur between proteins in an aqueous solution with dissociable charge groups (amino acids) on the surface, close to their point of zero charge (PZC), as first elucidated by Kirkwood and Shumaker [7,8]. The Kirkwood-Shumaker (KS) derivation is based on the thermodynamic perturbation theory around a noninteracting state that takes into account protein charge fluctuations. In the case of no ionic screening, apart from the usual Coulomb interaction, they also obtain a fluctuation interaction that scales as an inverse second power of the separation between the macroions. This scaling form is fundamentally different from the van der Waals interactions, exhibiting an inverse sixth power [9], that stem from dipolar fluctuations and act between electroneutral bodies. In fact, it can be shown that it is a consequence of the monopolar charge fluctuations and does not exist for macroions with a strictly fixed charge distribution. Kirkwood-Shumaker interaction pertains only to systems with flexible charge equilibrium that possess a nonzero capacitance, where the net charge is not a constant but depends on the underlying dissociation processes [10], implying furthermore that the effective charge on the macroion, e.g. the protein surface, is regulated and responds to the local solution conditions: pH , electrostatic potential, salt concentration, spatial dielectric constant profile, and the presence of other vicinal charged groups [11]. While the effects of charge regulation were analyzed on various levels

in the mean-field approximation [10,12–18], the fluctuation effects have not received a proportional amount of attention.

Recently, the KS theory experienced renewed interest when it was shown, using detailed Monte Carlo simulations [19], that indeed there exists an interaction between proteins that has the same salient features as the original approximate form of the KS interaction. An important step further was achieved by consistently including the charge-regulation free energy [10], derivable from the Parsegian-Ninham model [20], in the theoretical framework that allowed one to derive analytically and exactly the interaction free energy on the Gaussian fluctuation level [21], leading to an exact form of the KS interaction for the three-dimensional system with planar geometry. The full exact solutions for charge-regulation interaction, beyond the Gaussian fluctuation ansatz, have been found also in the case of a family of one-dimensional models solvable by the transfer-matrix formalism [22].

The aim of this paper is to present an improved theory of fluctuation interaction for two small and distant spherical macroions subject to charge regulation. The problem is formulated in a way that allows for decoupling of the charge-regulation part and the interaction part, of which the former can be treated exactly while the latter can be dealt with on the Debye-Hückel (DH) level. This allows us to derive a closed-form expression for the total interaction and compare it with various approximate forms, including the original KS expression. We show that our generalized fluctuation interaction reduces exactly to the KS result in the limit of large separations between macroions, where the macroion charge autocorrelation function is assumed to be independent of the separation between them, consistent with the original KS perturbation theory derivation. This assumption, implicit in the original KS derivation, breaks down for any finite separation. Apart from going beyond this limitation of the original theory of KS interactions, we are also able to go beyond the KS result in terms of deriving realistic pH and ionic-strength-dependent interactions between protein macroions with known amino acid composition.

The paper is arranged as follows. In Sec. II we introduce a model consisting of two spherical macroions immersed in a monovalent salt solution, with charge-regulated surface

*natasa.adzic@ijs.si

charges described with an appropriate free-energy term. The theory of electrostatic interactions for such a system is derived using the field-theoretic approach, described in Appendix A. Three different cases of charge regulation are considered (Sec. III): a fully symmetric system, consisting of two identical macroions with both charges spanning the interval $[-e, e]$; a semisymmetric system, composed of two identical macroions with charges spanning the asymmetric interval $[-e, (\alpha - 1)e]$ ($\alpha > 1$); and a completely asymmetric system composed of one negative and one positive macroion with charges $[-e, 0]$ and $[0, e]$, respectively. For all three cases we calculate the average charge, the charge-charge cross-correlation function, the charge-charge autocorrelation function, and the total interaction potential obtained numerically using the exact evaluation of the full partition function as well as via two simplifying and illuminating approximation methods (Sec. IV): the saddle-point method and the Gaussian approximation method, both giving an analytical closed form for the full charge-regulation interaction, including the thermal fluctuations. In Sec. V we show how this theory can be generalized to be applicable to a system of proteinlike macroions with specific amino acid composition. In Sec. VI we present a summary and comment on the connection with experiments and simulations.

II. MODEL

We consider a model system composed of two charged spherical macroions in a 1:1 salt solution (Fig. 1). The charge of the macroions is not constant, but is described by a dissociation surface free-energy density cost corresponding to the Parsegian-Ninham charge-regulation model, as discussed in [21], of the general lattice-gas form

$$f_0(\varphi(\vec{r})) = i\sigma_0\varphi(\vec{r}) - \alpha k_B T \frac{\sigma_0}{e_0} \ln(1 + be^{i\beta e_0\varphi(\vec{r})}), \quad (1)$$

where e_0 is the elementary charge, β is the inverse of the thermal energy $k_B T$. α quantifies the number of dissociation sites, and $\ln b = \beta\mu_S$, where μ_S is the free energy of charge

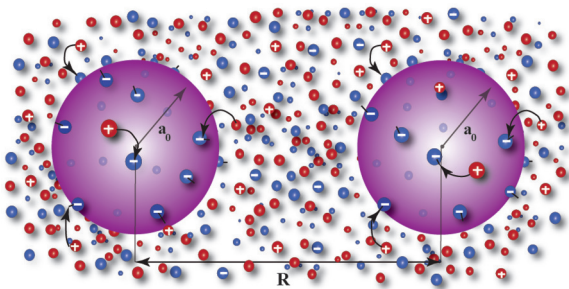


FIG. 1. (Color online) Schematic representation of the model: two charge-regulated macroions immersed in a 1:1 salt solution, with positive and negative ions indicated in red and blue, respectively. The dissociation sites and the dissociation process itself at the surface of the macroions are indicated with arrows. The solution is composed of salt ions that can be exchanged with the surface sites. In the Ninham-Parsegian model of charge regulation, the charge group dissociation proceeds through (de)protonation of the dissociable charge groups. In the case of proteins these are the dissociable amino acids.

dissociation. In the case of protonation of the surface charge one furthermore has $\ln b = -\ln 10(pH - pK)$ [21], where pK is the dissociation constant and pH indicates its value in the bulk, differing from the local value of pH at the dissociation sites exactly by the value of the local electrostatic potential, as implied by the second term in the logarithmic function of the above equation. The local electrostatic potential also depends on the ionic strength of the solution as well as on the vicinity of other dissociable charge groups or macroions [16].

Above $\varphi(\vec{r})$ is the local fluctuating potential that needs to be integrated over to get the final partition function. The mean-field Poisson-Boltzmann (PB) approximation is obtained by identifying $\varphi(\vec{r}) \rightarrow i\phi = i\phi_{PB}$ [21]. The total dissociation free energy for a spherical macroion of radius a_0 , sufficiently small so that one can assume that the electrostatic potential is uniform over its surface $\varphi(|\vec{r}| = a_0) = \varphi$, can be written in the form

$$f(\varphi) = \oint_S f_0(\varphi(\vec{r})) d^2\vec{r} \rightarrow iNe_0\varphi - \alpha k_B T N \ln(1 + be^{i\beta e_0\varphi}), \quad (2)$$

where N is the number of absorption sites satisfying $\int dS \sigma_0 = Ne_0$ and $\alpha > 1$ is a coefficient of asymmetry determining the width of the interval spanned by the particle's effective charge $e(\phi)$ as a function of the mean-field potential on its surface $\phi = \phi(a_0)$:

$$e(\phi = \phi(a_0)) = \frac{\partial f(\phi)}{\partial \phi} = e_0 N \left[\frac{\alpha}{2} - 1 - \frac{\alpha}{2} \tanh \left(-\frac{1}{2} (\ln b - \beta e_0 \phi) \right) \right]. \quad (3)$$

The effective charge of the macroion can thus fluctuate in the interval $-Ne_0 < e < (\alpha - 1)Ne_0$, $\alpha > 1$. When $\alpha = 2$ the charge interval is by definition symmetric $[-Ne_0, Ne_0]$. All of the expressions for the charge regulation referred to above are just variants of the surface lattice-gas free energies [21] with a variable number of dissociation sites that describe the dissociation of the charge moieties on the surface of the macroions. In addition we have taken the limit of small macroions, implying that the surface potential on the macroions is a constant $f(\varphi) = \oint_{|\vec{r}|=a_0} f_0(\varphi(\vec{r})) d^2\vec{r}$.

Assuming that the fluctuating electrostatic potential of one macroion is $\phi_1(a) = \varphi_1$ and of the other one is $\phi_2(a) = \varphi_2$, located at \vec{r}_1 and \vec{r}_2 , respectively, the partition function of the system can be derived in the field-theoretic form (see Appendix A)

$$\mathcal{Z} = \int \int d\varphi_1 e^{-\beta f(\varphi_1)} G(\varphi_1, \varphi_2) e^{-\beta f(\varphi_2)} d\varphi_2, \quad (4)$$

where the partition function has already been normalized by dividing by the bulk system partition function [23], obtained for $f(\varphi) = 0$, and $G(\varphi_1, \varphi_2)$ is the propagator of the field, defined with the values of the potential φ_1 and φ_2 at the location of the first and the second particle, respectively, derived in

Appendix A:

$$G(\varphi_1, \varphi_2) = \exp \left[-\frac{\beta}{2} \begin{pmatrix} \varphi_1 \\ \varphi_2 \end{pmatrix}^T \begin{pmatrix} G(\vec{r}_1, \vec{r}_1) & G(\vec{r}_1, \vec{r}_2) \\ G(\vec{r}_1, \vec{r}_2) & G(\vec{r}_2, \vec{r}_2) \end{pmatrix}^{-1} \begin{pmatrix} \varphi_1 \\ \varphi_2 \end{pmatrix} \right], \quad (5)$$

where the matrix of the Green's functions for the bulk composed of a 1:1 electrolyte in the DH approximation is given as

$$\begin{pmatrix} G(\vec{r}_1, \vec{r}_1) & G(\vec{r}_1, \vec{r}_2) \\ G(\vec{r}_1, \vec{r}_2) & G(\vec{r}_2, \vec{r}_2) \end{pmatrix} = \begin{pmatrix} \frac{1}{4\pi\epsilon\epsilon_0} \frac{e^{-\kappa a}}{a} & \frac{1}{4\pi\epsilon\epsilon_0} \frac{e^{-\kappa R}}{R} \\ \frac{1}{4\pi\epsilon\epsilon_0} \frac{e^{-\kappa R}}{R} & \frac{1}{4\pi\epsilon\epsilon_0} \frac{e^{-\kappa a}}{a} \end{pmatrix}. \quad (6)$$

Here we assume that the two macroions cannot come closer than $a = 2a_0$. Variations on the above form are possible and would contain the factor $\frac{e^{-\kappa(R-a)}}{R(1+\kappa a)}$ for the separation dependence of $G(\vec{r}, \vec{r}')$. We will comment on the detailed choice of the form for the DH interaction later.

The charge-regulation energy term $e^{-\beta f(\varphi)}$ can now be expanded as a binomial [22]

$$\begin{aligned} e^{-\beta f(\varphi)} &= e^{-i\beta N e_0 \varphi} (1 + b e^{i\beta e_0 \varphi})^{\alpha N} \\ &= \sum_{n=0}^{\alpha N} \binom{\alpha N}{n} b^n e^{-i\beta N e_0 \varphi} e^{i\beta e_0 n \varphi}. \end{aligned} \quad (7)$$

The integral (4) then becomes

$$\begin{aligned} \mathcal{Z} &= \frac{1}{\mathcal{Z}_0} \int \int d\varphi_1 d\varphi_2 \sum_n^{\alpha N} \sum_{n'}^{\alpha N} a_n a_{n'} e^{-i\beta e_0 (N-n)\varphi_1} \\ &\quad \times \exp \left[-\frac{\beta}{2} \begin{pmatrix} \varphi_1 \\ \varphi_2 \end{pmatrix}^T \begin{pmatrix} G(\vec{r}_1, \vec{r}_1) & G(\vec{r}_1, \vec{r}_2) \\ G(\vec{r}_1, \vec{r}_2) & G(\vec{r}_2, \vec{r}_2) \end{pmatrix}^{-1} \begin{pmatrix} \varphi_1 \\ \varphi_2 \end{pmatrix} \right. \\ &\quad \left. \times e^{-i\beta e_0 (N-n')\varphi_2} \right], \end{aligned} \quad (8)$$

where $a_n(\alpha) = \binom{\alpha N}{n} b^n$ for any α .

Introducing the dimensionless variables $\tilde{R} = \kappa R$ and $\tilde{a} = \kappa a$, one can rewrite the partition function for two equal macroions with both charges allowed to vary in the interval $[-N e_0, N e_0]$ in the form

$$\mathcal{Z} = \sum_n^{2N} \sum_{n'}^{2N} a_n(2) a_{n'}(2) e^{-\beta \mathcal{F}_{N,N}(n, n', \tilde{R})}, \quad (9)$$

where we introduced $\mathcal{F}_{N,N}(n, n', \tilde{R})$ as

$$\begin{aligned} \mathcal{F}_{N,N}(n, n', \tilde{R}) &= \frac{e_0^2 \kappa}{8\pi\epsilon\epsilon_0} \left(\frac{e^{-\tilde{a}}}{\tilde{a}} [(N-n)^2 + (N-n')^2] \right. \\ &\quad \left. + 2 \frac{e^{-\tilde{R}}}{\tilde{R}} (N-n)(N-n') \right). \end{aligned} \quad (10)$$

Clearly, we have incorporated exactly the charge-regulation free energy for each of the macroions, while the electrostatic coupling between the two macroions is included approximately via the DH propagator. The configuration of this particular example is symmetric, as the two macroions are identical and are described by the same charge-regulation free energy. The asymmetric configuration, corresponding to

unequal charge-regulation free energies for the two macroions, is addressed next.

In order to describe two equal macroions with a regulated charge in the interval $-N e_0 < e < 0$ we take as a model expression (2) with $\alpha = 1$, i.e.,

$$f(\varphi) = i M e_0 \varphi - \alpha k_B T N \ln(1 + b e^{i\beta e_0 \varphi}), \quad (11)$$

where $M = N$, and with the partition function

$$\mathcal{Z} = \sum_n^N \sum_{n'}^N a_n(1) a_{n'}(1) e^{-\beta \mathcal{F}_{N,N}(n, n', \tilde{R})}. \quad (12)$$

Furthermore, charge regulation in the interval $0 < e < N e_0$ is described by

$$f(\varphi) = -k_B T N \ln(1 + b e^{i\beta e_0 \varphi}), \quad (13)$$

corresponding to the protonization of neutral state ($M = 0$), with the partition function for two equal macroions obtained in the form

$$\mathcal{Z} = \sum_{n=0}^N \sum_{n'=0}^N a_n(1) a_{n'}(1) e^{-\mathcal{F}_{0,0}(n, n', \tilde{R})}. \quad (14)$$

Finally, for an asymmetric case where the two macroions are different, one with charge in the allowed interval $[0, N e_0]$ and the other one spanning the interval $[-N e_0, 0]$, the partition function is obviously obtained in the form

$$\mathcal{Z} = \sum_{n=0}^N \sum_{n'=0}^N a_n(1) a_{n'}(1) e^{-\mathcal{F}_{N,0}(n, n', \tilde{R})}. \quad (15)$$

These results for the partition function derived above can be written succinctly in a single formula as

$$\mathcal{Z} = \sum_n^{\alpha N} \sum_{n'}^{\alpha N} a_n(\alpha) a_{n'}(\alpha) e^{-\beta \mathcal{F}_{N,M}(n, n', \tilde{R})}, \quad (16)$$

where one can distinguish three different cases: (a) $M = N$, $\alpha = 2$, the fully symmetric system (the macroions are identical, both with charge spanning the symmetric interval $[-N e_0, N e_0]$); (b) $M = N$, $\alpha > 2$, the semisymmetric system (the macroions are identical, both with charge spanning the asymmetric interval $[-N e_0, \alpha N e_0]$); and (c) $N \neq 0$, $M = 0$, $\alpha = 1$, the asymmetric system (one particle is positive, with charge fluctuating $[0, N e_0]$, the other negative with charge spanning the interval $[-N e_0, 0]$). The partition function (16) can be evaluated exactly only numerically, as we will do, in addition to providing two explicit analytical approximations.

III. SYMMETRIC-ASYMMETRIC CHARGES ON PROTEINS

With this we proceed to calculate the average value of the charge of the macroions $\langle e_{1,2} \rangle$, charge cross correlation $\langle e_1 e_2 \rangle$, and autocorrelation function $\langle e_1 - \langle e_1 \rangle \rangle^2$ for all three systems. The thermodynamic averages can be written as

$$\langle \dots \rangle = \frac{1}{\mathcal{Z}} \sum_{n, n'}^{\alpha N} a_n(\alpha) a_{n'}(\alpha) \dots e^{-\beta \mathcal{F}_{N,M}(n, n', \tilde{R})}. \quad (17)$$

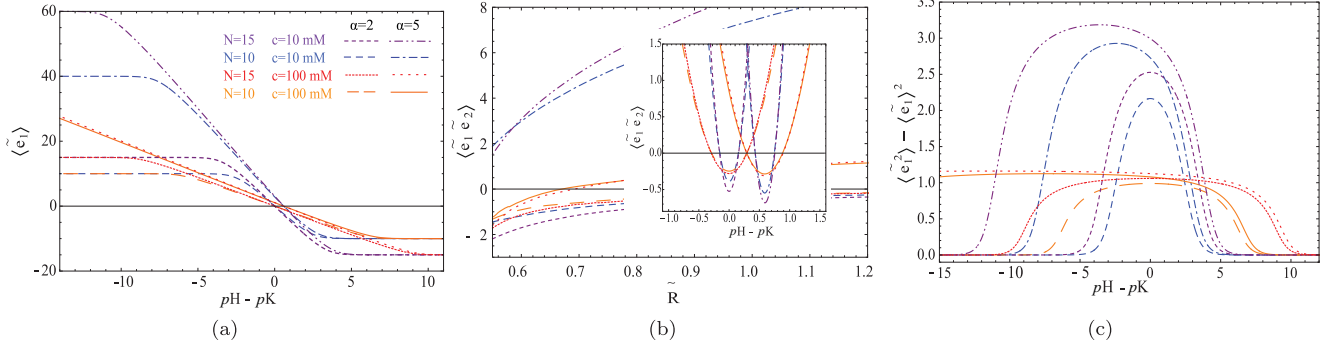


FIG. 2. (Color online) Symmetric system: (a) average charge of macroions, (b) charge cross-correlation function, and (c) autocorrelation function. All averages are obtained by exact evaluation of the partition function. Two systems are shown: a fully symmetric system with $\alpha = 2$ and the semisymmetric case, which takes the asymmetry coefficient to be $\alpha = 5$. Each line style corresponds to a choice of parameters (number of adsorption sites N and salt concentration c) and the system under consideration, as described in (a). The dimensionless diameter of the macroions is set to be $\tilde{a} = 0.5$ and the separation between them is $\tilde{R} = 1$. The \tilde{R} dependence is plotted at the PZC $pH - pK = 0$.

In this way we can write, e.g., the dimensionless average charge of the particle $\langle \tilde{e}_1 \rangle = \langle e_1 \rangle / e_0$ as

$$\langle \tilde{e}_1 \rangle = \langle (n - M) \rangle. \quad (18)$$

In a similar way, other averages are calculated exactly from the full partition function and are plotted as functions of \tilde{R} and $pH - pK$, for different values of the number of adsorption sites N and salt concentration c , keeping fixed the diameter of the macroions \tilde{a} (see Figs. 2 and 4).

In a fully symmetric system (Fig. 2, $\alpha = 2$), the average charge is allowed to vary in a symmetric interval, reaching the point of zero charge (PZC) for $pH = pK$. Away from the PZC, the average charge changes almost linearly until it reaches saturation and stays constant for any value of $pH - pK$ [Fig. 2(a)]. The charge cross-correlation function, being negative close to the PZC, indicates that even in the fully symmetric system the macroion charges tend to fluctuate asymmetrically, charge fluctuation on one macroion being accompanied by a fluctuation of the opposite sign on the other macroion [Fig. 2(b)]. This is a robust property of the system, fully discernible also in the one-dimensional exact solutions [22]. Considering the charge cross-correlation function as a function of distance between macroions, plotted for fixed $pH - pK$, one can observe that at the PZC, the fluctuation asymmetry effect decreases as separation increases and it is strongest for smaller values of salt concentration, while close to the PZC, the asymmetry appears in the regime of larger salt concentration and smaller separations. The charge autocorrelation function is positive with the maximum centered at the PZC, being bigger for smaller salt concentration [Fig. 2(c)].

Finally, the interaction force is calculated as

$$\tilde{F}(\tilde{R}) = -\frac{d}{d\tilde{R}}[-\ln \mathcal{Z}(\tilde{R})]$$

and is shown in Fig. 3. Two identical macroions repel for most values of the parameters, but show a net attraction in the vicinity of the PZC. This attraction is of purely fluctuational origin, stemming from the asymmetric charge cross correlation. At the same value of dimensionless separation, the strength of this fluctuation attraction is larger in systems with larger salt concentration and a larger number of adsorption sites.

Concerning the semisymmetric system of macroions with both charges spanning the same asymmetric interval (Fig. 2, $\alpha = 5$), one can discern similar behavior of all averages as in the fully symmetric system. However here, the PZC is no longer determined by $pH = pK$, but is shifted, meaning that the concentration of the positive ions close to the macroion surfaces is different from the concentration of protons in the bulk. The autocorrelation function as a function $pH - pK$ is not centered anymore on the PZC, but the asymmetric fluctuations do again appear at the PZC [Fig. 2(b)], where one can observe net attraction between the macroions (Fig. 3, inside graph).

The behavior of the completely asymmetric system is shown in Figs. 4 and 5. Here, away from the PZC, the first macroion is positive and the second neutral, or the first can be neutral while the second can be negatively charged, depending on the value of $pH - pK$. In the region $-3 \lesssim pH - pK \lesssim 3$

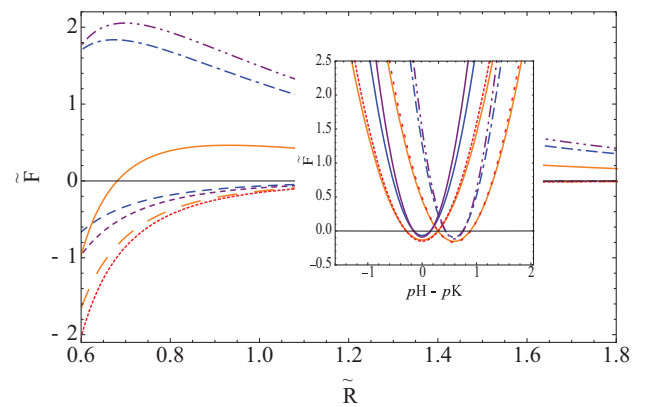


FIG. 3. (Color online) Interaction force for the fully symmetric system (solid lines) and the semisymmetric system (dashed lines). All averages are obtained by exact evaluation of the partition function. Each line style corresponds to a choice of parameters (number of adsorption sites N and salt concentration c) and the system under consideration, as described in Fig. 2(a). The \tilde{R} dependence is plotted at the PZC $pH - pK = 0$, while the $pH - pK$ dependence is plotted setting by $\tilde{R} = 1$. The dimensionless diameter of the macroions is taken to be $\tilde{a} = 0.5$.

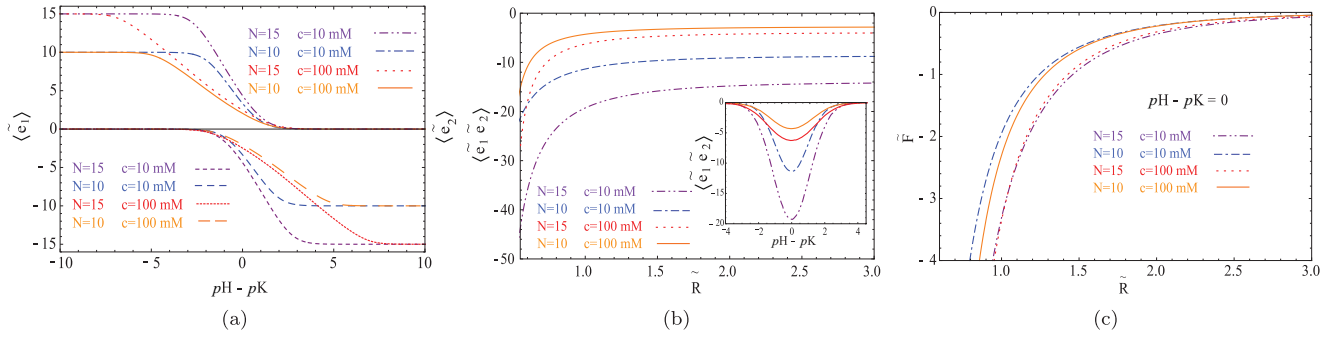


FIG. 4. (Color online) Asymmetric system: (a) average charge of macroions, (b) charge cross-correlation function, and (c) interaction force. All averages are obtained using the exact evaluation of the full partition function. Each line style corresponds to a choice of parameters (number of adsorption sites N and salt concentration c) as described in the legend. The dimensionless diameter of the macroions is set to be $\tilde{a} = 0.5$ and the separation between them is $\tilde{R} = 1$. The \tilde{R} dependence is plotted at a point determined with $pH - pK = 0$.

both macroions carry nonzero charge of opposite sign and at $pH = pK$ the system is electroneutral as a whole, i.e., the sum of average charges is equal to zero [Fig. 4(a)]. The charge cross-correlation function is always negative [Fig. 4(b)] and

one can observe only attraction [Fig. 4(c)]. The number of adsorption sites has the biggest influence on the intensity of the interaction.

The fluctuation effect shows an interesting twist in this system: The interaction force as a function of separation shows attraction also when one of the macroions is charged and the other reaches its point of zero charge [see Fig. 5(a)]. The origin of that attraction comes from the mean charge-induced charge interaction [see Fig. 5(b)], where one can observe a nonzero product $\langle \tilde{e}_i \rangle^2 (\langle \tilde{e}_j - \langle \tilde{e}_j \rangle \rangle^2)$ of nonzero charge $\langle \tilde{e}_i \rangle^2$ and autocorrelation function of zero charge $\langle \tilde{e}_j \rangle$. As is the case in the symmetric system, here also for the same dimensionless separation the attraction is significantly stronger in a solution with larger salt concentration.

IV. DISCUSSION

In the previous section we showed results obtained numerically using the exact evaluation of the full partition function. The aim of this section is to seek an analytical approximation that will provide better intuition about the behavior of the attractive interaction arising between identical macroions with fluctuating charge so that it can be compared with the original KS result for the attractive components as well as the DH result for the repulsive component, respectively. In order to do so, we will evaluate the partition function (16), introducing two different approximations, the saddle-point approximation and the Gaussian approximation, comparing the ensuing approximative results with the exact ones. The approximations refer to the evaluation of the partition function (4) and not to the evaluation of the field Green's function $G(\varphi_1, \varphi_2)$, which is always assumed to be of the DH form. All the approximations detailed below thus refer to the evaluation of the charge-regulation part of the partition function.

A. Saddle-point approximation

The saddle-point approximation consists of finding the dominant contribution to the partition function, corresponding to the minimum of the field action, which is then expanded around the minimum to the second order in deviation. The saddle-point approximation is usually referred to also as the mean-field approximation, but we need to distinguish the mean field in the treatment of the charge-regulation free

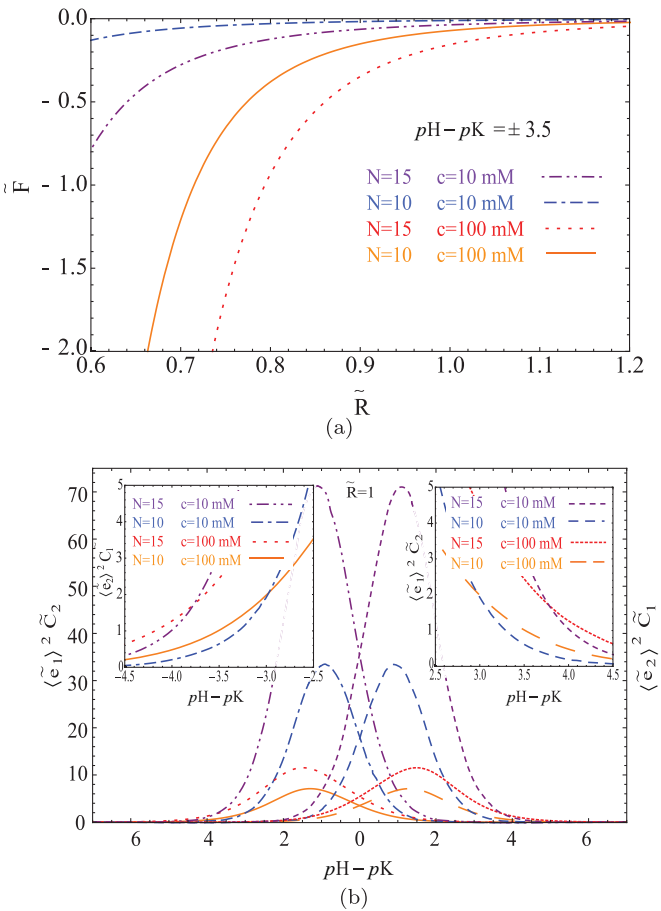


FIG. 5. (Color online) Asymmetric system: (a) interaction force plotted at $pH - pK = 3.5$ and (b) $\langle \tilde{e}_1 \rangle^2 \langle \tilde{e}_2 - \langle \tilde{e}_2 \rangle \rangle^2$ and $\langle \tilde{e}_2 \rangle^2 \langle \tilde{e}_1 - \langle \tilde{e}_1 \rangle \rangle^2$. All averages are obtained using the exact evaluation of the full partition function. Each line style corresponds to a choice of parameters (number of adsorption sites N and salt concentration c) as described in the legend. The dimensionless diameter of the macroions is set to be $\tilde{a} = 0.5$.

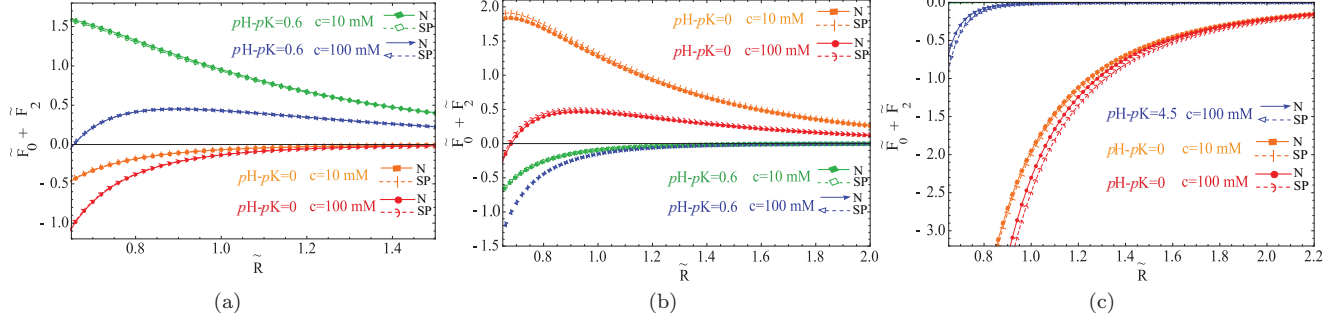


FIG. 6. (Color online) Total interaction force, obtained using the saddle-point approximation to evaluate the full partition function (SP), compared with numerical results, obtained using the exact evaluation of the full partition function (N) for the (a) fully symmetric system with $\alpha = 2$, (b) semisymmetric system with $\alpha = 5$, and (c) asymmetric system. Each line style corresponds to a different choice of parameters (number of adsorption sites N , salt concentration c , and $pH - pK$) as indicated. The dimensionless diameter of the macroions is set to be $\tilde{a} = 0.5$.

energy with the PB mean field, which refers to the interaction part. The procedure is detailed in Appendix B, where we derive expressions for the saddle-point free energy, as well as the fluctuation-induced free energy from the second-order correction (B9). With respect to that decomposition, one can distinguish the saddle-point interaction force \tilde{F}_0 and the fluctuation component of the interaction force \tilde{F}_2 with magnitudes given as

$$\tilde{F}_0 = k \frac{1 + \tilde{R}}{\tilde{R}^2} \tilde{a}^2 e^{2\tilde{a} - \tilde{R}} \times \frac{[\phi_1^* - (\tilde{a}/\tilde{R})e^{\tilde{a} - \tilde{R}} \phi_2^*][\phi_2^* - (\tilde{a}/\tilde{R})e^{\tilde{a} - \tilde{R}} \phi_1^*]}{[1 - (\tilde{a}/\tilde{R})^2 e^{-2(\tilde{R} - \tilde{a})}]^2} \quad (19)$$

and

$$\tilde{F}_2 = -\frac{1 + \tilde{R}}{\tilde{R}^3} \frac{\tilde{a}^2 e^{-2(\tilde{R} - \tilde{a})}}{h_1(\phi_1^*)h_2(\phi_2^*) - (\tilde{a}/\tilde{R})^2 e^{-2(\tilde{R} - \tilde{a})}}. \quad (20)$$

Here $k = \frac{4\pi\epsilon\epsilon_0}{\beta e_0^2 \kappa}$, while $h_1(\phi_1^*)$ and $h_2(\phi_2^*)$ are defined as

$$h_1(\phi_1^*) = 1 + \frac{k\tilde{a}}{\alpha b N} e^{\tilde{a}} e^{-\phi_1^*} (b + e^{\phi_1^*})^2, \quad (21)$$

$$h_2(\phi_2^*) = 1 + \frac{k\tilde{a}}{\alpha b N} e^{\tilde{a}} e^{-\phi_2^*} (b + e^{\phi_2^*})^2,$$

with ϕ_1^* and ϕ_2^* the solutions of the saddle-point equations (B3) and (B4) given in Appendix B. Since they are obtained numerically, this method does not give us a transparent analytical solution for the free energy and interaction force.

The sum of the saddle-point interaction force \tilde{F}_0 and the fluctuation force \tilde{F}_2 for symmetric, semisymmetric, and asymmetric systems are plotted as functions of separation \tilde{R} and compared with results obtained by exact evaluation of the full partition function (Fig. 6). One can notice that there is excellent agreement between both results obtained using these different methods. The saddle-point method decouples the total force into a saddle-point part and a fluctuation part, one being repulsive and the other attractive, respectively, except for the asymmetric system, where there is no repulsion whatsoever [Fig. 6(c)]. They can be differentiated based on the separation scaling of the interaction free energy. In the first case it decays exponentially with \tilde{R} , while in the second it decays exponentially with $2\tilde{R}$. The repulsive force decreases as

the system approaches the PZC, where it is identically equal to zero. In this regime the fluctuation component to the interaction force becomes the dominant one.

The main and important difference between the interactions calculated exactly or on the saddle-point level is that the attractive component of the interaction force in the latter case does not depend on pH , but is sensitive and increases with the salt concentration [Figs. 6(a) and 6(b)]. The full pH dependence of the interaction is thus not described properly by the saddle-point approximation.

B. Gaussian approximation

In this case the analytical evaluation of the partition function (16) is based on a Gaussian approximation for the binomial coefficient and is presented in Appendix C. The partition function in this case also decouples into two separate contributions, of which one decays exponentially with \tilde{R} and the other decays exponentially with $2\tilde{R}$. We will again refer to them as the mean and the fluctuation part of the interaction force, using the same notation as for the saddle-point approximation. One should note here that on this approximation level there is no real decoupling into the mean and fluctuation part. We differentiate them purely based on their separation scaling.

The mean interaction force \tilde{F}_0 can be obtained as

$$\tilde{F}_0 = k \frac{1 + \tilde{R}}{\tilde{R}^2} \tilde{a}^2 e^{2\tilde{a} - \tilde{R}} \frac{[(pH - pK) \ln 10]^2}{[1 + 2(k\tilde{a}/N)e^{\tilde{a}} + (\tilde{a}/\tilde{R})e^{-(\tilde{R} - \tilde{a})}]^2} \quad (22)$$

and the fluctuation force \tilde{F}_2 as

$$\tilde{F}_2 = -\frac{1 + \tilde{R}}{\tilde{R}^3} \frac{\tilde{a}^2 e^{-2(\tilde{R} - \tilde{a})}}{[1 + (4k\tilde{a}/\alpha N)e^{\tilde{a}}]^2 - (\tilde{a}^2/\tilde{R}^2)e^{-2(\tilde{R} - \tilde{a})}}. \quad (23)$$

Again both \tilde{F}_0 and \tilde{F}_2 are obtained in the same way and the separation into mean and fluctuation parts is arbitrary. Nevertheless, the separation scaling of the two is the same as for the mean-field and fluctuation contributions in the case of the saddle-point approximation, making the nomenclature reasonable.

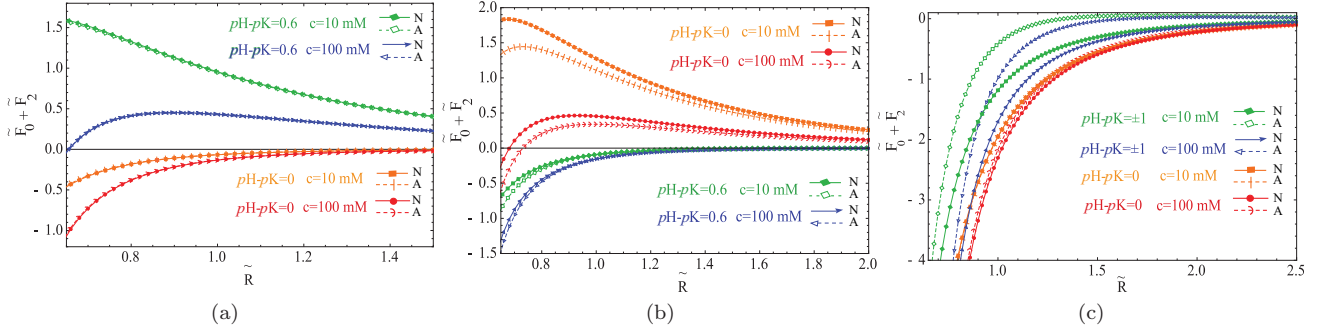


FIG. 7. (Color online) Analytical results for the total force, obtained using approximative evaluation of the full partition function (A), are compared with numerical results, obtained using exact evaluation of the full partition function (N) for the (a) fully symmetric system with $\alpha = 2$, (b) semisymmetric system with $\alpha = 5$, and (c) asymmetric system. Each line style corresponds to the choice of parameters (number of adsorption sites N , salt concentration c , and $pH - pK$) as indicated. The dimensionless diameter of the macroions is set to be $\tilde{a} = 0.5$.

The general form of the mean interaction force is given in Eq. (C4), which is valid for all three systems considered: fully symmetric, semisymmetric, and asymmetric. Because of its complexity, we display here only \tilde{F}_0 for the fully symmetric system (22). On the other hand, the fluctuation force (23) has the same universal form for all three types of systems. One can compare these results (22) and (23) with those obtained using the saddle-point approximation (19) and (20).

Clearly, the fluctuation force in the Gaussian approximation corresponds exactly to the fluctuating force in the saddle-point approximation if the saddle point is taken at the PZC $pH = pK$ and the mean potentials are $\phi_1^* = \phi_2^* = 0$. However, in general, the two approximations do not coincide and thus we cannot claim that \tilde{F}_2 is purely fluctuational in origin.

The mean and the fluctuation part to the interaction force are plotted as functions of dimensionless separation \tilde{R} in Fig. 7. The total interaction force obtained in this way is compared with the one obtained using the exact evaluation of the partition function. For the fully symmetric system, the Gaussian approximation fits perfectly the exact results [Fig. 7(a)]. Somewhat lesser agreement can be found in a semisymmetric system [Fig. 7(b)], while the analytical results do not work at all in the region away from the PZC in the asymmetric system [Fig. 7(c)].

In the fully symmetric system, the mean part of the interaction force is repulsive, decreasing on approach to the PZC, while in the asymmetric system, it is actually attractive as the macroions are on average oppositely charged. On the other hand, the fluctuation component to the interaction force is attractive no matter what the symmetry of the system and the pH of solution are, while it does depend on the salt concentration. Interestingly enough, on the Gaussian approximation level for the binomial coefficient the pH dependence of the autocorrelation function again drops out completely, which is contrary to the full numerical evaluation of the charge autocorrelation function.

C. Comparison with DH and KS forms

We now set our results against the mean-field DH theory of interactions between pointlike macroions and against the KS theory of charge-fluctuation forces. Obviously, without charge regulation the charge of both interacting macroions is

fixed and the DH form of the interaction should be recovered. Setting $\alpha = 0$ and $M = N$ in Eq. (16), one indeed gets the DH interaction force between two well-separated like-charged macroions in a salt solution

$$\tilde{F} \approx \frac{N^2 e^{-\tilde{R}}}{k \tilde{R}}. \quad (24)$$

Charge regulation, besides inducing attraction at the PZC, also introduces significant modifications in the mean-field interaction force (22), leading to its vanishing at the PZC. In the limit of large separations, the charge-regulated interaction force (22) in fact scales as

$$\tilde{F}_0 \approx \frac{1}{\tilde{R}} k \tilde{a}^2 e^{2\tilde{a}-\tilde{R}} \frac{[(pH - pK) \ln 10]^2}{[1 + 2(k\tilde{a}/N)e^{\tilde{a}}]^2}, \quad (25)$$

clearly showing a strong dependence on the solution pH .

As for the fluctuation component of the interaction force for two spherical pointlike macroions, we can cast its form in the Gaussian approximation, going to a limit of asymptotically large separation (23) as

$$\tilde{F}_2 \approx -\frac{1}{\tilde{R}^2} \frac{\tilde{a}^2 e^{-2(\tilde{R}-\tilde{a})}}{[1 + 2(k\tilde{a}/N)e^{\tilde{a}}]^2}. \quad (26)$$

In this limit the charge autocorrelation functions for the two macroions $\langle \Delta \tilde{e}_1^2 \rangle = \langle (\tilde{e}_1 - \langle \tilde{e}_1 \rangle)^2 \rangle$ are independent of the separation between them and can be calculated analytically using the same Gaussian approximation with the following result:

$$\langle \Delta \tilde{e}_1^2 \rangle \langle \Delta \tilde{e}_2^2 \rangle \approx \frac{k^2 \tilde{a}^2 e^{2\tilde{a}}}{[1 + 2(k\tilde{a}/N)e^{\tilde{a}}]^2}. \quad (27)$$

With this result the fluctuation component of the interaction force assumes the asymptotic form

$$\tilde{F}_2 \approx -\frac{e^{-2\tilde{R}}}{k^2 \tilde{R}^2} \langle \Delta \tilde{e}_1^2 \rangle \langle \Delta \tilde{e}_2^2 \rangle. \quad (28)$$

This actually coincides exactly with the original Kirkwood-Schumaker result [7,8] if we take into account the fact that they take the DH Green's function for two point charges with a finite-size scaling factor $e^{\tilde{a}}/(1 + \tilde{a})$, so that we would have to multiply Eq. (28) by $e^{-2\tilde{a}}(1 + \tilde{a})^2$. Again we note that on this approximation level the pH dependence of the autocorrelation function drops out completely, but is retained

TABLE I. The pK values of amino-acid functional groups in dilute aqueous solution, after Ref. [16].

AA	pK
Asp	3.71
Glu	4.15
Tyr	10.10
Arg	12.10
His	6.04
Lys	10.67
Cys	8.14

in the full numerical evaluation of the charge autocorrelation function.

V. PROTEINLIKE MACROIONS

The general theory formulated above can be straightforwardly applied to the interaction of proteinlike macroions. In a protein, the amino acids (AAs) Asp, Glu, Tyr, and Cys can be negatively charged, while Arg, Lys, and His can carry a positive charge, all depending on the solution conditions. The respective pK for the dissociation of the various amino acids are given at Table I [16].

In order to describe a protein macroion composed of these amino acids, one should write down the charge-regulation free energy in the form

$$f_p(\varphi) = i \sum_j N_j M_j e_0 \varphi - kT \sum_j N_j M_j \ln(1 + b_j e^{i\beta e_0 \varphi}) - kT \sum_k N_k M_k \ln(1 + b_k e^{i\beta e_0 \varphi}), \quad (29)$$

where j stands for negative AAs $j = \{\text{Asp, Glu, Tyr, Cys}\}$, while k stands for positive ones $k = \{\text{Arg, His, Lys}\}$. Here N_j and N_k are the numbers of adsorption sites on each positive AA and negative AA and since each of these AAs has one adsorption site it will be set to 1. In addition, M_j and M_k count how many times each AA occurs in the protein and b_j and b_k stand for $b_n = e^{-\ln 10(pH - pK_n)}$, where the pK_n for each

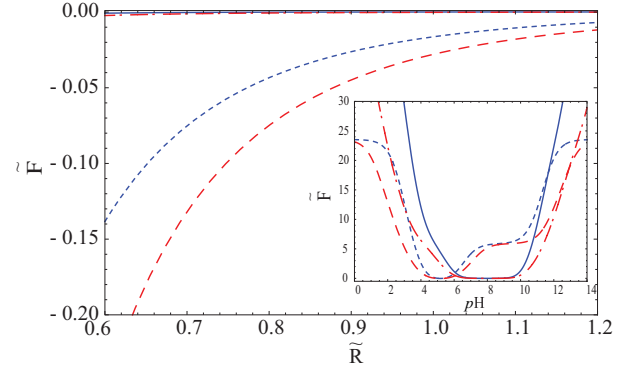


FIG. 9. (Color online) Generalized system: interaction force. All results are obtained by using the exact numerical evaluation of the full partition function. Each line style corresponds to a choice of system and the values of salt concentration c as indicated in Fig. 8(a). The functions bearing an \bar{R} dependence are plotted at the isoelectric point of the two systems: $pH = 5.15$ and 7.87 , respectively. The dimensionless diameter of the macroions is set to be $\bar{a} = 0.5$ and the separation between them is $\bar{R} = 1$.

AA is given in Table I. For pointlike macroions the spatial distribution of AAs on the surface of the protein is irrelevant and the above approximation is thus admissible.

The partition function for the system composed of two proteinlike macroions in a 1:1 salt solution is derived in the same way as explained in Sec. II and is given in Appendix D. Since the evaluation of Eq. (D2) is computationally time consuming, we consider only the behavior of two model systems, one (system I) composed of proteinlike macroions consisting of two Asp, two Glu, two Lys, and two His AAs and the other (system II) having four AAs more, two Tyr and two Arg. The results are shown in Figs. 8 and 9. The protein charge, as a function of pH , spans a symmetric interval with constant plateaus in the pH regions, which correspond to charging up an additional AA. The cross-correlation function in general follows the pattern of plateaus of the average charge, being positive everywhere except at the PZC, where an asymmetric charge distribution appears. The autocorrelation function and

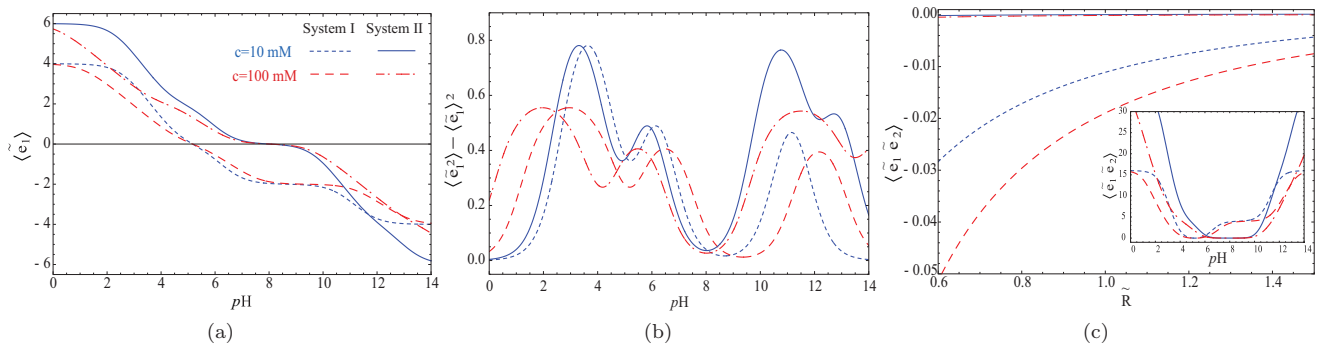


FIG. 8. (Color online) Generalized system: (a) average charge of macroions, (b) charge autocorrelation function, and (c) charge-charge cross-correlation function. All results are obtained by using the exact numerical evaluation of the full partition function. System I consists of two proteins, each of which consists of 2 Asp, 2 Glu, 2 Lys, and 2 His AAs, while system II has additional 2 Tyr and 2 Arg. The results are plotted for two different values of salt concentration $c = 10$ and 100 mM for each system. The dimensionless diameter of the macroions is set to be $\bar{a} = 0.5$ and the separation between them $\bar{R} = 1$. The functions bearing an \bar{R} dependence are plotted at the isoelectric point of the two systems: $pH = 5.15$ and 7.87 , respectively.

the charge cross correlation show opposite signs, with one being positive and the other negative, respectively.

Analyzing the behavior of the interaction force Fig. 9, one can see that two identical proteins mutually repel and that the strength of the interaction depends on the pH in the solution, following closely the behavior of the charge cross-correlation function. The repulsion is smaller in a solution of higher salt concentration, since the salt screens the protein charge and reduces the interaction. The repulsion disappears at the PZC, where the attraction sets in, increasing with salt concentration at a fixed dimensionless separation between the proteins. The attractive interaction is negligible for proteins composed of a larger number of amino acids, which does not correspond with our previous results, where the attraction is larger for a larger number of adsorption sites. This can be explained by analyzing the average charge of the protein [Fig. 8 (a)], where one can observe a plateau of zero charge for system II, which is not the case in system I. So it can be concluded that the strength of the fluctuation interaction depends on the rate of change of the charge of the macroion with pH , which of course depends on the type of the protein.

This can be derived also formally by following Lund and Jönsson [11]. The fluctuation part of the interaction force (28) is approximately proportional to the charge variance, which in turn follows from the macroion capacitance \mathcal{C} as

$$\langle(\bar{e} - \langle\bar{e}\rangle)^2\rangle \sim \mathcal{C} = \frac{\partial\bar{e}(\phi)}{\partial(\beta e_0\phi)} = -\frac{1}{\ln 10} \frac{\partial\bar{e}(\phi)}{\partial pH}, \quad (30)$$

as is clear also from Eq. (3). The strength of the fluctuation interaction therefore depends on the rate of change of the mean charge of the macroion with pH , i.e., its capacitance. This can be clearly discerned from Fig. 8(b), where we observe that system II has zero capacitance at its PZC, while system I has a nonzero capacitance at its PZC.

VI. CONCLUSION

We presented a theory describing electrostatic interaction between two spherical macroions, with nonconstant, fluctuating charge, surrounded by a monovalent bathing salt solution. The macroion charge fluctuations are described with the Parsegian-Ninham model of charge regulation, which effectively corresponds to a lattice-gas surface dissociation free energy. Our theory is based on two approximations: One assumes the macroions as pointlike, in the sense that the electrostatic potential on the surface of the macroion is uniform, and other treats the intervening salt solution on the Debye-Hückel level, assuming the electrostatic potential to be small, so that the Poisson-Boltzmann equation can be linearized. Choosing the proper charge-regulation energy, we analyzed the behavior of three different systems that differ in the symmetry of charge distribution. These are a symmetric system composed of two identical macroions with a symmetric as well as asymmetric charge-regulation intervals, corresponding to the fully symmetric and semisymmetric cases, and an asymmetric system, composed of oppositely charged macroions, allowing the case of having one charged and one uncharged particle.

We have shown that in charge-regulated systems, asymmetrical charge fluctuations appear near the PZC, engen-

dering strong attractive interactions of a general Kirkwood-Schumaker type, but with different functional dependences as argued in their original derivation. The fluctuational nature of the Kirkwood-Schumaker interaction is consistent also with the fact that it arises even between a charged and a charge neutral object, in the vicinity of the pH where the charged macroion becomes neutral itself. This is the case studied also in the context of the PB theory within the constant charge-regulation model, in fact corresponding to a linearized form of the full charge-regulation theory [24,25]. In this limit too the effects of charge regulation are crucial and lead to attraction. However, in the context of our approximations, the attractive interaction between a charged and a neutral surface stems from the coupling between the net charge of one and charge fluctuations of the other surface. Superficially, one would tend to see the attraction in the constant charge-regulation model as being grounded in the mean-field level, but caution should be exercised here. In our case too the Green's function pertains to the DH mean-field level and the attraction actually comes from the surface charge regulation. The constant-charge-regulation model must obviously capture some of the same physics.

The bathing solution with its pH and ionic strength therefore plays an important role in charge-regulated systems and the interactions to which they are subject. In all cases studied, the fluctuation attraction is larger for larger salt concentration in solution at the same dimensionless separation, while the repulsion is actually reduced at a fixed separation by increasing the salt concentration, consistent with the electrolyte screening effect. Furthermore, a stronger attraction is found in systems composed of identical macroions having a larger number of adsorption sites, giving rise to larger charge fluctuations.

The theory, developed for toy models, was then applied to the case of proteinlike macroions, with a different dissociation constant for different chargeable amino acids. For protein electrostatic interactions their strength depends on the rate of change of the charge of the macroion with respect to the solution pH , i.e., the molecular capacitance of the macroion, which is protein specific and connected with the capacitance of the protein charge distribution. Apart from this, salt concentration enhances the attraction between proteinlike macroions, as evidenced also in simulations and experiments in the case of, e.g., lysozyme in monovalent salt solutions [26,27]. In fact, understanding the details of the protein-protein interaction is our main motivation for developing further our theoretical approach, specifically the relation between the KS interaction, the patchiness effects, and van der Waals interactions between proteins in electrolyte solutions.

ACKNOWLEDGMENTS

N.A. acknowledges financial support from the Slovenian Research Agency under the young researcher grant. R.P. acknowledges financial support from the Slovenian Research Agency under Grant No. P1-0055 and would like to thank Professor Michal Borkovec and Dr. Gregor Trefalt for illuminating discussions on the subject of charge regulation and electrostatic interactions between charge-regulated macroions.

APPENDIX A: PATH-INTEGRAL FORMALISM

The field propagator at points \vec{r}_1 and \vec{r}_2 is defined as

$$G(\varphi_1, \varphi_2) = \int_{\varphi(\vec{r}_1)=\varphi_1}^{\varphi(\vec{r}_2)=\varphi_2} \mathcal{D}[\varphi(\vec{r})] \delta(\varphi(\vec{r}_1) - \varphi_1) \delta(\varphi(\vec{r}_2) - \varphi_2) \exp \left[-\frac{1}{2} \int d\vec{r} d\vec{r}' \varphi(\vec{r}) G^{-1}(\vec{r}, \vec{r}') \varphi(\vec{r}') \right], \quad (\text{A1})$$

where $G^{-1}(\vec{r}, \vec{r}')$ is the usual Debye-Hückel kernel of the form [4]

$$G^{-1}(\vec{r}, \vec{r}') = -\varepsilon_0 [\vec{\nabla} \varepsilon(\vec{r}) \vec{\nabla} - \varepsilon(\vec{r}) \kappa^2] \delta(\vec{r} - \vec{r}'), \quad (\text{A2})$$

where κ is the inverse Debye length. Using the δ function in the integral representation

$$\delta(\varphi(\vec{r}_1) - \varphi_1) = \int \frac{dk}{2\pi} e^{ik[\varphi(\vec{r}_1) - \varphi_1]} = \int \frac{dk}{2\pi} \exp \left(-ik\varphi_1 + ik \int d\vec{r} \rho_1(\vec{r}) \varphi(\vec{r}) \right), \quad (\text{A3})$$

where $\rho_1(\vec{r}) = \delta(\vec{r} - \vec{r}_1)$, one can rewrite the propagator as

$$G(\varphi_1, \varphi_2) = \int dk e^{-ik\varphi_1} \int dk' e^{-ik'\varphi_2} \int \mathcal{D}[\varphi(\vec{r})] \exp \left[-\frac{1}{2} \int d\vec{r} d\vec{r}' \varphi(\vec{r}) G^{-1}(\vec{r}, \vec{r}') \varphi(\vec{r}') + i \int t(\vec{r}) \varphi(\vec{r}) d^3\vec{r} \right], \quad (\text{A4})$$

where $t(\vec{r})$ stands for $t(\vec{r}) = k\rho_1(\vec{r}) + k'\rho_2(\vec{r})$. After integration over the field, one obtains

$$\begin{aligned} G(\varphi_1, \varphi_2) &= \frac{1}{\det G^{-1}(\vec{r}, \vec{r}')} \int dk e^{-ik\varphi_1} \int dk' e^{-ik'\varphi_2} \exp \left(-\frac{1}{2} \int d\vec{r} d\vec{r}' t(\vec{r}) G(\vec{r}, \vec{r}') t(\vec{r}') \right) \\ &= \frac{1}{\det G^{-1}(\vec{r}, \vec{r}')} \int_{-\infty}^{+\infty} \int_{-\infty}^{+\infty} dk dk' e^{-ik\varphi_1 - ik'\varphi_2} e^{-k^2 G(\vec{r}_1, \vec{r}_1)/2} e^{-k'^2 G(\vec{r}_2, \vec{r}_2)/2} e^{-kk' G(\vec{r}_1, \vec{r}_2)}. \end{aligned} \quad (\text{A5})$$

If one introduces a two-dimensional vector $(k k')$, this integral can be rewritten as

$$G(\varphi_1, \varphi_2) = \frac{1}{\det G^{-1}(\vec{r}, \vec{r}')} \int \int dk dk' \exp \left[-i \begin{pmatrix} \varphi_1 \\ \varphi_2 \end{pmatrix}^T \begin{pmatrix} k \\ k' \end{pmatrix} \right] \exp \left[-\frac{1}{2} \begin{pmatrix} k \\ k' \end{pmatrix}^T \begin{pmatrix} G(\vec{r}_1, \vec{r}_1) & G(\vec{r}_1, \vec{r}_2) \\ G(\vec{r}_1, \vec{r}_2) & G(\vec{r}_2, \vec{r}_2) \end{pmatrix} \begin{pmatrix} k \\ k' \end{pmatrix} \right]. \quad (\text{A6})$$

Since this is a Gaussian integral, it can be evaluated explicitly

$$G(\varphi_1, \varphi_2) = \exp \left[-\frac{\beta}{2} \begin{pmatrix} \varphi_1 \\ \varphi_2 \end{pmatrix}^T \begin{pmatrix} G(\vec{r}_1, \vec{r}_1) & G(\vec{r}_1, \vec{r}_2) \\ G(\vec{r}_1, \vec{r}_2) & G(\vec{r}_2, \vec{r}_2) \end{pmatrix}^{-1} \begin{pmatrix} \varphi_1 \\ \varphi_2 \end{pmatrix} \right]. \quad (\text{A7})$$

APPENDIX B: SADDLE-POINT APPROXIMATION

The partition function (4) can be evaluated using the saddle-point method, consisting of minimization of the field action $\frac{\partial A}{\partial \phi} = 0$, where the action can be written in the form

$$A(\phi_1, \phi_2) = f_1(\phi_1) + g(\phi_1, \phi_2) + f_2(\phi_2), \quad (\text{B1})$$

with g the logarithm of the Green's function, given as

$$g(\phi_1, \phi_2) = -\frac{1}{2} \begin{pmatrix} \phi_1 \\ \phi_2 \end{pmatrix}^T \begin{pmatrix} \tilde{G}(\vec{r}_1, \vec{r}_1) & \tilde{G}(\vec{r}_1, \vec{r}_2) \\ \tilde{G}(\vec{r}_1, \vec{r}_2) & \tilde{G}(\vec{r}_2, \vec{r}_2) \end{pmatrix}^{-1} \begin{pmatrix} \phi_1 \\ \phi_2 \end{pmatrix}. \quad (\text{B2})$$

The saddle-point equations are obtained as

$$N - \alpha N \frac{be^{-\phi_1}}{1 + be^{-\phi_1}} + \phi_1 \frac{4\pi\epsilon\epsilon_0}{\beta e_0^2 \kappa} \frac{1}{e^{-2\tilde{a}}/\tilde{a}^2 - e^{-2\tilde{R}}/\tilde{R}^2} \frac{e^{-\tilde{a}}}{\tilde{a}} - \phi_2 \frac{4\pi\epsilon\epsilon_0}{\beta e_0^2 \kappa} \frac{1}{e^{-2\tilde{a}}/\tilde{a}^2 - e^{-2\tilde{R}}/\tilde{R}^2} \frac{e^{-\tilde{R}}}{\tilde{R}} = 0, \quad (\text{B3})$$

$$M - \alpha N \frac{be^{-\phi_2}}{1 + be^{-\phi_2}} + \phi_2 \frac{4\pi\epsilon\epsilon_0}{\beta e_0^2 \kappa} \frac{1}{e^{-2\tilde{a}}/\tilde{a}^2 - e^{-2\tilde{R}}/\tilde{R}^2} \frac{e^{-\tilde{a}}}{\tilde{a}} - \phi_1 \frac{4\pi\epsilon\epsilon_0}{\beta e_0^2 \kappa} \frac{1}{e^{-2\tilde{a}}/\tilde{a}^2 - e^{-2\tilde{R}}/\tilde{R}^2} \frac{e^{-\tilde{R}}}{\tilde{R}} = 0. \quad (\text{B4})$$

Solutions of these equations are denoted by ϕ_1^* and ϕ_2^* . If one sets $M = 0$ and $\alpha = 1$, one deals with an asymmetric system, for $M = N$ and $\alpha = 2$, one deals with a fully symmetric system, and the choice $M = N$ and $\alpha > 2$ defines a symmetric system with an asymmetric interval of fluctuating charge, i.e., a semisymmetric system.

The action can be expanded around the SP solution up to the second order in deviation from ϕ_1^* and ϕ_2^* , yielding

$$A(\phi_1, \phi_2) = f_1(\phi_1^*) + g(\phi_1^*, \phi_2^*) + f_2(\phi_2^*) + \frac{1}{2} \frac{\partial^2 A(\phi_1, \phi_2)}{\partial \phi_1^2} \Big|_{\phi_1^*, \phi_2^*} \delta\phi_1^2 + \frac{\partial^2 A(\phi_1, \phi_2)}{\partial \phi_1 \partial \phi_2} \Big|_{\phi_1^*, \phi_2^*} \delta\phi_1 \delta\phi_2 + \frac{1}{2} \frac{\partial^2 A(\phi_1, \phi_2)}{\partial \phi_2^2} \Big|_{\phi_1^*, \phi_2^*} \delta\phi_2^2, \quad (\text{B5})$$

where $f_{1/2}(\phi_{1/2}^*)$ are given as

$$f_{1/2}(\phi_{1/2}^*) = -M\phi_{1/2}^* - \alpha N \ln(1 + be^{-\phi_{1/2}^*}). \quad (\text{B6})$$

If we denote second derivatives in the equation above by A_{11} , A_{12} , and A_{22} , respectively, we have

$$\begin{aligned} A_{11} &= -\alpha Nb \frac{e^{-\phi_1^*}}{(1 + be^{-\phi_1^*})^2} - \frac{4\pi\epsilon\epsilon_0}{\beta e_0^2 \kappa} \frac{1}{e^{-2\tilde{a}}/\tilde{a}^2 - e^{-2\tilde{R}}/\tilde{R}^2} \frac{e^{-\tilde{a}}}{\tilde{a}}, \\ A_{22} &= -\alpha Nb \frac{e^{-\phi_2^*}}{(1 + be^{-\phi_2^*})^2} - \frac{4\pi\epsilon\epsilon_0}{\beta e_0^2 \kappa} \frac{1}{e^{-2\tilde{a}}/\tilde{a}^2 - e^{-2\tilde{R}}/\tilde{R}^2} \frac{e^{-\tilde{a}}}{\tilde{a}}, \\ A_{12} &= \frac{4\pi\epsilon\epsilon_0}{\beta e_0^2 \kappa} \frac{1}{\frac{e^{-2\tilde{a}}}{\tilde{a}^2} - \frac{e^{-2\tilde{R}}}{\tilde{R}^2}} \frac{e^{-\tilde{R}}}{\tilde{R}}, \end{aligned} \quad (\text{B7})$$

so the saddle point and the fluctuation free energy are equal to

$$\beta\mathcal{F}_0 = -[f_1(\phi_1^*) + g(\phi_1^*, \phi_2^*) + f_2(\phi_2^*)] \quad (\text{B8})$$

and

$$\beta\mathcal{F}_2 = -\ln \frac{\det A_0}{\det A}, \quad (\text{B9})$$

where A_0 is a matrix, related to the partition function of the unperturbed system, with the elements

$$\begin{aligned} A_{11}^0 &= \frac{\partial^2 A_0(\phi_1, \phi_2)}{\partial \phi_1^2} = -\frac{4\pi\epsilon\epsilon_0}{\beta e_0^2 \kappa} \frac{1}{e^{-2\tilde{a}}/\tilde{a}^2 - e^{-2\tilde{R}}/\tilde{R}^2} \frac{e^{-\tilde{a}}}{\tilde{a}}, \\ A_{22}^0 &= \frac{\partial^2 A_0(\phi_1, \phi_2)}{\partial \phi_2^2} = -\frac{4\pi\epsilon\epsilon_0}{\beta e_0^2 \kappa} \frac{1}{e^{-2\tilde{a}}/\tilde{a}^2 - e^{-2\tilde{R}}/\tilde{R}^2} \frac{e^{-\tilde{a}}}{\tilde{a}}, \\ A_{12}^0 &= \frac{\partial^2 A_0(\phi_1, \phi_2)}{\partial \phi_1 \partial \phi_2} = \frac{4\pi\epsilon\epsilon_0}{\beta e_0^2 \kappa} \frac{1}{e^{-2\tilde{a}}/\tilde{a}^2 - e^{-2\tilde{R}}/\tilde{R}^2} \frac{e^{-\tilde{R}}}{\tilde{R}}. \end{aligned} \quad (\text{B10})$$

Finally, the saddle-point interaction force and the force due to the fluctuations around the saddle point are given as

$$\tilde{F}_0 = \frac{4\pi\epsilon\epsilon_0}{\beta e_0^2 \kappa} \frac{1 + \tilde{R}}{\tilde{R}^2} \frac{\tilde{a}^2 e^{2\tilde{a} - \tilde{R}} [\phi_1^* - (\tilde{a}/\tilde{R})e^{\tilde{a} - \tilde{R}} \phi_2^*] [\phi_2^* - (\tilde{a}/\tilde{R})e^{\tilde{a} - \tilde{R}} \phi_1^*]}{[1 - (\tilde{a}/\tilde{R})^2 e^{-2(\tilde{R} - \tilde{a})}]^2}, \quad (\text{B11})$$

$$\tilde{F}_2 = -\frac{1 + \tilde{R}}{\tilde{R}^3} \frac{\tilde{a}^2 e^{-2(\tilde{R} - \tilde{a})}}{h_1(\phi_1^*)h_2(\phi_2^*) - (\tilde{a}^2/\tilde{R}^2)e^{-2(\tilde{R} - \tilde{a})}}, \quad (\text{B12})$$

where

$$h_1(\phi_1^*) = 1 + \frac{4\pi\epsilon\epsilon_0\tilde{a}}{\beta e_0^2 \kappa N \alpha b} e^{\tilde{a}} e^{-\phi_1^*} (b + e^{\phi_1^*})^2, \quad h_2(\phi_2^*) = 1 + \frac{4\pi\epsilon\epsilon_0\tilde{a}}{\beta e_0^2 \kappa N \alpha b} e^{\tilde{a}} e^{-\phi_2^*} (b + e^{\phi_2^*})^2. \quad (\text{B13})$$

The saddle point and the fluctuation force are plotted as functions of dimensionless separation \tilde{R} in Fig. 6.

APPENDIX C: GAUSSIAN APPROXIMATION

The partition function (16) can be evaluated analytically if one takes a Gaussian approximation for the binomial coefficient

$$\binom{\alpha N}{n} = \frac{2^{\alpha N}}{\sqrt{\pi\alpha N/2}} e^{-(\alpha N - 2n)^2/2\alpha N}. \quad (\text{C1})$$

After the substitutions $x = \alpha N - 2n$ and $x' = \alpha M - 2n'$, summation can be transformed into the integral, when one assumes $N \gg 1$, so the partition function becomes

$$\mathcal{Z} = \int_{-\infty}^{\infty} dx \int_{-\infty}^{\infty} dx' e^{(1/2)(x+x')(pH-pK) \ln 10} e^{-(1/2\alpha N)(x^2+x'^2)} e^{-\beta\mathcal{F}(x, x', \tilde{R})}, \quad (\text{C2})$$

where

$$\mathcal{F}(x, x', \tilde{R}) = \frac{e_0^2 \kappa}{8\pi\epsilon\epsilon_0} \left(\frac{e^{-\kappa a}}{a} \{ [x + N(2 - \alpha)]^2 + [x' + M(2 - \alpha)]^2 \} + 2 \frac{e^{-\kappa R}}{R} [x + N(2 - \alpha)][x' + M(2 - \alpha)] \right). \quad (\text{C3})$$

This is a general Gaussian-type integral and can be calculated analytically, but since the solution is too cumbersome, it is not displayed here. The interaction force then follows as a sum of the mean contribution to the force and the fluctuation force as

$$\begin{aligned} \tilde{F}_0 &= k\tilde{a}^2 e^{2\tilde{a}-\tilde{R}} \frac{1+\tilde{R}}{\tilde{R}^2} \frac{[(pH-pK)\ln 10]^2}{\{1+2(k\tilde{a}/N)e^{\tilde{a}}+(\tilde{a}/\tilde{R})e^{-(\tilde{R}-\tilde{a})}\}^2} + \frac{(\alpha-2)k\tilde{a}^2 e^{2\tilde{a}-\tilde{R}}}{\alpha^2 N [1+(4k\tilde{a}e^{\tilde{a}}/\alpha N)]^2} \frac{1+\tilde{R}}{\tilde{R}^2} \\ &\times \left(-\frac{2\alpha(N+M)(pH-pK)\ln 10}{(1+\{1/[1+(4k\tilde{a}e^{\tilde{a}}/\alpha N)]^2\})(\tilde{a}/\tilde{R})e^{-(\tilde{R}-\tilde{a})}} + \frac{4\alpha M(\alpha N-1)(pH-pK)\ln 10 [1/1+(4k\tilde{a}e^{\tilde{a}}/\alpha N)]e^{-(\tilde{R}-\tilde{a})}}{(1-\{1/[1+(4k\tilde{a}e^{\tilde{a}}/\alpha N)]^2\})(\tilde{a}^2/\tilde{R}^2)e^{-2(\tilde{R}-\tilde{a})}} \right. \\ &\left. + \frac{(4\alpha M-8)(1+\{1/[1+(4k\tilde{a}e^{\tilde{a}}/\alpha N)]^2\})(\tilde{a}^2/\tilde{R}^2)e^{-2(\tilde{R}-\tilde{a})} - (\alpha-2)[1+\alpha(M^2/N^2)][4N/1+(4k\tilde{a}e^{\tilde{a}}/\alpha N)](\tilde{a}/\tilde{R})e^{-(\tilde{R}-\tilde{a})}}{(1-\{1/[1+(4k\tilde{a}e^{\tilde{a}}/\alpha N)]^2\})(\tilde{a}^2/\tilde{R}^2)e^{-2(\tilde{R}-\tilde{a})}} \right), \\ \tilde{F}_2 &= -\frac{1+\tilde{R}}{\tilde{R}^3} \frac{\tilde{a}^2 e^{-2(\tilde{R}-\tilde{a})}}{[1+(4/\alpha)(4\pi\epsilon_0\tilde{a}/\beta e_0^2\kappa N)e^{\tilde{a}}]^2 - (\tilde{a}^2/\tilde{R}^2)e^{-2(\tilde{R}-\tilde{a})}}. \end{aligned} \quad (C4)$$

The mean contributions to the force and fluctuation force are plotted as functions of separation \tilde{R} and the results are presented in Fig. 7. We note that the nomenclature “mean” and “fluctuation” do not have the same meaning in the context of the Gaussian approximation as they do in the saddle-point approximation. In fact, in the former the interaction free energy cannot be consistently separated into mean and fluctuation types. We use this separation based on the dimensionless separation scaling.

APPENDIX D: PROTEINLIKE MACROIONS

The partition function for the system of two pointlike proteins immersed in monovalent salt solution and containing seven types of dissociable AAs, negatively charged {Asp, Glu, Tyr, Cys} and positively charged {Arg, His, Lys}, can

be written as

$$\mathcal{Z} = \prod_{\ell=1,7}^{M_i^\ell, M_{i'}^\ell} \sum_{i_\ell, i'_\ell} b_\ell^{i_\ell+i'_\ell} \frac{M_i^\ell!}{i_\ell!(M_i^\ell-i_\ell)!} \frac{M_{i'}^\ell!}{i'_\ell!(M_{i'}^\ell-i'_\ell)!} e^{-\beta\mathcal{F}_{pp}}, \quad (D1)$$

where ℓ runs through {Asp, Glu, Tyr, Cys} and {Arg, His, Lys}, with

$$\begin{aligned} \mathcal{F}_{pp} &= \frac{e_0^2\kappa}{8\pi\epsilon_0} \left[\frac{e^{-\tilde{a}}}{\tilde{a}} \left(\sum_m (M_i^m - i)^2 + \sum_m (M_{i'}^m - i')^2 \right) \right. \\ &\left. + 2 \frac{e^{-\tilde{R}}}{\tilde{R}} \sum_m (M_i^m - i) \sum_m (M_{i'}^m - i') \right], \end{aligned} \quad (D2)$$

where the unprimed and the primed notation refer to the two protein macroions. Here M_i^ℓ counts how many times each of these seven amino acids occurs in a protein, while $M_{i'}^m$ is restricted to counting only negative amino acids. In addition, b_ℓ refers to the chemical energy of dissociation $b_\ell = e^{-\ln 10(pH-pK_\ell)}$, where the intrinsic pK_ℓ for the seven dissociable amino acids are given in Table I.

-
- [1] R. Piazza, *Curr. Opin. Colloid Interface Sci.* **8**, 515 (2004).
[2] T. Simonson, *Rep. Prog. Phys.* **66**, 737 (2003).
[3] D. Leckband and S. Sivasankar, *Colloids Surf. B* **14**, 83 (1999).
[4] A. Naji, M. Kanduč, J. Forsman, and R. Podgornik, *J. Chem. Phys.* **139**, 150901 (2013).
[5] N. I. Lebovka, *Adv. Polym. Sci.* **255**, 57 (2014).
[6] M. Borkovec, B. Jönsson, and G. J. M. Koper, *Surf. Colloid Sci.* **16**, 99 (2001).
[7] J. Kirkwood and J. B. Shumaker, *Proc. Natl. Acad. Sci. USA* **38**, 855 (1952).
[8] J. Kirkwood and J. B. Shumaker, *Proc. Natl. Acad. Sci. USA* **38**, 863 (1952).
[9] V. A. Parsegian, *Van der Waals Forces* (Cambridge University Press, Cambridge, 2005).
[10] S. H. Behrens and M. Borkovec, *J. Chem. Phys.* **111**, 382 (1999); M. Borkovec and S. H. Behrens, *J. Phys. Chem. B* **112**, 10795 (2008).
[11] M. Lund and B. Jönsson, *Q. Rev. Biophys.* **46**, 265 (2013).
[12] D. Chan, J. W. Perram, L. R. White, and T. W. Healy, *J. Chem. Soc. Faraday Trans. 1* **71**, 1046 (1974); D. Chan, T. W. Healy, and L. R. White, *ibid.* **72**, 2844 (1976).
[13] R. Podgornik and V. A. Parsegian, *Chem. Phys.* **154**, 477 (1991).
[14] R. Podgornik and V. A. Parsegian, *J. Phys. Chem.* **99**, 9491 (1995).
[15] S. L. Carnie and D. Y. Chan, *J. Colloid Interface Sci.* **161**, 260 (1993).
[16] R. J. Nap, A. Lošdorfer Božič, I. Szleifer, and R. Podgornik, *Biophys. J.* **107**, 1970 (2014).
[17] N. Boon and R. van Roij, *J. Chem. Phys.* **134**, 054706 (2011).
[18] R. R. Netz, *J. Phys.: Condens. Matter* **15**, S239 (2003).
[19] M. Lund and B. Jönsson, *Biochemistry* **44**, 5722 (2005); F. L. B. da Silva, M. Lund, B. Jönsson, and T. Åkesson, *J. Phys. Chem. B* **110**, 4459 (2006); F. L. B. da Silva and B. Jönsson, *Soft Matter* **5**, 2862 (2009).
[20] B. W. Ninham and V. A. Parsegian, *J. Theor. Biol.* **31**, 405 (1971).
[21] N. Adžić and R. Podgornik, *Eur. Phys. J. E* **37**, 49 (2014).

- [22] A. C. Maggs and R. Podgornik, *Europhys. Lett.* **108**, 68003 (2014).
- [23] H. Li and M. Kardar, *Phys. Rev. Lett.* **67**, 3275 (1991).
- [24] F. J. M. Ruiz-Cabello, P. Maroni, and M. Borkovec, *J. Chem. Phys.* **138**, 234705 (2013).
- [25] G. Trefalt, F. J. Montes Ruiz-Cabello, and M. Borkovec, *J. Phys. Chem. B* **118**, 6346 (2014).
- [26] M. Lund and B. Jönsson, *Biophys. J.* **85**, 2940 (2003).
- [27] R. A. Curtis, J. Ulrich, A. Montaser, J. M. Prausnitz, and H. W. Blanch, *Biotechnol. Bioeng.* **79**, 4 (2002).

PAPER

Semi-flexible compact polymers in two dimensional nonhomogeneous confinement

To cite this article: D Mareti *et al* 2019 *J. Phys. A: Math. Theor.* **52** 125001

View the [article online](#) for updates and enhancements.



IOP | ebooks™

Bringing you innovative digital publishing with leading voices to create your essential collection of books in STEM research.

Start exploring the collection - download the first chapter of every title for free.

Semi-flexible compact polymers in two dimensional nonhomogeneous confinement

D Marčetić¹, S Elezović-Hadžić^{2,5} , N Adžić³ and I Živić⁴

¹ Faculty of Natural Sciences and Mathematics, University of Banja Luka, M. Stojanovića 2, Bosnia and Herzegovina

² Faculty of Physics, University of Belgrade, PO Box 44, 11001 Belgrade, Serbia

³ Faculty of Physics, University of Vienna, Boltzmannngasse 5, A-1090 Vienna, Austria

⁴ Faculty of Science, University of Kragujevac, Radoja Domanovića 12, Kragujevac, Serbia

E-mail: dusanka.marcetic-lekic@pmf.unibl.org, suki@ff.bg.ac.rs, natasa.adzic@univie.ac.at and ivanz@kg.ac.rs

Received 24 October 2018, revised 9 January 2019

Accepted for publication 6 February 2019

Published 25 February 2019



CrossMark

Abstract

We have studied the compact phase conformations of semi-flexible polymer chains confined in two dimensional nonhomogeneous media, modelled by fractals that belong to the family of modified rectangular (MR) lattices. Members of the MR family are enumerated by an integer p ($2 \leq p < \infty$) and fractal dimension of each member of the family is equal to 2. The polymer flexibility is described by the stiffness parameter s , while the polymer conformations are modelled by weighted Hamiltonian walks (HWs). Applying an exact recurrence equations method, we have found that partition function Z_N for closed HWs consisting of N steps scales as $\omega^N \mu^{\sqrt{N}}$, where constants ω and μ depend on both p and s . We have calculated numerically the stiffness dependence of the polymer persistence length, as well as various thermodynamic quantities (such as free and internal energy, specific heat and entropy) for a large set of members of the MR family. Analysis of these quantities has shown that semi-flexible compact polymers on MR lattices can exist only in the liquid-like (disordered) phase, whereas the crystal (ordered) phase has not appeared. Finally, behavior of the examined system at zero temperature has been discussed.

Keywords: solvable lattice models, structures and conformations, phase diagrams, polymers

(Some figures may appear in colour only in the online journal)

⁵ Author to whom any correspondence should be addressed.

1. Introduction

Behaviour of a linear flexible polymer in various types of solvents has been extensively studied in the past and the subject is well understood, at least when the universal properties of polymer statistics are under consideration [1]. The canonical model of a linear polymer is the self-avoiding walk (SAW), which is a random walk that must not contain self-intersections. In this model, steps of the walk are usually identified with monomers, while the surrounding solvent is represented by a lattice [2]. In a good solvent (high temperature regime) polymer chain is in extended state, whereas in a bad solvent (low temperatures) it is in compact phase. Since in the compact phase a polymer fills up the space as densely as possible, it is often modelled by Hamiltonian walk (HW), which is a SAW that visits every site of the underlying lattice.

Most of real polymers, especially biologically important ones, are semi-flexible, but contrary to the flexible polymers, knowledge of their conformational properties is scarce. The measure of bending rigidity of a semi-flexible chain is its persistence length l_p , which can be understood as an average length of straight segments of the chain. In a good solvent the stiffness of the polymer only enlarges the persistence length, while in a bad one (when polymer is compact), an increase of the chain stiffness may promote the transition from a disordered phase (when polymer bends are randomly distributed over the polymer, with finite density) to an ordered crystalline phase (when large rod-like parts of the chain lie in parallel order, with zero density of bends). In order to study the compact phase of semi-flexible polymers on homogeneous lattices Flory introduced a model of polymer melting [3], in which a compact polymer is modelled by HW, while the bending rigidity is taken into account by assigning an extra energy to each bend of the chain. Applying the proposed model within the mean-field theory, it has been found [3] that there are two compact phases: disordered liquid-like and ordered crystal-like phase, and a phase transition caused by competition between the chain entropy and the stiffness of the polymer has emerged. At high temperatures, the entropy dominated disordered phase exists, in which the number of bends in the chain is comparable with the total number of monomers, and the persistence length is finite. At low temperatures bending energy dominates, so that polymer takes ordered crystalline form, in which bends exist only on the opposite edges of the underlying lattice. In this phase the persistence length becomes comparable to the lattice size. Using various techniques, in a series of papers [4–12], the existence and nature of phase transition between these two phases of compact polymers have been investigated, giving quite different results for the order of phase transition.

Besides being interesting from the pure physical point of view, semi-flexible compact polymer models are of great importance for better understanding of some biological systems and processes. For example, DNA condensation [13] and protein folding problem [14] take place in squeezed cellular environment and demand for compact states of these rigid polymers. For such systems, coarse-grained polymer models often present valuable tool in explaining the major features observed in experiments [15].

The Hamiltonian walk problem, even in its simplest form, with no interactions involved and on regular lattices, is a very difficult one. Exact enumeration of HWs, which is a prerequisite for further analysis of the compact polymer properties, is limited to rather small lattice sizes. For instance, HWs on L^2 square lattice have been enumerated up to size $L = 17$ [16], and on L^3 cube up to $L = 4$ [17], which is not sufficient to draw solid conclusions about asymptotic behavior for long compact chains (therefore approximate techniques, such as Monte Carlo algorithms [18, 19] have been used). In addition to the HWs enumeration, solving the semi-flexible HW problem requires their classification according to the number of bends, which makes it even less feasible. On the other hand, in real situations polymers are usually situated in nonhomogeneous media, so that models of semi-flexible compact polymers

should be extended to such environments. In that sense, as a first step towards more realistic situations, fractal lattices may be used as underlying lattices for semi-flexible HWs, which has been successfully accomplished for a broad range of polymer related problems [20–29]. Some deterministic fractal lattices have already been useful in exact studies of flexible HWs [30]. In these studies, emphasis has been put on establishing the scaling form of the number of very long walks, which is a long-standing issue in various polymer models [31]. Recently, a closely related problem of finding the scaling form of the partition function of semi-flexible HWs on 3- and 4-simplex lattices has been analyzed [32] in an exact manner. The method applied in [32] also enabled detailed analysis of various thermodynamic quantities, which brought about the conclusion that ordered crystal-like phase can not exist on these lattices. In order to resolve the question whether the inhomogeneity of the polymer environment always suppresses the crystal phase, it would be useful to extend this study on other nonhomogeneous lattices. In [33] an outline of a similar approach, applied on modified rectangular (MR) lattices, has been presented, and in this paper we generalize the applied method to the whole family of such lattices. Each member of this family is actually a square lattice with self-similarly removed bonds, where the manner in which the bonds are removed are characterized by an integer $p \geq 2$. None of the vertices is removed in this process, and fractal dimension of each of these lattices is 2, all that making them similar to the square lattice (on which most of the lattice polymer models are studied), and convenient for systematic analysis of the impact of defects in homogeneous environments on thermodynamic properties of the studied model.

The paper is organized as follows. In section 2 we describe the MR lattices for general scaling parameter p , then we introduce the model of semi-flexible HWs and the recurrence relations method for the exact evaluation of the partition function. In the same section we present specific results obtained for $p = 2$ MR lattice, and we analyze thermodynamic quantities concerning the studied model. In section 3 we generalize the method for lattice with arbitrary $p > 2$, and discuss the obtained general scaling form of the partition function. General thermodynamic behavior is presented in section 4, and the possibility of existence of different phases within the model is discussed. The behavior of the studied polymer model at temperature $T = 0$ (ground state) is examined in section 5. Summary of the obtained results and pertinent conclusions are given in section 6.

2. Semi-flexible closed HWs on the family of MR lattices

In this section the method of recurrence relations for studying the conformational properties of compact semi-flexible polymers is described. Polymer rings are modeled by closed HWs (Hamiltonian cycles), whereas the substrates on which the polymers are adsorbed are represented by fractals belonging to the MR family of fractals [34]. Members of MR fractal family are labeled by an integer p ($2 \leq p < \infty$), and can be constructed iteratively. For each particular p , at the first stage ($r = 1$) of the construction one has four points forming a unit square. Then, p unit squares are joined in the rectangle to obtain the ($r = 2$) construction stage. In the next step, p rectangles are joined into a square, and so on (see figure 1). The complete lattice is acquired in the limit $r \rightarrow \infty$. The lattice structure obtained in the r th stage is called the r th order fractal generator. It contains $N_r = 4p^{r-1}$ lattice sites, and fractal dimension is $d_f = 2$ for each fractal of the family.

To take into account the polymer stiffness property, to each bend of the walk we assign the weight factor $s = e^{-\varepsilon/k_B T}$ (stiffness parameter), where $\varepsilon > 0$ is the bending energy, T is the temperature, and k_B is the Boltzmann constant. Varying T and/or ε , the stiffness parameter can take values in the range $0 \leq s \leq 1$, where two opposite limits $s = 0$ and $s = 1$ coincide

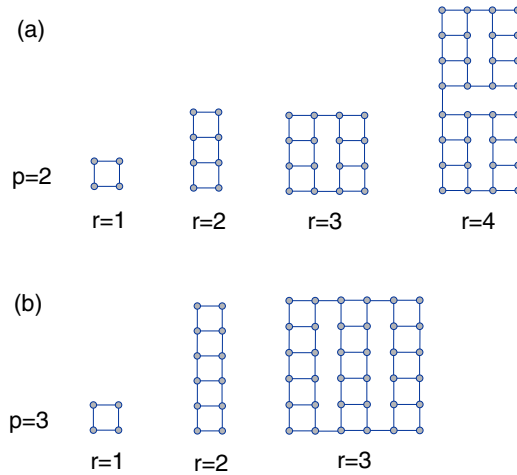


Figure 1. (a) First four steps of iterative construction of $p = 2$ MR fractal lattice. (b) First three steps in construction of $p = 3$ MR fractal.

with a fully rigid and a fully flexible polymer chain, respectively. To evaluate the partition function one has to sum the weights of all possible polymer conformations \mathcal{C}_N with N -steps: $Z_N = \sum_{\mathcal{C}_N} e^{-E(\mathcal{C}_N)/k_B T}$, where $E(\mathcal{C}_N) = \varepsilon N_b(\mathcal{C}_N)$ is the energy of an N -step conformation having N_b bends. The above partition function can be written as $Z_N = \sum_{\mathcal{C}_N} s^{N_b(\mathcal{C}_N)} = \sum_{N_b} g_{N,N_b} s^{N_b}$, where g_{N,N_b} is the number of N -step conformations with N_b bends (i.e. degeneracy of the energy level εN_b).

2.1. Recursion relations construction for $p = 2$ MR lattice

To calculate the partition function for the model under study, one has to enumerate all possible Hamiltonian cycle conformations. In general, this appears to be a very complicated task, but in this case the self-similarity of MR lattices allows systematic enumeration using an exact recursive method [33]. In order to explain this approach we present its application in the case of $p = 2$ MR lattice. In figure 2(a) an example of closed HW on the $p = 2$ MR lattice of order $r = 5$ is shown. Performing a coarse-graining process one notices in figure 2(b) that this walk can be decomposed into several parts corresponding to constitutive second order generators, which consist of one or two strands. As it can be seen in figures 2(c) and (d), this process can be repeated two more times, leading to a coarse-grained HW consisting of two one-strand parts within the two constituent $r = 4$ generators. It is quite obvious that figure 2(d) is general in the sense that any closed HW on generator of any order $(r + 1)$ can be decomposed into two open HWs, traversing the two constituent r th order generators. These two open HWs are of the same type, by which we mean that both of them enter and exit the r th order generator through vertices lying at the ends of the same longer edge of the generator, perpendicularly to that edge. We denote such conformations as B_1 -type HWs, and assign to them the function

$$B_1^{(r)}(s) = \sum_{N_b} \mathcal{B}_{1,N_b}^{(r)} s^{N_b}, \tag{2.1}$$

where $\mathcal{B}_{1,N_b}^{(r)}$ is the overall number of B_1 -type HWs with N_b bends, which traverse an r th order generator. Then, knowing $B_1^{(r)}(s)$, one can calculate the partition function

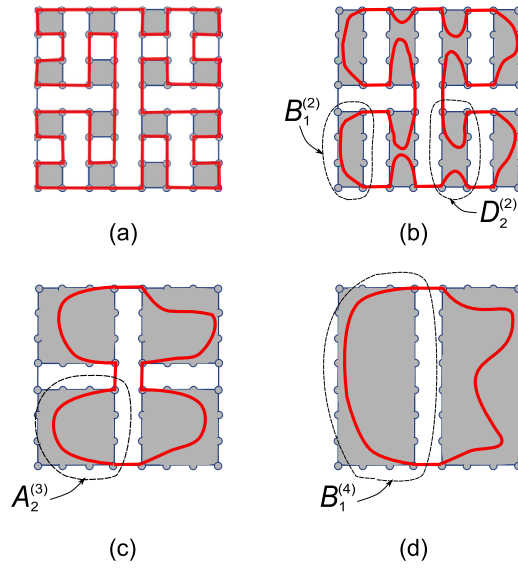


Figure 2. (a) Example of a semi-flexible Hamiltonian walk on the 5th order generator of $p = 2$ MR lattice. This walk has 42 bends, so that its statistical weight is equal to $e^{-42\epsilon/k_b T} = s^{42}$. Subsequent steps of the coarse-graining process are depicted in (b)–(d). Grey rectangles in (b)–(d) represent generators of order two, three and four, respectively, whereas curved lines correspond to the coarse grained parts of the walk. Different types of conformations within the $r = 2, 3$ and 4 generators are encircled. In (d) one can see that this closed Hamiltonian walk, observed on $r = 5$ generator, consists of two B_1 -type HWs which span the two constituent $r = 4$ generators. It is obvious that such decomposition of any closed Hamiltonian walk on generator of order $(r + 1)$ into the parts within the constituent r th order generators is the only possible one.

$$Z_c^{(r+1)} = \left(B_1^{(r)} \right)^2, \quad (2.2)$$

corresponding to all closed semi-flexible HWs on $(r + 1)$ th order lattice structure. The function $B_1^{(r)}(s)$ can be calculated recursively, utilizing the fact that each B_1 -type HW on any r th order generator can be decomposed into parts within the constituent $(r - 1)$ th generators (as depicted in figure 2(c)), and so on. As one continues HW decomposition into parts within lower order generators, careful inspection shows that altogether nine types of semi-flexible HW conformations can emerge, 5 one-stranded and 4 two-stranded (see figure 3), which differ by directions of the outer entering and exiting steps, as well as by the main direction of their strands within the generator (which can be either along longer or shorter edge). We denote these nine ‘traversing’ types of conformations as $A_1, A_2, B_1, B_2, B_3, D_1, D_2, E_1$ and E_2 , and to each of them (as for the B_1 -type) we assign a function

$$X^{(r)}(s) = \sum_{N_b} \mathcal{X}_{N_b}^{(r)} s^{N_b}, \quad X \in \{A_1, A_2, B_1, B_2, B_3, D_1, D_2, E_1, E_2\}, \quad (2.3)$$

with $\mathcal{X}_{N_b}^{(r)}$ being the number of HWs of the type X with N_b bends, on the r th order fractal structure. These functions can be thought of as restricted partition functions, and due to the self-similarity of the lattice, they obey the following recursion relations

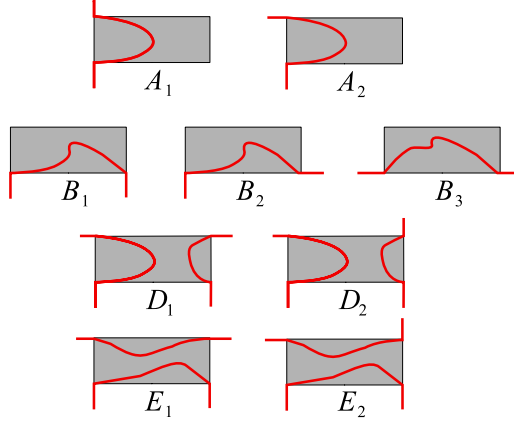


Figure 3. Possible types of semi-flexible HWs on the r th order lattice structure in the case $p = 2$.

$$\begin{aligned}
 A_1^{(r+1)} &= B_1^{(r)} D_1^{(r)}, & A_2^{(r+1)} &= B_1^{(r)} D_2^{(r)}, \\
 B_1^{(r+1)} &= \left(A_2^{(r)}\right)^2, & B_2^{(r+1)} &= A_1^{(r)} A_2^{(r)}, & B_3^{(r+1)} &= \left(A_1^{(r)}\right)^2, \\
 D_1^{(r+1)} &= 2E_2^{(r)} D_2^{(r)} + \left(B_2^{(r)}\right)^2, & D_2^{(r+1)} &= D_2^{(r)} E_1^{(r)} + E_2^{(r)} D_1^{(r)} + B_2^{(r)} B_3^{(r)}, \\
 E_1^{(r+1)} &= \left(D_2^{(r)}\right)^2, & E_2^{(r+1)} &= D_1^{(r)} D_2^{(r)}.
 \end{aligned} \tag{2.4}$$

Starting with their values for $r = 1$: $A_1^{(1)} = s^4$, $A_2^{(1)} = s^3$, $B_1^{(1)} = s^2$, $B_2^{(1)} = s^3$, $B_3^{(1)} = s^4$, $D_1^{(1)} = s^2$, $D_2^{(1)} = s$, $E_1^{(1)} = s^2$, and $E_2^{(1)} = s^3$, for any particular value of s one can, in principle, numerically find the values of the restricted partition functions for very large r values. In figure 4, construction of recursion relations for A - and B -type restricted partition functions, together with their initial conditions, is illustrated. In a similar way one can find recursive relations for the two-stranded partition functions, and the corresponding initial conditions.

Iterating restricted partition functions and using (2.2), one can obtain Z_c and, consequently, explore the thermodynamic behavior of the model. However, applying the recursion relations (2.4) for various values of s (between 0 and 1), one can show that there is a critical value of the bending parameter $s^* = 0.7366671$, such that for $s < s^*$ all restricted partition functions tend to 0 (and so does the overall partition function), whereas for $s > s^*$ they all become infinitely large, for $r \gg 1$. This can be explained by the coupling between the degeneracy g_{N,N_b} of energy levels $E(N_b) = \varepsilon N_b$ and the corresponding Boltzmann factor s^{N_b} . Degeneracies are such that they increase with the energy of levels attaining their maximum value, after which they decrease. At low temperatures (that is, for small s), degeneracies are not large enough to overcome small Boltzmann factors, but increasing the temperature they prevail and partition function iterates to infinity.

The fact that for $s > s^*$ restricted partition functions indefinitely grow makes the analysis of the thermodynamic behavior difficult, and therefore it is useful to introduce rescaled variables

$$x^{(r)} = \frac{X^{(r)}}{E_1^{(r)}}, \quad x \in \{a_1, a_2, b_1, b_2, b_3, d_1, d_2, e_2\}. \tag{2.5}$$

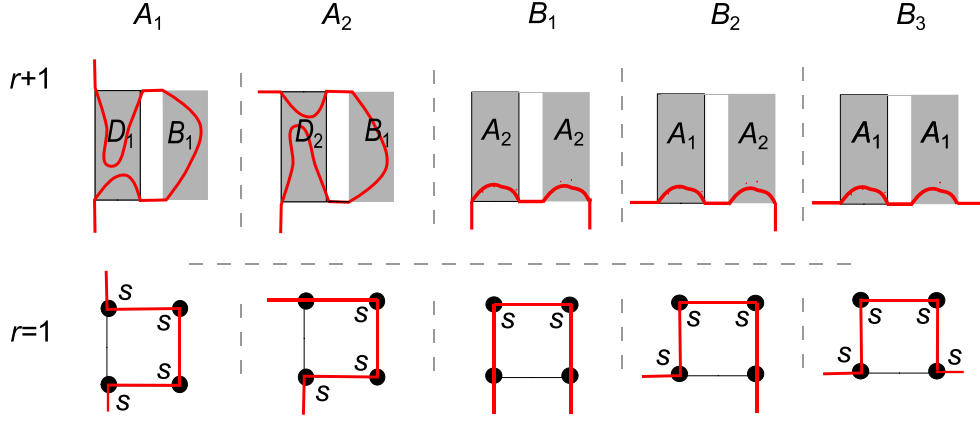


Figure 4. Top row: possible conformations of one-stranded types of semi-flexible HWs on the generator of order $(r + 1)$. Gray rectangles represent the r th order lattice structure, and curved lines correspond to coarse-grained walks. Bottom row: possible one-stranded semi-flexible HWs on the first order generator. Small black circles represent sites the lattice consists of.

These new variables fulfil the following recursion relations

$$\begin{aligned}
 a_1^{(r+1)} &= \frac{b_1^{(r)} d_1^{(r)}}{(d_2^{(r)})^2}, & a_2^{(r+1)} &= \frac{b_1^{(r)}}{d_2^{(r)}}, & e_2^{(r+1)} &= \frac{d_1^{(r)}}{d_2^{(r)}}, \\
 b_1^{(r+1)} &= \left(\frac{a_2^{(r)}}{d_2^{(r)}}\right)^2, & b_2^{(r+1)} &= \frac{a_1^{(r)} a_2^{(r)}}{(d_2^{(r)})^2}, & b_3^{(r+1)} &= \left(\frac{a_1^{(r)}}{d_2^{(r)}}\right)^2, \\
 d_1^{(r+1)} &= 2 \frac{e_2^{(r)}}{d_2^{(r)}} + \left(\frac{b_2^{(r)}}{d_2^{(r)}}\right)^2, & d_2^{(r+1)} &= \frac{1}{d_2^{(r)}} + \frac{e_2^{(r)} d_1^{(r)} + b_2^{(r)} b_3^{(r)}}{(d_2^{(r)})^2}, \quad (2.6)
 \end{aligned}$$

with the initial conditions

$$a_1^{(1)} = b_3^{(1)} = s^2, \quad a_2^{(1)} = b_2^{(1)} = e_2^{(1)} = s, \quad b_1^{(1)} = d_1^{(1)} = 1, \quad d_2^{(1)} = s^{-1}. \quad (2.7)$$

They are useful to operate with because it turns out that for any s in the region $0 < s \leq 1$, variables $a_i^{(r)}$ and $b_i^{(r)}$ quickly tend to 0, whereas $d_1^{(r)}$, $d_2^{(r)}$ and $e_2^{(r)}$ tend to some finite non-zero values. In particular, numerical analysis of (2.6) shows (see appendix A for some details) that

$$b_1^{(2k)}(s) \sim [\lambda_e(s)]^{2^k}, \quad b_1^{(2k+1)}(s) \sim [\lambda_o(s)]^{2^k}, \quad (2.8)$$

for $k \gg 1$, where λ_e and λ_o are finite functions of s (see figure 5).

Now, using the rescaled variable $b_1^{(r)}$, the partition function (2.2) may be written as

$$Z_c^{(r+1)} = \left(b_1^{(r)} E_1^{(r)}\right)^2, \quad (2.9)$$

so that, introducing variables

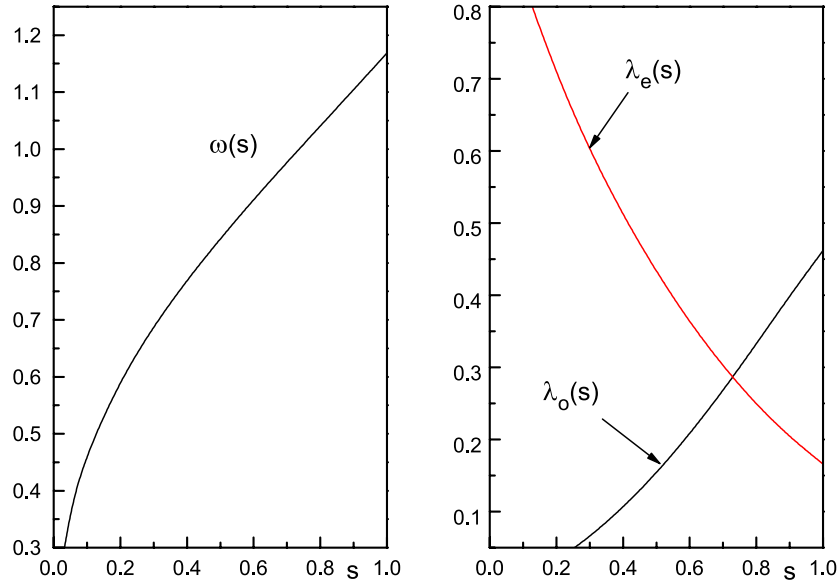


Figure 5. Dependence of ω (2.13), λ_e and λ_o (2.8) on the stiffness parameter s , for $p = 2$ MR lattice.

$$y_r = \frac{\ln Z_c^{(r)}}{N_r}, \quad q_r = \frac{\ln E_1^{(r)}}{N_r}, \quad (2.10)$$

where $N_r = 2^{r+1}$, one obtains

$$y_{r+1} = q_r + \frac{\ln b_1^{(r)}}{2^{r+1}}, \quad (2.11)$$

$$q_{r+1} = q_r + \frac{\ln d_2^{(r)}}{2^{r+1}}, \quad (2.12)$$

which follows from the recursion relation for $E_1^{(r)}$ (given in (2.4)) and definition (2.5). Numerically iterating recursion equation for q_r , for various values of s , one obtains that finite limiting value $\lim_{r \rightarrow \infty} q_r$ exists and it depends on s . Then, from (2.11) and (2.8) it follows that

$$\lim_{r \rightarrow \infty} y_r = \lim_{r \rightarrow \infty} q_r = \ln \omega(s), \quad (2.13)$$

meaning that the leading factor in the asymptotical behavior of $Z_c^{(r)}$ is ω^{N_r} . Values of $\omega(s)$ are depicted in figure 5. To find the next term in the asymptotical formula for $\ln Z_c^{(r)}$, we observe that, using (2.11)–(2.13), one obtains

$$y_{r+1} = \ln \omega + \frac{\ln b_1^{(r)}}{2^{r+1}} - \sum_{i=r}^{\infty} (q_{i+1} - q_i) = \ln \omega + \frac{\ln b_1^{(r)}}{2^{r+1}} - \sum_{i=r}^{\infty} \frac{\ln d_2^{(i)}}{2^{i+1}}. \quad (2.14)$$

Taking into account that $|\ln d_2^{(i)}|$ is less than some finite constant (which was numerically obtained), one can conclude that for $r \gg 1$ the following approximate relation follows

$$y_{r+1} \approx \ln \omega + \frac{\ln b_1^{(r)}}{2^{r+1}}. \quad (2.15)$$

Employing the relations (2.8), it further leads to the following form of the partition function:

$$Z_c^{(r)}(s) \sim [\omega(s)]^{N_r} \times \begin{cases} [\mu_e(s)]^{\sqrt{N_r}}, & \text{for } r \text{ even} \\ [\mu_o(s)]^{\sqrt{N_r}}, & \text{for } r \text{ odd} \end{cases}, \quad (2.16)$$

where $\mu_e(s) = [\lambda_o(s)]^{1/\sqrt{2}}$ and $\mu_o(s) = \lambda_e(s)$.

2.2. Thermodynamics of semi-flexible Hamiltonian cycles on $p = 2$ MR lattice

By definition, the free energy per monomer, in the thermodynamic limit, is equal to

$$f = -k_B T \lim_{r \rightarrow \infty} \frac{\ln Z_c^{(r)}}{N_r}, \quad (2.17)$$

so that, from (2.10) and (2.13), it follows

$$f = -k_B T \ln \omega = \varepsilon \frac{\ln \omega}{\ln s}. \quad (2.18)$$

Using already found values of $\omega(s)$, one can obtain $f(T)$, which is shown in figure 6.

Internal energy per monomer, in the thermodynamic limit, is equal to

$$u = \varepsilon \lim_{r \rightarrow \infty} \frac{\langle N_b^{(r)} \rangle}{N_r} = s \frac{\partial}{\partial s} (f \ln s), \quad (2.19)$$

where $N_b^{(r)}$ is the number of bends within the HW. Using (2.18) and (2.13), one obtains

$$\frac{u}{\varepsilon} = s \frac{\partial}{\partial s} (\ln \omega) = s \lim_{r \rightarrow \infty} q'_r, \quad (2.20)$$

where prime denotes derivative of q_r with respect to s . The recursion relation for q'_r follows from relation (2.12) and has the form

$$q'_{r+1} = q'_r + \frac{1}{N_r} \frac{(d_2^{(r)})'}{d_2^{(r)}}, \quad (2.21)$$

whereas from (2.6) one can directly obtain recursion relations for derivatives of $x^{(r)}$ (defined by (2.5)). Iterating all these relations, internal energy u can be calculated for any particular s .

Persistence length is defined as an average number of steps between two consecutive bends

$$l_p = \lim_{r \rightarrow \infty} \frac{N_r}{\langle N_b^{(r)} \rangle} = \frac{\varepsilon}{u}, \quad (2.22)$$

and can be evaluated directly from u .

Using expressions obtained for u , one can show that the heat capacity per monomer $c = \frac{\partial u}{\partial T}$ is equal to

$$c = k_B \ln^2 s \left[\frac{u}{\varepsilon} + s^2 \frac{\partial^2}{\partial s^2} (\ln \omega) \right]. \quad (2.23)$$

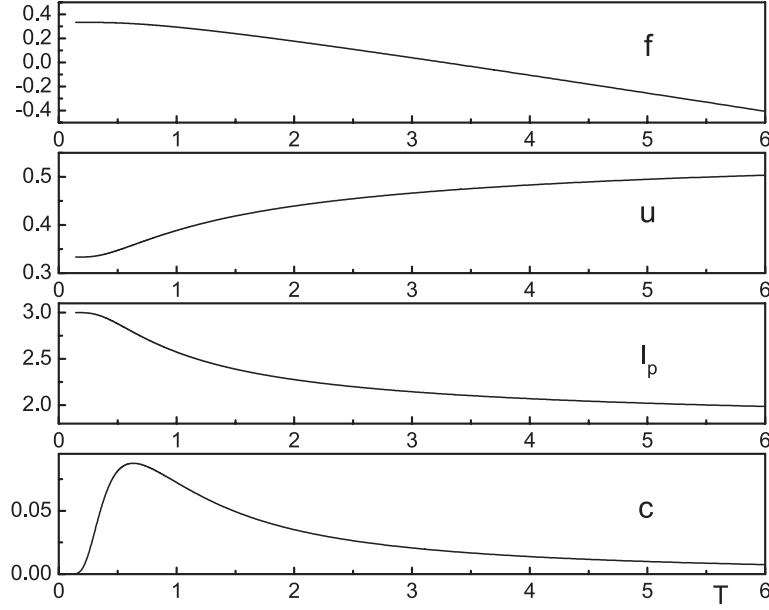


Figure 6. Free energy f (2.18), internal energy u (2.20), persistence length l_p (2.22), and heat capacity c (2.23) per monomer, in the thermodynamic limit, as functions of temperature T (f and u are measured in units of ε , c in units of k_B , and T in units of ε/k_B), for $p = 2$ MR lattice.

Since $\ln \omega = \lim_{r \rightarrow \infty} q_r$, this means that in order to calculate the heat capacity, in addition to already calculated u , one needs second derivatives of q_r , for $r \gg 1$. These derivatives can be obtained recursively using the relation

$$q''_{r+1} = q''_r + \frac{1}{N_r} \left[\frac{\left(d_2^{(r)} \right)''}{d_2^{(r)}} - \left(\frac{\left(d_2^{(r)} \right)'}{d_2^{(r)}} \right)^2 \right], \quad (2.24)$$

which follows directly from (2.21), together with recursion relations (2.6) for $x^{(r)}$ and corresponding recursive relations for their first and the second derivatives, which can be obtained straightforwardly. Temperature dependence of all evaluated thermodynamic quantities is depicted in figure 6, whereupon one can perceive that the free energy f and the persistence length of the polymer monotonically decrease with T , whereas the internal energy u is monotonically increasing function of T . Finally, the specific heat c is a non-monotonic function of temperature, displaying a maximum for some $T < 1$ (in the units of ε/k_B). These results imply that there is no finite order phase transition for the studied model. On the other hand, since for $s < s^*$ all restricted partition functions tend to 0, and for $s > s^*$ they tend to infinity, one could have expected different phases in these two regions, and therefore, existence of a phase transition. However, different polymer phases are characterized by different typical conformations. Here, that would be manifested by different mutual relationships between various restricted partition functions in the regions $s < s^*$ and $s > s^*$, but our precise and detailed numerical analysis could not detect any of these. This means that, formally speaking, structure of the recursion relations (2.4), together with their initial conditions (which are both determined by

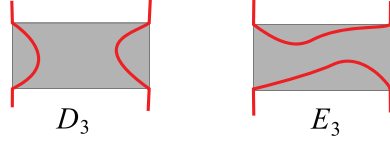


Figure 7. Two additional types of semi-flexible HWs on the r th order fractal structure, for any $p > 2$ MR lattice. Other possible conformations are of the same type as for $p = 2$ MR lattice, and they are depicted in figure 3.

the lattice topology and by the studied model) suppress abrupt change in orientational ordering of typical HW conformations, at any s value.

3. Generalization to MR lattices with $p > 2$

It is straightforward to generalize the method for lattices with $p > 2$. Due to the connectivity of the lattices and symmetry considerations, it follows that for any $p > 2$ there can be altogether eleven possible types of semi-flexible conformations. The nine ones, shown in figure 3, have already been introduced in the case of $p = 2$. Two additional ones needed in the case of $p > 2$ are shown in figure 7. In the upper part of figure 8 the only possible decomposition of any closed HW is shown, so that one concludes that the partition function of all closed semi-flexible conformations on the generator of order $(r + 1)$, for an arbitrary $p > 2$ member of the MR family, can be written as

$$Z_c^{(r+1)} = \left(B_1^{(r)}\right)^2 \left(D_3^{(r)}\right)^{p-2}. \quad (3.1)$$

Therefore, in a similar manner as in the case $p = 2$, one can iteratively calculate $Z_c^{(r+1)}$ for any r , which requires recursion relations for all eleven restricted partition functions. These relations have the following form

$$\begin{aligned} A_1^{(r+1)} &= B_1^{(r)} D_1^{(r)} \left(D_3^{(r)}\right)^{p-2}, & A_2^{(r+1)} &= B_1^{(r)} D_2^{(r)} \left(D_3^{(r)}\right)^{p-2}, \\ B_1^{(r+1)} &= \left(A_1^{(r)}\right)^{p-2} \left(A_2^{(r)}\right)^2, & B_2^{(r+1)} &= \left(A_1^{(r)}\right)^{p-1} A_2^{(r)}, & B_3^{(r+1)} &= \left(A_1^{(r)}\right)^p, \\ D_1^{(r+1)} &= 2D_2^{(r)} \left(D_3^{(r)}\right)^{p-2} E_2^{(r)} + (p-2) \left(D_2^{(r)}\right)^2 \left(D_3^{(r)}\right)^{p-3} E_3^{(r)} \\ &\quad + 2B_1^{(r)} B_2^{(r)} D_2^{(r)} \left(D_3^{(r)}\right)^{p-3} + (p-3) \left(B_1^{(r)}\right)^2 \left(D_2^{(r)}\right)^2 \left(D_3^{(r)}\right)^{p-4}, \\ D_2^{(r+1)} &= D_2^{(r)} \left(D_3^{(r)}\right)^{p-2} E_1^{(r)} + D_1^{(r)} \left(D_3^{(r)}\right)^{p-2} E_2^{(r)} + (p-2) D_1^{(r)} D_2^{(r)} \left(D_3^{(r)}\right)^{p-3} E_3^{(r)} \\ &\quad + B_1^{(r)} B_3^{(r)} D_2^{(r)} \left(D_3^{(r)}\right)^{p-3} + B_1^{(r)} B_2^{(r)} D_1^{(r)} \left(D_3^{(r)}\right)^{p-3} \\ &\quad + (p-3) \left(B_1^{(r)}\right)^2 D_1^{(r)} D_2^{(r)} \left(D_3^{(r)}\right)^{p-4}, \\ D_3^{(r+1)} &= 2D_1^{(r)} \left(D_3^{(r)}\right)^{p-2} E_1^{(r)} + (p-2) \left(D_1^{(r)}\right)^2 \left(D_3^{(r)}\right)^{p-3} E_3^{(r)} \\ &\quad + 2B_1^{(r)} B_3^{(r)} D_1^{(r)} \left(D_3^{(r)}\right)^{p-3} + (p-3) \left(B_1^{(r)}\right)^2 \left(D_1^{(r)}\right)^2 \left(D_3^{(r)}\right)^{p-4}, \\ E_1^{(r+1)} &= \left(D_2^{(r)}\right)^2 \left(D_3^{(r)}\right)^{p-2}, & E_2^{(r+1)} &= D_1^{(r)} D_2^{(r)} \left(D_3^{(r)}\right)^{p-2}, \\ E_3^{(r+1)} &= \left(D_1^{(r)}\right)^2 \left(D_3^{(r)}\right)^{p-2}. \end{aligned} \quad (3.2)$$

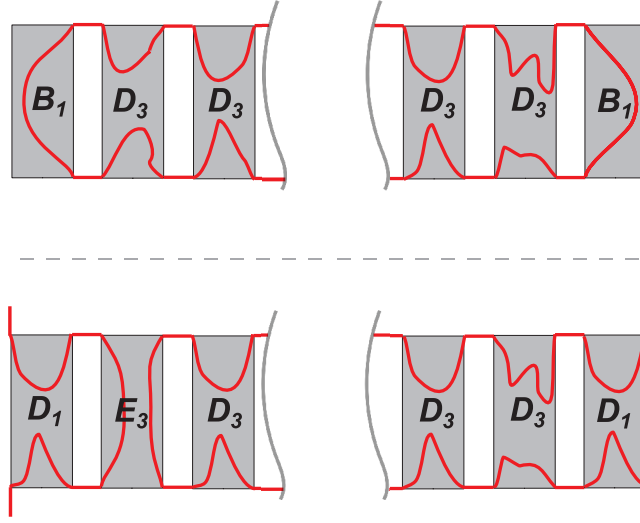


Figure 8. Upper part: decomposition of any closed semi-flexible HW on the generator of order $(r + 1)$, for an arbitrary $p > 2$ MR lattice. Grey rectangles represent p generators of order r . Lower part: example of a D_3 -type conformation on generator of order $(r + 1)$, illustrating occurrence of E_3 -type conformations on MR lattices with $p > 2$. The E_3 part can exist on any of the $(p - 2)$ inner r th order generators, so that such conformations correspond to the term $(p - 2) (D_1^{(r)})^2 (D_3^{(r)})^{p-3} E_3^{(r)}$ in the recursion relation for restricted partition function D_3 , given in (3.2).

The initial values for the new variables are given by $D_3^{(1)} = 1$ and $E_3^{(1)} = s^4$, while for the other variables they are the same as for the $p = 2$ case. For each restricted partition function recursion relation is obtained by decomposing the corresponding HW conformation on the generator of order $(r + 1)$ into parts within the constituent r th order generators. In the lower part of figure 8 an example of D_3 -type conformation on the generator of order $(r + 1)$ is depicted, illustrating occurrence of E_3 -type conformation. Since E_3 -type conformation within the $(r + 1)$ th order generator can traverse any of its $(p - 2)$ inner r th order generators, such conformations have overall weight equal to $(p - 2) (D_1^{(r)})^2 (D_3^{(r)})^{p-3} E_3^{(r)}$, which is, therefore, one of the terms in the recursion relation for restricted partition function D_3 , as can be seen in (3.2).

As in the case of $p = 2$ MR fractal, it is convenient to rescale the set of variables $X \in \{A_1, A_2, B_1, B_2, B_3, D_1, D_2, D_3, E_2, E_3\}$ by dividing them with the variable E_1 , thus introducing the new ones

$$x^{(r)} = \frac{X^{(r)}}{E_1^{(r)}}, \quad x \in \{a_1, a_2, b_1, b_2, b_3, d_1, d_2, d_3, e_2, e_3\}. \quad (3.3)$$

Then, directly from (3.2) follows that these new variables obey recurrence equation (B.1), given in appendix B, whereas the equation for E_1 becomes

$$E_1^{(r+1)} = (d_2^{(r)})^2 (d_3^{(r)})^{p-2} (E_1^{(r)})^p, \quad (3.4)$$

so that the partition function (3.1) in new variables gets the form

$$Z_c^{(r+1)} = \left(b_1^{(r)}\right)^2 \left(d_3^{(r)}\right)^{p-2} \left(E_1^{(r)}\right)^p. \quad (3.5)$$

Iterating these recursion relations, one can find that, for all s values, all variables a and b tend to zero, while variables d and e tend to some finite constants, which depend on the parity of the generator order. For arbitrary p we find, similarly to equation (2.8), that b_1 approaches zero as

$$b_1^{(2k)}(s) \sim [\lambda_e(s)]^{p^k}, \quad b_1^{(2k+1)}(s) \sim [\lambda_o(s)]^{p^k}, \quad (3.6)$$

where constants λ_e and λ_o depend on the fractal parameter p . Following the same procedure as in section 2.1, for the asymptotic behavior of the partition function, for general p we again obtain the scaling form

$$Z_c^{(r)}(s) \sim [\omega(s)]^{N_r} \times \begin{cases} [\mu_e(s)]^{\sqrt{N_r}}, & \text{for } r \text{ even} \\ [\mu_o(s)]^{\sqrt{N_r}}, & \text{for } r \text{ odd} \end{cases}, \quad (3.7)$$

where now $\mu_e(s) = [\lambda_o(s)]^{1/\sqrt{p}}$ and $\mu_o(s) = \lambda_e(s)$. Dependence of ω on the stiffness parameter s , for various values of p , is given in figure 9, where one can observe that for very large p the quantity ω approaches the unit value, ceasing to depend on s . Also, one may notice that $\omega(s=1)$ is smaller for lattices with higher value of p , meaning that the number of fully flexible HWs on equally large lattices is smaller for higher p . The reason for this is that the number of edges, and therefore connectivity of lattices, decreases with p . Values of μ_e and μ_o , as functions of s , are shown in figure 10, for various values of p , where one can see that μ_e decreases, while μ_o increases with s , for each member of the MR family.

The asymptotic form (3.7) obtained for the partition function, implies that correction to the leading term in the free energy is proportional to the square root of the number of steps of the walk. This can be compared with the similar correction terms obtained for flexible compact polymers on other lattices. For homogeneous d -dimensional environments such a correction in flexible polymer models is related to surface effects, which arise due to the fact that at low temperatures a polymer forms a compact globule, whose surface is proportional to $N^{(d-1)/d}$, with N being the number of monomers in globule [35]. Results obtained for flexible HWs on some fractal lattices imply that simple generalization of such correction term for nonhomogeneous environments is not possible [30]. In particular, correction term on all studied fractal lattices is of the same form μ^{N^σ} as for regular lattices, but σ is non-universal, i.e. it depends not only on fractal dimension, but also on other lattice characteristics. Here we have found the same value $\sigma = 1/2$ for each member (with the same fractal dimension 2) of the MR fractal family, meaning that σ depends neither on parameters by which these lattices differ, nor on the stiffness parameter s . This can be compared with the results $\sigma = 0$ and $\sigma = 1/2$, obtained for semi-flexible HWs on 3- and 4-simplex fractal lattices, respectively, for all values of s [32]. To the best of our knowledge, impact of the polymer rigidity on σ in the case of semi-flexible compact polymers on homogeneous lattices has not yet been studied, but on the bases of these results one could expect that it might be universal. That would also be in accord with recent conclusion that some other critical exponents, corresponding to semi-flexible SAW on the square lattice, also do not depend on s [36].

4. Thermodynamics of semi-flexible Hamiltonian cycles for general p

Thermodynamic functions for semi-flexible Hamiltonian cycles on MR lattices with $p > 2$ may be obtained using the recurrence equation (B.1), given in appendix B and expressions

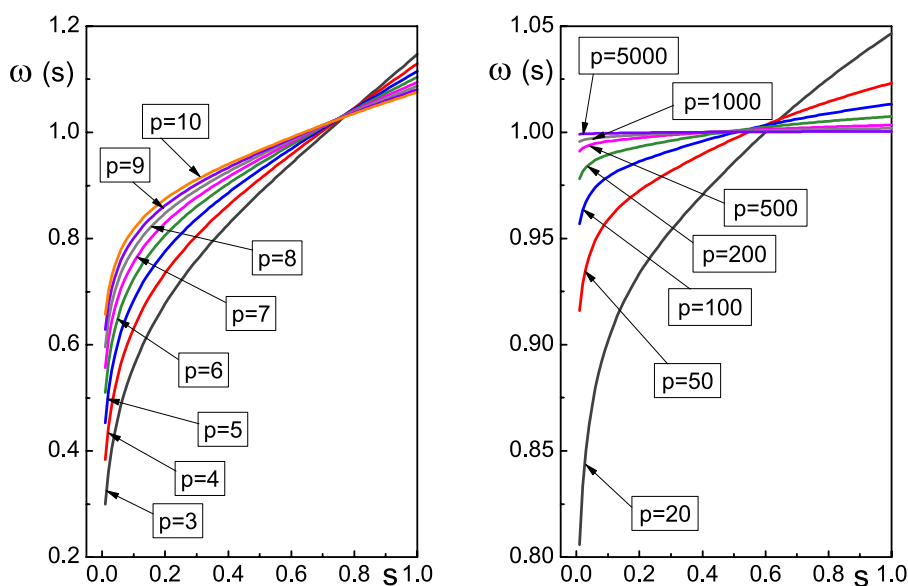


Figure 9. Stiffness dependence of the base ω in (3.7), for various members of the MR family, labelled by parameter p .

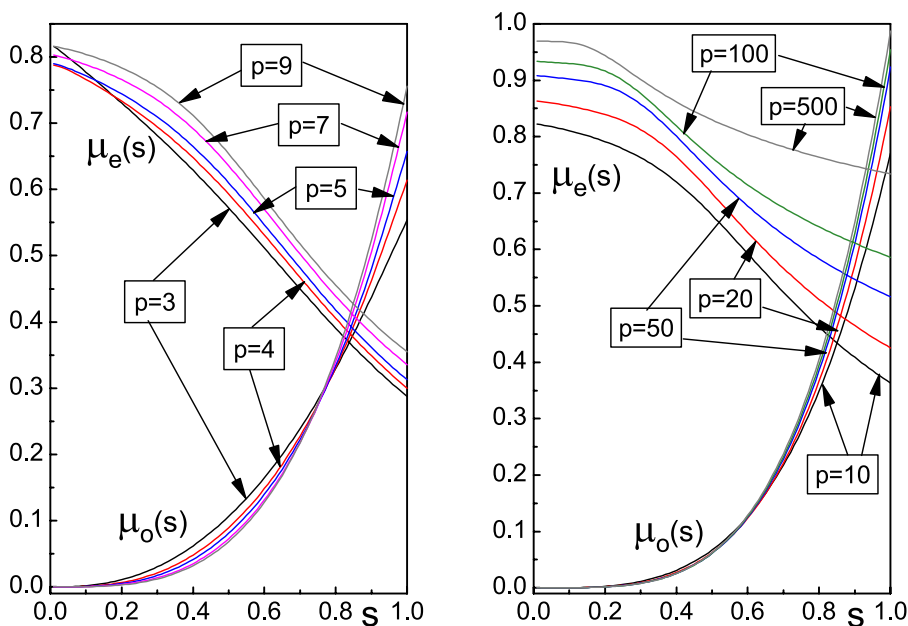


Figure 10. Stiffness dependence of the bases μ in the stretched exponential factor in (3.7), for various members of the MR family, labelled by parameter p .

$$q_{r+1} = q_r + \frac{1}{4p^r} \left(2 \ln d_2^{(r)} + (p-2) \ln d_3^{(r)} \right), \quad (4.1)$$

$$q'_{r+1} = q'_r + \frac{1}{4p^r} \left(2 \frac{(d_2^{(r)})'}{d_2^{(r)}} + (p-2) \frac{(d_3^{(r)})'}{d_3^{(r)}} \right), \quad (4.2)$$

$$q''_{r+1} = q''_r + \frac{1}{4p^r} \left[2 \frac{(d_2^{(r)})''}{d_2^{(r)}} - 2 \left(\frac{(d_2^{(r)})'}{d_2^{(r)}} \right)^2 \right] + \frac{1}{4p^r} \left[(p-2) \frac{(d_3^{(r)})''}{d_3^{(r)}} - (p-2) \left(\frac{(d_3^{(r)})'}{d_3^{(r)}} \right)^2 \right], \quad (4.3)$$

that correspond to the equations (2.12), (2.21) and (2.24) (obtained for $p = 2$ case), respectively.

The obtained numerical results for the persistence length l_p as function of temperature T , for different MR fractals, are depicted in figure 11, where one can see that l_p decreases with temperature, implying that number of polymer bends increases with T . Dependence of free and internal energy on T is presented in figure 12, for various members of the MR family. One perceives that f monotonically decreases, while u monotonically increases with T , for each p . Also, in the limit of very large p , one can conclude that both f and u go to zero. The obtained increment of internal energy with temperature is in accordance with the fact that at lower temperatures energetic effects dominate, so that low energy levels with conformations consisting of smaller number of bends are more populated. At higher temperatures, all energy levels become populated and internal energy saturates (i.e. becomes constant). This saturation is faster on fractals with larger values of p , for which the internal energy is generally smaller. The reason for this lies in the connectivity of the vertices. For lattices oriented as in figure 1 there are more vertical than horizontal edges, and for lattices with larger value of p this anisotropy becomes larger. The walks follow preferred direction and make smaller number of turns which reduces energy and increases persistence length. Described behavior of internal energy implies that specific heat should have a peak in the low temperature region, which we have numerically confirmed and displayed in figures 13 and 14, where specific heat as a function of T is shown. In these figures one can notice that besides one pronounced peak in specific heat landscape, there is another small peak at low temperatures, for fractals with $p \geq 4$. This effect in specific heat behaviour is known as Schottky anomaly (see, for instance [37]) and appears in systems with a finite number of energy levels.

We finish our discussion inferring that within the studied compact polymer phase there is no finite order phase transition, due to the fact that entropy and specific heat are continuous, smooth functions of temperature. One might challenge this conclusion, because it is based on numerical calculations, however, these calculations were performed with high precision, only by iterating exact recursion relations. For instance, the free energy is obtained by calculating $\omega(s)$ (see (2.18)), which is a limiting value of variable q_r that quickly saturates upon iterations. Furthermore, calculations were performed for a large number of s values, therefore functions $f(T)$ presented in figures 6 and 12 are obtained with high accuracy and one might be pretty sure, only relying on these figures, that the free energy is a differentiable function of T . Of course, this was further confirmed by

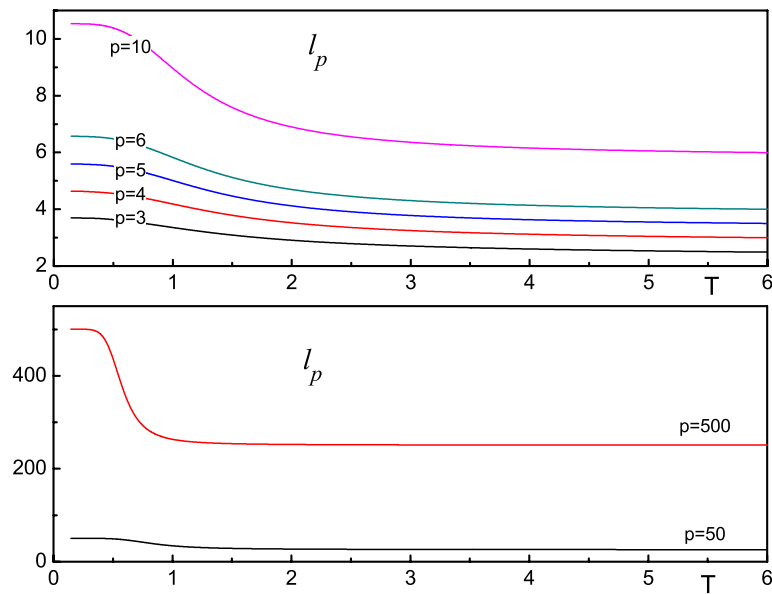


Figure 11. Persistence length l_p as a function of temperature, for various values of parameter p that enumerates members of the MR family.

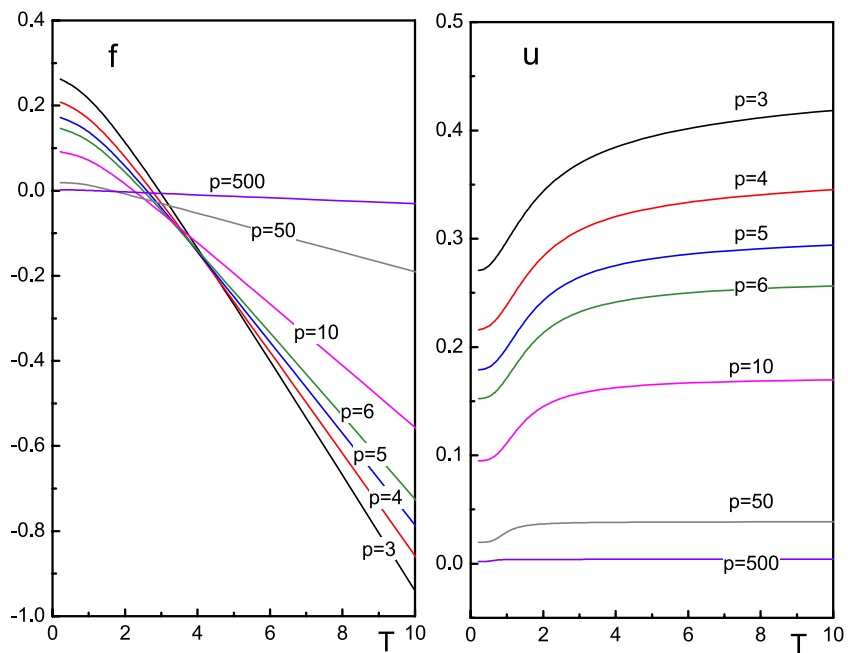


Figure 12. Free energy f and internal energy u as functions of temperature, for various values of parameter p that enumerates members of the MR family.

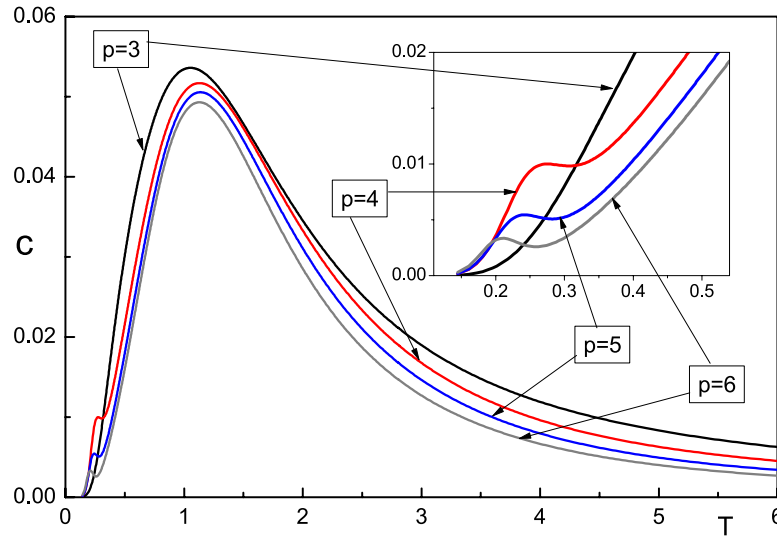


Figure 13. Specific heat c as a function of temperature T , for MR fractals labelled by $p = 3, 4, 5$, and 6 . Inset graph highlights additional small peaks that have appeared for $p = 4, 5$ and 6 fractals.

calculating the other thermodynamic functions, which, although defined through partial derivatives with respect to s , can be done without actual numerical differentiation, but again iteratively, utilizing the fact that derivatives of q_r obey recurrence relations (4.2) and (4.3). Since the persistence length l_p is finite at any T (for finite p), the polymer system is always in liquid-like (disordered) phase, and the transition to the crystal (ordered) phase is not possible. The existence of only disordered compact phase has also been observed in the case of semi-flexible HW on 3- and 4-simplex lattices [32]. The absence of crystal phase on the studied family of lattices stems from their asymmetry in horizontal and vertical direction. For each MR fractal there are more vertical than horizontal bonds. This discrepancy is more pronounced for larger p lattices, implying smaller number of bends in compact conformations since they are forced by the lattice in the vertical direction. Nevertheless, on such lattices conformations still have a large number of horizontal steps that prevent an ordered state that can exist on the square lattice [11].

5. Ground states and frustration

In order to achieve a minimal energy state at $T = 0$, in this section only conformations with a minimal number of bends will be considered. First we analyse the case of $p = 2$ lattice. Since the conformation D_2 makes the smallest number of bends on the unit square, one expects that the ground state, in this case, would be comprised of HW conformations with the maximal possible number of D_2 type on each unit square. Contribution of the ground state to the whole partition function is of the form $Z_0 = N_0 s^{N_{b0}}$, with N_0 being the number of ground state HWs and N_{b0} being the number of bends in each of these conformations. This term in the partition function can be obtained from the relation (2.2) and recurrence equation (2.4), keeping only the terms with conformations of the type D_2 . Then, some of the variables drop, and the system (2.4) reduces to

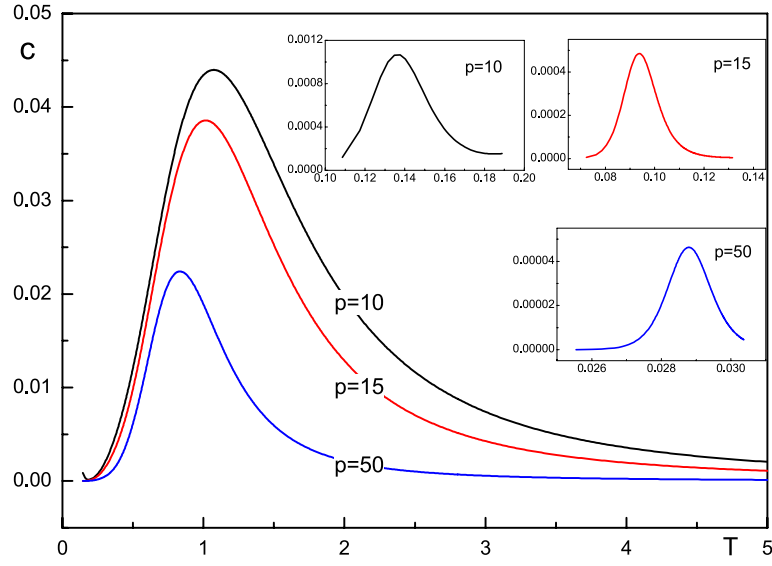


Figure 14. Specific heat as function of temperature, for $p = 10$, $p = 15$ and $p = 50$ fractals. Inset graphs show small peaks for these fractals. For higher p , peaks are smaller and pulled toward lower temperatures.

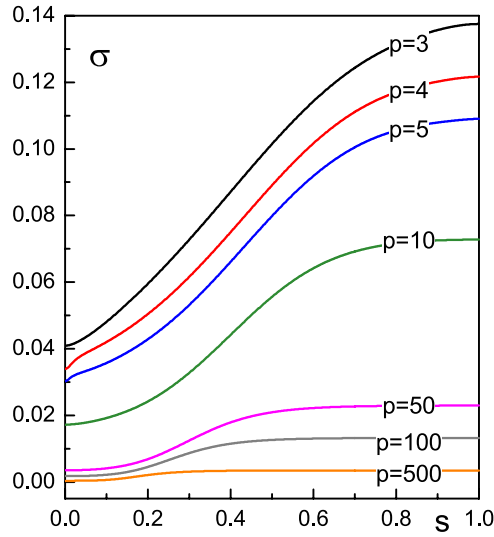


Figure 15. Entropy per monomer σ , in thermodynamic limit, as a function of the stiffness parameter s , for various members of the MR fractal family (labelled by p).

$$\begin{aligned}
 A_2^{(r+1)} &= B_1^{(r)} D_2^{(r)}, & B_1^{(r+1)} &= \left(A_2^{(r)}\right)^2, \\
 D_2^{(r+1)} &= D_2^{(r)} E_1^{(r)}, & E_1^{(r+1)} &= \left(D_2^{(r)}\right)^2.
 \end{aligned}
 \tag{5.1}$$

Solving this system exactly, from (2.2) we obtained Z_0 on the r th order fractal structure

Table 1. Entropies per monomer σ^* at temperature $T = 0$, for various p fractals of the MR family. We see that σ^* (and consequently the number of ground state conformations) decreases with p .

p	3	4	5	10	50	100	500
σ^*	0.040902	0.033925	0.030247	0.016914	0.0034679	0.0017333	0.00034658

$$Z_{0r} = s^{(\sqrt{2})^{r+1}[1+(-1)^{r+1}] + \frac{2}{3}2^r + \frac{4}{3}(-1)^r}. \quad (5.2)$$

In this case the ground state is non-degenerate, with the only one conformation leading to the zero entropy. From the number of bends in this conformation, given by $N_{b0r} = (\sqrt{2})^{r+1}[1 + (-1)^{r+1}] + \frac{2}{3}2^r + \frac{4}{3}(-1)^r$, we could calculate the ground state energy per site in the thermodynamic limit, as $u_0 = \varepsilon \lim_{r \rightarrow \infty} \frac{N_{b0r}}{2^{r+1}}$. The obtained value is $\frac{u_0}{\varepsilon} = \frac{1}{3}$, which is verified numerically and can be seen in figure 6.

For $p > 2$ equations are more complicated, and we have not been able to extract exact expressions for the number of ground state conformations, but numerically we have calculated the entropies per site, in the thermodynamic limit, in the whole range of stiffness parameter s (see figure 15). One can observe that for $p > 2$ fractals, ground state entropies per monomer do not vanish, meaning that there are exponentially large number of ground state conformations, which is a characteristic of geometrically frustrated systems. Limiting values of entropies for various MR fractals are given in table 1.

6. Summary and conclusion

We have studied a model of compact semi-flexible polymer rings modelled by closed HWs on the family of MR fractal lattices, whose members are labelled by an integer $p \geq 2$. All lattices from the family have the same fractal dimension ($d_f = 2$) and the coordination number (three), but their vertices are connected differently. Lattices can be obtained from the square lattice by deleting some bonds from it, which induces anisotropy between horizontal and vertical direction. By applying an exact method of recurrence relations, we have established the scaling form of the corresponding partition function (given by equation (3.7)) on the whole family of fractals. There is a leading exponential factor with a base ω , which depends on the lattice parameter p , as well as on the stiffness parameter s . For each p studied, we have found numerically that ω is increasing function of s , and that it changes more slowly on fractals with higher p . Correction to the leading exponential factor is stretched exponential factor of the same form for each fractal of the considered family, in the whole range of s values.

From the obtained partition function we have evaluated the set of thermodynamic quantities (free and internal energy, specific heat and entropy) as well as the polymer persistence length, as functions of the stiffness parameter s (or temperature T). We have found that all these quantities are differentiable functions of s . For each member of the MR family, we have found that all these quantities are monotonic functions of T , except for the specific heat, which has a maximum at low temperatures. Since the entropy and specific heat are continuous, smooth functions of temperature, there is no finite order phase transition, and the studied polymer system can exist only in disordered phase.

Eventually, we have analysed the ground state of the studied model. For $p = 2$ fractal we have found that the ground state is non-degenerate, and that the only ground state conformation has the persistence length $l_p = 3$. So, on average, there is one bend after every three steps, and there are no long straight segments in this conformation. The number of left/right

and up/down turns are comparable and this conformation is disordered. On the other hand, for fractals with $p > 2$, the ground state is degenerate, with exponentially large number of conformations, producing the residual entropy. The number of ground state conformations is maximal for $p = 3$ and decreases with p . Persistence length is the smallest for $p = 3$ ground state, and becomes larger, for larger p . However, all these ground state conformations have many bends and do not represent ordered ground states. In fact, we have geometrically frustrated systems, where geometry of the lattices is in conflict with the condition for minimal energy (i.e. minimal number of bends) and the requirement that all vertices are occupied only once. Geometric frustration suppresses ordered ground states and possibility of ordered phase at any T . The studied model describes disordered, liquid-like compact phase of semi-flexible polymers. Although MR lattices have some resemblance to the square lattice (on which the ordered phase can exist), an anisotropy of vertical and horizontal directions (small for $p = 2$, and greater for $p > 2$), causes that ordered phase can not exist on these lattices.

The main conclusion of this paper that inhomogeneity of the environment, in which the model was studied, suppresses the crystal phase of semiflexible polymers is in accord with the conclusions obtained in [32] for the same model applied on 3- and 4-simplex fractal lattices. Whereas there are no results for this model on homogeneous lattices that have symmetry similar to 3- and 4-simplex lattices (such as triangular or tetragonal ones), the family of MR lattices provides an infinite spectrum of nonhomogeneous lattices which differ from the square lattice by having smaller number of bonds, while the number of vertices is the same. Therefore, conclusion obtained here might imply that any kind of inhomogeneity can suppress occurring of the ordered phase. However, we think that this issue should be further inspected by performing similar studies on other nonhomogeneous lattices, and it could be of practical significance to expand the study of examined model into a more realistic case, when polymers are situated in three-dimensional fractal space.

Acknowledgments

This paper is part of the work within the project No. 171015, funded by the Ministry of Education, Science and Technological Development of the Republic of Serbia.

Appendix A

Here we give some additional details of the analysis of recursion relations (2.6) for the rescaled variables $x^{(r)}$ in the case of $p = 2$ MR lattice, given in section 2.1. For any $0 < s \leq 1$, by iterating (2.6), one obtains

$$\begin{aligned} \lim_{k \rightarrow \infty} d_1^{(2k+1)}(s) &= d_1^o(s), & \lim_{k \rightarrow \infty} d_2^{(2k+1)}(s) &= d_2^o(s), & \lim_{k \rightarrow \infty} e_2^{(2k+1)}(s) &= e_2^o(s), \\ \lim_{k \rightarrow \infty} d_1^{(2k)}(s) &= d_1^e(s), & \lim_{k \rightarrow \infty} d_2^{(2k)}(s) &= d_2^e(s), & \lim_{k \rightarrow \infty} e_2^{(2k)}(s) &= e_2^e(s), \end{aligned} \quad (\text{A.1})$$

where dependence of the limiting values $d_1^{o,e}$, $d_2^{o,e}$ and $e_2^{o,e}$ on s is depicted in figure A1.

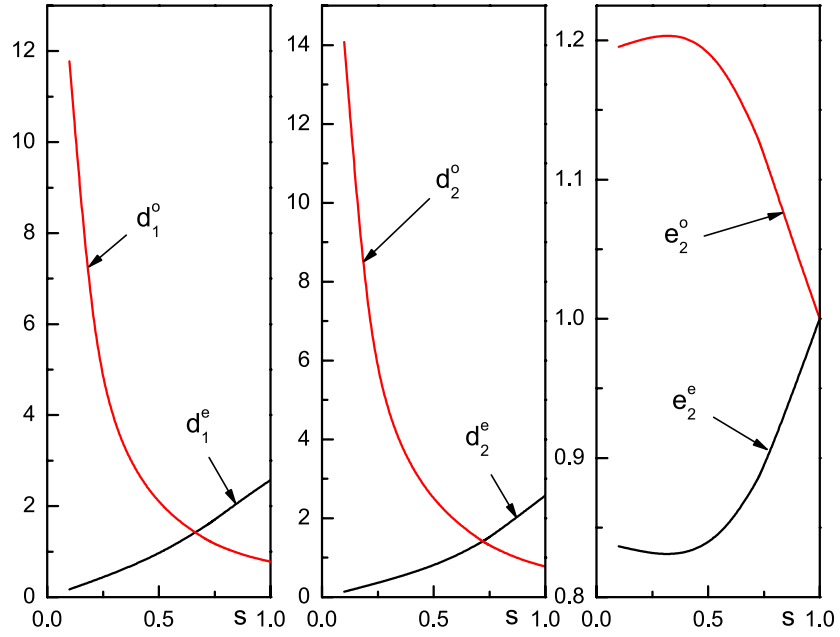


Figure A1. Dependence of the limiting values $d_1^{o,e}$, $d_2^{o,e}$ and $e_2^{o,e}$, defined in (A.1), on the stiffness parameter s , for $p = 2$ MR lattice.

Furthermore, the following relations are satisfied

$$d_2^o d_2^e = d_3^o d_3^e = 2, \quad e_2^o e_2^e = 1, \tag{A.2}$$

so that using relations (2.6), for large r one obtains the asymptotic recursion relation

$$b_1^{(r+2)} \approx \frac{1}{4} \left(b_1^{(r)} \right)^2, \tag{A.3}$$

which implies that

$$b_1^{(2k)}(s) \sim [\lambda_e(s)]^{2^k}, \quad b_1^{(2k+1)}(s) \sim [\lambda_o(s)]^{2^k}, \tag{A.4}$$

for $k \gg 1$. Dependence of λ_e and λ_o on values of the bending parameter s , obtained by numerical iteration of $\frac{\ln b_1^{(r)}(s)}{2^{[r/2]}}$, is depicted in figure 5.

Appendix B

In this appendix we give recurrence relations for the rescaled variables $x^{(r)}$ in the case of $p > 2$ MR lattice, defined in section 3 by (3.3). Directly from recurrence relations (3.2) one obtains

$$\begin{aligned}
a_1^{(r+1)} &= \frac{b_1^{(r)} d_1^{(r)}}{\left(d_2^{(r)}\right)^2}, & a_2^{(r+1)} &= \frac{b_1^{(r)}}{d_2^{(r)}}, & b_1^{(r+1)} &= \left(\frac{a_2^{(r)}}{d_2^{(r)}}\right)^2 \left(\frac{a_1^{(r)}}{d_3^{(r)}}\right)^{p-2}, \\
b_2^{(r+1)} &= \frac{a_1^{(r)} a_2^{(r)}}{\left(d_2^{(r)}\right)^2} \left(\frac{a_1^{(r)}}{d_3^{(r)}}\right)^{p-2}, & b_3^{(r+1)} &= \left(\frac{a_1^{(r)}}{d_2^{(r)}}\right)^2 \left(\frac{a_1^{(r)}}{d_3^{(r)}}\right)^{p-2}, \\
d_1^{(r+1)} &= 2 \frac{e_2^{(r)}}{d_2^{(r)}} + (p-2) \frac{e_3^{(r)}}{d_3^{(r)}} + 2 \frac{b_1^{(r)} b_2^{(r)}}{d_2^{(r)} d_3^{(r)}} + (p-3) \left(\frac{b_1^{(r)}}{d_3^{(r)}}\right)^2, \\
d_2^{(r+1)} &= \frac{1}{d_2^{(r)}} + \frac{d_1^{(r)} e_2^{(r)}}{\left(d_2^{(r)}\right)^2} + \frac{(p-2) d_1^{(r)} e_3^{(r)} + b_1^{(r)} b_3^{(r)}}{d_2^{(r)} d_3^{(r)}} + \frac{b_1^{(r)} b_2^{(r)} d_1^{(r)}}{\left(d_2^{(r)}\right)^2 d_3^{(r)}} + (p-3) \frac{\left(b_1^{(r)}\right)^2 d_1^{(r)}}{d_2^{(r)} \left(d_3^{(r)}\right)^2}, \\
d_3^{(r+1)} &= 2 \frac{d_1^{(r)}}{\left(d_2^{(r)}\right)^2} + (p-2) \frac{\left(d_1^{(r)}\right)^2 e_3^{(r)}}{\left(d_2^{(r)}\right)^2 d_3^{(r)}} + 2 \frac{b_1^{(r)} b_3^{(r)} d_1^{(r)}}{\left(d_2^{(r)}\right)^2 d_3^{(r)}} + (p-3) \frac{\left(b_1^{(r)}\right)^2 \left(d_1^{(r)}\right)^2}{\left(d_2^{(r)}\right)^2 \left(d_3^{(r)}\right)^2}, \\
e_2^{(r+1)} &= \frac{d_1^{(r)}}{d_2^{(r)}}, & e_3^{(r+1)} &= \left(\frac{d_1^{(r)}}{d_2^{(r)}}\right)^2.
\end{aligned} \tag{B.1}$$

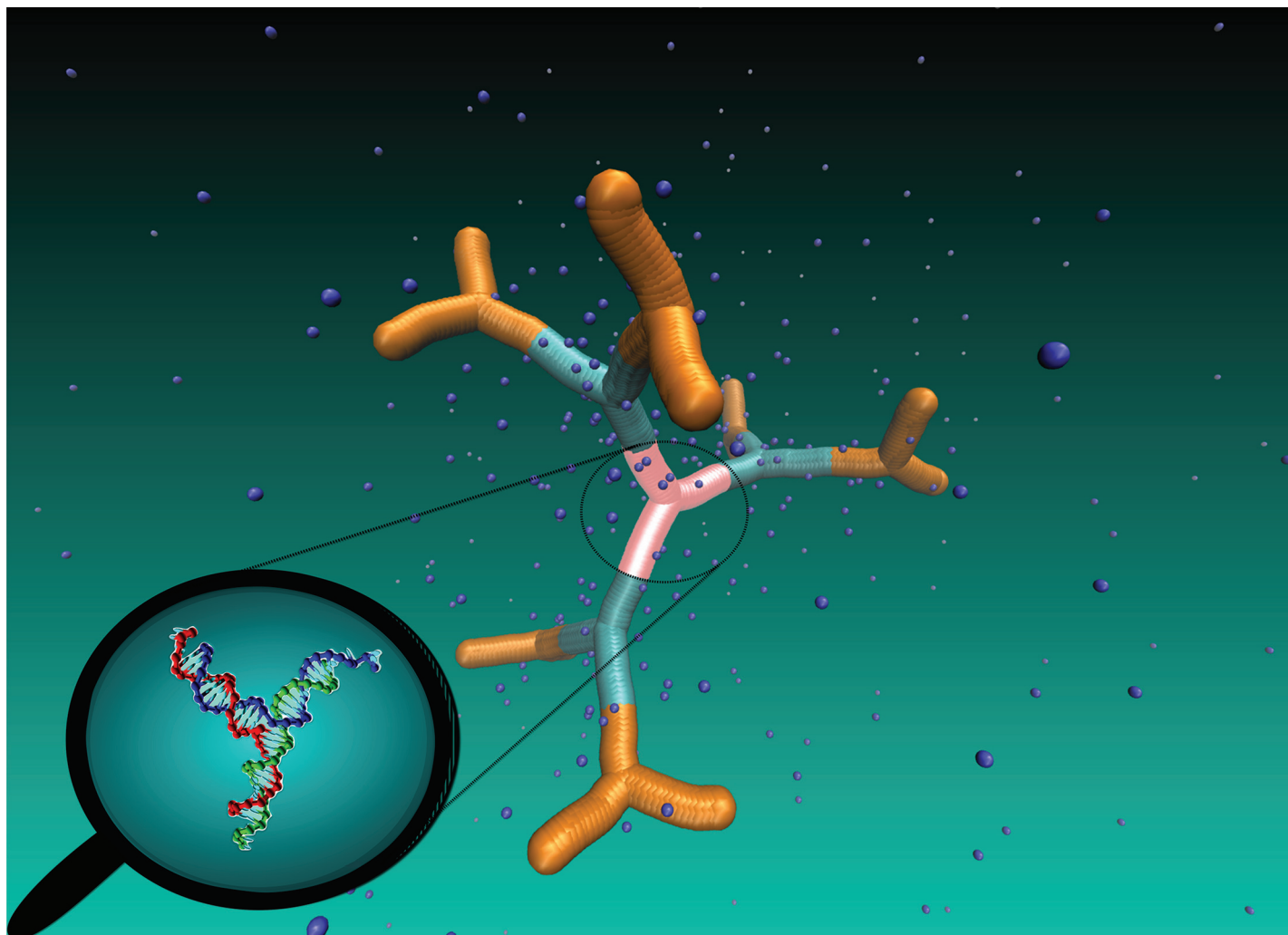
ORCID iDs

S Elezović-Hadžić  <https://orcid.org/0000-0001-8148-5828>

References

- [1] de Gennes P-G 1979 *Scaling Concepts in Polymer Physics* (Ithaca, NY: Cornell University Press)
- [2] Vanderzande C 1998 *Lattice Models of Polymers* (Cambridge: Cambridge University Press)
- [3] Flory P J 1956 *Proc. R. Soc. A* **234** 60
- [4] Gujrati P D 1980 *J. Phys. A: Math. Gen.* **13** L437
- [5] Saleur H 1986 *J. Phys. A: Math. Gen.* **19** 2409
- [6] Baumgartner A and Yoon D L 1983 *J. Chem. Phys.* **79** 521
- [7] Doniach S, Garel T and Orland H 1996 *J. Chem. Phys.* **105** 1601
- [8] Irback A and Sandelin E 1999 *J. Chem. Phys.* **110** 12256
- [9] Dijkstra M and Frenkel D 1994 *Phys. Rev. E* **50** 349
- [10] Gujrati P D and Corsi A 2001 *Phys. Rev. Lett.* **87** 025701
Corsi A and Gujrati P D 2003 *Phys. Rev. E* **68** 031502
- [11] Jacobsen J L and Kondev J 2004 *Phys. Rev. E* **69** 066108
Jacobsen J L and Kondev J 2004 *Phys. Rev. Lett.* **92** 210601
- [12] Krawczyk J, Owczarek A L and Prellberg T 2009 *Physica A* **388** 104
Krawczyk J, Owczarek A L and Prellberg T 2010 *Physica A* **389** 1619
- [13] Starostin E L 2013 *J. Chem. Phys.* **138** 164903
- [14] Karshikoff A, Nilsson L and Ladenstein R 2015 *FEBS J.* **282** 3899
- [15] Nuebler J, Fudenberg G, Imakaev M, Abdennura N and Mirny L A 2018 *Proc. Natl Acad. Sci.* **115** 6697
- [16] Jacobsen J L 2007 *J. Phys. A: Math. Theor.* **40** 14667
- [17] Schram R D and Schiessel H 2013 *J. Phys. A: Math. Theor.* **46** 485001
- [18] Oberdorf R, Ferguson A, Jacobsen J L and Kondev J 2006 *Phys. Rev. E* **74** 051801
- [19] Jacobsen J L 2008 *Phys. Rev. Lett.* **100** 118102
- [20] Dhar D and Singh Y 2005 Linear and branched polymers on fractals *Statistics of Linear Polymers in Disordered Media* ed B K Chakrabarti (Amsterdam: Elsevier)

- [21] Giacometti A and Maritan A 1992 *J. Phys. A: Math. Gen.* **25** 2753
- [22] Živić I, Milošević S and Stanley E H 1994 *Phys. Rev. E* **49** 636
- [23] Marenduzzo D, Maritan A and Seno F 2002 *J. Phys. A: Math. Gen.* **35** L233
- [24] Dhar D 2005 *Phys. Rev. E* **71** 031801
- [25] Vidanović I, Arsenijević S and Elezović-Hadžić S 2011 *Eur. Phys. J. B* **81** 291
- [26] Pretti M 2016 *Phys. Rev. E* **93** 032110
- [27] Maji J, Seno F, Trovato A and Bhattacharjee S M 2017 *J. Stat. Mech.* **073203**
- [28] Cheraghalizadeh J, Najafi M N, Mohammadzadeh H and Saber A 2018 *Phys. Rev. E* **97** 042128
- [29] Oliveira T J, Dantas W G, Prellberg T and Stilck J F 2018 *J. Phys. A: Math. Theor.* **51** 054001
- [30] Bradley R M 1989 *J. Phys. A: Math. Gen.* **22** L19
Stajić J and Elezović-Hadžić S 2005 *J. Phys. A: Math. Gen.* **38** 5677
Elezović-Hadžić S, Marčetić D and Maletić S 2007 *Phys. Rev. E* **76** 011107
Lekić D and Elezović-Hadžić S 2010 *J. Stat. Mech.* **P02021**
- [31] Roy A K and Chakrabarti B K 1987 *J. Phys. A: Math. Gen.* **20** 215
Blavatska V and Janke W 2009 *J. Phys. A: Math. Theor.* **42** 015001
Fricke N and Janke W 2014 *Phys. Rev. Lett.* **113** 255701
Fricke N and Janke W 2017 *J. Phys. A: Math. Theor.* **50** 264002
- [32] Lekić D and Elezović-Hadžić S 2011 *Physica A* **390** 1941
- [33] Lekić D, Elezović-Hadžić S and Adžić N 2016 *Contemp. Mater.* **VII-2** 166 (*Conference Paper in IX Int. Scientific Conf. Contemporary Materials 2016, Banja Luka: Academy of Sciences and Arts of the Republic of Srpska*)
- [34] Dhar D 1978 *J. Math. Phys.* **18** 577
Dhar D 1978 *J. Math. Phys.* **19** 5
Dhar D and Vannimenus J 1978 *J. Phys. A: Math. Gen.* **20** 199
- [35] Owczarek A L, Prellberg T and Brak R 1993 *Phys. Rev. Lett.* **70** 951
Duplantier B 1993 *Phys. Rev. Lett.* **71** 4274
Grassberger P and Hsu H P 2002 *Phys. Rev. E* **65** 031807
Baiesi M, Orlandini E and Stella A L 2007 *Phys. Rev. Lett.* **99** 058301
Baiesi M and Orlandini E 2014 *Phys. Rev. E* **89** 062601
- [36] Živić I, Elezović-Hadžić S and Milošević S 2018 *Phys. Rev. E* **98** 062133
- [37] Tari A 2003 *The Specific Heat of Matter at Low Temperatures* (London: Imperial College Press)

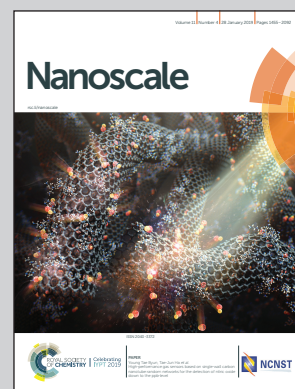


Showcasing research from the University of Vienna and the Technical University of Vienna, Austria, Forschungszentrum Jülich, Germany, and Cornell University, USA.

Structure and stimuli-responsiveness of all-DNA dendrimers: theory and experiment

How can we create nanocages, *i.e.*, robust and stable objects with regular voids and tunable properties? Short segments of DNA molecules synthesized to build a Y-shaped unit are the perfect building-blocks for the controllable design of a new family of dendrimers. These novel nanoconstructs are charged and void-containing assemblies, characterized with high rigidity and remarkable resistance to added salt. The investigated properties indicate these DNA-dendrimers as candidates for functional nanocarriers and as building blocks for engineering biocompatible artificial materials.

As featured in:



See Nataša Adžić *et al.*, *Nanoscale*, 2019, 11, 1604.



Cite this: *Nanoscale*, 2019, **11**, 1604

Structure and stimuli-responsiveness of all-DNA dendrimers: theory and experiment

Clemens Jochum,^a †^a Nataša Adžić,^b †^b Emmanuel Stiakakis,^c Thomas L. Derrien,^d †^d Dan Luo,^d Gerhard Kahl^e and Christos N. Likos^b †^b

We present a comprehensive theoretical and experimental study of the solution phase properties of a DNA-based family of nanoparticles - dendrimer-like DNA molecules (DL-DNA). These charged DNA dendrimers are novel macromolecular aggregates, which hold high promise in targeted self-assembly of soft matter systems in the bulk and at interfaces. To describe the behaviour of this family of dendrimers (with generations ranging from G1 to G7), we use a theoretical model in which base-pairs of a single DL-DNA molecule are modeled by charged monomers, whose interactions are chosen to mimic the equilibrium properties of DNA correctly. Experimental results on the sizes and conformations of DL-DNA are based on static and dynamic light scattering; and molecular dynamics simulations are employed to model the equilibrium properties of DL-DNA, which compare favorably to the findings from experiments while at the same time providing a host of additional information and insight into the molecular structure of the nanostructures. We also examine the salt-responsiveness of these macromolecules, finding that despite the strong screening of electrostatic interactions brought about by the added salt, the macromolecules shrink only slightly, their size robustness stemming from the high bending rigidity of the DNA-segments. The study of these charged dendrimer systems is an important field of research in the area of soft matter due to their potential role for various interdisciplinary applications, ranging from molecular cages and carriers for drug delivery in a living organism to the development of dendrimer- and dendron-based ultra-thin films in the area of nanotechnology. These findings are essential to determine if DL-DNA is a viable candidate for the experimental realization of cluster crystals in the bulk, a novel form of solid with multiple site occupancy.

Received 18th July 2018,
Accepted 5th October 2018

DOI: 10.1039/c8nr05814h

rsc.li/nanoscale

Introduction

All-DNA constructs are complex self-assemblies made solely by DNA. The creation of such nanostructures was initiated in the early 1980s when Seeman proposed the use of DNA as a programmable nanoscale building material,¹ laying the foundation for structural DNA nanotechnology.^{2,3} This interdisciplinary research field has had a striking impact on nanoscience and nanotechnology, demonstrating the construction of a remarkably rich assortment of multidimensional all-

DNA nanoarchitectures^{4–10} with promising applications in areas such as molecular and cellular biophysics,^{11–15} macromolecular crystallography,¹⁶ inorganic nanoparticle templated self-assembly for nanoelectronics,^{17–19} protein assembly,^{11,20–23} drug delivery²⁴ and biotechnology.²⁵

Very recently, the area of DNA-based self-assembly has been embraced by the research field of soft-matter physics for fabricating all-DNA particles with engineered shape and interaction potentials that could serve as model systems for exploring unconventional bulk phase behaviour of diverse states of matter such as gels^{26–28} and liquid crystals.^{29,30} In 2004, Luo and co-workers,³¹ demonstrated the fabrication of a novel dendrimer-like DNA (DL-DNA) construct. The DL-DNA particles were synthesized in a controlled step-wise fashion from the enzymatic ligation of Y-shaped DNA (Y-DNA) building blocks with rigid arms and specifically designed hybridization regions known as “sticky-ends”, leading to the formation of a highly charged and void-containing macromolecular assembly with tree-like architecture (see Methods for more details). Here, we perform a joint experimental/theoretical analysis of the shapes, sizes, and forms of these constructs, demonstrat-

^aInstitute for Theoretical Physics, TU Wien, Wiedner Hauptstraße 8-10, A-1040 Vienna, Austria. E-mail: clemens.jochum@tuwien.ac.at

^bFaculty of Physics, University of Vienna, Boltzmannstraße 5, A-1090 Vienna, Austria. E-mail: natasa.adzic@univie.ac.at

^cInstitute of Complex Systems 3, Forschungszentrum Jülich, Leo-Brandt-Strasse, D-52425 Jülich, Germany

^dDepartment of Biological and Environmental Engineering, Cornell University, Ithaca, New York 14853-5701, USA

^eInstitute for Theoretical Physics and Center for Computational Materials Science, TU Wien, Wiedner Hauptstraße 8-10, A-1040 Vienna, Austria

†These authors contributed equally to this work.

ing their unique properties. We show that they are different from both sterically and charge-dominated dendrimers, they possess a regular spherical shape with voids, and are robust to the influence of added salt.

DL-DNA molecules are a clear example of novel functional nanostructures that can be assembled with remarkable control and subnanometer precision through programmable sticky-end cohesions. Unlike other chemical dendrimers, their built-in modularity allows tailored reshaping of the dendritic scaffold in terms of surface functionalization³² and internal structure modification³³ by employing standard tools from bio-functional chemistry. Thus, these DNA-based dendritic architectures have been envisioned to play a promising role in developing nano-barcodes,^{34,35} DNA-based vaccine³⁶ technologies, and functioning as a structural scaffold as well as a structural probe involving multiplexed molecular sensing processes.^{37,38} Furthermore, from the fundamental research perspective, their polyelectrolyte character and inherently open architecture near their center of mass endow the DL-DNA particles with an ultrasoft repulsive potential³⁹ and penetrability; features which make the DL-DNA molecules optimal candidates for the experimental realization of the recently proposed cluster-crystal structure.^{40–42}

The investigation of the structural properties of DL-DNAs at a single particle level, including their responsiveness to charge screening, is imperative for the development of emerging applications and for the understanding of intriguing collective phenomena related to this type of novel soft material. Broadly speaking, access on global molecular characteristics such as particle diameter and spatial structure at a very coarse-grained level is feasible with numerous scattering techniques. However, probing in detail the internal and surface morphology of a complex nanostructure is a challenging task. To this end, we adopted an approach of tackling the above issues by combining experiments and simulations to profound insights from the latter into quantities and properties not accessible to experimental techniques. As a prerequisite for establishing the reliability of the latter, we first validate the model by comparing results from the simulation approach with accessible experimental findings.

System description

The building block of the dendrimer of interest is the Y-DNA unit, a three-armed structure consisting of double-stranded DNA (dsDNA), formed *via* hybridization of three single-stranded DNA chains (ssDNA), each of which has partially complementary sequences to the other two. Each arm is made up of 13 base-pairs and a single-stranded sticky end with four nucleobases, see Fig. 1. While a single Y-DNA corresponds to the first dendrimer generation, G1, attaching further Y-DNA elements yields DL-DNA of higher generations, as shown in Fig. 2. This attachment is achieved by enzymatic ligation, where the single-stranded ends of two different arms form a regular double-strand through base-pairing. In this paper we

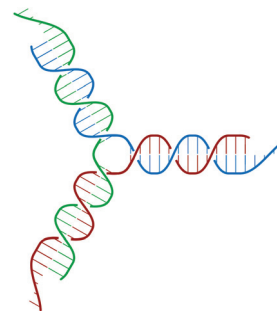


Fig. 1 Sketch of the Y-DNA structure: three ssDNA chains (colored red, green, and blue) assemble to form a star-like configuration with sticky ends.

study experimentally and computationally DL-DNA macromolecules from the first generation, G1, up to the sixth generation, G6. We extend the theoretical model also to G7 dendrimer for selective quantities that spread light on the dendrimers' internal structure. Subgenerations of a G_N dendrimer will be indicated by g_i , $i = 1, 2, \dots, N$.

In order to build a model of the DL-DNA nanostructures, we start with a simple and widely used approach by assuming a bead-spring DNA model, where the interactions and the corresponding parameters are carefully chosen to mimic the structural properties of a single dsDNA chain.^{43,44} This particle-based model for a dsDNA, which is presented in the following, has already been introduced in recent theoretical studies of polyelectrolyte brushes^{43–45} and its validity has been tested in comparison with experiments in the context of salt-dependent forces between DNA-grafted colloids.^{46–49} Accordingly, each Y-DNA arm is modeled as a chain of charged monomers consisting of a single dsDNA junction monomer followed by twelve dsDNA chain monomers and a single-stranded end group of four monomers. While the first thirteen monomers correspond to base pairs, the last four represent single nucleobases. The connection between two Y-configurations is established by replacing four + four ssDNA monomers with four dsDNA monomers, see Fig. 2. The numbers of constituents of each generation are given in Table 1.

The beads of the DNA-strands carry electric charges; mobile counterions are introduced in order to preserve the electro-neutrality of the system. Additionally, we also introduce different concentrations of monovalent salt ions, Na^+ and Cl^- , with the purpose of studying the influence of salt on the conformational characteristics of DL-DNA. The properties of each particle type can be seen in Table 2. The steric interaction is described *via* a truncated and vertically shifted Lennard-Jones potential, which is equivalent to the Weeks–Chandler–Andersen (WCA) potential, here with a possible horizontal shifting by $r_{\alpha\beta}$ as follows:

$$V_{\text{steric}}^{\alpha\beta}(r) = \begin{cases} \infty & \text{if } r < r_{\alpha\beta}, \\ 4\epsilon \left[\left(\frac{\sigma}{r - r_{\alpha\beta}} \right)^{12} - \left(\frac{\sigma}{r - r_{\alpha\beta}} \right)^6 + \frac{1}{4} \right] & \text{if } r_{\alpha\beta} \leq r \leq \sqrt[6]{2}\sigma + r_{\alpha\beta}, \\ 0 & \text{if } r > \sqrt[6]{2}\sigma + r_{\alpha\beta}, \end{cases} \quad (1)$$

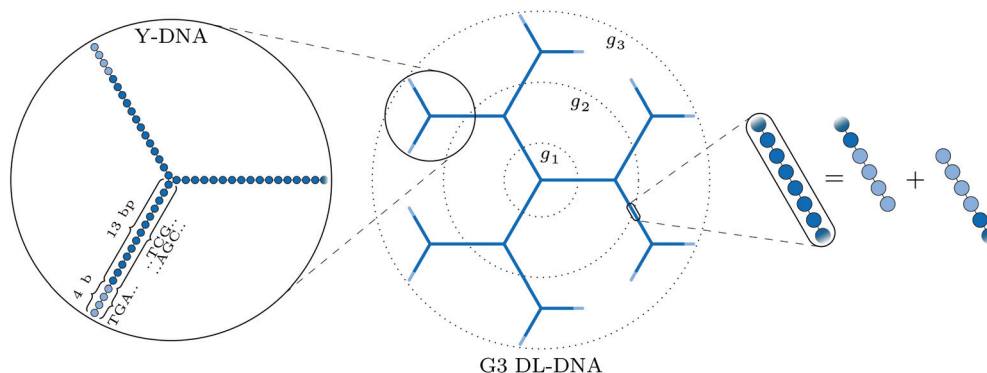


Fig. 2 Schematic representation of our DL-DNA model: the left part shows the representation of a single Y-DNA according to our particle-based model; the middle part shows how the union of Y-DNAs *via* enzymatic ligation gives rise to a dendrimer-like structure; the rightmost part shows the equivalence of two combined sticky ends to regular dsDNA at the connection of two Y-DNAs in our model.

Table 1 Characteristic numbers N_Y (*i.e.*, number of Y-DNAs), N_{bp} (*i.e.*, number of base pairs), and N_{mon} (*i.e.*, number of monomers) for DL-DNA of different generations

Generation	N_Y	N_{bp}	N_{mon}
G1	1	39	51
G2	4	168	192
G3	10	426	474
G4	22	942	1038
G5	46	1974	2166
G6	94	3666	4422

Table 2 Properties of system's constituents. The radii at the last column refer to the model in eqn (1)

Particle type	Mass m [u]	Charge q [e]	Radius r_α [Å]
Regular monomer (M^-)	660	-1	9
Y-junction monomer (M^-)	660	-1	9
Sticky end-linker (M^-)	330	-1	9
Counterions (C^+)	20	+1	2
Salt particles (S^\pm)	20	± 1	2

with the following parameters values: $\sigma = 4 \text{ \AA}$, $\epsilon = 1 \text{ kJ mol}^{-1}$ and $r_{\alpha\beta} = r_\alpha + r_\beta - \sigma$ (with $\alpha, \beta = M^-, C^+$, or S^\pm , referring to monomers, counterions, and counter/co-ions belonging to the salt particles, respectively), where $r_{M^-} = 9 \text{ \AA}$ and $r_{C^+} = r_{S^\pm} = 2 \text{ \AA}$.

This way, the excluded volume interaction between counterion particles reduces to the usual WCA interaction, diverging at zero separation, while the potential between monomers and ions diverges at a center-to-center distance of 7 \AA and the interaction between monomers diverges at the distance of 14 \AA , accounting for the larger size of the monomers. Thus, the steric interaction acts in the range of $r \leq 18.5 \text{ \AA}$, corresponding to the value of the effective DNA helix diameter, which is approximately equal 20 \AA .

Consecutive monomers along dsDNA- or ssDNA-strands are connected with bonds described by a harmonic bonding potential:

$$V_b(r) = \frac{k_b}{2}(r - l_b)^2, \quad (2)$$

where the spring constant takes the value $k_b = 210 \text{ kJ (mol \AA}^2)^{-1}$, giving a dispersion of about 0.15 \AA , which is consistent with the values observed in structural studies of DNA.^{50,51} The equilibrium bond length is $l_b = 3.4 \text{ \AA}$, (which renders the spring constant equivalent to $k_b l_b^2 \approx 10^3 k_B T$) corresponding to the typical distance between base pairs in DNA.^{44,50} Comparing the bond length l_b with the steric monomer-monomer interaction offset $r_{M-M} = 14 \text{ \AA}$ reveals that neighbouring monomers in a straight configuration are located in the divergent regime of the WCA potential. Therefore, we set the WCA steric interaction to only act between monomers which are *not* within the same chain and additionally exclude the steric interaction between the first five monomers located at the Y-DNA junctions.

The stiffness of dsDNA is modeled *via* a harmonic bending-angle potential $V_{bend}(\phi)$, which acts on the angle ϕ between the bonds connecting any monomer (index j) to the two neighbouring monomers (indices $j + 1$ and $j - 1$):

$$V_{bend}(\phi) = \frac{k_\phi}{2}(\phi - \pi)^2, \quad (3)$$

where the constant of bending energy, k_ϕ , takes the values:

$$k_\phi = \begin{cases} 750 \text{ kJ mol}^{-1} & \text{for stiff chains,} \\ 150 \text{ kJ mol}^{-1} & \text{for sticky ends,} \\ 0 & \text{for the fully flexible Y-junction.} \end{cases} \quad (4)$$

The bending energy constant value $k_\phi = 750 \text{ kJ mol}^{-1}$ is chosen to reproduce the typical persistence length $L = 500\text{--}1000 \text{ \AA}$ of dsDNA at low ionic strength.⁵² While the bonds between the three central junction monomers are the same as between all other monomers, the Y-arms are fully flexible, *i.e.*, the bending energy constant is chosen to be zero. Since the

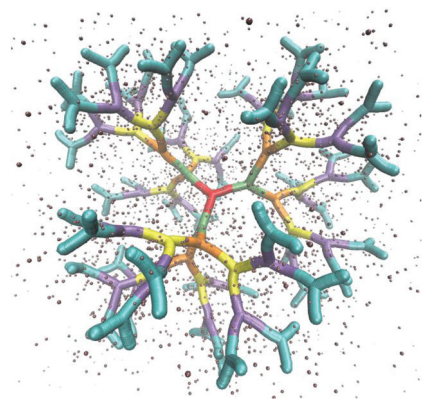


Fig. 3 Simulation snapshot of a G6 dendrimer. Each color corresponds to a different dendrimer generation. The figure shows only a small fraction of simulation box. Small spheres represent counterions.

persistence length of unpaired ssDNAs is lower than for dsDNAs,^{53,54} the degree of flexibility of the ssDNA end group monomer is set to $k_{\phi} = 150 \text{ kJ mol}^{-1}$.

Since each monomer bears an elementary charge $q_M = -e < 0$, a corresponding number of counterions with charge $e > 0$ is added to ensure overall electroneutrality of the system. Any two charged species α and β interact additionally *via* the Coulomb interaction

$$\frac{V_C(r)}{k_B T} = \lambda_B \frac{q_{\alpha} q_{\beta}}{r}, \quad (5)$$

where r denotes interparticle separation, $q_{\alpha} q_{\beta} \in e, -e$, and the Bjerrum length $\lambda_B = \frac{e^2}{\epsilon_r \epsilon_0 k_B T}$ is set to $\lambda_B = 7 \text{ \AA}$. Water is treated as uniformly dielectric with dielectric constant $\epsilon_r = 80$.

The above described model is used in Molecular Dynamics (MD) simulations, details of the latter are given in Methods. A representative simulation snapshot for a G6 dendrimer is shown in Fig. 3, where monomers pertaining to different sub-generations are presented by different colors.

It can be seen that the connections between successive branching points are rather rigid segments with a strong overlap between neighboring monomers, while the sticky ends (*i.e.*, the segments pertaining to ssDNA belonging to the outermost sub-generation) show a less stiff behaviour. Counterions are found to be absorbed into the interior of the dendrimer to a high degree.

Methods

Here, we briefly specify some of the experimental as well as simulation techniques employed in this work.

Experimental

DNA sequences and synthesis of DL-DNA

The DL-DNA nanostructures were fabricated following the synthetic procedure described in the reference,³⁵ which is based

on two assembly procedures: (a) self-assembly and (b) enzyme-assisted assembly. Briefly, DL-DNA was prepared from a core three-arm DNA junction (Y-DNA), having each arm terminated with a non-palindromic four-base-long sticky-end. We designate this Y-DNA as a first dendrimer generation (G1). To build up the next generation (G2), the above all-DNA tri-functional core was hybridized with three other Y-DNAs with sticky-ends complementary to the core Y-DNA. The cohesions points were enzymatically sealed using T4 DNA ligase (Promega). Additional generations (G3, G4, G5, *etc.*) were created by repeatedly ligating Y-DNAs to the sticky-ends of the previous generation. The Y-DNA building block is synthesized by annealing of three partially complementary single-stranded DNAs (ssDNAs) at equal molar ratio, employing a one-pot approach. Purification of excess DNA was performed using a combination amicon ultra spin columns as well as dialysis.

The sequences of DNA strands used to create the DL-DNA constructs are slightly modified compared to those reported in reference³⁵ in order to minimize the total number of different strands necessary for synthesizing all-DNA dendrimers up to the 6th generation. The sequences of DNA strands were designed using the program SEQUIN.⁵⁵ All DNA strands used in this study were purchased from Integrated DNA Technologies, Inc. (<http://www.idtdna.com>), phosphorylated at their 5'-end, and purified by denaturing polyacrylamide gel electrophoresis. The DNA strand concentrations were determined by measuring the absorbance at 260 nm with a micro-volume spectrometer (NanoDrop 2000).

DNA sequences and construction scheme for synthesizing the all-DNA dendrimers used in this study are listed below. The bold letters correspond to sticky-end sequence and p indicates the position of the phosphate modification.

DNA strand sequences:

- Y_{1a}: 5'-p-TGAC TGGATCCGCATGACATTCGCCGTAAG-3'
- * Y_{2a}: 5'-p-GTCA TGGATCCGCATGACATTCGCCGTAAG-3'
- ◇ Y_{3a}: 5'-p-ATCG TGGATCCGCATGACATTCGCCGTAAG-3'
- △ Y_{4a}: 5'-p-GCAA TGGATCCGCATGACATTCGCCGTAAG-3'
- Y_{1b}: 5'-p-TGAC CTTACGGCGAATGACCGAATCAGCCT-3'
- * Y_{2b}: 5'-p-CGAT CTTACGGCGAATGACCGAATCAGCCT-3'
- ◇ Y_{3b}: 5'-p-TTGC CTTACGGCGAATGACCGAATCAGCCT-3'
- △ Y_{4b}: 5'-p-GTCA CTTACGGCGAATGACCGAATCAGCCT-3'
- Y_{1c}: 5'-p-TGAC AGGCTGATTCGGTTCATGCGGATCCA-3'
- * Y_{2c}: 5'-p-CGAT AGGCTGATTCGGTTCATGCGGATCCA-3'
- ◇ Y_{3c}: 5'-p-TTGC AGGCTGATTCGGTTCATGCGGATCCA-3'
- △ Y_{4c}: 5'-p-GTCA AGGCTGATTCGGTTCATGCGGATCCA-3'

DL-DNA construction scheme:

- 1st generation DL-DNA: G1 = Y₁ = Y_{1a} + Y_{1b} + Y_{1c}
- 2nd generation DL-DNA: G2 = G1 + 3 × Y₂,
where Y₂ = Y_{2a} + Y_{2b} + Y_{2c}
- 3rd generation DL-DNA: G3 = G2 + 6 × Y₃,
where Y₃ = Y_{3a} + Y_{3b} + Y_{3c}
- 4th generation DL-DNA: G4 = G3 + 12 × Y₄,
where Y₄ = Y_{4a} + Y_{4b} + Y_{4c}
- 5th generation DL-DNA: G5 = G4 + 24 × Y₅,
where Y₅ = Y_{1a} + Y_{2b} + Y_{2c}
- 6th generation DL-DNA: G6 = G5 + 48 × Y₆,

$$\text{where } Y_6 = Y_3 = Y_{3a} + Y_{3b} + Y_{3c}$$

Agarose gel electrophoresis was employed to confirm the successful assembly of all-DNA dendrimers. As shown in Fig. 4, the desired DL-DNA constructs migrate as single bands, showing decreasing mobility with increasing generation. The disparity in the sharpness of the bands is likely to be a result of the increased flexibility of the larger dendrimers, which can explore a variety of conformations, leading to a diffuse band. The G1 band is likely more diffuse due to having moved further through the gel.

Light scattering experiments

Dynamic light scattering (DLS) and static light scattering (SLS) experiments were performed by employing an ALV goniometer setup equipped with a helium-neon laser operating at $\lambda = 632.8$ nm. The effective hydrodynamic radii of the DL-DNA constructs in dilute aqueous solutions at different conditions of salinity (NaCl) were measured with DLS. The Brownian motion of the DL-DNA molecules was recorded in terms of the time auto-correlation function of the polarized light scattering intensity, $G(q, t)$, using an ALV-5000 multi-tau digital correlator. The measurement consisted of obtaining the intermediate scattering (field) function $C(q, t) = \sqrt{(G(q, t) - 1)/\beta}$ at several scattering wave vectors $q = (4\pi n/\lambda)(\sin(\theta)/2)$, where β is an instrumental factor related to the spatial coherence constant and depends only on the detection optics, n the refractive index of the solvent, and θ the scattering angle. $C(q, t)$ was analyzed *via* an Inverse Laplace Transform (ILT) using the CONTIN algorithm⁵⁶ and the average relaxation time was determined from the peak of the distribution of relaxation times. The translational diffusion coefficient, $D = \Gamma/q^2$, was

found to be q -independent (Γ is the measured relaxation rate). The hydrodynamic radius was extracted from the measured diffusion coefficient D assuming validity of the Stokes–Einstein relation, $R_H = kT/6\pi\eta D$ (k is the Boltzmann constant, T the absolute temperature, and η the solvent viscosity) for spherical objects, (see Fig. 5).

The radius of gyration R_g of the higher DL-DNA generations was extracted from SLS experiments in very dilute aqueous solutions. The scattered intensity of the solution I_{sol} , the solvent I_{solv} , and the pure toluene I_{tol} were recorded over an angular range from 15° to 150° corresponding to scattering vector q in a range of $3.46 \times 10^3 < q < 2.55 \times 10^2 \text{ nm}^{-1}$. The pure toluene was used as a scattering-angle-independent standard to account the dependence of the scattering volume on the scattering angle. Thus, the scattered intensity I of the DL-DNA particles was determined as follows: $I(q) = (I_{\text{sol}}(q) - I_{\text{solv}}(q))/I_{\text{tol}}(q)$. The R_g was obtained from SLS experiments by performing a Guinier plot: $\ln(I(q)) = \ln(I(0)) - (q^2 R_g^2)/3$. All experiments reported here were performed at room temperature.

Simulation

To simulate the behaviour of the above described macromolecular system with given interactions we employ molecular dynamic (MD) simulations. Simulations are performed using two independent platforms, namely ESPResSo^{57,58} and LAMMPS.⁵⁹ The time step used is $\Delta t = 10^{-3}\tau$, where $\tau = \sqrt{m\sigma^2/\epsilon}$, so that the total running time of the simulations extends over 100 ns (*i.e.*, over 10^9 simulation steps). The box size is chosen to keep the total particle density, ρ_p , independent of dendrimer generation. This number density is set to the value of $\rho_p = 5 \times 10^{-7} \text{ \AA}^{-3}$ in order to avoid self-interaction

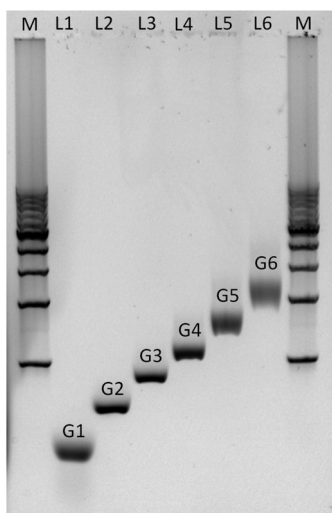


Fig. 4 Non-denaturing agarose gel (0.5%) electrophoresis analysis of the assembly of DL-DNA. The electrophoretic mobility of purified all-DNA dendrimers up to 6th generation is demonstrated. Lane M: 1 Kbp double-stranded DNA marker (bottom to the top: 1 Kbp to 10 Kbp with a 1 Kbp step), lane 1: G1, lane 2: G2, lane 3: G3, lane 4: G4, lane 5: G5 and lane 6: G6.

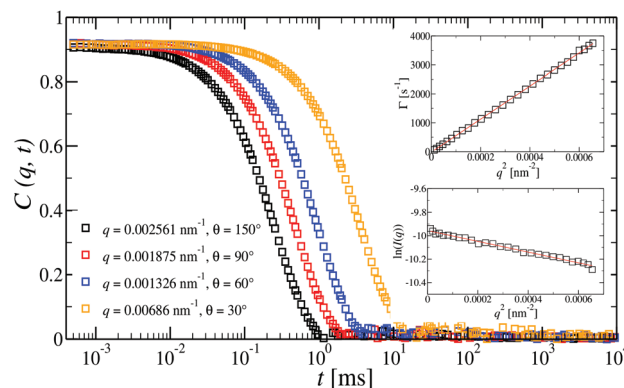


Fig. 5 Intermediate scattering functions, $C(q, t)$, at different angles for a dilute G6 all-DNA dendrimer aqueous solution at a concentration of 15 nM and under mild-salinity conditions (50 mM NaCl). For such dilute regime only a single translational diffusion process is observed. Indeed, the $C(q, t)$ is a single diffusive relaxation which is clearly confirmed by the q^2 dependence of the decay rate, $D = \Gamma$ (top inset). Bottom inset: The natural logarithm of the reduced static light scattering intensity for the G6 dendrimer as a function of q^2 (Guinier plot). In both insets, the slopes (red lines) were used for the extraction of the R_H (top) and R_g (bottom).

via periodic boundaries while keeping the box size small at the same time.

Canonical ensemble is applied and periodic boundary condition are applied. The evaluation of electrostatic interactions is performed using the Ewald summation method⁶⁰ and the multilevel summation method^{61,62} (MSM) for ESPResSo and LAMMPS, respectively, with a relative force accuracy of 10^{-5} . Langevin thermostat is chosen and set to preserve the temperature of $T = 298$ K. We use 1000 snapshots of a simulation run over $0.1 \mu\text{s}$ (after equilibration) of a single DL-DNA molecule to obtain results that follow.

Results and discussion

Comparison between experiment and simulation

The overall size of the dendrimer can be characterized by its radius of gyration R_g or its hydrodynamic radius R_H . In principle, these quantities can be determined in simulations; they are also experimentally accessible by means of different scattering techniques, *e.g.*, SANS, SAXS, or dynamic light scattering. However, in this contribution, we only calculate the radius of gyration, R_g , from simulated systems *via* the following expression:

$$R_g^2 = \frac{1}{N} \left\langle \sum_{i=1}^N (r_i - r_{\text{com}})^2 \right\rangle, \quad (6)$$

where N is the total number of monomers constituting the DL-DNA, r_i denotes the positions of the individual monomers, and r_{com} stands for the center of mass of the molecule. This quantity is readily accessible in MD simulations and enables us to assign a typical size to the molecule described by the employed model. The hydrodynamic radius R_H was experimentally determined using dynamic light scattering and measuring the diffusion coefficient in diluted dendrimer solutions. Though the two radii are different by definition, one measuring spatial extent and the other hydrodynamic drag, they differ in their values only by a small amount so that a comparison of R_g from simulation with R_H from experiment is a good way to validate the model. Moreover, static light scattering has been also employed to determine R_g for dendrimers of higher generation numbers.

A comparison of the results originating from experiment, R_H , and simulation, R_g , is presented in Fig. 6. For G1 to G5 the results of R_g and R_H show excellent agreement, indicating the appropriateness of the underlying model. The two sets of data show small discrepancies for DL-DNAs of higher generations, *i.e.*, for G6 DL-DNAs; therefore, we show here also experimental values of R_g for G5 and G6 DL-DNAs. As experiments show, for G5 DL-DNAs the radius of gyration coincides with the hydrodynamic radius $R_g = R_H$, which on the other hand, fits nicely with the obtained simulation value. This matching between results of static and dynamic light scattering for G5 justifies our choice of comparing two different quantities that characterize the size of a dendrimers of lower generation

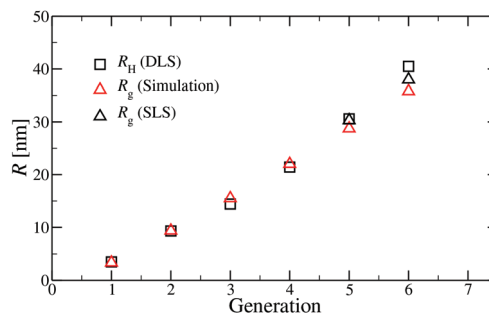


Fig. 6 Hydrodynamic radius R_H (as extracted from experiment) and radius of gyration R_g (as predicted in simulation) as functions of the generation index of DL-DNAs (as labeled). For DL-DNA of G5 and G6 experimental values of R_g are also provided.

numbers. We observe that both the experimental and simulation data exhibit a concave shape as function of generation index, reflecting the non-linear growth of the dendrimer with increasing generation number. This feature can be explained by the observed increase of the molecules' sphericity with the growing monomer density at the periphery of the DL-DNA. As the sphericity of the dendrimer increases, as it is the case for G6 DL-DNAs, the ratio between the experimentally measured radius of gyration and the hydrodynamic radius deviates from 1 and goes toward smaller values, *i.e.*, $R_g/R_H = 0.94$. For the sake of comparison, the theoretical value of this ratio is 0.778 for a homogeneous hard sphere⁶⁴ and 1.0 for hollow spheres with an infinitely thin shell.⁶⁵ Therefore, the significant discrepancy observed between the experimental R_H and R_g obtained from simulation for G6 DL-DNAs and probably also for higher generations becomes reasonable and one has to employ static light scattering in order to obtain better agreement with the results of the performed simulations.

Conformational analysis

A more detailed analysis of the form factor $F_{\text{mm}}(q)$ of the dendrimer provides a deeper insight into the structural properties of the dendrimer. The form factor is defined as

$$F_{\text{mm}}(q) = 1 + \frac{1}{N} \left\langle \sum_{i \neq j}^N \exp[-i(\mathbf{q} \cdot \mathbf{r}_{ij})] \right\rangle, \quad (7)$$

where the summation runs over all inter-monomer distances r_{ij} and the brackets $\langle \dots \rangle$ stand for an average over all conformations, which restores rotational symmetry; here, \mathbf{q} denotes the scattering wavevector, allowing to look at different scales within the molecule. At coarse length scales, $qR_g \lesssim 1$, the above expression reduces to the Guinier law:⁶⁶

$$F_{\text{mm}}(q) \simeq N \exp\left[\frac{-(qR_g)^2}{3}\right], \quad (8)$$

which represents a useful relation between the form factor and the radius of gyration within the regime $qR_g \lesssim 1$. *Via* this

expression, the radius of gyration can be extracted from experimental form factor data in the small wave-vector limit.

An overview of the results for $F_{\text{mm}}(q)$ from simulation is given in Fig. 7, where this function is shown on different scales. As eqn (8) implies, the form factor becomes equal to the total number of monomers of the molecule in the limit of small wave vectors, *i.e.*, for $q \rightarrow 0$. Further, we observe oscillations in $F_{\text{mm}}(q)$ for $q\sigma \sim 10^{-1}$; the first local minimum becomes more pronounced with increasing generation index, signifying that these larger molecules possess a more spherical shape and that the sharpness of the molecules' boundary at the outermost shell increases. The rigidity of the dsDNA strands within the molecule reflects in the large wave-vector behaviour of $F_{\text{mm}}(q)$, namely, the form factor satisfies the law $F_{\text{mm}}(q) \sim q^{-1}$ in the limit of large wave vectors.⁶³ This is the typical scaling law for scattering from rigid rods, which is in contrast to flexible dendrimers, which usually scale with $\sim q^{-4}$ in the same range of q , according to Porod's law.⁶⁷ This outcome can be better understood in the context of scattering from fractal aggregates: it can be shown⁶⁸ that for arbitrary systems of scatterers the scattering intensity $F_{\text{mm}}(q)$ scales with the wave vector as

$$F_{\text{mm}}(q) \sim (qR)^{-2D_m+D_s} \quad \text{for } R^{-1} < q < a^{-1}, \quad (9)$$

where D_m and D_s are the mass and surface fractal dimensions, respectively. The size of a single monomer is a , while the size of the whole system is denoted as R . In the case of solid spheres the mass dimension D_m is equal to the system's spatial dimension d ($D_m = d = 3$), while the surface dimension is $D_s = d - 1 = 2$, which results in the well-known Porod's law, $F_{\text{mm}}(q) \sim q^{-4}$. On the other hand, a rigid dendrimer can be characterized as a single fractal aggregate. Therefore, its fractal dimension, D , is equal to the fractal mass and surface dimensions, $D = D_m = D_s < d$, obeying the scaling law

$$F_{\text{mm}}(q) \sim (qR_g)^{-D} \quad \text{for } qR_g > 1, \quad (10)$$

with $D = 1$. By analyzing the form factor in this way, we have obtained a beautiful reflection of the distinctive behaviours of flexible and rigid dendrimers.

Additional insight into the conformational features of DL-DNAs can be acquired by analyzing the monomer–monomer pair correlation function. In Fig. 8 the radial distribution function $g_{\text{mm}}(r)$ for DL-DNAs of generations G1 and G5 is plotted as a function of the distance r , given in units of the equilibrium bond length l_b . The well-defined maxima which occur at equidistant positions indicate that the bonds between the monomers are rather stiff. The first and largest peak represents the nearest neighbour separation along the Y-DNA arms. The height of the maxima scales with r^{-2} , which is the rate at which the volume of the spherical shells increases. The two curves of $g_{\text{mm}}(r)$ are identical for G1 and G5 in this regime.

Another quantity that provides detailed information about the complex internal structure of DL-DNAs is the density profile of the constituents of the macromolecule with respect to the center of mass of the dendrimer:

$$\rho(r) = \left\langle \sum_{i=1}^{N_m} \delta(r - r_i + r_{\text{com}}) \right\rangle, \quad (11)$$

where the summation runs over all particles of a particular type, such as the monomers or the counterions; the vectors r_i denote the corresponding positions of the particles. In Fig. 9 the density profiles for specific components of DL-DNA molecules are shown, focusing on a G3 (Fig. 9(a)) and a G6

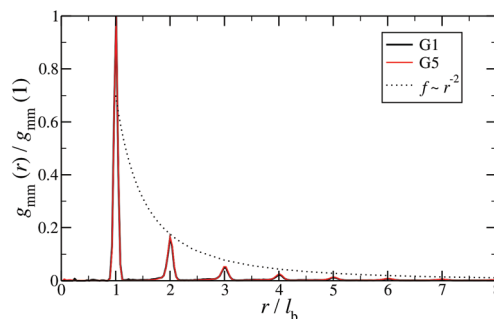


Fig. 8 Monomer–monomer radial distribution function $g_{\text{mm}}(r)$ for DL-DNAs of generations G1 and G5 plotted as functions of distance r , given in units of the equilibrium bond length l_b .

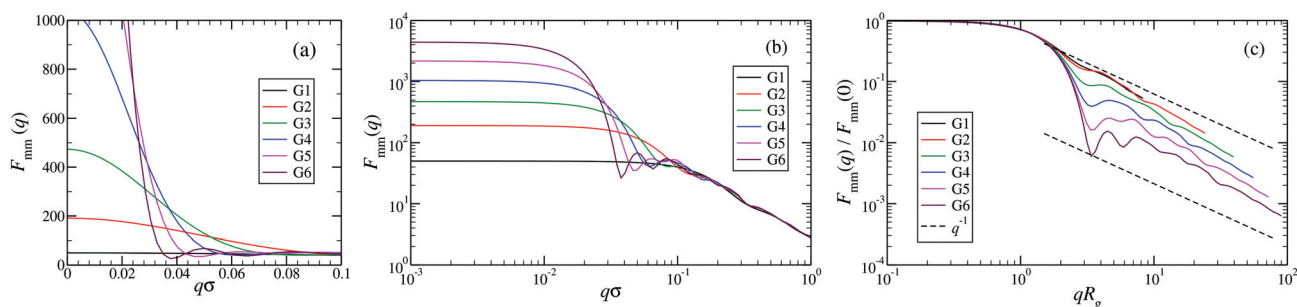


Fig. 7 The form factor $F_{\text{mm}}(q)$ of the DL-DNAs of generation G1 to G6 (as labeled) obtained from simulations, given as a function of the dimensionless wave-vector. Data are shown: (a) on a linear scale; (b) on a double-logarithmic scale; and (c) on a double-logarithmic scale with $\lim_{q \rightarrow 0} F_{\text{mm}}(q)$ rescaled to 1. The dashed lines in panel (c), *i.e.*, $F_{\text{mm}}(q) \sim q^{-1}$, correspond to the typical scaling law for the scattering from rigid rods⁶³ for large q -values.

(Fig. 9(b)) dendrimer, respectively. The different entities considered are (i) all monomers (without distinction; “total”), (ii) the monomers pertaining to a specific subgeneration, g_i , and (iii) the counterions. The monomers are regularly distributed in concentric-like structures such that only minor overlap between subsequent subgenerations exists. This kind of behaviour is typical for charged macromolecules with rigid bonds:^{69,70} the strong Coulomb repulsion, combined with rigidity and the dendritic character prevent backfolding of the outer monomers towards the interior of the molecule, a feature that is in contrast to the standard dense-core model of dendrimers with flexible bonds.^{71,72} This rigidity is in addition reinforced by the Coulomb repulsion between like-charged monomers, resulting in a complete suppression of backfolding. Because the Y-DNAs of the individual subgenerations exhibit a transition at the junction, where one inward-facing arm splits into two outward facing arms, the corresponding density profiles feature a double-peak. This double-peak feature is not as pronounced in subgenerations with higher index g_i , as the spatial distribution of these higher subgenerations is less coherent and more flattened out.

The counterion density distribution closely follows the monomer density due to the system’s propensity towards local charge neutrality and the spatial structure of the counterions is less pronounced due to an entropic ‘smearing out’ of the profiles. Overall, we obtain, especially for higher generations, almost flat-density molecules, whose monomer- and counterion-profiles are tunable by varying the generation index, GN . Contrary to the usual, dense-core, flexible dendrimers,^{67,72} the

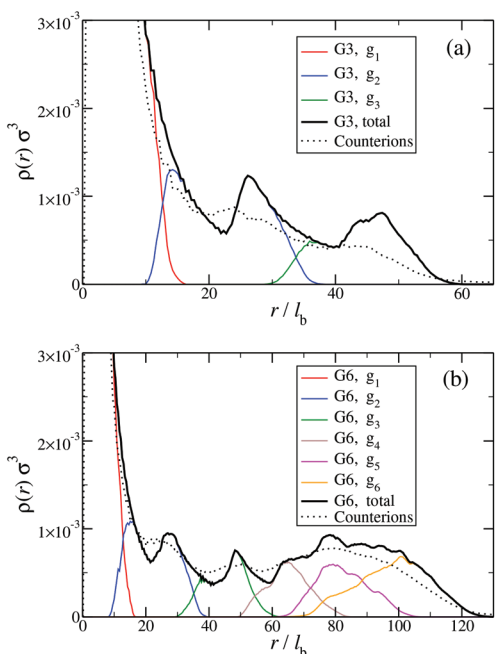


Fig. 9 Monomer and counterion density profiles $\rho(r)$ as functions of r , given in units of the equilibrium bond length l_b ; $\rho(r)$ is shown for different entities of the system (as labeled and see text). Data are shown (a) for a G3 DL-DNA and (b) for a G6 DL-DNA.

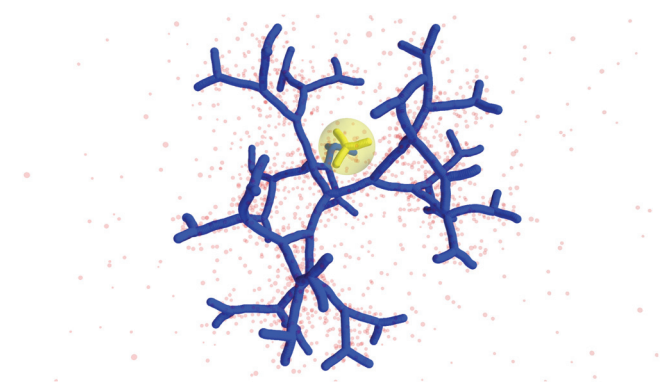


Fig. 10 Simulation snapshot of G5 DL-DNA. The encircled G1 DL-DNA is inserted to the figure to guide the eye to better visualization of the void size.

monomer profile of the DL-DNA does not monotonically drop as one moves from the center of the molecule towards its periphery, but it remains rather flat and constant (with modulations close to the junction points). Moreover, these nanostructures feature very low local monomer packing in their interior, $\rho(r)\sigma^3 \sim 10^{-3}$ (see Fig. 9), as opposed to typical values $\rho(r)\sigma^3 \sim 1$ for flexible dendrimers.⁶⁷ Accordingly, they offer a great deal of empty space (voids) in their interior, capable of accommodating smaller molecules, such as a G1-dendrimer, as demonstrated in Fig. 10. Due to their ‘uniform-density’ interior, DL-DNA constructs are also suitable for an analytical description using the Poisson–Boltzmann theory,^{73,74} since the constant ion density inside the molecule simplifies analytical calculations.

In the following, a more detailed analysis of the counterion condensation is presented. In our investigation we have encircled each arm of the individual Y-DNA elements by a tube of radius r ; we have then counted the percentage of ions $Q_i(r)$ captured in those cylinders. The dependence of $Q_i(r)$ on the tube radius r is depicted in Fig. 11(a). Even though the considered system is electro-neutral, a difference in the value of $Q_i(r)$ of approximately 20% between G1 and G5 dendrimers can be observed for tube radii larger than $3r_{M-C}$. This observation is a direct consequence of an increase in the available volume provided by the larger dendrimers. The same effect can be seen in Fig. 11(b), where the total amount of counterions absorbed by the dendrimers is shown, expressed *via* function $Q_s(r)$. When the radius of the sphere r that encircles the dendrimer exceeds the size of the dendrimer r_{max} only 40% of counterions are absorbed by a G1 DL-DNA, whereas this percentage grows with increasing dendrimer generation number and approaches 90% in the case of a G5 DL-DNA. It is also worth noticing that the transition of the counterion profile from the interior to the exterior becomes increasingly sharp as the dendrimer generation index grows: accordingly, high-G DL-DNA’s act as osmotic dendrimers, in full analogy with the osmotic polyelectrolyte stars,^{75–77} which capture the counterions in their interior. However, in contrast to these, DL-DNA’s

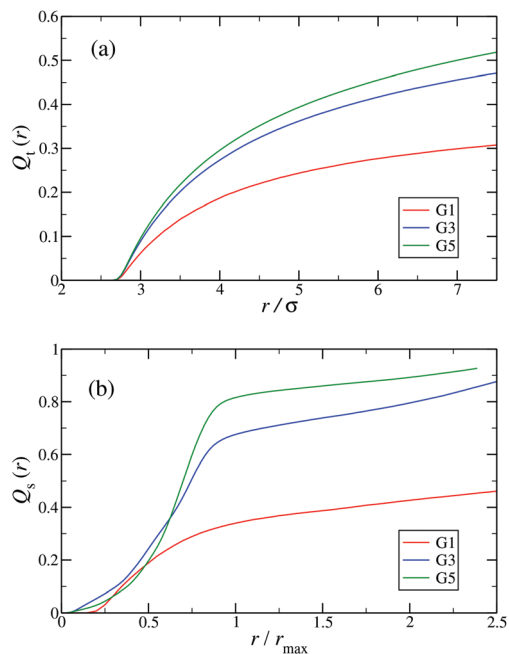


Fig. 11 (a) Percentage of total counterions, $Q_t(r)$, captured in tubes of radius r surrounding each arm of the Y-DNA elements as a function of r (in units of σ). (b) Percentage of total counterions, $Q_s(r)$, captured in spheres of radius r centered at the center of mass of the DL-DNA r_{com} as a function of r/r_{\max} , where r_{\max} denotes the maximum distance between a DNA-monomer and r_{com} . The graphs are shown for dendrimers G1, G3, and G5 (as labeled).

are very robust against salinity, maintaining their size essentially unaffected by addition of large quantities of monovalent salt, as it will be shown in what follows.

In Fig. 12 the probability of the nearest junction-to-junction separation of successive subgenerations g_i and g_{i+1} within a G6 DL-DNA is shown as a function of distance given in units of bond length. Since each branch extending from junction to junction point consists of 30 monomers, the peak of this function is located slightly above $29l_b$ for the innermost branches and its position decreases monotonically as one moves away toward the exterior of the molecule, (*i.e.*, towards the outer

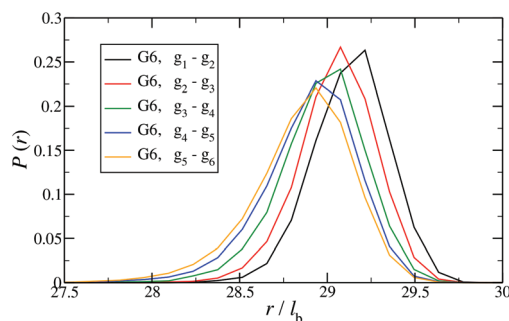


Fig. 12 Probability for the nearest junction-to-junction separation of successive subgenerations g_i and g_{i+1} within a G6 DL-DNA given in units of the equilibrium bond length l_b .

subgroups) while the variance increases at the same time. The shrinkage of bond lengths belonging to the outer branches is a consequence of osmotic swelling which tends, on one hand, to stretch central (inner) branches, while on the other hand, it allows a slightly higher flexibility of the branches belonging to higher subgenerations. To understand the physics behind this, we need to consider the osmotic pressure from the counterions trapped in the interior of the molecule, which tries to swell the dendrimer by exercising an outward force at a fictitious spherical surface of radius r_{\max} that surrounds the molecule, touching the free tips of the outermost Y-junctions (composed of 4-bases long ssDNA). This force is transmitted to the interior of the dendrimer, but the number of Y-junction tips among which it is partitioned is halved each time the subgeneration index decreases by one. Accordingly, the innermost generations are pulled more strongly than the outermost ones; thus they are more rigid, more straight-line looking. This effect is also observable in the simulation snapshot (see Fig. 3), where it can be seen that the innermost branches are more rigid, having the shape of a straight line, while the branches belonging to the outermost subgenerations expose a more wiggly behaviour. This interpretation is corroborated by the analysis of angular fluctuations in what follows.

In order to analyze the internal freedom of the typical conformations of the dendrimers, we measure in the simulations two kinds of bond angles, namely ϕ and θ , for the individual subgenerations. Here, ϕ is defined, according to eqn (3), as the angle between two consecutive bonds within a Y-arm; it is consequently a reliable measure of the rigidity of the Y-DNA arms. The angles θ_i ($i = 1, 2, 3$), on the other hand, are defined as the angles between the vectors pointing along the three arms of the Y-DNA, whereby an arm vector is defined as the vector connecting the first and last monomer of a specific Y-DNA arm, *i.e.*, the arm is assumed to be fully rigid. Each Y-DNA element is characterized by three of these angles: θ_1 , θ_2 , and θ_3 . For fully rigid connections between successive Y-junctions in the dendrimer, one would find $\phi = \pi$ and $\theta_i = 2\pi/3$ for all i .

In Fig. 13(a) the probability distribution $P(\phi)$ of the angle ϕ for the innermost generations, g_1 , is shown for DL-DNAs of different generation index. The distributions all exhibit a pronounced maximum close to the value of a fully rigid dendrimer, *i.e.*, $\phi \cong \pi$. This feature again demonstrates that the interactions of our model tend to keep the monomer chains straight. A slight but visible enhancement of the peak (*i.e.*, a reduction of the fluctuations) can be seen for the G7 dendrimer. This indicates, that its inner generation is more stretched and thus more straight as the number of generation grows. This feature is one manifestation of the increased osmotic stretching force from the counterions. If we focus on a G7 molecule and look at the stretching of the various generations g_i within the G7 DL-DNA, Fig. 13(b), a similar trend can be observed: the distribution is rather sharply peaked close to the angle $\phi = \pi$, pointing to stretched connections between the junction points. Again, one can notice that the probability distribution $P(\phi)$ for higher subgenerations displays a ‘leakage’ to smaller ϕ -values, indicating that the branches belonging to the

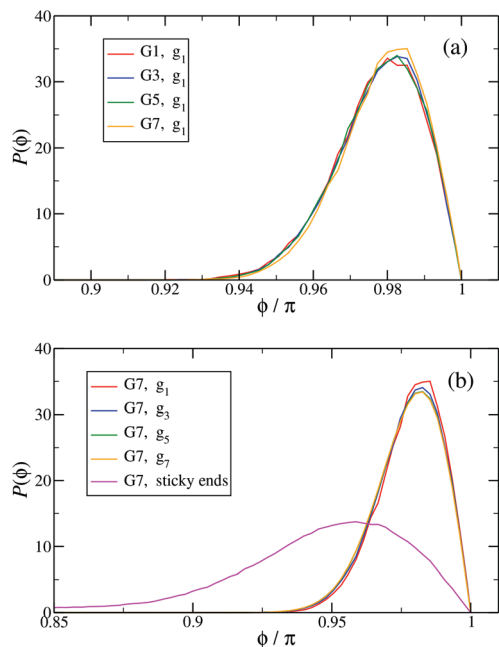


Fig. 13 The probability distribution $P(\phi)$ of angle ϕ of (a) the innermost subgeneration g_1 for DL-DNAs of generation index G1–G7 (as labeled) and (b) individual subgenerations within a G7 DL-DNA (as labeled). The distribution $P(\phi)$ is normalized as $\int_0^\pi P(\phi) d\phi = 1$.

outermost subgenerations are more flexible compared to the innermost branches, which is consistent with the finding on the inter-bonding separation (see Fig. 12) and our interpretation of its physical origin. In addition, we also show in Fig. 13(b) the probability distribution of angle ϕ corresponding to those parts of the chains that are characterized as a sticky-end. As it is expected, the function spreads over a wider range of possible conformational angles, reflecting the fact that sticky ends exhibit a significantly more flexible behaviour.

Fig. 14 shows the corresponding probability distributions $P(\theta_i)$ for the angles θ_i ($i = 1, 2, 3$), for DL-DNAs of different generation index. In particular, in Fig. 14(a) we focus on the innermost generation, g_1 , of various GN-dendrimers and we do not distinguish between the three angles θ_i , $i = 1, 2, 3$, since their distributions coincide by symmetry. The distinction is being made in Fig. 14(b), for which we collected statistics of outer angle θ_3 and inner angles $\theta_{1,2}$ to determine the three individual distributions $P_i(\theta)$ for the three angles denoted in the insets. Here, we can see that the most probable angle of the innermost subgeneration, g_1 , of dendrimers of different generations is centered around $\theta_i = 2\pi/3$, confirming the rigidity of the Y-branches. However, the width of these distributions increases with decreasing generation number GN, as the amplitude of the fluctuations in θ_i correlates negatively with the size of the dendrimer branch attached to the corresponding arm. With growing generation number, the number of branches grows more rapidly, so that the fluctuations in the angle θ become less probable due to the reduced available

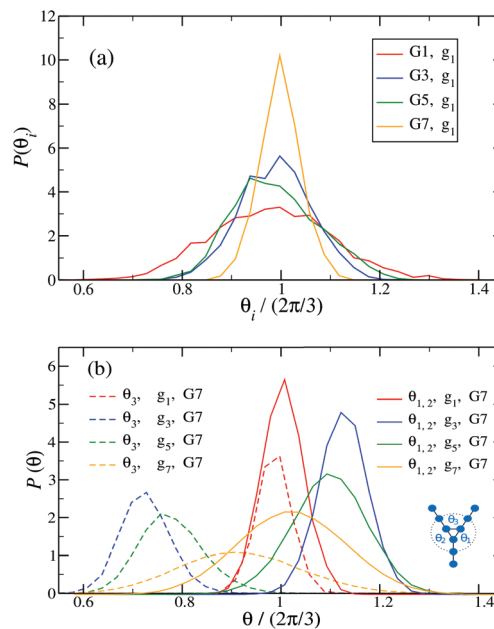


Fig. 14 $P(\theta_i)$, i.e., (a) the probability distribution of angles θ_i , ($i = 1, 2, 3$) of the innermost subgeneration g_1 for DL-DNA of generation index G1–G7 (as labeled) and (b) the probability distribution of outer angle θ_3 (dashed lines) and the inner angles θ_i , ($i = 1, 2$) (solid lines) of the individual subgeneration within a G7 DL-DNA (as labeled). Each $P(\theta_i)$ is normalized as $\int_0^\pi P(\theta_i) d\theta_i = 1$.

volume and the restrictions due to the mutual electrostatic repulsions between the different arms. When examining the distributions of different subgenerations within a G7 DL-DNA, Fig. 14(b), the emergence of differently centered peaks of $P(\theta_3)$ and $P(\theta_{1,2})$ for the corresponding intermediate subgenerations can be observed.

This phenomenon can be explained by the deformation of Y-DNAs from a conformation with $\theta_i = 2\pi/3$, $i = 1, 2, 3$, into a configuration with $\theta_i > 2\pi/3$, with $i = 1, 2$, and $\theta_3 < 2\pi/3$. This change is caused by the monomers pertaining to the outer (inner) generations that pull (push), respectively, monomers of the intermediate subgenerations outwards *via* steric and electrostatic interactions. This phenomenon does not occur for Y-DNAs of the last subgeneration, i.e., g_7 in the examined case, as these Y-DNAs are not constrained by subgenerations of higher index.

Finally, in Fig. 15 the distribution $P(\theta_\Sigma)$ is shown for a G7 DL-DNA, where $\theta_\Sigma = \sum_{i=1}^3 \theta_i$. The data provide evidence that the Y-DNA of the innermost subgeneration, whose arms are subject to outward forces caused by the subsequent generations, is almost completely planar, i.e., $\theta_\Sigma \approx 2\pi$. With increasing generation index, however, the Y-DNAs' deviation from the planar configuration becomes more pronounced, i.e., $\theta_\Sigma < 2\pi$. Underlying to this behaviour are two opposite effects: Coulomb repulsion and the aforementioned outward forces drive the Y-DNAs towards a planar configuration, but at the

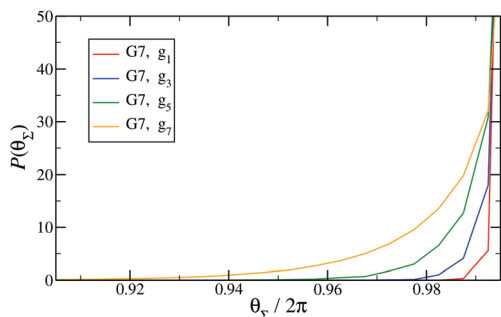


Fig. 15 $P(\theta_\Sigma)$, *i.e.*, the probability distribution of the sum of the three junction angles θ_Σ of the individual subgenerations within a G7 DL-DNA (as labeled). $P(\theta_\Sigma)$ is normalized as $\int_0^{2\pi} P(\theta_\Sigma) d\theta_\Sigma = 1$.

same time this planarity reduces the number of configurations available to the Y-DNAs and therefore their entropy. As we proceed to the outermost generations, the branches of the Y-junctions have more freedom to fluctuate and entropic contributions become enhanced, enabling fluctuations of the Y-junctions that deviate from planarity.

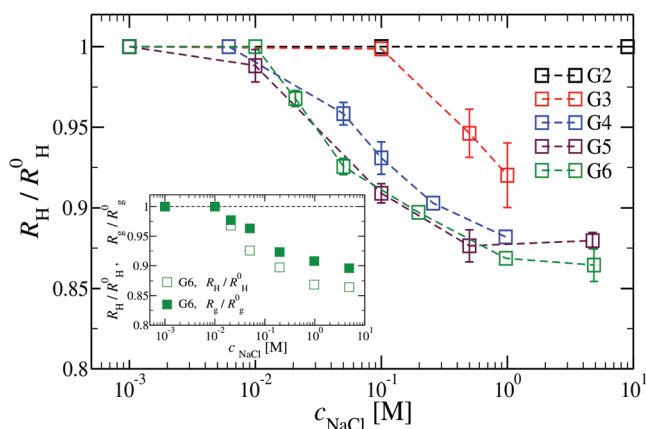


Fig. 16 The effect of different NaCl concentrations on the hydrodynamic radius R_H for DL-DNA of generations G2 to G6 (as labeled). The inset shows a comparison between the R_H - and the R_g -shrinkage (as compared to respective salt-free values R_H^0 and R_g^0) for a G6 DL-DNA.

Influence of salt on conformational properties of DL-DNA

We have also analyzed the effect of a finite salt concentration (NaCl) on the overall size of the dendrimer. The experiments are performed for different values of salt concentrations, extending from a low salt regime ($c = 0.1$ mM) up to very high salt concentrations ($c \approx 5$ M). Due to numerical limitations, only salt concentration up to $c \approx 30$ mM could be considered in simulations. Results for the hydrodynamic radius, as obtained from the experiment, are summarized in Fig. 16. By adding salt essentially no change in the size of the dendrimer is observable up to a concentration of $c = 10$ mM.

This observation is confirmed in the simulations (see Table 3). The absence of any significant shrinking at low salt concentrations is the consequence of the rigidity of the molecule, *i.e.*, the high persistence length. In order to overcome the stiffness of the molecule, one has to proceed to higher salt concentrations, *i.e.*, above $c = 10$ mM; under such conditions the screening of the charge of the molecule starts to affect the Coulomb interaction between the monomers, inducing thereby the shrinking of the molecule. This reduction in size is more pronounced for higher dendrimer generations and it can range from approximately 10% to 15% for extremely high salt concentrations (*i.e.*, $c \sim 1$ M). Throughout, the decrease of R_H is generation-dependent and the critical salt concentration at which the molecule starts to shrink differs from generation to generation. The inset of Fig. 16 shows the comparison of the experimental results for the radius of gyration and for the hydrodynamic radius of G6 DL-DNA under the change of salt concentration. Both quantities show the same trend but with slightly more expressed shrinkage of R_H over R_g .

We have performed simulations of G4 DL-DNA for various values of salt concentration, and the resulting radius of gyration as a function of salt concentration is given in Fig. 17(a). The comparison with the hydrodynamic radius obtained from experiments is also shown. From simulation, we observe the shrinking of the molecule by approximately 7% when varying the salt concentration from $c = 1$ mM to $c = 30$ mM, while the experiments show the shrinkage by approximately 5% when varying the salt concentration from $c = 1$ mM to $c = 50$ mM. In Fig. 17(b) we present the form factors, comparing two sets of simulation data corresponding to different salt regimes. The curves unambiguously demonstrate that the added salt does

Table 3 Comparison of the results for the radius of gyration, R_g , obtained in simulations and for the hydrodynamic radius, R_H , extracted from experiment (as labeled) over six generations of DL-DNA. Experiments are performed for a salt concentration of 0.1 mM. Simulations are carried out both for the salt-free regime ($c_0 = 0$ mM) and using a salt concentration of $c_1 = 1$ mM with different simulation packages (as labeled)

Generation	$R_{H/c=0.1\text{ mM}}^{\text{exp}}$ [nm]	$R_{g/c=0\text{ mM}}^{\text{ESPResSo}}$ [nm]	$R_{g/c=0\text{ mM}}^{\text{LAMMPS}}$ [nm]	$R_{g/c=1\text{ mM}}^{\text{LAMMPS}}$ [nm]
G1	3.5	3.30	3.37	—
G2	9.31	9.60	9.37	9.6
G3	14.42	15.75	15.52	15.4
G4	21.43	22.14	22.02	21.6
G5	30.58	28.87	28.75	28.2
G6	40.49	36.02	35.8	—

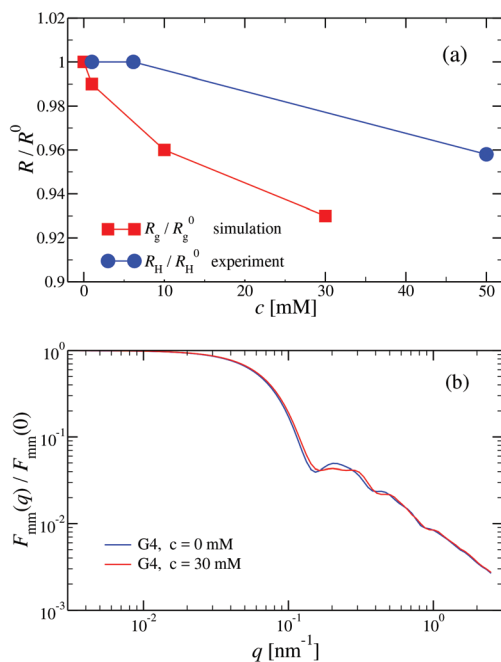


Fig. 17 (a) Hydrodynamic radius R_H , as extracted from experiments, and radius of gyration R_g , obtained from simulation, (as labeled) as functions of the NaCl concentration (given in mM) for a G4 DL-DNA. (b) Form factor $F_{mm}(q)$ as a function of q for a G4 DL-DNA for salt concentrations $c = 0$ mM and $c = 30$ mM (as labeled), obtained from simulation.

not have any impact on the rigidity of the dendrimer, *i.e.*, in the regime of large wave vectors the form factor satisfies the above mentioned q^{-1} scaling law irrespective of the salt concentration. From these data one can conclude that the Coulomb interactions do stretch the bonds between the monomers, but the related effect is subdominant when compared to the role that rigidity has in suppressing significant changes in bond lengths.

The shrinking of flexible, charged polymers upon addition of salt can be physically traced back to the screening of the electrostatic interaction or to the enhanced osmotic pressure from the co- and counterions at the exterior of the macromolecule.⁷⁶ For the case at hand, it is not clear that the same physical mechanism is at work, since the shrinkage is minimal and the molecular architecture is different. To shed light into the mechanism behind the size reduction of the nanoparticle, we look at the density profiles with and without salt. In Fig. 18(a) and (b), the monomer density profile for a G4 DL-DNA is shown for the salt-free case and for a NaCl salt solution of concentration $c = 30$ mM, respectively. One can notice that the only difference between corresponding monomer profiles under different salt conditions appears for the outermost subgeneration g_4 . In the salt solution enhanced backfolding of the outermost branches arises, resulting in the small shrinkage of the dendrimer's radius of gyration, observed at Fig. 17(a). The interior of the dendrimer remains unaffected by the added salt, an additional manifestation of the combined effect of rigidity and branched architecture of

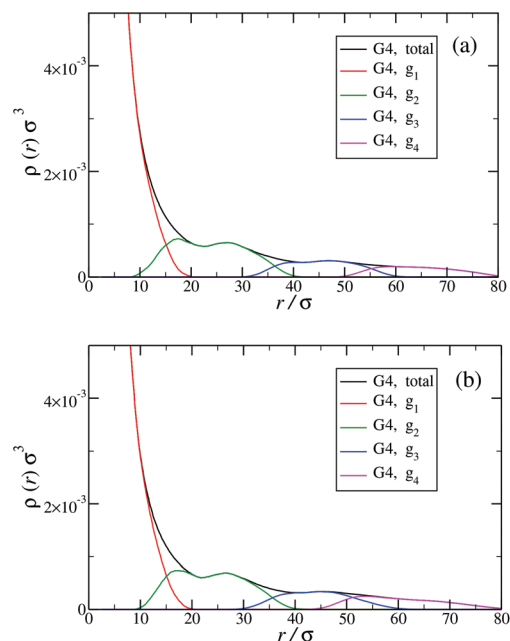


Fig. 18 Monomer density profile for G4 DL-DNA: (a) salt-free regime, $c = 0$ mM; (b) $c = 30$ mM.

the novel DL-DNA constructs. These are remarkably resistant macromolecules, which nevertheless feature a very low internal monomer concentration, allowing them to absorb counterions or smaller molecules in their interior. In addition, whereas salinity is expected to affect the effective interactions between such dendrimers, practically it does not affect their sizes and shapes, rendering them thus as prime candidates for molecules with tunable, ultrasoft effective repulsions.

Conclusions

We have investigated the structural properties of DL-DNA at a single particle level with sizes ranging from G1 to G7. Additionally, we probed the salt-responsiveness of the complex nanostructure of said molecules with regards to backfolding of dendritic arms, providing a thorough investigation of the structural properties of these all-DNA nanostructures. Through a combination of experiments and molecular modeling we provide an advancement of our understanding of such dendritic DNA constructs, which is essential for developing applications and investigating novel phenomena related to this type of soft material.

In colloidal polymer network terms, the high-G DL-DNA and ionic microgels share some common characteristics. Both, highly permeable to solvent molecules, can act as efficient absorbers of their own counterions under salt-free conditions, and at a very coarse-grained level their internal structure has a core-shell morphology. However, our results revealed that the DL-DNA's scaffold architecture and its inherent rigidity grant these all-DNA nanostructures with low internal monomer con-

centration, regular voids in their interior and, at the same time, a resilience against the addition of salt; intriguing and promising features which are absent in ionic microgels and which are expected to have significant impact on the dendrimers' collective behaviour. More specific, experimental as well as computational results show that varying the salt concentration only minimally affects the conformation and does not cause any backfolding of dendritic arms. This low salt-responsiveness allows for adjusting the effective interaction between different DL-DNA molecules without the dendrimers collapsing or their structure deforming significantly. In addition, the monomer density profiles revealed that high-G DL-DNA are dendrimers with almost flat density and internal cavities with generation-independent size. The cavity space, located at the dendrimer's center of mass, was found to be comparable to the size of G1, implying that the void interior can be engineered at subnanometer precision (at the level of a single level) by simply adjusting the arm length of the Y-DNA building block belonging to the first generation; thus allowing full control over the degree of dendrimer interpenetrability. We believe that the above properties make these highly charged tailored empty-core/shell nanostructures ideal candidates for exploring novel forms of self-assembly such as cluster crystallization in the bulk. The current work sets the pivotal point for the investigation on the many-body properties of concentrated DL-DNA systems, which will be the subject of the future work.

Conflicts of interest

There are no conflicts of interest to declare.

Acknowledgements

This work has been supported by the Austrian Science Fund (FWF) under grant number I 2866-N36 and by the Deutsche Forschungsgemeinschaft (DFG) under grant number STI 664/3-1. Computation time at the Vienna Scientific Cluster (VSC) is gratefully acknowledged.

References

- 1 N. C. Seeman, *J. Theor. Biol.*, 1982, **99**, 237–247.
- 2 A. V. Pinheiro, D. Han, W. M. Shih and H. Yan, *Nat. Nanotechnol.*, 2011, **6**, 763–772.
- 3 N. C. Seeman and H. F. Sleiman, *Nat. Rev. Mater.*, 2017, **3**, 17068.
- 4 N. R. Kallenbach, R. Ma and N. C. Seeman, *Nature*, 1983, **305**, 829–831.
- 5 T. J. Fu and N. C. Seeman, *Biochemistry*, 1993, **32**, 3211–3220.
- 6 E. Winfree, F. Liu, L. A. Wenzler and N. C. Seeman, *Nature*, 1998, **394**, 539–544.
- 7 Y. He, T. Ye, M. Su, C. Zhang, A. E. Ribbe, W. Jiang and C. Mao, *Nature*, 2008, **452**, 198–201.
- 8 P. W. Rothmund, *Nature*, 2006, **440**, 297–302.
- 9 S. M. Douglas, H. Dietz, T. L. B. Högberg, F. Graf and W. M. Shih, *Nature*, 2009, **459**, 414–418.
- 10 Y. Ke, L. L. Ong, W. M. Shih and P. Yin, *Science*, 2012, **338**, 1177–1183.
- 11 S. M. Douglas, J. J. Chou and W. M. Shih, *Proc. Natl. Acad. Sci. U. S. A.*, 2007, **104**, 6644–6648.
- 12 Y. Sannohe, M. Endo, Y. Katsuda, K. Hidaka and H. Sugiyama, *J. Am. Chem. Soc.*, 2010, **132**, 16311–16313.
- 13 C. Steinhauer, R. Jungmann, T. L. Sobey, F. C. Simmel and P. Tinnefeld, *Angew. Chem., Int. Ed.*, 2009, **48**, 8870–8873.
- 14 R. Jungmann, M. S. Avendaño, J. B. Woehrstein, M. Dai, W. M. Shih and P. Yin, *Nat. Methods*, 2014, **11**, 313–318.
- 15 Y. Suzuki, M. Endo, Y. Katsuda, K. Ou, K. Hidaka and H. Sugiyama, *Nat. Commun.*, 2015, **6**, 8052.
- 16 J. Zheng, J. J. Birktoft, Y. Chen, T. Wang, R. Sha, P. E. Constantinou, S. L. Ginell, C. Mao and N. C. Seeman, *Nature*, 2009, **461**, 74–77.
- 17 A. Kuzyk, R. Schreiber, Z. Fan, G. Pardatscher, E. M. Roller, A. Högele, F. C. Simmel, A. O. Govorov and T. Liedl, *Nature*, 2012, **483**, 311–314.
- 18 G. P. Acuna, F. M. Möller, P. Holzmeister, S. Beater, B. Lalkens and P. Tinnefeld, *Science*, 2012, **338**, 506–510.
- 19 W. Ma, L. Xu, A. F. de Moura, X. Wu, H. Kuang, C. Xu and N. A. Kotov, *Chem. Rev.*, 2017, **117**, 8041–8093.
- 20 A. Udomprasert, M. N. Bongiovanni, R. Sha, W. B. Sherman, T. Wang, P. S. Arora, J. W. Canary, S. L. Gras and N. C. Seeman, *Nat. Nanotechnol.*, 2014, **9**, 537–541.
- 21 D. N. Selmi, R. J. Adamson, H. Attrill, A. D. Goddard, R. J. C. Gilbert, A. Watts and A. J. Turberfield, *Nano Lett.*, 2011, **11**, 657–660.
- 22 N. D. Derr, B. S. Goodman, R. Jungmann, A. E. Leschziner, W. M. Shih and S. L. Reck-Peterson, *Science*, 2012, **338**, 662–665.
- 23 F. Praetorius and H. Dietz, *Science*, 2017, **335**, 5488.
- 24 E. S. Andersen, M. Dong, M. M. Nielsen, K. Jahn, R. Subramani, W. Mamdouh, M. M. Golas, B. Sander, H. Stark, C. L. P. Oliveira, S. Pedersen, V. Birkedal, F. Besenbacher, K. V. Gothelf and J. Kjems, *Nature*, 2009, **459**, 73–76.
- 25 F. Praetorius, B. Kick, K. L. Behler, M. N. Honemann and H. Dietz, *Nature*, 2017, **552**, 84–87.
- 26 F. Romano and F. Sciortino, *Phys. Rev. Lett.*, 2015, **114**, 078104.
- 27 S. Biffi, R. Cerbino, F. Bomboi, E. M. Paraboschi, R. Asselta and F. S. T. Bellini, *Proc. Natl. Acad. Sci. U. S. A.*, 2013, **110**, 15633–15637.
- 28 F. Bomboi, F. Romano, M. Leo, J. Fernandez-Castanon, R. Cerbino, T. Bellini, F. Bordi, P. Filetici and F. Sciortino, *Nat. Commun.*, 2016, **7**, 13191.
- 29 M. Salamonczyk, J. Zhang, G. Portale, C. Zhu, E. Kentzinger, J. T. Gleeson, A. Jakli, C. D. Michele, J. K. G. Dhont, S. Sprunt and E. Stiakakis, *Nat. Commun.*, 2016, **7**, 13358.

- 30 M. Siavashpouri, C. H. Wachauf, M. J. Zakhary, F. Praetorius, H. Dietz and Z. Dogic, *Nat. Mater.*, 2017, **16**, 849–856.
- 31 Y. G. Li, Y. D. Tseng, S. Y. Kwon, L. D'Espaux, J. S. Bunch, P. L. McEuen and D. Luo, *Nat. Mater.*, 2004, **3**, 38–42.
- 32 D. Yang, M. R. Hartman, T. Derrien, S. Hamada, D. An, K. G. Yancey, R. Cheng, M. Ma and D. Luo, *Acc. Chem. Res.*, 2014, **47**, 1902–1911.
- 33 T. Zhou, P. Chen, L. Niu, J. Jin, D. Liang, Z. Li, Z. Yang and D. Liu, *Angew. Chem., Int. Ed.*, 2012, **51**, 11271–11274.
- 34 Y. G. Li, Y. T. H. Cu and D. Luo, *Nat. Biotechnol.*, 2005, **23**, 885–889.
- 35 S. H. Um, J. B. Lee, S. Y. Kwon, Y. Li and D. Luo, *Nat. Protoc.*, 2006, **1**, 995–1000.
- 36 Y. H. Roh, K. Lee, J. J. Ye and D. Luo, *Methods Mol. Biol.*, 2014, **1143**, 159–179.
- 37 S. H. Um, J. B. Lee, N. Park, S. Y. Kwon, C. C. Umbach and D. Luo, *Nat. Mater.*, 2006, **5**, 797–801.
- 38 H. M. Meng, X. Zhang, Y. Lv, Z. Zhao, N. N. Wang, T. Fu, H. Fan, H. Liang, L. Qiu, G. Zhu and W. Tan, *ACS Nano*, 2014, **8**, 6171–6181.
- 39 C. N. Likos, *Soft Matter*, 2006, **2**, 478–498.
- 40 C. N. Likos, R. Blaak and A. Wynveen, *J. Phys.: Condens. Matter*, 2008, **20**, 494221.
- 41 D. A. Lenz, B. M. Mladek, C. N. Likos, G. Kahl and R. Blaak, *J. Phys. Chem. B*, 2011, **115**, 7218–7226.
- 42 D. A. Lenz, B. M. Mladek, C. N. Likos, G. Kahl and R. Blaak, *J. Chem. Phys.*, 2016, **144**, 204901.
- 43 A. Wynveen and C. N. Likos, *Phys. Rev. E: Stat., Nonlinear, Soft Matter Phys.*, 2009, **80**, 010801.
- 44 A. Wynveen and C. N. Likos, *Soft Matter*, 2009, **6**, 163–171.
- 45 P. S. Crozier and M. J. Stevens, *J. Chem. Phys.*, 2003, **118**, 3855.
- 46 K. Kegler, M. Salomo and F. Kremer, *Phys. Rev. Lett.*, 2007, **98**, 058304.
- 47 K. Kegler, M. Konieczny, G. Dominguez-Espinosa, C. Gutsche, M. Salomo, F. Kremer and C. N. Likos, *Phys. Rev. Lett.*, 2008, **100**, 118302.
- 48 C. G. Baumann, S. B. Smith, V. A. Bloomfield and C. Bustamante, *Proc. Natl. Acad. Sci. U. S. A.*, 1997, **94**, 6185–6190.
- 49 J. R. Wenner, M. C. Williams, I. Rouzina and V. A. Bloomfield, *Biophys. J.*, 2002, **82**, 3160–3169.
- 50 H. M. Berman, W. K. Olson, D. L. Beveridge, J. Westbrook, A. Gelbin, T. Demeny, S. H. Hsien, A. R. Srinivasan and B. Schneider, *Biophys. J.*, 1992, **63**, 751–759.
- 51 A. Wynveen, D. J. Lee, A. A. Kornyshev and S. Leikin, *Nucleic Acids Res.*, 2008, **36**, 5540–5551.
- 52 J. F. Marko and E. D. Siggia, *Macromolecules*, 1995, **28**, 8759–8770.
- 53 B. Tinland, A. Pluen, J. Sturm and G. Weill, *Macromolecules*, 1997, **30**, 5763–5765.
- 54 H. Chen, S. P. Meisburger, S. A. Pabit, J. L. Sutton, W. W. Webb and L. Pollack, *Proc. Natl. Acad. Sci. U. S. A.*, 2012, **109**, 799–804.
- 55 N. C. Seeman, *J. Biomol. Struct. Dyn.*, 1990, **8**, 573–581.
- 56 S. W. Provencher, *Comput. Phys. Commun.*, 1982, **27**, 213–227.
- 57 A. Arnold, K. Breitsprecher, F. Fahrenberger, S. Kesselheim, O. Lenz and C. Holm, *Entropy*, 2013, **15**, 4569–4588.
- 58 H. J. Limbach, A. Arnold, B. A. Mann and C. Holm, *Comput. Phys. Commun.*, 2006, **174**, 704–727.
- 59 S. Plimpton, *J. Comp. Physiol.*, 1995, **117**, 1–19.
- 60 P. P. Ewald, *Ann. Phys.*, 1921, **369**, 253–287.
- 61 D. J. Hardy, M. A. Wolff, J. Xia, K. Schulten and R. D. Skeel, *J. Chem. Phys.*, 2016, **144**, 114112.
- 62 D. J. Hardy, Z. Wu, J. C. Phillips, J. E. Stone, R. D. Skeel and K. Schulten, *J. Chem. Theory Comput.*, 2015, **11**, 766–779.
- 63 N. J. Wagner, L. M. Walker and B. Hammouda, *Macromolecules*, 1995, **28**, 5075–5081.
- 64 G. S. Grest, L. J. Fetters, J. S. Huang and D. Richter, *Advances in Chemical Physics*, 1996, vol. 94, pp. 67–163.
- 65 S. U. Egelhaaf and P. Schurtenberger, *J. Phys. Chem.*, 1994, **98**, 8560–8573.
- 66 A. Guinier and G. Fournet, *Small angle scattering of X-rays*, J. Wiley & Sons, New York, 1955.
- 67 I. O. Götze and C. N. Likos, *Macromolecules*, 2003, **36**, 8189–8197.
- 68 C. M. Sorensen, *Aerosol Sci. Technol.*, 2001, **35**, 648–687.
- 69 R. Blaak, S. Lehmann and C. N. Likos, *Macromolecules*, 2008, **41**, 4452–4458.
- 70 S. Huißmann, A. Wynveen, C. N. Likos and R. Blaak, *J. Phys.: Condens. Matter*, 2010, **22**, 232101.
- 71 H. M. Harreis, C. N. Likos and M. Ballauff, *J. Chem. Phys.*, 2003, **118**, 1979.
- 72 M. Ballauff and C. N. Likos, *Angew. Chem., Int. Ed.*, 2004, **43**, 2998–3020.
- 73 J. S. Klos, *Phys. Chem. Chem. Phys.*, 2018, **20**, 2693–2703.
- 74 T. Colla, C. N. Likos and Y. Levin, *J. Chem. Phys.*, 2014, **141**, 234902.
- 75 A. Jusufi, C. N. Likos and H. Löwen, *Phys. Rev. Lett.*, 2002, **88**, 018301.
- 76 A. Jusufi, C. N. Likos and H. Löwen, *J. Chem. Phys.*, 2002, **116**, 11011.
- 77 J. Zhang, M. P. Lettinga, J. K. G. Dhont and E. Stiakakis, *Phys. Rev. Lett.*, 2014, **113**, 268303.

EPJ E

Soft Matter and
Biological Physics

EPJ.org
your physics journal

Eur. Phys. J. E (2014) **37**: 49

DOI 10.1140/epje/i2014-14049-6

Field-theoretic description of charge regulation interaction

Nataša Adžić and Rudolf Podgornik

edp sciences



Società
Italiana
di Fisica

 Springer

Field-theoretic description of charge regulation interaction

Nataša Adžić^{1,a} and Rudolf Podgornik^{1,2}

¹ Department of Theoretical Physics, J. Stefan Institute, 1000 Ljubljana, Slovenia

² Department of Physics, Faculty of Mathematics and Physics, University of Ljubljana, 1000 Ljubljana, Slovenia

Received 14 March 2014 and Received in final form 14 May 2014

Published online: 25 June 2014 – © EDP Sciences / Società Italiana di Fisica / Springer-Verlag 2014

Abstract. In order to find the exact form of the electrostatic interaction between two proteins with dissociable charge groups in aqueous solution, we have studied a model system composed of two macroscopic surfaces with charge dissociation sites immersed in a counterion-only ionic solution. Field-theoretic representation of the grand canonical partition function is derived and evaluated within the mean-field approximation, giving the Poisson-Boltzmann theory with the Ninham-Parsegian boundary condition. Gaussian fluctuations around the mean field are then analyzed in the lowest-order correction that we calculate *analytically* and *exactly*, using the path integral representation for the partition function of a harmonic oscillator with time-dependent frequency. The first-order (one loop) free-energy correction gives the interaction free energy that reduces to the zero-frequency van der Waals form in the appropriate limit but in general gives rise to a monopolar fluctuation term due to charge fluctuation at the dissociation sites. Our formulation opens up the possibility to investigate the Kirkwood-Shumaker interaction in more general contexts where their original derivation fails.

1 Introduction

Kirkwood and Shumaker were the first to realize, more than half a century ago, that there might exist anomalously long-range interactions between proteins in aqueous solutions stemming from thermal charge fluctuations of dissociable charge groups on their surface [1,2]. Within the framework of statistical mechanical *perturbation theory* they showed that this interaction is different from the standard van der Waals (vdW) interaction [3], ubiquitous between neutral bodies, primarily because of its extremely long range. The Kirkwood-Shumaker (KS) interaction was shown to scale with a lower inverse power of separation between two proteins than the vdW interaction. Furthermore and contrary to vdW interactions, the KS forces are not universal, but depend on whether and how the protein charge can respond to the local electrostatic potential, a salient property of dissociable charge groups that is usually referred to as *charge regulation* and was first formalized by Ninham and Parsegian [4].

Charge regulation implies that the effective charge on a macroion, *e.g.* protein surface, responds to the local solution conditions, such as local pH, local electrostatic potential, salt concentration, dielectric constant variation and most importantly the presence of other vicinal charged groups [5]. Although charge regulation is an old concept, modern theories of electrostatic interaction be-

tween macroions immersed in Coulomb fluids [6] mostly deal with constant surface charge of a macroion, bypassing the complications introduced by charge regulation [7–10]. Constant charge is of course a very stringent approximation and holds only in a very restricted part of the parameter space. In general, however, the charge of a macroion surface with dissociable groups always depends strongly on the acid-base equilibrium that defines the fraction of acidic (basic) groups that are dissociated [11–13], and it is necessary to incorporate this property consistently into a theoretical formulation. Our goal in this work is thus to find a theoretical description which would take into account charge regulation of dissociable surface groups and would allow to generalize the original Ninham-Parsegian derivation to include the contribution of fluctuations around the mean field, as well as to pave the way towards other approximations that go beyond the simple mean-field *Ansatz*.

We will first show what is the correct free energy that corresponds to the Ninham-Parsegian mean-field charge regulation theory [4]. It will furthermore become clear as we proceed that the KS interactions in fact correspond to Gaussian monopolar charge fluctuations around the Ninham-Parsegian state, different from the dipolar fluctuations at the origin of the standard vdW forces. We will derive explicitly an exact expression for the one-loop correction of the free energy in the case of a counterion-only system in a planar parallel slab geometry. The theory presented here, while being explicitly formulated only

^a e-mail: natasa.adzic@ijs.si

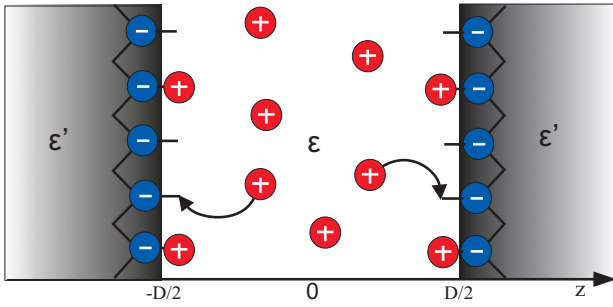


Fig. 1. Schematic representation of two charged planar surfaces at a separation D with charge dissociation sites distributed uniformly along the surfaces and with counterions between the surfaces. The counterions originate from the charge dissociation of the dissociable groups (AC) through the reaction $AC \leftrightarrow A^- + C^+$.

for a restricted model, allows for many generalizations of the monopolar fluctuation interactions that can be derived within the same formalism. We will nevertheless not pursue these generalizations here and relegate further developments to subsequent publications.

The plan of the paper is as follows: in sect. 2 we start from the simplest model that retains the salient features of charge regulation, composed of two planar parallel macromolecular surfaces with surface distributed charge dissociation sites, immersed in a Coulomb fluid composed of counterions only. We base our analysis on a field-theoretic description of the system's partition function, whose Hamiltonian is generalized to include a surface term which describes properly the charge regulation and consequently the local charge fluctuation at the macromolecular surfaces. This model is introduced in sect. 3 together with its full free energy and is shown to coincide with the Ninham-Parsegian *Ansatz* for the charge dissociation equilibrium on the mean-field level and to reduce to the Poisson-Boltzmann (PB) equation with the charge regulation boundary condition in sect. 4. In sect. 6 we address the Gaussian fluctuations around this mean-field solution with its charge regulation boundary condition that can in fact be solved *exactly* and *analytically*. The exact one-loop free-energy correction is obtained by using the path-integral approach for a harmonic oscillator with time-dependent frequency with all the relevant technical details relegated to appendix A. Finally in sect. 7 we present numerical results and comment upon its relevance for the KS interaction in the Conclusions sect. 8.

2 The model

We consider two flat parallel plates, located at $z = \pm D/2$ and immersed into an aqueous solvent, that carry dissociable charge groups of the type $AC \leftrightarrow A^- + C^+$, where the counterion C is released into the aqueous solution, fig. 1. We do not specify the identity of the released counterion but assume it is the only mobile species in the considered model. Furthermore we assume a grand canonical ensemble for the counterions, specified by a fixed value

of the activity. The number of the counterions in the solution is thus not fixed but depends on the dissociation state of the surfaces. While in standard formulations of the counterion-only Coulomb fluids with fixed boundary charge the grand canonical formulation is just a step towards the final canonical ensemble, corresponding to a fixed number of charges, in our case this is not fixed and the grand canonical description is natural.

We need to note that in the Ninham-Parsegian model the released counterion is a proton and the aqueous solution contains a salt mixture at a specified ionic strength for both monovalent and divalent complements [4]. While this model can be formalized in the same way as our simplified model, we first solve the simplified case in order to derive the proper level of description as well as to investigate the salient features of fluctuations in a case, where they can be treated exactly.

In order to describe the surface charge dissociation we introduce a lattice gas model with its own surface free-energy contribution. This surface part of the free energy stems from the charge dissociation equilibrium and describes the (free) energy penalty for a finite surface charge density. We show furthermore that on the mean-field level our formulation yields *exactly* the same result as the Ninham-Parsegian charge regulation *Ansatz*, which is not explicitly based on any surface free energy. The equilibrium distribution of the counter ions is then obtained from the saddle-point equation, that corresponds to the minimum of the complete, *i.e.* volume plus surface, free energy. The dielectric constant in the region between the walls is taken as ϵ , while outside that region it is assumed to be in general different and equal to ϵ' .

3 Field-theoretic description of the model

For describing this model system of interacting particles it is advantageous to use the field-theoretic formalism to derive the partition function. The configurational part of the Hamiltonian of an auxiliary system of N counterions, with a fixed surface charge density σ_0 on the bounding surfaces, can be written as

$$H = \frac{1}{2} \sum_{i \neq j} u(\vec{r}_i, \vec{r}_j) e_i e_j + \sum_{i=1}^N \oint u(\vec{r}, \vec{r}_i) \sigma_0 d^2 \vec{r}, \quad (1)$$

where \oint implies an integration over all the charged bounding surfaces and $u(\vec{r}, \vec{r}_i)$ is the electrostatic interaction kernel, *i.e.* Green's function of the Coulomb potential, which satisfies the relation

$$\nabla^2 u(\vec{r}, \vec{r}_i) = -\frac{\delta(\vec{r} - \vec{r}_i)}{\epsilon \epsilon_0}. \quad (2)$$

The canonical configurational partition function of the system can then be represented by an integral over all positions of the counterions

$$Q_N = \int d\vec{r}_1 \dots d\vec{r}_N e^{-\beta H}. \quad (3)$$

After applying the Hubbard-Stratonovich transformation, one can obtain the grand canonical partition function as a functional integral over the fluctuating electrostatic potential $\varphi(\vec{r})$

$$\mathcal{Z} = \int \mathcal{D}[\varphi(\vec{r})] e^{-\mathcal{S}[\varphi(\vec{r})]}, \quad (4)$$

with the field-action of the form:

$$\begin{aligned} \mathcal{S}[\varphi(\vec{r})] = & \frac{1}{2} \beta \epsilon \epsilon_0 \int d^3 \vec{r} |\nabla \varphi(\vec{r})|^2 + \tilde{\lambda} \int d^3 \vec{r} e^{i \beta e \varphi(\vec{r})} \\ & + i \beta \oint d^2 \vec{r} \sigma_0 \varphi(\vec{r}), \end{aligned} \quad (5)$$

Here $\tilde{\lambda}$ is the absolute activity that will be obtained self-consistently. The above field-action is universal in terms of the non-linear volume interaction term, the second term in the above equation, that corresponds exactly to the van't Hoff ideal osmotic pressure of the counterions. This is a well-known result [14], which on the weak coupling mean-field level, using substitution $\varphi \rightarrow i \phi_{\text{MF}}$, gives the PB equation with fixed charged density boundary condition $\vec{n} \cdot \vec{\nabla} \phi_{\text{MF}} = \sigma_0$ [6].

We now generalize this free-energy *Ansatz* so that it will contain also a surface part, not necessarily linear in the surface fluctuating potential, by assuming that the surface free energy in eq. (5) can be modified as

$$i \oint \sigma_0 \varphi(\vec{r}) d^2 \vec{r} \longrightarrow \oint f(\varphi(\vec{r})) d^2 \vec{r}, \quad (6)$$

where $f(\varphi(\vec{r}))$ is a general non-linear function of the local potential. The exact form of this surface free-energy is not universal and depends on the model of the surface-ion interaction [15]. Here, we will delimit ourselves to a surface lattice gas model, which was introduced in a different context by Fleck and Netz [16], and derive the corresponding free energy, as well as show that the same model in fact corresponds exactly to the Ninham-Parsegian charge regulation theory [17]. The surface lattice gas model of dissociable charged groups gives [16, 19]

$$f(\varphi(\mathbf{r})) = i \sigma_0 \varphi(\mathbf{r}) - k_B T \frac{|\sigma_0|}{e_0} \ln \left(1 + e^{\beta \mu_S + i \beta e_0 \varphi(\mathbf{r})} \right), \quad (7)$$

where μ_S is the free energy of dissociation. In the argument of the logarithm function one can recognize the partition function for a system with uncharged ground state and a charged state with an effective energy $\beta \mu_S + i \beta e_0 \varphi(\vec{r})$. It is possible to generalize this model with other surface free energies [20–22] that can capture other details of the surface-ion interaction. Furthermore, in the limit of $\beta \mu_S \rightarrow \infty$, the sites are completely undissociated, the bounding surfaces are uncharged and there is no contribution to the surface free energy. In the opposite limit, $\beta \mu_S \rightarrow -\infty$, the bounding surfaces are completely dissociated and we are back to the fixed surface charge $f(\varphi(\mathbf{r})) = i \sigma_0 \varphi(\mathbf{r})$.

The complete field action of the model at hand thus assumes the form

$$\begin{aligned} \mathcal{S}[\varphi(\vec{r})] = & \frac{1}{2} \beta \epsilon \epsilon_0 \int d^3 \vec{r} |\nabla \varphi(\vec{r})|^2 + \tilde{\lambda} \int d^3 \vec{r} e^{i \beta e \varphi(\vec{r})} \\ & + i \beta \oint d^2 \vec{r} \sigma_0 \varphi(\mathbf{r}) - \oint d^2 \vec{r} \frac{|\sigma_0|}{e_0} \\ & \times \ln \left(1 + e^{-\beta \mu_S + i \beta e_0 \varphi(\mathbf{r})} \right). \end{aligned} \quad (8)$$

While the volume part presents an exact field-theoretic representation of the counterion partition function, the surface part pertains to a specific model of the interaction between the mobile charges and the bounding surfaces.

4 Mean-field approximation

The functional integral eq. (4), with the field-action functional $\mathcal{S}[\varphi(\vec{r})]$ decomposed as

$$\mathcal{S}[\varphi(\vec{r})] = \int_V f_V(\varphi(\vec{r})) d^3 r + \oint_S f_S(\varphi(\vec{r})) d^2 r \quad (9)$$

can not be evaluated exactly, since it is in general not Gaussian. One thus has to take recourse to various approximations of which the mean-field approximation, being equivalent to the saddle-point approximation, is the most straightforward one.

The mean-field potential $\phi_{\text{MF}}(\vec{r})$ of the field-action eq. (9) is defined as a solution of the saddle-point equation corresponding to $\delta \mathcal{S}[\varphi(\vec{r})] = 0$ at $\varphi(\vec{r}) = i \phi_{\text{MF}}(\vec{r})$ where $\phi_{\text{MF}}(\vec{r})$ is thus a solution of

$$\nabla \left(\frac{\partial f_V(\phi_{\text{MF}}(\vec{r}))}{\partial \nabla \phi_{\text{MF}}(\vec{r})} \right) - \frac{\partial f_S(\phi_{\text{MF}}(\vec{r}))}{\partial \phi_{\text{MF}}(\vec{r})} = 0 \quad (10)$$

and

$$-\beta \epsilon \epsilon_0 \frac{\partial \phi_{\text{MF}}(\vec{r})}{\partial \vec{n}} = \frac{\partial f_S(\phi_{\text{MF}}(\vec{r}))}{\partial \phi_{\text{MF}}(\vec{r})} = \sigma(\phi_{\text{MF}}(\vec{r})), \quad (11)$$

where \vec{n} is the normal vector to the bounding surface(s), and $\sigma(\phi_{\text{MF}}(\vec{r}))$ is the effective surface charge at the bounding surface(s). *In extenso* the first equation is exactly the standard PB equation for the counterion-only system

$$\nabla^2 \phi_{\text{MF}}(\vec{r}) = - \frac{\tilde{\lambda} e}{\epsilon \epsilon_0} e^{-\beta e \phi_{\text{MF}}(\vec{r})}, \quad (12)$$

while the second saddle-point equation with $f(\varphi(\vec{r}))$ from eq. (7) reduces to the boundary condition

$$-\beta \epsilon \epsilon_0 \frac{\partial \phi_{\text{MF}}(\vec{r})}{\partial \vec{n}} = - \frac{\sigma_0}{2} \left(1 + \tanh \frac{1}{2} (-\beta \mu_S + \beta e_0 \phi_{\text{MF}}) \right). \quad (13)$$

Obviously the above surface charge density can span the interval $[-\sigma_0, 0]$.

Assuming that $\beta \mu_S = -\ln 10(pH - pK)$, with $pK = -\log K$ and K being the dissociation equilibrium constant

while $pH = -\log[H^+]$ with $[H^+]$ the concentration of the protons in the bath, the above boundary condition coincides exactly with the charge regulation boundary condition of the Ninham-Parsegian site-dissociation model [17]. Should there be more than one type of dissociable groups the proper generalization was introduced in ref. [18].

For the planar geometry the mean-field solution of eq. (12) depends only on the z coordinate and has the form

$$\phi_{\text{MF}}(z) = \frac{1}{\beta e} \ln[\cos^2(\alpha z)], \quad (14)$$

where α can be determined from the boundary condition eq. (13) as

$$(1+b)\alpha \tan(\alpha D/2) + b\alpha \tan^3(\alpha D/2) = \frac{1}{\mu}, \quad (15)$$

with b being related to the dissociation free energy as $\ln b = \beta \mu_S$. Here μ is the Gouy-Chapman length, which represents the characteristic distance at which a counterion interacts with a macromolecular flat surface, of surface charge σ_0 , with an energy $k_B T$ and is defined as $\mu = 2\epsilon_0 \epsilon / e \beta \sigma_0$.

5 Second-order (Gaussian) correction

After solving the mean-field equations, one proceeds to analyze the fluctuations around the mean-field potential by evaluating the partition function eq. (4) for the field-action functional $\mathcal{S}[\phi(\vec{r}) = \phi_{\text{MF}}(\vec{r}) + \delta\phi(\vec{r})]$. To the lowest Gaussian order in the field fluctuations $\delta\phi(\vec{r})$ the field-action can be expanded

$$\mathcal{S}[\phi(\vec{r})] = \mathcal{S}[\phi_{\text{MF}}(\vec{r}) + \delta\phi(\vec{r})] = S_{\text{MF}}[\phi_{\text{MF}}] + \mathcal{S}_2[\delta\phi(\vec{r})], \quad (16)$$

where

$$\begin{aligned} \mathcal{S}_2[\delta\phi(\vec{r})] &= \frac{1}{2} \int \int \frac{\delta^2 S}{\delta\phi(\vec{r})\delta\phi(\vec{r}')} \Big|_{\text{MF}} \delta\phi(\vec{r})\delta\phi(\vec{r}') d^3\vec{r}d^3\vec{r}' \\ &+ \frac{1}{2} \oint \mathcal{C}_S(\phi(\vec{r}')) \Big|_{\text{MF}} \delta\phi(\vec{r}')^2 d^2\vec{r}, \end{aligned} \quad (17)$$

and obviously decomposes into a volume and surface term just like the complete field action. Above we introduced the Hessian of the volume part of the field-action as

$$\frac{1}{2} \frac{\delta^2 S}{\delta\phi(\vec{r})\delta\phi(\vec{r}')} \Big|_{\text{MF}} = \frac{1}{2} \beta \left(u^{-1}(\vec{r}, \vec{r}') - \frac{\beta \tilde{\lambda}}{\cos^2(\alpha z)} \delta^3(\vec{r} - \vec{r}') \right), \quad (18)$$

while \mathcal{C}_S is the surface capacitance due to the non-linear coupling of surface charge and surface electrostatic potential

$$\mathcal{C}_S(\vec{r}) = \frac{\partial^2 f(\phi_{\text{MF}}(\vec{r}))}{\partial(\beta e \phi_{\text{MF}}(\vec{r}))^2} = \frac{\partial \sigma}{\partial(\beta e \phi_{\text{MF}}(\vec{r}))}. \quad (19)$$

We will show later on that in the original theory of KS interactions it is this surface capacitance that quantifies the thermal charge fluctuations [5].

The decomposition of the field action eq. (17) induces a decomposition of the partition function into a product of the saddle-point partition function and its first-order correction, so that finally

$$\begin{aligned} \mathcal{Z} &= e^{-\frac{1}{2} \ln[\det \beta u(\vec{r}, \vec{r}')] } \times e^{\mathcal{S}[\phi_{\text{MF}}(\vec{r})]} \\ &\times \int \mathcal{D}[\delta\phi(\vec{r})] e^{\mathcal{S}_2[\delta\phi(\vec{r})]} = \mathcal{Z}_{\text{MF}} \times \mathcal{Z}_2. \end{aligned} \quad (20)$$

The last term is due to Gaussian fluctuation around the saddle-point and thus corresponds to the one-loop correction in the free energy.

In order to proceed we first introduce the appropriate field Green's function

$$\begin{aligned} \mathcal{G}(\delta\phi_1(\vec{r}), \delta\phi_2(\vec{r})) &= \\ \int_{\delta\phi_1}^{\delta\phi_2} \mathcal{D}[\delta\phi(\vec{r})] e^{\frac{1}{2} \iint \frac{\delta^2 S}{\delta\phi(\vec{r})\delta\phi(\vec{r}')} \Big|_{\text{MF}} \delta\phi(\vec{r})\delta\phi(\vec{r}') d^3\vec{r}d^3\vec{r}'} \end{aligned} \quad (21)$$

that describes the field, or better the propagation of Gaussian electrostatic potential fluctuations and will allow us to formally separate the bulk and the surface terms in the calculation of the one-loop partition function.

Since the kernel $u^{-1}(\vec{r}, \vec{r}')$ is isotropic in the transverse directions $\rho = (x, y)$, one can introduce the Fourier-Bessel transform of the fluctuating potential as

$$\delta\phi(\vec{r}) = \delta\phi(\rho, z) = \int_0^\infty dQ J_0(Q\rho) \delta\phi(Q, z), \quad (22)$$

where $\delta\phi(Q, z)$ depends only on the magnitude of the 2D transverse wave vector, $Q = |\mathbf{Q}|$. With this notation the complete Green's function can be presented as the product

$$\mathcal{G}(\delta\phi_1(\vec{r}), \delta\phi_2(\vec{r})) = \Pi_Q \mathcal{G}_Q(\delta\phi(Q, z_1), \delta\phi(Q, z_2)), \quad (23)$$

where $\mathcal{G}_Q(\delta\phi(Q, z_1), \delta\phi(Q, z_2))$ can be furthermore derived in the form

$$\begin{aligned} \mathcal{G}_Q(\delta\phi(Q, z_1), \delta\phi(Q, z_2)) &= \\ \int_{\delta\phi(Q, z_1)}^{\delta\phi(Q, z_2)} \mathcal{D}[\delta\phi(Q, z)] \exp \left[-\frac{1}{2} \beta \epsilon \epsilon_0 \int_{z=z_1}^{z=z_2} dz \right. \\ &\times \left. \left(\left(\frac{d\delta\phi}{dz} \right)^2 - \left(Q^2 + \frac{2\alpha^2}{\cos^2(\alpha z)} \right) \delta\phi^2 \right) \right]. \end{aligned} \quad (24)$$

Obviously this is nothing but the Feynman propagator of a harmonic oscillator with time-dependent frequency, where the z coordinate plays the role of "time" [23], and the Wick's rotation makes the action real instead of imaginary as in quantum mechanics. The general method of solving this type of functional integrals was described by

$$\begin{aligned} Z_2(D) = & \Pi_Q \sqrt{\frac{2e^{-DQ}Q(\alpha^2 + Q^2)}{2\pi((\alpha \tan[\frac{\alpha D}{2}] + Q)^2 - (\alpha \tan[\frac{\alpha D}{2}] - Q)^2 e^{-2DQ})}} \\ & \times \sqrt{\frac{1}{C_{S_1}C_{S_2} + \beta\epsilon'\epsilon_0(C_{S_1} + C_{S_2})Q + (\beta\epsilon\epsilon_0)^2 N^2 + (\beta\epsilon'\epsilon_0)^2 Q^2 + (\beta\epsilon\epsilon_0)(C_{S_1} + C_{S_2} + 2\beta\epsilon'\epsilon_0 Q)M}}, \end{aligned} \quad (26)$$

$$\begin{aligned} M = & \frac{Q(\alpha \tan[\frac{\alpha D}{2}] + Q)^2 + (\alpha^2 + \alpha^2 \tan^2[\frac{\alpha D}{2}])(\alpha \tan[\frac{\alpha D}{2}] + Q)}{(\alpha \tan[\frac{\alpha D}{2}] + Q)^2 - (\alpha \tan[\frac{\alpha D}{2}] - Q)^2 e^{-2DQ}} \\ & - \frac{Q(\alpha \tan[\frac{\alpha D}{2}] - Q)^2 - (\alpha^2 + \alpha^2 \tan^2[\frac{\alpha D}{2}])(\alpha \tan[\frac{\alpha D}{2}] - Q)e^{-2DQ}}{(\alpha \tan[\frac{\alpha D}{2}] + Q)^2 - (\alpha \tan[\frac{\alpha D}{2}] - Q)^2 e^{-2DQ}}; \\ N^2 = & M^2 - \frac{4e^{-2DQ}Q^2(\alpha^2 + Q^2)^2}{\left[(\alpha \tan[\frac{\alpha D}{2}] + Q)^2 - (\alpha \tan[\frac{\alpha D}{2}] - Q)^2 e^{-2DQ}\right]^2}. \end{aligned} \quad (27)$$

Khandekar and Lawande [24] and was adapted to this particular case as described in detail in appendix A.

The partition function, or specifically the part stemming from Gaussian fluctuations, eq. (20), around the mean-field can now be cast into the following form:

$$\begin{aligned} Z_2(D) = & \Pi_Q \int \mathcal{D}[\delta\phi_1(\vec{r})\delta\phi_2(\vec{r})] \\ & \times \tilde{\mathcal{G}}_Q(0, \delta\phi_1(\vec{r})) \times e^{-\frac{1}{2} \int_{S_1} d^2r C_{S_1} (\phi_{MF}) \delta\phi_1^2(\vec{r})} \\ & \times \mathcal{G}_Q(\delta\phi_1(\vec{r}), \delta\phi_2(\vec{r})) \times e^{-\frac{1}{2} \int_{S_2} d^2r C_{S_2} (\phi_{MF}) \delta\phi_2^2(\vec{r})} \\ & \times \tilde{\mathcal{G}}_Q(\delta\phi_2(\vec{r}), 0), \end{aligned} \quad (25)$$

where $\tilde{\mathcal{G}}_Q$ stands for the Green's function eq. (24) but with $\alpha = 0$, as there are no counterions behind the two bounding surfaces. The exact form eq. (A.18) thus still remains valid but evaluated explicitly for vanishing α . Of course in that case the functional integral can be evaluated directly in a trivial fashion. In addition, one needs to take the dielectric constant as ϵ' for $\tilde{\mathcal{G}}_Q(0, \delta\phi_1(\vec{r}))$ and $\tilde{\mathcal{G}}_Q(\delta\phi_2(\vec{r}), 0)$, but as ϵ for $\mathcal{G}_Q(\delta\phi_1(\vec{r}), \delta\phi_2(\vec{r}))$ in the definition eq. (24).

One could see the above formula as describing fluctuations behind the surface at $z = z_1$, described by $\tilde{\mathcal{G}}_Q(\epsilon'; 0, \delta\phi_1(\vec{r}); \infty)$, fluctuations behind the surface at $z = z_2$, described by $\tilde{\mathcal{G}}_Q(\epsilon'; \delta\phi_2(\vec{r}), 0; \infty)$, fluctuations in the space between the two surfaces for $z_1 < z < z_2$, described in their turn by $\mathcal{G}_Q(\epsilon; \delta\phi_1(\vec{r}), \delta\phi_2(\vec{r}); D)$, and finally all of them coupled through the surface capacitance and the surface potential fluctuations at the two surfaces at $z = z_1$ and $z = z_2$ corresponding to the two exponential terms.

After integration over the boundary electrostatic potential fluctuations the final exact form of the partition function can be written as

see eq. (26) above

with the functions M and N defined as

see eqs. (27) above

We have thereby derived the explicit and exact forms of the partition function in the form of a mean-field term and the one-loop or Gaussian fluctuation correction that has not been calculated before.

What remains now is the evaluation of the corresponding free energy and specifically the part of this free energy that depends on the separation between the bounding surfaces, *i.e.* the interaction free energy.

6 Second-order correction: Interaction free energy

Knowing the partition function for Gaussian fluctuations around the mean field, one can straightforwardly calculate the second-order or the one-loop correction to the free energy as

$$\frac{\mathcal{F}_2(D)}{S} = -k_B T \ln \frac{Z_2(D)}{Z_2(D \rightarrow \infty)}, \quad (28)$$

where we subtracted the free energy corresponding to infinite separation that contains the bulk free energy as well as the surface self-energies.

Assuming furthermore that the surfaces have identical properties, *i.e.*, $C_{S_1} = C_{S_2} = C_S$ we get the one-loop correction as

$$\begin{aligned} \frac{\mathcal{F}_2(D)}{S} = & \frac{k_B T}{4\pi} \int_0^\infty Q dQ \ln \left[\frac{1}{(\alpha^2 + Q^2)} \Delta_{11}^2(Q) \right] \\ & + \frac{k_B T}{4\pi} \int_0^\infty Q dQ \ln \left(1 - \Delta_{12}^2(Q) e^{-2QD} \right), \end{aligned} \quad (29)$$

$$\Delta_{11}(Q) = \frac{\mathcal{C}_S(\alpha \tan[\alpha D/2] + Q) + \beta\epsilon_0[\epsilon'Q(\alpha \tan[\alpha D/2] + Q) + \epsilon\{Q(\alpha \tan[\alpha D/2] + Q) + (\alpha^2 + \alpha^2 \tan^2[\alpha D/2])\}]}{\mathcal{C}_S + \beta\epsilon_0Q(\epsilon' + \epsilon)}, \quad (30)$$

$$\Delta_{12}(Q) = \frac{\mathcal{C}_S(\alpha \tan[\alpha D/2] - Q) + \beta\epsilon_0[\epsilon'Q(\alpha \tan[\alpha D/2] - Q) - \epsilon\{Q(\alpha \tan[\alpha D/2] - Q) - (\alpha^2 + \alpha^2 \tan^2[\alpha D/2])\}]}{\mathcal{C}_S(\alpha \tan[\alpha D/2] + Q) + \beta\epsilon_0[\epsilon'Q(\alpha \tan[\alpha D/2] + Q) + \epsilon\{Q(\alpha \tan[\alpha D/2] + Q) + (\alpha^2 + \alpha^2 \tan^2[\alpha D/2])\}]} \quad (31)$$

where we defined the following quantities:

see eqs. (30) and (31) above

The second-order correction free energy eq. (29) consists of two integrals. The first one corresponds to that part of the self-energy of the two bounding surfaces that depends on the inter surface separation, while the second integral represents a generalization of the zero-frequency (classical) vdW-Lifshitz term [25]. In fact it can be easily seen that in the limit of no mobile ions between the surfaces, corresponding to $\alpha = 0$, it reduces exactly to the zero-frequency vdW term with

$$\Delta_{12}^2(Q) = \left(\frac{\epsilon' - \epsilon}{\epsilon' + \epsilon}\right)^2, \quad (32)$$

while the first term vanishes. With mobile ions present, the second-order correction is however very different from this limit. In the limit of fixed surface charge ($\mathcal{C}_{S_1} = \mathcal{C}_{S_2} = 0$) and no dielectric discontinuity ($\epsilon' = \epsilon$), the integral reduces to the known result [26]:

$$\begin{aligned} \frac{\mathcal{F}_2(D)}{S} &= \frac{k_B T}{4\pi} \int_0^\infty \tilde{Q} d\tilde{Q} \ln \left[\frac{1}{(\tilde{\alpha}^2 + \tilde{Q}^2)} \right. \\ &\times \left. \left(\frac{2\tilde{Q} + 2\tilde{Q}^2 + \tilde{\alpha}^2 + 1}{2\tilde{Q}} \right)^2 \right] + \frac{k_B T}{4\pi} \int_0^\infty \tilde{Q} d\tilde{Q} \\ &\times \ln \left(1 - \left(\frac{1 + \tilde{\alpha}^2}{2\tilde{Q} + 2\tilde{Q}^2 + \tilde{\alpha}^2 + 1} \right)^2 e^{-2\tilde{D}\tilde{Q}} \right), \end{aligned} \quad (33)$$

leading to the attractive pressure which scales as $\ln \tilde{D} \times \tilde{D}^{-3}$ in a system composed of mobile counterions and fixed surface charge. At the end we also consider a formal limit of the free energy corresponding to no dielectric discontinuity $\epsilon' = \epsilon$, as well as no mobile ions $\alpha \rightarrow 0$, but nevertheless assuming a non-vanishing surface capacitance \mathcal{C} . While this limit is not meaningful in our model, we will nevertheless use it to show how the KS result [1,2], which is based on a linear response formalism and considers no coupling between the mean-field solution and the corresponding values of the capacitances, is obtained from our conceptual framework.

The KS limit could be obtained more directly if instead of a counterion-only case dealt with here, we would consider a uni-univalent salt as indeed was considered by Kirkwood and Shumaker in their derivation of the long

range interaction between protein molecules with dissociable surface groups [1,2]. Nevertheless, for $\alpha \rightarrow 0$ our general result reduces to

$$\Delta_{12}^2(Q) = \left(\frac{\mathcal{C}}{\mathcal{C} + 2\beta\epsilon\epsilon_0 Q} \right)^2, \quad (34)$$

which in its turn, to the lowest order in the surface capacitance leads to the disjoining pressure

$$p = -\frac{\partial}{\partial D} \left(\frac{\mathcal{F}_2(D)}{S} \right) \sim \mathcal{C}^2 D^{-1}. \quad (35)$$

As it depends quadratically on the surface capacitance, this interaction presents the contribution of monopolar fluctuations in the surface charge to the free energy. This can be easily confirmed by evaluating the free energy of two fluctuating charge distributions in the Gaussian approximation explicitly. Let us now show that interaction pressure eq. (35) corresponds exactly to the KS interaction between two planar surfaces.

In fact, the disjoining pressure eq. (35) starts to become more familiar when we realize that a Hamaker-type summation [3] for two thin planar surface sheets with a pair interaction of the KS form scaling as $\mathcal{V}(R) \sim R^{-2}$, gives the interaction pressure as [1]

$$p = \frac{F(R)}{S} = -\frac{\partial}{\partial D} \int_D^\infty 2\pi R dR \mathcal{V}(R) \sim D^{-1}. \quad (36)$$

The two forms of the disjoining pressure, eqs. (35) and (36), are thus identical, meaning that the KS interaction is nothing but a monopolar fluctuation interaction. This is clear from the fact that the separation dependence of the fluctuation interaction free energy between two surfaces is slower than in the case of standard vdW interactions that stem from dipolar fluctuations between either two semi-infinite media or two thin layers, scaling respectively as [3]

$$p = \frac{F(R)}{S} = -\frac{A(D)}{12\pi D^2} \quad \text{and/or} \quad -\frac{2A(D)a^2}{\pi D^5}, \quad (37)$$

respectively.

The KS fluctuation forces thus originate in monopolar fluctuations and follow a different scaling either between point particles, R^{-2} , or between fluctuating surface layers, D^{-1} , then in the case of dipolar fluctuations. They arise directly from surface capacitance that is non-zero only for a surface free energy that is non-linear, *i.e.* at least quadratic, w.r.t. the local electrostatic potential.

$$\frac{\tilde{\mathcal{F}}_2(\tilde{D})}{\tilde{\mathcal{S}}} = \frac{1}{2}\Xi \int_0^\infty \tilde{Q}d\tilde{Q} \ln \left[1 - e^{-2\tilde{Q}\tilde{D}} \right. \\ \left. \times \left(\frac{2(1+\Delta)b(1+\tan^2[\frac{\tilde{\alpha}\tilde{D}}{2}]) (\tilde{\alpha} \tan[\frac{\tilde{\alpha}\tilde{D}}{2}] - \tilde{Q}) - (1+b+b\tan^2(\frac{\tilde{\alpha}\tilde{D}}{2}))^2 [2\Delta\tilde{Q}(\tilde{\alpha} \tan[\frac{\tilde{\alpha}\tilde{D}}{2}] - \tilde{Q}) - (1+\Delta)(\tilde{\alpha}^2 + \tilde{\alpha}^2 \tan^2[\frac{\tilde{\alpha}\tilde{D}}{2}])]}{2(1+\Delta)b(1+\tan^2[\frac{\tilde{\alpha}\tilde{D}}{2}]) (\tilde{\alpha} \tan[\frac{\tilde{\alpha}\tilde{D}}{2}] + \tilde{Q}) + (1+b+b\tan^2(\frac{\tilde{\alpha}\tilde{D}}{2}))^2 [2\tilde{Q}(\tilde{\alpha} \tan[\frac{\tilde{\alpha}\tilde{D}}{2}] + \tilde{Q}) + (1+\Delta)(\tilde{\alpha}^2 + \tilde{\alpha}^2 \tan^2[\frac{\tilde{\alpha}\tilde{D}}{2}])]} \right)^2 \right]. \quad (42)$$

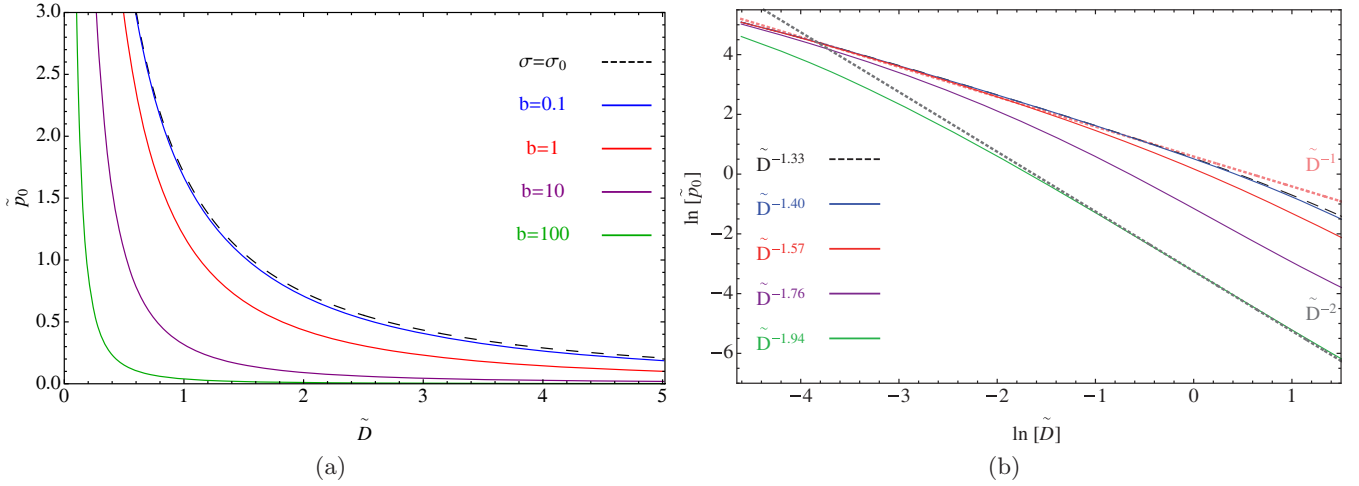


Fig. 2. (a) Rescaled mean-field disjoining pressure plotted as a function of rescaled surfaces separation for different values of parameter b . The curve $\sigma = \sigma_0$ corresponds to $b = 0$. (b) Rescaled mean-field pressure from (a) plotted in a log-log plot. The two dotted lines represent the scalings \tilde{D}^{-1} and \tilde{D}^{-2} introduced solely to guide the eye. Obviously the scaling \tilde{D}^{-1} for mean-field pressure sets in for small and \tilde{D}^{-2} for large values of the dimensionless separation.

7 Numerical results

It is convenient to introduce dimensionless quantities by using the Gouy-Chapman length scale μ and $\sigma_0^2/2\epsilon\epsilon_0$ as the disjoining pressure scale. Hence, the length scale (\mathbf{r}, D) , the free energy (F), the disjoining pressure (p) and the surface capacitance (\mathcal{C}) can all be rescaled into dimensionless variables $\tilde{\mathbf{r}} = \mathbf{r}/\mu$, $\tilde{D} = D/\mu$, $\tilde{F} = F/(\frac{\sigma_0^2}{2\epsilon\epsilon_0})\mu^3$, $\tilde{p} = p/(\frac{\sigma_0^2}{2\epsilon\epsilon_0})$ and $\tilde{\mathcal{C}} = \mu\mathcal{C}$, respectively. We also introduce the dielectric mismatch with $\Delta = (\epsilon - \epsilon')/(\epsilon + \epsilon')$. With these definitions, the mean-field free energy becomes

$$\frac{\tilde{\mathcal{F}}_0(\tilde{D})}{\tilde{\mathcal{S}}} = \tilde{\alpha}^2 \tilde{D} + 2 \ln[1 + \tilde{\alpha}^2], \quad (38)$$

where $\tilde{\alpha} = \mu\alpha$ is the solution of the boundary condition

$$(1+b)\tilde{\alpha} \tan(\tilde{\alpha}\tilde{D}/2) + b\tilde{\alpha} \tan^3(\tilde{\alpha}\tilde{D}/2) = 1. \quad (39)$$

The rescaled surface capacitance in terms of $\tilde{\alpha}$ is then equal to

$$\tilde{\mathcal{C}}_{S_1, S_2} = 2\beta\epsilon\epsilon_0 b \frac{1 + \tan^2[\tilde{\alpha}\tilde{D}/2]}{(1+b+b\tan^2[\tilde{\alpha}\tilde{D}/2])^2}, \quad (40)$$

which goes to zero for large values of b , $\lim_{b \rightarrow \infty} \tilde{\mathcal{C}}_{S_1, S_2} \rightarrow 0$ as well as for vanishing b , $\lim_{b \rightarrow 0} \tilde{\mathcal{C}}_{S_1, S_2} \rightarrow 0$. We also

invoke a coupling parameter Ξ , analogous to the one introduced by Netz and Moreira [27], given as

$$\Xi = \frac{e_0^3 \sigma_0}{8\pi(\epsilon\epsilon_0 k_B T)^2} \quad (41)$$

for monovalent counterions. For a counterion-only system with fixed surface charge the magnitude of the coupling parameter defines a weak- and a strong-coupling regime [6]. In our case the existence of the surface free energy introduces also other length scales that preclude a direct introduction of a unique electrostatic coupling parameter and it is thus in general not possible to establish the presence of the weak and the strong coupling limits *strictu sensu* as exact limits of the partition function.

While the weak coupling limit can therefore not be derived as an exact limit, the saddle-point can be defined for any field-action. As explained in detail in ref. [6] we thus use the saddle-point solution as the *proxy* for the weak coupling limit and evaluate the contribution of the fluctuations around the saddle-point to the free energy.

The surface interaction part of the Gaussian fluctuating free energy from eq. (29), in a dimensionless form is then given as

see eq. (42) above

We first investigate the surface separation dependence of the interaction free energy and the disjoining pressure

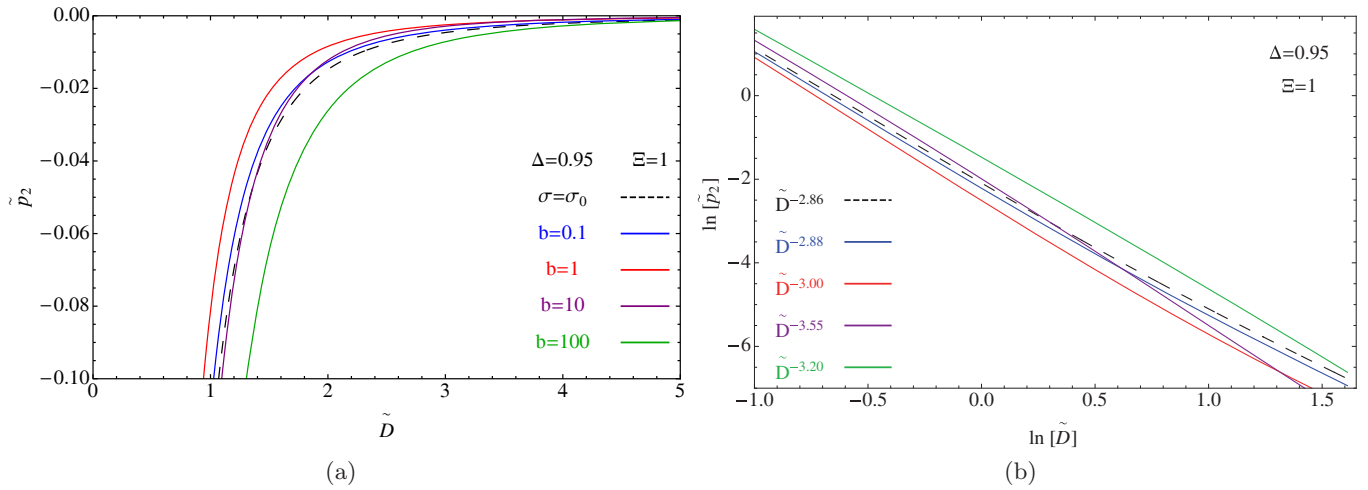


Fig. 3. (a) Rescaled fluctuation disjoining pressure as a function of rescaled surface separation is plotted for different values of parameter b with a fixed dielectric jump $\Delta = 0.95$, and coupling parameter $\Xi = 1$. (b) Rescaled fluctuation disjoining pressure from (a) plotted in a log-log plot to show the effective scaling of the disjoining pressure with the intersurface separation. The scaling exponent is typically comparable with the case of the counterion-only Coulomb fluid between two surfaces with fixed charges, which is -3 , but its exact value depends on b .

between the surfaces pertaining to that dependence. The mean-field rescaled pressure is shown in fig. 2(a), as a function of the surface dissociation energy $\ln b = \beta\mu_S$ in a lin-lin and log-log plots. Clearly, the higher the energy penalty for charge dissociation at the surface, b , the lower is the interaction pressure between the two surfaces until for large enough energy penalty the interaction remains close to zero for all intersurface separations. The scaling of the mean-field disjoining pressure with the separation is shown in fig. 2(b). For constant surface charge $\sigma = \sigma_0$, *i.e.*, corresponding formally to $b = 0$, the asymptotic forms of the mean-field interaction pressure are $\lim_{D \rightarrow \infty} \tilde{p}_0(D) \sim \tilde{D}^{-2}$ and $\lim_{D \rightarrow 0} \tilde{p}_0(D) \sim \tilde{D}^{-1}$, see ref. [28]. This is in fact also what we observe in the case of charge regulation, with the proviso that the regime of validity of the two limits depends additionally on the value of b ; the smaller its value the more extended is the region of \tilde{D}^{-1} scaling.

Because the surface capacitance depends on the mean-field solution, the fluctuation correction to the free energy and the corresponding disjoining pressure also depend on the surface dissociation energy, as can be discerned from fig. 3(a). This is very different from the standard vdW interactions that do not depend on the mean-field solution, at least in the standard DLVO formulation [3]. The scaling of the fluctuation part of the interaction pressure, fig. 3(b), shows a robust value of the scaling exponent close to -3 , close to its value for the case of a counterion-only Coulomb fluid between two surfaces with fixed charges, where the fluctuation disjoining pressure scales exactly as $\sim \ln D \times D^{-3}$, see ref. [6] for details. The exact value of the scaling exponent in the charge-regulated case, however, depends on the value of the surface interaction parameter b . Since the dielectric mismatch in this case is not zero, the monopolar and vdW dipolar fluctuation interactions,

stemming from the surface capacitance and the dielectric mismatch respectively, are always mixed together and can not be disentangled in the separation dependence of the fluctuation pressure.

Adding the mean-field and the fluctuation contribution together, fig. 4, we note that for large values of the surface dissociation energy, the fluctuation contribution becomes dominant, a simple consequence of the fact that the mean field vanishes while the fluctuation part remains finite. While in general the fluctuation part is always subdominant to the mean-field solution, in this case the matters are a bit more complicated as the charge regulation can wipe out the mean field entirely but not the fluctuation part. The fluctuation disjoining pressure for a vanishing mean field again depends crucially on the presence of the dielectric mismatch at the bounding surfaces and does not necessarily coincide with the standard vdW interaction. In fact for the case of complete dielectric homogeneity, $\Delta = 0$ see fig. 5, the interaction pressure scaling exponent is in general smaller than for $\Delta \neq 0$. Asymptotically for small separations in fact it approaches one, just as for the KS interaction. For larger separations it tends to a larger value but does not approach -3 as the fluctuations it corresponds to, being due to the presence of counterions between the surfaces, are never purely dipolar.

Finally, in order to get an idea about the strength of the attractive interaction we compare the fluctuation disjoining pressure p_2 with the pure van der Waals pressure given as $p_{\text{vdW}} = -H(\Delta)/12\pi D^3$, see ref. [3], where $H(\Delta)$ is a Hamaker coefficient, which for illustration purposes we chose to be 4.3 zJ [29]. We choose a large dielectric inhomogeneity ($\Delta = 0.95$), and a separation between the surfaces of 1 nm ($D = 1 \text{ nm}$), bearing maximal surface charge $\sigma_0 = 0.5e_0/\text{nm}^2$. With the given set of parameters, we calculate the fluctuation disjoining pressure $p_{b=0}$ correspond-

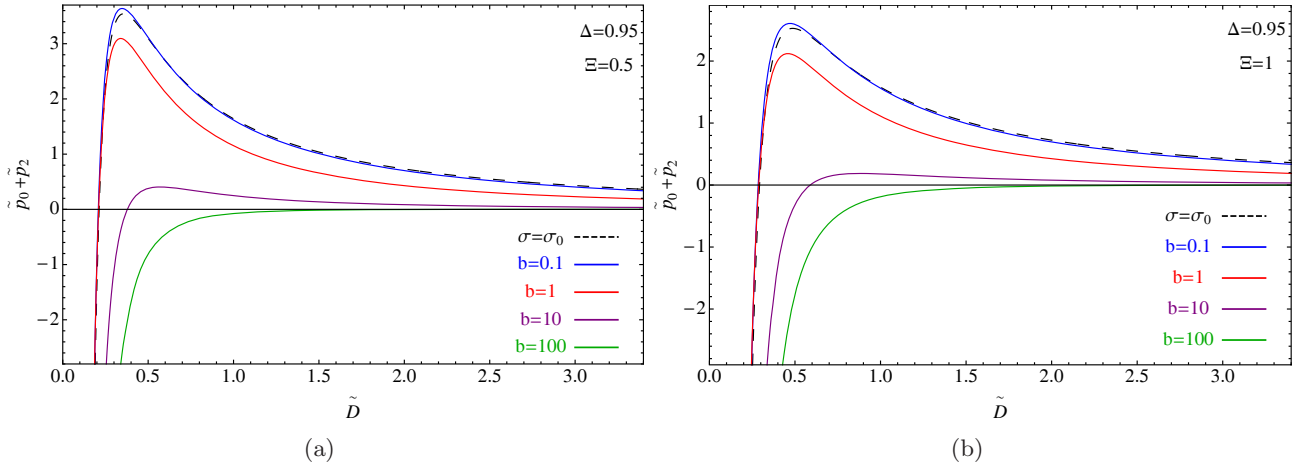


Fig. 4. Rescaled total disjoining pressure as a function of the rescaled surface separation plotted for different values of the parameter b , fixed dielectric jump $\Delta = 0.95$ and for the following values of the coupling parameter: (a) $\Xi = 0.5$; (b) $\Xi = 1$.

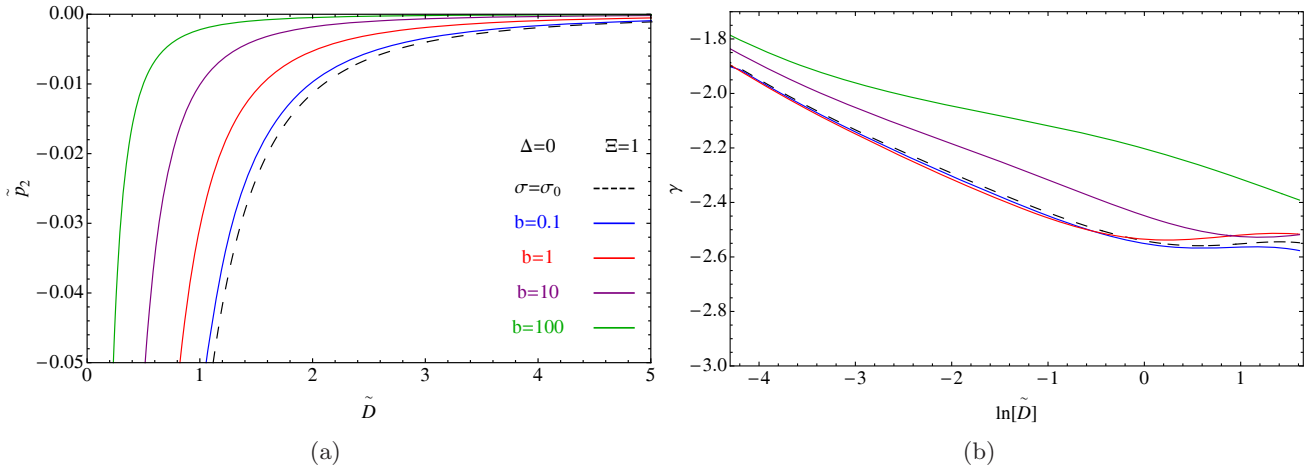


Fig. 5. (a) Rescaled fluctuation disjoining pressure as a function of rescaled surface separation is plotted for different values of the parameter b but without any dielectric jump, $\Delta = 0$, and $\Xi = 1$. (b) The scaling exponent γ for the effective scaling of the disjoining pressure with the intersurface separation is defined as $\tilde{p}_2 \sim \tilde{D}^\gamma$. For small separations it approaches -1 asymptotically, whereas for large separations it tends to a value close but not equal to -3 .

ing to a maximal charge at the surfaces, and the fluctuating disjoining pressure $p_{b=100}$, corresponding to the case of electroneutral surfaces. One finds that for this specific choice of parameters the fluctuating pressure is comparable to the vdW disjoining pressure: $p_{\text{vdW}} = -1.1$ atm while $p_{b=100} = -1.3$ atm and $p_{b=0} = -0.8$ atm.

8 Conclusion

In this paper we derived a theory describing electrostatic interactions between macromolecular surfaces bearing dissociable charge groups immersed in an aqueous solution of dissociated counterions. Introducing a surface free energy corresponding to a simple model of charge regulation, and formulating it in a field-theoretic language, we derived the mean-field solution which is related to the Ninham-Parsegian charge regulation theory and also obtained an

exact solution for the second-order fluctuations around the mean field. The fluctuation contribution to the total free energy is related to vdW interactions but is fundamentally modified by the presence of dissociable charges on the bounding surfaces as well as the counterions dissolved in the space between them.

While for the model discussed, containing an additional surface term usually not present in Coulomb fluids with fixed charges on interacting surfaces, a weak-coupling approximation can not be consistently defined, we proceed from the observation that the saddle-point and the fluctuations around the saddle-point can be defined for any field action [6]. The range of validity of this approximation should eventually be ascertained once compared with detailed simulations of the same microscopic model.

What our methodology also clearly identifies is the monopolar nature of the fluctuation interactions between charge-regulated surfaces that singles them out from the

dipolar fluctuation interactions as is the case for vdW fluctuation interactions. This sets the two types of interactions fundamentally apart as the range and scaling characteristics of the two are vastly different. It also emerges quite straightforwardly that the two types of fluctuation interactions are not additive but are fundamentally intertwined and can only be decoupled in extreme limiting cases of either no dielectric discontinuity or in the case of no surface capacitance. More specific predictions regarding the role of monopolar fluctuation interactions between dissociable charge groups corresponding to deprotonated and protonated molecular groups, as is the case for proteins, will be forthcoming once the model considered is generalized to include the intervening salt solution at a set value of the solution pH.

Suffice it to say at this point that in an appropriate limit our theory is related to the KS interactions known to be relevant in the protein context. More importantly though, it allows to consistently generalize the theory of KS interactions, or indeed any electrostatic interaction that presumes charge regulation, in such a way that one can use advanced concepts and methods of the Coulomb fluid theory to solve it approximately. In this way we pave the way to new developments in the theory of KS and related interactions that would not be conceivable within their original theoretical framework [1,2]. The field-theoretic framework in fact allows to formulate a single-particle partition function which can be used as a proxy for the strong-coupling approximation, also not consistently definable in the case where the field action contains additional surface terms, as in the model introduced here [6]. We are currently working to extend the present formulation to the case of symmetric as well as asymmetric ionic mixtures containing monovalent and polyvalent ions.

N. A. is grateful to Anže Lošdorfer Božič for constructive advice regarding this work. N. A. acknowledges the financial support by the Slovenian Research Agency under the young researcher grant. R.P. acknowledges the financial support by the Slovenian Research Agency under the grant P1-0055. R.P. would like to thank the hospitality of Prof. R.R. Netz during his stay at the Freie Universität and the Technische Universität in Berlin as a visiting professor, where parts of this work were performed.

Appendix A. Exact evaluation of the path integral

The path integral in eq. (24) can be written in the form [24]

$$\begin{aligned} \mathcal{G}_p(\delta\phi(Q, z_1), \delta\phi(Q, z_2)) = & \\ & \sqrt{\frac{1}{2\pi}} \exp\left[-\frac{1}{2} \int_{-d}^d dz \int_0^1 d\mu \mathcal{R}(z, z, \mu)\right] \\ & \times \exp\left[-\frac{\beta\epsilon\epsilon_0}{2} (\delta\phi(Q, z_2) f'(z_2) - \delta\phi(Q, z_1) f'(z_1))\right], \end{aligned} \quad (\text{A.1})$$

where $f(z)$ is a solution of the equation of motion given as

$$\ddot{f} - \mu \left(Q^2 + \frac{2\alpha^2}{\cos^2(\alpha z)} \right) f = 0, \quad (\text{A.2})$$

where $f = f(z; \mu)$. The Green's function equation is

$$\frac{d^2}{dz^2} Q(z, z'|\mu) - \mu \left(Q^2 + \frac{2\alpha^2}{\cos^2(\alpha z)} \right) Q(z, z'|\mu) = -\delta(z-z'), \quad (\text{A.3})$$

with $Q(-d, z'|\mu) = Q(d, z'|\mu) = 0$. The resolvent $\mathcal{R}(z, z'|\mu)$ obeys the equation

$$\begin{aligned} \frac{d^2}{dz^2} \mathcal{R}(z, z'|\mu) - \mu \left(Q^2 + \frac{2\alpha^2}{\cos^2(\alpha z)} \right) \mathcal{R}(z, z'|\mu) = \\ \delta(z-z') \left(Q^2 + \frac{2\alpha^2}{\cos^2(\alpha z)} \right), \end{aligned} \quad (\text{A.4})$$

with $\mathcal{R}(-d, z'|\mu) = \mathcal{R}(d, z'|\mu) = 0$. We can see that the resolvent satisfies $\mathcal{R}(z, z'|\mu) = -\left(Q^2 + \frac{2\alpha^2}{\cos^2(\alpha z')} \right) Q(z, z'|\mu)$. The Green's function $Q(z, z'|\mu)$ has the form

$$Q(z, z'|\mu) = \begin{cases} g(z, \mu) h(z', \mu) / \Delta(\mu), & z < z', \\ g(z', \mu) h(z, \mu) / \Delta(\mu), & z > z', \end{cases} \quad (\text{A.5})$$

where $g(z, \mu)$ and $h(z, \mu)$ are two linearly independent solutions of eq. (A.2) satisfying the conditions

$$g(-d; \mu) = h(d; \mu) = 0 \quad (\text{A.6})$$

and

$$\Delta(\mu) = \dot{g}(-d, \mu) h(-d, \mu) = -g(d, \mu) \dot{h}(d, \mu). \quad (\text{A.7})$$

The integration of the resolvent operator yields

$$\begin{aligned} \int_{-d}^d \mathcal{R}(z, z|\mu) dz = - \int_{-d}^d \left(Q^2 + \frac{2\alpha^2}{\cos^2(\alpha z)} \right) Q(z, z|\mu) dz = \\ [-1/\Delta(\mu)] \int_{-d}^d \left(Q^2 + \frac{2\alpha^2}{\cos^2(\alpha z)} \right) g(z, \mu) h(z, \mu) dz. \end{aligned} \quad (\text{A.8})$$

Consider now the equation satisfied by g

$$\ddot{g} - \mu \left(Q^2 + \frac{2\alpha^2}{\cos^2(\alpha z)} \right) g = 0 \quad (\text{A.9})$$

and differentiating it with respect to μ , we have

$$-\left(Q^2 + \frac{2\alpha^2}{\cos^2(\alpha z)} \right) g = \ddot{g}_\mu + \mu \left(Q^2 + \frac{2\alpha^2}{\cos^2(\alpha z)} \right) g_\mu. \quad (\text{A.10})$$

Inserting this into the resolvent integral and integrating by parts, one can get

$$\begin{aligned} \int_{-d}^d \mathcal{R}(z, z|\mu) dz = [-1/\Delta(\mu)] \\ \times [\dot{g}_\mu(-d, \mu) h(-d, \mu) - \dot{h}(d, \mu) g_\mu(d, \mu)] = \\ -g_\mu(d, \mu) / g(d, \mu) - \dot{g}_\mu(-d, \mu) / \dot{g}(-d, \mu), \end{aligned} \quad (\text{A.11})$$

from which it follows that

$$\int_0^1 d\mu \int_{-d}^d dz \mathcal{R}(z, z|\mu) = \ln [g(d, \mu)/\dot{g}(-d, \mu)]|_0^1 = \ln[(g(d, 1)/\dot{g}(-d, 1))(\dot{g}(-d, 0)/g(d, 0))]. \quad (\text{A.12})$$

As $g(d, 0)/\dot{g}(-d, 0) = 2d = D$, we have

$$\exp \left[-\frac{1}{2} \int_0^1 d\mu \int_{-d}^d dz \mathcal{R}(z, z|\mu) \right] = [D\dot{g}(-d, 1)/g(d, 1)]^{\frac{1}{2}}. \quad (\text{A.13})$$

Now, the solution of the equation of motion is given as a linear combination of the solutions g and h as

$$f(z, 1) = \delta\phi_2 g(z, 1)/g(d, 1) + \delta\phi_1 h(z, 1)/h(-d, 1), \quad (\text{A.14})$$

so the exponent in the propagator eq. (A.1) becomes

$$\begin{aligned} & \exp \left[-\frac{\beta\epsilon\epsilon_0}{2} (\delta\phi(Q, z_2)f'(z_2) - \delta\phi(Q, z_1)f'(z_1)) \right] = \\ & \exp \left[-\frac{\beta\epsilon\epsilon_0}{2} \left(\delta\phi^2(Q, d) \frac{\dot{g}(d, 1)}{g(d, 1)} \right. \right. \\ & \left. \left. - 2\delta\phi(Q, d)\delta\phi(Q, -d) \frac{\dot{g}(-d, 1)}{g(d, 1)} \right. \right. \\ & \left. \left. - \delta\phi^2(Q, -d) \frac{\dot{h}(-d, 1)}{h(-d, 1)} \right) \right]. \quad (\text{A.15}) \end{aligned}$$

Finally the propagator can be written as

$$\begin{aligned} \mathcal{G}_p(\delta\phi(Q, -d), \delta\phi(Q, d)) = & \\ & \sqrt{\frac{D\dot{g}(-d, 1)}{2\pi g(d, 1)}} \exp \left[-\frac{\beta\epsilon\epsilon_0}{2} \left(\delta\phi^2(Q, d) \frac{\dot{g}(d, 1)}{g(d, 1)} \right. \right. \\ & \left. \left. - 2\delta\phi(Q, d)\delta\phi(Q, -d) \frac{\dot{g}(-d, 1)}{g(d, 1)} \right. \right. \\ & \left. \left. - \delta\phi^2(Q, -d) \frac{\dot{h}(-d, 1)}{h(-d, 1)} \right) \right]. \quad (\text{A.16}) \end{aligned}$$

Solutions $g(z, 1)$ and $h(z, 1)$, which satisfy eq. (A.2) when $\mu = 1$ and boundary conditions eq. (A.6), are given as

$$\begin{aligned} g(z) = & \frac{\sinh[Q(d+z)](Q^2 \cot[\alpha d] + \alpha^2 \tan[\alpha z])}{\alpha(Q^2 + \alpha^2)} \\ & + \frac{\alpha Q \cosh[Q(d+z)](1 + \cot[\alpha d] \tan[\alpha z])}{\alpha(Q^2 + \alpha^2)}, \\ h(z) = & \frac{\sinh[Q(-d+z)](Q^2 \cot[\alpha d] - \alpha^2 \tan[\alpha z])}{\alpha(Q^2 + \alpha^2)} \\ & + \frac{\alpha Q \cosh[Q(-d+z)](-1 + \cot[\alpha d] \tan[\alpha z])}{\alpha(Q^2 + \alpha^2)}. \quad (\text{A.17}) \end{aligned}$$

After inserting these solutions back into eq. (A.16), one obtains the final result in the explicit form:

$$\begin{aligned} \mathcal{G}_Q \left(\delta\phi \left(Q, -\frac{D}{2} \right), \delta\phi \left(Q, \frac{D}{2} \right) \right) = & \\ & \sqrt{\frac{A}{2\pi B}} \times \exp \left[-\frac{\beta\epsilon\epsilon_0}{2B} \left(\left[\delta\phi^2 \left(Q, -\frac{D}{2} \right) + \delta\phi^2 \left(Q, \frac{D}{2} \right) \right] C \right. \right. \\ & \left. \left. - 2\delta\phi \left(Q, -\frac{D}{2} \right) \delta\phi \left(Q, \frac{D}{2} \right) A \right) \right], \quad (\text{A.18}) \end{aligned}$$

where $z_2 = D/2$, $z_1 = -D/2$ while A , B and C are defined as

$$\begin{aligned} A &= Q(\alpha^2 + Q^2) \cot^2(\alpha D/2); \\ B &= 2\alpha Q \cosh(DQ) \cot(\alpha D/2) \\ & \quad + (\alpha^2 + Q^2 \cot^2(\alpha D/2)) \sinh(DQ); \\ C &= Q \cosh(DQ) (2\alpha^2 + (\alpha^2 + Q^2) \cot^2(\alpha D/2)) \\ & \quad + 2\alpha(\alpha^2 + Q^2 + Q^2 \cos(\alpha D)) \csc(\alpha D) \sinh(DQ). \quad (\text{A.19}) \end{aligned}$$

References

1. J. Kirkwood, J.B. Shumaker, Proc. Natl. Acad. Sci. U.S.A. **38**, 855 (1952).
2. J. Kirkwood, J.B. Shumaker, Proc. Natl. Acad. Sci. U.S.A. **38**, 863 (1952).
3. V.A. Parsegian, *Van der Waals Forces* (Cambridge University Press, Cambridge, 2005).
4. B.W. Ninham, V.A. Parsegian, J. Theor. Biol. **31**, 405 (1973).
5. M. Lund, B. Jönsson, Q. Rev. Biophys. **46**, 265 (2013).
6. A. Naji, M. Kanduč, J. Forsman, R. Podgornik, J. Chem. Phys. **139**, 150901 (2013).
7. D. Chan, J.W. Perram, L.R. White, T.W. Healy, J. Chem. Soc., Faraday Trans. 1 **71**, 1046 (1975).
8. D. Chan, T.W. Healy, L.R. White, J. Chem. Soc., Faraday Trans. 1 **72**, 2844 (1976).
9. N. Boon, R. van Roij, J. Chem. Phys. **134**, 054706 (2011).
10. R.R. Netz, J. Phys.: Condens. Matter **15**, S239 (2003).
11. M. Lund, B. Jönsson, Biochemistry **44**, 5722 (2005).
12. F.L.B. da Silva, M. Lund, B. Jonsson, T. Åkesson, J. Phys. Chem. B **110**, 4459 (2006).
13. F.L.B. da Silva, B. Jonsson, Soft Matter **5**, 2862 (2009).
14. R. Podgornik, B. Žekš, J. Chem. Soc., Faraday Trans. II **84**, 611 (1988).
15. T. Markovich, A. Andelman, R. Podgornik, arXiv: 1305.3142v1 [cond-mat.soft] (2013).
16. C.C. Fleck, R.R. Netz, Eur. Phys. J. E **22**, 261 (2007).
17. B.W. Ninham, V.A. Parsegian, J. Theor. Biol. **31**, 405 (1970).
18. C. Fleck, R.R. Netz, H.H. von Grünberg, Biophys. J. **82**, 76 (2002).
19. I. Borukhov, D. Andelman, H. Orland, Electrochim. Acta **46**, 221 (2000).
20. D. Ben-Yaakov, D. Andelman, R. Podgornik, D. Harries, Curr. Opin. Colloids Interface Sci. **16**, 542 (2011).

21. D. Ben-Yaakov, D. Andelman, R. Podgornik, J. Chem. Phys. **134**, 074705-1 (2011).
22. D.S. Dean, R.R. Horgan, Phys. Rev. E **65**, 061603 (2002).
23. C. Grosche, F. Steiner, *Handbook of Feynman Path Integrals* (Springer, 1998).
24. D.C. Khandekar, S.V. Lawande, Phys. Rep. **137**, 115 (1986).
25. R. Podgornik, J. Chem. Phys. **91**, 5840 (1989).
26. M. Kanduč, R. Podgornik, Eur. Phys. J. E **23**, 265 (2007).
27. A.G. Moreira, R.R. Netz, Europhys. Lett. **52**, 705 (2000).
28. D. Andelman, in *Soft Condensed Matter Physics in Molecular and Cell Biology*, edited by W.C.K. Poon, D. Andelman (Taylor & Francis, 2006) pp. 97–122.
29. R. Podgornik, R.H. French, V.A. Parsegian, J. Chem. Phys. **124**, 044709 (2006).

Titrateable macroions in multivalent electrolyte solutions: Strong coupling dressed ion approach

Nataša Adžić and Rudolf Podgornik

Citation: *The Journal of Chemical Physics* **144**, 214901 (2016); doi: 10.1063/1.4952980

View online: <http://dx.doi.org/10.1063/1.4952980>

View Table of Contents: <http://scitation.aip.org/content/aip/journal/jcp/144/21?ver=pdfcov>

Published by the [AIP Publishing](#)

Articles you may be interested in

[Theoretical analysis of aqueous solutions of mixed strong electrolytes by a smaller-ion shell electrostatic model](#)

J. Chem. Phys. **140**, 054513 (2014); 10.1063/1.4862689

[Solution processable carbon nanotube network thin-film transistors operated in electrolytic solutions at various pH](#)

Appl. Phys. Lett. **101**, 223101 (2012); 10.1063/1.4768683

[Miniaturized diamond field-effect transistors for application in biosensors in electrolyte solution](#)

Appl. Phys. Lett. **90**, 063901 (2007); 10.1063/1.2454390

[Conductance of symmetric electrolyte solutions: Formulation of the dressed-ion transport theory \(DITT\)](#)

J. Chem. Phys. **111**, 10986 (1999); 10.1063/1.480462

[An empirical relation to predict ultrasonic velocity in electrolytic solutions](#)

J. Acoust. Soc. Am. **101**, 1191 (1997); 10.1121/1.418112



NEW Special Topic Sections

NOW ONLINE
Lithium Niobate Properties and Applications:
Reviews of Emerging Trends

AIP | Applied Physics
Reviews

Titrateable macroions in multivalent electrolyte solutions: Strong coupling dressed ion approach

Nataša Adžić^{1,a)} and Rudolf Podgornik^{1,2}

¹Department of Theoretical Physics, J. Stefan Institute, 1000 Ljubljana, Slovenia

²Department of Physics, Faculty of Mathematics and Physics, University of Ljubljana, 1000 Ljubljana, Slovenia

(Received 7 April 2016; accepted 17 May 2016; published online 1 June 2016)

We present a theoretical description of the effect of polyvalent ions on the interaction between titrateable macroions. The model system consists of two point-like macroions with dissociable sites, immersed in an asymmetric ionic mixture of monovalent and polyvalent salts. We formulate a *dressed ion strong coupling theory*, based on the decomposition of the asymmetric ionic mixture into a weakly electrostatically coupled monovalent salt and into polyvalent ions that are strongly electrostatically coupled to the titrateable macro-ions. The charge of the macroions is not considered as fixed, but is allowed to respond to local bathing solution parameters (electrostatic potential, pH of the solution, and salt concentration) through a simple *charge regulation* model. The approach presented, yielding an effective polyvalent-ion mediated interaction between charge-regulated macroions at various solution conditions, describes the strong coupling equivalent of the Kirkwood-Schumaker interaction. *Published by AIP Publishing.* [<http://dx.doi.org/10.1063/1.4952980>]

I. INTRODUCTION

Charged colloidal particles such as proteins,¹ surfactant micelles and vesicles,² and nanoparticles³ are seldom describable as possessing a fixed charge or a fixed potential, though this notion does not cease to be popular.⁴ A more realistic point of view considers colloidal particles immersed in an aqueous electrolyte solution as possessing ionizable surface groups that respond to the local solution conditions.^{5,6} Formally this perspective is equivalent to the assumption that one can characterize the chargeable surface of the colloid particles with a specific free energy describing the dissociation/association equilibrium of surface ionizable groups or adsorption/desorption equilibrium of charged ions from solution to the surface⁷ and is referred to as *charge regulation* (CR). This concept was first introduced implicitly by Linderstrom-Lang almost a century ago in the context of pH titration of proteins⁸ and was later invoked through “proton occupation variables” in the context of protein charge-fluctuation interactions by Kirkwood and Schumaker in the 1950s^{9,10} as well as in the context of dissociable lipid membrane interactions by Ninham and Parsegian in the 1970s,¹¹ based on the generalization of the boundary condition within the Poisson-Boltzmann (PB) theory of electrostatic interactions.¹²

The implementation details of the CR paradigm can vary. Chemical dissociation equilibrium of surface binding sites with the corresponding law of mass action was introduced already in Ref. 11 and was later generalized in different contexts.^{13–16} A surface-site partition function or indeed a surface free energy model leads to the same basic self-consistent boundary conditions for surface dissociation equilibrium, but without an explicit connection with the law of

mass action.^{7,17–27} The relationship between various boundary conditions that can be derived was elucidated recently.²³

Charge regulation has been invoked and widely applied in the context of various colloidal systems: stability and inter-surface forces due to the electrostatic double-layers,^{7,28} dissociation of amino acids and the corresponding electrostatic protein-protein interactions,^{29,31–33} charge regulation of protein aggregates and viral shells,³⁴ and of polyelectrolytes and polyelectrolyte brushes,^{35–38} as well as charge regulation of charged lipid membranes.^{39–41} Here, we specifically dedicate ourselves to the problem of the connection between charge regulation and electrostatic interactions between proteins in ionic solutions.^{1,30} We recently showed how the Kirkwood-Schumaker (KS) interaction^{9,10} follows directly from charge regulation, based on different surface free energy models,^{19–21} and presented a theory of fluctuation interaction between macroions subject to charge regulation, thereby generalizing the KS perturbation approach.^{9,10}

We formulated this generalized KS problem by decoupling the system composed of two charge-regulated macroions and an intervening bathing ionic solution into two parts: the solution part and the surface part.^{19–21} These were then treated within separate approximation schemes. The solution part was treated on the linearized weak-coupling Debye-Hückel (DH) level,⁴² while the surface part was shown to be amenable to an exact evaluation. This decomposition allowed us to derive a closed-form expression for the total effective interaction between macroions that we were able to connect with the original KS expression. In fact, our generalized fluctuation-mediated interaction reduces exactly to the KS result in the limit of large separations between macroions and in fact presents a one-loop (Gaussian fluctuation) correction to the mean-field DH result. As such, it is only valid for a weakly charged system, where the salt ions mediating the mean-field as well as fluctuation interactions are electrostatically weakly

^{a)}natasa.adzic@ijs.si

coupled to the macroions. No such approximations were necessary in a 1D model that can be evaluated exactly²¹ and supports the conclusions based on the weak coupling (WC) approximation.

We now change the perspective and consider a case where the bathing solution contains not only weakly charged monovalent salt ions but also polyvalent ions that are strongly electrostatically coupled to the charged macroions, mediating the interaction between them. A possible realization would correspond to a mixture of multivalent ions in a bathing solution of monovalent ions, a situation rather typical in the context of e.g., semiflexible biopolymers, where multivalent ions are believed to play a key role in their condensation.^{43,44} With the presence of polyvalent ions in the system, the WC paradigm in general breaks down and the existence of KS interactions becomes dubious.⁴² However, there exists a theory, the *dressed ion theory*, based on an asymmetric treatment of the different components of the bathing electrolyte solution, that would allow us to analyze the effect of charge regulation of macroions also in the presence of polyvalent salt ions in the bathing solution.^{43,44} It is based on the fact that one can use the WC DH approach in order to describe the monovalent salt ions, while a strong coupling (SC) approach is preferable for the polyvalent ion part. This combined *weak-strong coupling* approach^{43,44} effectively leads to dressed interactions between polyvalent ions and thus also affects the interactions mediated by polyvalent counterions between two like charge-regulated macroions. The ensuing effective interactions between macroions would then correspond to a *generalized KS interaction*, mediated by strongly coupled salt ions and not by weakly coupled monovalent salt. This generalized KS interaction would consequently also cease to be fluctuational in nature, i.e., of the type proposed in the original work of Kirkwood and Shumaker,^{9,10} but would show a different behavior stemming from the polyvalent ion mediated interactions coupled to the charge regulation response of the dissociation equilibrium at the macroion surfaces.

Our approach as detailed below is composed of disjointed parts brought together to describe this new type of generalized KS interaction, and a short *guided tour* through the conceptual and calculational flowchart is thus in order. The dissociable surfaces of the two identical macroions, representing two proteins with dissociable amino acids, are described with a charge-regulation surface free energy that allows the effective charge to vary between a positive and a negative maximal value. We then contract the macroion to a point particle merely as a calculational device, since we can then disregard the angular distribution of the dissociable groups along the surface, remaining solely with the monopolar charge as the only characteristics of the macroion. The bathing solution for the macroions, assuming to be an ionic mixture of monovalent salt and polyvalent ions, is then treated within the *dressed ion theory*, i.e., the monovalent salt is described within the WC and the polyvalent ions within the SC paradigm, an approximate approach that has already proved valuable in other contexts.^{43,44} We then further approximate the non-linear surface charge regulation free energy with a Gaussian expansion proved to be a good description on the WC level.^{19,20} Finally, we study the obtained

expressions for the effective generalized KS interaction between the macroions in the various parts of the parameter space and comment on the results.

The dressed ion theory, as a variant of the SC theory,⁴² does not hold the same status as the *original SC theory*, valid *exactly* for a counterion-only system in the limit of large coupling constant.^{45–47} In fact the regime of validity of this approach can be only checked against explicit-ion Monte Carlo simulations, showing that the dressed ion theory can indeed give quantitatively accurate results in a wide range of realistic parameter values.^{43,44,48}

II. GENERAL FORMALISM

A. Model

We study the system which consists of two equal titratable macroions immersed in a bathing solution, itself composed of a mixture of monovalent salt ions as well as polyvalent ions of valency q , see Fig. 1. Two macroions, representing for instance two titratable proteins in the context of a second virial coefficient pair-interaction calculation, immersed in a monovalent salt solution with a small admixture of multivalent salt, are located at \mathbf{r}_1 and \mathbf{r}_2 so that their separation is equal to $|\mathbf{r}_1 - \mathbf{r}_2| = R$. The macroions are assumed to be identical with a radius of $a/2$ and can have either sign. Furthermore, the macroions are charge-regulated with adsorption sites, which can exchange a proton from the environment, and are described with the lattice gas free energy, see below, with a site number coefficient of $\alpha = 2$. This implies that there are twice as many proton adsorption/dissociation sites as there are negative fixed charges. This allows the total charge of the macroion to span negative as well as positive values, a basic tenet of our charge regulation model.

The macroion charge is thus not fixed, but responds to the local solution conditions. We also assume that the macroions are “small” in the specific sense that the angular variation of the local electrostatic potential along their surface is negligible.

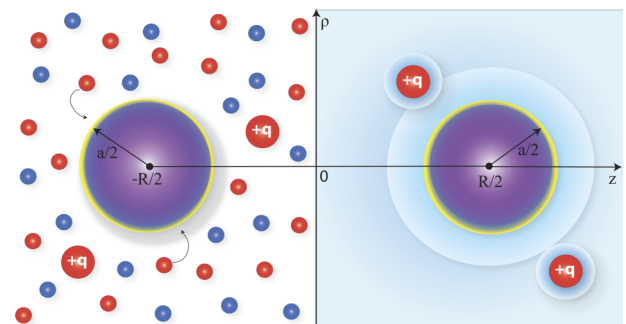


FIG. 1. Schematic representation of the model: two charge regulated macroions, representing two proteins with titratable surface groups, immersed in a mixture of monovalent-polyvalent salt solution. The microscopic model (left) shows the different types of ions and the surface dissociation equilibrium on the surface of the macroion. The coarse-grained dressed ion model (right) shows the effective DH potential (light colored corona) of the macroion as well as the polyvalent solution ions. In a cylindrical coordinate system with the z -axis connecting the two macroions, having its origin in the middle between the macroions, the macroions are located at $\mathbf{r}_1 = (x, y, -R/2)$ and $\mathbf{r}_2 = (x, y, R/2)$, respectively.

This implies that we only deal with effective monopolar fluctuations, disregarding the subdominant higher multipolar fluctuations that would correspond to a generalization of the full van der Waals interaction potential.⁴⁹ The higher multipolar KS interactions remain as a possible future topic of our investigation.

B. Charge regulation

For charge-regulated titratable macroions we have recently introduced several models,^{19,20} based on a charge dissociation free energy that generalizes the law of mass action charge-regulation approach of Ninham and Parsegian.¹¹ In these models the charge regulation is described by a surface free energy $f_S(\mathbf{r}) = f_S(\phi(\mathbf{r}))$ that depends on the surface electrostatic potential $\phi(\mathbf{r})$. For each macroion the total charge regulation free energy $F[\phi(\mathbf{r})]$ would thus be a functional of the surface potential amount to

$$F[\phi(\mathbf{r})] = \oint_S f_S(\phi(\mathbf{r})) d^2\mathbf{r}, \quad (1)$$

where S is the surface area of the macroion. At this point we simplify matters by furthermore assuming that the macroions are spherical and of vanishing radius, i.e., they are point particles. Of course this approximation will only work for sufficiently large separations between them and small separation regime would need to be analyzed separately. It will soon become clear why this type of approximation simplifies the calculation substantially.

While the approximation of contracting the macroion to a point particle is a convenient analytical device to make the calculations tractable, it obviously entails some additional limitations to their validity. The most severe one is the disregard of non-spherically symmetric charge fluctuations, or equivalently of fluctuating higher order multipoles. A macroion of finite extension, with an angular distribution of surface dissociable sites, will typically show fluctuating monopoles, dipoles, etc., that depend on the local electrostatic potential. The point-particle simplification retaining only the monopolar fluctuations can be argued to be the most important contribution in the large separation limit, while the higher order multipoles are subdominant. In addition, higher order multipoles—starting with the dipole—would invariably couple the charge fluctuation interaction with the standard van der Waals interaction.

In addition, the point macroion approximation disregards the electrostatic interaction between dissociable groups, as they are represented by a single point-like charge regulated moiety. A finite size of the macroion with angular dependence of the dissociation site distribution would bring in also the electrostatic interactions between the sites on the same macroion, which could furthermore lead to potentially important new facets in the interaction between two macroions. While this line of reasoning can certainly be pursued, and will be in the future, it is important to have the “baseline” point-macroion results first in order to assess the importance of other contributions.

Assuming then that the macroion is located at (\mathbf{r}_0) and has a vanishing radius $a \rightarrow 0$, the integral of the dissociation

free energy over the surface of the macroion, Eq. (1), simply gives a total dissociation energy of the point-like macroion as a *function* of the local potential at the point $\mathbf{r} = \mathbf{r}_0$. The point-like approximation for the macroion therefore disregards the angular variation of the local electrostatic potential along the surface of the macroions and can describe only monopolar charge regulation, while higher multipoles are ignored.

In the next step one needs to assume a model for $f_S(\phi(\mathbf{r}))$. We already invoked several models^{19,20} related to the original Ninham-Parsegian model.¹¹ Focusing on a simple two-parameter model we introduce the following *ansatz* for a charge regulated point-like macroion:²⁰

$$F(\phi(\mathbf{r}_0)) = \lim_{a \rightarrow 0} \oint_S f_S(\phi(\mathbf{r})) d^2\mathbf{r} \\ \rightarrow -Ne_0\phi(\mathbf{r}_0) - \alpha Nk_B T \log \left(1 + be^{-\beta e_0\phi(\mathbf{r}_0)} \right), \quad (2)$$

where $\phi(\mathbf{r}_0)$ is now the local electrostatic potential at the position of the ion, while N and α are two parameters characterizing the dissociation process. The site number coefficient α quantifies the number of dissociation sites, and $\log b = \beta\mu_S$ incorporates the free energy of charge dissociation μ_S .

In the case of protonation of the titratable surface charge, it furthermore follows that $\log b = \log 10(pH - pK)$, where pK is the dissociation constant and $pH = -\log[H^+]$ is the proton concentration in the bulk, differing from the local value of pH at the dissociation site.^{19,20} It is straightforward to see that the free energy Eq. (2) is composed of the electrostatic energy of N fixed negatively charged sites with the total charge $-Ne_0$ and αN lattice gas sites, that can be filled with adsorbing protons from the solution; in fact $1 + e^\mu$ is nothing but the lattice gas partition function for single occupation sites, with zero energy for the empty site and μ for the filled site, while $\log(1 + e^\mu)$ is just the corresponding grand canonical surface pressure.

The form of the charge regulation free energy then allows us to derive the effective charge of the charge-regulated macroion as a function of the local electrostatic potential in the form

$$e(\phi) = \frac{\partial F(\phi)}{\partial \phi}, \quad (3)$$

where $F(\phi)$ is the dissociation free energy Eq. (2) yielding

$$e(\phi) = e_0 N \left(\left(\frac{\alpha}{2} - 1 \right) - \frac{\alpha}{2} \tanh \left[-\frac{1}{2} (\ln b - \beta e_0 \phi) \right] \right). \quad (4)$$

The effective charge of the macroion then varies in the interval $-Ne_0 < e(\phi) < (\alpha - 1)Ne_0$. Choosing the site number coefficient to be $\alpha = 2$, one thus remains with a symmetric charge regulated macroion whose effective charge varies within the interval $-Ne_0 < e(\phi) < +Ne_0$. This is the generic charge regulation model that we will consider as a simple description of the protein charge regulation in what follows.

C. Field theory—general formalism

We proceed by writing the partition function through the Hubbard-Stratonovich transform for the Coulomb potential as explained in detail elsewhere.⁵⁰ This leads to a field theory,

where the classical partition function is represented as a functional integral over the fluctuating electrostatic potential. Two explicit exact limiting results are then obtainable from this representation in the case of a counterion-only system:⁴² the saddle-point of this field-theory in fact corresponds to the mean-field Poisson-Boltzmann (PB) approximation, while the Gaussian fluctuation correction together with the PB theory constitutes the *WC theory*; the first order virial expansion of the partition function then constitutes the *SC theory*, unrelated to the PB approximation. The latter can be further generalized in the case of a mixed system by treating the monovalent salt on the WC level while the polyvalent ions are described on the SC level, i.e., their contribution to the partition function is written as a second order virial expansion theory. This approximation was dubbed the “dressed ion theory.”^{43,44}

Assuming that the fluctuating electrostatic potential of the macroions is $\phi(\mathbf{r} = \mathbf{r}_1) = \varphi_1$ and of the other one is $\phi(\mathbf{r} = \mathbf{r}_2) = \varphi_2$, located at \mathbf{r}_1 and \mathbf{r}_2 , respectively, the partition function of the system within the dressed ion theory can be derived in the field-theoretic form as^{19,20}

$$\mathcal{Z} = \iint d\varphi_1 e^{-\beta F(\varphi_1)} G(\varphi_1, \varphi_2) e^{-\beta F(\varphi_2)} d\varphi_2, \quad (5)$$

where $F(\varphi)$ is charge regulation free energy, Eq. (2), evaluated at imaginary values of the fluctuating electrostatic potential, and the field propagator or the Green function, giving the probability of field configurations with $\phi(\mathbf{r} = \mathbf{r}_1) = \varphi_1$ and $\phi(\mathbf{r} = \mathbf{r}_2) = \varphi_2$, is given by

$$G(\varphi_1, \varphi_2) = \int \mathcal{D}[\varphi(\mathbf{r})] e^{-\beta H[\varphi]} \delta(\varphi(\mathbf{r}_1) - \varphi_1) \delta(\varphi(\mathbf{r}_2) - \varphi_2), \quad (6)$$

with the bulk field action,

$$-\beta H[\varphi] = -\beta H_0[\varphi] + \lambda_c \int d\mathbf{r} e^{i\beta q e \varphi(\mathbf{r})}, \quad (7)$$

where λ_c is the fugacity of the polyvalent ions with valency q and $H_0[\varphi]$ is the DH field Hamiltonian

$$\begin{aligned} -\beta H_0[\varphi] &= \frac{1}{2} \epsilon \epsilon_0 \int d\mathbf{r} d\mathbf{r}' \varphi(\mathbf{r}) u_{DH}^{-1}(\mathbf{r}, \mathbf{r}') \varphi(\mathbf{r}') \\ &= \frac{1}{2} \epsilon \epsilon_0 \int ((\nabla \varphi(\mathbf{r}))^2 + \kappa^2 \varphi^2(\mathbf{r})) d\mathbf{r}. \end{aligned} \quad (8)$$

Here we have assumed that the monovalent salt is weakly coupled to the rest of the charges and can be treated on the DH level. The inverse square of Debye length was introduced as

$$\kappa^2 = 4\pi \ell_B n_b = 4\pi \ell_B (2n_0 + qc_0), \quad (9)$$

with ℓ_B the Bjerrum length and obviously $n_b = 2n_0 + qc_0$, where n_0 is the bulk concentration of the monovalent salt and c_0 is the bulk concentration of the multivalent ions, assumed to originate in dissociation of a $q:1$ salt. The DH interaction kernel $u_{DH}^{-1}(\mathbf{r}, \mathbf{r}')$ implies a screened effective DH interaction potential

$$u_{DH}(\mathbf{r}, \mathbf{r}') = \frac{1}{4\pi \epsilon \epsilon_0} \frac{e^{-\kappa|\mathbf{r}-\mathbf{r}'|}}{|\mathbf{r}-\mathbf{r}'|} = \frac{1}{4\pi \epsilon \epsilon_0} \tilde{u}_{DH}(\mathbf{r}, \mathbf{r}') \quad (10)$$

between the polyvalent ions and the macroions. On this level the polyvalent ions are thus treated explicitly, but their interactions with the macroions are described with

a dressed electrolyte-mediated effective DH potential. By explicit polyvalent ions we understand the fact that in the final expressions the positions of the polyvalent ions still need to be traced over, while the monovalent salt is present only via its screening length.

The strong asymmetry in the system, implied by the presence of polyvalent mobile ions, together with their small concentration leads straightforwardly to the virial expansion for their contribution to the partition function that yields to the lowest order,^{43,44,48}

$$e^{-\beta H[\varphi]} = e^{-\frac{1}{2}\beta \int d\mathbf{r} d\mathbf{r}' \varphi(\mathbf{r}) u_{DH}(\mathbf{r}, \mathbf{r}') \varphi(\mathbf{r}')} \times (1 + \lambda_c \int_V d\mathbf{r}_0 e^{i\beta q e \varphi(\mathbf{r}_0)} + \dots), \quad (11)$$

furthermore implying that the propagator $G(\varphi_1, \varphi_2)$ can be decomposed into

$$G(\varphi_1, \varphi_2) = G_0(\varphi_1, \varphi_2) + \lambda_c \int_V d\mathbf{r}_0 G_1(\varphi_1, \varphi_2; \mathbf{r}_0). \quad (12)$$

The propagator $G_1(\varphi_1, \varphi_2; \mathbf{r}_0)$ describes the field propagation from macro-ion at \mathbf{r}_1 to macro-ion at \mathbf{r}_2 mediated by the presence of the polyvalent ion q at \mathbf{r}_0 integrated over the fluctuating potential at the positions of both macroions. Formally this can be expressed as

$$G_1(\varphi_1, \varphi_2; \mathbf{r}_0) = \int \mathcal{D}[\varphi(\mathbf{r})] \delta(\varphi(\mathbf{r}_1) - \varphi_1) e^{-\beta H_1[\varphi; \mathbf{r}_0]} \delta(\varphi(\mathbf{r}_2) - \varphi_2), \quad (13)$$

where the effective field action $H_1[\varphi; \mathbf{r}_0]$ can be decomposed into the DH part due to the weakly coupled monovalent salt ions and the coupling between fluctuating potential and the polyvalent ion of valency q located at \mathbf{r}_0 , i.e.,

$$\beta H_1[\varphi; \mathbf{r}_0] = \beta H_0[\varphi] - i\beta \int \rho(\mathbf{r}_0) \varphi(\mathbf{r}) d\mathbf{r}. \quad (14)$$

The last term describes the interaction with the polyvalent ion with density,

$$\rho(\mathbf{r}_0) = q\delta(\mathbf{r} - \mathbf{r}_0).$$

This formal expression for the propagator $G_1(\varphi_1, \varphi_2; \mathbf{r}_0)$ is thus identical to the partition function of two macroions at positions $\mathbf{r}_{1,2}$ with set values of the fluctuating potential $\varphi_{1,2}$ interacting via the DH interaction with an additional point particle of charge qe_0 at \mathbf{r}_0 at the positions of the two point-like macroions. The functional integral in Eq. (13) simply indicates the summation over all fluctuating potentials that satisfy these constraints.

With these definitions the full dressed ion partition function can then be cast into the sum of two disjoint terms, one corresponding to two isolated polyvalent ions interacting directly via DH potential and the other describing the polyvalent ion mediated interaction,

$$\begin{aligned} \mathcal{Z} &= \iint d\varphi_1 e^{-\beta F(\varphi_1)} \left[G_0(\varphi_1, \varphi_2) \right. \\ &\quad \left. + \lambda_c \int_V d\mathbf{r}_0 G_1(\varphi_1, \varphi_2; \mathbf{r}_0) \right] e^{-\beta F(\varphi_2)} d\varphi_2 = \mathcal{Z}_0 + \lambda_c \mathcal{Z}_1, \end{aligned} \quad (15)$$

with obvious definitions for the two terms in the sum. \mathcal{Z}_0 and \mathcal{Z}_1 by definition then give the zero order and the first order

polyvalent ion virial expansion contributions in the partition function. \mathcal{Z}_0 has been already analyzed in Ref. 20 and \mathcal{Z}_1 will be evaluated below. The above decomposition of the full partition function $\mathcal{Z} = \mathcal{Z}(R)$ is the essence of the dressed ion theory and the corresponding free energy will describe the interactions between the two macroions as a function of their separation and model parameters.

D. Dressed ion theory and charge regulation

The first order virial expanded Green function $G_1(\varphi_1, \varphi_2; \mathbf{r}_0)$ can be reduced to Gaussian functional integrals, see Appendix, and can be derived in an explicit form

$$G_1(\varphi_1, \varphi_2; \mathbf{r}_0) = \frac{\exp\left(\frac{1}{2}\tilde{\Phi}_i(\mathbf{r}_0)G^{-1}_{ij}(\mathbf{r}_1, \mathbf{r}_2)\tilde{\Phi}_j(\mathbf{r}_0)\right)}{\sqrt{\det G_{ij}(\mathbf{r}_1, \mathbf{r}_2)}}, \quad (16)$$

where we introduced

$$\Phi_i(\mathbf{r}_0) = i\varphi_1 + qe_0u_{DH}(\mathbf{r}_0, \mathbf{r}_i) \quad (17)$$

and

$$G_{ij}(\mathbf{r}_1, \mathbf{r}_2) = k_B T \begin{pmatrix} a^{-1} & u_{DH}(\mathbf{r}_1, \mathbf{r}_2) \\ u_{DH}(\mathbf{r}_1, \mathbf{r}_2) & a^{-1} \end{pmatrix}, \quad (18)$$

for $i, j = 1, 2$. From the above expressions it is clear that the macroions interact with themselves as well as with the polyvalent ion whose position within the system will be finally integrated over. The terms with a^{-1} describe the self-interaction of the macroions with diameter a , while the interaction between the macroions as well as between the macroions and the polyvalent ion are given by the DH screened interaction potential. In a cylindrical coordinate system with the z -axis connecting the two macroions, having its origin in the middle between the macroions, themselves separated by R , the position of the polyvalent ion with respect to both

macroions can be written as $|\mathbf{r}_0 - \mathbf{r}_1| = \sqrt{\rho_0^2 + (R/2 + z_0)^2}$ and $|\mathbf{r}_0 - \mathbf{r}_2| = \sqrt{\rho_0^2 + (R/2 - z_0)^2}$, respectively.

Going back to the definition of the partition function \mathcal{Z}_1 , Eq. (15), one can finally write

$$\mathcal{Z}_1 = \lambda_c \int_V d\mathbf{r}_0 \int d\varphi_1 e^{-\beta F(\varphi_1)} \left[G_1(\varphi_1, \varphi_2) \right] e^{-\beta F(\varphi_2)} d\varphi_2. \quad (19)$$

While the Green function $G_1(\varphi_1, \varphi_2)$ is Gaussian in the two fields, the surface field action $F(\varphi)$ is not. Additional considerations are therefore needed to proceed. First we note, as amply elucidated in Ref. 20, that an *exact* method of evaluation of \mathcal{Z}_1 is available if one expands the surface field action into a series, yielding

$$e^{-\beta F(\varphi)} = e^{-i\beta N e_0 \varphi} (1 + b e^{i\beta e_0 \varphi})^{2N} \\ = \sum_{n=0}^{2N} \binom{2N}{n} e^{-i\beta N e_0 \varphi} b^n e^{i\beta e_0 n \varphi}. \quad (20)$$

While the above expansion, giving a sum over surface terms linear in the fluctuating potential, could in principle be used for a direct numerical evaluation of the partition function, we have already shown^{19,20} that an additional approximation, simplifying the calculation extensively, yields an accurate result that compares well with the exact summation. This further step relies on the Gaussian approximation for the binomial coefficient in the above expansion,

$$\lim_{N \gg 1} \binom{2N}{n} \simeq \frac{2^{2N}}{\sqrt{\pi N}} e^{-\frac{(N-n)^2}{N}}, \quad (21)$$

valid strictly in the limit of a large number of adsorption sites, $N \gg 1$. Introducing the auxiliary fields $x_1 = N - n_1$ and $x_2 = N - n_2$, summation in Eq. (20) can thus be replaced with an integration, so that the partition function assumes a much simplified and easily calculable form

$$\mathcal{Z}_1 = \lambda_c \int_V d\mathbf{r}_0 \int d\varphi_1 d\varphi_2 \int dx_1 dx_2 \frac{e^{s(q^2; \mathbf{r}_1, \mathbf{r}_2) + \ln 10 (pH - pK)(x_1 + x_2) - \frac{x_1^2 - x_2^2}{N}}}{\sqrt{\det G_{ij}(\mathbf{r}_1, \mathbf{r}_2)}} \exp \left[-\frac{1}{2} \varphi_i G^{-1}_{ij}(\mathbf{r}_1, \mathbf{r}_2) \varphi_j + i\beta e_0 \varphi_i (-x_i + q y_i) \right]. \quad (22)$$

Here the effective interaction matrix $G_{ij}(\mathbf{r}_1, \mathbf{r}_2)$ has been already defined in Eq. (18), while $G^{-1}_{ij}(\mathbf{r}_1, \mathbf{r}_2)$ is its matrix inverse. In addition we introduced two additional auxiliary fields with no other role but to make the notation more compact,

$$y_1 = \frac{a^2}{1 - \frac{a^2}{R^2} e^{-2\kappa R}} \left(\frac{1}{a} \tilde{u}_{DH}(\mathbf{r}_0, \mathbf{r}_1) - \frac{e^{-\kappa R}}{R} \tilde{u}_{DH}(\mathbf{r}_0, \mathbf{r}_2) \right) \quad (23)$$

and

$$y_2 = \frac{a^2}{1 - \frac{a^2}{R^2} e^{-2\kappa R}} \left(\frac{e^{-\kappa R}}{R} \tilde{u}_{DH}(\mathbf{r}_0, \mathbf{r}_1) - \frac{1}{a} \tilde{u}_{DH}(\mathbf{r}_0, \mathbf{r}_2) \right). \quad (24)$$

The effective self-energy of the polyvalent ion, $s(q^2; \mathbf{r}_1, \mathbf{r}_2)$, mediated by both macroions, is proportional to the square of the polyvalent ion charge and is given by

$$s(q^2; \mathbf{r}_1, \mathbf{r}_2) = \frac{1}{2} q^2 \frac{l_B a}{1 - \frac{a^2}{R^2} e^{-2\kappa R}} \times \left(\tilde{u}_{DH}^2(\mathbf{r}_0, \mathbf{r}_1) + \tilde{u}_{DH}^2(\mathbf{r}_0, \mathbf{r}_2) - 2 \frac{a}{R} e^{-\kappa R} \tilde{u}_{DH}(\mathbf{r}_0, \mathbf{r}_1) \tilde{u}_{DH}(\mathbf{r}_0, \mathbf{r}_2) \right). \quad (25)$$

After integrating out the x_i -auxiliary fields and the fluctuating potentials of the two macroions, φ_1, φ_2 , one obtains the final result in the form of an integration over the position of the polyvalent ion,

$$\mathcal{Z}_1 = \mathcal{Z}_0 \lambda_c \int_V d\mathbf{r}_0 \times \exp \left[\frac{q \ell_B N (pH - pK) \ln 10 (\tilde{u}_{DH}(\mathbf{r}_0, \mathbf{r}_1) + \tilde{u}_{DH}(\mathbf{r}_0, \mathbf{r}_2))}{2 + N l_B \frac{1}{a} [1 + \frac{a}{R} e^{-\kappa R}]} \right] \times \exp \left[\frac{1}{2} q^2 \ell_B^2 (C_{11} \tilde{u}_{DH}^2(\mathbf{r}_0, \mathbf{r}_1) + C_{22} \tilde{u}_{DH}^2(\mathbf{r}_0, \mathbf{r}_2) - 2C_{12} \tilde{u}_{DH}(\mathbf{r}_0, \mathbf{r}_1) \tilde{u}_{DH}(\mathbf{r}_0, \mathbf{r}_2)) \right], \quad (26)$$

where \mathcal{Z}_0 is the partition function of a system of two isolated charge-regulated macroions on the WC approximation level, already derived within the context of the weakly coupled macroions in monovalent salt solution^{19,20} and given by

$$\mathcal{Z}_0 = \frac{\exp \left[\frac{N[(pH-pK) \ln 10]^2}{2 + N l_B \frac{1}{a} [1 + \frac{a}{R} e^{-\kappa R}]} \right]}{\sqrt{\frac{4}{N^2} + \frac{2}{N} \frac{l_B}{a} + \frac{l_B^2}{a^2} \left[1 - \frac{a^2}{R^2} e^{-2\kappa R} \right]}}. \quad (27)$$

Above we also introduced the generalized self and mutual capacitances as

$$C_{11} = C_{22} = \frac{\frac{l_B}{a} + \frac{2}{N}}{\left(\frac{l_B}{a} + \frac{2}{N} \right)^2 - \frac{e^{-2\kappa R}}{R^2 l_B^2}}; \quad (28)$$

$$C_{12} = \frac{\frac{l_B e^{-\kappa R}}{R}}{\left(\frac{l_B}{a} + \frac{2}{N} \right)^2 - \frac{e^{-2\kappa R}}{R^2 l_B^2}}.$$

While they do not have the standard form of the capacitances, since they both contain also contributions from mutual interactions, in the limit of large separations between the macroions they do reduce to the expected values. The difference in the definition of capacitances is a consequence of the fact that the dressed ion theory is not Gaussian as far as the fluctuating potential is concerned, in contrast to

the WC case analyzed before,^{19,20} but is a non-linear SC theory. Capacitance is a WC concept, pertaining to Gaussian fluctuations and thus does not have a direct equivalent in the SC theory.

We now write down the free energy difference between the state where the two macroions are at a finite spacing R and the state corresponding to two isolated macroions with $R \rightarrow \infty$. This SC free energy difference, Eq. (15), finally assumes the form

$$\beta \mathcal{F} = -\ln[\mathcal{Z}_0] - \lambda_c \frac{\mathcal{Z}_1}{\mathcal{Z}_0} = \tilde{\mathcal{F}}_0 + c_0 \tilde{\mathcal{F}}_1. \quad (29)$$

Here, in the grand canonical ensemble, the fugacity λ_c is identical to polyvalent ion concentration in the bulk c_0 and

$$\tilde{\mathcal{F}}_0 = -\ln[\mathcal{Z}_0], \quad (30)$$

where \mathcal{Z}_0 is defined in Eq. (27) and extensively analyzed in Refs. 19 and 20. For the sake of completeness we nevertheless write it down in an explicit form

$$\tilde{\mathcal{F}}_0 = -\frac{N[(pH-pK) \ln 10]^2}{2 + N l_B \frac{1}{a} [1 + \frac{a}{R} e^{-\kappa R}]} + \frac{1}{2} \ln \left(1 + N \frac{l_B}{2a} + \frac{l_B^2}{(2a)^2} N^2 \left[1 - \frac{a^2}{R^2} e^{-2\kappa R} \right] \right). \quad (31)$$

On the other hand, $\tilde{\mathcal{F}}_1$, as defined above yields the final expression

$$\tilde{\mathcal{F}}_1 = \int_V d\mathbf{r}_0 \left(\exp \left[\frac{q N (pH - pK) \ln 10 (u_{DH}(\mathbf{r}_0, \mathbf{r}_1) + u_{DH}(\mathbf{r}_0, \mathbf{r}_2))}{2 + N l_B \frac{1}{a} [1 + \frac{a}{R} e^{-\kappa R}]} \right] \times \exp \left[\frac{1}{2} q^2 (C_{11} u_{DH}^2(\mathbf{r}_0, \mathbf{r}_1) + C_{22} u_{DH}^2(\mathbf{r}_0, \mathbf{r}_2) - 2C_{12} u_{DH}(\mathbf{r}_0, \mathbf{r}_1) u_{DH}(\mathbf{r}_0, \mathbf{r}_2)) \right] - 1 \right), \quad (32)$$

with explicitly subtracted free energy value of two isolated macroions with $R \rightarrow \infty$. The structure of this complicated expression is as follows: the first exponent corresponds to the screened DH interactions of the q -valent polyvalent ion with both macroions, whose charge is determined by the bulk pH of the solution and is proportional to $pH - pK$, while the second exponent corresponds to the electrostatic self-interaction of the polyvalent ion in the presence of both macroions. Finally the product of the two expressions needs to be integrated over all the possible positions of the polyvalent ion. The constants C_{11} and C_{22} , Eq. (28), can be interpreted as generalized self-capacitances and mutual capacitance C_{12}

of the macroions, originating in the interaction between the three charged particles. At the end, we subtracted the non-interacting part of two isolated macroions proportional simply to the volume of the system V .

In addition, we note that both $\tilde{\mathcal{F}}_0(R)$ as well as $\tilde{\mathcal{F}}_1(R)$ contain parts which are due to *polyion mediated* interaction between the macroions, proportional to $qN(pH - pK)$, as well as *polyion self-interaction* mediated by the macroions and proportional to q^2 . The division into a “mean interaction” and “fluctuations” is thus not possible due to the fact that our theory is not of a mean-field type that would allow for fluctuations around the mean-field configuration.

In the case of absent charge regulation, where the system consists of two macroions with fixed charge Ne_0 , immersed in the same bathing solution with a strongly

coupled oppositely charged polyvalent ion, one can repeat the above analysis and obtain the final free energy in the form

$$\tilde{\mathcal{F}}_0 + c_0\tilde{\mathcal{F}}_1 = N^2l_B \left(\frac{1}{a} + \frac{e^{-\kappa R}}{R} \right) - c_0 \int_V d\mathbf{r}_0 \left(\exp \left[qN (u_{DH}(\mathbf{r}_0, \mathbf{r}_1) + u_{DH}(\mathbf{r}_0, \mathbf{r}_2)) \right] - 1 \right). \quad (33)$$

This is very instructive, since obviously without charge regulation the self-interaction contributions proportional to q^2 are absent, and the interaction energy reduces to the macroion-macroion repulsion proportional to the charge squared, $(Ne_0)^2$, and a contribution stemming from the interaction of macroions with the polyvalent ion, proportional to the product of both charges, $q(Ne_0)$. The above equations represent the final result of the dressed ion theory for the interaction between two identical point-like charge regulated macroions in the presence of small concentrations of a polyvalent salt and they have to be evaluated numerically.

III. RESULTS AND DISCUSSION

The effective interaction free energy between the charge-regulated macroions is obtained directly from Eq. (27) after performing the numerical integration over volume in Eq. (32). We calculate the total interaction free energy, $\beta\mathcal{F}(R)$, as a function of the separation between the macroions as

$$\beta\mathcal{F}(R) = \tilde{\mathcal{F}}_0(R) + c_0\tilde{\mathcal{F}}_1(R). \quad (34)$$

We study the separation dependence of the force,

$$\tilde{F}(\tilde{R}) = -\frac{d\tilde{\mathcal{F}}_0(\tilde{R})}{d\tilde{R}} - c_0 \frac{d\tilde{\mathcal{F}}_1(\tilde{R})}{d\tilde{R}} = \tilde{F}_0(\tilde{R}) + \tilde{F}_1(\tilde{R}), \quad (35)$$

for different values of the parameters, differentiating in particular the case of $pH - pK = 0$, i.e., the point of zero charge (PZC), corresponding to macroions that are on the average uncharged. In spite of this, the self-energy of the polyvalent ion in this case still contains the non-vanishing electrostatic self-interaction of the polyvalent ion mediated by both charge regulated macroions.

We first analyze the term $\tilde{F}_1(R)$, obtained from Eq. (32), which corresponds to the interaction force mediated by the polyvalent q -ion only. Obviously, see Figure 2(a), this interaction force leads to an attractive contribution to the force at PZC, stemming solely from the self-interaction of the macroions, whose magnitude depends quadratically on q . The screening effect of the monovalent salt is clearly discernible. In summary, the polyvalent self-interaction at PZC yields an attractive interaction that gets stronger and more long-ranged on increase of the valency q of the polyvalent ion and on decrease of the monovalent salt concentration n_0 . We should note that this PZC polyvalent ion-mediated attraction in the SC dressed ion approach is much stronger than the residual WC (KS) attraction between charge regulated macroions in a monovalent salt solution (black lines) Fig. 2(a).

We have not specified yet the sign of the q polyvalent ion. In fact the product $q(pH - pK)$ can have either sign. In Fig. 2 we thus study how the sign of polyvalent ions modifies the polyvalent ion-mediated contribution to the total interaction force. For both cases, $q(pH - pK)$ positive, Fig. 2(b), and for $q(pH - pK)$ negative, Fig. 2(c), the interaction force corresponds to attractive polyvalent ion-mediated forces but of vastly different magnitude, being much larger in the former case than in the latter. In both cases the attraction is again larger in the lower screening regime (less n_0 , bigger q).

The total interaction force between the two titratable macroions, $\tilde{F}(\tilde{R}) = \tilde{F}_0(\tilde{R}) + \tilde{F}_1(\tilde{R})$, is presented in Figs. 3 and 4. Obviously, the interaction force is attractive when $q(pH - pK) \geq 0$, due to the strongly coupled polyvalent ion mediated interaction, and is in general screened by the monovalent salt. Interestingly enough, in this case even the

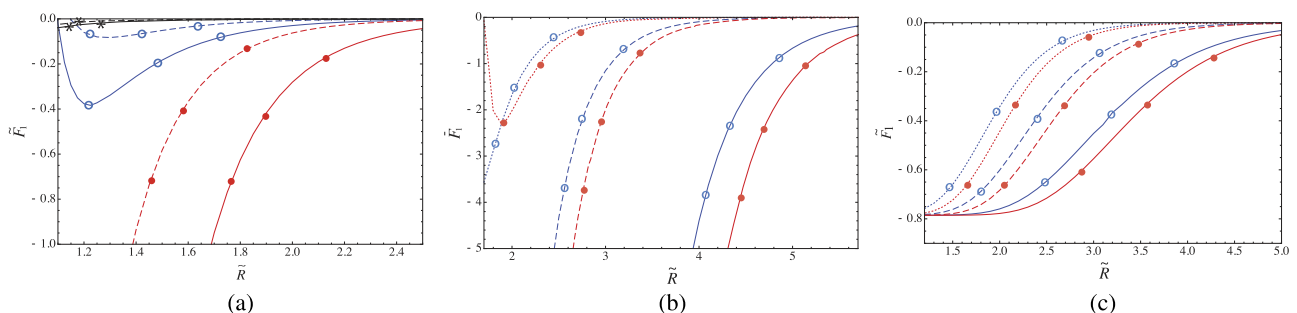


FIG. 2. Interaction force contribution $\tilde{F}_1(R)$, calculated from Eq. (32), originating in the presence of polyvalent ions, for (a) $pH - pK = 0$; (b) $pH - pK = 3$; and (c) $pH - pK = -3$. Blue lines (marked with an open circle), $q = 3$; red lines (marked with a filled circle), $q = 4$; black lines (marked with star), $q = 0$ (standing for the attraction coming from Eq. (31)). Solid lines correspond $n_0 = 150$ mM, dashed $n_0 = 300$ mM, while dotted stand for $n_0 = 500$ mM in (b) and (c), while in (a) monovalent salt concentration is chosen as $n_0 = 100$ mM solid lines and $n_0 = 150$ mM dashed lines. Macroions diameter $a = 1$ nm, number of adsorption sites $N = 7$, and $c_0 = 1$ mM.

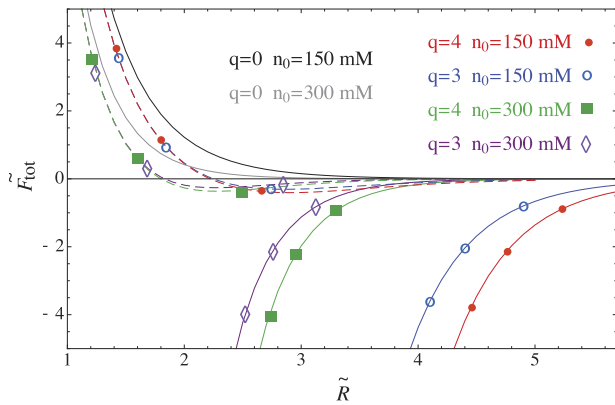


FIG. 3. The total interaction force for $pH-pK=3$ (solid lines) and $pH-pK=-3$ (dashed lines), at fixed values of parameters as shown in legend. Macroions of diameter $a = 1$ nm, with the number of adsorption sites $N = 7$ and salt concentration $c_0 = 1$ mM.

interaction at small separations remains attractive and the bare macroion repulsion is not observed. The reason for this is not the polyion mediated electrostatic attraction but its size: in fact for small separation the polyvalent counterion cannot enter the space between the macroions and thus exerts an additional effective osmotically generated attraction between them in general akin to the depletion effect, already noticed in a similar context for net-neutral surfaces at small separations.⁴⁸ In the opposite case, when $q(pH-pK) < 0$, the repulsion in general prevails, except at large separations where one can detect a small residual attraction, possibly as a consequence of an asymmetrical charge fluctuation due to charge regulation. At smaller separations the bare repulsion between macroions is reduced partly due to the charge regulation effects and partly due to depletion effects. In Fig. 4 one can additionally notice how the two cases, one with small $pH-pK$, immersed in a solution of low salt concentration, and the other one with large $pH-pK$, but immersed in concentrated salt solution, have quite similar behavior, indicating that the valency of the polyion and the screening of the monovalent salt somehow act in parallel.

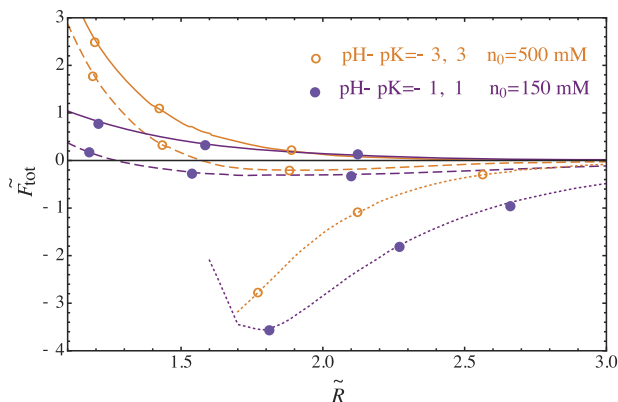


FIG. 4. Total interaction force between macroions with small $pH-pK$ values at low salt concentration compared with the total interaction force in concentrated salt solutions between macroions with large $pH-pK$. Dotted lines correspond to q being a counterion, dashed q is coion, while solid lines stand for $q=0$. Macroions diameter $a = 1$ nm, number of adsorption sites $N = 7$, and $c_0 = 1$ mM.

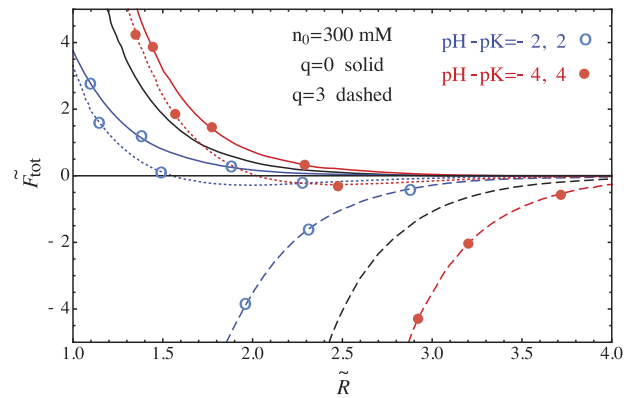


FIG. 5. The comparison of the total interaction force for non-regulated case (black full line) with total regulated interaction force at $q(pH-pK) < 0$ (dotted lines) and $q(pH-pK) > 0$ (dashed lines), at fixed values of parameters as shown in legend. Macroions of diameter $a = 1$ nm, with the number of adsorption sites $N = 7$ and salt concentration $c_0 = 1$ mM.

In Fig. 5 the total interaction force is now compared for the two cases with and without charge regulation, Eqs. (32) and (33), respectively. The charge non-regulated case corresponds to fixed values of the macroion charge equal to Ne_0 . Here, one can notice the important effect of charge regulation through the polyvalent mediated interaction, ruled by the pH value, which determines the overall strength of the charge regulation interaction, that can then appear as either smaller or larger than the one corresponding non-regulated interaction energy. This non-monotonic effect of charge regulation hinges on the two terms in the dressed ion free energy that respond differently to titration of the macroion charges.

The dressed ion theory obviously predicts an attractive interaction between charge regulated macroions, which can sometimes dominate the overall interaction. This is different from the WC case,^{19,20} where the fluctuation attraction, or the KS interaction, is subdominant to the DH repulsion, except close to the PZC, where it indeed becomes dominant. In the SC dressed ion theory the attraction can clearly become dominant either with or without the charge regulation, though it can be stronger in the latter case and remains important for any value of pH . The salt effect acts mostly to quench the correlation polyvalent ion-mediated attraction and diminish its spatial range.

The mesoscale model of charge regulation introduced depends only on the difference $pH-pK$ as a free parameter and the value of pK should be taken from other considerations. The physical dimensions of the interaction force can be obtained by multiplying the dimensionless force with $k_B T/l_B$. Since $k_B T$ is 4.114 pN nm and l_B is 0.7 nm this then leads to the physical force of the order ~ 10 pN at nanometer-ranged separations. The interaction force of that order of magnitude is found, for example, in the experiments with charge-regulated silica particles in the presence of multivalent cations as described in Ref. 51.

The attraction between two identical charge regulated macroions, seen in the dressed ion theory, has a different origin from the WC KS interactions, where they are due to thermal monopolar charge fluctuations around the mean-field solution, enabled by the dissociation equilibrium of

the surface of the macroion. In the dressed ion theory, the polyvalent ion-mediated attraction could be seen as being due to the *electrostatic bridging interaction* involving the polyvalent ion. This should in general not be confused with the *s.c. salt bridging interaction* sometimes invoked even in weakly coupled monovalent salt solutions.

IV. CONCLUSION

The main goal of this research was to present a theoretical description for the phenomenon of charge regulation as affected by the presence of polyvalent ions. We formulated a SC dressed ion theory, describing the electrostatic interactions between macroions undergoing charge regulation processes, in a mixture of monovalent-polyvalent salt solution. Using the proper description of charge regulation, suitable for treating it in the field-theoretic framework, the partition function is derived in the form of a virial expansion valid for small concentration of the polyvalent salt. The first term in such expansion corresponds to the direct interaction between titratable macroions in a monovalent salt solution, while the first order correction stems from the interaction of the polyvalent ion with each macroion. The asymmetry in the ionic solution allowed us to decouple the system into the monovalent salt component, addressed on a weak coupling level, while the polyvalent ion component was assumed to be strongly coupled with macroions. In both cases, titration of the macroions is treated on the Gaussian approximation level involving an expansion of the exact charge regulation free energy valid in general for highly charged macroions.

We have shown that the presence of polyvalent ion brings about a strong attraction between two symmetrically charged macroions. In the case when polyvalent ion acts like a counterion, the attraction is big enough to overcome repulsion between the macroions, while in the opposite case, the repulsion between macroions turns into a small attraction at large separations due to the asymmetric charge fluctuations at macroions surface, induced by the presence of the polyvalent salt. The polyvalent-ion mediated attraction remains appreciable even at conditions, when macroions reach

the point of zero charge. From the derived expressions for the free energy of interaction, it is clear that the polyvalent ion-mediated attractive contribution stems from the charge-induced charge type of the interaction, since it is proportional to the square of the polyvalent ion charge. Our results show that the polyvalent ion-mediated attraction is significantly stronger than the KS interaction, obtained for the same system described in the WC regime, i.e., without any polyvalent salt. We therefore derived a generalized form of the KS interaction, with the range of validity extended to the regime, where their original KS derivation fails.

By calculating the interaction between point-like charge regulated macroions in the WC and SC approximations, based within the field representation of the partition function, we have opened a new way to analyze the interactions between proteins in ionic solutions. Our approach brings together the charge regulation theory as well as the general WC and SC dichotomy of the field representation of the partition function of Coulomb fluids. The results seem interesting and we will endeavor to compare them with detailed Monte Carlo simulations in the near future.

ACKNOWLEDGMENTS

N.A. acknowledges the financial support by the Slovenian Research Agency under the young researcher grant. R.P. acknowledges the financial support by the Slovenian Research Agency under the grant P1-0055. The authors would also like to thank Profs. Mikael Lund, David Andelman, and Michal Borkovec as well as Dr. Tomer Markovich and Dr. Gregor Trefalt for illuminating discussions on the subject of charge regulation and electrostatic interactions between charge-regulated macroions.

APPENDIX: FLUCTUATING ELECTROSTATIC POTENTIAL PROPAGATOR

The propagator $G_1(\varphi_1, \varphi_2)$, describing how the electrostatic potential propagates from one macroion to another in the presence of a polyvalent ion q at \mathbf{r}_0 , is given as

$$G_1(\varphi_1, \varphi_2) = \int \mathcal{D}[\varphi(\mathbf{r})] \delta(\varphi(\mathbf{r}_1) - \varphi_1) \delta(\varphi(\mathbf{r}_2) - \varphi_2) e^{-\frac{1}{2} \int d\mathbf{r} d\mathbf{r}' \varphi(\mathbf{r}) u_{DH}^{-1}(\mathbf{r}, \mathbf{r}') \varphi(\mathbf{r}') + i\beta \int_V \rho(\mathbf{r}) \varphi(\mathbf{r}) d\mathbf{r}} \quad (\text{A1})$$

with $\rho = q\delta(\mathbf{r} - \mathbf{r}_0)$. The delta function entering the above expression can be written via a Fourier integral representation as

$$\delta(\varphi(\mathbf{r}_i) - \varphi_i) = \int d\mathbf{k} e^{ik(\varphi(\mathbf{r}_i) - \varphi_i)} = \int d\mathbf{k} e^{-ik\varphi_i + ik \int d\mathbf{r} \rho_i(\mathbf{r}) \varphi(\mathbf{r})}, \quad (\text{A2})$$

where $\rho_i(\mathbf{r}) = \delta(\mathbf{r} - \mathbf{r}_i)$, $i = 1, 2$. One notes that this is an ordinary and not a functional Fourier integral representation, as the propagator is defined for two vertex points in the real space. Our strategy now will be to first evaluate the functional integral over the fluctuating electrostatic potential field $\varphi(\mathbf{r})$ and then calculate the remaining integral over the auxiliary fields stemming from the Fourier representation of the delta functions. Therefore it follows that

$$G_1(\varphi_1, \varphi_2) = \int dk_1 e^{-ik_1\varphi_1} \int dk_2 e^{-ik_2\varphi_2} \int \mathcal{D}[\varphi(\mathbf{r})] \times \exp \left[-\frac{1}{2} \int d\mathbf{r} d\mathbf{r}' \varphi(\mathbf{r}) u_{DH}^{-1}(\mathbf{r}, \mathbf{r}') \varphi(\mathbf{r}') + i \int [t(\mathbf{r}) + \beta q e_0 \delta(\mathbf{r} - \mathbf{r}_0)] \varphi(\mathbf{r}) d^3\mathbf{r} \right] \quad (\text{A3})$$

with the field $t(\mathbf{r})$ denoting

$$t(\mathbf{r}) = k_1 \rho_1(\mathbf{r}) + k_2 \rho_2(\mathbf{r}).$$

The above integral is a general Gaussian functional integral for the fluctuating potential $\varphi(\mathbf{r})$ and can be evaluated explicitly and exactly. The result is then an ordinary Gaussian integral over the variables k_1 and k_2 .

One has in fact

$$\delta(\varphi(\mathbf{r}_1) - \varphi_1) \delta(\varphi(\mathbf{r}_2) - \varphi_2) = \int dk_1 e^{ik_1(\varphi(\mathbf{r}_1) - \varphi_1)} \int dk_2 e^{ik_2(\varphi(\mathbf{r}_2) - \varphi_2)} \quad (\text{A4})$$

after which one can derive

$$G_1(\varphi_1, \varphi_2) = \det u_{DH}^{-1/2}(\mathbf{r}, \mathbf{r}') \int dk_1 e^{-ik_1\varphi_1} \int dk_2 e^{-ik_2\varphi_2} e^{-\frac{1}{2} \int d\mathbf{r} d\mathbf{r}' [t(\mathbf{r}) + \beta q e_0 \delta(\mathbf{r} - \mathbf{r}_0)] u_{DH}(\mathbf{r}, \mathbf{r}') [t(\mathbf{r}') + \beta q e_0 \delta(\mathbf{r}' - \mathbf{r}_0)]} \\ = \det u_{DH}^{-1/2}(\mathbf{r}, \mathbf{r}') \int_{-\infty}^{+\infty} \int_{-\infty}^{+\infty} dk_1 dk_2 e^{-ik_1\varphi_1 - ik_2\varphi_2} \times e^{-\frac{1}{2} k_1^2 u_{DH}(\mathbf{r}_1, \mathbf{r}_1) - \frac{1}{2} k_2^2 u_{DH}(\mathbf{r}_2, \mathbf{r}_2) - k_1 k_2 u_{DH}(\mathbf{r}_1, \mathbf{r}_2)} \\ \times e^{-\frac{1}{2} \beta^2 q^2 e_0^2 u_{DH}(\mathbf{r}_0, \mathbf{r}_0) - \frac{1}{2} \beta q e_0 [2k_1 u_{DH}(\mathbf{r}_0, \mathbf{r}_1) + 2k_2 u_{DH}(\mathbf{r}_0, \mathbf{r}_2)]}. \quad (\text{A5})$$

The fluctuating electrostatics potential propagator has thus been reduced to simple integrals in the variable $\mathbf{k} = (k_1, k_2)$.

The vacuum fluctuations term, $\det u_{DH}^{-1/2}(\mathbf{r}, \mathbf{r}')$, as well as the polyvalent ion bare self-interaction term $e^{-\frac{1}{2} \beta^2 q^2 e_0^2 u_{DH}(\mathbf{r}_0, \mathbf{r}_0)}$, will be neglected since they do not depend on the separation between the point-like macroions and thus make no contribution to the interactions between them. If the macroions had finite dimensions $\det u_{DH}^{-1/2}(\mathbf{r}, \mathbf{r}')$ would describe the thermal Casimir (van der Waals) interactions between them.

If one introduces a 2D wave-vector \mathbf{k} , together with the Einstein summation convention, this integral can be rewritten simply as

$$G_1(\varphi_1, \varphi_2) = \iint d^2\mathbf{k} e^{-f(\mathbf{k})}, \quad (\text{A6})$$

where we introduced the function $f(\mathbf{k})$ as

$$f(\mathbf{k}) = k_j (i\varphi_j + \beta q e_0 u_{DH}(\mathbf{r}_0, \mathbf{r}_j)) + \frac{1}{2} k_j u_{DH}(\mathbf{r}_j, \mathbf{r}_l) k_l. \quad (\text{A7})$$

Since this is a Gaussian integral, it can be evaluated explicitly as

$$G_1(\varphi_1, \varphi_2) = \det u_{DH}^{-1/2}(\mathbf{r}, \mathbf{r}') \exp \left[\frac{1}{2} (i\varphi_i + \beta q e_0 u_{DH}(\mathbf{r}_0, \mathbf{r}_i)) u_{DH}^{-1}(\mathbf{r}_i, \mathbf{r}_j) (i\varphi_j + \beta q e_0 u_{DH}(\mathbf{r}_0, \mathbf{r}_j)) \right]. \quad (\text{A8})$$

The above expressions typically involve the Coulomb or the DH self-interaction $u_{DH}(\mathbf{r}, \mathbf{r})$, or indeed its inverse. This quantity is not unambiguously defined because the field representation does not describe the sizes of the charges in a consistent description. However, one usually assumes that the finite size can be approximately included as an ultraviolet cutoff in the Fourier space, or indeed by assuming that one has the Coulomb self-energy $u_{DH}(\mathbf{r}, \mathbf{r}) \sim 1/4\pi\epsilon\epsilon_0 a$, where a is the radius of the charge; to be consistent one needs to take $\kappa a \rightarrow 0$ in the DH expression, which gives its bare Coulomb limit.

⁴E. J. Verwey and J. T. G. Overbeek, *Theory of the Stability of Lyophobic Colloids* (Elsevier, Amsterdam, 1948).

⁵S. H. Behrens and M. Borkovec, *J. Phys. Chem. B* **103**, 2918-2928 (1999).

⁶S. H. Behrens and M. Borkovec, *J. Chem. Phys.* **111**, 382-385 (1999).

⁷R. Podgornik and V. A. Parsegian, *J. Chem. Phys.* **99**, 9491-9496 (1995).

⁸K. Linderstrom-Lang, C. R. Trav. Lab. Carlsberg. **15**, 1-28 (1924).

⁹J. Kirkwood and J. B. Shumaker, *Proc. Natl. Acad. Sci. U. S. A.* **38**, 855 (1952).

¹⁰J. Kirkwood and J. B. Shumaker, *Proc. Natl. Acad. Sci. U. S. A.* **38**, 863 (1952).

¹¹B. W. Ninham and V. A. Parsegian, *J. Theor. Biol.* **31**, 405-428 (1971).

¹²T. Markovich, D. Andelman, and R. Podgornik, in *Handbook of Lipid Membranes*, edited by C. Safinya and J. Raedler (Taylor & Francis, 2016), Chap. 9.

¹³D. Chan, J. W. Perram, L. R. White, and T. W. Healy, *J. Chem. Soc., Faraday Trans. 1* **71**, 1046-1057 (1975).

¹⁴D. C. Prieve and E. Ruckenstein, *J. Theor. Biol.* **56**, 205-228 (1976).

¹⁵R. Pericet-Camara, G. Papastavrou, S. H. Behrens, and M. Borkovec, *J. Phys. Chem. B* **108**, 19467-19475 (2004).

¹⁶H. H. von Grunberg, *J. Colloid Interface Sci.* **219**, 339-344 (1999).

¹⁷G. S. Longo, M. Olvera de la Cruz, and I. Szleifer, *Soft Matter* **8**, 1344-1354 (2012).

¹A. Warshel, P. K. Sharma, M. Kato, and W. W. Parson, *Biochim. Biophys. Acta* **1764**, 1647-1676 (2006).

²W. M. Gelbart, A. Ben-Shaul, and D. Roux, *Micelles, Membranes, Microemulsions, and Monolayers*, 1st ed. (Partially Ordered Systems) (Springer, 1994).

³A. E. Nel, L. Madler, D. Velegol, T. Xia, E. M. Hoek, P. Somasundaran, F. Klaessig, V. Castranova, and M. Thompson, *Nat. Mater.* **8**, 543-557 (2009).

- ¹⁸G. S. Longo, M. Olvera de la Cruz, and I. Szleifer, *ACS Nano* **7**, 2693-2704 (2013).
- ¹⁹N. Adžić and R. Podgornik, *Euro. Phys. J. E* **37**, 49 (2014).
- ²⁰N. Adžić and R. Podgornik, *Phys. Rev. E* **91**, 022715 (2015).
- ²¹A. C. Maggs and R. Podgornik, *EPL* **108**, 68003 (2014).
- ²²T. Markovich, D. Andelman, and R. Podgornik, *Europhys. Lett.* **106**, 16002 (2014).
- ²³T. Markovich, D. Andelman, and R. Podgornik, *EPL* **113**, 26004 (2016).
- ²⁴H. Diamant and D. Andelman, *J. Phys. Chem.* **100**, 13732 (1996).
- ²⁵P. M. Biesheuvel, *J. Colloid Interface Sci.* **257**, 514-522 (2004).
- ²⁶D. Ben-Yaakov, D. Andelman, D. Harries, and R. Podgornik, *J. Phys.: Condens. Matter* **21**, 424106 (2009).
- ²⁷D. Ben-Yaakov, D. Andelman, R. Podgornik, and D. Harries, *Curr. Opin. Colloid Interface Sci.* **16**, 542-550 (2011).
- ²⁸R. Podgornik and V. A. Parsegian, *Chem. Phys.* **154**, 477-483 (1991).
- ²⁹D. Leckband and S. Sivasankar, *Colloids Surf., B* **14**, 83-97 (1999).
- ³⁰D. Leckband and J. Israelachvili, *Q. Rev. Biophys.* **34**, 105-267 (2001).
- ³¹M. Lund and B. Jonsson, *Biochemistry* **44**, 5722 (2005).
- ³²F. L. Barroso da Silva, M. Lund, B. Jonsson, and T. Åkesson, *J. Phys. Chem. B* **110**, 4459 (2006).
- ³³F. L. Barroso da Silva and B. Jonsson, *Soft Matter* **5**, 2862 (2009).
- ³⁴R. J. Nap, A. L. Bozic, I. Szleifer, and R. Podgornik, *Biophys. J.* **107**, 1970 (2014).
- ³⁵R. R. Netz, *J. Phys.: Condens. Matter* **15**, S239 (2003).
- ³⁶I. Borukhov, D. Andelman, R. Borrega, M. Cloitre, L. Leibler, and H. Orland, *J. Phys. Chem. B* **104**, 11027 (2000).
- ³⁷R. Kumar, B. G. Sumpter, and S. M. Kilbey, *J. Chem. Phys.* **136**, 234901 (2012).
- ³⁸R. Kumar, B. G. Sumpter, and S. M. Kilbey, *Langmuir* **27**, 10615 (2011).
- ³⁹W. B. S. de Lint, P. M. Biesheuvel, and H. Verweij, *J. Colloid Interface Sci.* **251**, 131 (2002).
- ⁴⁰C. Y. Leung, L. C. Palmer, S. Kewalramani, B. Qiao, S. I. Stupp, M. Olvera de la Cruz, and M. J. Bedzyk, *Proc. Natl. Acad. Sci. U. S. A.* **110**, 16309 (2013).
- ⁴¹G. Pabst, N. Kucerka, N. Mu-Ping, and J. Katsaras, *Liposomes, Lipid Bilayers and Model Membranes: From Basic Research to Application* (CRC Press, New York, 2014).
- ⁴²A. Naji, M. Kanduč, J. Forsman, and R. Podgornik, *J. Chem. Phys.* **139**, 150901 (2013).
- ⁴³M. Kanduc, A. Naji, J. Forsman, and R. Podgornik, *J. Chem. Phys.* **132**, 124701 (2010).
- ⁴⁴M. Kanduc, A. Naji, J. Forsman, and R. Podgornik, *Phys. Rev. E* **84**, 011502 (2011).
- ⁴⁵R. R. Netz, *Eur. Phys. J. E* **5**, 557 (2001).
- ⁴⁶A. G. Moreira and R. R. Netz, *Eur. Phys. J. E* **8**, 33 (2002).
- ⁴⁷H. Boroudjerdi, Y. W. Kim, A. Naji, R. R. Netz, X. Schlagberger, and A. Serr, *Phys. Rep.* **416**, 129 (2005).
- ⁴⁸M. Kanduč, A. Naji, J. Forsman, and R. Podgornik, *J. Chem. Phys.* **137**, 174704 (2012).
- ⁴⁹R. H. French, V. A. Parsegian, R. Podgornik *et al.*, *Rev. Mod. Phys.* **82**, 1887-1944 (2010).
- ⁵⁰R. Podgornik and B. Žekš, *J. Chem. Soc., Faraday Trans. 2* **84**, 611-631 (1988).
- ⁵¹V. Valmacco, M. Elzbieciak-Wodka, D. Herman, G. Trefalt, P. Maroni, and M. Borkovec, *J. Colloid Interface Sci.* **427**, 108-115 (2016).

UNIVERSITY OF LJUBLJANA
FACULTY OF MATHEMATICS AND PHYSICS
DEPARTMENT OF PHYSICS

Nataša Adžić

**VARIETIES AND PHENOMENOLOGY
OF ELECTROSTATIC INTERACTIONS
IN PROTEIN PHYSICS**

Doctoral thesis

ADVISER: Prof. Dr. Rudolf Podgornik

Ljubljana, 2016

UNIVERZA V LJUBLJANI
FAKULTETA ZA MATEMATIKO IN FIZIKO
ODDELEK ZA FIZIKO

Nataša Adžić

**RAZNOLIKOST IN FENOMENOLOGIJA
ELEKTROSTATIČNIH INTERAKCIJ
V FIZIKI PROTEINOV**

Doktorska disertacija

MENTOR: Prof. Dr. Rudolf Podgornik

Ljubljana, 2016

Acknowledgements

First and foremost, I thank my adviser, professor *Rudolf Podgornik*. His immense knowledge and bright ideas were the most important ingredients for successful realization of this Thesis. Constantly spreading his charisma and sense of humour, he was always taking care for the friendly and inspiring working atmosphere. It was a great pleasure and honour for me to work under his guidance. I am infinitely grateful for the constant support, help, motivation, enthusiasm, patience and freedom he provided me with.

Special thanks go to *Anže Lošdorfer Božič*, my first office-mate, whose unrestricted help I could always count on.

Additionally, I am thankful to professor *Primož Zihlerl* and *Matej Kanduč* for reading the Thesis thoroughly and giving useful comments and suggestions which helped to improve it.

I thank professor *Mikael Lund* and *Björn Persson* for hosting me at Lund University and sharing with me tactics and tricks for studying the Coulomb fluids with Monte Carlo simulations. I also thank *Gregor Trefalt* and professor *Michal Borkovec* for useful discussions on the charge regulation problems.

The ones who gave a special essence to my PhD path are those who have been fighting the similar battles in the field of Science. So, the young researches of F1 department: *Zala, Ivana, Urška, Labrini, Urša, Anže, Luca, Matej, Andreas, Bing, Tilen, Žiga, Jan, Vasja, Luka, Ivan, Admir, Ambrož, Denis, Dario*, thank you for the alliance. I am also enormously thankful to my friends *Dragana, Nevena, Jelena, Ivna, Danijela, Biljana, Mojca, Vladimir, Miroslav, Rok* for all their love, support, adventurism and all unforgettable and humorous moments we had at and out of the Institute...

My gratitude to the chief of our department, professor *Svjetlana Fajfer* is beyond the words, for her mother-like care for all the students in the department, which made our workplace feel like home. Moreover, my thanks goes to department secretary *Nevenka Hauschild* for helping me with all administrative tasks. I am also grateful to professor *Bosiljka Tadić* for the nice moments and books we shared.

And last but not least, I thank my *family* for their unceasing support.

The Thesis was completed at the Department of Theoretical Physics, Jožef Stefan Institute with the financial support of the Slovenian Research Agency under the young researcher grant.

Abstract

The main subject of this Thesis was the full examination of all varieties of electrostatic interaction, existing between proteins immersed in an ionic solution. Inspired by the work of Kirkwood and Shumaker, our goal was to investigate the interaction that they had proposed in a more general theoretic framework, obtaining the results also valid in the regimes where the original derivation fails. The general idea was to broaden the existing modern field-theoretic approach to the statistical mechanics of Coulomb fluid, by including within this framework the concept of charge regulation in the form of an additional field-dependent general surface free energy. This line of thought would be a significant contribution to the development of the theory of electrostatic interactions between macromolecules, based on the generalization of the most up-to-date formal approach that has heretofore still been restricted to a narrow part of the parameter space corresponding to the constant charge on the macromolecular surface. However, the charge of a macroion surface with dissociable molecular groups always depends strongly on the acid–base equilibrium, which defines the fraction of acidic (basic) groups that are dissociated, and it was necessary to incorporate this property consistently into a field-theoretic formulation of this system and to see to what kind of consequences it may lead. Our work leads to a complete reformulation of the theory of electrostatic interaction between macromolecules that bear dissociable charge groups and allows for a consistent inclusion of surface chemical parameters such as dissociation energy as well as solution parameters such as pH into a general theory of electrostatic interactions between macromolecules. The field-theoretic framework of the theory allows to consistently generalize the ideas of Kirkwood and Shumaker, or indeed of any electrostatic interaction that includes charge regulation, in such a way that one can use advanced concepts and methods of the Coulomb fluid statistical mechanics in order to analyze its salient features in various regions of the parameter space. In this work we have analyzed four different model systems. The first two model systems relate to counterion-mediated electrostatic interactions of planar charge regulated surfaces treated in the weak electrostatic coupling regime and electrostatic interaction of two point-like charge regulated macroions, again treated in the weak electrostatic coupling regime. The other two model systems investigate how the presence of polyvalent, strongly electrostatically coupled ions in the bathing solution influences the interactions between charge regulated macroions, firstly described within the model of charged spheres and then within the model of flat charged plates. All four model systems also capture and explain in detail the phenomenon of electrostatic attraction between electroneutral macroions. In this way, we were able to cover a large portion of the parameter space in the case of charge regulated macroions, paving the way to new developments in the theory of electrostatic interactions not conceivable within the original theoretical framework as pioneered by Kirkwood and Shumaker.

Keywords: electrostatics, charge regulation, weak coupling, strong coupling, dressed ions, proteins

PACS: 78.30.cd, 82.35.Rs, 87.10.Ca, 87.15.km

Izvleček

Glavna tema doktorske disertacije je celosten pregled vseh vrst elektrostatičnih interakcij med proteini v ionski raztopini. Cilj, motiviran z delom Kirkwooda in Shumakerja (KS), je opis elektrostatičnih interakcij med proteini v bolj splošnem teoretičnem okviru, s katerim smo prišli tudi do rezultatov, veljavnih v režimu, ki ga originalna KS teorija ne uspe opisati. Splošna ideja pristopa je formulacija problema v jeziku teorije polja, ki bi razširil obstoječi opis coulombskih tekočin z vključitvijo regulacije naboja preko dodatnega površinskega člana v prosti energiji. Standardne teorije elektrostatičnih interakcij so omejene na ozek del parametrskega prostora, ki ustreza konstantnemu naboju na površini makromolekule, tako da omenjena razširitev predstavlja pomemben prispevek k razvoju teorije elektrostatičnih interakcij med makromolekulami. Še posebej zato, ker naboj na površinah makromolekul ni konstanten, ampak je močno odvisen od kislinsko-bazičnega ravnotežja disociirajočih molekularnih delcev na površinah makromolekul. V tezi tako predstavimo reformulacijo teorije elektrostatičnih interakcij, ki zajema tudi koloide z nabitimi disociabilnimi skupinami. V okviru teorije polja to napravimo tako, da v teorijo vključimo kemijske parametre, ki se nanašajo na disociabilne površine, ter parametre raztopine, kot je denimo pH vrednost. Na ta način začrtamo smer, v kateri lahko posplošimo ideje Kirkwooda in Shumakerja oziroma opišemo kakršnekoli elektrostatične interakcije, ki zajemajo regulacijo naboja. V disertaciji analiziramo štiri različne sisteme: dva sistema opisujeta šibko interakcijo tako za ravne plošče, regulacijsko nabite v raztopini protiionov, kot tudi točkastih makroionov regulacijskega naboja v raztopini monovalentne soli. Druga dva sistema opisujeta vpliv polivalentnih ionov, ki inducirajo močne ionske korelacije, na interakcije med makroioni s fluktuirajočim nabojem, ki jih enkrat modeliramo kot točkaste ione, drugič pa kot ravne plošče. Vsi štirje modeli opišejo pojav elektrostatičnega privlaka med elektronevtralnimi makroioni. Na ta način uspemo pokriti veliko območje parametrskega prostora in utremo pot razvoju novih teorij elektrostatičnih interakcij med proteini.

Ključne besede: elektrostatika, regulacija naboja, šibka sklopitev, močna sklopitev, teorija odetih ionov, proteini

PACS: 78.30.cd, 82.35.Rs, 87.10.Ca, 87.15.km

Contents

1 Introduction	13
1.1 Electrostatic interactions in colloidal matter	13
1.2 Proteins, charge regulation and Kirkwood – Shumaker interaction	15
1.3 Overview of the Thesis	20
2 Theoretical background	23
2.1 Qualitative understanding of Coulomb fluids	23
2.2 Field-theoretic approach	25
2.2.1 Weak-coupling limit	28
2.2.2 Strong-coupling limit	29
2.2.3 Dressed counterions theory	30
2.3 Charge regulation phenomenology	32
3 Counterion-mediated interactions of planar charge regulated surfaces	37
3.1 Model	38
3.2 Field-theoretic description of model	39
3.3 Mean-field approximation	40
3.4 Second-order (Gaussian) correction	41
3.5 Second-order correction — interaction free energy	44
3.6 Numerical results	46
3.7 Conclusions	50
4 Titrating macroions in monovalent salt solution	51
4.1 Model	51
4.2 Symmetric–asymmetric charges on proteins	55
4.3 Discussion	58
4.3.1 Saddle-point approximation	60
4.3.2 Gaussian approximation	61
4.3.3 Comparison with Debye–Hückel and Kirkwood– Shumaker forms	62
4.4 Protein-like macroions	63
4.5 Conclusions	67
5 Titrating macroions in polyvalent salt solution	69
5.1 General formalism	70
5.1.1 Model	70
5.1.2 Charge regulation	70
5.1.3 Field-theory – general formalism	72

5.1.4	Dressed ion theory and charge regulation	74
5.1.5	Approximate macroion interaction free energy	78
5.2	Results and discussion	80
5.3	Conclusions	84
6	Salt-mediated interactions of planar charge regulated surfaces	87
6.1	General formalism	88
6.1.1	Model	88
6.1.2	Charge regulation	88
6.1.3	Dressed ion theory	90
6.2	Planar surfaces in presence of monovalent salt	91
6.2.1	Derivation of partition function	91
6.2.2	Comparison with van der Waals and Kirkwood–Shumaker interactions	93
6.3	Planar surfaces in presence of polyvalent salt	95
6.3.1	Derivation of partition function	95
6.3.2	Comparison with fixed charge results	97
6.3.3	Results and discussion	98
6.4	Conclusions	101
7	Concluding remarks	103
A	Exact evaluation of Feynman path integral	107
B	Derivation of field propagator $G(\varphi_1, \varphi_2)$	111
C	Saddle-point approximation	113
D	Gaussian approximation	115
E	Derivation of field propagator $G_1(\varphi_1, \varphi_2)$	117
F	Saddle-point and Gaussian fluctuations of volume integral \mathcal{F}	119
G	Self energy of polyvalent ion	121
Razširjeni povzetek		123
H.1	Uvod	123
H.1.1	Proteini, regulacija naboja in interakcija Kirkwood-Shumakerja	124
H.2	Interakcije površin reguliranega naboja v prisotnosti protiionov	125
H.3	Interakcije točkastih makroionov reguliranega naboja v prisotnosti monovalentne soli	128
H.4	Interakcije točkastih makroionov reguliranega naboja v prisotnosti polivalentne soli	130
H.5	Interakcije površin reguliranega naboja v prisotnosti polivalentne soli	131
H.6	Zaključek	132
Bibliography		135

Chapter 1

Introduction

1.1 Electrostatic interactions in colloidal matter

Electrostatic interaction is of fundamental importance in governing the behavior of biological systems on molecular level [1, 2]. Soft and biological materials are typically composed of macromolecules such as polymers, colloids, and proteins [3, 4, 5, 6]. These macromolecules usually acquire charge when dipped into a polar solution such as water [7]. This happens due to dissociation of chemical groups on their surface, while releasing mobile ions into the solution. Another mechanism of charging involves small charged molecules, such as salt ions that can physically or chemically adsorb to a surface, thereby leading to an effective surface charge. In practice, one typically encounters a mixture of these two mechanisms, so that the effective charge of a surface is controlled by the distribution of acidic and basic surface groups, solution pH, and bulk concentration of charged solutes. In a salt solution, each charged object (macromolecule, macroion) is surrounded by a cloud of neutralizing oppositely charged microscopic ions, referred to as *counterions*, as well as ions of the same sign, referred to as *coions*. These particles form loosely bound ionic clouds around macroions and in this way tend to screen their charges. The distribution of charges in an ionic cloud is given by the competition between electrostatic interactions, acting to bind them, and the entropy of ions in solution, which tends to disperse them [8]. In order to understand the behavior of macromolecules, one then needs to understand the behavior of ionic clouds they are surrounded with [9, 10].

A century long history of electrostatic interactions in colloidal matter starts with Louis Georges Gouy and David Leonard Chapman, who were the first to seek a tractable description for many-body Coulomb systems, while considering a problem of counterion distribution near a planar charged wall, known as the *double layer problem* [11, 12]. Deriving and solving the Poisson–Boltzmann (PB) equation, they found that counterion distribution profile decays algebraically as a function of the separation from the wall with a characteristic, Gouy–Chapman length, which is proportional to the surface charge density of the wall. Ten years later, Peter Debye and Erich Hückel contributed significantly to the understanding of ionic screening in electrolyte solutions [13]. By linearizing the Poisson–Boltzmann equation, they found that the screening leads to an exponential decay of the potential around a point-like charge. This Debye–Hückel (DH) screening is connected with the linearization approximation valid for small potentials in the system, which is usually the case when charges involved in are small enough (for example the charged mem-

branes have the surface charge $\sigma \sim 1 e_0/\text{nm}^2$ in 1:1 salt solution, when DH screening length in water at room temperature becomes $\kappa^{-1} = 0.305 \text{ nm}/\sqrt{n_0 [\text{mM}]}$, where the salt concentration n_0 is given in moles). With these two approaches one could describe the repulsion between like-charge macromolecules in an ionic solution [14]. Two decades later, when the Poisson–Boltzmann electrostatic repulsion was combined with the van der Waals attraction, it was possible to explain the stability of colloidal systems and processes of coagulation through the theory put forward by Boris Derjaguin, Lev Landau, Evert Verwey, and Theodoor Overbeek, also known as the DLVO theory [15, 16]. Being of a mean-field type, this theory fails to describe the strongly-correlated systems, such as a macroion in a polyvalent salt solution [17].

Strong correlations were first observed in a computer simulations by Lars Gulbrand and coworkers, based on a suggestion by Dušan Bratko at that time working at the University of Ljubljana, in the form of a strange attraction between like-charged surfaces that may exist due to correlations between the charges in the vicinity of the charged, bounding walls in the system [18]. This observation represents one of the major advances in colloid science in the past century and ranks among the top scientific discoveries of that time. Soon after the like-charge attraction was predicted theoretically using simulations, it has been observed also in experiments by Johan Marra in 1986 [19], when studying the interaction between two planar surfaces bearing charge of the same sign, immersed into an aqueous solution with dispersed divalent ions originating in the dissociation of calcium chloride. Later on, this phenomenon has been verified in various experiments, while a simple, intuitive theoretical picture explaining it remained an unsolved problem.

A significant improvement of theoretical approaches to many-body electrostatics came with Samuel Edwards and Andrew Lenard who were the first to implement a field theoretical approach to the charged systems, deriving the grand canonical partition function as a functional integral over a fluctuating potential [20]. Subsequently, in 1988, Rudolf Podgornik and Boštjan Žekš showed that the saddle-point of the field-theoretic formulation corresponds to the PB equation [21]. With this realization it became possible to go beyond the PB results, calculating the one-loop (Gaussian) corrections to the mean-field solution [22]. Due to the perturbative nature of the loop formalism, the attraction obtained in such a way helped only in improving the PB theory [23], but not in actually describing the like-charge attraction. Continuing in the same framework, Andre Moreira and Roland Netz were the ones who succeeded to unveil the conceptual framework standing behind this phenomenon [24, 25]. They defined the *strong coupling limit*, *SC*, relevant for highly correlated systems, in contrast to the *weak coupling limit*, *WC*, corresponding to the mean field theories. Their work was then extended by Ali Naji [26, 27, 28, 29] and later continued by Matej Kanduč and Rudolf Podgornik who, all together, contributed in providing a complete and systematic view of Coulomb fluids, composed of macromolecular surfaces with *fixed* charge distribution [10, 30, 31, 32, 33]. They also managed to upgrade the WC–SC dichotomy, deriving the proper theoretic description for asymmetric ionic mixtures, known as the *dressed counterion theory* [34, 35, 36].

Nowadays, it is a well-known fact that two like-charged macromolecules will repel or attract depending on the composition of the ionic cloud [37]. Although it is counter-intuitive that there exists an attraction between like-charged objects, it

1.2. Proteins, charge regulation and Kirkwood – Shumaker interaction

does actually happen if the cloud is composed of multivalent counterions, e.g. DNA condensation observed in the presence of multivalent cations [38, 39, 40]. This is only one manifestation of the complexity of the many-body Coulomb systems, stemming from the long-ranged nature of the interaction potential, making it a challenging problem of mesoscopic physics [1, 41].

Especially interesting players in a diverse world of colloidal electrostatics are proteins. Proteins exhibit extraordinary behavior, whose complexity has made them elusive and difficult-to-understand, especially for theoretical physicists chasing a deep understanding of fundamental laws of the protein world [42, 43]. Our main motivation was then to find proper equations describing proteins' dance, performed for a wide range of melodies played by the electrolyte solution they are surrounded with.

1.2 Proteins, charge regulation and Kirkwood – Shumaker interaction

Protein is a macromolecule composed of amino-acid (AA) subunits, bounded together with peptide bonds [43, 45]. Such polypeptide chain forms the primary structure of a protein. Due to the hydrogen bonds between non-neighboring amino acids it can be folded into an alpha-helix or a beta-sheet, representing the secondary protein structure [46, 47, 48]. The tertiary structure occurs as a result of further folding and bonding of the secondary structure. Interactions between two or more tertiary subunits lead to the quaternary structure [49], which is the most common stage of protein aggregation found in nature (Fig. 1.1). Besides, this is the most relevant stage for analysis, since the proteins express their biological function when

they are in a compactified form [50, 51]. Governed by electrostatic interactions, proteins in a quaternary structure may also form protein complexes (Fig. 1.2), such as proteasome, DNA/RNA polymerase, viral capsids, etc [52].

As biomolecules, proteins play an essential role in a vast number of processes within living organisms, including DNA replication, catalyzing metabolic reactions,

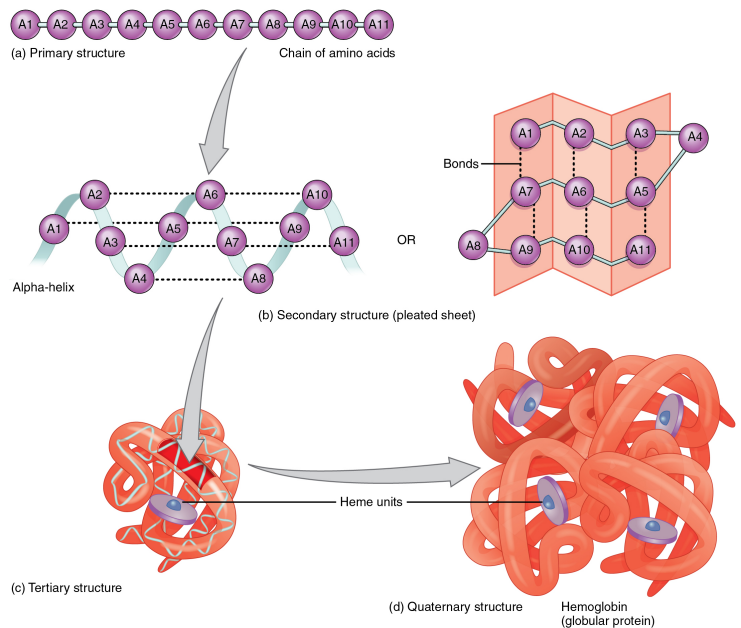


Figure 1.1: From primary to quaternary protein structure. The example shown is hemoglobin, a protein in red blood cells, which transports oxygen to body tissues [44].

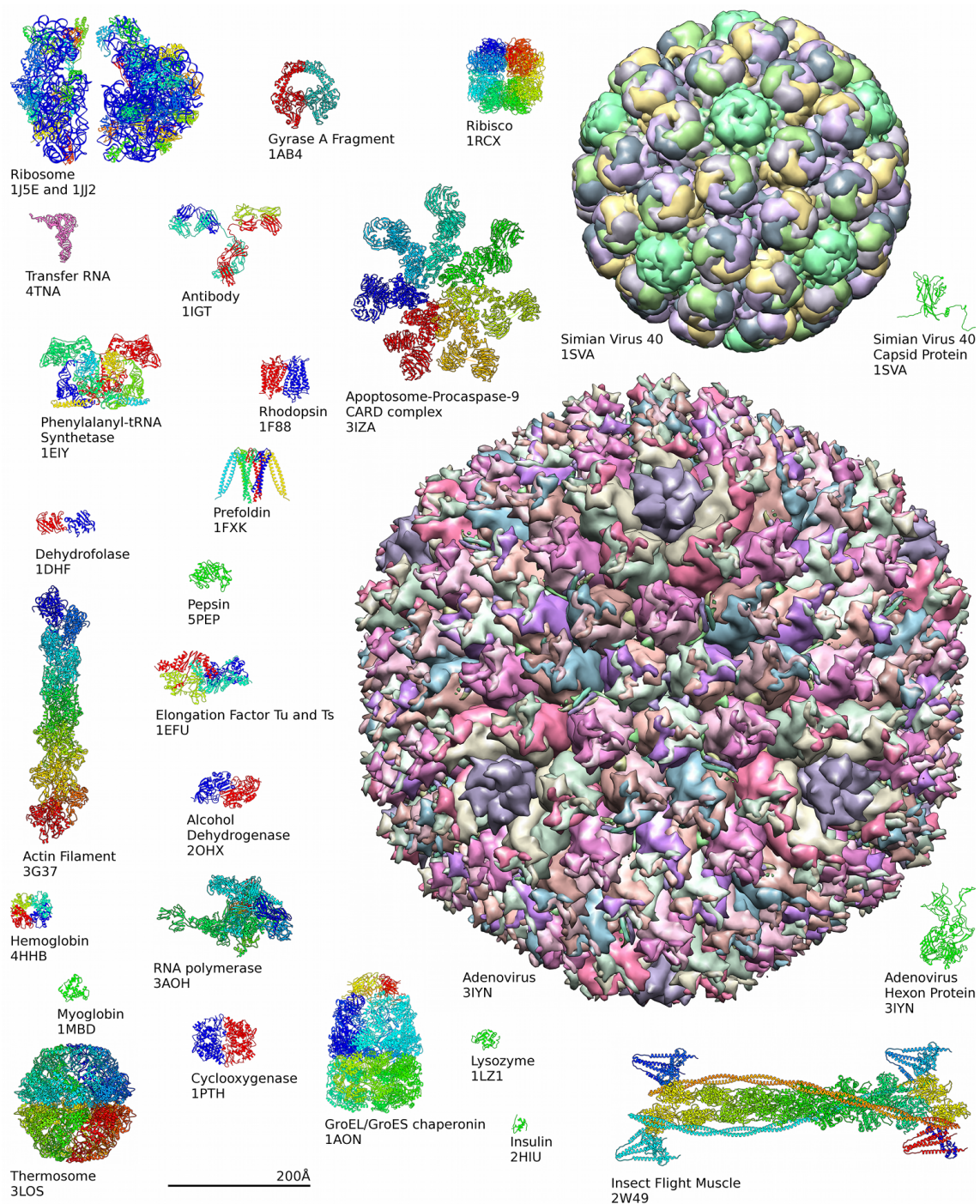


Figure 1.2: Examples of protein structures and complexes of different sizes as available from the PDB and EMDB [53].

1.2. Proteins, charge regulation and Kirkwood – Shumaker interaction

cell signaling, immune responses, etc. Some have a structural function, like the proteins in cytoskeleton or a mechanical function, like actin and myosin in muscle fiber [54]. In order to obtain a fundamental understanding of the majority of these processes, it is crucial to understand the electrostatic interactions that determine the complicated behavior of proteins. This is not an easy task, since the proteins' behavior cannot be captured with standard theories of colloidal electrostatics. What makes them so unique and challenging from theoretic perspective is their complex structure featuring many unique properties which may lead to exotic electrostatics. Namely, protein is an amphoteric molecule due to the amino acids it is composed of. Having the same general structure, each amino acid consists of the carboxylic acid group $-\text{COOH}$ which acts like a base, α -amino group $-\text{NH}_2$ which behaves like an acid, and also a variable side group (which determines the AA species). Since the carboxylic and amino groups build a peptide bond (Fig. 1.3), the charge on the protein predominantly comes from a side chain, i.e., some of the side chains contain molecular groups that can become either *deprotonated* (donating a proton into the solution), making them negatively charged, or conversely, *protonated* (accepting a proton from the solution), making them positively charged. Amino acids with side chains that can be deprotonated are aspartic and glutamic acid (Fig. 1.4), while the protonated ones are arginine, hystidine and lysine (Fig. 1.5).

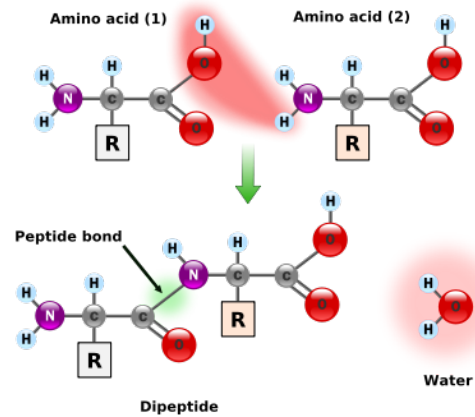


Figure 1.3: Amino acids making a peptide bond [55].

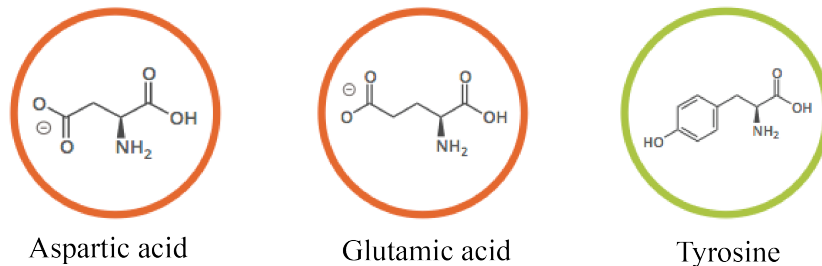


Figure 1.4: Amino acids which may bring a negative charge to a protein: by deprotonation of carboxylate on the side chain of aspartic and glutamic acid $\text{RCOOH} \rightarrow \text{RCOO}^- + \text{H}^+$ and by deprotonation of hydroxyl of the phenyl group of tyrosine $\text{ROH} \rightarrow \text{RO}^- + \text{H}^+$.

To summarize, whenever a protein is in a polar aqueous solution, the following processes of dissociation and association may proceed on its dissociable moieties lying on protein's surface:

- deprotonation of carboxylate on the side chain of aspartic and glutamic acid $\text{RCOOH} \rightarrow \text{RCOO}^- + \text{H}^+$;
- deprotonation of hydroxyl of the phenyl group of tyrosine $\text{ROH} \rightarrow \text{RO}^- + \text{H}^+$;

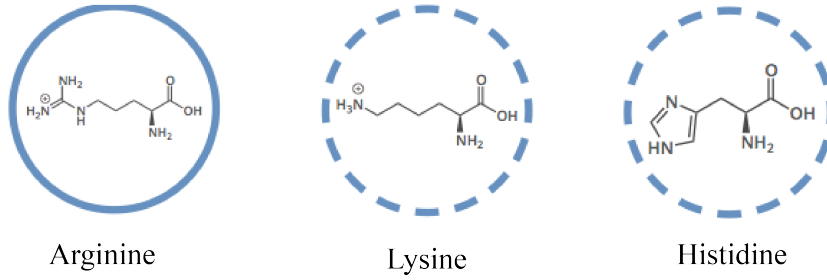


Figure 1.5: Amino acids which may bring a positive charge to a protein: by protonation of amine group of arginine and lysine and by protonation of secondary amine of histidine $\text{RNH}_3^+ \rightarrow \text{RNH}_2 + \text{H}^+$ and $\text{RNH}_2^+ \rightarrow \text{RNH} + \text{H}^+$.

- protonation of amine group of arginine and lysine $\text{RNH}_2^+ \rightarrow \text{RNH} + \text{H}^+$ and $\text{RNH}_3^+ \rightarrow \text{RNH}_2 + \text{H}^+$;
- secondary amine group of histidine can also contribute a charge $\text{RNH}_2^+ \rightarrow \text{RNH} + \text{H}^+$;
- terminal groups: deprotonation of carboxylate $\text{RCOOH} \rightarrow \text{RCOO}^- + \text{H}^+$ and protonation of α -amino $\text{RNH}_2 + \text{H}^+ \rightarrow \text{RNH}_3^+$;
- cysteine can contribute to the charge of the protein, since it consists of thiol functional end group that is a weak acid, but usually it is disregarded from consideration due to the reactivity of the thiol group which makes disulfide bonds.

The energy for dissociation of carboxyl group in water environment is roughly $14 k_B T$ making this reaction favorable [56]. Because of protonation and deprotonation processes that charge up the susceptible amino acids, the dissociation equilibrium mostly depends on the pH of solution. Each of these amino acids has its intrinsic value of pH (denoted as pK) at which it becomes charged. The respective pK s for the dissociation of the various amino acids are given at Table 1.1. For a protein,

	Asp	Glu	Tyr	Arg	His	Lys	Cys
pK	3.71	4.15	10.10	12.10	6.04	10.67	8.14

Table 1.1: pK values of amino acids' functional groups (side chains) in dilute aqueous solution, Ref. [57].

at the pH range in which it contains both a negative carboxylate and a positive α -ammonium group, one can say that a molecule is a *zwitterion*. The pH value at which the molecule has exactly zero net charge is called the *isoelectric point* (or the point of zero charge (PZC), as it is going to be used later on in the Thesis). Their mutual difference and sensitivity to solution condition can generate a wide range of diverse properties of the complexes they form [58].

One nice example of how the protein charge can respond to changes in the local electrostatic potential, coupled to the solution pH, can be seen in (Fig. 1.6), where it is shown how the surface charge of inner/outer virus shell (composed of proteins)

1.2. Proteins, charge regulation and Kirkwood – Shumaker interaction

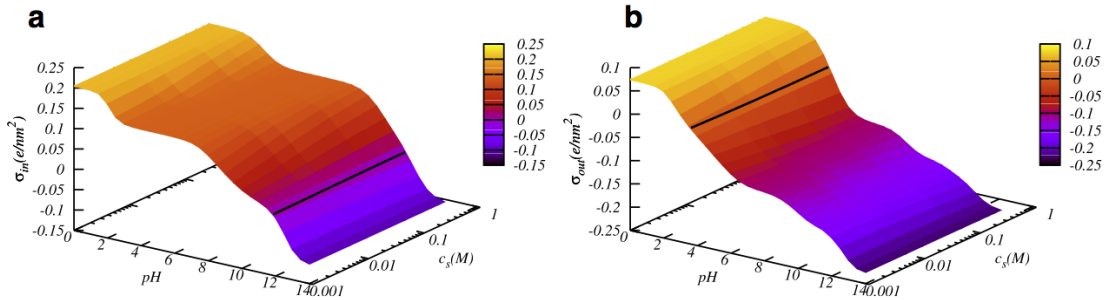


Figure 1.6: Surface charge density of inner (a) and outer (b) shell of virus capsid as a function of solution pH and salt concentration. The isoelectric point is marked with a black line. The virus under consideration is bacteriophage PP7 [57].

changes with solution pH and its salt concentration [57].

The response of the protein charge to the local electrostatic potential is a salient property of dissociable charge groups of the protein surface, see above, that is usually referred to as *charge regulation* and was first introduced in an analytical model by Barry Ninham and Adian Parsegian [59]. Charge regulation implies that the effective charge on a macroion, e.g. protein surface, responds to the local solution conditions, such as local pH, local electrostatic potential, salt concentration, dielectric constant variation and most importantly the presence of other vicinal charged groups [60]. Although charge regulation is an old concept introduced by Kaj Ulrik Linderström-Lang a century ago, modern theories of electrostatic interaction between macroions immersed in Coulomb fluids [10] mostly deal with constant surface charge of a macroion, bypassing the complications introduced by charge regulation [61, 62, 63]. For proteins this cannot work.

Since amino acids can be positively or negatively charged (or neutral), depending on the local solution conditions, the charge of the protein surface is never fixed, but at any finite temperature actually fluctuates. The existence of anomalously long-range interactions between proteins in aqueous solutions, stemming from thermal charge fluctuations of dissociable charge groups on their surface, was first examined by John Kirkwood and John Shumaker more than half a century ago [64, 65]. They studied two spherical protein molecules in an aqueous solution, supposing that one protein has ν_1 groups of intrinsic charge e_i , and the other protein ν_2 groups of intrinsic charge e_k . Defining the proton occupation number x , they wrote the charge of each protein as:

$$\begin{aligned} q_i^{(1)} &= e_i^{(1)} + e_0 x_i^{(1)}, \\ q_k^{(2)} &= e_k^{(2)} + e_0 x_k^{(2)}. \end{aligned} \quad (1.1)$$

By allowing the charge to fluctuate, it was expected that fluctuation in charge should lead to fluctuations in the electrostatic interaction, defined by:

$$V = \sum_{i=1}^{\nu_1} \sum_{k=1}^{\nu_2} \frac{q_i^{(1)} q_k^{(2)}}{\epsilon R_{ik}^{(12)}}. \quad (1.2)$$

Within the framework of statistical-mechanical *perturbation theory* they showed that when proteins reach their isoelectric point, that is, when the net charge vanishes $\langle q^{(1)} \rangle = \langle q^{(2)} \rangle = 0$, the following interaction energy remains:

$$W^{(11)}(R) = -\frac{\langle \Delta q^{(1)^2} \rangle \langle \Delta q^{(2)^2} \rangle}{2\epsilon^2 R^2 k_B T} \neq \frac{1}{R^6}. \quad (1.3)$$

The Kirkwood–Shumaker (KS) interaction was shown to scale with a lower inverse power of separation between two proteins than the notoriously long-ranged van der Waals (vdW) interaction [66]. Furthermore and contrary to vdW interactions, the KS forces are not universal, but depend on whether and how the protein charge can respond to the local electrostatic potential.

Experiments and simulations [60, 67, 68, 69] show that thermally generated charge fluctuations may indeed produce an extra attractive contribution to the interaction when proteins are close to their isoelectric point (typical situation in physiological solution). The anomalously long-range nature of that interaction can be responsible for self-assembly processes [70, 71]. Nowadays, fundamental laws of physics standing behind these processes are incomplete and one of the main aims of this doctoral research was to acquire a deeper theoretic understanding of these biologically important issues.

1.3 Overview of the Thesis

The main goal of this Thesis is to present a theory of electrostatic interactions that includes the charge regulation phenomenon in its general formalism, and, in such a way, to capture and explain all the possible effects that may ensue from this complicated thermal exchange of charges in biological matter.

In Chapter 2, we briefly present the theoretical background, starting with the history of charge regulation interaction on one side, and field-theoretic description developed for systems with fixed charges on the other. This will constitute an introduction to what follows, which is a generalized field-theoretic description of charge regulation which will be presented for four model systems in the next four chapters.

In Chapter 3, we start from the simplest model system composed of two macroscopic planar parallel surfaces with charge dissociation sites immersed in counterion-only ionic solution. A surface lattice gas model is employed and the corresponding surface part of the free energy is derived, showing that it corresponds exactly to the Ninham–Parsegian charge regulation theory. With this included in the field-theoretic representation of the grand canonical partition function, evaluated in the saddle-point approximation, we obtain *analytically and exactly* a solution also for the Gaussian fluctuations around the mean-field. This solution leads to vdW-like KS interaction, but it is fundamentally modified by the presence of dissociable charges on the bounding surfaces as well as by the counterions dissolved in the space between them.

In Chapter 4, we study the behavior of two macroions with dissociable charge groups, regulated by local variables such as pH of a solution and electrostatic potential, immersed in a monovalent salt solution, considering the cases where the net

charge can either change the sign or remains of the same sign depending on these local parameters. The charge regulation is in both cases described by the proper free energy function for each of the macroions, while the coupling between the charges is evaluated on the approximate DH level. The charge correlation functions and the ensuing charge fluctuation forces are calculated analytically and numerically. Strong attraction between like-charged macroions is found close to the point of zero charge, specifically due to *asymmetric, anticorrelated charge fluctuations* of the macroion charges. The general theory is then implemented for a system of two protein-like macroions, generalizing the form and magnitude of the KS interaction.

In Chapter [5](#), we present a theory describing the influence of polyvalent ions on the behavior of the titratable macroions. The model system consists of two spherical macroions with dissociable sites on their surfaces immersed in a mixture of monovalent and polyvalent salt. A dressed ion theory is then formulated [\[10\]](#), set in the field-theoretic framework, treating the monovalent salt in a weak coupling approximation, while the polyvalent ions are strongly coupled with macroions. Fluctuations of macroions' charge are regulated by local parameters (local electrostatic potential, pH of the solution, salt concentration). The charge regulation is described in the approximation of the point-like macroions. Our theory describes the attraction of macroions reaching the PZC and gives the general expression for the KS interaction.

In Chapter [6](#), we present a theory describing the effect of polyvalent ions on the interaction of charge regulated surfaces. The dressed-ion theory is again employed and the generalized KS interaction in planar geometry is derived.

The results are summarized in Chapter [7](#) where we also discuss possible ways of further developing the theory of charge regulation interactions.

Chapter 2

Theoretical background

In this Chapter we briefly present a field theoretic framework developed for Coulomb fluids, which is going to be used as a starting point in our research. Later on in the Thesis, we generalize it to the wider parameter and model space, to be valid for systems of our interest – those undergoing charge regulation processes. Charge regulation is not a new concept and its history will be outlined at the end of this Chapter.

2.1 Qualitative understanding of Coulomb fluids

Under the concept of *Coulomb fluids* one considers an ionic solution whose behavior is governed by electrostatic interactions. In an ionic environment each charged object (macromolecule, macroion) will be surrounded by a cloud of neutralizing particles (counterions) and the particles of the same sign (coions), which tend to screen their charge. The interaction of macromolecules strongly depends on the composition of the ionic cloud they are surrounded with. From a theoretical viewpoint, such a system represents a many-body problem, being challenging to handle because of its enormous degree of complexity. In order to get a qualitative understanding of Coulomb systems, certain complexities can be overcome by introducing various models and approximations.

The most common theoretical approach starts from a “primitive model“ where the molecular nature of the solution is neglected and treated as a continuous dielectric medium, while the ions are treated as structureless point-like or hard-sphere particles. In reality, the structure of the solvent is locally perturbed around particles, bringing about additional short-ranged solvent-mediated interactions [72, 73, 74, 75]. In most cases, the specific effects of ions as well as image charges due to dielectric inhomogeneities are neglected [73, 76]. Such models are a coarse-grained simplification of the real situation, but can nonetheless lead to a systematic and clear understanding of electrostatic effects.

To get a better impression about the length scales governing the behavior of Coulomb fluids, consider a flat plane of area S and surface charge $-\sigma$, surrounded from one side with N mobile, q -valent counterions of elementary charge e_0 (Fig. 2.1). Since the system has to be electroneutral, the number of mobile counterions will be determined by the following condition:

$$\sigma S = Nqe_0. \tag{2.1}$$

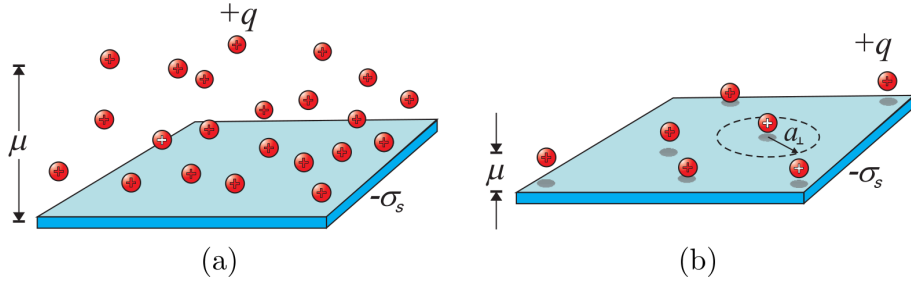


Figure 2.1: Schematic representation of two limiting regimes for counterions in the vicinity of a charged surface: (a) weak-coupling – counterions form a three dimensional diffuse layer; and (b) strong-coupling regime - counterions form a two dimensional layer at the surface [76].

The interaction Hamiltonian in units of thermal energy $k_B T$ for this system is:

$$\beta H = \sum_{i>j} \frac{q^2 l_B}{|\mathbf{r}_i - \mathbf{r}_j|} + \frac{1}{\mu} \sum_{i=1}^N z_i, \quad (2.2)$$

where \mathbf{r}_i stands for the coordinate of i -th counterion and z_i is its separation from the surface. The *Bjerrum length*

$$l_B = \frac{\beta e_0^2}{4\pi\epsilon\epsilon_0}, \quad (2.3)$$

represents the distance at which two unit charges interact electrostatically with the energy of $k_B T$. It is equal to $l_B \sim 0.7$ nm in water at room temperature. The other characteristic length is the *Gouy-Chapman length*

$$\mu = \frac{e_0}{2\pi q l_B \sigma}, \quad (2.4)$$

which gives the distance at which the counterion interacts electrostatically with the surface of surface charge density σ with the energy of $k_B T$. It also measures the thickness of the counterion layer at a charged surface, $\langle z \rangle \sim \mu$.

For planar systems where no other length scales are present, a dimensionless parameter can be introduced, which measures the ratio of the Bjerrum and Gouy-Chapman lengths,

$$\Xi \equiv \frac{q^2 l_B}{\mu}. \quad (2.5)$$

This parameter is also known as the *electrostatic coupling parameter* and was first introduced by Andre Moreira and Roland Netz [25]. It is the only parameter that governs the physical behaviour of this system, and can also be expressed as

$$\Xi = \frac{(e_0 q)^3 \sigma}{8\pi(\epsilon\epsilon_0 k_B T)^2}. \quad (2.6)$$

It scales with the cube of the counterion's valence, implying that the valence is one of the main factors that determines the behavior of the system.

One can also determine the lateral separation, a_{\perp} , between two neighboring counterions from the condition:

$$\pi a_{\perp}^2 = \frac{S}{N}. \quad (2.7)$$

Using a electroneutrality condition, Eq. (2.1), one gets an important relation

$$a_{\perp}/\mu \sim \sqrt{\Xi}, \quad (2.8)$$

which provides a deeper insight into the meaning of the electrostatic coupling parameter. Namely, if the lateral separation between counterions is much smaller than their distance from the surface, then $\Xi \ll 1$ and the system is in the *weak-coupling regime*. In this case counterions have many neighbors and form a three dimensional diffuse layer at the surface. Such a system can be described with a mean-field approximation.

On the other hand, if the lateral separation is much larger than their distance from the surface, the coupling parameter is large, $\Xi \gg 1$, defining the *strong-coupling regime*, where the counterions are surrounded by a hole of size a_{\perp} from which other counterions are depleted and form a quasi two-dimensional layer close to the surface [29, 77].

2.2 Field-theoretic approach

The essence of modern theories of Coulomb fluids [10, 78, 79] is based on field-theoretic approach, which starts from the functional integral representation of partition function [21, 80], useful in studying charged colloidal and biological systems, in which long-range electrostatic interactions play an important role. Here we first derive the grand canonical partition function for a charged system and then we outline the domains of applicability that could be reached with their basic results.

Consider the system of N mobile point-like particles of charge e_i in the electrostatic field of an external charge density distribution $\rho_e(\mathbf{r})$. For describing such an ensemble of electrostatically interacting particles it is suitable to use field-theoretic formalism to evaluate the partition function [81]. The configurational part of Hamiltonian of the system can be written as:

$$H = \frac{1}{2} \sum_{i \neq j} u(\mathbf{r}_i, \mathbf{r}_j) e_i e_j + \sum_{i=1}^N \int e_i u(\mathbf{r}, \mathbf{r}_i) \rho_e(\mathbf{r}) d^3 \mathbf{r}, \quad (2.9)$$

where $u(\mathbf{r}, \mathbf{r}_i)$ is the Green's function of the Coulomb interaction, which satisfies the relation:

$$\nabla^2 u(\mathbf{r}, \mathbf{r}_i) = -\frac{\delta(\mathbf{r} - \mathbf{r}_i)}{\epsilon \epsilon_0}, \quad (2.10)$$

i.e.

$$u(\mathbf{r}, \mathbf{r}_i) = \frac{1}{4\pi\epsilon\epsilon_0|\mathbf{r} - \mathbf{r}_i|}. \quad (2.11)$$

The operator inverse to the Green's function is referred to as the Coulomb interaction kernel [82], and is obviously given by

$$u^{-1}(\mathbf{r}, \mathbf{r}_i) = \epsilon\epsilon_0 \nabla^2 \delta(\mathbf{r} - \mathbf{r}_i). \quad (2.12)$$

The total charge density operator is given by:

$$\hat{\rho}(\mathbf{r}) = \sum_{i=1}^N e_i \delta(\mathbf{r} - \mathbf{r}_i). \quad (2.13)$$

Chapter 2. Theoretical background

The canonical partition function of the system is conventionally given by the configurational integral over all positions of the charged particles:

$$Q_N = \int d\mathbf{r}_1 \dots d\mathbf{r}_N \exp(-\beta H), \quad (2.14)$$

where the integration over kinetic degrees of freedom, being trivial in this context, is taken out of consideration. Then, Hamiltonian can be written as:

$$H = \frac{1}{2} \int d^3\mathbf{r} d^3\mathbf{r}' \hat{\rho}(\mathbf{r}) u(\mathbf{r}, \mathbf{r}') \hat{\rho}(\mathbf{r}') - Nu(\mathbf{r}, \mathbf{r}) + \int d^3\mathbf{r} d^3\mathbf{r}' \hat{\rho}(\mathbf{r}) u(\mathbf{r}, \mathbf{r}') \rho_e(\mathbf{r}'). \quad (2.15)$$

Here we subtracted the self-interaction term. The canonical partition function takes the form:

$$Q_N = \int d\mathbf{r}_1 \dots d\mathbf{r}_N \exp \left(-\frac{1}{2} \beta \int d^3\mathbf{r} d^3\mathbf{r}' \hat{\rho}(\mathbf{r}) u(\mathbf{r}, \mathbf{r}') \hat{\rho}(\mathbf{r}') + \beta Nu(\mathbf{r}, \mathbf{r}) - \beta \int d^3\mathbf{r} d^3\mathbf{r}' \hat{\rho}(\mathbf{r}) u(\mathbf{r}, \mathbf{r}') \rho_e(\mathbf{r}') \right). \quad (2.16)$$

In order to proceed, the partition function given by Eq. (2.16) can be further transformed, mainly because the density operator $\hat{\rho}$ enters in a quadratic fashion. In the next step it is suitable to introduce a unit operator as the decomposition of the unit in the form:

$$1 = \int \mathcal{D}[\hat{\rho}(\mathbf{r})] \delta(\hat{\rho} - \rho) = \iint \mathcal{D}[\hat{\rho}(\mathbf{r})] \mathcal{D}[\phi(\mathbf{r})] \exp \left(i \int d^3\mathbf{r} \phi(\mathbf{r}) \left[\sum_{i=1}^N e_i \delta^3(\mathbf{r} - \mathbf{r}_i) - \hat{\rho}(\mathbf{r}) \right] \right), \quad (2.17)$$

where we used the integral representation of the delta function. This unit operator can be introduced into the partition function at no cost. Now, the partition function becomes:

$$\begin{aligned} Q_N &= [\exp(\beta u(0))]^N \\ &\times \int d\mathbf{r}_1 \dots d\mathbf{r}_N \int \mathcal{D}[\hat{\rho}(\mathbf{r})] \int \mathcal{D}[\phi(\mathbf{r})] \exp \left(-i\beta \int \hat{\rho}(\mathbf{r}) \phi(\mathbf{r}) d^3\mathbf{r} + i\beta \sum_{i=1}^N e_i \phi(\mathbf{r}_i) \right) \\ &\times \exp \left(-\frac{1}{2} \beta \iint d^3\mathbf{r} d^3\mathbf{r}' \hat{\rho}(\mathbf{r}) u(\mathbf{r}, \mathbf{r}') \hat{\rho}(\mathbf{r}') - \beta \iint d^3\mathbf{r} d^3\mathbf{r}' \hat{\rho}(\mathbf{r}) u(\mathbf{r}, \mathbf{r}') \rho_e(\mathbf{r}') \right), \end{aligned} \quad (2.18)$$

where $u(0) = u(\mathbf{r}, \mathbf{r})$. Let us now introduce $\tilde{\rho}$ as a sum of charge density of counterions and external charge density:

$$\tilde{\rho}(\mathbf{r}) = \hat{\rho}(\mathbf{r}) + \rho_e. \quad (2.19)$$

After inserting $\tilde{\rho}$ into the partition function, we get:

$$\begin{aligned} Q_N &= [\exp(\beta u(0))]^N \exp \left(-\frac{1}{2} \beta \iint d^3\mathbf{r} d^3\mathbf{r}' \rho_e(\mathbf{r}) u(\mathbf{r}, \mathbf{r}') \rho_e(\mathbf{r}') \right) \\ &\times \int \mathcal{D}[\phi(\mathbf{r})] \int d^3\mathbf{r}_1 \dots d^3\mathbf{r}_N \exp \left(i\beta \sum_{i=1}^N e_i \phi(\mathbf{r}_i) \right) \exp \left(i\beta \int \rho_e(\mathbf{r}) \phi(\mathbf{r}) d^3\mathbf{r} \right) \\ &\times \int \mathcal{D}[\tilde{\rho}(\mathbf{r})] \exp \left(-\frac{1}{2} \beta \iint d^3\mathbf{r} d^3\mathbf{r}' \tilde{\rho}(\mathbf{r}) u(\mathbf{r}, \mathbf{r}') \tilde{\rho}(\mathbf{r}') - i\beta \int d^3\mathbf{r} \tilde{\rho} \phi(\mathbf{r}) \right). \end{aligned} \quad (2.20)$$

The part $\exp(-\frac{1}{2}\beta \int \int d^3\mathbf{r}d^3\mathbf{r}'\rho_e(\mathbf{r})u(\mathbf{r},\mathbf{r}')\rho_e(\mathbf{r}'))$ can be taken out of the integration over fields, as it does not enter the averaging, and can be shortly denoted as $e^{\beta\omega_e}$, where the ω_e corresponds to the electrostatic energy of external charge. If we look at integral over $\tilde{\rho}$ in Eq. (2.20), we can see that it represents a Gaussian integral of the form

$$\int \exp\left(-\frac{1}{2}\mathbf{v}^T\mathbf{A}\mathbf{v} + \mathbf{J}^T\mathbf{v}\right)d^N\mathbf{v} = \frac{(2\pi)^{N/2}}{\sqrt{\det\mathbf{A}}} \exp\left(\frac{1}{2}\mathbf{J}^T\mathbf{A}^{-1}\mathbf{J}\right), \quad (2.21)$$

so it can be exactly solved. Furthermore by taking $\mathbf{v} = -i \int d^3\mathbf{r}\tilde{\rho}$, we will have:

$$\begin{aligned} & \int \mathcal{D}[\tilde{\rho}(\mathbf{r})] \exp\left(\frac{1}{2}\beta \int \int d^3\mathbf{r}d^3\mathbf{r}'(-i\tilde{\rho})(\mathbf{r})u(\mathbf{r},\mathbf{r}')(-i\tilde{\rho})(\mathbf{r}') + \beta \int d^3\mathbf{r}(-i\tilde{\rho})\phi(\mathbf{r})\right) = \\ & \frac{(2\pi)^{N/2}}{\sqrt{\det\beta u}} \exp\left(-\frac{1}{2}\beta \int \int d^3\mathbf{r}d^3\mathbf{r}'\phi(\mathbf{r})u^{-1}(\mathbf{r},\mathbf{r}')\phi(\mathbf{r}')\right). \end{aligned} \quad (2.22)$$

With this included, the partition function becomes

$$\begin{aligned} Q_N &= \lambda^N e^{\beta\omega_e} \int \mathcal{D}[\phi(\mathbf{r})] \exp\left(i\beta \int \rho_e(\mathbf{r})\phi(\mathbf{r})d^3\mathbf{r}\right) \left[\int d^3\mathbf{r}_i \exp\left(i\beta \sum_{i=1}^N e_i\phi(\mathbf{r}_i)\right)\right]^N \\ &\quad \times \exp\left(-\frac{1}{2}\beta \int \int d^3\mathbf{r}d^3\mathbf{r}'\phi(\mathbf{r})u^{-1}(\mathbf{r},\mathbf{r}')\phi(\mathbf{r}') - \frac{1}{2}\ln(\det\beta u(\mathbf{r},\mathbf{r}'))\right), \end{aligned} \quad (2.23)$$

where $\lambda' = \exp(\beta u(0))$. After the transition to the grand-canonical ensemble, the partition function transforms according to:

$$\mathcal{Z} = \sum_{N=0}^{\infty} \frac{\lambda^N}{N!} Q_N, \quad (2.24)$$

where λ is the fugacity (absolute activity) given by $\lambda = \exp(\beta\mu)$.

$$\begin{aligned} \mathcal{Z} &= \exp\left(-\frac{1}{2}\ln(\det\beta u(\mathbf{r},\mathbf{r}'))\right) \\ &\quad \times \int \mathcal{D}[\phi(\mathbf{r})] \exp\left(-\frac{1}{2}\beta \int d^3\mathbf{r}d^3\mathbf{r}'\phi(\mathbf{r})u^{-1}(\mathbf{r},\mathbf{r}')\phi(\mathbf{r}') + i\beta \int d^3\mathbf{r}\rho_e(\mathbf{r})\phi(\mathbf{r})\right) \\ &\quad \times \sum_{N=0}^{\infty} \frac{(\lambda\lambda')^N}{N!} \left[\int d^3\mathbf{r}_i \exp\left(i\beta e_i\phi(\mathbf{r}_i)\right)\right]^N. \end{aligned} \quad (2.25)$$

Denoting the product $\lambda\lambda'$ as $\tilde{\lambda}$, and using the definition of the exponential function $e^x = \sum_{N=0}^{\infty} x^N/N!$, the grand-canonical partition function finally yields:

$$\begin{aligned} \mathcal{Z} &= \exp\left(-\frac{1}{2}\ln(\det\beta u(\mathbf{r},\mathbf{r}'))\right) \\ &\quad \times \int \mathcal{D}[\phi(\mathbf{r})] \exp\left[-\frac{1}{2}\beta \int d^3\mathbf{r}d^3\mathbf{r}'\phi(\mathbf{r})u^{-1}(\mathbf{r},\mathbf{r}')\phi(\mathbf{r}') + i\beta \int d^3\mathbf{r}\rho_e(\mathbf{r})\phi(\mathbf{r})\right. \\ &\quad \left.+ \tilde{\lambda} \int d^3\mathbf{r} \exp\left(i\beta e\phi(\mathbf{r})\right)\right]. \end{aligned} \quad (2.26)$$

or in a simplified form:

$$\mathcal{Z} = [\det \beta u(\mathbf{r}, \mathbf{r}')]^{-\frac{1}{2}} \int \mathcal{D}[\phi(\mathbf{r})] \exp\left(-H(\phi(\mathbf{r}))\right), \quad (2.27)$$

where H is the field-action or the field Hamiltonian, defined as:

$$H = \frac{1}{2}\beta \int d^3\mathbf{r} \phi(\mathbf{r}) u^{-1}(\mathbf{r}, \mathbf{r}') \phi(\mathbf{r}') - i\beta \int d^3\mathbf{r} \rho_e(\mathbf{r}) \phi(\mathbf{r}) - \sum_i \lambda_i \int d^3\mathbf{r} \exp\left(i\beta e_i \phi(\mathbf{r})\right). \quad (2.28)$$

Here, e_i are the charges of the mobile ions present in the system, and λ_i is the fugacity of the i -th ion species. After introducing dimensionless quantities:

$$\tilde{\lambda} = \Xi \mu^3 \lambda, \quad \tilde{\phi}(\tilde{\mathbf{r}}) = \beta e_0 q \phi(\mathbf{r}), \quad \tilde{\rho}(\tilde{\mathbf{r}}) = \frac{\mu}{2\pi\sigma} \rho(\mathbf{r}), \quad \tilde{u}^{-1}(\tilde{\mathbf{r}}, \tilde{\mathbf{r}}') = \frac{\mu^5}{4\pi\epsilon\epsilon_0} u^{-1}(\mathbf{r}, \mathbf{r}') \quad (2.29)$$

one obtains a dimensionless field-action or the field Hamiltonian in the form:

$$\tilde{H} = \frac{1}{2} \int d^3\tilde{\mathbf{r}} \tilde{\phi}(\tilde{\mathbf{r}}) \tilde{u}^{-1}(\tilde{\mathbf{r}}, \tilde{\mathbf{r}}') \tilde{\phi}(\tilde{\mathbf{r}}') - i \int d^3\tilde{\mathbf{r}} \tilde{\rho}_e(\tilde{\mathbf{r}}) \tilde{\phi}(\tilde{\mathbf{r}}) - \sum_i \tilde{\lambda}_i \int d^3\tilde{\mathbf{r}} \exp\left(i\tilde{\phi}(\tilde{\mathbf{r}})\right), \quad (2.30)$$

leading to the partition function:

$$\tilde{\mathcal{Z}} = \int \mathcal{D}[\tilde{\phi}(\tilde{\mathbf{r}})] \exp\left(-\frac{\tilde{H}(\tilde{\phi})}{\Xi}\right). \quad (2.31)$$

Here the meaning of the electrostatic coupling parameter in the field theoretic framework is clearly indicated, namely, Ξ can be used as an expansion parameter in two limiting regimes discussed next. One needs to note that the partition function has to be written as a functional integral over all the fluctuating potential configurations.

2.2.1 Weak-coupling limit

For small values of the coupling parameter, $\Xi \rightarrow 0$, at sufficiently low surface charges, low ion valencies, high permittivity constants, or high temperatures, charged systems can be treated in the weak-coupling regime, which is formally equivalent to a saddle-point approximation, also equivalent to a mean-field approximation. This leads to the PB theory of electrostatic interactions in ionic solutions [14, 15, 16].

The saddle-point approximation consists in evaluating the configuration that corresponds to a minimum, or, in general, extremum, of the field-action functional. The extremum of the functional is obtained from its variation or from its first functional derivative

$$\left. \frac{\delta H}{\delta \phi(\mathbf{r})} \right|_{\text{MF}} = 0. \quad (2.32)$$

The index MF stands for mean-field, since in general the mean-field approximation on the level of field-action is obtained from a saddle-point. In order to remain faithful to the historical path to the MF equation, as it has been introduced as

the PB equation, we define the electrostatic potential as $\varphi = -i\phi_{\text{MF}}$, so that the saddle-point equation becomes:

$$\nabla^2 \varphi_{\text{MF}}(\mathbf{r}) = -\frac{1}{\epsilon\epsilon_0}[\rho_e(\mathbf{r}) + en_{\text{MF}}(\mathbf{r})], \quad (2.33)$$

where $n_{\text{MF}}(\mathbf{r})$ is the mean-field density of the mobile ions. In the case of a two-component system, composed of monovalent salt ($i = \pm 1$) of the same fugacity, one gets

$$\nabla^2 \varphi_{\text{MF}} = -\frac{1}{\epsilon\epsilon_0}[\rho_e - 2\tilde{\lambda}e \sinh(\beta e\varphi_{\text{MF}})], \quad (2.34)$$

which reduces to the well known DH equation in the limit of high monovalent salt concentration when the potential becomes small. In this case the last term in Eq. (2.30) can be linearized, after which one derives the well known DH result:

$$\nabla^2 \varphi_{\text{MF}} = -\frac{1}{\epsilon\epsilon_0}(\rho_e - \kappa^2 \varphi_{\text{MF}}). \quad (2.35)$$

In the case of monovalent salt and low surface charges ($\Xi \rightarrow 0$) the PB/DH theories are quantitatively correct even when compared with more sophisticated approaches [56]. Nevertheless, for finite values of Ξ one can search for the corrections to the mean field solution in terms of an expansion of the field action around the mean-field solution. Thus, to the second (Gaussian) order

$$H = H_{\text{MF}}[\varphi_{\text{MF}}] + \frac{1}{2} \iint \frac{\delta^2 H}{\delta\varphi(\mathbf{r})\delta\varphi(\mathbf{r})} \Big|_{\text{MF}} \delta\varphi(\mathbf{r})\delta\varphi(\mathbf{r}') d^3\mathbf{r}d^3\mathbf{r}'. \quad (2.36)$$

Gaussian fluctuations around the saddle-point represent the first correction to the mean-field solution, and they are governed by the Hessian operator of the second derivatives of the field action with respect to the fluctuating electrostatic potential.

In spite of the fact that the Hessian does not depend on the terms describing the external charges in the field action, calculation of the free energy corresponding to the Gaussian fluctuations is not an easy task, especially in the case of a non-uniform distribution of mobile ions. It has been calculated exactly for a system composed of two uniformly charged flat plates immersed in a counterions-only solution, where the mean-field density of counterions depends on the transverse spatial coordinate [30]. It was shown that the correlations give an attractive contribution to the total free energy as a function of the intersurface separation, but are not large enough to overcome the mean-field repulsion of two symmetrically charged surfaces. In the systems with dielectric discontinuities, those attractive contributions correspond to the thermal component (zero Matsubara frequency) of the van der Waals attractions [31].

The limitations of the PB theory become practically important in highly charged systems, where ion-ion correlations begin to influence the electrostatic properties of the charged system [29, 77].

2.2.2 Strong-coupling limit

Even though the PB approach can be systematically improved with perturbative corrections around the mean-field solution, such an approach must be renounced

sooner or later, and recourse should be taken in the fundamentally different reformulation of the partition function evaluation, based on the concept of strong-coupling [10, 29, 32, 76, 77, 83, 84].

The strong-coupling theory includes only the contributions of single particle interactions between a single counterion and the surface charges on the bounding surfaces, valid for large coupling parameter $\Xi \rightarrow \infty$, when polyvalent counterions are present in the bathing solution. In that case the partition function can be expanded in terms of fugacity:

$$\mathcal{Z} = \mathcal{Z}^{(0)} + \lambda \mathcal{Z}^{(1)} + \mathcal{O}(\lambda^2), \quad (2.37)$$

which is nothing but the virial expansion, where the zeroth-order term stands for the bare electrostatic interaction of charged surfaces without counterions, while the first-order term corresponds to the one-particle contribution:

$$\mathcal{Z}^{(0)} = \mathcal{Z}|_{\lambda=0} = \exp(-\beta W_{00}), \quad (2.38)$$

with the energy of a bare macroion

$$W_{00} = \frac{1}{2} \int \rho_e(\mathbf{r}) u(\mathbf{r}, \mathbf{r}') \rho_e(\mathbf{r}') d\mathbf{r} d\mathbf{r}'. \quad (2.39)$$

The one-particle contribution or indeed the first order virial term can be obtained as

$$\mathcal{Z}^{(1)} = \frac{\partial}{\partial \lambda} \mathcal{Z}|_{\lambda=0} = \mathcal{Z}^{(0)} \int d\mathbf{r} \exp(-\beta W_{self}(\mathbf{r}) - \beta W_{0c}(\mathbf{r})), \quad (2.40)$$

with:

$$W_{self}(\mathbf{r}) = \frac{1}{2} (e_0 q)^2 u(\mathbf{r}, \mathbf{r}), \quad (2.41)$$

corresponding to the counterion self energy and

$$W_{0c}(\mathbf{r}) = e_0 q \int d\mathbf{r}' u(\mathbf{r}, \mathbf{r}') \rho_e(\mathbf{r}') \quad (2.42)$$

to the macroion-counterion interaction energy, respectively. Counterion-counterion interaction are excluded from the strong-coupling consideration due to the one-particle nature of the description.

2.2.3 Dressed counterions theory

The boundaries between these two theoretical approaches to charged systems are given by the electrostatic coupling parameter [24, 83], which in its two opposite limits leads to the PB mean-field description on one hand, and the strong-coupling theory on the other hand (Fig. 2.2). In experiments it is not easy to prepare a solution composed of counterions only.

In real systems, the entire solution composed of the macromolecule and the polyvalent counterions is always accompanied by the presence of monovalent salt ions. This brings an asymmetry to Coulomb fluids, whose constituents are differently coupled: polyvalent counterions are strongly coupled, while the monovalent salt ions

are weakly coupled. Even though there is no theory that could take into account both cases, it is still possible to construct a theory that selectively uses different descriptions for different components of the system. Such a combined approach leads to the strong-coupling theory of *dressed (screened) counterions* [34]. It starts with a field Hamiltonian:

$$H[\varphi] = \frac{1}{2} \int d\mathbf{r} d\mathbf{r}' \varphi(\mathbf{r}) u^{-1}(\mathbf{r}, \mathbf{r}') \varphi(\mathbf{r}') - \frac{\lambda_c}{\beta} \int d\mathbf{r} \exp\left(-i\beta q e_0 \varphi(\mathbf{r})\right) - \frac{\lambda_+}{\beta} \int d\mathbf{r} \exp\left(-i\beta e_0 \varphi(\mathbf{r})\right) - \frac{\lambda_-}{\beta} \int d\mathbf{r} \exp\left(i\beta e_0 \varphi(\mathbf{r})\right). \quad (2.43)$$

When monovalent salt ions are in equilibrium with the bulk reservoir, their fugacities are to the lowest order the same and equal to the bulk concentration $\lambda_+ = \lambda_- = n_0$. Then the sum of the terms corresponding to the monovalent ions gives the cosine function, which in the limit of small potentials, relevant for the weak-coupling regime, can be expanded to the second-order with respect to the potential:

$$-\frac{2n_0}{\beta} \int d\mathbf{r} \cos(\beta e_0 \varphi(\mathbf{r})) \approx \frac{1}{2} \epsilon \epsilon_0 \kappa^2 \int d\mathbf{r} d\mathbf{r}' \varphi(\mathbf{r}) \varphi(\mathbf{r}') \delta(\mathbf{r} - \mathbf{r}'). \quad (2.44)$$

Here, $\kappa = \sqrt{8\pi l_B n_0}$ is the Debye screening parameter for monovalent salt ions. The field Hamiltonian can be modified into the approximate form:

$$H[\varphi] = \frac{1}{2} \int d\mathbf{r} d\mathbf{r}' \varphi(\mathbf{r}) u_{DH}^{-1}(\mathbf{r}, \mathbf{r}') \varphi(\mathbf{r}') - \frac{\lambda_c}{\beta} \int d\mathbf{r} e^{-i\beta q e_0 \varphi(\mathbf{r})}, \quad (2.45)$$

where the Coulomb's interaction kernel is replaced by the screened Debye–Hückel kernel, defined as:

$$u_{DH}^{-1}(\mathbf{r}, \mathbf{r}') \varphi(\mathbf{r}') = -\epsilon \epsilon_0 (\nabla^2 - \kappa^2) \delta(\mathbf{r} - \mathbf{r}') \quad (2.46)$$

Since the polyvalent ions are strongly coupled to the external charge, one can proceed further by repeating the procedure from the previous section, expanding the partition function in terms of the polyvalent ion's fugacity to the first order:

$$\mathcal{Z} = \mathcal{Z}_0 + \lambda_c \mathcal{Z}_1. \quad (2.47)$$

This approximate form of the partition function is then referred to as the dressed counterion theory.

The most interesting outcome of the dressed counterion theory is a proper description of the polyvalent counterion-mediated attraction appearing between same-charged flat plates, arising due to the strong screening of macroion's charge [34, 35]. Moreover this theory successfully describes also the attraction between neutral dielectrics induced by multivalent ions [36].

A significant step further was accomplished by Ali Naji and his coworkers [75, 85, 86, 87] who generalized the dressed ion theory by considering the effects of randomly disordered charge distributions at the surfaces in the system with dielectric inhomogeneity, including the salt image effects. Their results lead to the new phenomenon in the Coulomb world, highlighting an anti-fragile behavior of multivalent counterions that reduce the entropy of a disordered system, making randomly charged

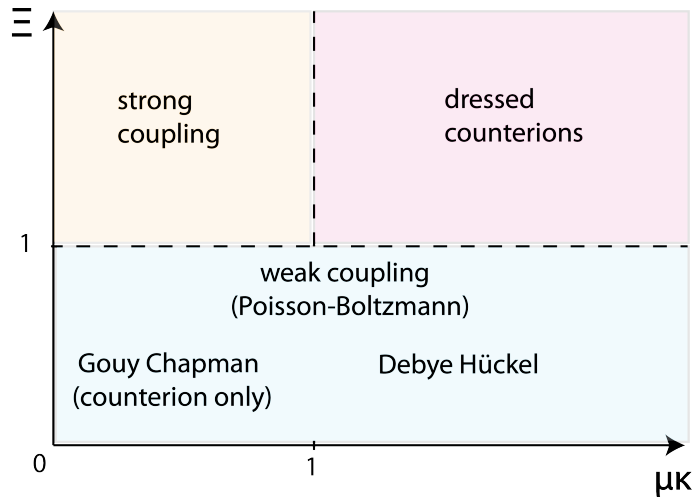


Figure 2.2: Phase diagram of the applicability of different approximations that follow from the field-theoretic description of charged surfaces in a salt solution. For small coupling parameter one is in the weak-coupling regime, described by the PB equation. Depending on the amount of salt, one is either in the Gouy–Chapman counterion-only system, or the Debye–Hückel regime, corresponding to large salt concentrations. Highly correlated systems can be described by the strong-coupling theory for counterions, while for asymmetric salt mixtures, dressed counterions theory becomes valid.

surfaces attract stronger than the corresponding ones with a uniform distribution of charge. This represents another manifestation of the complicated and unpredictable features of Coulomb fluids.

A more detailed insight of the application of the field theoretic approach to various electrostatic models can be found in the doctoral Thesis of Matej Kanduč [88].

Common to all these theoretic approaches (and the others up to date) is that they are developed and tested in the case of the *fixed* macroion’s charge, and as such they fail to describe the systems of macroions whose charge can fluctuate and in general responds to the solution conditions, i.e. is charge regulated.

2.3 Charge regulation phenomenology

As already mentioned in Chapter 1, charged objects undergoing the processes of ion exchange with the environment can show exotic behavior due to fluctuations of their charge. Once dipped into the polar solution, the charge of the macromolecule is determined by the local environmental conditions, i.e. by charge regulation, which implies that the effective charge on a macroion responds to the local solution conditions, such as local pH, local electrostatic potential, salt concentration, dielectric constant variation, and the presence of other vicinal charged groups [60].

The concept of charge regulation was first introduced by Linderström-Lang a century ago [89]. Although the processes of ion dissociation and adsorption had been well studied by chemists in the 19th century, he was the first to discuss the boundary condition of the DH equation and its modification due to the degree of

ion dissociation at macromolecule's surfaces. His work was predominantly oriented to the study of protein structure, where he gave a huge contribution, proving experimentally how the hydrogen ion exchange rules protein folding [90, 91].

The proper theoretic description of charge regulation effects was first established by Barry Ninham and Adrian Parsegian in the '70s of the last century [59]. Their aim was to improve the DLVO theory in order to describe the behavior of biological cells, specifically their charged membranes. It was also observed that some enzymes at cell surface act according to their microenvironment [92]. At that time it had been known that the presence of ionizable groups on cell membranes modifies the local electrostatic potential. So they were aware that the electrostatic theories based on the constant surface potential or the constant surface charge boundary conditions are not relevant for such biological systems. It was necessary to derive a self-consistent theory where the surface charge depends on the local electrostatic potential.

Ninham and Parsegian started from the model that takes two flat plates with ionizable groups at the surface, undergoing a chemical dissociation reaction:



whose dissociation constant is given through the law of mass action as:

$$K = \frac{[\text{H}^+]_s[\text{A}^-]}{[\text{AH}]} = [\text{H}^+]_s \frac{\alpha}{1 - \alpha}. \quad (2.49)$$

Here, α is the degree of dissociation and $[\text{H}^+]_s$ represents the concentration of hydrogen ions at the surface. The crucial step in their theory is posing the equilibrium condition for hydrogen ions as:

$$[\text{H}^+]_s = [\text{H}^+] \exp(-\beta e_0 \phi_s), \quad (2.50)$$

where ϕ_s is the surface potential, so that the concentration of the hydrogen ions at the surface is related to the concentration of the hydrogen ions in the bulk through the Boltzmann equilibrium condition involving surface potential. Introducing the notations $\text{pH} = -\log[\text{H}^+]$ and $\text{p}K = -\log K$, the degree of dissociation can be obtained, combining the equations above, in the following form:

$$\alpha = \frac{1}{1 + \exp(-(pH - pK) \ln 10) \exp(-\beta e_0 \phi_s)}. \quad (2.51)$$

In this way the charge at the surface is obviously regulated by the surface electrostatic potential. This was the charge regulation boundary condition for the PB equation they solved for the flat plates immersed in a monovalent salt solution with a small concentration of divalent cations.

Dennis Prieve and Eli Ruckenstein generalized the Ninham–Parsegian model by applying multiple ionic equilibria to the surfaces that contain acidic sites which can be deprotonated and basic sites which can be protonated [93, 94]. For each acidic and basic site the dissociation constant is defined and a complicated non-linear boundary condition is formulated. They then numerically solved the PB equation for an isolated surface and managed to reproduce behavior of the surface potential upon pH variation, applying the theory to human erythrocytes.

For two interacting double layer surfaces, the high non-linearity in boundary condition makes the nonlinear PB equation far more complicated to solve, so their estimated analytical solutions had been provided on the level of approximate boundary conditions, i.e. constant surface charge and constant surface potential. It is observed that at the isoelectric point, the net surface charge tended to vanish.

Later on in the '90s, Steven Carnie and Derek Chan came up with an idea how to tame the highly non-linear charge regulated boundary condition to be accessible for theoretical treatment [95, 96]. Namely, they suggested that the dissociation at the surface can be modeled by a linear relation between surface charge and surface potential in the following way:

$$\sigma = K_1 - K_2\psi. \quad (2.52)$$

The constants K_1 and K_2 are determined from the imposed assumption that the surface charge as a function of surface potential ψ can be expressed in terms of surface charge being a function of the potential of an isolated surface, ψ_{iso} :

$$\sigma(\psi) = \sigma(\psi_{iso}) + \left. \frac{\partial\sigma(\psi)}{\partial\psi} \right|_{\psi=\psi_{iso}} (\psi - \psi_{iso}). \quad (2.53)$$

From this, it is clear that the constant K_2 has dimensions of surface capacitance, defined as $K_2 = -\left. \frac{\partial\sigma(\psi)}{\partial\psi} \right|_{\psi=\psi_{iso}}$. Such linearized boundary condition, together with the linearized PB equation gave the set of self-consistent equations, which they solved for the models of two spherical colloidal particles in a monovalent salt solution as well as for two flat charged plates. It had been shown that the interaction energy of the linearized charge regulation model lies always between the solutions provided by the constant charge approximation model and the constant surface potential approximation model.

Several years later, the Carnie–Chan’s model, derived in the limit of small surface potentials, was extended by Sven Behrens and Michal Borkovec to be valid for arbitrary surface potentials [97]. They considered two flat charged surfaces immersed in an electrolyte solution, distinguishing two subsystems, each of which was described by its own equation of state. The inner layer was characterized by chemical properties of the surface, and the diffuse part composed of mobile ions was governed by DH equation. The equilibrium between these two subsystems is achieved by imposing the condition that the charge distribution of inner layer is equal to the charge density of the diffuse layer. They introduced a charge regulation parameter p that relates the true interaction energy $W^{(reg)}$ with energies of two limiting cases – constant charge model (cc), and constant potential (cp) model as:

$$p = \frac{W^{(reg)}(L) - W^{(cp)}(L)}{W^{(cc)}(L) - W^{(cp)}(L)}. \quad (2.54)$$

The values of p are then between 0 for the constant potential and 1 for the constant charge conditions. Geometrically, from the surface charge – surface potential diagram, it is determined that for large surface distances $L \rightarrow \infty$ one has

$$p = \frac{C^D}{C^D + C^I}, \quad (2.55)$$

where C^D and C^I are the capacitances of the diffuse and the inner layer respectively. The behavior of real systems depends on the interplay between these two capacitances. Domination of one capacitance determines the choice of the approximation (cc)/(cp). By measuring the capacitance, one can determine the regulation parameter and knowing the regulation parameter, one can get charge regulation interaction energy by calculating the approximate energy of (cc) and (cp) models.

In the last decade many experiments were performed by Borkovec and his coworkers using the atomic force microscope for studying the aggregation of colloidal particles [67, 68, 98, 99, 100, 101]. The most interesting scenario they found is that the charge regulation phenomenon has the essential effect on electro-neutral systems, where the attraction may appear. They explained it in the framework of the Chan–Borkovec formalism based on the regulation parameter p . The measured force between such objects always satisfied the profile in between the constant charge approximation and the constant potential approximation. They were also experimenting with the influence of the solution properties on the charge regulation effect, and found that multivalent ions increase the attractive interaction between electro-neutral objects [99, 102, 103, 104, 105, 106], a puzzle without a proper theoretical explanation. Comparing their measurements with the PB theory they found that the latter fails at small separations as well as at higher salt concentrations.

A lot of progress has been made in understanding the charge regulation phenomena, but the tricky part concerning the interactions between charge regulated objects stayed theoretically poorly understood and explained. Even the KS interaction had been somehow forgotten. Just recently it experienced rebirth when Mikael Lund and Bo Jönsson studied the protein–protein interactions using Monte Carlo simulations [60, 69, 107]. In the framework of statistical mechanics they introduced the *protein capacitance*, C , as ability of the protein charge, Q , to fluctuate:

$$C \equiv \langle Q^2 \rangle - \langle Q \rangle^2 = -\frac{\partial Q}{\partial(\beta e_0 \phi)}. \quad (2.56)$$

This quantity is useful, since it can be experimentally measured from the titration curve:

$$C \ln 10 = -\frac{\partial Q}{\partial(\text{pH})}. \quad (2.57)$$

This means that the KS interaction is directly related to charge regulation, i.e. to the dependence of the charge on the pH of the solution! This was an important signal for me that allowed me to undertake a fundamental study of how the charge regulation and interactions between charged macromolecules are related on various levels of the statistical mechanics of Coulomb systems.

With the introduction of the capacitance, continuing in the framework of statistical mechanics energy perturbation expansion, Lund and Jönsson recovered a fluctuation-driven interaction between two point charges as:

$$\beta \mathcal{A} = \frac{l_B \langle Q_A \rangle \langle Q_B \rangle}{R} - \frac{l_B^2}{2R^2} (C_A \langle Q_B \rangle^2 + C_B \langle Q_A \rangle^2 + C_A C_B), \quad (2.58)$$

where the first term stands for the direct Coulomb interaction, while the following term represents the interaction of the fluctuation type, already introduced by Kirkwood and Shumaker. Using the coarse-grained representation of proteins, where

each amino acid is represented with a single bead, and allowing that each bead can exchange a proton with the bathing solution, they developed a Monte Carlo simulation scheme by defining the trial energy of a “charge regulation Monte Carlo move” as:

$$\Delta U = \Delta U_{el} \pm (\text{pH} - \text{p}K_0) \ln 10, \quad (2.59)$$

where ΔU_{el} is the change in the electrostatic energy, $\text{p}K_0$ is the dissociation constant of an isolated amino acid, (+) applies when protonating an amino acid, while (−) applies when deprotonating an amino acid. Simulations proved first the existence of a long ranged attraction when proteins reach their isoelectric point, and then also the original KS conceptual framework.

Charge regulation has a long history of development, and has been invoked and widely applied in the context of various colloidal systems: stability and intersurface forces due to the electrostatic double-layers [108, 109], dissociation of amino acids and the corresponding electrostatic protein–protein interactions [60, 70, 110], charge regulation of protein aggregates and viral shells [57], and of polyelectrolytes and polyelectrolyte brushes [62, 111, 112, 113], as well as charge regulation of charged lipid membranes [114, 115, 116]. However, in spite of this, modern theories of electrostatic interaction between macroions immersed in Coulomb fluids [10] mostly deal with constant surface charge of a macroion, bypassing the complications introduced by charge regulation [61, 62, 96].

It is therefore our aim to construct a theory that will include the charge regulation phenomenon within the field-theoretic formalism and explain consequences stemming out from it.

Chapter 3

Counterion-mediated interactions of planar charge regulated surfaces

For describing protein's behavior governed by electrostatics, it is crucial to understand a phenomenon of charge regulation. As it is mentioned in the Chapter [2](#), a lot of work has been done in this field, but a general theory describing the interactions of objects undergoing charge regulation processes at diverse circumstances have still been lacking. In the last decade significant progress has been made in developing an elegant field theoretic framework for describing the various properties of Coulomb fluids, but they are limited to particles with a constant surface charge. A constant charge is a very stringent approximation and it holds only in a very restricted part of the parameter space, since in many biological systems, macroions bear dissociable groups on their surface, so that their charge always depends strongly on the acid-base equilibrium that defines the fraction of acidic (basic) groups that are dissociated [\[71\]](#). The challenge is to incorporate this property consistently into a theoretical formulation. In order to do so, it is natural to start from analyzing counter-ion mediated interaction in the simplest geometries, such as a planar plates with dissociable surfaces.

In this Chapter we start with the simplest model that retains the salient features of charge regulation, composed of two planar parallel macromolecular surfaces with surface distributed charge dissociation sites, immersed in a Coulomb fluid composed of counterions only. We base our analysis on a field-theoretic description of the system's partition function, whose Hamiltonian will be generalized to include a surface term that describes properly the charge regulation and consequently the local charge fluctuation at the macromolecular surfaces. The problem is set in the weak-coupling regime. Going beyond the mean-field level, we address the Gaussian fluctuations around this mean-field solution with its charge-regulation boundary condition. That is the main task of interest here, since we expect that the exotic electrostatics hides in loop corrections to the mean-field solution. We will be able to calculate one-loop correction exactly and analytically by using the path-integral approach for the harmonic oscillator with time-depended frequency. Finally, we present numerical results and comment upon its relevance for the KS interaction.

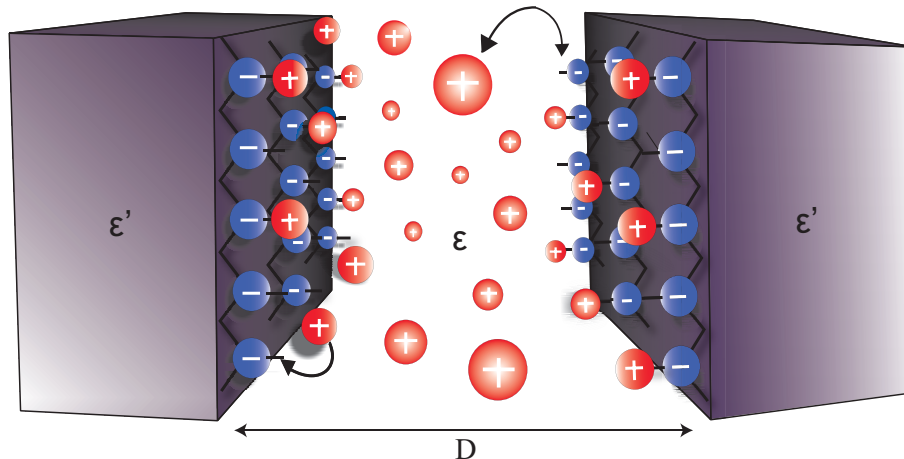


Figure 3.1: Schematic representation of two charged planar surfaces at a separation D with charge dissociation sites distributed uniformly along the surfaces and with counterions between the surfaces. The counterions originate from the charge dissociation of the dissociable groups (AC) through the reaction $AC \leftrightarrow A^- + C^+$.

3.1 Model

We consider two flat parallel plates, located at $z = \pm D/2$ and immersed into an aqueous solvent that carry dissociable charge groups of the type $AC \leftrightarrow A^- + C^+$, where the counterion C is released into the aqueous solution (Fig. 3.1). We do not specify the identity of the released counterion but assume it to be the only mobile species in the considered model. Furthermore, we assume a grand canonical ensemble for the counterions, specified by a fixed value of the activity. The number of the counterions in the solution is thus not fixed but depends on the dissociation state of the surfaces. While in standard formulations of the counterion-only Coulomb fluids with fixed boundary charge the grand-canonical formulation is just a step towards the final canonical ensemble, corresponding to a fixed number of charges, in our case this is not fixed and the grand canonical description is natural.

We need to note that in the Ninham–Parsegian model the released counterion is a proton and the aqueous solution contains a salt mixture at a specified ionic strength for both monovalent and divalent complements [59]. While this model can be formalized in the same way as our simplified model, we first solve the simplified case in order to derive the proper level of description as well as to investigate the salient features of fluctuations in a case, where they can be treated exactly.

In order to describe the surface charge dissociation, we introduce a lattice gas model with its own surface free energy contribution. This surface part of the free energy stems from the charge dissociation equilibrium and describes the (free) energy penalty for a finite surface charge density. We show furthermore that on the mean-field level, our formulation yields *exactly* the same result as the Ninham–Parsegian charge regulation *ansatz*, which is not explicitly based on any surface free energy. The equilibrium distribution of the counterions is then obtained from the saddle-point equation, which corresponds to the minimum of the complete, that is the volume and surface free energy terms. The dielectric constant in the region between the walls is taken as ϵ , while outside that region it is assumed to be in general different and equal to ϵ' . Dielectric inhomogeneity (jump) is a common phenomenon

in biological systems, since bio macro-molecules have a dielectric constant ($\sim 2-5$), while the water, as the most common solvent, has a dielectric constant around 80. The existence of dielectric inhomogeneity may lead to the image forces, which on the weak coupling level considered here, do not play an important role [31].

3.2 Field-theoretic description of model

In order to describe this model system of interacting particles it is advantageous to use the field-theoretic formalism to derive the partition function. The configurational part of the Hamiltonian of an auxiliary system of N counterions, with a fixed surface charge density σ_0 on the bounding surfaces, can be written as

$$H = \frac{1}{2} \sum_{i \neq j} u(\mathbf{r}_i, \mathbf{r}_j) e_i e_j + \sum_{i=1}^N \oint u(\mathbf{r}, \mathbf{r}_i) \sigma_0 d^2 \mathbf{r}, \quad (3.1)$$

where \oint implies an integration over all the charged bounding surfaces and $u(\mathbf{r}, \mathbf{r}_i)$ is the electrostatic interaction kernel, i.e. Green's function of the Coulomb potential, which satisfies the relation

$$\nabla^2 u(\mathbf{r}, \mathbf{r}_i) = -\frac{\delta(\mathbf{r} - \mathbf{r}_i)}{\epsilon \epsilon_0}. \quad (3.2)$$

The canonical configurational partition function of the system can then be represented by an integral over all positions of the counterions

$$Q_N = \int d\mathbf{r}_1 \dots d\mathbf{r}_N \exp(-\beta H). \quad (3.3)$$

After applying the Hubbard–Stratonovich transformation, one can obtain the grand canonical partition function as a functional integral over the fluctuating electrostatic potential $\varphi(\mathbf{r})$

$$\mathcal{Z} = \int \mathcal{D}[\varphi(\mathbf{r})] \exp\left(-\mathcal{S}[\varphi(\mathbf{r})]\right), \quad (3.4)$$

with the field-action of the form:

$$\begin{aligned} \mathcal{S}[\varphi(\mathbf{r})] &= \frac{1}{2} \beta \epsilon \epsilon_0 \int d^3 \mathbf{r} |\nabla \varphi(\mathbf{r})|^2 + \tilde{\lambda} \int d^3 \mathbf{r} \exp(i\beta e \varphi(\mathbf{r})) + \\ &+ i\beta \oint d^2 \mathbf{r} \sigma_0 \varphi(\mathbf{r}). \end{aligned} \quad (3.5)$$

Here, $\tilde{\lambda}$ is the absolute activity and will be obtained self-consistently. The above field-action is universal in terms of the non-linear volume interaction term, the second term in the above equation corresponds exactly to the van't-Hoff ideal osmotic pressure of the counter ions. This is a well-known result [21], which on the weak coupling mean-field level, using substitution $\varphi \rightarrow i\phi_{MF}$, gives the PB equation with fixed charged density boundary condition $\mathbf{n} \cdot \nabla \phi_{MF} = \sigma_0$ [10].

We now generalize this free energy *ansatz* so that it will contain also the surface part, not necessarily linear in the surface fluctuating potential, by assuming that the surface free energy in Eq. (3.5) can be modified as

$$i \oint \sigma_0 \varphi(\mathbf{r}) d^2 \mathbf{r} \longrightarrow \oint f(\varphi(\mathbf{r})) d^2 \mathbf{r}, \quad (3.6)$$

where $f(\varphi(\mathbf{r}))$ is a general non-linear function of the local potential. The exact form of this surface free energy is not universal and depends on the model of the surface–ion interaction [117, 118]. Here, we will delimit ourselves to a surface lattice gas model, which was introduced in a different context by Fleck and Netz [119], and derive the corresponding free energy, as well as show that the same model in fact corresponds exactly to the Ninham–Parsegian charge regulation theory [59]. The surface lattice gas model of dissociable charged groups gives [119, 120]

$$f(\varphi(\mathbf{r})) = i\sigma_0\varphi(\mathbf{r}) - k_B T \frac{|\sigma_0|}{e_0} \ln(1 + \exp(\beta\mu_S + i\beta e_0\varphi(\mathbf{r}))), \quad (3.7)$$

where μ_S is the free energy of dissociation. In the argument of the logarithm function one can recognize the partition function for a system with uncharged ground state and a charged state with an effective energy $\beta\mu_S + i\beta e_0\varphi(\mathbf{r})$. It is possible to generalize this model with other surface free energies [121, 122] that can capture other details of the surface–ion interaction. Furthermore, in the limit of $\beta\mu_S \rightarrow \infty$, the sites are completely undissociated, the bounding surfaces are uncharged and there is no contribution to the surface free energy. In the opposite limit, $\beta\mu_S \rightarrow -\infty$, the bounding surfaces are completely dissociated and we are back to the fixed surface charge $f(\varphi(\mathbf{r})) = i\sigma_0\varphi(\mathbf{r})$.

The complete field action of the model at hand thus assumes the form

$$\begin{aligned} \mathcal{S}[\varphi(\mathbf{r})] = & \frac{1}{2}\beta\epsilon\epsilon_0 \int d^3\mathbf{r} |\nabla\varphi(\mathbf{r})|^2 + \tilde{\lambda} \int d^3\mathbf{r} \exp(i\beta e_0\varphi(\mathbf{r})) + \\ & i \oint d^2\mathbf{r} \sigma_0\varphi(\mathbf{r}) - k_B T \oint d^2\mathbf{r} \frac{|\sigma_0|}{e_0} \ln(1 + \exp(-\beta\mu_S + i\beta e_0\varphi(\mathbf{r}))). \end{aligned} \quad (3.8)$$

While the bulk part presents an exact field-theoretic representation of the counterion partition function, the surface part pertains to a specific model of the interaction between the mobile charges and the bounding surfaces.

3.3 Mean-field approximation

The functional integral Eq. (3.4) with the field-action functional $\mathcal{S}[\varphi(\mathbf{r})]$ decomposed as

$$\mathcal{S}[\varphi(\mathbf{r})] = \int_V f_V(\varphi(\mathbf{r})) d^3r + \oint_S f_S(\varphi(\mathbf{r})) d^2r, \quad (3.9)$$

and can not be evaluated exactly, since it is in general not Gaussian. One thus has to take recourse to various approximations of which the mean-field approximation, being equivalent to the saddle-point approximation, is the most straightforward one. The mean-field potential $\phi_{\text{MF}}(\mathbf{r})$ of the field-action Eq. (3.9) is defined as a solution of the saddle-point equation corresponding to $\delta\mathcal{S}[\varphi(\mathbf{r})] = 0$ at $\varphi(\mathbf{r}) = i\phi_{\text{MF}}(\mathbf{r})$ where $\phi_{\text{MF}}(\mathbf{r})$ is thus a solution of

$$\nabla \left[\frac{\partial f_V(\phi_{\text{MF}}(\mathbf{r}))}{\partial \nabla \phi_{\text{MF}}(\mathbf{r})} \right] - \frac{\partial f_S(\phi_{\text{MF}}(\mathbf{r}))}{\partial \phi_{\text{MF}}(\mathbf{r})} = 0, \quad (3.10)$$

and

$$-\beta\epsilon\epsilon_0 \frac{\partial \phi_{\text{MF}}(\mathbf{r})}{\partial \mathbf{n}} = \frac{\partial f_S(\phi_{\text{MF}}(\mathbf{r}))}{\partial \phi_{\text{MF}}(\mathbf{r})} = \sigma(\phi_{\text{MF}}(\mathbf{r})), \quad (3.11)$$

where \mathbf{n} is the normal vector to the bounding surface(s), and $\sigma(\phi_{\text{MF}}(\mathbf{r}))$ is the effective surface charge at the bounding surface(s). *In extenso* the first equation is exactly the standard PB equation for the counterion-only system

$$\nabla^2 \phi_{\text{MF}}(\mathbf{r}) = -\frac{\tilde{\lambda}e}{\epsilon\epsilon_0} \exp(-\beta e \phi_{\text{MF}}(\mathbf{r})), \quad (3.12)$$

while the second saddle-point equation with $f(\varphi(\mathbf{r}))$ from Eq. (3.7) reduces to the boundary condition

$$-\beta\epsilon\epsilon_0 \frac{\partial \phi_{\text{MF}}(\mathbf{r})}{\partial \mathbf{n}} = -\frac{\sigma_0}{2} \left[1 + \tanh\left(\frac{1}{2}(-\beta\mu_S + \beta e_0 \phi_{\text{MF}})\right) \right]. \quad (3.13)$$

Obviously, the above surface charge density can span the interval $[-\sigma_0, 0]$. Assuming that $\beta\mu_S = -\ln 10(\text{pH} - \text{p}K)$, with $\text{p}K = -\log K$ and K being the dissociation equilibrium constant while $\text{pH} = -\log [\text{H}^+]$ with $[\text{H}^+]$ the concentration of the protons in the bath, the above boundary condition coincides exactly with the charge regulation boundary condition of the Ninham–Parsegian site-dissociation model [59]. Should there be more than one type of dissociable groups the proper generalization was introduced in Ref. [79]. For the planar geometry the mean-field solution of Eq. (3.12) depends only on the z coordinate and has the form

$$\phi_{\text{MF}}(z) = \frac{1}{\beta e} \ln(\cos^2(\alpha z)), \quad (3.14)$$

where α can be determined from the boundary condition Eq. (3.13) as

$$(1+b)\alpha \tan(\alpha D/2) + b\alpha \tan^3(\alpha D/2) = \frac{1}{\mu}, \quad (3.15)$$

with b being related to the dissociation free energy as $\ln b = \beta\mu_S$. Here μ is the Gouy–Chapman length.

3.4 Second-order (Gaussian) correction

After solving the mean-field equations, one proceeds to analyze the fluctuations around the mean-field potential by evaluating the partition function Eq. (3.4) for the field-action functional $\mathcal{S}[\phi(\mathbf{r}) = \phi_{\text{MF}}(\mathbf{r}) + \delta\phi(\mathbf{r})]$. To the lowest Gaussian order in the field fluctuations $\delta\phi(\mathbf{r})$ the field-action can be expanded

$$\mathcal{S}[\phi(\mathbf{r})] = \mathcal{S}[\phi_{\text{MF}}(\mathbf{r}) + \delta\phi(\mathbf{r})] = S_{\text{MF}}[\phi_{\text{MF}}] + \mathcal{S}_2[\delta\phi(\mathbf{r})] \quad (3.16)$$

where

$$\begin{aligned} \mathcal{S}_2[\delta\phi(\mathbf{r})] &= \frac{1}{2} \int \int \frac{\delta^2 S}{\delta\phi(\mathbf{r})\delta\phi(\mathbf{r})} \Big|_{\text{MF}} \delta\phi(\mathbf{r})\delta\phi(\mathbf{r}') d^3\mathbf{r} d^3\mathbf{r}' + \\ &+ \frac{1}{2} \oint \mathcal{C}_S(\phi(\mathbf{r}')) \Big|_{\text{MF}} \delta\phi(\mathbf{r}')^2 d^2\mathbf{r}, \end{aligned} \quad (3.17)$$

Chapter 3. Counterion-mediated interactions of planar charge regulated surfaces

and obviously decomposes into a volume and a surface term just like the complete field action. Above we introduced the Hessian of the volume part of the field-action as

$$\frac{1}{2} \frac{\delta^2 S}{\delta\phi(\mathbf{r})\delta\phi(\mathbf{r})} \Big|_{\text{MF}} = \frac{1}{2}\beta \left[u^{-1}(\mathbf{r}, \mathbf{r}') - \frac{\beta\tilde{\lambda}}{\cos^2(\alpha z)} \delta^3(\mathbf{r} - \mathbf{r}') \right]; \quad (3.18)$$

where \mathcal{C}_S is the surface capacitance due to the nonlinear coupling of surface charge and surface electrostatic potential

$$\mathcal{C}_S(\mathbf{r}) = \frac{\partial^2 f(\phi_{\text{MF}}(\mathbf{r}))}{\partial(\beta e\phi_{\text{MF}}(\mathbf{r}))^2} = \frac{\partial\sigma}{\partial(\beta e\phi_{\text{MF}}(\mathbf{r}))}. \quad (3.19)$$

We will show later on that in the original theory of KS interactions, it is this surface capacitance that quantifies the thermal charge fluctuations [60].

The decomposition of the field action Eq. (3.17) induces a decomposition of the partition function into a product of the saddle-point partition function and its first order correction, so that finally

$$\begin{aligned} \mathcal{Z} &= \exp\left(-\frac{1}{2} \ln(\det \beta u(\mathbf{r}, \mathbf{r}'))\right) \times \exp(\mathcal{S}[\phi_{\text{MF}}(\mathbf{r})]) \\ &\times \int \mathcal{D}[\delta\phi(\mathbf{r})] \exp(\mathcal{S}_2[\delta\phi(\mathbf{r})]) = \mathcal{Z}_{\text{MF}} \times \mathcal{Z}_2. \end{aligned} \quad (3.20)$$

The last term is due to Gaussian fluctuation around the saddle point and thus corresponds to the one-loop correction in the free energy. In order to proceed we first introduce the appropriate field Green's function

$$\begin{aligned} \mathcal{G}(\delta\phi_1(\mathbf{r}), \delta\phi_2(\mathbf{r})) &= \\ &\int_{\delta\phi_1}^{\delta\phi_2} \mathcal{D}[\delta\phi(\mathbf{r})] \exp\left(\frac{1}{2} \iint \frac{\delta^2 S}{\delta\phi(\mathbf{r})\delta\phi(\mathbf{r})} \Big|_{\text{MF}} \delta\phi(\mathbf{r})\delta\phi(\mathbf{r}') d^3\mathbf{r} d^3\mathbf{r}'\right) \end{aligned} \quad (3.21)$$

that describes the field, or better, the propagation of the fluctuations of the Gaussian electrostatic potential. This will allow us to formally separate the bulk and the surface terms in the calculation of the one-loop partition function. Since the kernel $u^{-1}(\mathbf{r}, \mathbf{r}')$ is isotropic in the transverse directions $\rho = (x, y)$, one can introduce the Fourier–Bessel transform of the fluctuating potential as

$$\delta\phi(\mathbf{r}) = \delta\phi(\rho, z) = \int_0^\infty dQ J_0(Q\rho) \delta\phi(Q, z), \quad (3.22)$$

where $\delta\phi(Q, z)$ depends only on the magnitude of the 2D transverse wave vector, $Q = |\mathbf{Q}|$. With this notation, the complete Green's function can be presented as the product

$$\mathcal{G}(\delta\phi_1(\mathbf{r}), \delta\phi_2(\mathbf{r})) = \Pi_Q \mathcal{G}_Q(\delta\phi(Q, z_1), \delta\phi(Q, z_2)), \quad (3.23)$$

where $\mathcal{G}_Q(\delta\phi(Q, z_1), \delta\phi(Q, z_2))$ can be furthermore derived in the form

$$\begin{aligned} \mathcal{G}_Q(\delta\phi(Q, z_1), \delta\phi(Q, z_2)) &= \\ &\int_{\delta\phi(Q, z_1)}^{\delta\phi(Q, z_2)} \mathcal{D}[\delta\phi(Q, z)] \exp\left(-\frac{1}{2}\beta\epsilon\epsilon_0 \int_{z_1}^{z_2} dz \left[\left(\frac{d\delta\phi}{dz}\right)^2 - \left(Q^2 + \frac{2\alpha^2}{\cos^2(\alpha z)}\right) \delta\phi^2 \right]\right). \end{aligned} \quad (3.24)$$

3.4. Second-order (Gaussian) correction

Obviously, this is nothing but the Feynman propagator of a harmonic oscillator with time-depended frequency, where the z coordinate plays the role of time [123], and the Wick's rotation makes the action real instead of imaginary as in quantum mechanics. The general method of solving this type of functional integrals was described by Khandekar and Lawande [124] and was adapted to this particular case as described in detail in Appendix A.

The partition function, or specifically the part stemming from Gaussian fluctuations, Eq. (3.20), around the mean-field can now be cast into the following form

$$\begin{aligned} \mathcal{Z}_2(D) &= \Pi_Q \int \mathcal{D}[\delta\phi_1(\mathbf{r})\delta\phi_2(\mathbf{r})] \\ &\tilde{\mathcal{G}}_Q(0, \delta\phi_1(\mathbf{r})) \times \exp\left(-\frac{1}{2} \int_{S_1} d^2r \mathcal{C}_{S_1}(\phi_{\text{MF}}) \delta\phi_1^2(\mathbf{r})\right) \times \mathcal{G}_Q(\delta\phi_1(\mathbf{r}), \delta\phi_2(\mathbf{r})) \\ &\times \exp\left(-\frac{1}{2} \int_{S_2} d^2r \mathcal{C}_{S_2}(\phi_{\text{MF}}) \delta\phi_2^2(\mathbf{r})\right) \times \tilde{\mathcal{G}}_Q(\delta\phi_2(\mathbf{r}), 0), \end{aligned} \quad (3.25)$$

where $\tilde{\mathcal{G}}_Q$ stands for the Green's function Eq. (3.24) but with $\alpha = 0$, as there are no counterions behind the two bounding surfaces. The exact form Eq. (A.18) thus still remains valid but evaluated explicitly for vanishing α . Of course in that case the functional integral can be evaluated directly in a trivial fashion. In addition, one needs to take the dielectric constant as ϵ' for $\tilde{\mathcal{G}}_Q(0, \delta\phi_1(\mathbf{r}))$ and $\tilde{\mathcal{G}}_Q(\delta\phi_2(\mathbf{r}), 0)$, but as ϵ for $\mathcal{G}_Q(\delta\phi_1(\mathbf{r}), \delta\phi_2(\mathbf{r}))$ in the definition Eq. (3.24).

One could see the above formula as describing fluctuations behind the surface at $z = z_1$, described by $\tilde{\mathcal{G}}_Q(\epsilon'; 0, \delta\phi_1(\mathbf{r}); \infty)$, fluctuations behind the surface at $z = z_2$, described by $\tilde{\mathcal{G}}_Q(\epsilon'; \delta\phi_2(\mathbf{r}), 0; \infty)$, fluctuations in the space between the two surfaces for $z_1 < z < z_2$, described in their turn by $\mathcal{G}_Q(\epsilon; \delta\phi_1(\mathbf{r}), \delta\phi_2(\mathbf{r}); D)$, and finally all of them coupled through the surface capacitance and the surface potential fluctuations at the two surfaces at $z = z_1$ and $z = z_2$ corresponding to the two exponential terms.

After integration over the boundary electrostatic potential fluctuations the final exact form of the partition function can be written as

$$\begin{aligned} \mathcal{Z}_2(D) &= \Pi_Q \sqrt{\frac{2 \exp(-DQ)Q(\alpha^2 + Q^2)}{2\pi(\alpha \tan(\alpha D/2) + Q)^2 - (\alpha \tan(\alpha D/2) - Q)^2 \exp(-2DQ)}} \\ &\sqrt{\frac{1}{\mathcal{C}_{S_1}\mathcal{C}_{S_2} + \beta\epsilon'\epsilon_0(\mathcal{C}_{S_1} + \mathcal{C}_{S_2})Q + (\beta\epsilon\epsilon_0)^2 N^2 + (\beta\epsilon'\epsilon_0)^2 Q^2 + (\beta\epsilon\epsilon_0)(\mathcal{C}_{S_1} + \mathcal{C}_{S_2} + 2\beta\epsilon'\epsilon_0 Q)M}}}; \end{aligned} \quad (3.26)$$

with the functions M and N defined as

$$\begin{aligned} M &= \frac{Q(\alpha \tan(\alpha D/2) + Q)^2 + (\alpha^2 + \alpha^2 \tan^2(\alpha D/2))(\alpha \tan(\alpha D/2) + Q)}{(\alpha \tan(\alpha D/2) + Q)^2 - (\alpha \tan(\alpha D/2) - Q)^2 \exp(-2DQ)} \\ &- \frac{Q(\alpha \tan(\alpha D/2) - Q)^2 - (\alpha^2 + \alpha^2 \tan^2(\alpha D/2))(\alpha \tan(\alpha D/2) - Q) \exp(-2DQ)}{(\alpha \tan(\alpha D/2) + Q)^2 - (\alpha \tan(\alpha D/2) - Q)^2 \exp(-2DQ)} \\ N^2 &= M^2 - \frac{4 \exp(-2DQ)Q^2(\alpha^2 + Q^2)^2}{\left[(\alpha \tan(\alpha D/2) + Q)^2 - (\alpha \tan(\alpha D/2) - Q)^2 \exp(-2DQ)\right]^2}. \end{aligned} \quad (3.27)$$

We have thereby derived the explicit and exact expressions of the partition function in the form of a mean-field term and the one-loop or Gaussian fluctuation correction that has not been calculated before.

What remains now is the evaluation of the corresponding free energy and specifically the part of this free energy that depends on the separation between the bounding surfaces, i.e. the interaction free energy.

3.5 Second-order correction — interaction free energy

Knowing the partition function for Gaussian fluctuations around the mean-field, one can straightforwardly calculate the second-order or the one-loop correction to the free energy as

$$\frac{\mathcal{F}_2(D)}{S} = -k_B T \ln \frac{\mathcal{Z}_2(D)}{\mathcal{Z}_2(D \rightarrow \infty)}, \quad (3.28)$$

where we subtracted the free energy corresponding to infinite separation, which contains the bulk free energy as well as the surface self-energies. Assuming furthermore that the surfaces have identical properties, i.e., $\mathcal{C}_{S_1} = \mathcal{C}_{S_2} = \mathcal{C}_S$, we get the one-loop correction as:

$$\begin{aligned} \frac{\mathcal{F}_2(D)}{S} &= \frac{k_B T}{4\pi} \int_0^\infty Q dQ \ln \left(\frac{1}{(\alpha^2 + Q^2)} \Delta_{11}^2(Q) \right) \\ &+ \frac{k_B T}{4\pi} \int_0^\infty Q dQ \ln \left(1 - \Delta_{12}^2(Q) \exp(-2QD) \right), \end{aligned} \quad (3.29)$$

where we defined the following quantities

$$\begin{aligned} \Delta_{11}(Q) &= \frac{\mathcal{C}_S(\alpha \tan(\alpha D/2) + Q) + \beta \epsilon_0 \epsilon' Q(\alpha \tan(\alpha D/2) + Q)}{\mathcal{C}_S + \beta \epsilon_0 Q(\epsilon' + \epsilon)} + \\ &+ \frac{\beta \epsilon_0 \{ \epsilon [Q(\alpha \tan(\alpha D/2) + Q) + (\alpha^2 + \alpha^2 \tan^2(\alpha D/2))] \}}{\mathcal{C}_S + \beta \epsilon_0 Q(\epsilon' + \epsilon)}; \end{aligned} \quad (3.30)$$

$$\begin{aligned} \Delta_{12}(Q) &= \frac{\mathcal{A}}{\mathcal{B}} \\ \mathcal{A} &= \mathcal{C}_S(\alpha \tan(\alpha D/2) - Q) + \beta \epsilon_0 \{ \epsilon' Q(\alpha \tan(\alpha D/2) - Q) \\ &- \epsilon [Q(\alpha \tan(\alpha D/2) - Q) - (\alpha^2 + \alpha^2 \tan^2(\alpha D/2))] \}; \\ \mathcal{B} &= \mathcal{C}_S(\alpha \tan(\alpha D/2) + Q) + \beta \epsilon_0 \{ \epsilon' Q(\alpha \tan(\alpha D/2) + Q) \\ &+ \epsilon [Q(\alpha \tan(\alpha D/2) + Q) + (\alpha^2 + \alpha^2 \tan^2(\alpha D/2))] \}. \end{aligned} \quad (3.31)$$

The second-order correction free energy Eq. (3.29) consists of two integrals. The first one corresponds to part of the self-energy of the two bounding surfaces that depends on the inter surface separation, while the second integral represents a generalization of the zero-frequency (classical) van der Waals–Lifshitz term [80]. In fact, it can be easily seen that in the limit of no mobile ions between the surfaces, corresponding to $\alpha = 0$, it reduces exactly to the zero-frequency van der Waals term with

$$\Delta_{12}^2(Q) = \left(\frac{\epsilon' - \epsilon}{\epsilon' + \epsilon} \right)^2, \quad (3.32)$$

3.5. Second-order correction — interaction free energy

while the first term vanishes. With mobile ions present, the second order correction is however very different from this limit. In the limit of fixed surface charge ($\mathcal{C}_{S_1} = \mathcal{C}_{S_2} = 0$) and no dielectric discontinuity ($\epsilon' = \epsilon$), the integral reduces to the known result [31]:

$$\begin{aligned} \frac{\mathcal{F}_2(D)}{S} &= \frac{k_B T}{4\pi} \int_0^\infty \tilde{Q} d\tilde{Q} \ln \left(\frac{1}{\tilde{\alpha}^2 + \tilde{Q}^2} \times \left(\frac{2\tilde{Q} + 2\tilde{Q}^2 + \tilde{\alpha}^2 + 1}{2\tilde{Q}} \right)^2 \right) \\ &+ \frac{k_B T}{4\pi} \int_0^\infty \tilde{Q} d\tilde{Q} \ln \left(1 - \left(\frac{1 + \tilde{\alpha}^2}{2\tilde{Q} + 2\tilde{Q}^2 + \tilde{\alpha}^2 + 1} \right)^2 \exp(-2\tilde{D}\tilde{Q}) \right), \end{aligned} \quad (3.33)$$

leading to the attractive pressure that scales as $\ln \tilde{D} \times \tilde{D}^{-3}$ in a system composed of mobile counterions and fixed surface charge. At the end we also consider a formal limit of the free energy corresponding to no dielectric discontinuity $\epsilon' = \epsilon$, as well as no mobile ions $\alpha \rightarrow 0$, but nevertheless assuming a non-vanishing surface capacitance \mathcal{C} . While this limit is not meaningful in our model, we will nevertheless use it to show how the KS result [64, 65], which is based on a linear response formalism and considers no coupling between the mean-field solution and the corresponding values of the capacitances, is obtained from our conceptual framework.

The KS limit could be obtained more directly if instead of a counterion-only case dealt with here, one considers a monovalent salt as indeed was considered by Kirkwood and Shumaker in their derivation of the long range interaction between protein molecules with dissociable surface groups [64, 65]. Nevertheless, for $\alpha \rightarrow 0$ our general result reduces to

$$\Delta_{12}^2(Q) = \left(\frac{\mathcal{C}}{\mathcal{C} + 2\beta\epsilon\epsilon_0 Q} \right)^2, \quad (3.34)$$

which in its turn, to the lowest order in the surface capacitance leads to the disjoining pressure

$$p = -\frac{\partial}{\partial D} \left[\frac{\mathcal{F}_2(D)}{S} \right] \sim \mathcal{C}^2 D^{-1}. \quad (3.35)$$

As it depends quadratically on the surface capacitance, this interaction presents the contribution of monopolar fluctuations in the surface charge to the free energy. This can be easily confirmed by evaluating the free energy of two fluctuating charge distributions in the Gaussian approximation explicitly. Let us now show that interaction pressure Eq. (3.35) corresponds exactly to the KS interaction between two planar surfaces.

In fact, the disjoining pressure Eq. (3.35) starts to become more familiar when we realize that a Hamaker-type summation [66] for two thin planar surface sheets with a pair interaction of the KS scaling $\mathcal{V}(R) \sim R^{-2}$, gives the interaction pressure as [64]

$$p = \frac{F(R)}{S} = -\frac{\partial}{\partial D} \int_D^\infty 2\pi R dR \mathcal{V}(R) \sim D^{-1}. \quad (3.36)$$

The two forms of the disjoining pressure, Eqs. (3.35) and (3.36), are thus identical, meaning that the KS interaction is nothing but a monopolar fluctuation interaction. This is clear from the fact that the separation dependence of the fluctuation interaction free energy between two surfaces is slower in the case of standard vdW

interaction that stems from dipolar fluctuations between either two semi-infinite media or two thin layers, scaling respectively as [66]

$$p = \frac{F(R)}{S} = -\frac{A(D)}{12\pi D^2} \quad \text{and/or} \quad -\frac{2A(D)a^2}{\pi D^5}. \quad (3.37)$$

The KS fluctuation forces thus originate in monopolar fluctuations and follow a different scaling than in the case of dipolar fluctuations, either between point particles, R^{-2} , or between fluctuating surface layers, D^{-1} . They arise directly from surface capacitance that is non-zero only for the surface free energy that is non-linear, i.e. at least quadratic, with respect to the local electrostatic potential.

3.6 Numerical results

It is convenient to introduce dimensionless quantities by using the Gouy–Chapman length scale μ and $\sigma_0^2/2\epsilon\epsilon_0$ as the disjoining pressure scale. Hence, the length scale (\mathbf{r}, D) , the free energy (F) , the disjoining pressure (p) and the surface capacitance (\mathcal{C}) can all be rescaled into dimensionless variables $\tilde{\mathbf{r}} = \mathbf{r}/\mu$, $\tilde{D} = D/\mu$, $\tilde{F} = F/\left(\frac{\sigma_0^2}{2\epsilon\epsilon_0}\right)\mu^3$, $\tilde{p} = p/\left(\frac{\sigma_0^2}{2\epsilon\epsilon_0}\right)$, and $\tilde{\mathcal{C}} = \mu\mathcal{C}$ respectively. We also introduce the dielectric mismatch $\Delta = (\epsilon - \epsilon')/(\epsilon + \epsilon')$. With these definitions, the mean-field free energy becomes

$$\frac{\tilde{\mathcal{F}}_0(\tilde{D})}{\tilde{S}} = \tilde{\alpha}^2 \tilde{D} + 2 \ln(1 + \tilde{\alpha}^2), \quad (3.38)$$

where $\tilde{\alpha} = \mu\alpha$ is the solution of the boundary condition

$$(1 + b)\tilde{\alpha} \tan(\tilde{\alpha}\tilde{D}/2) + b\tilde{\alpha} \tan^3(\tilde{\alpha}\tilde{D}/2) = 1. \quad (3.39)$$

The rescaled surface capacitance in terms of $\tilde{\alpha}$ is then equal to

$$\tilde{\mathcal{C}}_{S_1, S_2} = 2\beta\epsilon\epsilon_0 b \frac{1 + \tan^2(\tilde{\alpha}\tilde{D}/2)}{[1 + b + b \tan^2(\tilde{\alpha}\tilde{D}/2)]^2}, \quad (3.40)$$

which goes to zero for large values of b , $\lim_{b \rightarrow \infty} \tilde{\mathcal{C}}_{S_1, S_2} \rightarrow 0$ as well as for vanishing b , $\lim_{b \rightarrow 0} \tilde{\mathcal{C}}_{S_1, S_2} \rightarrow 0$. We also invoke a coupling parameter Ξ , analogous to the one introduced by Netz and Moreira [24], given as

$$\Xi = \frac{e_0^3 \sigma_0}{8\pi(\epsilon\epsilon_0 k_B T)^2}, \quad (3.41)$$

for monovalent counterions. For a counterion-only system with fixed surface charge, the magnitude of the coupling parameter defines a weak- and a strong-coupling regime [10]. In our case, the existence of the surface free energy introduces also other length scales that preclude a direct introduction of a unique electrostatic coupling parameter and it is thus in general not possible to establish the presence of the weak and the strong-coupling limits *strictu sensu* as exact limits of the partition function.

While the weak-coupling limit can therefore not be derived as an exact limit, the saddle-point can be defined for any field-action. As explained in detail in Ref. [10] we thus use the saddle-point solution as the *proxy* for the weak coupling limit and evaluate the contribution of the fluctuations around the saddle-point to the free energy.

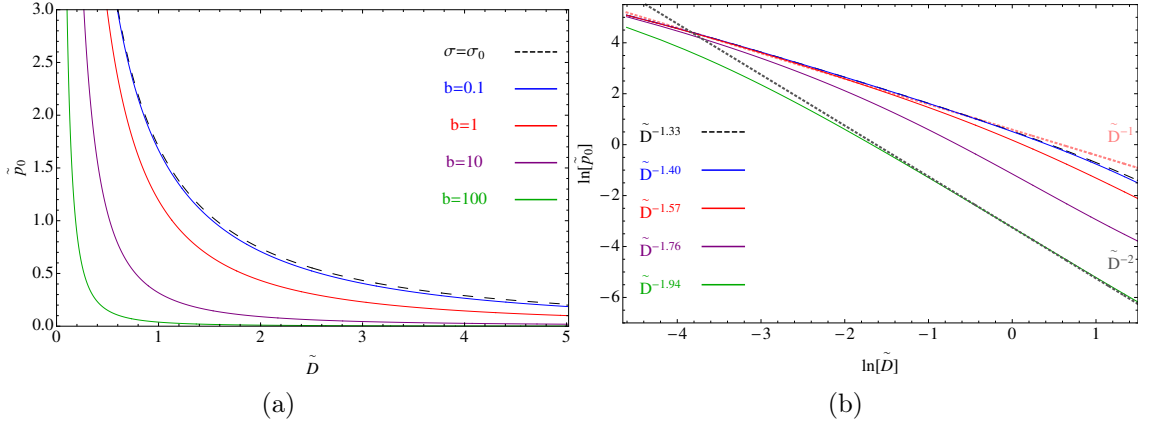


Figure 3.2: (a) Rescaled mean-field disjoining pressure plotted as a function of rescaled surface separation for different values of parameter b . The curve $\sigma = \sigma_0$ corresponds to $b = 0$. (b) Rescaled mean-field pressure from (a) plotted in a log-log plot. The two dotted lines represent the scalings \tilde{D}^{-1} and \tilde{D}^{-2} introduced solely to guide the eye. Obviously the scaling \tilde{D}^{-1} for mean-field pressure sets in for small and \tilde{D}^{-2} for large values of the dimensionless separation.

The surface interaction part of the Gaussian fluctuating free energy from Eq. (3.29), in a dimensionless form is then given as:

$$\frac{\tilde{\mathcal{F}}_2(\tilde{D})}{\tilde{S}} = \frac{1}{2} \Xi \int_0^\infty \tilde{Q} d\tilde{Q} \ln \left(1 - e^{-2\tilde{Q}\tilde{D}} \times \left(\frac{\mathcal{P}}{\mathcal{Q}} \right)^2 \right), \quad (3.42)$$

with

$$\begin{aligned} \mathcal{P} &= 2(1 + \Delta)b(1 + \tan^2(\frac{\tilde{\alpha}\tilde{D}}{2}))(\tilde{\alpha} \tan(\frac{\tilde{\alpha}\tilde{D}}{2}) - \tilde{Q}) \\ &\quad - (1 + b + b \tan^2(\frac{\tilde{\alpha}\tilde{D}}{2}))^2 [2\Delta\tilde{Q}(\tilde{\alpha} \tan(\frac{\tilde{\alpha}\tilde{D}}{2}) - \tilde{Q}) - (1 + \Delta)(\tilde{\alpha}^2 + \tilde{\alpha}^2 \tan^2(\frac{\tilde{\alpha}\tilde{D}}{2}))]; \\ \mathcal{Q} &= 2(1 + \Delta)b(1 + \tan^2(\frac{\tilde{\alpha}\tilde{D}}{2}))(\tilde{\alpha} \tan(\frac{\tilde{\alpha}\tilde{D}}{2}) + \tilde{Q}) \\ &\quad + (1 + b + b \tan^2(\frac{\tilde{\alpha}\tilde{D}}{2}))^2 [2\tilde{Q}(\tilde{\alpha} \tan(\frac{\tilde{\alpha}\tilde{D}}{2}) + \tilde{Q}) + (1 + \Delta)(\tilde{\alpha}^2 + \tilde{\alpha}^2 \tan^2(\frac{\tilde{\alpha}\tilde{D}}{2}))]. \end{aligned} \quad (3.43)$$

We first investigate the surface separation dependence of the interaction free energy and the disjoining pressure between the surfaces pertaining to that dependence. The mean-field rescaled pressure is shown in (Fig. 3.2) (a), as a function of the surface dissociation energy $\ln b = \beta\mu_S$ in a lin-lin and log-log plots. Clearly, the higher the energy penalty for charge dissociation at the surface, b , the lower is the interaction pressure between the two surfaces, until for large enough energy penalty the interaction remains close to zero for all intersurface separations. The scaling of the mean-field disjoining pressure with the separation is shown in (Fig. 3.2) (b). For constant surface charge $\sigma = \sigma_0$, i.e., corresponding formally to $b = 0$, the asymptotic forms of the mean-field interaction pressure are $\lim_{D \rightarrow \infty} \tilde{p}_0(D) \sim \tilde{D}^{-2}$ and $\lim_{D \rightarrow 0} \tilde{p}_0(D) \sim \tilde{D}^{-1}$, see Ref. [41]. This is in fact also what we observe in the case

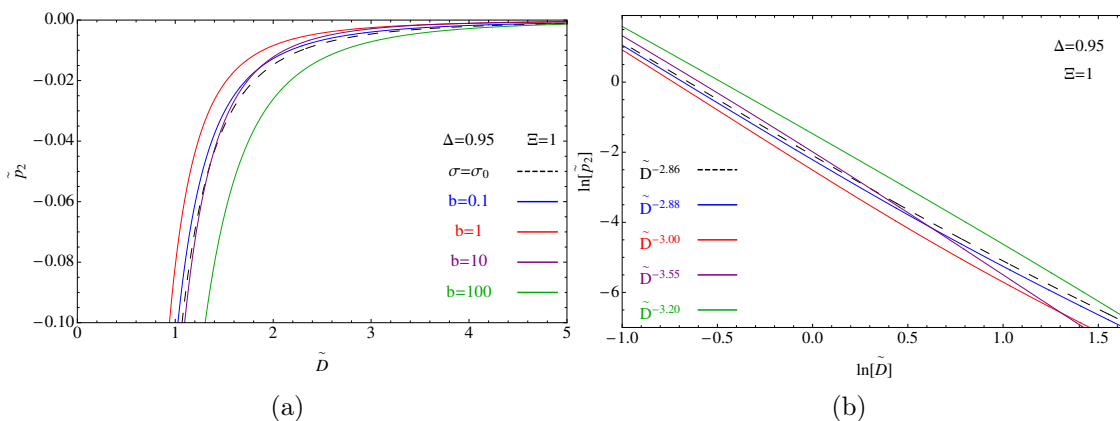


Figure 3.3: (a) Rescaled fluctuation disjoining pressure as a function of rescaled surface separation is plotted for different values of parameter b with a fixed dielectric jump $\Delta = 0.95$, and coupling parameter $\Xi = 1$. (b) Rescaled fluctuation disjoining pressure from (a) plotted in a log-log plot to show the effective scaling of the disjoining pressure with the intersurface separation. The scaling exponent is typically comparable with the case of the counterion-only Coulomb fluid between two surfaces with fixed charges, which is -3 , but its exact value depends on b .

of charge regulation, with the proviso that the regime of validity of the two limits depends additionally on the value of b ; the smaller its value the more extended the region of \tilde{D}^{-1} scaling.

Because the surface capacitance depends on the mean-field solution, the fluctuation correction to the free energy and the corresponding disjoining pressure also depend on the surface dissociation energy, as can be discerned from (Fig. 3.3) (a). This is very different from the standard vdW interactions that do not depend on the mean-field solution, at least in the standard DLVO formulation [66]. The scaling of the fluctuation part of the interaction pressure, (Fig. 3.3) (b), shows a robust value of the scaling exponent close to -3 , close to its value for the case of a counterion-only Coulomb fluid between two surfaces with fixed charges, where the fluctuation disjoining pressure scales exactly as $\sim \ln D \times D^{-3}$, see Ref. [10] for details. The exact value of the scaling exponent in the charge-regulated case, however, depends on the value of the surface interaction parameter b . Since the dielectric mismatch in this case is not zero, the monopolar and vdW dipolar fluctuation interactions, stemming from the surface capacitance and the dielectric mismatch respectively, are always mixed together and can not be disentangled in the separation dependence of the fluctuation pressure.

Adding the mean-field and the fluctuation contribution together, (Fig. 3.4), we note that for large values of the surface dissociation energy, the fluctuation contribution becomes dominant, a simple consequence of the fact that the mean-field vanishes while the fluctuation part remains finite. While in general the fluctuation part is always subdominant to the mean-field solution, in this case the matters are a bit more complicated as the charge regulation can wipe out the mean-field entirely but not the fluctuation part. The fluctuation disjoining pressure for a vanishing mean-field again depends crucially on the presence of the dielectric mismatch at the bounding surfaces and does not necessarily coincide with the standard vdW interaction. In fact, for the case of complete dielectric homogeneity, $\Delta = 0$ see

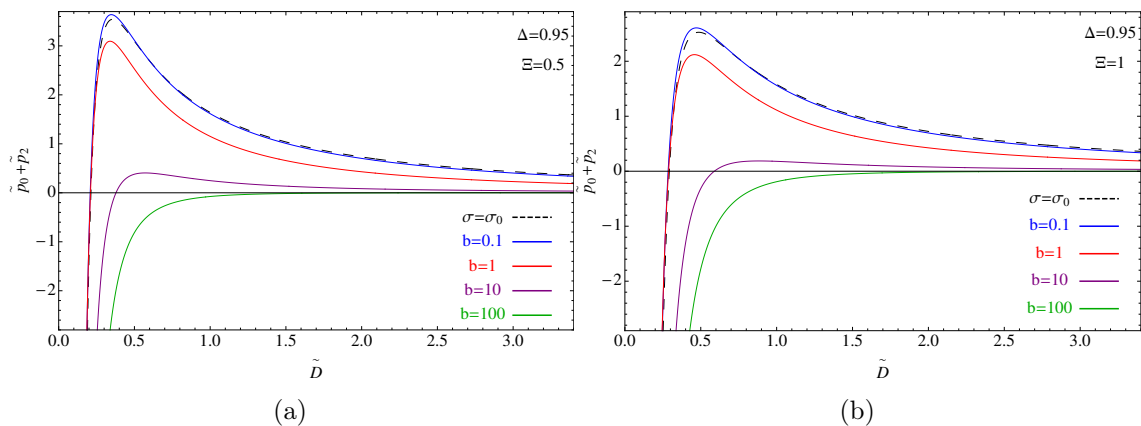


Figure 3.4: Rescaled total disjoining pressure as a function of the rescaled surface separation plotted for different values of the parameter b , fixed dielectric jump $\Delta = 0.95$ and for the following values of the coupling parameter: (a) $\Xi = 0.5$; (b) $\Xi = 1$.

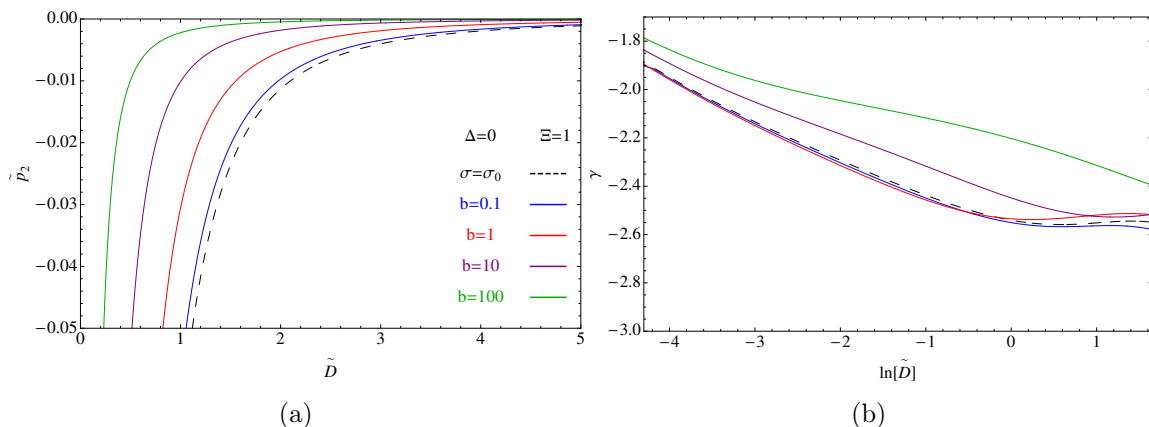


Figure 3.5: (a) Rescaled fluctuation disjoining pressure as a function of rescaled surface separation is plotted for different values of the parameter b but without any dielectric jump, $\Delta = 0$, and $\Xi = 1$. (b) The scaling exponent γ for the effective scaling of the disjoining pressure with the intersurface separation is defined as $\tilde{p}_2 \sim \tilde{D}^\gamma$. For small separations it approaches -1 asymptotically, whereas for large separations it tends to a value close but not equal to -3 .

(Fig. 3.5), the interaction pressure scaling exponent is in general smaller than for $\Delta \neq 0$. Asymptotically for small separations in fact it approaches one, just as for the KS interaction. For larger separations it tends to a larger value but does not approach -3 as the fluctuations it corresponds to, being due to the presence of counter ions between the surfaces, are never purely dipolar.

Finally, in order to get an idea about the strength of the attractive interaction we compare the fluctuation disjoining pressure p_2 with the pure vdW pressure given as $p_{vdW} = -H(\Delta)/12\pi D^3$ [66], where $H(\Delta)$ is a Hamaker coefficient, which for illustration purposes we chose to be 4.3 zJ [125]. We choose a large dielectric inhomogeneity ($\Delta = 0.95$), and a separation between the surfaces of 1 nm ($D = 1$ nm), bearing maximal surface charge $\sigma_0 = 0.5$ e₀/nm². With the given set of parameters,

we calculate the fluctuation disjoining pressure $p_{b=0}$ corresponding to a maximal charge at the surfaces, and the fluctuating disjoining pressure $p_{b=100}$, corresponding to the case of electroneutral surfaces. One finds that for this specific choice of parameters the fluctuating pressure is comparable to the vdW disjoining pressure: $p_{vdW} = -1.1$ bar while $p_{b=100} = -1.3$ bar and $p_{b=0} = -0.8$ bar.

3.7 Conclusions

In this Chapter, we derived a theory describing electrostatic interactions between macromolecular surfaces bearing dissociable charge groups immersed in an aqueous solution of dissociated counterions. Introducing a surface free energy corresponding to a simple model of charge regulation, and formulating it in a field-theoretic language, we derived the mean-field solution related to the Ninham–Parsegian charge regulation theory and also obtained an exact solution for the second-order fluctuations around the mean-field. The fluctuation contribution to the total free energy is related to vdW interactions but is fundamentally modified by the presence of dissociable charges on the bounding surfaces as well as the counterions dissolved in the space between them.

While for the model discussed, containing an additional surface term usually not present in Coulomb fluids with fixed charges on interacting surfaces, a weak-coupling approximation can not be consistently defined, we proceed from the observation that the saddle-point and the fluctuations around the saddle-point can be defined for any field action [10]. The range of validity of this approximation should eventually be ascertained once compared with detailed simulations of the same microscopic model.

What our methodology also clearly identifies, is the monopolar nature of the fluctuation interactions between charge-regulated surfaces that singles them out from the dipolar fluctuation interactions as is the case for vdW fluctuation interactions. This sets the two types of interactions fundamentally apart as the range and scaling characteristics of the two are vastly different. It also emerges quite straightforwardly that the two types of fluctuation interactions are not additive but are fundamentally intertwined and can only be decoupled in extreme limiting cases of either no dielectric discontinuity or in the case of no surface capacitance. More specific predictions regarding the role of monopolar fluctuation interactions between dissociable charge groups corresponding to deprotonated and protonated molecular groups, as is the case for proteins, will be forthcoming once the model considered is generalized to include the intervening salt solution at a set value of the solution pH, which is going to be a subject of the Chapter 4.

Suffice it to say at this point that in an appropriate limit our theory is related to the KS interactions known to be relevant in the protein context. More importantly though, it allows to consistently generalize the theory of KS interactions, or indeed any electrostatic interaction that presumes charge regulation, in such a way that one can use advanced concepts and methods of the Coulomb fluid theory to solve it approximately. In this way, we pave the way to new developments in the theory of KS and related interactions that would not be conceivable within their original theoretical framework [64, 65].

Chapter 4

Titrating macroions in monovalent salt solution

In Chapter 3 we set a proper theoretical framework for describing charge-regulation interactions, where we solved a problem of counterion-mediated interactions between charge-regulated surfaces. In biological systems, it is more common situation to have proteins in a solution where the salt ions are ubiquitous components (as in a physiological solution, where the concentration of monovalent salt is approximately 0.1 M). So now we proceed with studying a system, more related to the one also found in nature. Again, we start from the simplest model, that takes two spherical macroions with dissociable groups immersed in monovalent salt solution, corresponding more closely to the original KS model.

The aim of this Chapter is to present an improved theory of fluctuation interaction for two small and distant spherical macroions subject to charge regulation. The problem will be formulated in the way that allows for decoupling of the charge regulation part and the interaction part, of which the former can be treated exactly while the latter can be described on the DH level. This allows us to derive a closed form expression for the total interaction and compare it with various approximate forms, including the original KS expression. Furthermore, we will be able to go beyond the KS result and derive realistic pH and ionic strength dependent interactions between protein macroions with known amino acid composition.

4.1 Model

We consider a model system composed of two charged spherical macroions in a 1:1 salt solution (Fig 4.1). The charge of the macroions is not constant, but is described by a dissociation surface free energy density cost corresponding to the Parsegian-Ninham charge regulation model, as discussed in Chapter 3, of the general lattice gas form

$$f_0(\varphi(\mathbf{r})) = i\sigma_0\varphi(\mathbf{r}) - \alpha k_B T \frac{\sigma_0}{e_0} \ln \left(1 + b \exp(i\beta e_0\varphi(\mathbf{r})) \right), \quad (4.1)$$

where α quantifies the number of dissociation sites and $\ln b = -\ln 10(\text{pH} - \text{p}K) = \beta\mu_S$, where $\text{p}K$ is the dissociation constant and μ_S is the free energy of charge dissociation. Here $\varphi(\mathbf{r})$ is the local fluctuating potential that needs to be integrated over to get the final partition function. The mean-field PB approximation is obtained by identifying $\varphi(\mathbf{r}) \rightarrow i\phi = i\phi_{\text{PB}}$ [126]. The total dissociation free energy for a

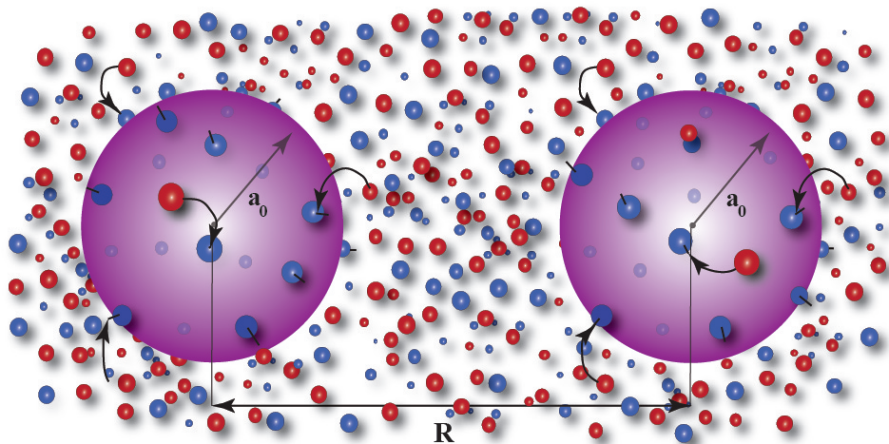


Figure 4.1: Schematic representation of the model: two charge-regulated ions immersed in 1:1 salt solution.

spherical macroion of a radius a_0 , sufficiently small so that one can assume that the electrostatic potential is uniform over its surface, $\varphi(|\mathbf{r}| = a_0) = \varphi$, and can be written in the form

$$\begin{aligned}
 f(\varphi) &= \oint_S f_0(\varphi(\mathbf{r})) d^2\mathbf{r} \longrightarrow \\
 &\longrightarrow iN e_0 \varphi - \alpha k_B T N \ln(1 + b \exp(i\beta e_0 \varphi)), \quad (4.2)
 \end{aligned}$$

where N is the number of absorption sites satisfying $\int dS \sigma_0 = N e_0$, and $\alpha > 1$ is a coefficient of asymmetry, determining the width of the interval spanned by the particle's effective charge $e(\phi)$ as a function of the mean-field potential on its surface $\phi = \phi(a_0)$:

$$\begin{aligned}
 e(\phi = \phi(a_0)) &= \frac{\partial f(\phi)}{\partial \phi} = \\
 e_0 N \left[\left(\frac{\alpha}{2} - 1 \right) - \frac{\alpha}{2} \tanh \left(-\frac{1}{2} (\ln b - \beta e_0 \phi) \right) \right]. \quad (4.3)
 \end{aligned}$$

The effective charge of the macroion can thus fluctuate in the interval $-N e_0 < e < (\alpha - 1) N e_0$, $\alpha > 1$. When $\alpha = 2$ the charge interval is by definition symmetric $[-N e_0, N e_0]$. All of the expressions for the charge regulation referred to above are just variants of the surface lattice gas free energies [126] with a variable number of dissociation sites that describe the dissociation of the charge moieties on the surface of the macroions. In addition, we have taken the limit of small macroions, $a_0 \rightarrow 0$, implying that the surface potential on the macroions is a constant, $f(\varphi) = \oint_{|\mathbf{r}|=a_0} f_0(\varphi(\mathbf{r})) d^2\mathbf{r}$.

While the approximation of treating the macroion as a point-like particle is a convenient analytical device to make the calculations tractable, it obviously entails some additional limitations to their validity. The most severe one is the disregard of non-spherically symmetric charge fluctuations, or equivalently of fluctuating higher order multipoles. A macroion of finite extension, with an angular distribution of surface dissociable sites, will typically show fluctuating monopoles, dipoles etc. that depend on the local electrostatic potential. The point-particle simplification retaining only the monopolar fluctuations can be argued to be the most important

contribution in the large separation limit, while the higher order multipoles are subdominant. In addition, higher order multipoles - starting with the dipole - would invariably couple the charge fluctuation interaction with the standard van der Waals interaction.

In addition, the point macroion approximation disregards the electrostatic interaction between dissociable groups, as they are represented by a single point-like charge regulated moiety. A finite size of the macroion with angular dependence of the dissociation site distribution would bring in also the electrostatic interactions between the sites on the same macroion, which could furthermore lead to potentially important new facets in the interaction between two macroions. While this line of reasoning can certainly be pursued, and will be in the future, it is important to have the “baseline“ point-macroion results first in order to assess the importance of other contributions.

Assuming that the fluctuating electrostatic potential of one macroion is $\phi_1(a) = \varphi_1$ and of the other one is $\phi_2(a) = \varphi_2$, located at \mathbf{r}_1 and \mathbf{r}_2 , respectively, the partition function of the system can be derived in the field-theoretic form, see Appendix B:

$$\mathcal{Z} = \iint d\varphi_1 \exp(-\beta f(\varphi_1)) G(\varphi_1, \varphi_2) \exp(-\beta f(\varphi_2)) d\varphi_2, \quad (4.4)$$

where the partition function has already been normalized by dividing with the bulk system partition function [127], obtained for $f(\varphi) = 0$. $G(\varphi_1, \varphi_2)$ is the propagator of the field, defined with the values of the potential φ_1 and φ_2 at the location of the first and the second particle respectively, derived in Appendix B:

$$G(\varphi_1, \varphi_2) = \exp\left(-\frac{\beta}{2} \begin{pmatrix} \varphi_1 \\ \varphi_2 \end{pmatrix}^T \begin{pmatrix} G(\mathbf{r}_1, \mathbf{r}_1) & G(\mathbf{r}_1, \mathbf{r}_2) \\ G(\mathbf{r}_1, \mathbf{r}_2) & G(\mathbf{r}_2, \mathbf{r}_2) \end{pmatrix}^{-1} \begin{pmatrix} \varphi_1 \\ \varphi_2 \end{pmatrix}\right), \quad (4.5)$$

where the matrix of Green’s functions for the bulk composed of a 1:1 electrolyte in the DH approximation is given as:

$$\begin{pmatrix} G(\mathbf{r}_1, \mathbf{r}_1) & G(\mathbf{r}_1, \mathbf{r}_2) \\ G(\mathbf{r}_1, \mathbf{r}_2) & G(\mathbf{r}_2, \mathbf{r}_2) \end{pmatrix} = \begin{pmatrix} (\exp(-\kappa a)/4\pi\epsilon\epsilon_0 a) & (\exp(-\kappa R)/4\pi\epsilon\epsilon_0 R) \\ (\exp(-\kappa R)/4\pi\epsilon\epsilon_0 R) & (\exp(-\kappa a)/4\pi\epsilon\epsilon_0 a) \end{pmatrix}, \quad (4.6)$$

Here we assumed that the two macroions can not come closer than $a = 2a_0$. The DH screening is given as $\kappa = \sqrt{8\pi l_B c}$, where c is the salt concentration. Variations on the above form are possible that would contain the factor $\exp(-\kappa(R-a))/R(1+\kappa a)$ for the separation dependence of $G(\mathbf{r}, \mathbf{r})$. We will comment on the detailed choice of the form for the DH interaction later.

The charge regulation energy term $\exp(-\beta f(\varphi))$ can now be expanded as a binomial [128]:

$$\begin{aligned} \exp(-\beta f(\varphi)) &= \exp(-i\beta N e_0 \varphi) [1 + b \exp(i\beta e_0 \varphi)]^{\alpha N} = \\ &= \sum_{n=0}^{\alpha N} \binom{\alpha N}{n} b^n \exp(-i\beta N e_0 \varphi) \exp(i\beta e_0 n \varphi). \end{aligned} \quad (4.7)$$

The integral (4.4) then becomes:

$$\mathcal{Z} = \frac{1}{\mathcal{Z}_0} \iint d\varphi_1 d\varphi_2 \sum_n^{\alpha N} \sum_{n'}^{\alpha N} a_n a_{n'} \exp(-i\beta e_0(N-n)\varphi_1) \times \exp\left(-\frac{\beta}{2} \begin{pmatrix} \varphi_1 \\ \varphi_2 \end{pmatrix}^T \begin{pmatrix} G(\mathbf{r}_1, \mathbf{r}_1) & G(\mathbf{r}_1, \mathbf{r}_2) \\ G(\mathbf{r}_1, \mathbf{r}_2) & G(\mathbf{r}_2, \mathbf{r}_2) \end{pmatrix}^{-1} \begin{pmatrix} \varphi_1 \\ \varphi_2 \end{pmatrix}\right) \exp(-i\beta e_0(N-n')\varphi_2) \quad (4.8)$$

where $a_n(\alpha) = \binom{\alpha N}{n} b^n$ for any α .

Introducing the dimensionless variables $\tilde{R} = R/lB$, $\tilde{a} = a/lB$ and $\tilde{\kappa} = \kappa lB$, one can rewrite the partition function for two equal macroions with both charges allowed to vary in the interval $[-Ne_0, Ne_0]$ in the form:

$$\mathcal{Z} = \sum_n^{2N} \sum_{n'}^{2N} a_n(2) a_{n'}(2) \exp\left(-\beta \mathcal{F}_{N,N}(n, n', \tilde{R})\right), \quad (4.9)$$

where we introduced $\mathcal{F}_{N,N}(n, n', \tilde{R})$ as:

$$\mathcal{F}_{N,N}(n, n', \tilde{R}) = \frac{1}{2} \left\{ \frac{e^{-\tilde{\kappa}\tilde{a}}}{\tilde{a}} [(N-n)^2 + (N-n')^2] + 2 \frac{e^{-\tilde{\kappa}\tilde{R}}}{\tilde{R}} (N-n)(N-n') \right\}. \quad (4.10)$$

Clearly, we have incorporated exactly the charge regulation free energy for each of the macroions, while the electrostatic coupling between the two macroions is included approximately *via* the DH propagator. The configuration of this particular example is symmetric, as the two macroions are identical and are described by the same charge regulation free energy. The asymmetric configuration, corresponding to unequal charge regulation free energies for the two macroions, is addressed next.

In order to describe two equal macroions with a regulated charge in the interval $-Ne_0 < e < 0$ we take as a model expression Eq. (6) with $\alpha = 1$, *i.e.*,

$$f(\varphi) = iMe_0\varphi - \alpha k_B T N \ln(1 + b \exp(i\beta e_0\varphi)), \quad (4.11)$$

where $M = N$ and with the partition function

$$\mathcal{Z} = \sum_n^N \sum_{n'}^N a_n(1) a_{n'}(1) \exp\left(-\beta \mathcal{F}_{N,N}(n, n', \tilde{R})\right). \quad (4.12)$$

Furthermore, charge regulation in the interval $0 < e < Ne_0$ is described by

$$f(\varphi) = -k_B T N \ln(1 + b \exp(i\beta e_0\varphi)), \quad (4.13)$$

corresponding to the protonation of neutral state ($M = 0$), with the partition function for two equal macroions obtained in the form:

$$\mathcal{Z} = \sum_{n=0}^N \sum_{n'=0}^N a_n(1) a_{n'}(1) \exp\left(-\mathcal{F}_{0,0}(n, n', \tilde{R})\right). \quad (4.14)$$

4.2. Symmetric–asymmetric charges on proteins

Finally, for an asymmetric case, where the two macroions are different, one with charge in the allowed interval $[0, Ne_0]$ and the other one spanning the interval $[-Ne_0, 0]$, the partition function is obviously obtained in the form

$$\mathcal{Z} = \sum_{n=0}^N \sum_{n'=0}^N a_n(1)a_{n'}(1) \exp\left(-\mathcal{F}_{N,0}(n, n', \tilde{R})\right), \quad (4.15)$$

These results for the partition function derived above can be written succinctly in a single formula as:

$$\mathcal{Z} = \sum_n^{\alpha N} \sum_{n'}^{\alpha N} a_n(\alpha)a_{n'}(\alpha) \exp\left(-\beta\mathcal{F}_{N,M}(n, n', \tilde{R})\right), \quad (4.16)$$

where one can distinguish three different cases:

- $M = N, \alpha = 2$ - full symmetric system (the macroions are identical, both with charge spanning the symmetric interval $[-Ne_0, Ne_0]$);
- $M = N, \alpha > 2$ - semi-symmetric system (the macroions are identical, both with charge spanning the asymmetric interval $[-Ne_0, \alpha Ne_0]$);
- $N \neq 0, M = 0, \alpha = 1$ - asymmetric system (one particle is positive, with charge fluctuating $[0, Ne_0]$, the other negative with charge spanning the interval $[-Ne_0, 0]$).

The partition function Eq. (4.16) can be evaluated exactly only numerically, as we will do as well, in addition to providing two explicit analytical approximations.

4.2 Symmetric–asymmetric charges on proteins

We proceed to calculate the average value of the charge of the macroions $\langle e_{1,2} \rangle$, charge cross correlation $\langle e_1 e_2 \rangle$ and auto-correlation function $\langle e_1 - \langle e_1 \rangle \rangle^2$ for all three systems. The thermodynamic averages can be written as

$$\langle \dots \rangle = \frac{1}{\mathcal{Z}} \sum_{n, n'}^{\alpha N} a_n(\alpha)a_{n'}(\alpha) \dots \exp\left(-\beta\mathcal{F}_{N,M}(n, n', \tilde{R})\right). \quad (4.17)$$

In this way, we can write e.g. the dimensionless average charge of the particle, $\langle \tilde{e}_1 \rangle = \langle e_1 \rangle / e_0$ as:

$$\langle \tilde{e}_1 \rangle = \langle (n - M) \rangle. \quad (4.18)$$

In a similar way, other averages are calculated exactly from the full partition function and are plotted as functions of \tilde{R} and $\text{pH} - \text{p}K$, for different values of the number of absorption sites N and salt concentration c , keeping fixed the diameter of the macroions \tilde{a} , see (Figs. 4.2, 4.3, 4.5 and 4.6).

In a fully symmetric system (Fig. 4.2) (solid lines), the average charge is allowed to vary in a symmetric interval, reaching the point of zero charge (PZC) for $\text{pH} = \text{p}K$. Away from PZC, the average charge changes almost linearly until it reaches saturation and stays constant for any value of $\text{pH} - \text{p}K$ (Fig. 4.2(a)). The charge auto-correlation function is positive with the maximum centered at the PZC, being larger

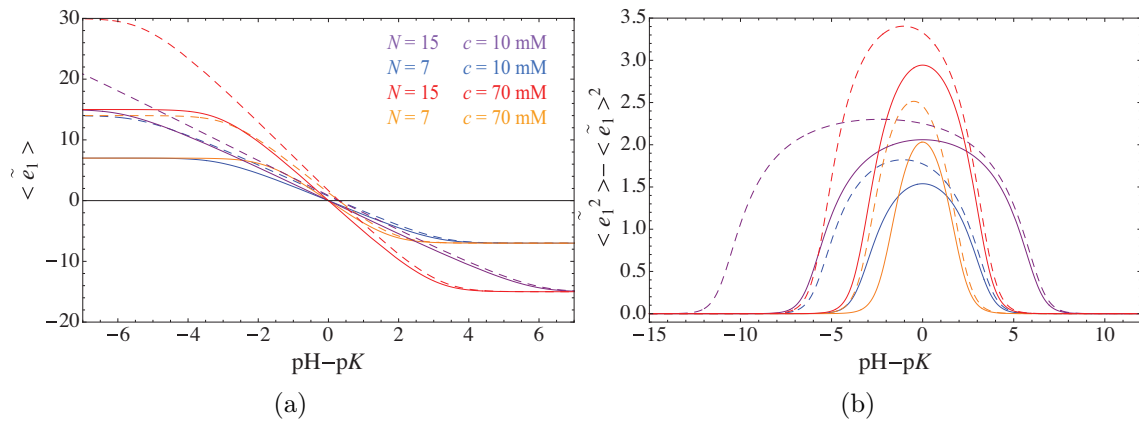


Figure 4.2: Symmetric system: (a) The average charge of macroions; (b) Auto-correlation function. All averages are obtained by exact evaluation of the partition function. Solid lines correspond to a fully-symmetric system ($\alpha = 2$), while dashed lines represent the semi-symmetric case which takes asymmetry coefficient to be $\alpha = 3$. Each color corresponds to a choice of parameters (number of adsorption sites N and salt concentration c) as described in panel (a). The dimensionless diameter of the macroions is $\tilde{a} = 1$ and separation between them $\tilde{R} = 1.5$.

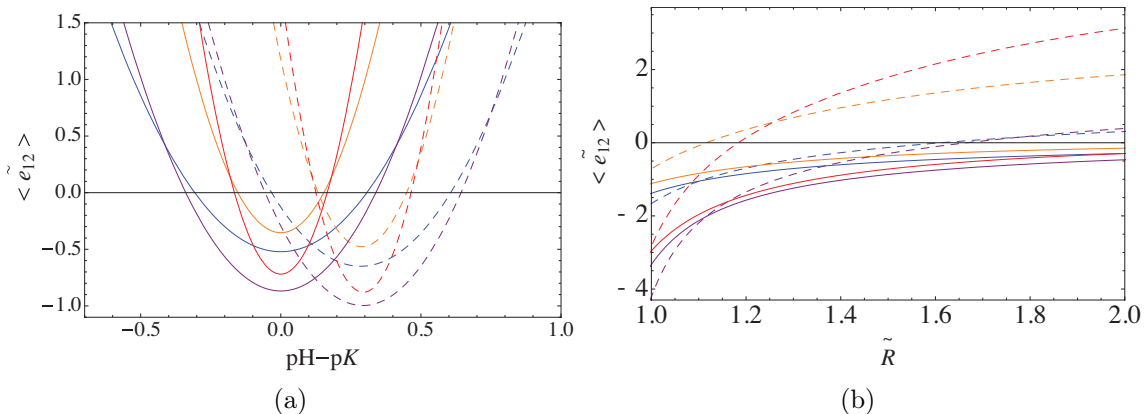


Figure 4.3: Charge cross-correlation function for fully-symmetric system (solid lines) and semi-symmetric system (dashed lines): (a) pH-dependence at $R = 1.5$; (b) R -dependence at $\text{pH} - \text{pK} = 0$. All averages are obtained by exact evaluation of the partition function. Each color corresponds to a choice of parameters (number of adsorption sites N and salt concentration c) as described in Fig. 4.2 (a). The dimensionless diameter of the macroions is taken as $\tilde{a} = 1$.

for larger number of adsorption sites and salt concentration (Fig. 4.2(b)). The charge cross correlation function, being negative close to the PZC, indicates that even in the fully symmetric system the macroion charges prefer to fluctuate asymmetrically: charge fluctuation on one macroion being accompanied with a fluctuation of the opposite sign on the other macroion (Fig. 4.3)(a). This is a robust property of the system, fully discernable also in the 1-dimensional exact solutions [128]. Considering the charge cross correlation function as a function of distance between macroions, plotted for fixed $\text{pH} = \text{pK}$ (Fig. 4.3)(b), one can observe that at the PZC, fluctua-

4.2. Symmetric–asymmetric charges on proteins

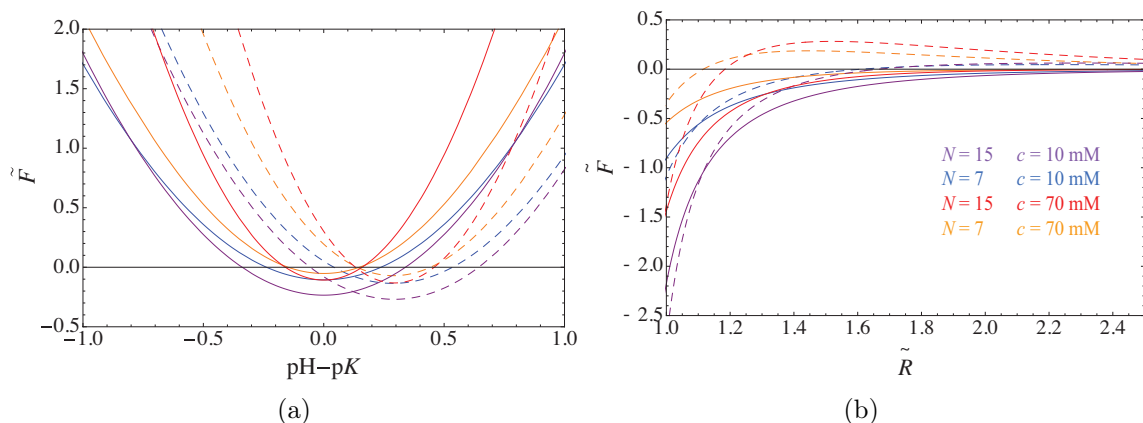


Figure 4.4: The interaction force for fully-symmetric system (solid lines) and semi-symmetric system (dashed lines), plotted as: (a) pH-dependence at $R = 1.5$; (b) R -dependence at $\text{pH} - \text{p}K = 0$. All averages are obtained by exact evaluation of the partition function. Each color corresponds to a choice of parameters (number of adsorption sites N and salt concentration c) as described in panel (b). The dimensionless diameter of the macroions is taken as $\tilde{a} = 1$.

tion asymmetry effect decreases as separation increases, and it is the strongest for larger number of adsorption sites and smaller values of salt concentration.

Finally, the interaction force is calculated as

$$\tilde{F}(\tilde{R}) = -\frac{d}{d\tilde{R}}[-\ln \mathcal{Z}(\tilde{R})],$$

and it is shown in (Figs. 4.4 and 4.7). Two identical macroions repel for most values of the parameters, but show a net attraction in the vicinity of the PZC. This attraction is of purely fluctuational origin, stemming from the asymmetric charge cross-correlation. At the same value of dimensionless separation, the strength of this fluctuation attraction is larger in systems with a larger number of adsorption sites and smaller salt concentration.

Concerning the semi-symmetric system of macroions with both charges spanning the same asymmetric interval (Figs. 4.2 - 4.4) (dashed lines), one discerns similar behavior of all averages as in the fully symmetric system. However here, the PZC is no longer determined by $\text{pH} = \text{p}K$, but is shifted, meaning that the concentration of the positive ions close to the macroion surfaces is different from the concentration of protons in the bulk. The auto-correlation function as a function $\text{pH} - \text{p}K$ is not centered anymore on the PZC, but the asymmetric fluctuations do again appear at the PZC, (Fig. 4.3), where one can observe net attraction between the macroions, (Fig. 4.4) (dashed lines).

The behavior of the completely asymmetric system is shown in (Figs. 4.5- 4.7). Here, away from PZC, the first macroion is positive, the second neutral, or the first can be neutral, while the second can be negatively charged, depending on the value of $\text{pH} - \text{p}K$. In the region $-3 \lesssim \text{pH} - \text{p}K \lesssim 3$ both macroions carry nonzero charge of opposite sign, and at $\text{pH} = \text{p}K$, the system is electroneutral as a whole, i.e. the sum of average charges is equal to zero, Fig 4.5(a). The charge cross correlation function is always negative (Fig. 4.6(a)) and one can observe only

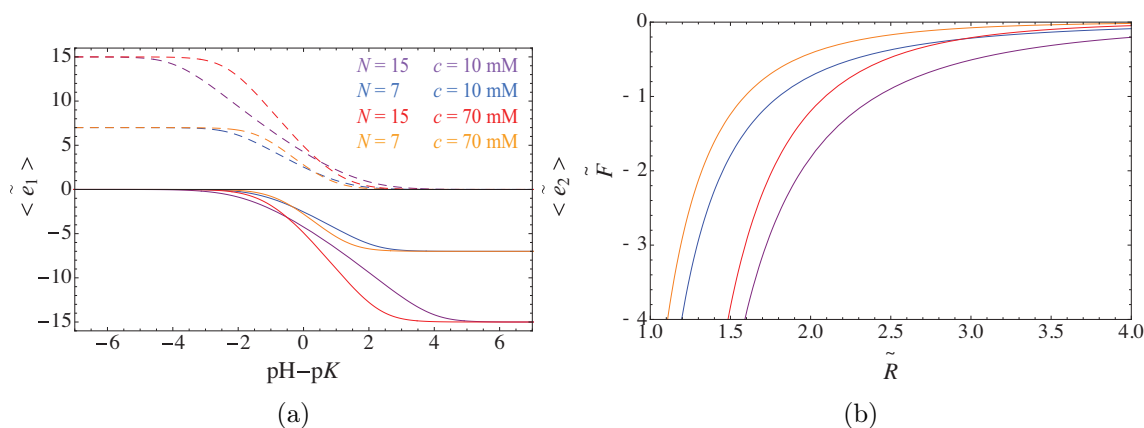


Figure 4.5: Asymmetric system: (a) The average charge of one particle (solid lines) and the other (dashed lines); (b) the interaction force at $\text{pH} = \text{p}K$. All averages are obtained using the exact evaluation of full partition function. Each color corresponds to a choice of parameters (number of adsorption sites N and salt concentration c) as described in (a). The dimensionless diameter of the macroions is $\tilde{a} = 1$ and the separation between them $\tilde{R} = 1.5$.

attraction (Fig. 4.5)(b). The number of adsorption sites has the biggest influence on the intensity of interaction.

The fluctuation effect shows an interesting twist in this system: the interaction force as a function of separation shows attraction also when one of the macroions is charged and the other one reaching its point of zero charge, see (Fig. 4.7)(a). The origin of that attraction comes from the mean charge-induced charge interaction, see (Fig. 4.7)(b), where one can observe non-zero product $\langle \tilde{e}_i \rangle^2 \langle (\tilde{e}_j - \langle \tilde{e}_j \rangle)^2 \rangle$ of non-zero charge $\langle \tilde{e}_i \rangle^2$ and autocorrelation function of zero charge $\langle \tilde{e}_j \rangle$. As it is the case in the symmetric system, here also for the same separation the attraction is significantly stronger in a solution with larger number of adsorption sites and smaller salt concentration.

4.3 Discussion

In the previous section we showed results obtained numerically using the exact evaluation of the full partition function [129]. The aim of this section is to seek an analytical approximation that will provide a better intuition about the behavior of the attractive interaction arising between identical macroions with fluctuating charge, so that it can be compared with the original KS result for the attractive components as well as the DH result for the repulsive component, respectively. In order to do so, we will evaluate the partition function, Eq. (4.16), introducing two different approximations, the *saddle-point* approximation and the “*Gaussian*” approximation, comparing the ensuing approximative results with the exact ones. The approximations refer to the evaluation of the partition function Eq. (4.4) and not to the evaluation of the field Green’s function, $G(\varphi_1, \varphi_2)$, which is always assumed to be of the DH form. All the approximations detailed below thus refer to the evaluation of the charge regulation part of the partition function.

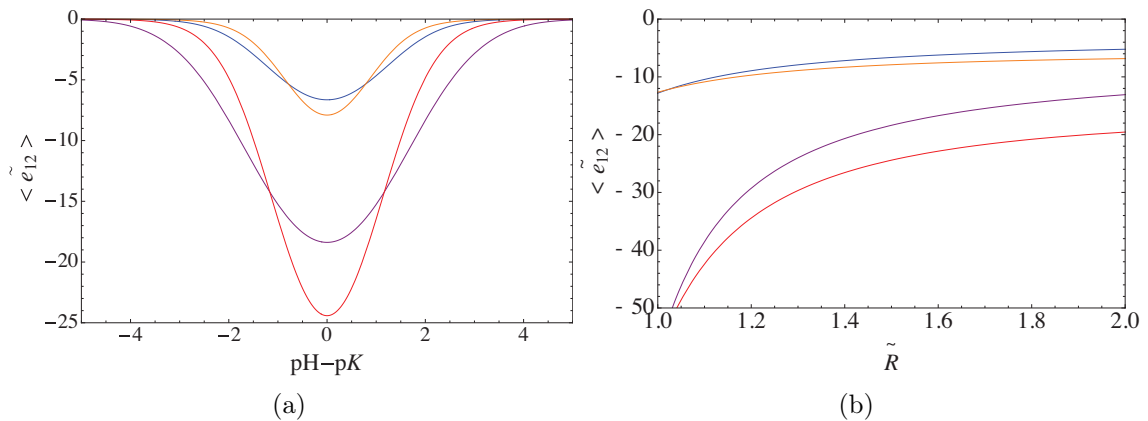


Figure 4.6: Asymmetric system — charge cross-correlation function (a) pH-dependence at $R = 1.5$; (b) R -dependence at $\text{pH} - \text{p}K = 0$. All averages are obtained using the exact evaluation of full partition function. Each color corresponds to a choice of parameters (number of adsorption sites N and salt concentration c) as described in Fig. 4.5(a). The dimensionless diameter of the macroions is $\tilde{a} = 1$.

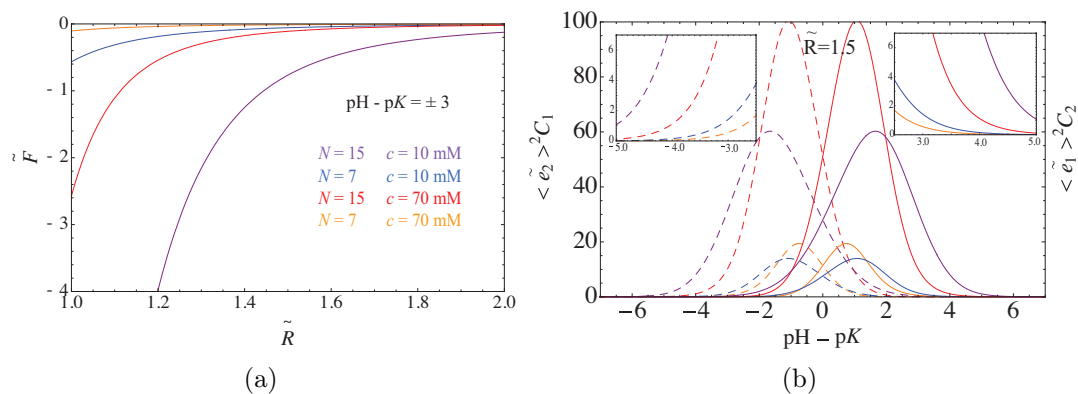


Figure 4.7: Asymmetric system: (a) the interaction force plotted at $\text{pH} - \text{p}K = 3$; (b) $\langle \tilde{e}_1 \rangle^2 \langle (\tilde{e}_2 - \langle \tilde{e}_2 \rangle)^2 \rangle$ (solid lines) and $\langle \tilde{e}_2 \rangle^2 \langle (\tilde{e}_1 - \langle \tilde{e}_1 \rangle)^2 \rangle$ (dashed lines). All averages are obtained using the exact evaluation of full partition function. Each color corresponds to a choice of parameters (number of adsorption sites N and salt concentration c) as described in (a). The dimensionless diameter of the macroions is $\tilde{a} = 1$.

4.3.1 Saddle-point approximation

The saddle-point approximation consists of finding the dominant contribution to the partition function, corresponding to the minimum of the field action, which is then expanded around the minimum to the second-order in deviation. The saddle-point approximation is usually referred to also as the mean-field approximation, but we need to distinguish the mean-field in the treatment of the charge regulation free energy with the PB mean-field, which refers to the interaction part. The procedure is detailed in Appendix C, where we derive expressions for the saddle-point free energy, as well as the fluctuation induced free energy from the second-order correction Eq. (C.9). With respect to that decomposition, one can distinguish the saddle-point interaction force, \tilde{F}_0 , and the fluctuation component of the interaction force, \tilde{F}_2 , with magnitudes given by:

$$\begin{aligned} \tilde{F}_0 &= \frac{1 + \tilde{\kappa}\tilde{R}}{\tilde{R}^2} \tilde{a}^2 \exp(2\tilde{\kappa}\tilde{a} - \tilde{\kappa}\tilde{R}) \\ &\times \frac{\left[\phi_1^* - \frac{\tilde{a}}{\tilde{R}} \exp(\tilde{\kappa}(\tilde{a} - \tilde{R}))\phi_2^*\right] \left[\phi_2^* - \frac{\tilde{a}}{\tilde{R}} \exp(\tilde{\kappa}(\tilde{a} - \tilde{R}))\phi_1^*\right]}{\left[1 - \left(\frac{\tilde{a}}{\tilde{R}}\right)^2 \exp(-2\tilde{\kappa}(\tilde{R} - \tilde{a}))\right]^2} \end{aligned} \quad (4.19)$$

and:

$$\tilde{F}_2 = -\frac{1 + \tilde{\kappa}\tilde{R}}{\tilde{R}^3} \frac{\tilde{a}^2 \exp(-2\tilde{\kappa}(\tilde{R} - \tilde{a}))}{h_1(\phi_1^*)h_2(\phi_2^*) - \frac{\tilde{a}^2}{\tilde{R}^2} \exp(-2\tilde{\kappa}(\tilde{R} - \tilde{a}))}. \quad (4.20)$$

Here $h_1(\phi_1^*)$ and $h_2(\phi_2^*)$ are defined by:

$$\begin{aligned} h_1(\phi_1^*) &= 1 + \frac{\tilde{a}}{\alpha b N} \exp(\tilde{\kappa}\tilde{a}) \exp(-\phi_1^*)(b + e^{\phi_1^*})^2; \\ h_2(\phi_2^*) &= 1 + \frac{\tilde{a}}{\alpha b N} \exp(\tilde{\kappa}\tilde{a}) \exp(-\phi_2^*)(b + e^{\phi_2^*})^2, \end{aligned} \quad (4.21)$$

with ϕ_1^* and ϕ_2^* the solutions of the saddle-point equations, Eqs. (C.3) and (C.4), given in the Appendix C. Since they are obtained numerically, this method does not give us a transparent analytical solution for the free energy and interaction force.

The sum of the saddle-point interaction force, \tilde{F}_0 , and the fluctuation force, \tilde{F}_2 , for symmetric, semi-symmetric and asymmetric systems are plotted as functions of separation \tilde{R} and compared with results obtained with exact evaluation of the full partition function, (Fig. 4.8). One can notice that there is a good agreement between both results obtained using these different methods. The saddle-point method decouples the total force into a saddle-point part and a fluctuation part, one being repulsive and the other attractive, respectively, except for the asymmetric system, where there is no repulsion whatsoever and where the agreement is not so good as in the previous two cases, (Fig. 4.8)(c). They can be differentiated based on the separation scaling of the interaction free energy. In the first case it decays exponentially with \tilde{R} , while in the second it decays exponentially with $2\tilde{R}$. The repulsive force decreases as the system is approaching the PZC, where it is identically equal to zero. In this regime the fluctuation component to the interaction force becomes the dominant one.

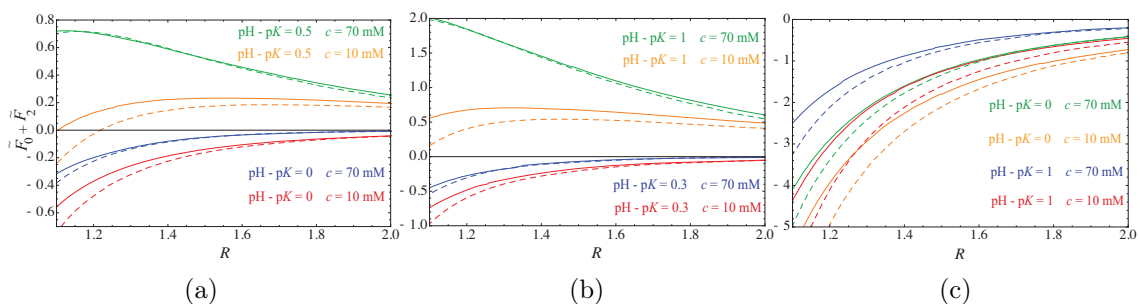


Figure 4.8: Total interaction force, obtained using the saddle-point approximation to evaluate the full partition function, (dashed lines) compared with numerical results, obtained using the exact evaluation of the full partition function, (solid lines). (a) fully symmetric system ($\alpha = 2$); (b) semi-symmetric system with $\alpha = 3$; (c) asymmetric system. Each color corresponds to a different choice of parameters (salt concentration c and $\text{pH} - \text{pK}$) as indicated. The dimensionless diameter of the macroions is $\tilde{a} = 1$ and number of adsorption sites $N = 7$.

4.3.2 Gaussian approximation

In this case the analytical evaluation of the partition function Eq. (4.16), is based on a Gaussian approximation for the binomial coefficient, and it is presented in Appendix D.

The partition function in this case also decouples into two separate contributions, of which one decays exponentially with \tilde{R} , and the other one decays exponentially with $2\tilde{R}$. We will again refer to them as the “mean“ and the “fluctuation“ part of the interaction force, using the same notation as for the saddle-point approximation. One should note here that on this approximation level there is no real decoupling into the mean and fluctuation part. We differentiate them purely based on their scaling with separation.

The mean interaction force, \tilde{F}_0 , can be obtained as:

$$\tilde{F}_0 = \frac{1 + \tilde{\kappa}\tilde{R}}{\tilde{R}^2} \tilde{a}^2 \exp(2\tilde{\kappa}\tilde{a} - \tilde{\kappa}\tilde{R}) \frac{[(\text{pH} - \text{pK}) \ln 10]^2}{\left[1 + 2\frac{\tilde{a}}{N} \exp(\tilde{\kappa}\tilde{a}) + \frac{\tilde{a}}{\tilde{R}} \exp(-\tilde{\kappa}(\tilde{R} - \tilde{a}))\right]^2} \quad (4.22)$$

and the fluctuation force, \tilde{F}_2 , as:

$$\tilde{F}_2 = -\frac{1 + \tilde{\kappa}\tilde{R}}{\tilde{R}^3} \frac{\tilde{a}^2 \exp(-2\tilde{\kappa}(\tilde{R} - \tilde{a}))}{\left(1 + \frac{4\tilde{a}}{\alpha N} \exp(\tilde{\kappa}\tilde{a})\right)^2 - \frac{\tilde{a}^2}{\tilde{R}^2} \exp(-2\tilde{\kappa}(\tilde{R} - \tilde{a}))}. \quad (4.23)$$

Again both \tilde{F}_0 and \tilde{F}_2 are obtained in the same way and the separation into “mean“ and “fluctuation“ part is arbitrary. Nevertheless, the separation scaling of the two is the same as for the mean-field and fluctuation contribution in the case of the saddle-point approximation, making the nomenclature reasonable.

The general form of mean interaction force is given in Eq. (D.4), valid for all three systems considered: fully symmetric, semi-symmetric and asymmetric. Because of its complexity, we display here only \tilde{F}_0 for the fully symmetric system, Eq. (4.22).

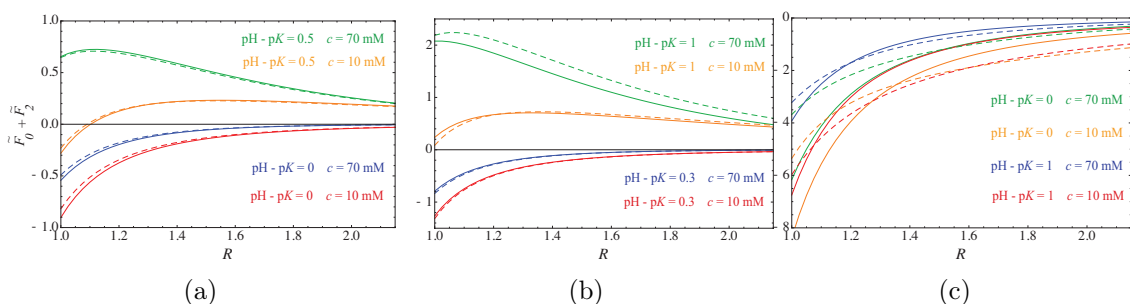


Figure 4.9: Analytical results for the total force, obtained using approximative evaluation of full partition function, (dashed lines) are compared with numerical results, obtained using exact evaluation of full partition function, (solid lines). (a) fully symmetric system ($\alpha = 2$); (b) semi-symmetric system with $\alpha = 3$; (c) asymmetric system. Each color suits to the corresponding choice of parameters (salt concentration c , and $\text{pH} - \text{pK}$) as it is shown at figures. The dimensionless diameter of the macroions is $\tilde{a} = 1$ and number of adsorption sites $N = 7$.

On the other side, the fluctuation force, Eq. (4.23), has the same, universal form for all three types of systems. One can compare these results, Eqs. (4.22), (4.23), with those obtained using the saddle-point approximation, Eqs. (4.19) (4.20).

Clearly, the fluctuation force in the Gaussian approximation corresponds exactly to the fluctuating force in the saddle-point approximation, if the saddle-point is taken at the PZC, $\text{pH} = \text{pK}$, and the mean-potentials are $\phi_1^* = \phi_2^* = 0$. However, in general the two approximations do not coincide and thus we can not claim that \tilde{F}_2 is purely fluctuational in origin.

The mean and the fluctuation part to the interaction force are plotted as functions of dimensionless separation \tilde{R} in (Fig. 4.9). The total interaction force obtained in this way is compared with the one obtained using the exact evaluation of the partition function. For the fully symmetric system, the Gaussian approximation fits perfectly the exact results (Fig. 4.9)(a). A good agreement is found in a semi-symmetric system (Fig. 4.9)(b), while the analytical results do not work quite well in the region away from PZC in the asymmetric system (Fig. 4.9)(c).

In the fully symmetric system, the mean part of the interaction force is repulsive, decreasing on approach to the PZC, while in the asymmetric system, it is actually attractive as the macroions are on the average oppositely charged. On the other hand, the fluctuation component to the interaction force is attractive no matter what the symmetry of the system and the pH of solution, while it does depend on the salt concentration. Interestingly enough, on the Gaussian approximation level for the binomial coefficient the pH-dependence of the auto-correlation function again drops out completely, which is contrary to the full numerical evaluation of the charge auto-correlation function.

4.3.3 Comparison with Debye–Hückel and Kirkwood–Shumaker forms

We now set our results against the mean-field DH theory of interactions between point-like macroions, and against the KS theory of charge fluctuation forces. Obviously, without charge regulation the charge of both interacting macroions is fixed

and the DH form of the interaction should be recovered. Setting $\alpha = 0$ and $M = N$ in Eq. (4.16), one indeed gets the DH interaction force between two well separated like-charged macroions in a salt solution:

$$\tilde{F} \approx N^2 \frac{\exp(-\tilde{\kappa}\tilde{R})}{\tilde{R}}. \quad (4.24)$$

Charge regulation, besides inducing attraction at the PZC, also introduces significant modifications in the mean-field interaction force, Eq. (4.22), leading to its vanishing at the PZC. In the limit of large separations, the charge-regulated interaction force Eq. (4.22), in fact scales as:

$$\tilde{F}_0 \approx \frac{1}{\tilde{R}} \tilde{a}^2 \exp(2\tilde{\kappa}\tilde{a} - \tilde{\kappa}\tilde{R}) \frac{[(\text{pH} - \text{p}K) \ln 10]^2}{(1 + 2\frac{\tilde{a}}{N} \exp(\tilde{\kappa}\tilde{a}))^2}, \quad (4.25)$$

clearly showing a strong dependence on the solution pH.

As for the fluctuation component of the interaction force for two spherical point-like macroions, we can cast its form in the Gaussian approximation, going to a limit of large separation, Eq. (4.23), as

$$\tilde{F}_2 \approx -\frac{\tilde{\kappa}}{\tilde{R}^2} \frac{\tilde{a}^2 \exp(-2\tilde{\kappa}(\tilde{R} - \tilde{a}))}{[1 + 2\frac{\tilde{a}}{N} \exp(\tilde{\kappa}\tilde{a})]^2}. \quad (4.26)$$

The charge auto-correlation function for the two macroions, $\langle \Delta \tilde{e}_1^2 \rangle = \langle (\tilde{e}_1 - \langle \tilde{e}_1 \rangle)^2 \rangle$, is calculated analytically using the same Gaussian approximation and the following form is obtained:

$$\langle \Delta \tilde{e}_1^2 \rangle \langle \Delta \tilde{e}_2^2 \rangle \approx \frac{\tilde{a}^2 \exp(2\tilde{\kappa}\tilde{a})}{(1 + 2\frac{\tilde{a}}{N} \exp(\tilde{\kappa}\tilde{a}))^2}. \quad (4.27)$$

With this result the fluctuation component of the interaction force assumes the asymptotic form:

$$\tilde{F}_2 \approx -\frac{\tilde{\kappa} \exp(-2\tilde{\kappa}\tilde{R})}{\tilde{R}^2} \langle \Delta \tilde{e}_1^2 \rangle \langle \Delta \tilde{e}_2^2 \rangle. \quad (4.28)$$

This actually coincides exactly with the original Kirkwood Shumaker result [64, 65] if we take into account the fact that they take the DH Green's function for two point charges with a finite size-scaling factor $\exp(\tilde{\kappa}\tilde{a})/(1 + \tilde{a})$, so that we would have to multiply Eq. (4.28) by $\exp(-2\tilde{\kappa}\tilde{a})(1 + \tilde{a})^2$. Again we note that on this approximation level the pH-dependence of the auto-correlation function drops out completely, but is retained in the full numerical evaluation of the charge auto-correlation function.

4.4 Protein-like macroions

The general theory formulated above can be straightforwardly applied to the interaction of protein-like macroions at large separations. In a protein, the amino acids Asp, Glu, Tyr and Cys can be negatively charged, while Arg, Lys and His can carry a positive charge, all depending on the solution conditions. The respective $\text{p}K$'s for the dissociation of the various amino acids are given at the Table 1.1.

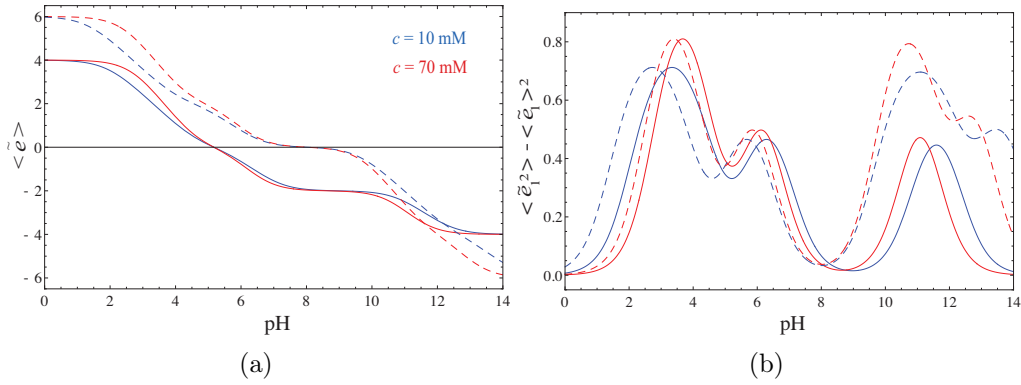


Figure 4.10: Generalized system: (a) The average charge of macroions; (b) charge auto-correlation function. All results are obtained by using the exact numerical evaluation of the full partition function. Solid lines correspond to a system of two proteins, each of which consists of 2 Asp, 2 Glu, 2 Lys, 2 His, while dashed lines represent the system which has additional 2 Tyr and 2 Arg. Blue color corresponds to the value of salt concentration $c = 10$ mM, while the red color corresponds to the $c = 70$ mM. The dimensionless diameter of the macroions is $\tilde{a} = 1$ and separation between them $\tilde{R} = 1.5$.

In order to describe a protein macroion composed of these amino acids, one should write down the charge regulation free energy in the form:

$$f_p(\varphi) = i \sum_j N_j M_j e_0 \varphi - kT \sum_j N_j M_j \ln(1 + b_j \exp(i\beta e_0 \varphi)) - kT \sum_k N_k M_k \ln(1 + b_k \exp(i\beta e_0 \varphi)), \quad (4.29)$$

where j stands for negative AAs $j = \{\text{Asp, Glu, Tyr, Cys}\}$, while k stands for positive ones $k = \{\text{Arg, His, Lys}\}$. N_j, N_k are the numbers of adsorption sites on each positive and negative AAs and since each of these AAs has one adsorption site it will be set to 1. M_j, M_k count how many times each of AAs occurs in the protein, and b_j, b_k stand for $b_n = \exp(-(\text{pH} - \text{p}K_n) \ln 10)$, where $\text{p}K_n$ for each AA is given in Table 1.1. For point-like macroions the spatial distribution of AAs on the surface of the protein is irrelevant and the above approximation is thus admissible.

The partition function for the system of two point-like proteins immersed in monovalent salt solution and containing seven types of dissociable AAs, negatively charged $\{\text{Asp, Glu, Tyr, Cys}\}$ and positively charged $\{\text{Arg, His, Lys}\}$, can be written as:

$$\mathcal{Z} = \prod_{\ell=1,7} \sum_{i_\ell, i'_\ell}^{M_i^\ell, M_{i'}^\ell} b_\ell^{i_\ell + i'_\ell} \frac{M_i^\ell!}{i_\ell! (M_i^\ell - i_\ell)!} \frac{M_{i'}^\ell!}{i'_\ell! (M_{i'}^\ell - i'_\ell)!} \exp(-\beta \mathcal{F}_{pp}). \quad (4.30)$$

where ℓ runs through $\{\text{Asp, Glu, Tyr, Cys}\}$ and $\{\text{Arg, His, Lys}\}$, with:

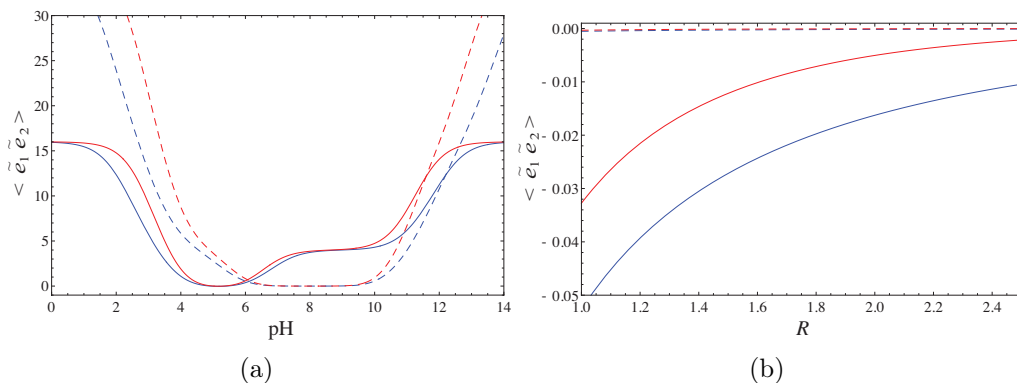


Figure 4.11: Generalized system: charge cross correlation function - (a) pH dependence; (b) R -dependence. All results are obtained by using the exact numerical evaluation of the full partition function. Solid lines correspond to a system of two proteins, each of which consists of 2 Asp, 2 Glu, 2 Lys, 2 His, while dashed lines represent the system which has additional 2 Tyr and 2 Arg. Blue color corresponds to the value of salt concentration $c = 10$ mM, while the red color corresponds to the $c = 70$ mM. The functions bearing \tilde{R} -dependence are plotted at isoelectric point of two systems: $\text{pH} = 5.15$ and $\text{pH} = 8$ respectively, while the function bearing pH-dependence are plotted at fixed separation $\tilde{R} = 1.5$. The dimensionless diameter of the macroions is $\tilde{a} = 1$.

$$\mathcal{F}_{pp} = \frac{1}{2} \left\{ \frac{e^{-\tilde{\kappa}\tilde{a}}}{\tilde{a}} \left[\sum_m (M_i^m - i)^2 + \sum_m (M_{i'}^m - i')^2 \right] + 2 \frac{e^{-\tilde{\kappa}\tilde{R}}}{\tilde{R}} \sum_m (M_i^m - i) \sum_m (M_{i'}^m - i') \right\}, \quad (4.31)$$

where the unprimed/primed notations referred to the two protein macroions. M_i^ℓ counts how many times each of these seven amino-acids occurs in a protein, while M_i^m is restricted on counting only negative amino acids. b_ℓ refer to the chemical energy of dissociation: $b_\ell = \exp(-(\text{pH} - \text{p}K_\ell) \ln 10)$, where the intrinsic $\text{p}K_\ell$ for the seven dissociable amino-acids are given in the Table [1.1](#).

Since the evaluation of Eq. [\(4.30\)](#), is computationally time consuming, we consider only the behavior of two model systems, one (system I) composed of protein-like macro-ions consisting of 2 Asp, 2 Glu, 2 Lys, 2 His, and the other (system II) having 4 AAs more - 2 Tyr and 2 Arg. The results are shown in (Figs. [4.10](#) - [4.12](#)). The protein charge, as a function of pH, spans a symmetric interval with constant plateaus in the pH regions, that correspond to charging up an additional AA. The cross-correlation function in general follows the pattern of plateaus of the average charge, being positive everywhere except at the PZC, where asymmetric charge distribution appears. The auto-correlation function and the charge cross-correlation show opposite signs, with one being positive and the other negative, respectively.

Analyzing the behavior of the interaction force, one can see that two identical proteins mutually repel and that the strength of the interaction depends on pH in the solution, following closely the behavior of the charge cross-correlation function. The repulsion is smaller in a solution of higher salt concentration, since the salt

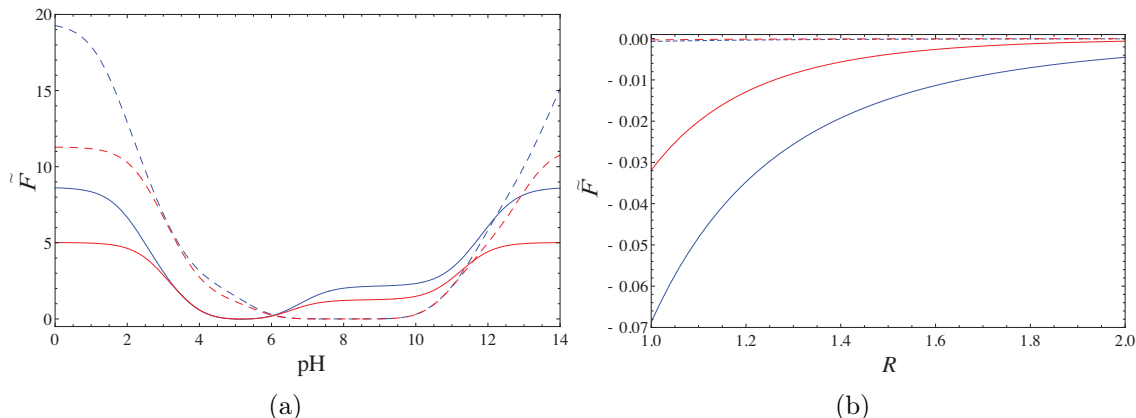


Figure 4.12: Generalized system: interaction force - (a) pH-dependence; (b) R -dependence. All results are obtained by using the exact numerical evaluation of the full partition function. Solid lines correspond to a system of two proteins, each of which consists of 2 Asp, 2 Glu, 2 Lys, 2 His, while dashed lines represent the system which has additional 2 Tyr and 2 Arg. Blue color corresponds to the value of salt concentration $c = 10$ mM, while the red color corresponds to the $c = 70$ mM. The functions bearing \tilde{R} -dependence are plotted at isoelectric point of two systems: $\text{pH} = 5.15$ and $\text{pH} = 8$ respectively, while the function bearing pH-dependence are plotted at fixed separation $\tilde{R} = 1.5$. The dimensionless diameter of the macroions is $\tilde{a} = 1$.

screens the protein charge and reduces the interaction. The repulsion disappears at the PZC, where the attraction sets in, increasing with salt concentration at a fixed dimensionless separation between the proteins. The attractive interaction is negligible for proteins composed of a larger number of amino-acids, which is not in correspondence with our previous results, where the attraction is larger for a larger number of adsorption sites. This can be explained by analyzing the average charge of the protein, (Fig. 4.10) (a), where one can observe a plateau of zero charge for the system II, which is not the case in system I, so it can be concluded that the strength of the fluctuation interaction depends on the rate of change of the charge of the macroion with pH, which of course depends on the type of the protein.

This can be derived also formally by following Lund and Jönsson [60]. The fluctuation part of the interaction force, Eq. (4.28), is approximately proportional to the charge variance, which in its turn follows from the macroion capacitance \mathcal{C} , as

$$\langle(\tilde{e} - \langle\tilde{e}\rangle)^2\rangle \sim \mathcal{C} = \frac{\partial\tilde{e}(\phi)}{\partial(\beta e_0\phi)} = -\frac{1}{\ln 10} \frac{\partial\tilde{e}(\phi)}{\partial\text{pH}}, \quad (4.32)$$

as is clear also from Eq. (4.3). The strength of the fluctuation interaction therefore depends on the rate of change of the mean charge of the macroion with pH, i.e. its capacitance. This can be clearly discerned from (Fig. 4.10)(b), where we observe that the system II has zero capacitance at its PZC, while system I has a non-zero capacitance at its PZC.

4.5 Conclusions

We presented a theory describing electrostatic interaction between two spherical macroions, with non-constant, fluctuating charge, surrounded by a monovalent bathing salt solution. The macroion charge fluctuations are described with the Parsegian–Ninham model of charge regulation, which effectively corresponds to the lattice gas surface dissociation free energy. Our theory is based on two approximations: one assumes the macroions as point-like, in the sense that the electrostatic potential on the surface of the macro-ion is uniform, whereas the other one treats the intervening salt solution on the DH level, assuming the electrostatic potential to be small, such that the PB equation can be linearized. Choosing the proper charge regulation energy, we analyzed the behavior of three different systems that differ in the symmetry of charge distribution. These are: a symmetric system composed of two identical macroions with a symmetric as well as asymmetric charge regulation intervals, corresponding to the fully symmetric and semi-symmetric cases, and an asymmetric system, composed of oppositely charged macroions, allowing the case of having one charged and one uncharged particle.

We have shown that in charge-regulated systems, asymmetrical charge fluctuations appear near the PZC, engendering strong attractive interactions of a general Kirkwood–Schumaker type, but with different functional dependencies as argued in their original derivation. The fluctuational nature of the KS interaction is consistent also with the fact that it arises even between a charged and a charge-neutral object, in the vicinity of the pH where the charged macroion becomes neutral itself. This is the case studied also in the context of the PB theory within the constant charge regulation model, in fact corresponding to a linearized form of the full charge-regulation theory [68, 98]. In this limit too, the effects of charge regulation are crucial and lead to attraction. However, in the context of our approximations, the attractive interaction between a charged and a neutral surface stems from the coupling between the net charge of one, and charge fluctuations of the other surface. Off-hand one would tend to see the attraction in the constant charge regulation model as being grounded in the mean-field level but caution should be exercised here. In our case too the Green’s function pertains to the DH mean-field level, and the attraction actually comes from the surface charge regulation. Constant charge regulation model must obviously capture some of the same physics.

The bathing solution with its pH and ionic strength therefore plays an important role in charge regulated systems, and the interactions to which they are subject. In all cases studied, the fluctuation attraction is larger for smaller salt concentration in solution at the same dimensionless separation, as well as the repulsion, which is actually reduced at a fixed separation by increasing the salt concentration, consistent with the electrolyte screening effect. Furthermore, a stronger attraction is found in systems composed of identical macroions having a larger number of adsorption sites, giving rise to larger charge fluctuations.

The theory, developed for toy models, was then applied to the case of protein-like macroions, with different dissociation constant for different chargeable amino acids. For protein electrostatic interactions their strength depends on the rate of change of the charge of the macroion with respect to the solution pH, i.e. the molecular capacitance of the macroion, which is protein specific and connected with the capacitance of the protein charge distribution. Apart from this, salt concentration reduces

the attraction between protein-like macroions, as is noted also in simulations and experiments in the case of e.g. lysozyme in monovalent salt solutions [69]. In fact, understanding the details of the protein–protein interaction is our main motivation for developing further our theoretical approach, specifically the relation between the KS interaction, the patchiness effects and vdW interactions between proteins in electrolyte solutions.

Chapter 5

Titrating macroions in polyvalent salt solution

We now change the perspective and consider a case where the bathing solution contains not only a weakly coupled monovalent salt but also polyvalent ions that are strongly coupled to the charged macroions, mediating the interaction between them. A possible realization would correspond to a mixture of multivalent ions in a bathing solution of monovalent ions, a situation rather typical in the context of semiflexible biopolymers, where multivalent ions are believed to play a key role in their condensation [34, 35]. With the presence of polyvalent ions in the system, the weak-coupling paradigm in general breaks down and the existence of KS interactions becomes dubious [10]. However, there exists the *dressed ion theory* based on an asymmetric treatment of the different components of the bathing electrolyte solution that allows to analyze the effect of charge regulation of macroions also in the presence of polyvalent mediating ions in the bathing solution [29, 34, 35, 77]. It is based on the fact that one can use the weak coupling DH approach in order to describe the monovalent salt ions, while a strong-coupling approach is preferable for the polyvalent ion part. This combined weak/strong-coupling approach [34, 35] effectively leads to dressed interactions between polyvalent ions and thus also affects the interactions mediated by polyvalent counterions between two like charge-regulated macroions. The ensuing effective interactions between macroions would then correspond to a *generalized KS interaction*, mediated by strongly coupled salt ions and not by weakly coupled monovalent salt. This generalized KS interaction would consequently also cease to be fluctuational in nature, i.e. of the type proposed in the original work of Kirkwood and Shumaker [64, 65], but would show a different behavior stemming from the polyvalent ion mediated interactions coupled to the charge regulation response of the dissociation equilibrium at the macroion surfaces.

Our approach is composed of disjointed parts brought together to describe this new type of generalized KS interaction, and a short guided tour through the conceptual and calculational flowchart is thus in order. The dissociable surfaces of the two identical macroions are described with a charge-regulation surface free energy that allows the effective charge to vary between a positive and negative maximal value. We then contract the macroion to a point particle merely as a calculational device, since we can then disregard the angular distribution of the dissociable groups along the surface, remaining solely with the monopolar charge as the only characteristics of the macroion. The bathing solution for the macroions, assuming to be an ionic

mixture of monovalent salt and polyvalent ions, is then treated within the dressed ion theory, i.e. the monovalent salt is described within the weak-coupling and the polyvalent ions within the strong-coupling paradigm, an approximate approach that has already proved valuable in different contexts [34, 35]. We then further approximate the non-linear surface charge regulation free energy with a Gaussian expansion proved to be a good description on the weak-coupling level (Chapter 4). Finally, we introduce another (admittedly optional) saddle-point approximation to evaluate the partition function in an analytic form, though exact numerical quadratures are easily available. We finally study the obtained expressions for the effective generalized KS interaction between the macroions in the various parts of the parameter space and comment on the results.

The dressed ion theory, as a variant of the strong-coupling theory [10], does not hold the same status as the original strong-coupling theory, valid exactly for a counterion-only system in the limit of large coupling constant [56, 83, 130]. In fact the regime of validity of this approach can be only checked against explicit-ion Monte Carlo simulations, showing that the dressed ion theory can indeed give quantitatively accurate results in a wide range of realistic parameter values [34, 35, 36].

5.1 General formalism

5.1.1 Model

The system under consideration consists of two equal titratable macroions immersed in a bathing solution, itself composed of a mixture of monovalent salt ions as well as polyvalent ions of valency q , see (Fig. 5.1). Two macroions, representing two titratable proteins, are located at \mathbf{r}_1 and \mathbf{r}_2 so that their separation is equal to $|\mathbf{r}_1 - \mathbf{r}_2| = R$. The macroions are assumed to be identical with a radius of $a/2$ and can have either sign. Furthermore, the macroions are charge-regulated with adsorption sites which can exchange a proton from the environment, and are described with the lattice gas free energy, see below, with a site number coefficient of $\alpha = 2$. This implies that there are twice as many proton adsorption/dissociation sites as there are negative fixed charges. This allows the total charge of the macroion to span negative as well as positive values, a basic tenet of our charge regulation model.

The macroion charge is thus not fixed, but responds to the local solution conditions. We also assume that the macroions are “small“ in the specific sense that the angular variation of the local electrostatic potential along their surface is negligible. This implies that we only deal with effective monopolar fluctuations, disregarding the subdominant higher multipolar fluctuations that would correspond to a generalization of the full vdW interaction potential [131]. The higher multipolar KS interactions remain as a possible future topic of our investigation.

5.1.2 Charge regulation

For charge-regulated titratable macroions we have already introduced several models in Chapter 4, based on a charge dissociation free energy that generalizes the law of mass action charge-regulation approach of Ninham and Parsegian [59]. In these models the charge regulation is described by a surface free energy $f_S(\mathbf{r}) = f_S(\phi(\mathbf{r}))$ that depends on the surface electrostatic potential $\phi(\mathbf{r})$. For each macroion the

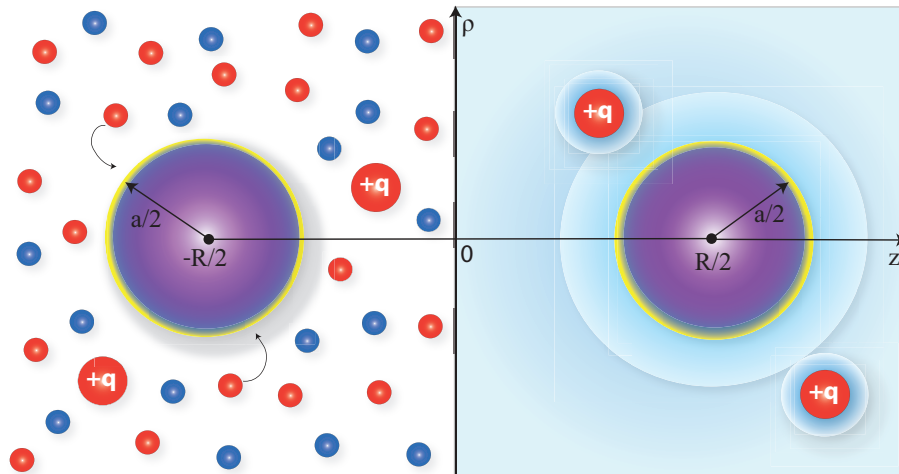


Figure 5.1: Schematic representation of the model: two charge regulated macroions, representing two proteins with titratable surface groups, immersed in a mixture of monovalent/polyvalent salt solution. The microscopic model (left) shows the different types of ions and the surface dissociation equilibrium on the surface of the macroion. The coarse-grained dressed ion model (right) shows the effective DH potential (light coloured corona) of the macroion as well as the polyvalent solution ions. In a cylindrical coordinate system with the z -axis connecting the two macroions, having its origin in the middle between the macroions, the macroions are located at $\mathbf{r}_1 = (0, 0, -R/2)$, and $\mathbf{r}_2 = (0, 0, R/2)$, respectively.

total charge regulation free energy $F[\phi(\mathbf{r})]$ would thus be a functional of the surface potential amount to

$$F[\phi(\mathbf{r})] = \oint_S f_S(\phi(\mathbf{r})) d^2\mathbf{r}, \quad (5.1)$$

where S is the surface area of the macroion. At this point we simplify matters by furthermore assuming that the macroions are spherical and of vanishing radius, i.e. they are point particles. Of course this approximation will only work for sufficiently large separations between them and small separation regime would need to be analyzed separately. It will soon become clear why this type of approximation simplifies the calculation substantially.

Assuming then that the macroion is located at (\mathbf{r}_0) and has a vanishing radius $a \rightarrow 0$, the integral of the dissociation free energy over the surface of the macroion, Eq. (5.1), simply gives a total dissociation energy of the point-like macroion as a function of the local potential at the point $\mathbf{r} = \mathbf{r}_0$. The point-like approximation for the macroion therefore disregards the angular variation of the local electrostatic potential along the surface of the macroions and can describe only monopolar charge regulation, while higher multipoles are ignored.

In the next step one needs to assume a model for $f_S(\phi(\mathbf{r}))$. We already invoked several models Eq (4.16) related to the original Ninham-Parsegian model [59]. Focusing on a simple two-parameter model we introduce the following ansatz for a charge regulated point-like macroion

$$F(\phi(\mathbf{r}_0)) = \lim_{a \rightarrow 0} \oint_S f_S(\phi(\mathbf{r})) d^2\mathbf{r} \rightarrow -Ne_0\phi(\mathbf{r}_0) - \alpha Nk_B T \ln \left(1 + b \exp(-\beta e_0\phi(\mathbf{r}_0)) \right), \quad (5.2)$$

where $\phi(\mathbf{r}_0)$ is now the local electrostatic potential at the position of the ion, while N and α are two parameters characterizing the dissociation process. The site number coefficient α quantifies the number of dissociation sites, and $\ln b = \beta\mu_S$, incorporates the free energy of charge dissociation μ_S .

In the case of protonation of the titratable surface charge, it furthermore follows that $\ln b = (\text{pH} - \text{p}K) \ln 10$, where $\text{p}K$ is the dissociation constant and $\text{pH} = -\log [\text{H}^+]$ is the proton concentration in the bulk, differing from the local value of pH at the dissociation site. It is straightforward to see that the free energy Eq. (5.2) is composed of the electrostatic energy of N fixed negatively charged sites with the total charge $-Ne_0$ and αN lattice gas sites, that can be filled with adsorbing protons from the solution; in fact $1 + e^\mu$ is nothing but the lattice gas partition function for single occupation sites, with zero energy for the empty site and μ for the filled site, while $\ln(1 + e^\mu)$ is just the corresponding grand canonical surface pressure.

The form of the charge regulation free energy then allows us to derive the effective charge of the charge-regulated macroion as a function of the local electrostatic potential in the form

$$e(\phi) = \frac{\partial F(\phi)}{\partial \phi} \quad (5.3)$$

where $F(\phi)$ is the dissociation free energy Eq. (5.2) yielding

$$e(\phi) = e_0 N \left[\left(\frac{\alpha}{2} - 1 \right) - \frac{\alpha}{2} \tanh \left(-\frac{1}{2} (\ln b - \beta e_0 \phi) \right) \right]. \quad (5.4)$$

The effective charge of the macroion then varies in the interval $-Ne_0 < e(\phi) < (\alpha - 1)Ne_0$. Choosing the site number coefficient to be $\alpha = 2$, one thus remains with a symmetric charge regulated macroion whose effective charge varies within the interval $-Ne_0 < e(\phi) < +Ne_0$. This is the generic charge regulation model that we will consider as a simple description of the protein charge regulation in what follows.

5.1.3 Field-theory – general formalism

We proceed by writing the partition function through the Hubbard-Stratonovich transform for the Coulomb potential as explained in detail in Chapter 2. This leads to a field theory, where the classical partition function is represented as a functional integral over the fluctuating electrostatic potential. Two explicit exact limiting results are then obtainable from this representation in the case of a counterion-only system [10]: the saddle-point of this field theory in fact corresponds to the mean-field PB approximation, while the Gaussian fluctuation correction together with the PB theory constitutes the weak-coupling theory; the first order virial expansion of the partition function then constitutes the strong-coupling theory, unrelated to the PB approximation. The latter can be further generalized in the case of a mixed system by treating the monovalent salt on the weak-coupling level while the polyvalent ions are described on the strong-coupling level, i.e. their contribution to the partition function is written as a second-order virial expansion theory. This approximation was dubbed the “dressed ion theory“ [34, 35].

Assuming that the fluctuating electrostatic potential of the macroions is $\phi(\mathbf{r} = \mathbf{r}_1) = \varphi_1$ and of the other one is $\phi(\mathbf{r} = \mathbf{r}_2) = \varphi_2$, located at \mathbf{r}_1 and \mathbf{r}_2 respectively,

the partition function of the system within the dressed ion theory can be derived in the field-theoretic form as:

$$\mathcal{Z} = \iint d\varphi_1 \exp\left(-\beta F(i\varphi_1)\right) G(\varphi_1, \varphi_2) \exp\left(-\beta F(i\varphi_2)\right) d\varphi_2, \quad (5.5)$$

where $F(i\varphi)$ is charge regulation free energy, Eq. (5.2), evaluated at imaginary values of the fluctuating electrostatic potential, and the field propagator or the Green function, giving the probability of field configurations with $\phi(\mathbf{r} = \mathbf{r}_1) = \varphi_1$ and $\phi(\mathbf{r} = \mathbf{r}_2) = \varphi_2$, is given by

$$G(\varphi_1, \varphi_2) = \int \mathcal{D}[\varphi(\mathbf{r})] \exp\left(-\beta H[\varphi]\right) \delta(\varphi(\mathbf{r}_1) - \varphi_1) \delta(\varphi(\mathbf{r}_2) - \varphi_2) \quad (5.6)$$

with the bulk field action:

$$-\beta H[\varphi] = -\beta H_0[\varphi] + \lambda_c \int d\mathbf{r} \exp\left(i\beta q e \varphi(\mathbf{r})\right), \quad (5.7)$$

where λ_c is the fugacity of the polyvalent ions with valency q and $H_0[\varphi]$ is the DH interaction kernel

$$\begin{aligned} -\beta H_0[\varphi] &= \frac{1}{2} \epsilon \epsilon_0 \int d\mathbf{r} d\mathbf{r}' \varphi(\mathbf{r}) u_{DH}^{-1}(\mathbf{r}, \mathbf{r}') \varphi(\mathbf{r}') \\ &= \frac{1}{2} \epsilon \epsilon_0 \int [(\nabla \varphi(\mathbf{r}))^2 + \kappa^2 \varphi^2(\mathbf{r})] d\mathbf{r}. \end{aligned} \quad (5.8)$$

Here we have assumed that the monovalent salt is weakly coupled to the rest of the charges and can be treated on the DH level. The inverse square of Debye length was introduced as $\kappa^2 = 4\pi \ell_B n_D$, with ℓ_B the Bjerrum length and $n_D = 2n_0 + qc_0$, where n_0 is the bulk concentration of the monovalent salt and c_0 is the bulk concentration of the multivalent ions, assumed to originate in dissociation of a $q:1$ salt. The above interaction kernel implies a screened effective DH interaction potential

$$u_{DH}(\mathbf{r}, \mathbf{r}') = \frac{1}{4\pi \epsilon \epsilon_0} \frac{\exp(-\kappa |\mathbf{r} - \mathbf{r}'|)}{|\mathbf{r} - \mathbf{r}'|} = \frac{1}{4\pi \epsilon \epsilon_0} \tilde{u}_{DH}(\mathbf{r}, \mathbf{r}') \quad (5.9)$$

between the polyvalent ions and the macroions. On this level the polyvalent ions are thus treated explicitly, but their interactions with the macroions are described with a dressed electrolyte-mediated effective DH potential.

The strong asymmetry in the system, implied by the presence of polyvalent mobile ions, together with their small concentration leads straightforwardly to the expansion for their contribution to the partition function that yields to the lowest order [34, 35, 36]

$$\begin{aligned} \exp\left(-\beta H[\varphi]\right) &= \exp\left(-\frac{1}{2}\beta \int d\mathbf{r} d\mathbf{r}' \varphi(\mathbf{r}) u_{DH}(\mathbf{r}, \mathbf{r}') \varphi(\mathbf{r}')\right) \left[1 + \right. \\ &\quad \left. \lambda_c \int_V d\mathbf{r}_0 \exp\left(i\beta q e \varphi(\mathbf{r}_0)\right) + \dots\right], \end{aligned} \quad (5.10)$$

furthermore implying that the propagator $G(\varphi_1, \varphi_2)$ can be decomposed into

$$G(\varphi_1, \varphi_2) = G_0(\varphi_1, \varphi_2) + \lambda_c \int_V d\mathbf{r}_0 G_1(\varphi_1, \varphi_2; \mathbf{r}_0). \quad (5.11)$$

The propagator $G_1(\varphi_1, \varphi_2; \mathbf{r}_0)$, describes the field propagation from macroion at \mathbf{r}_1 to macro-ion at \mathbf{r}_2 mediated by the presence of the polyvalent ion q at \mathbf{r}_0 integrated over the fluctuating potential at the positions of both macroions. Formally this can be expressed as

$$G_1(\varphi_1, \varphi_2; \mathbf{r}_0) = \int \mathcal{D}[\varphi(\mathbf{r})] \delta(\varphi(\mathbf{r}_1) - \varphi_1) \exp\left(-\beta H_1[\varphi; \mathbf{r}_0]\right) \delta(\varphi(\mathbf{r}_2) - \varphi_2), \quad (5.12)$$

where the effective field action $H_1[\varphi; \mathbf{r}_0]$ can be decomposed into the DH part due to the weakly coupled monovalent salt ions and the part that originates in screened electrostatic interactions mediated by the polyvalent ion of valency q located at \mathbf{r}_0 , i.e.

$$\beta H_1[\varphi; \mathbf{r}_0] = \beta H_0[\varphi] - i\beta \int \rho(\mathbf{r}_0) \varphi(\mathbf{r}) d\mathbf{r} \quad (5.13)$$

The last term describes the interaction with the polyvalent ion with density

$$\rho(\mathbf{r}_0) = q\delta(\mathbf{r} - \mathbf{r}_0). \quad (5.14)$$

This formal expression for the propagator $G_1(\varphi_1, \varphi_2; \mathbf{r}_0)$ is thus identical to the partition function of two macroions at positions $\mathbf{r}_{1,2}$ with set values of the fluctuating potential $\varphi_{1,2}$ interacting via the DH interaction with an additional point particle of charge qe_0 at \mathbf{r}_0 at the positions of the two point-like macroions. The functional integral in Eq. (5.5) simply indicates the summation over all fluctuating potentials that satisfy these constraints.

With these definitions the full dressed ion partition function can then be cast into the form

$$\begin{aligned} \mathcal{Z} &= \iint d\varphi_1 \exp\left(-\beta F(\varphi_1)\right) \left[G_0(\varphi_1, \varphi_2) \right. \\ &\quad \left. + \lambda_c \int_V d\mathbf{r}_0 G_1(\varphi_1, \varphi_2; \mathbf{r}_0) \right] \exp\left(-\beta F(\varphi_2)\right) d\varphi_2 \\ &= \mathcal{Z}_0 + \lambda_c \mathcal{Z}_1 \end{aligned} \quad (5.15)$$

with obvious definitions. \mathcal{Z}_0 and \mathcal{Z}_1 thus give the zero order and the first order polyvalent ion virial expansion terms in the partition function. \mathcal{Z}_0 has been already analyzed in the Chapter 4, and \mathcal{Z}_1 will be evaluated below. The above decomposition of the full partition function $\mathcal{Z} = \mathcal{Z}(R)$ is the essence of the dressed ion theory and the corresponding free energy will describe the interactions between the two macroions as a function of their separation and model parameters.

5.1.4 Dressed ion theory and charge regulation

The first order virial expanded Green function $G_1(\varphi_1, \varphi_2; \mathbf{r}_0)$ can be reduced to Gaussian functional integrals (Appendix F), and can be derived in an explicit form

$$G_1(\varphi_1, \varphi_2; \mathbf{r}_0) = \frac{\exp\left(\frac{1}{2} \tilde{\Phi}_i(\mathbf{r}_0) G^{-1}_{ij}(\mathbf{r}_1, \mathbf{r}_2) \tilde{\Phi}_j(\mathbf{r}_0)\right)}{\sqrt{\det G_{ij}(\mathbf{r}_1, \mathbf{r}_2)}} \quad (5.16)$$

where we introduced

$$\Phi_i(\mathbf{r}_0) = i\varphi_1 + qe_0 u_{DH}(\mathbf{r}_0, \mathbf{r}_i), \quad (5.17)$$

and

$$G_{ij}(\mathbf{r}_1, \mathbf{r}_2) = k_B T \begin{pmatrix} a^{-1} & u_{DH}(\mathbf{r}_1, \mathbf{r}_2) \\ u_{DH}(\mathbf{r}_1, \mathbf{r}_2) & a^{-1} \end{pmatrix}, \quad (5.18)$$

for $i, j = 1, 2$. From the above expressions it is clear that the macroions interact with themselves as well as with the polyvalent ion whose position within the system will be finally integrated over. The diagonal terms describe the self-interaction¹ of the macroions of diameter a , while the interaction between the macroions as well as between the macroions and the polyvalent ion are given by the DH screened interaction potential. In a cylindrical coordinate system with the z -axis connecting the two macroions, having its origin in the middle between the macroions, themselves separated by R , the position of the polyvalent ion with respect to both macroions can be written as $|\mathbf{r}_0 - \mathbf{r}_1| = \sqrt{\rho_0^2 + (R/2 + z_0)^2}$, and $|\mathbf{r}_0 - \mathbf{r}_2| = \sqrt{\rho_0^2 + (R/2 - z_0)^2}$, respectively.

Going back to the definition of the partition function \mathcal{Z}_1 , Eq. (5.15), one can finally write

$$\mathcal{Z}_1 = \lambda_c \int_V d\mathbf{r}_0 \int d\varphi_1 \exp(-\beta F(\varphi_1)) \left[G_1(\varphi_1, \varphi_2) \right] \exp(-\beta F(\varphi_2)) d\varphi_2. \quad (5.19)$$

In order to proceed with explicit evaluation of this expression, we first expand the charge regulation free energy of the macroions with $\alpha = 2$, as

$$\begin{aligned} \exp(-\beta F(\varphi)) &= \exp(-i\beta N e_0 \varphi) (1 + b \exp(i\beta e_0 \varphi))^{2N} = \\ &= \sum_{n=0}^{2N} \binom{2N}{n} \exp(-i\beta N e_0 \varphi) b^n \exp(i\beta e_0 n \varphi). \end{aligned} \quad (5.20)$$

Note that this choice of parameter α implies that the effective macroion charge can be regulated in the symmetric interval $-N e_0 < e(\phi) < +N e_0$.

While the expansion Eq. (5.20) could in principle be used for a direct numerical evaluation of the partition function, we have already shown in Section 4.3.2, that an additional approximation, simplifying the calculation extensively, yields an accurate result that compares well with the exact summation [132]. This further step relies on the Gaussian approximation for the binomial coefficient

$$\binom{2N}{n} \simeq \frac{2^{2N}}{\sqrt{\pi N}} e^{-\frac{(N-n)^2}{N}}, \quad (5.21)$$

valid strictly in the limit of $N \gg 1$, i.e. in the limit of a large number of adsorption sites. Introducing the auxiliary fields $x_1 = N - n$ and $x_2 = N - n'$, summation in Eq. (5.20) can be replaced with an integral, so that the partition function becomes

¹In Chapter 4 we used screened interaction for macroion's self interaction, $\exp(-\kappa a)/a$, while here we find Coulomb interaction as a more suitable choice. The results do not crucially depend on the choice of self interaction, especially in the approximation which takes macroions as point-like particles.

$$\begin{aligned}
 \mathcal{Z}_1 &= \lambda_c \int_V d\mathbf{r}_0 \int d\varphi_1 d\varphi_2 \int dx_1 dx_2 \\
 &\times \frac{\exp\left(s(q^2; \mathbf{r}_1, \mathbf{r}_2) + \ln 10 (pH - pK)(x_1 + x_2) - \frac{x_1^2}{N} - \frac{x_2^2}{N}\right)}{\sqrt{\det G_{ij}(\mathbf{r}_1, \mathbf{r}_2)}} \\
 &\times \exp\left[-\frac{1}{2}\varphi_i G^{-1}_{ij}(\mathbf{r}_1, \mathbf{r}_2)\varphi_j + \nu\beta e_0\varphi_i(-x_i + qy_i)\right].
 \end{aligned} \tag{5.22}$$

Here the effective interaction matrix $G_{ij}(\mathbf{r}_1, \mathbf{r}_2)$ has been already defined in Eq. (5.18), while $G^{-1}_{ij}(\mathbf{r}_1, \mathbf{r}_2)$ is its matrix inverse. We also introduced two additional auxiliary fields with no other role but to make the notation more compact,

$$y_1 = \frac{a^2}{1 - \frac{a^2}{R^2}e^{-2\kappa R}} \left[\frac{1}{a}\tilde{u}_{DH}(\mathbf{r}_0, \mathbf{r}_1) - \frac{\exp(-\kappa R)}{R}\tilde{u}_{DH}(\mathbf{r}_0, \mathbf{r}_2) \right] \tag{5.23}$$

and

$$y_2 = \frac{a^2}{1 - \frac{a^2}{R^2}e^{-2\kappa R}} \left[\frac{\exp(-\kappa R)}{R}\tilde{u}_{DH}(\mathbf{r}_0, \mathbf{r}_1) - \frac{1}{a}\tilde{u}_{DH}(\mathbf{r}_0, \mathbf{r}_2) \right], \tag{5.24}$$

The effective self-energy of the polyvalent ion, $s(q^2; \mathbf{r}_1, \mathbf{r}_2)$, mediated by both macroions, is proportional to the square of the polyvalent ion charge and is given by

$$\begin{aligned}
 s(q^2; \mathbf{r}_1, \mathbf{r}_2) &= \frac{1}{2}q^2 \frac{l_B a}{1 - (a/R)^2 \exp(-2\kappa R)} \\
 &\times \left(\tilde{u}_{DH}^2(\mathbf{r}_0, \mathbf{r}_1) + \tilde{u}_{DH}^2(\mathbf{r}_0, \mathbf{r}_2) - 2\frac{a}{R} \exp(-\kappa R)\tilde{u}_{DH}(\mathbf{r}_0, \mathbf{r}_1)\tilde{u}_{DH}(\mathbf{r}_0, \mathbf{r}_2) \right).
 \end{aligned} \tag{5.25}$$

After integrating out the x_i -auxiliary fields and the fluctuating potentials of the two macroions, φ_1, φ_2 , one obtains the final result in the form

$$\begin{aligned}
 \mathcal{Z}_1 &= \mathcal{Z}_0 \lambda_c \int_V d\mathbf{r}_0 \exp\left(\frac{q l_B N (pH - pK) \ln 10 [\tilde{u}_{DH}(\mathbf{r}_0, \mathbf{r}_1) + \tilde{u}(\mathbf{r}_0, \mathbf{r}_2)]}{2 + N(l_B/a)[1 + (a/R)\exp(-\kappa R)]}\right) \times \\
 &\exp\left(\frac{1}{2}q^2 l_B^2 \left[C_{11}\tilde{u}_{DH}^2(\mathbf{r}_0, \mathbf{r}_1) + C_{22}\tilde{u}_{DH}^2(\mathbf{r}_0, \mathbf{r}_2) - 2C_{12}\tilde{u}_{DH}(\mathbf{r}_0, \mathbf{r}_1)\tilde{u}_{DH}(\mathbf{r}_0, \mathbf{r}_2) \right]\right).
 \end{aligned} \tag{5.26}$$

where \mathcal{Z}_0 is the partition function of a system of two isolated charge-regulated macroions on the weak-coupling approximation level, already derived within the context of the weakly coupled macroions in monovalent salt solution Eqs. (4.22) and (4.23) and given by

$$\mathcal{Z}_0 = \frac{\exp\left[\frac{N[(pH-pK)\ln 10]^2}{2+N(l_B/a)[1+(a/R)e^{-\kappa R}]}\right]}{\sqrt{\frac{4}{N^2} + \frac{2}{N}\frac{l_B}{a} + \frac{l_B^2}{a^2}\left[1 - \frac{a^2}{R^2}\exp(-2\kappa R)\right]}}. \tag{5.27}$$

Above we also introduced the generalized self and mutual capacitances as

$$\begin{aligned} C_{11} &= C_{22} = \frac{\frac{l_B}{a} + \frac{2}{N}}{\left[\frac{l_B}{a} + \frac{2}{N}\right]^2 - \frac{\exp(-2\kappa R)}{R^2/l_B^2}}; \\ C_{12} &= \frac{\frac{\exp(-\kappa R)}{R/l_B}}{\left[\frac{l_B}{a} + \frac{2}{N}\right]^2 - \frac{\exp(-2\kappa R)}{R^2/l_B^2}}. \end{aligned} \quad (5.28)$$

While they do not have the standard form of the capacitances, since they both contain also contributions from mutual interactions, in the limit of large separations between the macroions they do reduce to the expected values. The difference in the definition of capacitances is a consequence of the fact that the dressed ion theory is not Gaussian as far as the fluctuating potential is concerned, in contrast to the weak-coupling case analyzed before Eq. (4.27), but is a non-linear strong-coupling theory. Capacitance is a weak coupling concept, pertaining to Gaussian fluctuations and thus does not have a direct equivalent in the strong-coupling theory.

We now write down the free energy difference between the state where the two macroions are at a finite spacing R and the state corresponding to two isolated macroions with $R \rightarrow \infty$. This SC free energy difference, Eq (5.15), finally assumes the form:

$$\beta\mathcal{F} = -\ln(\mathcal{Z}_0) - \lambda_c \frac{\mathcal{Z}_1}{\mathcal{Z}_0} = \tilde{\mathcal{F}}_0 + c_0 \tilde{\mathcal{F}}_1. \quad (5.29)$$

In the grand canonical ensemble, the fugacity λ_c is identical to polyvalent ion concentration in the bulk c_0 , and

$$\tilde{\mathcal{F}}_0 = -\ln(\mathcal{Z}_0), \quad (5.30)$$

where \mathcal{Z}_0 is defined in Eq. (5.27), and extensively analyzed in Chapter 4. For the sake of completeness we nevertheless write it down in an explicit form

$$\begin{aligned} \tilde{\mathcal{F}}_0 &= -\frac{N[(\text{pH} - \text{pK}) \ln 10]^2}{2 + N(l_B/a)[1 + (a/R) \exp(-\kappa R)]} \\ &+ \frac{1}{2} \ln \left(1 + N \frac{l_B}{2a} + \frac{l_B^2}{(2a)^2} N^2 \left[1 - \frac{a^2}{R^2} \exp(-2\kappa R) \right] \right). \end{aligned} \quad (5.31)$$

On the other hand, $\tilde{\mathcal{F}}_1$ yields the final result as

$$\begin{aligned} \tilde{\mathcal{F}}_1 &= \int_V d\mathbf{r}_0 \left[\exp \left(\frac{qN(\text{pH} - \text{pK}) \ln 10 [u_{DH}(\mathbf{r}_0, \mathbf{r}_1) + u_{DH}(\mathbf{r}_0, \mathbf{r}_2)]}{2 + N(l_B/a)[1 + (a/R) \exp(-\kappa R)]} \right) \times \right. \\ &\left. \exp \left(\frac{1}{2} q^2 [C_{11} u_{DH}^2(\mathbf{r}_0, \mathbf{r}_1) + C_{22} u_{DH}^2(\mathbf{r}_0, \mathbf{r}_2) - 2C_{12} u_{DH}(\mathbf{r}_0, \mathbf{r}_1) u_{DH}(\mathbf{r}_0, \mathbf{r}_2)] \right) - 1 \right]. \end{aligned} \quad (5.32)$$

with explicitly subtracted free energy value of two isolated macroions with $R \rightarrow \infty$. The structure of this complicated expression is as follows: the first exponent corresponds to the screened DH interactions of the q -valent polyvalent ion with both macroions whose charge is determined by the bulk pH of the solution and is proportional to $\text{pH} - \text{pK}$, while the second exponent corresponds to the electrostatic

self-interaction of the polyvalent ion in the presence of both macroions. Finally the product of the two expressions needs to be integrated over all the possible positions of the polyvalent ion. The constants C_{11} and C_{22} , Eq (5.28), can be interpreted as generalized self-capacitances and mutual capacitance C_{12} of the macroions, originating in the interaction between the three charged particles. At the end, we subtracted the non-interacting part of two isolated macroions proportional simply to the volume of the system V .

In addition, we note that both $\tilde{\mathcal{F}}_0(R)$ as well as $\tilde{\mathcal{F}}_1(R)$ contain parts which are due to *polyion mediated* interaction between the macroions, proportional to $qN(\text{pH} - \text{p}K)$, as well as *polyion self-interaction* mediated by the macroions and proportional to q^2 . The division into a “mean interaction“ and “fluctuations“ is thus not possible due to the fact that our theory is not of a mean-field type that would allow for fluctuations around the mean-field configuration.

In the case of absent charge regulation, where the system consists of two macroions with fixed charge Ne_0 , immersed in the same bathing solution with a strongly coupled oppositely charged polyvalent ion, one can repeat the above analysis and obtain the free energy in the form

$$\tilde{\mathcal{F}}_0 + c_0\tilde{\mathcal{F}}_1 = N^2l_B \left(\frac{1}{a} + \frac{\exp(-\kappa R)}{R} \right) - c_0 \int_V d\mathbf{r}_0 \left[\exp \left(qN [u_{DH}(\mathbf{r}_0, \mathbf{r}_1) + u_{DH}(\mathbf{r}_0, \mathbf{r}_2)] \right) - 1 \right]. \quad (5.33)$$

This is very instructive, since obviously without charge regulation the self-interaction contributions proportional to q^2 is absent, and the interaction energy reduces to the macroion-macroion repulsion proportional to the charge squared, $(Ne_0)^2$, and a contribution stemming from the interaction of macro-ions with the polyvalent ion, proportional to the product of both charges, $q(Ne_0)$. The above equations represent the final result of the dressed ion theory for the interaction between two identical point-like charge regulated macroions in the presence of small concentrations of a polyvalent salt and they have to be evaluated numerically. In general they have to be evaluated numerically, but we will derive a simple analytical approximation below. While it is nice to have an explicit analytical form for the interaction, the final volume integration is simple enough and leads directly to numerical results.

5.1.5 Approximate macroion interaction free energy

The volume integration in Eq. (5.32) has to be done numerically. However, one can obtain an approximate form of this integral by evaluating it at the saddle-point level, amounting to Gaussian fluctuations around the most probably position of the polyvalent ion.

The partition function Eq (5.32) can then be approximated as

$$\tilde{\mathcal{F}}_1 = \int_V d\mathbf{r}_0 \exp \left(-\mathcal{S}(\mathbf{r}_0) \right) \simeq \frac{\exp \left(-\mathcal{S}(\mathbf{a}) \right)}{\sqrt{\det \left(\partial^2 \mathcal{S}(\mathbf{r} = \mathbf{a}) / (\partial \mathbf{r} \partial \mathbf{r}) \right)}} \quad (5.34)$$

the most probable position of the polyvalent ion corresponds to the equilibrium configuration of zero “force“ defined by

$$\nabla \mathcal{S}(\mathbf{a}) = \mathbf{0}. \quad (5.35)$$

One could refer to $\nabla \mathcal{S}(\mathbf{a})$ also as the generalized force on the polyvalent ion at the dressed ion theory level. Generalized because it is not of standard electrostatic nature but contains terms due to the charge regulation of both macroions amounting to self-interaction of the ions, i.e. terms proportional to q^2 . The solution of this condition is trivial, amounting to $\mathbf{a} = 0$, in the case when when the macroions and the polyvalent ion bear charges of opposite sign, i.e. $q(\text{pH} - \text{pK}) \geq 0$. If they are of the same sign, the minimum configuration does not exist. In the former case

$$\begin{aligned} \mathcal{S}(\mathbf{r}_0 = \mathbf{a}) &= \frac{4qN(\text{pH} - \text{pK}) \ln 10 l_B}{2 + N(l_B/a)[1 + (a/R) \exp(-\kappa R)]} \frac{\exp(-\frac{1}{2}\kappa R)}{R} \\ &+ 4q^2 l_B^2 \frac{[(l_B/a) + (2/N)] (\exp(-\kappa R)/R^2) - l_B(\exp(-2\kappa R)/R^3)}{(4/N^2) + (4/N)(l_B/a) + (l_B/a)^2 [1 - (a/R)^2 \exp(-2\kappa R)]} \end{aligned} \quad (5.36)$$

The Gaussian correction to the saddle-point solution is calculated in Appendix [F](#) and is given symbolically by

$$-\ln \tilde{\mathcal{F}}_1(R) \simeq \mathcal{S}(\mathbf{r}_0 = \mathbf{a}) + \frac{1}{2} \ln \det \frac{\partial^2 \mathcal{S}(\mathbf{r} = \mathbf{a})}{\partial \mathbf{r} \partial \mathbf{r}}. \quad (5.37)$$

The corresponding force $F(R)$ between macroions can then be derived *via* $F(R) = \frac{d}{dR} \tilde{\mathcal{F}}_1(R)$ with $\tilde{\mathcal{F}}_1(R)$ written above, and contains two terms, stemming from the saddle point configuration $\mathcal{S}(\mathbf{r}_0 = \mathbf{a})$ and from the Gaussian fluctuations in the position of the polyvalent ion around the saddle-point, when it exists. We present here only the force stemming from the saddle point configuration, which contains a term linear in q and corresponding to the interaction between charged macroion and the polyvalent ion, and the one quadratic in q corresponding to electrostatic self-interaction of the polyvalent ion in the presence of the macroions. It is straightforward to derive also the asymptotic forms of this interaction. The former has the asymptotic form

$$F_{sp}^{(1)} \approx -\frac{4qN(\text{pH} - \text{pK}) \ln 10}{2 + N(l_B/a)[1 + (a/R) \exp(-\kappa R)]} \frac{\kappa \exp(-\kappa R/2)}{R/2l_B} + \dots \quad (5.38)$$

and the latter as

$$F_{sp}^{(2)} \approx -2q^2(C_1 + C_2) \frac{\kappa \exp(-\kappa R)}{(R/l_B)^2} + \dots \quad (5.39)$$

where the capacitances have been defined in Eq. [\(5.28\)](#). The scaling of the force between the macroions on the level of the strong-coupling dressed ion theory is thus easily discernible. For the above expression to remain valid $q(\text{pH} - \text{pK}) \geq 0$ condition has to be fulfilled. Nevertheless, the approximation introduced does not work well, as it could be seen in [\(Fig. 5.2\)](#), and we will proceed with numerical evaluation of the full formula Eq. [\(5.32\)](#).

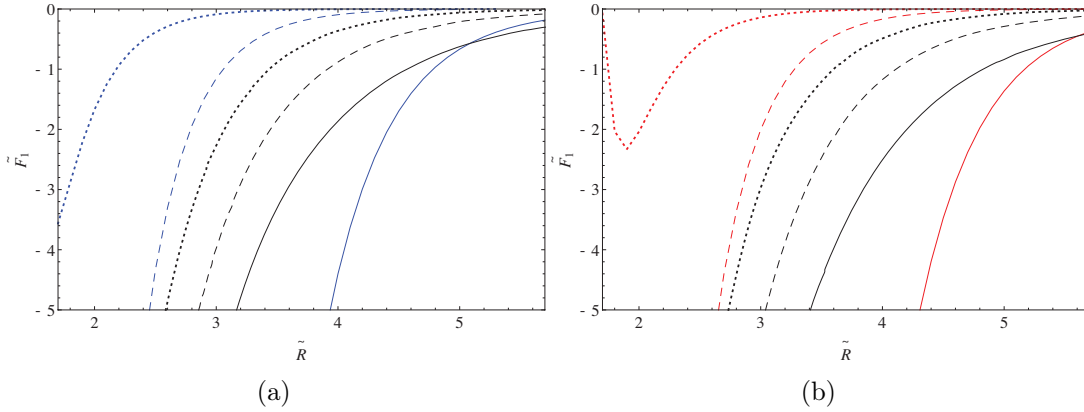


Figure 5.2: Comparison of the exact interaction force contribution $\tilde{F}_1(R)$ (calculated from Eq. (5.32)) (blue/red lines) with the saddle-point interaction force (Eqs. (5.38) and (5.39)) (black lines). (a) $q = 3$; (b) $q = 4$. Solid lines correspond $n_0 = 150$ mM, dashed $n_0 = 300$ mM, while dotted stand for $n_0 = 500$ mM. Macroions diameter is $a = 1$ nm, number of adsorption sites $N = 7$ and $c_0 = 1$ mM and $\text{pH} - \text{p}K = 3$.

5.2 Results and discussion

The effective interaction free energy between the charge-regulated macroions is obtained directly from Eq. (5.27) after performing the numerical integration over volume in Eq. (5.32). We calculate the total interaction free energy, $\beta\mathcal{F}(R)$, as a function of the separation between the macroions as

$$\beta\mathcal{F}(R) = \tilde{\mathcal{F}}_0(R) + c_0\tilde{\mathcal{F}}_1(R), \quad (5.40)$$

We study the separation dependence of the force:

$$\tilde{F}(\tilde{R}) = -\frac{d\tilde{\mathcal{F}}_0(\tilde{R})}{d\tilde{R}} - c_0\frac{d\tilde{\mathcal{F}}_1(\tilde{R})}{d\tilde{R}} = \tilde{F}_0(\tilde{R}) + \tilde{F}_1(\tilde{R}), \quad (5.41)$$

for different values of the parameters, differentiating in particular the case of PZC ($\text{pH} - \text{p}K = 0$) corresponding to macroions that are on the average uncharged. In spite of this, the self-energy of the polyvalent ion in this case still contains the non-vanishing electrostatic self-interaction of the polyvalent ion mediated by both charge regulated macroions.

We first analyze the term $\tilde{F}_1(R)$ from Eq. (5.32), which corresponds to the interaction free energy mediated by the polyvalent q -ion only, as seen in (Fig. 5.3(a)), this interaction free energy leads to an attractive contribution to the force at PZC, stemming solely from the self-interaction of the polyvalent ion, mediated by the charge regulation of the macroions, whose magnitude depends quadratically on q . The screening effect of the monovalent salt is clearly discernible. In summary, the polyvalent self-interaction at PZC yields an attractive interaction that gets stronger and more long-ranged on increase of the valency q of the polyvalent ion and on decrease of the monovalent salt concentration n_0 . We should note that this PZC polyvalent ion-mediated attraction in the strong-coupling dressed ion approach is much stronger than the residual weak-coupling (KS) attraction between charge regulated macroions in a monovalent salt solution (black lines) (Fig. 5.3(a)). We should

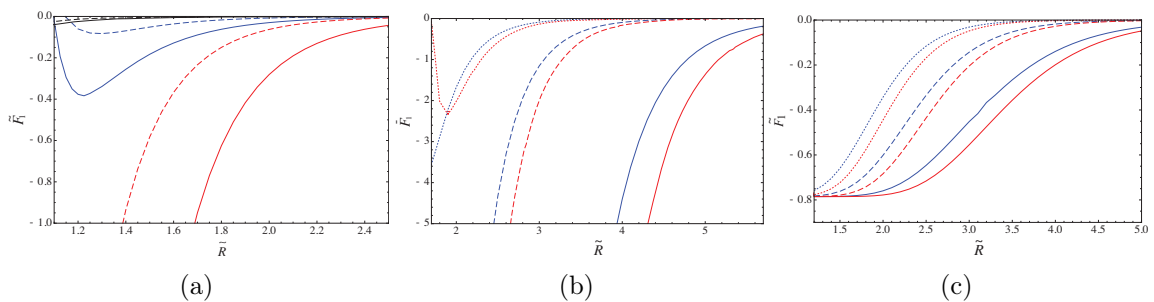


Figure 5.3: Interaction force contribution $\tilde{F}_1(R)$, calculated from Eq. (5.32), originating in the presence of polyvalent ions, for (a) $\text{pH} - \text{p}K = 0$; (b) $\text{pH} - \text{p}K = 3$ and (c) $\text{pH} - \text{p}K = -3$. Blue lines $q = 3$, red lines $q = 4$, black lines $q = 0$ (standing for the attraction coming from Eq. (5.31)). Solid lines correspond $n_0 = 150$ mM, dashed $n_0 = 300$ mM, while dotted stand for $n_0 = 500$ mM in (b) and (c), while in (a) monovalent salt concentration is chosen as $n_0 = 100$ mM solid lines and $n_0 = 150$ mM dashed lines. Macroions diameter $a = 1$ nm, number of adsorption sites $N = 7$ and $c_0 = 1$ mM.

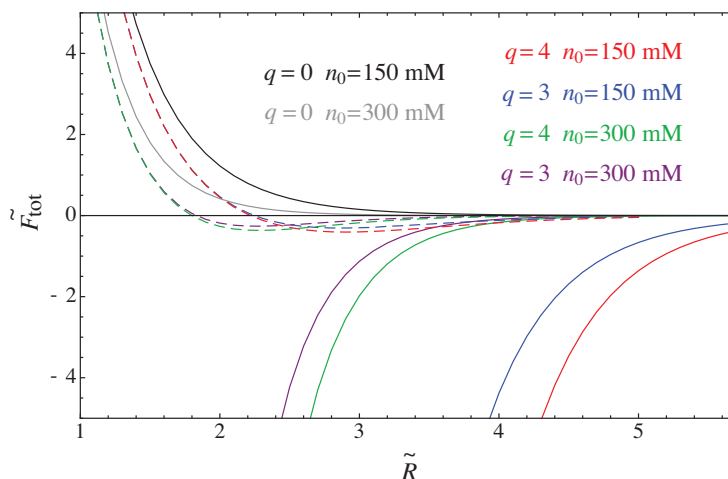


Figure 5.4: The total interaction force for $\text{pH} - \text{p}K = 3$ (solid lines) and $\text{pH} - \text{p}K = -3$ (dashed lines), at fixed values of parameters as shown in legend. Macroions' diameter is $a = 1$ nm, with the number of adsorption sites $N = 7$ and salt concentration $c_0 = 1$ mM.

stress out that these conclusions do not work for divalent ions. This is not a thing to worry about, since the strong-coupling theory is ion specific and it does not always work for divalent ions.

We have not specified yet the sign of the q polyvalent ion. In fact the product $q(\text{pH} - \text{p}K)$ can have either sign. In (Fig. 5.3) we thus study how the sign of polyvalent ions modifies the polyvalent ion-mediated contribution to the total interaction free energy. For both cases, $q(\text{pH} - \text{p}K)$ positive, (Fig. 5.3)(b), and for $q(\text{pH} - \text{p}K)$ negative, (Fig. 5.3)(c), the interaction free energy corresponds to attractive polyvalent ion-mediated forces but of vastly different magnitude, being much larger in the former case than in the latter. In both cases the attraction is again larger in the weak screening regime (smaller n_0 , large q).

The total interaction free energy between the two titratable macroions, $\tilde{F}(\tilde{R}) =$

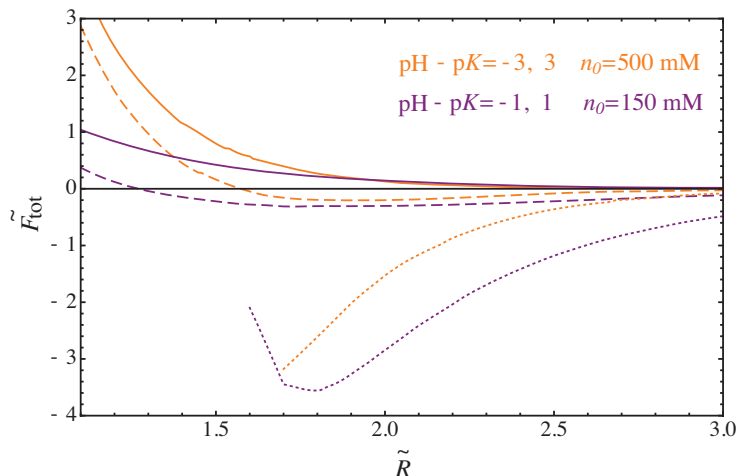


Figure 5.5: Total interaction force between macroions with small $\text{pH} - \text{p}K$ values at low salt concentration compared with the total interaction free energy in concentrated salt solutions between macroions with large $\text{pH} - \text{p}K$. Dotted lines correspond to q being a counter ion, dashed q is coion, while solid lines stand for $q = 0$. Macroions' diameter is $a = 1$ nm, number of adsorption sites $N = 7$ and $c_0 = 1$ mM.

$\tilde{F}_0(\tilde{R}) + \tilde{F}_1(\tilde{R})$, is presented in (Figs. 5.4 and 5.5). Obviously, the interaction force is attractive when $q(\text{pH} - \text{p}K) \geq 0$, due to the strongly coupled polyvalent ion mediated interaction, and is in general screened by the monovalent salt. Interestingly enough, in this case even the interaction at small separations remains attractive and the bare macroion repulsion is not observed. The reason for this is not the polyion mediated electrostatic attraction but its size: in fact for small separation the polyvalent counterion cannot enter the space between the macroions and thus exerts an additional effective osmotically generated attraction between them in general akin to the depletion effect, already noticed in a similar context for net-neutral surfaces at small separations [36]. In the opposite case, when $q(\text{pH} - \text{p}K) < 0$, the repulsion in general prevails, except at large separations where one can detect a small residual attraction, possibly as a consequence of an asymmetrical charge fluctuation due to charge regulation. At smaller separations the bare repulsion between macroions is reduced partly due to the charge regulation effects and partly due to depletion effects. In (Fig. 5.5) one can additionally notice how the two cases, one with small $\text{pH} - \text{p}K$, immersed in a solution of low salt concentration, and the other one with large $\text{pH} - \text{p}K$, but immersed in concentrated salt solution, have quite similar behavior, indicating that the valency of the polyion and the screening of the monovalent salt somehow act in parallel.

In (Fig. 5.6) the total interaction energy is now compared for the two cases with and without charge regulation, Eq. (5.32) and Eq. (5.33), respectively. The charge non-regulated case corresponds to fixed values of the macroion charge equal to Ne_0 . Here, one can notice the important effect of charge regulation through the polyvalent mediated interaction, ruled by the pH value, which determines the overall strength of the charge regulation interaction that can then appear as either smaller or larger than the one corresponding non-regulated interaction energy. This non-monotonic effect of charge regulation hinges on the two terms in the dressed ion free energy that respond differently to titration of the macroion charges.

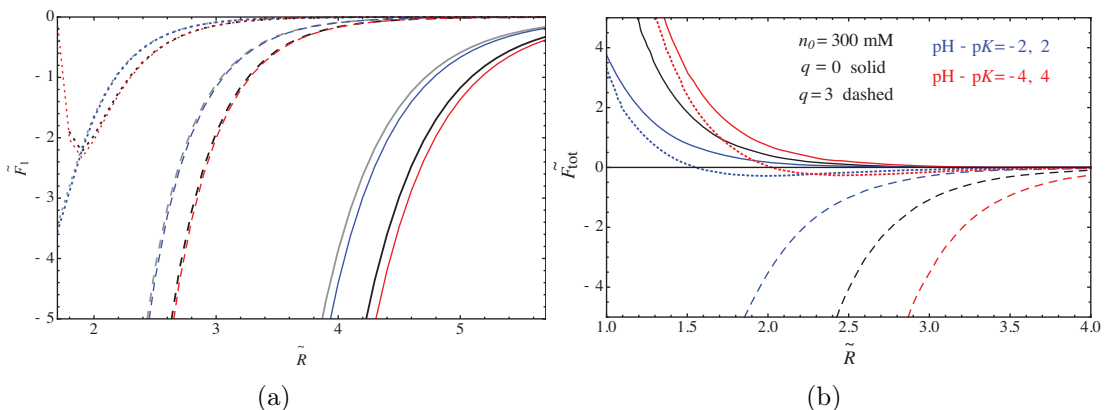


Figure 5.6: (a) The comparison of the interaction force \tilde{F}_1 for non-regulated case (calculated from Eq. (5.33) and presented with: $q = 4$ black lines and gray lines standing for $q = 3$) with regulated interaction force (calculated from Eq. (5.32) for $\text{pH} - \text{p}K = 3$ and presented with blue lines for $q = 3$ and red lines for $q = 4$). Solid lines correspond $n_0 = 150$ mM, dashed $n_0 = 300$ mM, while dotted stand for $n_0 = 500$ mM. (b) The comparison of the total interaction force for non-regulated case (black lines) with total regulated interaction force at $\text{pH} - \text{p}K = -2, -4$ (dotted lines) and $\text{pH} - \text{p}K = 2, 4$ (dashed lines), at fixed values of parameters as shown in legend. Macroions have diameter $a = 1$ nm, with the number of adsorption sites is $N = 7$ and salt concentration $c_0 = 1$ mM.

The dressed ion theory obviously predicts an attractive interaction between charge regulated macroions, which can sometimes dominate the overall interaction. This is different from the weak-coupling case (Chapters 3 and 4), where the fluctuation attraction, or the KS interaction, is subdominant to the DH repulsion, except close to the PZC, where it indeed becomes dominant. In the strong-coupling dressed ion theory the attraction can clearly become dominant either with or without the charge regulation, though it can be stronger in the latter case and remains important for any value of pH. The salt effect acts mostly to quench the correlation polyvalent ion-mediated attraction and diminish its spatial range.

The attraction between two identical charge regulated macroions, seen in the dressed ion theory, has a different origin from the weak-coupling KS interactions, where they are due to thermal monopolar charge fluctuations around the mean-field solution, enabled by the dissociation equilibrium of the surface of the macroion. In the dressed ion theory, the polyvalent ion-mediated attraction could be seen as being due to the *electrostatic bridging interaction* involving the polyvalent ion. This should in general not be confused with the so-called *salt bridging interaction* sometimes invoked even in weakly coupled monovalent salt solutions.

The mesoscale model of charge regulation introduced depends only on the difference $\text{pH} - \text{p}K$ as a free parameter and the value of $\text{p}K$ should be taken from other considerations. The physical dimensions of the interaction force can be obtained by multiplying the dimensionless force with $k_B T / l_B$. Since $k_B T$ is 4.114 pN nm and l_B is 0.7 nm this then leads to the physical force of the order ~ 1 pN at nanometer-ranged separations. The interaction force of that order of magnitude is found quite recently in the experiments with charge-regulated silica particles in dilute aqueous electrolyte solutions containing multivalent counterions, using direct

force measurements as described in Ref. [133]. Moreover, the similar experiments based on direct force measurement, confirmed that multivalent coions do not play an important role on charge regulation and the interaction of two symmetrically charged sulfate/amidine latex particles can be well described with standard PB theory [106]. Residual attraction at distant separation, our theory proposed, is not observed in mentioned experiments.

5.3 Conclusions

The main goal of this research was to present a theoretical description for the phenomenon of charge regulation as affected by the presence of polyvalent ions. We formulated a strong-coupling dressed ion theory, describing the electrostatic interactions between macroions undergoing charge regulation processes, in a mixture of monovalent-polyvalent salt solution. Using the proper description of charge regulation, suitable for treating it in the field theoretical framework, the partition function is derived in the form of a virial expansion valid for small concentration of the polyvalent salt. The first term in such expansion corresponds to the direct interaction between titratable macroions in a monovalent salt solution, while the first order correction, stems from the interaction of the polyvalent ion with each macroion. The asymmetry in the ionic solution allowed us to decouple the system into the monovalent salt component, addressed on a weak-coupling level, while the polyvalent ion component was assumed to be strongly coupled with macroions. In both cases, titration of the macroions is treated on the Gaussian approximation level involving an expansion of the exact charge regulation free energy valid in general for highly charged macroions

We have shown that the presence of polyvalent ion brings about a strong attraction between two symmetrically charged macroions. In the case when polyvalent ion acts like a counterion, the attraction is large enough to overcome repulsion between the macroions, while in the opposite case, the repulsion between macroions turns into a small attraction at large separations due to the asymmetric charge fluctuations at macroions surface, induced by the presence of the polyvalent salt. The polyvalent-ion mediated attraction remains appreciable even at conditions, when macroions reach the point of zero charge. From the derived expressions for the free energy of interaction, it is clear that the polyvalent ion-mediated attractive contribution stems from the charge – induced charge type of the interaction, since it is proportional to the square of the polyvalent ion charge. Our results show that the polyvalent ion-mediated attraction is significantly stronger than the KS interaction, obtained for the same system described in the weak-coupling regime, i.e. without any polyvalent salt. We therefore derived a generalized form of the KS interaction, with the range of validity extended to the regime, where their original KS derivation fails.

By calculating the interaction between point-like charge regulated macroions in the weak-coupling and strong-coupling approximations, based within the field representation of the partition function, we have opened a new way to analyze the interactions between proteins in ionic solutions. Our approach brings together the charge regulation theory as well as the general weak-coupling and strong-coupling dichotomy of the field representation of the partition function of Coulomb fluids. The results seem interesting and we will endeavor to compare them with detailed

Monte Carlo simulations in the near future.

Chapter 6

Salt-mediated interactions of planar charge regulated surfaces

In Chapter 5 we derived the dressed ion theory for charge regulated point-like particles immersed in a mixture of salt ions [134]. Here, we continue with the analysis of the influence of polyvalent ions on charge regulation in order to complete our analytical journey through the charge regulation phenomena. To do so, we will first define another tractable system set in a planar geometry in order to complete the analysis of the system we had started from: the double layer problem with titration sites immersed in a salt mixture. Bathing ions will be treated in conceptually the same way as we in Chapter 5: we take the monovalent salt as weakly coupled with the surfaces while the polyvalent ions are strongly coupled. Within this model we then proceed to derive the dressed ion theory for charge regulated planar bounding surfaces. Contrary to the point-like macroion case, here we investigate the case where the titration sites span an infinite surface and thus analyze the thermodynamic limit of finite surface densities of all the quantities analysed. The obtained results will be relevant for systems where the separation between charged macromolecules is much smaller than their size. The non-vanishing size of the titrating macroion will introduce additional formal difficulties and one of the goals of this Chapter is to find a way to overcome them and arrive at the understanding of how the spatial distribution of charge fluctuations at the surfaces affects their mutual interaction in the presence of polyvalent ions.

As we have seen in Chapter 1, the double layer problem has never stopped to be an interesting calculational device for theoretical physicists. The hundred years long history of different attempts to understand it includes also the successful description of diverse biological phenomena on one side, but also testifies to the challenging nature of some problems that needed decades to be solved on the other. This is certainly the case with the attraction of similarly-charged surfaces in the presence of polyvalent ions. We saw that its proper theoretical description was given in 2010, by Matej Kanduč and coworkers [34], and this Chapter will provide an extension of their work, broadening it to include also the charge regulation phenomenon in its formalism.

Since the problem of charge regulated surfaces affected by salt has not been studied before in a field-theoretic manner, we start from a uniform distribution of titrating sites spread over the planar parallel plates, immersed in a monovalent salt solution, and then extend the theory to the case where the mixture of monovalent

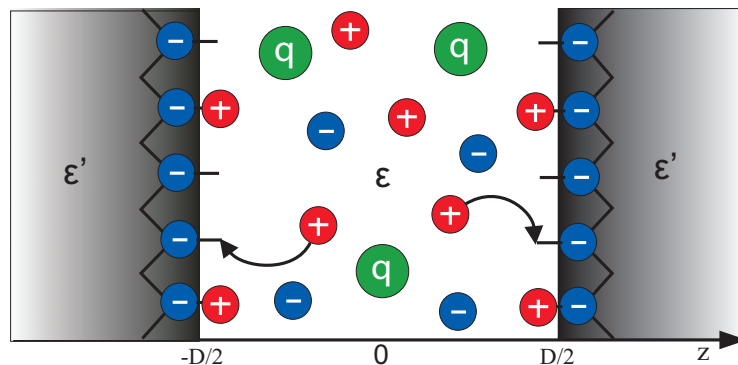


Figure 6.1: Schematic representation of two charged planar surfaces at a separation D with charge dissociation sites distributed uniformly along the surfaces with dissociable groups (AC) undergoing the reaction $AC \leftrightarrow A^- + C^+$. In between the surfaces there is a mixture of monovalent/polyvalent salt.

and polyvalent salt is present. As a final outcome we will obtain a generalized KS interaction for planar geometry and it will be possible to compare it with the ever present vdW interaction. The chosen model will allow us also to understand how the charge regulation affects the like-charge attraction.

6.1 General formalism

6.1.1 Model

The system of interest consists of two flat plates, bearing the surface charge which can fluctuate due to the absorption/dissociation of ions at the surface. The number of adsorption sites is equal on both surfaces and it is uniformly distributed across the surfaces. The system is immersed in a water described with dielectric constant ϵ . Both a monovalent 1:1 and polyvalent salt $q:1$ ions are dissolved in between. Behind the surfaces there is a medium of dielectric constant ϵ' , where one cannot find any ions (Fig. 6.1). The plates are separated by a distance D .

6.1.2 Charge regulation

To describe a charge regulation at the surface, we again start from the surface lattice gas model, corresponding to the Ninham–Parsegian charge regulation theory [59] where the surface free energy assumes the form:

$$f(\varphi(\mathbf{r})) = i\sigma\varphi(\mathbf{r}) - \alpha k_B T \frac{|\sigma|}{e_0} \ln \left(1 + \exp(\beta\mu_S + i\beta e_0\varphi(\mathbf{r})) \right), \quad (6.1)$$

We kept the same notation for the parameters: σ is maximal density of negative surface charge, uniformly distributed over surface, φ stands for the electrostatic potential, the asymmetry coefficient is $\alpha = 2$, chemical dissociation energy is $\mu_S = -(\text{pH} - \text{pK}) \ln 10$ and $b = \exp(\beta\mu_S)$. The total charge at the surface is consequently able to fluctuate in the interval $-\sigma S \leq e \leq \sigma S$. The total free energy Eq. (6.1) is then obtained from the integral over the surface:

$$F[\varphi(\mathbf{r})] = \oint_S f_S(\varphi(\mathbf{r})) d^2\mathbf{r}, \quad (6.2)$$

so that $F[\varphi(\mathbf{r})]$ is a functional of the surface potential. It enters the partition function as $\exp(-\beta F[\varphi(\mathbf{r})])$, so that it becomes equal:

$$\begin{aligned} \exp(-\beta F[\varphi(\mathbf{r})]) &= \\ \exp\left(-i\beta \int d^2\rho \sigma \varphi(\rho, z_{1/2}) + \alpha \int d^2\rho \frac{\sigma}{e_0} \ln\left(1 + b \exp(i\beta e_0 \varphi(\rho, z_{1/2}))\right)\right). \end{aligned} \quad (6.3)$$

For the purpose of further analysis, it is going to be suitable to switch to the discrete representation in the following way:

$$\exp\left(-\int d^2\rho f_S(\varphi_1(\rho))\right) \rightarrow \Pi_{\rho} \exp\left(-f_S(\varphi_1(\rho))\right), \quad (6.4)$$

so that one can use the same trick as already used in Chapters [4](#) and [5](#):

$$\exp\left(-\beta f_S(\varphi_1(\rho))\right) = \sum_{n=0}^{\alpha\tilde{\sigma}} \binom{\alpha\tilde{\sigma}}{n} b^n \exp(-i\beta e_0 \tilde{\sigma} \varphi) \exp(i\beta e_0 n \varphi), \quad (6.5)$$

where $\tilde{\sigma} = \sigma/e_0$. The binomial coefficient will be treated on the level of the Gaussian approximation, as explained before:

$$\binom{\alpha\tilde{\sigma}}{n} = \frac{2^{\alpha\tilde{\sigma}}}{\sqrt{\pi\alpha\tilde{\sigma}}} \exp\left(-\frac{(\alpha\tilde{\sigma} - 2n)^2}{2\alpha\tilde{\sigma}}\right). \quad (6.6)$$

We now introduce the notation $\tilde{x} = \alpha\tilde{\sigma} - 2n$, and switch from the summation to integration, obtaining:

$$\begin{aligned} \exp\left(-\beta f_S(\varphi_1(\rho))\right) &= \\ \int d\tilde{x} \exp\left(-\frac{1}{2} \frac{\tilde{x}^2}{\alpha\tilde{\sigma}} - \frac{1}{2} \tilde{x} [i\tilde{\varphi}(\rho) + \ln b]\right) \exp\left(-i\left[\tilde{\sigma} - \frac{1}{2}\alpha\tilde{\sigma}\right]\tilde{\varphi}(\rho)\right) \exp\left(\frac{1}{2} \ln b \alpha\tilde{\sigma}\right). \end{aligned} \quad (6.7)$$

Going back to the full surface free energy, one can write it as a functional integral over the new variable $\tilde{x}(\rho)$:

$$\begin{aligned} \Pi_{\rho} \exp\left(-\beta f_S(\varphi_1(\rho))\right) &= \\ \Pi_{\rho} \int \mathcal{D}[\tilde{x}(\rho)] \exp\left(-\frac{1}{2} \int d^2\rho \frac{\tilde{x}^2(\rho)}{\alpha\tilde{\sigma}} - \frac{1}{2} \int d^2\rho \tilde{x}(\rho) [i\tilde{\varphi}(\mathbf{r}) + \ln b]\right) \\ \times \exp\left(-i \int d^2\rho \left[\tilde{\sigma} - \frac{1}{2}e\alpha\tilde{\sigma}\right]\tilde{\varphi}(\mathbf{r}) \exp\left(\frac{1}{2} \ln b \alpha\tilde{\sigma}\right)\right). \end{aligned} \quad (6.8)$$

For further developments, it is going to be suitable to deal with the above evaluation in the Fourier-Bessel representation. The Fourier-Bessel transform of the functions $g = \{x, \varphi\}$ can be written explicitly as:

$$g(\rho, z) = \frac{1}{2\pi} \int Q dQ J_0(Q\rho) g(Q, z). \quad (6.9)$$

Therefore, the surface free energy term can be transformed as:

$$\begin{aligned} & \Pi_{\boldsymbol{\rho}} \exp\left(-\beta f_S(\varphi_1(\boldsymbol{\rho}))\right) \rightarrow \\ & \Pi_Q \int \mathcal{D}[x(Q)] \exp\left(-\frac{1}{2\alpha\sigma} \int Q dQ x^2(Q) - \frac{1}{2} \ln b \int dQ x(Q) \delta(Q)\right) \\ & \times \exp\left(-i \int Q dQ \varphi(Q) \left[\frac{1}{2}x(Q) + \left(\tilde{\sigma} - \frac{1}{2}\alpha\tilde{\sigma}\right) \frac{\delta(Q)}{Q}\right]\right) \exp\left(\frac{1}{2} \ln b \alpha \tilde{\sigma}\right), \end{aligned} \quad (6.10)$$

where the following identities have been used [135]

$$\int_0^\infty \rho d\rho J_0(\rho Q) J_0(\rho Q') = \frac{1}{Q} \delta(Q - Q'),$$

and

$$\int_0^\infty \rho d\rho J_0(\rho Q) = \frac{\delta(Q)}{Q}.$$

6.1.3 Dressed ion theory

To describe such system, we again start from partition function written as a functional integral over the local fluctuational potential:

$$\mathcal{Z} = \int \mathcal{D}[\varphi(\mathbf{r})] \exp\left(-\beta F[\varphi(\mathbf{r})]\right) \exp\left(-\beta H[\varphi(\mathbf{r})]\right) \exp\left(-\beta F[\varphi(\mathbf{r})]\right), \quad (6.11)$$

with the field Hamiltonian Eq. (5.10):

$$\begin{aligned} H[\varphi] &= \frac{1}{2} \int d\mathbf{r} d\mathbf{r}' \varphi(\mathbf{r}) u^{-1}(\mathbf{r}, \mathbf{r}') \varphi(\mathbf{r}') \\ & - \frac{\lambda_+}{\beta} \int d\mathbf{r} \exp(-i\beta e_0 \varphi(\mathbf{r})) - \frac{\lambda_-}{\beta} \int d\mathbf{r} \exp(i\beta e_0 \varphi(\mathbf{r})) - \frac{\lambda_c}{\beta} \int d\mathbf{r} \exp(-i\beta q e_0 \varphi(\mathbf{r})). \end{aligned} \quad (6.12)$$

Taking the monovalent salt as weakly coupled to the rest of the charges, one can decompose the bulk field Hamiltonian as:

$$-\beta H[\varphi] = -\beta H_0[\varphi] + \lambda_c \int d\mathbf{r} \exp(i\beta q e_0 \varphi(\mathbf{r})), \quad (6.13)$$

where the monovalent salt is treated on the DH level so that the interaction kernel is given as the screened effective DH interaction potential:

$$\begin{aligned} -\beta H_0[\varphi] &= \frac{1}{2} \epsilon \epsilon_0 \int d\mathbf{r} d\mathbf{r}' \varphi(\mathbf{r}) u_{DH}^{-1}(\mathbf{r}, \mathbf{r}') \varphi(\mathbf{r}') \\ &= \frac{1}{2} \epsilon \epsilon_0 \int ((\nabla \varphi(\mathbf{r}))^2 + \kappa^2 \varphi^2(\mathbf{r})) d\mathbf{r}. \end{aligned} \quad (6.14)$$

Here we again introduced the inverse square of Debye length as $\kappa^2 = 4\pi \ell_B n_b$ and $n_b = 2n_0 + qc_0$, where n_0 is the bulk concentration of the monovalent salt and c_0 is the bulk concentration of the multivalent ions, assumed to originate in dissociation of a $q:1$ salt.

We now invoke the dressed ion approximation for the rest of the system. Assuming that the fugacity of polyvalent salt is small enough, one is then allowed to use the following expansion:

$$\begin{aligned} \mathcal{Z} &= \int \mathcal{D}[\varphi(\mathbf{r})] \exp\left(-\beta F_{S_1}[\varphi(\mathbf{r})]\right) \exp\left(-\frac{\beta}{2} \int d\mathbf{r} d\mathbf{r}' \varphi(\mathbf{r}) u_{DH}^{-1}(\mathbf{r}, \mathbf{r}') \varphi(\mathbf{r}')\right) \\ &\quad \times \left[1 + \lambda_c \int d\mathbf{r}_0 \exp\left(-i\beta q e_0 \varphi(\mathbf{r}_0)\right) + \dots\right] \exp\left(-\beta F_{S_2}[\varphi(\mathbf{r})]\right). \end{aligned} \quad (6.15)$$

Thus we obtained a decomposition of the partition function into the part corresponding to the monovalent salt system and the part due to the one particle polyvalent ion contribution:

$$\mathcal{Z} = \mathcal{Z}_0 + \lambda_c \mathcal{Z}_1. \quad (6.16)$$

We proceed by calculating the partition function \mathcal{Z}_0 first.

6.2 Planar surfaces in presence of monovalent salt

6.2.1 Derivation of partition function

When the bathing solution is composed of only the monovalent salt, the partition function for a weakly coupled system is then given as:

$$\begin{aligned} \mathcal{Z} &= \int \mathcal{D}[\varphi(\mathbf{r})] \exp\left(-\beta F_{S_1}[\varphi(\mathbf{r})]\right) \\ &\quad \times \exp\left(-\frac{\beta}{2} \int d\mathbf{r} d\mathbf{r}' \varphi(\mathbf{r}) u_{DH}^{-1}(\mathbf{r}, \mathbf{r}') \varphi(\mathbf{r}')\right) \exp\left(-\beta F_{S_2}[\varphi(\mathbf{r})]\right). \end{aligned} \quad (6.17)$$

Due to the symmetry of the system it is going to be more suitable to deal with the problem in the Fourier–Bessel space. So we again write the Fourier–Bessel representation of the potential φ :

$$\varphi(\rho, z) = \frac{1}{2\pi} \int Q dQ J_0(Q\rho) \varphi(Q, z), \quad (6.18)$$

where Q stands for 2D transverse wave vector, $Q = |\mathbf{Q}|$ and then the partition function becomes:

$$\begin{aligned} \mathcal{Z}_0 &= \int \mathcal{D}[\varphi(Q, z)] \exp\left(-\beta F_{S_1}[\varphi(Q, z_1)]\right) \\ &\quad \times \exp\left(\frac{1}{2}\beta\epsilon\epsilon_0 \int Q dQ \int dz \left[\left(\frac{d\varphi(Q, z)}{dz}\right)^2 + p^2 \varphi^2(Q, z)\right]\right) \exp\left(-\beta F_{S_2}[\varphi(Q, z_2)]\right), \end{aligned} \quad (6.19)$$

where $p = \sqrt{Q^2 + \kappa^2}$. From the above equation one can easily identify the field propagator:

$$\begin{aligned} \mathcal{G}_p\left(\varphi(Q, z_1), \varphi(Q, z_2)\right) &= \\ &= \int_{\varphi(Q, z_1)}^{\varphi(Q, z_2)} \mathcal{D}[\varphi(Q, z)] \exp\left(-\frac{1}{2}\beta\epsilon\epsilon_0 \int_{z=z_1}^{z=z_2} dz \left[\left(\frac{d\varphi(Q, z)}{dz}\right)^2 + (Q^2 + \kappa^2)\varphi^2\right]\right), \end{aligned} \quad (6.20)$$

Chapter 6. Salt-mediated interactions of planar charge regulated surfaces

where the complete Green's function can be represented as the product over the wave vector:

$$\mathcal{G}\left(\varphi_1(\mathbf{r}), \varphi_2(\mathbf{r})\right) = \Pi_Q \mathcal{G}_p\left(\varphi(Q, z_1), \varphi(Q, z_2)\right). \quad (6.21)$$

The propagator $\mathcal{G}_p\left(\delta\phi(Q, z_1), \delta\phi(Q, z_2)\right)$ can be now identified as the Feynman propagator of a harmonic oscillator with constant frequency, where the z coordinate plays the role of time [123], and the Wick's rotation makes the action real instead of imaginary as in quantum mechanics. This type of integral is straightforward to solve [124], obtaining:

$$\begin{aligned} \mathcal{G}_p\left(\varphi(Q, z_1), \varphi(Q, z_2)\right) &= \sqrt{\frac{\beta\epsilon\epsilon_0 p}{2\pi \sinh(pD)}} \\ &\exp\left(-\frac{1}{2}\beta\epsilon\epsilon_0 \begin{bmatrix} \varphi(Q, z_1) \\ \varphi(Q, z_2) \end{bmatrix}^T \begin{bmatrix} p \coth(pD) & -p/\sinh(pD) \\ -p/\sinh(pD) & p \coth(pD) \end{bmatrix} \begin{bmatrix} \varphi(Q, z_1) \\ \varphi(Q, z_2) \end{bmatrix}\right). \end{aligned} \quad (6.22)$$

Now we can proceed with the calculation of the partition function, which takes the form:

$$\begin{aligned} \mathcal{Z} &= \Pi_Q \iint d\varphi_1(Q) d\varphi_2(Q) \\ &\exp\left(-f_S(\varphi_1(Q, z_1))\right) \mathcal{G}_p\left(\varphi(Q, z_1), \varphi(Q, z_2)\right) \exp\left(-f_S(\varphi_2(Q', z_2))\right). \end{aligned} \quad (6.23)$$

Invoking next the result obtained for the surface part of the partition function, Eq. (6.10), we remain with:

$$\begin{aligned} &\exp\left(-f_S(\varphi_1(Q, z_1))\right) \exp\left(-f_S(\varphi_2(Q', z_2))\right) = \iint \mathcal{D}[x_1(Q)] \mathcal{D}[x_2(Q)] \\ &\exp\left(-\frac{1}{2\alpha\tilde{\sigma}} \int Q dQ [x_1^2(Q) + x_2^2(Q)]\right) \exp\left(-i \int Q dQ [\varphi_1(Q) + \varphi_2(Q)] [\tilde{\sigma} - \frac{1}{2}\alpha\tilde{\sigma}]\right) \\ &\exp\left(-\frac{1}{2} \int dQ \delta(Q) [x_1(Q)(\ln b + i\varphi_1) + x_2(Q)(\ln b + i\varphi_2)]\right). \end{aligned} \quad (6.24)$$

Integrating the partition function Eq. (6.23) over the x -variable, one is left with the integral over all possible values of the surface potentials φ_1 and φ_2 :

$$\begin{aligned} \mathcal{Z} &= \Pi_Q \iint d\varphi_1(Q) d\varphi_2(Q) \sqrt{\frac{\beta\epsilon\epsilon_0 p}{2\pi \sinh(pD)}} \exp\left(-\frac{\beta\epsilon\epsilon_0}{2} \begin{bmatrix} \varphi_1(Q) \\ \varphi_2(Q) \end{bmatrix}^T \right. \\ &\left. \begin{bmatrix} p \coth(pD) + (\alpha\tilde{\sigma}(\beta e_0)^2)/(4\beta\epsilon\epsilon_0) & -p/\sinh(pD) \\ -p/\sinh(pD) & p \coth(pD) + (\alpha\tilde{\sigma}(\beta e_0)^2)/(4\beta\epsilon\epsilon_0) \end{bmatrix} \begin{bmatrix} \varphi_1(Q) \\ \varphi_2(Q) \end{bmatrix}\right) \\ &\times \exp\left(i\beta e_0 \delta(Q) [\varphi_1(Q) + \varphi_2(Q)] \left[\frac{1}{4} \ln b \alpha\tilde{\sigma} - \left(\tilde{\sigma} - \frac{1}{2}\alpha\tilde{\sigma}\right)\right]\right). \end{aligned} \quad (6.25)$$

Eventually the partition function assumes the final form:

$$\begin{aligned} \mathcal{Z} = & \exp\left(-\left[\frac{\alpha\tilde{\sigma}}{4}\ln b - \left(\tilde{\sigma} - \frac{\alpha}{2}\tilde{\sigma}\right)\right]^2 \frac{\tilde{\kappa}\coth(\tilde{\kappa}\tilde{D}) + \alpha\tilde{\sigma}\pi + \tilde{\kappa}/\sinh(\tilde{\kappa}\tilde{D})}{\tilde{\kappa}^2 + 2\pi\alpha\tilde{\sigma}\tilde{\kappa}\coth(\tilde{\kappa}\tilde{D}) + (\alpha\tilde{\sigma}\pi)^2}\right) \\ & \Pi_{\tilde{Q}} \sqrt{\frac{\tilde{p}}{(2\pi)\sinh(\tilde{p}\tilde{D})}} \sqrt{\frac{1}{(\tilde{p}\coth(\tilde{p}\tilde{D}) + \alpha\pi\tilde{\sigma})^2 - (\tilde{p}/\sinh(\tilde{p}\tilde{D}))^2}}, \end{aligned} \quad (6.26)$$

where we introduced dimensionless quantities $\tilde{D} = D/l_B$, $\tilde{\kappa} = \kappa l_B$ and $\tilde{\sigma} = \tilde{\sigma} l_B^2$, and

$$\mathcal{F}(D) = -k_B T \ln \frac{\mathcal{Z}(D)}{\mathcal{Z}(D \rightarrow \infty)}. \quad (6.27)$$

After subtraction of the bulk free energy $\ln \mathcal{Z}(D \rightarrow \infty)$, one obtains the interaction free energy $\mathcal{F}(D)_{00} = \mathcal{F}(D)_{01} + \mathcal{F}(D)_{02}$ as the sum of two contributions:

$$\beta\mathcal{F}_{01}/S = \left[\frac{\alpha\tilde{\sigma}}{4}\ln b - \left(\tilde{\sigma} - \frac{\alpha}{2}\tilde{\sigma}\right)\right]^2 \frac{\tilde{\kappa}\coth(\tilde{\kappa}\tilde{D}) + \alpha\tilde{\sigma}\pi + \tilde{\kappa}/\sinh(\tilde{\kappa}\tilde{D})}{\tilde{\kappa}^2 + 2\pi\alpha\tilde{\sigma}\tilde{\kappa}\coth(\tilde{\kappa}\tilde{D}) + (\alpha\tilde{\sigma}\pi)^2}, \quad (6.28)$$

and

$$\beta\mathcal{F}_{02}/S = \frac{1}{2} \int \tilde{Q} d\tilde{Q} \ln \left[1 - \left(\frac{\alpha\tilde{\sigma}\pi - \tilde{p}}{\alpha\tilde{\sigma}\pi + \tilde{p}} \right)^2 \exp(-2\tilde{p}\tilde{D}) \right]. \quad (6.29)$$

The first term gives the interaction between two equally-charged plates with fluctuating charge, while the second one leads to the attraction, which becomes dominant at the point of zero charge where the first term vanishes.

6.2.2 Comparison with van der Waals and Kirkwood–Shukmaker interactions

The above results are obtained by neglecting the (dielectric) region behind the surfaces where in principle the electrostatic field can propagate. Allowing the field to propagate behind the surfaces, the dielectric jump at the boundary comes into play and the partition function for such a system becomes

$$\begin{aligned} \mathcal{Z} = & \Pi_Q \iint d\varphi_1(Q) d\varphi_2(Q) \mathcal{G}_p(\varphi(Q, z_1), 0) \exp\left(-f_S(\varphi_1(Q, z_1))\right) \\ & \times \mathcal{G}_p(\varphi(Q, z_1), \varphi(Q, z_2)) \exp\left(-f_S(\varphi_2(Q, z_2))\right) \mathcal{G}_p(0, \varphi(Q, z_2)), \end{aligned} \quad (6.30)$$

where the Green's functions describing the propagation of the field in the semi-infinite region behind the surfaces are obtained from the general propagator Eq. (6.22):

$$\mathcal{G}_Q(\varphi(Q, z_1), 0) = \exp\left(-\frac{1}{2}\beta\epsilon'\epsilon_0 Q\varphi_1^2\right) \quad \text{and} \quad \mathcal{G}_Q(\varphi(Q, z_2), 0) = \exp\left(-\frac{1}{2}\beta\epsilon'\epsilon_0 Q\varphi_2^2\right), \quad (6.31)$$

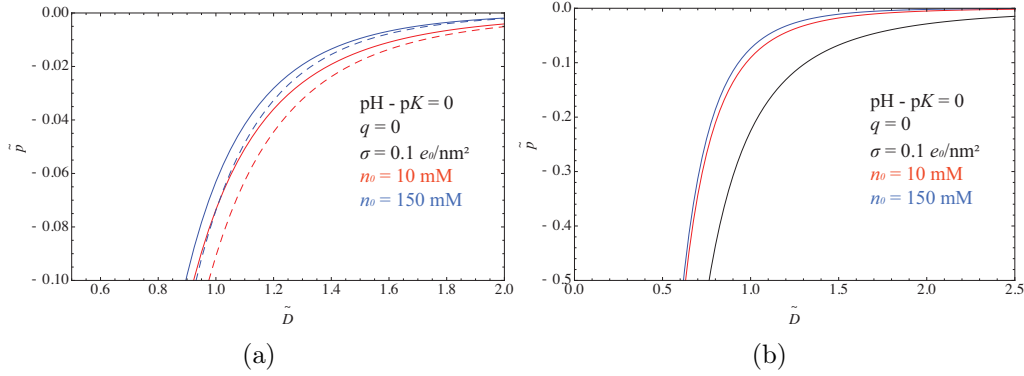


Figure 6.2: The interaction pressure, obtained from the derivative of the free energy, at PZC. (a) pressure calculated according to Eq. (6.32) (solid lines) is compared with the KS pressure calculated from Eq. (6.29) (dashed lines). (b) KS pressure is compared with the vdW interaction Eq. (6.34) (black line).

where we assumed that there is no salt behind the surfaces, so that $p = Q$ and $D \rightarrow \infty$. The free energy for such a system then yields the expression:

$$\beta\mathcal{F}(\tilde{D})/S = \left[\frac{\alpha\tilde{\sigma}}{4} \ln b - \left(\tilde{\sigma} - \frac{\alpha}{2}\tilde{\sigma} \right) \right]^2 \frac{\tilde{\kappa} \coth(\tilde{\kappa}\tilde{D}) + \alpha\tilde{\sigma}\pi + \tilde{\kappa}/\sinh(\tilde{\kappa}\tilde{D})}{\tilde{\kappa}^2 + 2\pi\alpha\tilde{\sigma}\tilde{\kappa} \coth(\tilde{\kappa}\tilde{D}) + (\alpha\tilde{\sigma}\pi)^2} + \frac{1}{2} \int Q dQ \ln \left(1 - \left[\frac{\alpha\tilde{\sigma}\pi + \epsilon' \tilde{Q}/\epsilon - \tilde{p}}{\alpha\tilde{\sigma}\pi + \epsilon' \tilde{Q}/\epsilon + \tilde{p}} \right]^2 \exp(-2\tilde{p}\tilde{D}) \right). \quad (6.32)$$

The first interaction term, corresponding to repulsion stayed unchanged but the attractive term is strongly modified. It can be said that the attraction in the previous case, Eq. (6.29), corresponds to the KS fluctuation interaction, while here we have the case of intertwined KS and vdW interaction acting in parallel.

In the case of no charge regulation $\alpha = 0$, the attraction reduces to the van der Waals interaction:

$$\beta\mathcal{F}_{vdw}/S = \frac{1}{2} \int \tilde{Q} d\tilde{Q} \ln \left(1 - \left[\frac{\epsilon' \tilde{Q} - \epsilon \tilde{p}}{\epsilon' \tilde{Q} + \epsilon \tilde{p}} \right]^2 \exp(-2\tilde{p}\tilde{D}) \right), \quad (6.33)$$

which is solvent dependent [136]. Taking the limit of no salt between the plates, one can get the zero order van der Waals– Lifshitz interaction in the famous form [21]:

$$\beta\mathcal{F}_{vdw}/S = \frac{1}{2} \int \tilde{Q} d\tilde{Q} \ln \left(1 - \left[\frac{\epsilon - \epsilon'}{\epsilon + \epsilon'} \right]^2 \exp(-2\tilde{Q}\tilde{D}) \right). \quad (6.34)$$

The results are shown in (Fig. 6.2). The comparison of two attractive contributions, Eq. (6.29) and Eq. (6.32), is shown in (Fig. 6.2)(a). One observes that the pure KS attraction is slightly bigger than the one calculated for the system with a dielectric jump. In other words, in the system with charge regulation the contribution of image forces reduces the attraction! Also, the non-additivity of the two type of forces becomes obvious, while the sensitivity to parameters change is quite small. What is not expected is that both types of attraction are smaller than the standard vdW attraction, Eq. (6.34).

6.3 Planar surfaces in presence of polyvalent salt

6.3.1 Derivation of partition function

The presence of polyvalent ions in the bathing solution decouples the total partition function into the weak-coupling one \mathcal{Z}_0 , and the one particle contribution \mathcal{Z}_1 , as we showed in Eq. (6.15), where we obtained \mathcal{Z}_1 in the following form:

$$\begin{aligned} \mathcal{Z}_1 &= \lambda_c \int d\mathbf{r}_0 \int \mathcal{D}[\varphi(\mathbf{r})] \exp\left(-\beta F_{S_1}[\varphi(\mathbf{r})]\right) \exp\left(-\beta F_{S_2}[\varphi(\mathbf{r})]\right) \\ &\times \exp\left(-\frac{\beta}{2} \int d\mathbf{r} d\mathbf{r}' \varphi(\mathbf{r}) u_{DH}^{-1}(\mathbf{r}, \mathbf{r}') \varphi(\mathbf{r}') - i\beta \int d\mathbf{r} \rho(\mathbf{r}; \mathbf{r}_0) \varphi(\mathbf{r})\right). \end{aligned} \quad (6.35)$$

The integration $d\mathbf{r}_0$ should be performed over all the available polyvalent ion positions in the slab between the surfaces. The point charge qe_0 is given as an integral over the density $\rho(\mathbf{r}; \mathbf{r}_0) = qe_0 \delta(\mathbf{r} - \mathbf{r}_0)$, or indeed by writing it in cylindric coordinates $\rho(\mathbf{r}) = qe_0 \frac{\delta(\rho - \rho_0)}{\rho} \delta(\varphi - \varphi_0) \delta(z - z_0)$. In the Fourier–Bessel representation the partition function becomes:

$$\begin{aligned} \mathcal{Z}_1 &= 2\pi \int d\rho_0 \rho_0 \int dz_0 \Pi_Q \int \mathcal{D}[\varphi(Q, z)] \exp\left(-\beta \tilde{f}_{S_1}(\varphi(Q, z_1))\right) \\ &\times \exp\left(\frac{1}{2} \beta \epsilon \epsilon_0 \int dz \left\{ \left[\frac{d\varphi(Q, z)}{dz} \right]^2 + p^2 \varphi^2(Q, z) \right\} \right. \\ &\left. - i\beta qe_0 \int dz J_0(Q\rho_0) \delta(z - z_0) \varphi(Q, z) \right) \exp\left(-\beta \tilde{f}_{S_2}(\varphi(Q, z_2))\right). \end{aligned} \quad (6.36)$$

The field propagator in this case has a more complicated form, given by:

$$\begin{aligned} \mathcal{G}_p(\varphi(Q, z_1), \varphi(Q, z_2)) &= \frac{1}{2} \beta \epsilon \epsilon_0 \int_{-D/2}^{D/2} dz_0 \left\{ \left[\frac{d\varphi(Q, z)}{dz} \right]^2 + p^2 \varphi^2(Q, z) \right\} \\ &- i\beta qe_0 \int_{-D/2}^{D/2} dz J_0(Q\rho_0) \delta(z - z_0) \varphi(Q, z). \end{aligned} \quad (6.37)$$

and is analogous to the 1D forced harmonic oscillator with constant frequency and with imaginary 'time', with an explicit solution in the form [124]:

$$\begin{aligned} \mathcal{G}_p(\varphi(Q, z_1), \varphi(Q, z_2)) &= \\ &\frac{\beta \epsilon \epsilon_0 p}{2 \sinh(pD)} [(\varphi(Q, z_1))^2 + \varphi(Q, z_2)^2] \cosh(pD) - 2\varphi(Q, z_1) \varphi(Q, z_2) \\ &- i \frac{\varphi(Q, z_2)}{\sinh(pD)} \int_{-D/2}^{D/2} dz \sinh(p[z + D/2]) \beta qe_0 J_0(Q\rho_0) \delta(z - z_0) \\ &- i \frac{\varphi(Q, z_1)}{\sinh(pD)} \int_{-D/2}^{D/2} dz \sinh(p[D/2 - z]) \beta qe_0 J_0(Q\rho_0) \delta(z - z_0) \\ &+ \frac{(\beta qe_0 J_0(Q\rho_0))^2}{\beta \epsilon \epsilon_0 p \sinh pD} \int_{-D/2}^{D/2} dz \int_0^z du \sinh(p[u + D/2]) \sinh(p[D/2 - z]) \delta(z - z_0) \delta(u - z_0). \end{aligned} \quad (6.38)$$

Chapter 6. Salt-mediated interactions of planar charge regulated surfaces

where $z_1 = -D/2$, $z_2 = D/2$, are the positions of the first and second plate, respectively, while z_0 is the position of the polyvalent ion. For $\varphi(Q, z_1)$ and $\varphi(Q, z_2)$ we will now use the notation φ_1 and φ_2 . Then:

$$\begin{aligned} \mathcal{G}_p(\varphi(Q, z_1), \varphi(Q, z_2)) &= \frac{\beta\epsilon\epsilon_0 p}{2 \sinh(pD)} [(\varphi_1^2 + \varphi_2^2) \cosh(pD) - 2\varphi_1\varphi_2] \\ &- i \frac{\beta q e_0 J_0(Q\rho_0) \sinh(p[D/2 + z_0])}{\sinh(pD)} \varphi_2 - i \frac{\beta q e_0 J_0(Q\rho_0) \sinh(p[D/2 - z_0])}{\sinh(pD)} \varphi_1 \\ &+ \frac{(\beta q e_0 J_0(Q\rho_0))^2 \sinh(p[D/2 + z_0]) \sinh(p[D/2 - z_0])}{\beta\epsilon\epsilon_0 p \sinh(pD)}. \end{aligned} \quad (6.39)$$

Going back to the partition function and introducing the surface parts, one can derive the following expression:

$$\begin{aligned} \mathcal{Z}_1 &= 2\pi \int d\rho_0 \rho_0 \int dz_0 \Pi_Q \\ &\times \exp\left(\frac{[\beta q e_0 J_0(Q\rho_0)]^2 \sinh(p[D/2 + z_0]) \sinh(p[D/2 - z_0])}{\beta\epsilon\epsilon_0 p \sinh pD}\right) \\ &\times \int d\varphi(Q, z_1) d\varphi(Q, z_2) \exp\left(-\frac{1}{2} \begin{bmatrix} \varphi(Q, z_1) \\ \varphi(Q, z_2) \end{bmatrix}^T \right. \\ &\times \left. \begin{bmatrix} \beta\epsilon\epsilon_0 p \coth(pD) + (\alpha\tilde{\sigma}\beta e_0)^2/4 & -\beta\epsilon\epsilon_0 p/\sinh(pD) \\ -\beta\epsilon\epsilon_0 p/\sinh(pD) & \beta\epsilon\epsilon_0 p \coth(pD) + \alpha\tilde{\sigma}(\beta e_0)^2/4 \end{bmatrix} \begin{bmatrix} \varphi(Q, z_1) \\ \varphi(Q, z_2) \end{bmatrix} \right) \\ &\times \exp\left(\begin{bmatrix} \varphi(Q, z_1) \\ \varphi(Q, z_2) \end{bmatrix}^T \begin{bmatrix} -i\beta q e_0 J_0(Q\rho_0) \sinh(p[D/2 + z_0])/\sinh(pD) \\ -i\beta q e_0 J_0(Q\rho_0) \sinh(p[D/2 - z_0])/\sinh(pD) \\ +i\beta e_0 \delta(Q) [\ln b \alpha\tilde{\sigma}/4 - (\tilde{\sigma} - (\alpha/2)\tilde{\sigma})] \\ +i\beta e_0 \delta(Q) [\ln b \alpha\tilde{\sigma}/4 - (\tilde{\sigma} - (\alpha/2)\tilde{\sigma})] \end{bmatrix} \right). \end{aligned} \quad (6.40)$$

After the integration over the surface potential we obtain:

$$\begin{aligned} \mathcal{Z}_1 &= 2\pi \int d\rho_0 \rho_0 \int dz_0 \mathcal{Z}_0 \\ &\times \exp\left[q \left[\frac{\alpha\tilde{\sigma}}{4} \ln b - \left(\tilde{\sigma} - \frac{\alpha}{2}\tilde{\sigma}\right) \right] \frac{\cosh(\tilde{\kappa}\tilde{z}_0) \left[\alpha\pi\tilde{\sigma} + \tilde{\kappa} \coth\left(\frac{\tilde{\kappa}\tilde{D}}{2}\right) \right] \operatorname{csch}(\tilde{\kappa}\tilde{D}) \sinh\left(\frac{\tilde{\kappa}\tilde{D}}{2}\right)}{\tilde{\kappa}^2 + \alpha\pi\tilde{\sigma}\tilde{\kappa} \coth(\tilde{\kappa}\tilde{D}) + (\alpha\pi\tilde{\sigma})^2} \right] \\ &\times \exp\left(q^2 \int \tilde{Q} d\tilde{Q} [J_0(Q\rho_0)]^2 \operatorname{csch}(\tilde{p}\tilde{D}) \frac{\alpha\pi\sigma \operatorname{csch}(\tilde{p}\tilde{D}) - \cosh(2\tilde{p}\tilde{z}_0) [\tilde{p} + \alpha\pi\sigma \coth(\tilde{p}\tilde{D})]}{\tilde{p}^2 + \alpha\pi\alpha\tilde{\sigma}\tilde{p} \coth(\tilde{p}\tilde{D}) + (\alpha\tilde{\sigma}\pi)^2} \right) \\ &\times \exp\left(q^2 \int \tilde{Q} d\tilde{Q} [J_0(Q\rho_0)]^2 \operatorname{csch}(\tilde{p}\tilde{D}) \frac{\cosh(\tilde{p}\tilde{D}) - \cosh(2\tilde{p}\tilde{z}_0)}{\tilde{p}} \right). \end{aligned} \quad (6.41)$$

Total free energy is then decomposed into:

$$\beta\mathcal{F} = -\ln \mathcal{Z}_0 - \lambda_c \frac{\mathcal{Z}_1}{\mathcal{Z}_0}, \quad (6.42)$$

so that one can identify the one particle contribution to the free energy as:

$$\begin{aligned}
 \beta\mathcal{F}_1 = & -2\pi c_0 \int d\tilde{\rho}_0 \tilde{\rho}_0 \int_{-D/2}^{D/2} d\tilde{z}_0 \left[\exp \left(q \left[\frac{\alpha\tilde{\sigma}}{4} (\text{pH} - \text{p}K) \ln 10 - \left(\tilde{\sigma} - \frac{\alpha}{2} \tilde{\sigma} \right) \right. \right. \right. \\
 & \left. \left. \left. \times \frac{\cosh(\tilde{\kappa}\tilde{z}_0) \left[\alpha\pi\tilde{\sigma} + \tilde{\kappa} \coth(\tilde{\kappa}\frac{\tilde{D}}{2}) \right] \text{csch}(\tilde{\kappa}\tilde{D}) \sinh(\tilde{\kappa}\frac{\tilde{D}}{2})}{\tilde{\kappa}^2 + \alpha\pi\tilde{\sigma}\tilde{\kappa} \coth(\tilde{\kappa}\tilde{D}) + (\alpha\pi\tilde{\sigma})^2} \right) \right) \\
 & \times \exp \left(q^2 \int \tilde{Q} d\tilde{Q} [J_0(Q\rho_0)]^2 \text{csch}(\tilde{p}\tilde{D}) \frac{\alpha\pi\sigma \text{csch}(\tilde{p}\tilde{D}) - \cosh(2\tilde{p}\tilde{z}_0) [\tilde{p} + \alpha\pi\sigma \coth(\tilde{p}\tilde{D})]}{\tilde{p}^2 + \alpha\pi\alpha\tilde{\sigma}\tilde{p} \coth(\tilde{p}\tilde{D}) + (\alpha\tilde{\sigma}\pi)^2} \right) \\
 & \times \exp \left(q^2 \int \tilde{Q} d\tilde{Q} [J_0(Q\rho_0)]^2 \left[\text{csch}(\tilde{p}\tilde{D}) \frac{\cosh(\tilde{p}\tilde{D}) - \cosh(2\tilde{p}\tilde{z}_0)}{\tilde{p}} - \frac{1}{\tilde{p}} \right] \right) - 1 \Big].
 \end{aligned} \tag{6.43}$$

Above we subtracted the bulk term as well as the polyvalent ion self-energy term W_{self} which is given by:

$$W_{self} = q^2 \int \tilde{Q} d\tilde{Q} \frac{[J_0(Q\rho_0)]^2}{\tilde{p}}. \tag{6.44}$$

Written in the Q representation, it is not entirely obvious that this corresponds exactly to the ion self-energy, so an explicit proof is given in Appendix [G](#).

The two terms in the final expression, Eq. [\(6.43\)](#), can then be differentiated, leading to one term that corresponds to the linear coupling between the charge of the polyvalent ion and the surface charge and the other term being proportional to the square of the charge of the polyvalent ion. The first term thus corresponds to the direct electrostatic interaction, while the second one stands for the interaction of the type charge-induced charge electrostatic interaction.

At the point of zero charge ($\text{pH} = \text{p}K$, $\alpha = 2$), the first term vanishes and one is left with the fluctuating charge interaction due to the charge regulation in the presence of a strongly coupled polyvalent ion. Since the fluctuations of the surface charge at PZC are inhomogeneous along the plate, the integral in the exponent depends on the position vector ρ_0 which runs over the whole plate.

6.3.2 Comparison with fixed charge results

The problem of polyvalent ion mediated interaction between the flat plates with fixed charge was solved by Matej Kanduč and coworkers [\[34\]](#). We are first going to check whether our theory reduces to that limit.

If one considers only the term stemming from the ion-surface interaction and take the limit $\alpha = 0$, corresponding to no charge regulation in the system, then one is left with:

$$\beta\mathcal{F}_1 = -Sc_0 \int_{-D/2}^{D/2} d\tilde{z}_0 \exp \left(-q\sigma \cosh(\kappa z_0) \frac{\exp(-\kappa D/2)}{\kappa[1 - \exp(-\kappa D)]} \right), \tag{6.45}$$

which reduces exactly to the known result if neglecting the term $\exp(-\kappa D)$ in the denominator. This difference has its origin in the different models studied. Namely, contrary to our model, the one with the fixed charge was developed for the system where the salt is allowed to penetrate into the region behind the surfaces, but in

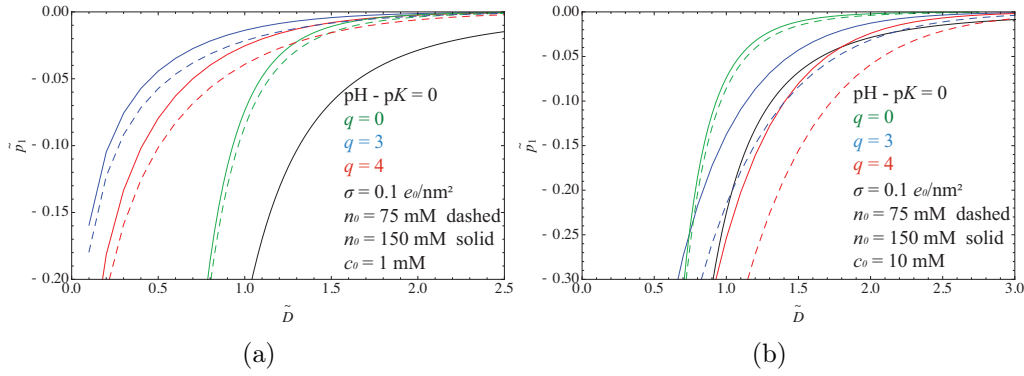


Figure 6.3: The interaction pressure at PZC, stemming from the presence of the polyvalent ions, with (a) $c_0 = 1$ mM and (b) $c_0 = 10$ mM. The values of other parameters are given in the inset. Black lines stand for the vdW interaction.

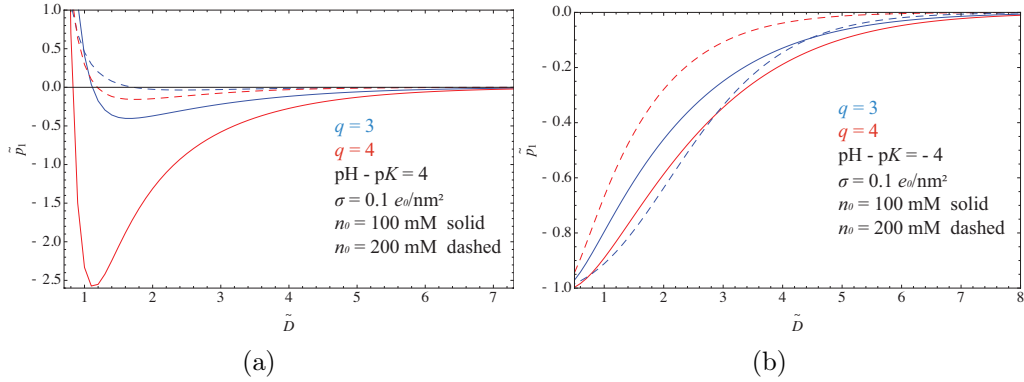


Figure 6.4: The interaction pressure \tilde{p}_1 , calculated from Eq. (6.43), plotted for (a) $\text{pH} - \text{pK} = 4$ and (b) $\text{pH} - \text{pK} = -4$. The values of other parameters are given in inset.

our model there are no salt ions behind the surface, neither does the field penetrate into the region behind the surfaces. The difference is due solely in order to reduce the complexity of the problem.

6.3.3 Results and discussion

After the numerical evaluation of Eq. (6.43), the interaction pressure, $p = -\frac{\partial \mathcal{F}/S}{\partial D}$, is plotted as a function of the plate separation, (Figs. 6.3–6.8).

First we analyze one particle contribution to the interaction pressure, originating in the presence of polyvalent ions. At the PZC (Fig. 6.3), the attractive contribution arises due to the fluctuations of surface charge enhanced by the strongly coupled polyvalent ion in the intervening solution. As we have seen from the formula Eq. (6.43), this is the charge-induced charge type of electrostatic interaction. As expected, this attraction increases for larger ion valencies and smaller screening. It can be either smaller or larger than the vdW interaction, depending on the concentration of the polyvalent ions.

When the system is not in the vicinity of the PZC, two scenarios are possible: one, where the surface and polyvalent ions are oppositely charged, (Fig. 6.4) (a),

6.3. Planar surfaces in presence of polyvalent salt

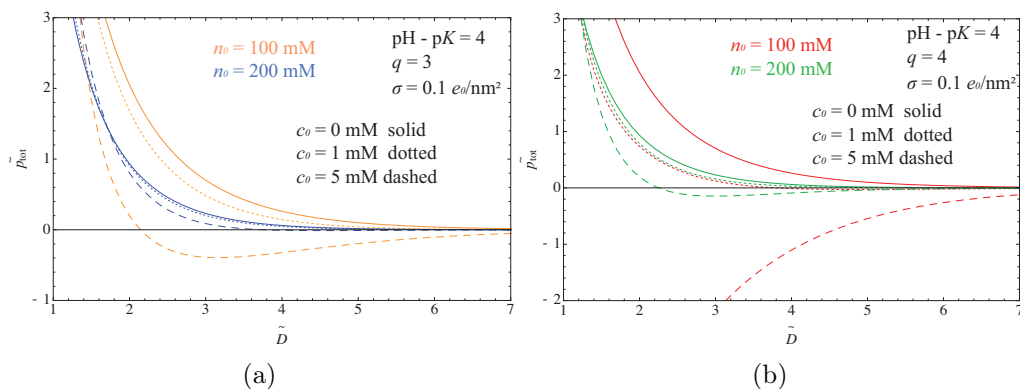


Figure 6.5: The total interaction pressure $\tilde{p}_0 + \tilde{p}_1$, plotted for (a) $q = 3$ and $q = 4$. The values of other parameters are given in the inset. q is counterion with respect to macroions' charge.

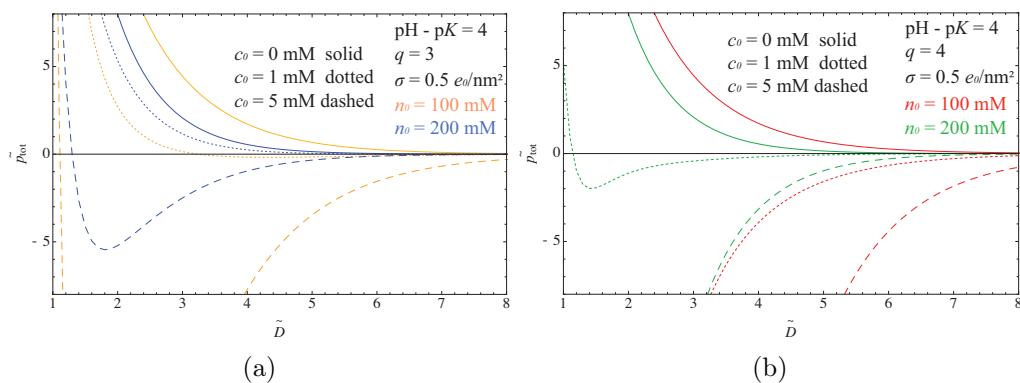


Figure 6.6: Total interaction pressure $\tilde{p}_0 + \tilde{p}_1$, plotted for (a) $q = 3$; (b) $q = 4$. The values of other parameters are given in the inset. q is counterion with respect to macroions' charge.

and the other, where they bear the charge of the same sign, (Fig. 6.4) (b). In both cases the interaction is attractive, but with obvious differences in the overall behavior. Namely, when q is a counterion with respect to macroions' charge, the strong attraction arises in the regime of high valency and small screening, which has its maximum at small surface separations and is then fast reduced as the plates become more distant. Here, polyvalent ions successfully screen the plate charge and tend to bring them closer. The monovalent salt also plays a significant role, since its concentration can drastically affect this kind of behavior: for larger concentration of monovalent salt, all the charges can be completely screened, so that the attraction is neutralized. On the other hand, if q is a coion with respect to macroions' charge, a small attraction arises, but it is not so sensitive to changes of the parameters such as pH of the solution, monovalent salt concentration, or ion valency.

How this affects a total interaction can be seen from (Figs. 6.5–6.8). Polyvalent ions always reduce the mutual repulsion of two equally-charged plates. Except at the point of zero charge, where the repulsion vanishes and attractive fluctuation forces become dominant, the overall repulsion can be overcome in the case of strongly coupled polyvalent ions with oppositely charged surfaces. While this is not always

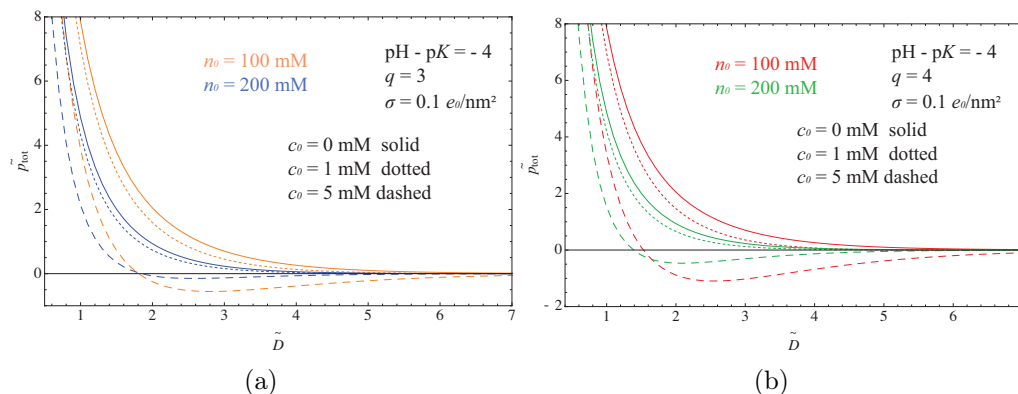


Figure 6.7: The total interaction pressure $\tilde{p}_0 + \tilde{p}_1$, plotted for (a) $q = 3$ and $q = 4$. The values of other parameters are given in the inset. q is coion with respect to macroions' charge.

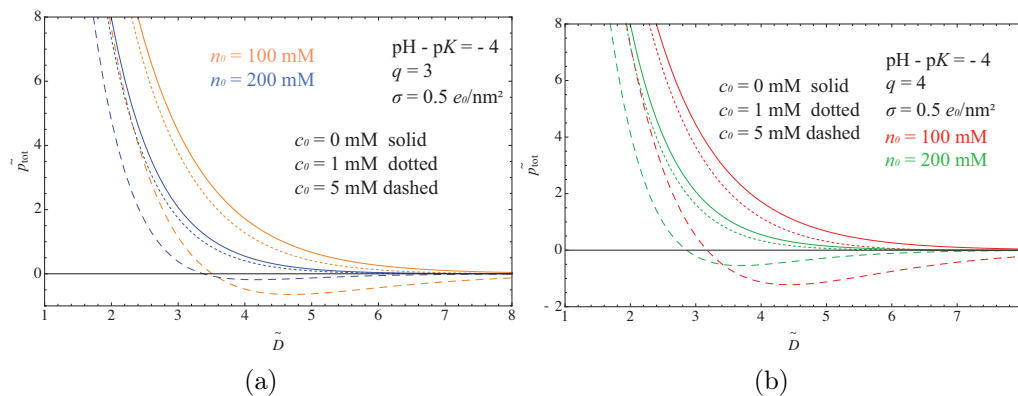


Figure 6.8: The total interaction pressure $\tilde{p}_0 + \tilde{p}_1$, plotted for (a) $q = 3$ and $q = 4$. The values of other parameters are given in the inset. q is coion with respect to macroions' charge.

the case, it is the usual state of affairs for smaller monovalent salt screening, larger polyvalent ion valencies and of course, larger concentration of polyvalent ions, see (Fig. 6.5). Interestingly enough, the repulsion can be more easily overcome if the surfaces bear larger charge density, (Fig. 6.6), which is due to the stronger coupling with polyvalent salt and dominant correlation effects.

In the other case, when the polyvalent ions bear charge of the same sign as the surfaces, the mutual repulsion is slightly reduced, irrespective of the ion valency or the surface charge, (Figs. 6.7 and 6.8). It thus appears that in the presence of polyvalent coions, the interaction can be described sufficiently well by the weak-coupling theory. This phenomenon was experimentally discovered recently in the laboratory of Michal Borkovec [106]. Nevertheless, for bigger concentrations of polyvalent salt ions, the derived theory predicts also that repulsion at large separations can be turned into a small attraction as a consequence of charge regulation, when the asymmetric charge fluctuations can result with the attraction in the regime when the surfaces are far apart.

The appearance of the pure attraction between same-charge surfaces is observed in the experiments with atomic force microscope when measuring the direct

force between negatively charged interfaces in the presence of cationic multivalent oligoamines [137]. The attraction is proved with charge-reversal effect, since the highly charged counterions attract strongly to the surface leading to the occurrence of the attraction. A better experimental insight into charge regulation phenomenon is given by the same research group [103, 133, 138] measuring the force between planar silica substrate having the possibility to adsorb an ion from solution and reduce its charge. They find that charge regulation effect has the important role at short surfaces' separations, i.e. 1 nm distances if immersed in a monovalent salt solution, while the presence of multivalent counterions increases this range 2-3 times. Beyond this range their results agree with standard PB theory even for the multivalent electrolytes, which contradicts to the many theoretical and computational studies [10, 18]. All this requires a more detailed investigations to address the range of validity of theories standing for multivalent ions.

The mentioned experiments provide a strong guarantee for the reasonableness of a qualitative outcome that our theories predict [139]. For validity distinction it is necessary to employ Monte Carlo simulations. As far as the comparison of our theoretical results with the case of proteins is concerning, nowadays experimental techniques allow only indirect protein-protein interaction measurements through determination of the second virial coefficient in dilute solution conditions, which can only tell us about if the attraction or repulsion prevails. But even on that level, the charge regulation phenomena in a form of attraction between proteins at PZC is experimentally observed when studying therapeutical monoclonal antibodies at different solution conditions, using both dynamic and static light scattering [140, 141].

6.4 Conclusions

The aim of this Chapter is to draw final conclusions from the study of the dressed ion strong-coupling theory, describing the electrostatic interactions between charge regulated planar surfaces. The dressed ion theory is generally based on the decomposition of the system's partition function into the strong-coupling part due to the presence of polyvalent ions and the weak-coupling part due to the monovalent salt ions. This decomposition eventually leads to two additive terms in the free energy, one based on the weakly-coupled partition function and the other one based on the strong-coupling one particle partition function. Both terms take equally into account the exact form of the surface free energy which describes the surface charge regulation.

The weak-coupling partition function describes the repulsion between two equally-charged surfaces. It exhibits a pronounced pH-dependence, so that it vanishes at the PZC. Moreover, it also gives an attractive contribution which then becomes dominant at the PZC, and representing an intertwined vdW-KS interaction. One can decouple these two parts by first taking the limit of vanishing dielectric jump in the system, when the KS interaction remains intact, or equivalently by taking the no charge regulation limit in the system, when it is the vdW interaction turn to become dominant.

The one particle dressed ion contribution to the partition function was calculated to describe the effect of polyvalent ions on the charge-regulated systems. That was the tricky part of the problem, since the polyvalent ions induce intensive charge

fluctuations at the surfaces that are not homogeneously distributed over the plates, which then brings fourth additional formal difficulties into the mathematical developments. Nevertheless, the problem can be solved in the Fourier-Bessel space employing a Feynman path integral in the form of a forced harmonic oscillator and all the following relations are then basically exact.

The results showed that two electroneutral surfaces at the PZC can attract in monovalent salt solutions as well as when polyvalent ions are in addition present in the bathing medium. In the first case, the attraction stems from the monopolar charge fluctuations induced by charge regulation, while in the second case, the attraction follows as a result of the charge-induced charge type of interaction, again, as a consequence of the surface charge regulation. Increasing the valency of the polyvalent salt ions, or increasing their concentration, leads to the attraction becoming more pronounced.

The theory derived in this section describes in particular the attraction of two equally-charged surfaces undergoing the charge regulation processes in the presence of polyvalent ions. We obtained pH-dependent properties of such interaction and we showed how it behaves as a function of different parameters. The underlying weak-coupling repulsion can be overcome by the polyvalent ion mediated attraction only when the surfaces and polyvalent ions bear charges of opposite sign, i.e. when the polyion is also the counterion. In the opposite case, the polyvalent ions do not have a significant influence on the strength of electrostatic interaction which then remains mostly repulsive. Only in the regime where their concentration is large enough, does the attraction appears at large plate separations, where the repulsion disappears and the asymmetric charge fluctuations become the dominant feature of the interaction. This is an additional interesting twist of the strong-coupling behavior of the unpredictable charge regulation phenomenon.

To conclude, we have made an important contribution and uncovered an important new regime of the double layer theory, by going beyond the standard description with the charge regulation model and at the same time also broadened its range of validity to polyvalent salt solutions. In this Chapter we completed our analysis of strongly coupled charge regulated objects in the dressed ion theory as well as proposed a new formulation to the charge regulation theory in general.

Chapter 7

Concluding remarks

In conclusion, it is important to indicate that this work represents an extension of a century-long history of the theory of electrostatic interactions in the colloid milieu. Coulomb fluids composed of macromolecules in an ionic solution represent a quintessential many-body problem, and are as such challenging to analyze, especially due to the long-range nature of the electrostatic interactions. This made a strong imprint on the development of this scientific area, since usually the theoretical approaches proposed had to be limited to the narrow parameter space, where the relevant approximations retain their validity, thus making the overall progress in the knowledge difficult and stepwise. Introducing the tools from a field-theoretic description of Coulomb fluids, significant formal progress was made possible and the era of the modern theoretical description of Coulomb fluids was ushered in. Nevertheless, even such modern theories are necessarily restricted to the parameter space corresponding to fixed colloidal or macromolecular charges. As is well recognized, this assumption is usually not realistic, especially in the world of proteins with dissociable protonable–deprotonable amino acids, where pronounced charge regulation effects enabling fluctuating surface charges are the general rule. This Thesis is devoted entirely to the generalized theory of colloidal electrostatic interactions, describing the effects brought upon by relaxing the fixed macroion charge restraint and leading to charge regulated macroions. Of course, it can only be based on additional approximations but we believe that it nevertheless describes the salient fundamental features of the behavior of charge-regulated macroions in colloidal ionic solutions. This general endeavour was partitioned into the analysis of four model systems, chosen to represent some fundamental general features of the charge regulated systems.

The first advance was achieved by introducing the free energy that corresponds exactly to the Ninham–Parsegian chemical equilibrium description of charge regulation, and by formulating the field-theoretic description of charge regulation in the case of two planar charge regulated bounding surfaces, immersed in a counterion-only solution. It is exactly this reformulation of the charge regulation problem that opened up the way to new developments such as going beyond the mean field Ninham–Parsegian solution, and to calculate exactly and analytically the contribution of Gaussian fluctuations and the inhomogeneous distribution of counterions between the bounding surfaces. The one-loop Gaussian correction to the mean-field solution brought forth an attractive contribution stemming from the intertwined monopolar KS fluctuation interaction and the dipolar vdW fluctuation interaction, which can in fact be decoupled for certain limiting cases. A similar situation was

identified also when the interaction between the bounding surfaces was mediated not only by counterions but also by the addition of monovalent salt ions. In this case the salt ions were treated on the DH level, while the contribution of charge regulation of the bounding surfaces was calculated exactly. This in general shows that the solution of the full statistical-mechanical problem can be achieved with different levels of approximation for the bulk part and for the surface charge regulated part.

In the case of two small spherical charge-regulated macroions in a monovalent salt solution, based on the approximation of point-like macroions, we based our theoretical approach on treating the salt on a weak-coupling level, while the surface charge regulated part was included exactly. The ensuing electrostatic interaction showed pronounced pH-dependent behavior, with attraction dominant at the PZC. Since this system is related to the original KS model, the obtained attraction in this limit corresponds to the original KS result. Moreover, we also showed that this attraction stems from an asymmetric charge fluctuations which appears strictly at the PZC. The charge regulation part of the free energy did not take into account the details of the distribution of dissociable sites along the macroion surface but assumed an uniform distribution of sites, each of which has an equal probability to be neutralized. This theoretical approach was then generalized to the system of protein-like macroions, characterized with an assumed amino acid composition, where each of the dissociable amino acids is defined by its neutralization point pK. In this way, more realistically describing the real system, the resulting theory was able to describe an additional phenomenon concerning the attraction at the PZC, viz. the attraction does not appear always exactly at the PZC, pending on the details of the protein composition. The attraction is in fact proportional to the protein capacitance, i.e., the rate of change of its charge with the local electrostatic potential in the vicinity of the PZC, which in its turn depends on the details of the amino-acid composition. All these are also well known and experimentally confirmed facts.

A special theoretical challenge was to broaden the charge regulation theory to be valid also in the strong electrostatic coupling regime. In that case, the original KS result is inapplicable, and no other approximate results were available. The problem was formulated and solved for two model systems, one based on the point-like macroions in a mixture of monovalent and polyvalent salt solution and the other based on two charge regulated flat plates immersed in the same type of an asymmetric ionic solution. The dressed ion theory was taken as the point of departure and reformulated for the charge regulated component of the solution, by decoupling the salt components into a weak-coupling part (monovalent salt ions) and the strong-coupling part (polyvalent salt ions). In both cases the macroion charge or the bounding surface charge is regulated with the local solution conditions, allowing the local charge to fluctuate. The effects of the polyvalent ions are conceptually related in both model systems: the first order correction to the mean-field weak-coupling solution gives rise to an attractive force, where two types of attraction can be in general distinguished: one describes the attraction as stemming from the coupling of the polyvalent ions with the charged surfaces and the other stemming from the charge-induced charge type of interaction, relevant in the vicinity of the PZC. They have significantly different behavior depending on whether the polyvalent ions enter as a counterions or as a coions. In the first case, strong attraction appears, which may overcome repulsion between same-charged objects, while in the latter case, the

attractive contribution is not strong enough to modify the dominant repulsion. Only at larger separations, a small attraction may arise, due to the asymmetric surface charge fluctuations. The attraction at the PZC is larger for higher ion valency and smaller salt screening. A generalized KS attraction, however, different from the original formulation, is therefore obtained also for strongly coupled systems in these two geometries.

In this Thesis we presented a theoretic framework for the description of charge regulated systems in an ionic solution, and was strongly motivated by the challenges of the protein-protein electrostatic interactions. Though the advances achieved are non-negligible, there remains a lot of room for improvement and generalizations. First, the validity of the theoretical approaches presented should be checked by the Monte Carlo simulations, which is already planned in the near future. Furthermore, the macroions were described either within the simplest possible model as point-like macroions, neglecting the spatial distribution of adsorption sites, or within the flat infinitely extended surface model, with uniform distribution of dissociation sites. Both these models can be generalized and ammended. Especially interesting would be to see how the patchy charge distributions affect the charge regulation interaction. It would be also possible to go deeper into the numerics and implement the results to the interactions between concrete proteins. Concerning further theoretical development, the inclusion of multipolar moments as well as polarization effects is particularly called for. This will allow for a deeper and more complete understanding of the protein-protein interactions.

Appendix A

Exact evaluation of Feynman path integral

The path integral in Eq. (3.24) can be written in the form [124]:

$$\begin{aligned} \mathcal{G}_p(\delta\phi(Q, z_1), \delta\phi(Q, z_2)) = & \\ \sqrt{\frac{1}{2\pi}} \exp\left(-\frac{1}{2} \int_{-d}^d dz \int_0^1 d\mu \mathcal{R}(z, z, \mu)\right) & \\ \times \exp\left(-\frac{\beta\epsilon\epsilon_0}{2} \left[\delta\phi(Q, z_2) f'(z_2) - \delta\phi(Q, z_1) f'(z_1)\right]\right), & \end{aligned} \quad (\text{A.1})$$

where $f(z)$ is a solution of the equation of motion given by:

$$\ddot{f} - \mu \left[Q^2 + \frac{2\alpha^2}{\cos^2(\alpha z)} \right] f = 0, \quad (\text{A.2})$$

where $f = f(z; \mu)$. The Green's function equation is:

$$\frac{d^2}{dz^2} Q(z, z'|\mu) - \mu \left[Q^2 + \frac{2\alpha^2}{\cos^2(\alpha z)} \right] Q(z, z'|\mu) = -\delta(z - z'), \quad (\text{A.3})$$

with $Q(-d, z'|\mu) = Q(d, z'|\mu) = 0$. The resolvent $\mathcal{R}(z, z'|\mu)$ obeys the equation:

$$\begin{aligned} \frac{d^2}{dz^2} \mathcal{R}(z, z'|\mu) - \mu \left[Q^2 + \frac{2\alpha^2}{\cos^2(\alpha z)} \right] \mathcal{R}(z, z'|\mu) = & \\ \delta(z - z') \left[Q^2 + \frac{2\alpha^2}{\cos^2(\alpha z)} \right], & \end{aligned} \quad (\text{A.4})$$

with $\mathcal{R}(-d, z'|\mu) = \mathcal{R}(d, z'|\mu) = 0$. We can see that the resolvent satisfies $\mathcal{R}(z, z'|\mu) = -\left[Q^2 + \frac{2\alpha^2}{\cos^2(\alpha z')} \right] Q(z, z'|\mu)$. The Green's function $Q(z, z'|\mu)$ has the form:

$$Q(z, z'|\mu) = \begin{cases} g(z, \mu) h(z', \mu) / \Delta(\mu), & z < z' \\ g(z', \mu) h(z, \mu) / \Delta(\mu), & z > z' \end{cases} \quad (\text{A.5})$$

Appendix A. Exact evaluation of Feynman path integral

where $g(z, \mu)$ and $h(z, \mu)$ are two linearly independent solutions of Eq. (A.2) satisfying the conditions:

$$g(-d; \mu) = h(d; \mu) = 0, \quad (\text{A.6})$$

and

$$\Delta(\mu) = \dot{g}(-d, \mu)h(-d, \mu) = -g(d, \mu)\dot{h}(d, \mu). \quad (\text{A.7})$$

The integration of the resolvent operator yields:

$$\begin{aligned} \int_{-d}^d \mathcal{R}(z, z|\mu) dz &= - \int_{-d}^d \left(Q^2 + \frac{2\alpha^2}{\cos^2(\alpha z)} \right) Q(z, z|\mu) dz = \\ &= \left[-\frac{1}{\Delta(\mu)} \right] \int_{-d}^d \left[Q^2 + \frac{2\alpha^2}{\cos^2(\alpha z)} \right] g(z, \mu) h(z, \mu) dz. \end{aligned} \quad (\text{A.8})$$

Consider now the equation satisfied by function g :

$$\ddot{g} - \mu \left[Q^2 + \frac{2\alpha^2}{\cos^2(\alpha z)} \right] g = 0, \quad (\text{A.9})$$

and differentiating it with respect to μ , we have:

$$- \left[Q^2 + \frac{2\alpha^2}{\cos^2(\alpha z)} \right] g = \ddot{g}_\mu + \mu \left[Q^2 + \frac{2\alpha^2}{\cos^2(\alpha z)} \right] g_\mu. \quad (\text{A.10})$$

Inserting this into the resolvent integral and integrating by parts, one can get:

$$\begin{aligned} \int_{-d}^d \mathcal{R}(z, z|\mu) dz &= \left[-\frac{1}{\Delta(\mu)} \right] \left[\dot{g}_\mu(-d, \mu)h(-d, \mu) - \dot{h}(d, \mu)g_\mu(d, \mu) \right] = \\ &= \frac{g_\mu(d, \mu)}{g(d, \mu)} - \frac{\dot{g}_\mu(-d, \mu)}{\dot{g}(-d, \mu)}, \end{aligned} \quad (\text{A.11})$$

from which it follows that:

$$\int_0^1 d\mu \int_{-d}^d dz \mathcal{R}(z, z|\mu) = \ln \left(\frac{g(d, \mu)}{\dot{g}(-d, \mu)} \right) \Big|_0^1 = \ln \left(\frac{g(d, 1)}{\dot{g}(-d, 1)} \frac{\dot{g}(-d, 0)}{g(d, 0)} \right). \quad (\text{A.12})$$

As $g(d, 0)/\dot{g}(-d, 0) = 2d = D$, we have:

$$\exp \left(-\frac{1}{2} \int_0^1 d\mu \int_{-d}^d dz \mathcal{R}(z, z|\mu) \right) = \left[D \frac{\dot{g}(-d, 1)}{g(d, 1)} \right]^{\frac{1}{2}}. \quad (\text{A.13})$$

Now, the solution of the equation of motion is given as a linear combination of the solutions g and h as:

$$f(z, 1) = \delta\phi_2 \frac{g(z, 1)}{g(d, 1)} + \delta\phi_1 \frac{h(z, 1)}{h(-d, 1)}, \quad (\text{A.14})$$

so the exponent in the propagator Eq. (A.1) becomes:

$$\begin{aligned} & \exp \left(-\frac{\beta\epsilon\epsilon_0}{2} \left[\delta\phi(Q, z_2)f'(z_2) - \delta\phi(Q, z_1)f'(z_1) \right] \right) = \\ & \exp \left(-\frac{\beta\epsilon\epsilon_0}{2} \left[\delta\phi^2(Q, d)\frac{\dot{g}(d, 1)}{g(d, 1)} - \right. \right. \\ & \left. \left. - 2\delta\phi(Q, d)\delta\phi(Q, -d)\frac{\dot{g}(-d, 1)}{g(d, 1)} - \delta\phi^2(Q, -d)\frac{\dot{h}(-d, 1)}{h(-d, 1)} \right] \right). \end{aligned} \quad (\text{A.15})$$

Finally the propagator can be written as:

$$\begin{aligned} & \mathcal{G}_p \left(\delta\phi(Q, -d), \delta\phi(Q, d) \right) = \\ & \sqrt{\frac{D\dot{g}(-d, 1)}{2\pi g(d, 1)}} \exp \left(-\frac{\beta\epsilon\epsilon_0}{2} \left[\delta\phi^2(Q, d)\frac{\dot{g}(d, 1)}{g(d, 1)} - \right. \right. \\ & \left. \left. - 2\delta\phi(Q, d)\delta\phi(Q, -d)\frac{\dot{g}(-d, 1)}{g(d, 1)} - \delta\phi^2(Q, -d)\frac{\dot{h}(-d, 1)}{h(-d, 1)} \right] \right). \end{aligned} \quad (\text{A.16})$$

Solutions $g(z, 1)$ and $h(z, 1)$, which satisfy equation Eq. (A.2) when $\mu = 1$ and boundary conditions Eq. (A.6), are given by:

$$\begin{aligned} g(z) &= \frac{\sinh(Q[d+z])[Q^2 \cot(\alpha d) + \alpha^2 \tan(\alpha z)]}{\alpha(Q^2 + \alpha^2)} \\ &+ \frac{\alpha Q \cosh(Q[d+z])[1 + \cot(\alpha d) \tan(\alpha z)]}{\alpha(Q^2 + \alpha^2)}, \\ h(z) &= \frac{\sinh(Q[-d+z])[Q^2 \cot(\alpha d) - \alpha^2 \tan(\alpha z)]}{\alpha(Q^2 + \alpha^2)} \\ &+ \frac{\alpha Q \cosh(Q[-d+z])[-1 + \cot(\alpha d) \tan(\alpha z)]}{\alpha(Q^2 + \alpha^2)}. \end{aligned} \quad (\text{A.17})$$

After inserting these solutions back into the equation Eq. (A.16), one obtains the final result in the explicit form:

$$\begin{aligned} & \mathcal{G}_Q \left(\delta\phi(Q, -\frac{D}{2}), \delta\phi(Q, \frac{D}{2}) \right) = \\ & \sqrt{\frac{A}{2\pi B}} \exp \left(-\frac{\beta\epsilon\epsilon_0}{2B} \left\{ \left[\delta\phi^2(Q, -\frac{D}{2}) + \delta\phi^2(Q, \frac{D}{2}) \right] C - 2\delta\phi(Q, -\frac{D}{2})\delta\phi(Q, \frac{D}{2})A \right\} \right), \end{aligned} \quad (\text{A.18})$$

where $z_2 = D/2$, $z_1 = -D/2$ while A , B and C are defined by

$$\begin{aligned} A &= Q(\alpha^2 + Q^2) \cot^2(\alpha D/2) \\ B &= 2\alpha Q \cosh(DQ) \cot(\alpha D/2) + [\alpha^2 + Q^2 \cot^2(\alpha D/2)] \sinh(DQ) \\ C &= Q \cosh(DQ) [2\alpha^2 + (\alpha^2 + Q^2) \cot^2(\alpha D/2)] + \\ &+ 2\alpha[\alpha^2 + Q^2 + Q^2 \cos(\alpha D)] \csc(\alpha D) \sinh(DQ). \end{aligned} \quad (\text{A.19})$$

Appendix B

Derivation of field propagator

$G(\varphi_1, \varphi_2)$

The field propagator at points \mathbf{r}_1 and \mathbf{r}_2 is defined by:

$$G(\varphi_1, \varphi_2) = \int_{\varphi(\mathbf{r}_1)=\varphi_1}^{\varphi(\mathbf{r}_2)=\varphi_2} \mathcal{D}[\varphi(\mathbf{r})] \delta(\varphi(\mathbf{r}_1) - \varphi_1) \delta(\varphi(\mathbf{r}_2) - \varphi_2) \times \exp\left(-\frac{1}{2} \int d\mathbf{r} d\mathbf{r}' \varphi(\mathbf{r}) G^{-1}(\mathbf{r}, \mathbf{r}') \varphi(\mathbf{r}')\right), \quad (\text{B.1})$$

where $G^{-1}(\mathbf{r}, \mathbf{r}')$ is the usual Debye-Hückel kernel of the form [10]:

$$G^{-1}(\mathbf{r}, \mathbf{r}') = -\varepsilon_0 [\nabla \varepsilon(\mathbf{r}) \nabla - \varepsilon(\mathbf{r}) \kappa^2] \delta(\mathbf{r} - \mathbf{r}'), \quad (\text{B.2})$$

where κ is the inverse Debye length. Using the delta function in integral representation:

$$\delta(\varphi(\mathbf{r}_1) - \varphi_1) = \int \frac{dk}{2\pi} \exp\left(ik[\varphi(\mathbf{r}_1) - \varphi_1]\right) = \int \frac{dk}{2\pi} \exp\left(-ik\varphi_1 + ik \int d\mathbf{r} \rho_1(\mathbf{r}) \varphi(\mathbf{r})\right), \quad (\text{B.3})$$

where $\rho_1(\mathbf{r}) = \delta(\mathbf{r} - \mathbf{r}_1)$, one can rewrite the propagator as:

$$G(\varphi_1, \varphi_2) = \int dk \exp(-ik\varphi_1) \int dk' \exp(-ik'\varphi_2) \int \mathcal{D}[\varphi(\mathbf{r})] \exp\left(-\frac{1}{2} \int d\mathbf{r} d\mathbf{r}' \varphi(\mathbf{r}) G^{-1}(\mathbf{r}, \mathbf{r}') \varphi(\mathbf{r}') + i \int t(\mathbf{r}) \varphi(\mathbf{r}) d^3\mathbf{r}\right), \quad (\text{B.4})$$

where $t(\mathbf{r})$ stands for $t(\mathbf{r}) = k\rho_1(\mathbf{r}) + k'\rho_2(\mathbf{r})$. After integration over the field, one obtains:

$$G(\varphi_1, \varphi_2) = \frac{1}{\det G^{-1}(\mathbf{r}, \mathbf{r}')} \int dk \exp(-ik\varphi_1) \int dk' \exp(-ik'\varphi_2) \times \exp\left(-\frac{1}{2} \int d\mathbf{r} d\mathbf{r}' t(\mathbf{r}) G(\mathbf{r}, \mathbf{r}') t(\mathbf{r}')\right)$$

Appendix B. Derivation of field propagator $G(\varphi_1, \varphi_2)$

$$\begin{aligned}
&= \frac{1}{\det G^{-1}(\mathbf{r}, \mathbf{r}')} \int_{-\infty}^{+\infty} \int_{-\infty}^{+\infty} dk dk' \exp(-ik\varphi_1 - ik'\varphi_2) \\
&\times \exp\left(-\frac{1}{2}k^2 G(\mathbf{r}_1, \mathbf{r}_1)\right) \exp\left(-\frac{1}{2}k'^2 G(\mathbf{r}_2, \mathbf{r}_2)\right) \exp\left(-kk' G(\mathbf{r}_1, \mathbf{r}_2)\right).
\end{aligned} \tag{B.5}$$

If one introduces a 2D vector $(k \ k')$, this integral can be rewritten as:

$$\begin{aligned}
G(\varphi_1, \varphi_2) &= \frac{1}{\det G^{-1}(\mathbf{r}, \mathbf{r}')} \iint dk dk' \exp\left(-i \begin{pmatrix} \varphi_1 \\ \varphi_2 \end{pmatrix}^T \begin{pmatrix} k \\ k' \end{pmatrix}\right) \\
&\times \exp\left(-\frac{1}{2} \begin{pmatrix} k \\ k' \end{pmatrix}^T \begin{pmatrix} G(\mathbf{r}_1, \mathbf{r}_1) & G(\mathbf{r}_1, \mathbf{r}_2) \\ G(\mathbf{r}_1, \mathbf{r}_2) & G(\mathbf{r}_2, \mathbf{r}_2) \end{pmatrix} \begin{pmatrix} k \\ k' \end{pmatrix}\right).
\end{aligned} \tag{B.6}$$

Since this is a Gaussian integral, it can be evaluated explicitly:

$$G(\varphi_1, \varphi_2) = \exp\left(-\frac{\beta}{2} \begin{pmatrix} \varphi_1 \\ \varphi_2 \end{pmatrix}^T \begin{pmatrix} G(\mathbf{r}_1, \mathbf{r}_1) & G(\mathbf{r}_1, \mathbf{r}_2) \\ G(\mathbf{r}_1, \mathbf{r}_2) & G(\mathbf{r}_2, \mathbf{r}_2) \end{pmatrix}^{-1} \begin{pmatrix} \varphi_1 \\ \varphi_2 \end{pmatrix}\right). \tag{B.7}$$

Appendix C

Saddle-point approximation

The partition function Eq. (4.16) can be evaluated using the saddle-point method, consisting of minimization of the field action $\partial A/\partial\phi = 0$, where the action can be written in the form:

$$A(\phi_1, \phi_2) = f_1(\phi_1) + g(\phi_1, \phi_2) + f_2(\phi_2), \quad (\text{C.1})$$

with g the logarithm of the Green's function, given by:

$$g(\phi_1, \phi_2) = -\frac{1}{2} \begin{pmatrix} \phi_1 \\ \phi_2 \end{pmatrix}^T \begin{pmatrix} \tilde{G}(\mathbf{r}_1, \mathbf{r}_1) & \tilde{G}(\mathbf{r}_1, \mathbf{r}_2) \\ \tilde{G}(\mathbf{r}_1, \mathbf{r}_2) & \tilde{G}(\mathbf{r}_2, \mathbf{r}_2) \end{pmatrix}^{-1} \begin{pmatrix} \phi_1 \\ \phi_2 \end{pmatrix}. \quad (\text{C.2})$$

The saddle-point equations are obtained as:

$$N - \alpha N \frac{b \exp(-\phi_1)}{1 + b \exp(-\phi_1)} + \phi_1 \frac{4\pi\epsilon\epsilon_0}{\beta e_0^2 \kappa} \frac{1}{\exp(-2\tilde{a})/\tilde{a}^2 - \exp(-2\tilde{R})/\tilde{R}^2} \frac{\exp(-\tilde{a})}{\tilde{a}} - \phi_2 \frac{4\pi\epsilon\epsilon_0}{\beta e_0^2 \kappa} \frac{1}{\exp(-2\tilde{a})/\tilde{a}^2 - \exp(-2\tilde{R})/\tilde{R}^2} \frac{\exp(-\tilde{R})}{\tilde{R}} = 0; \quad (\text{C.3})$$

$$M - \alpha N \frac{b \exp(-\phi_2)}{1 + b \exp(-\phi_{1/2})} + \phi_2 \frac{4\pi\epsilon\epsilon_0}{\beta e_0^2 \kappa} \frac{1}{\exp(-2\tilde{a})/\tilde{a}^2 - \exp(-2\tilde{R})/\tilde{R}^2} \frac{\exp(-\tilde{a})}{\tilde{a}} - \phi_1 \frac{4\pi\epsilon\epsilon_0}{\beta e_0^2 \kappa} \frac{1}{\frac{e^{-2\tilde{a}}}{\tilde{a}^2} - \frac{e^{-2\tilde{R}}}{\tilde{R}^2}} \frac{e^{-\tilde{R}}}{\tilde{R}} = 0. \quad (\text{C.4})$$

Solutions of these equations are denoted as ϕ_1^* and ϕ_2^* . If one sets $M = 0$, $\alpha = 1$, one deals with an asymmetric system, for $M = N$, $\alpha = 2$, one deals with a fully symmetric system, while the choice $M = N$, $\alpha > 2$ defines a symmetric system with an asymmetric interval of fluctuating charge, i.e. a semi-symmetric system.

The action can be expanded around the saddle-point solution up to the second order in deviation from ϕ_1^* and ϕ_2^* , yielding:

$$A(\phi_1, \phi_2) = f_1(\phi_1^*) + g(\phi_1^*, \phi_2^*) + f_2(\phi_2^*) + \frac{1}{2} \left. \frac{\partial^2 A(\phi_1, \phi_2)}{\partial \phi_1^2} \right|_{\phi_1^*, \phi_2^*} \delta \phi_1^2 + \left. \frac{\partial^2 A(\phi_1, \phi_2)}{\partial \phi_1 \partial \phi_2} \right|_{\phi_1^*, \phi_2^*} \delta \phi_1 \delta \phi_2 + \frac{1}{2} \left. \frac{\partial^2 A(\phi_1, \phi_2)}{\partial \phi_2^2} \right|_{\phi_1^*, \phi_2^*} \delta \phi_2^2, \quad (\text{C.5})$$

where $f_{1/2}(\phi_{1/2}^*)$ are given as:

$$f_{1/2}(\phi_{1/2}^*) = -M \phi_{1/2}^* - \alpha N \ln(1 + b \exp(-\phi_{1/2}^*)). \quad (\text{C.6})$$

Appendix C. Saddle-point approximation

If we denote second derivatives in the equation above as A_{11} , A_{12} and A_{22} respectively, we will have:

$$\begin{aligned}
A_{11} &= -\alpha N b \frac{\exp(-\phi_1^*)}{[1 + b \exp(-\phi_1^*)]^2} - \frac{4\pi\epsilon\epsilon_0}{\beta e_0^2 \kappa} \frac{\exp(-\tilde{a})/\tilde{a}}{\exp(-2\tilde{a})/\tilde{a}^2 - \exp(-2\tilde{R})/\tilde{R}^2} \\
A_{22} &= -\alpha N b \frac{\exp(-\phi_2^*)}{(1 + b \exp(-\phi_2^*))^2} - \frac{4\pi\epsilon\epsilon_0}{\beta e_0^2 \kappa} \frac{\exp(-\tilde{a})/\tilde{a}}{\exp(-2\tilde{a})/\tilde{a}^2 - \exp(-2\tilde{R})/\tilde{R}^2} \\
A_{12} &= \frac{4\pi\epsilon\epsilon_0}{\beta e_0^2 \kappa} \frac{\exp(-\tilde{R})/\tilde{R}}{\exp(-2\tilde{a})/\tilde{a}^2 - \exp(-2\tilde{R})/\tilde{R}^2},
\end{aligned} \tag{C.7}$$

so that the saddle-point and the fluctuation free energy are equal to:

$$\beta \mathcal{F}_0 = -[f_1(\phi_1^*) + g(\phi_1^*, \phi_2^*) + f_2(\phi_2^*)], \tag{C.8}$$

and

$$\beta \mathcal{F}_2 = -\ln \frac{\det A_0}{\det A}, \tag{C.9}$$

where A_0 is a matrix, related to the partition function of the unperturbed system, with the elements:

$$\begin{aligned}
A_{11}^0 &= \frac{\partial^2 A_0(\phi_1, \phi_2)}{\partial \phi_1^2} = -\frac{4\pi\epsilon\epsilon_0}{\beta e_0^2 \kappa} \frac{\exp(-\tilde{a})/\tilde{a}}{\exp(-2\tilde{a})/\tilde{a}^2 - \exp(-2\tilde{R})/\tilde{R}^2} \\
A_{22}^0 &= \frac{\partial^2 A_0(\phi_1, \phi_2)}{\partial \phi_2^2} = -\frac{4\pi\epsilon\epsilon_0}{\beta e_0^2 \kappa} \frac{\exp(-\tilde{a})/\tilde{a}}{\exp(-2\tilde{a})/\tilde{a}^2 - \exp(-2\tilde{R})/\tilde{R}^2} \\
A_{12}^0 &= \frac{\partial^2 A_0(\phi_1, \phi_2)}{\partial \phi_1 \partial \phi_2} = \frac{4\pi\epsilon\epsilon_0}{\beta e_0^2 \kappa} \frac{\exp(-\tilde{R})/\tilde{R}}{\exp(-2\tilde{a})/\tilde{a}^2 - \exp(-2\tilde{R})/\tilde{R}^2}.
\end{aligned} \tag{C.10}$$

Finally, the saddle-point interaction force and the force due to the fluctuations around the saddle-point are given as:

$$\begin{aligned}
\tilde{F}_0 &= \frac{4\pi\epsilon\epsilon_0}{\beta e_0^2 \kappa} \frac{1 + \tilde{R}}{\tilde{R}^2} \tilde{a}^2 \exp(2\tilde{a} - \tilde{R}) \\
&\quad \times \frac{(\phi_1^* - \tilde{a}/\tilde{R} \exp(\tilde{a} - \tilde{R})\phi_2^*)(\phi_2^* - \tilde{a}/\tilde{R} \exp(\tilde{a} - \tilde{R})\phi_1^*)}{\left(1 - (\tilde{a}/\tilde{R})^2 \exp(-2(\tilde{R} - \tilde{a}))\right)^2}
\end{aligned} \tag{C.11}$$

$$\tilde{F}_2 = -\frac{1 + \tilde{R}}{\tilde{R}^3} \frac{\tilde{a}^2 \exp(-2(\tilde{R} - \tilde{a}))}{h_1(\phi_1^*)h_2(\phi_2^*) - (\tilde{a}^2/\tilde{R})^2 \exp(-2(\tilde{R} - \tilde{a}))}, \tag{C.12}$$

where:

$$\begin{aligned}
h_1(\phi_1^*) &= 1 + \frac{4\pi\epsilon\epsilon_0 \tilde{a}}{\beta e_0^2 \kappa N \alpha b} \exp(\tilde{a}) \exp(-\phi_1^*) (b + \exp(\phi_1^*))^2 \\
h_2(\phi_2^*) &= 1 + \frac{4\pi\epsilon\epsilon_0 \tilde{a}}{\beta e_0^2 \kappa N \alpha b} \exp(\tilde{a}) \exp(-\phi_2^*) (b + \exp(\phi_2^*))^2.
\end{aligned} \tag{C.13}$$

Appendix D

Gaussian approximation

The partition function Eq. (4.16) can be evaluated analytically, if one takes a Gaussian approximation for the binomial coefficient:

$$\binom{\alpha N}{n} = \frac{2^{\alpha N}}{\sqrt{\pi \alpha N / 2}} \exp\left(-\frac{(\alpha N - 2n)^2}{2\alpha N}\right). \quad (\text{D.1})$$

After substitution $x = \alpha N - 2n$ and $x' = \alpha M - 2n'$, summation can be transformed into the integral, when one assumes $N \gg 1$, so that the partition function becomes:

$$\begin{aligned} \mathcal{Z} &= \int_{-\infty}^{\infty} dx \int_{-\infty}^{\infty} dx' \exp\left(-\beta \mathcal{F}(x, x', \tilde{R})\right) \\ &\times \exp\left(\frac{1}{2}[x + x'][\text{pH} - \text{pK}] \ln 10\right) \exp\left(-\frac{1}{2\alpha N}[x^2 + x'^2]\right), \end{aligned} \quad (\text{D.2})$$

where

$$\begin{aligned} \mathcal{F}(x, x', \tilde{R}) &= \left(\frac{\exp(-\kappa a)}{a/l_B}\right) \left\{ [x + N(2 - \alpha)]^2 + [x' + M(2 - \alpha)]^2 \right\} \\ &+ 2\frac{\exp(-\kappa \tilde{R})}{\tilde{R}/l_B} [x + N(2 - \alpha)][x' + M(2 - \alpha)]. \end{aligned} \quad (\text{D.3})$$

This is a general Gaussian-type integral and can be calculated analytically, but since the solution is too cumbersome, it is not displayed here. The interaction force then follows as a sum of the mean contribution to the force and the fluctuation force as:

$$\begin{aligned} \tilde{F}_0 &= \tilde{a}^2 \exp(2\tilde{\kappa}\tilde{a} - \tilde{\kappa}\tilde{R}) \frac{1 + \tilde{\kappa}\tilde{R}}{\tilde{R}^2} \frac{[(\text{pH} - \text{pK}) \ln 10]^2}{\left(1 + 2\tilde{a}/N \exp(\tilde{\kappa}\tilde{a}) + \tilde{a}/\tilde{R} \exp(-\tilde{\kappa}(\tilde{R} - \tilde{a}))\right)^2} \\ &+ \frac{(\alpha - 2)\tilde{a}^2 \exp(2\tilde{\kappa}\tilde{a} - \tilde{\kappa}\tilde{R})}{\alpha^2 N (1 + \tilde{a} \exp(\tilde{\kappa}\tilde{a})/\alpha N)^2} \frac{1 + \tilde{\kappa}\tilde{R}}{\tilde{R}^2} \left(-\frac{2\alpha(N + M)(\text{pH} - \text{pK}) \ln 10}{\left(1 + \frac{(\tilde{a}/\tilde{R}) \exp(-\tilde{\kappa}(\tilde{R} - \tilde{a}))}{(1 + 4\tilde{a} \exp(\tilde{\kappa}\tilde{a})/\alpha N)^2}\right)^2} \right. \\ &+ \left. \frac{4\alpha M(\alpha N - 1)(\text{pH} - \text{pK}) \ln 10 \left[\exp(-\tilde{\kappa}(\tilde{R} - \tilde{a}))/ (1 + (4\tilde{a}/\alpha N) \exp(\tilde{\kappa}\tilde{a})) \right]}{\left(1 - \frac{(\tilde{a}/\tilde{R})^2 \exp(-2\tilde{\kappa}(\tilde{R} - \tilde{a}))}{(1 + 4\tilde{a} \exp(\tilde{\kappa}\tilde{a})/\alpha N)^2}\right)^2} \right) \end{aligned}$$

Appendix D. Gaussian approximation

$$\begin{aligned}
& + \frac{(4\alpha M - 8) \left[1 + [(\tilde{a}/\tilde{R})^2 \exp(-2\tilde{\kappa}(\tilde{R} - \tilde{a})) / (1 + 4\tilde{a} \exp(\tilde{\kappa}\tilde{a})/\alpha N)^2] \right]}{\left(1 - \frac{(\tilde{a}/\tilde{R})^2 \exp(-2\tilde{\kappa}(\tilde{R} - \tilde{a}))}{(1 + 4\tilde{a} \exp(\tilde{\kappa}\tilde{a})/\alpha N)^2} \right)^2} \\
& - \frac{(\alpha - 2) \left(1 + \alpha \frac{M^2}{N^2} \right) (4N / [1 + (4\tilde{a} \exp(\tilde{\kappa}\tilde{a})/\alpha N)]) (\tilde{a}/\tilde{R}) \exp(-\tilde{\kappa}(\tilde{R} - \tilde{a}))}{\left(1 - \frac{(\tilde{a}/\tilde{R})^2 \exp(-2\tilde{\kappa}(\tilde{R} - \tilde{a}))}{(1 + 4\tilde{a} \exp(\tilde{\kappa}\tilde{a})/\alpha N)^2} \right)^2} \\
\tilde{F}_2 = & - \frac{1 + \tilde{\kappa}\tilde{R}}{\tilde{R}^3} \frac{\tilde{a}^2 \exp(-2\tilde{\kappa}(\tilde{R} - \tilde{a}))}{(1 + (4/\alpha)(\tilde{a}/N) \exp(\tilde{\kappa}\tilde{a}))^2 - (\tilde{a}^2/\tilde{R})^2 \exp(-2\tilde{\kappa}(\tilde{R} - \tilde{a}))}.
\end{aligned} \tag{D.4}$$

We note that the nomenclature “mean“ and “fluctuation“ do not have the same meaning in the context of the Gaussian approximation as they do in the saddle-point approximation. In fact in the former the interaction free energy can not be consistently separated into a mean and fluctuation types. We use this separation based on the dimensionless separation scaling.

Appendix E

Derivation of field propagator

$G_1(\varphi_1, \varphi_2)$

The propagator $G_1(\varphi_1, \varphi_2)$, describing how the electrostatic potential propagates from one macroion to another in the presence of a polyvalent ion q at \mathbf{r}_0 , is given as::

$$G_1(\varphi_1, \varphi_2) = \int \mathcal{D}[\varphi(\mathbf{r})] \delta(\varphi(\mathbf{r}_1) - \varphi_1) \delta(\varphi(\mathbf{r}_2) - \varphi_2) \exp\left(-\frac{1}{2} \int d\mathbf{r} d\mathbf{r}' \varphi(\mathbf{r}) G^{-1}(\mathbf{r}, \mathbf{r}') \varphi(\mathbf{r}') + i\beta \int_V \rho(\mathbf{r}) \varphi(\mathbf{r}) d\mathbf{r}\right), \quad (\text{E.1})$$

with $\rho = q\delta(\mathbf{r} - \mathbf{r}_0)$. The delta function entering the above expression can be written via a Fourier integral representation as:

$$\delta(\varphi(\mathbf{r}_i) - \varphi_i) = \int dk \exp\left(ik(\varphi(\mathbf{r}_i) - \varphi_i)\right) = \int dk \exp\left(-ik\varphi_i + ik \int d\mathbf{r} \rho_i(\mathbf{r}) \varphi(\mathbf{r})\right), \quad (\text{E.2})$$

where $\rho_i(\mathbf{r}) = \delta(\mathbf{r} - \mathbf{r}_i)$, $i = 1, 2$. One notes that this is an ordinary and not a functional Fourier integral representation, as the propagator is defined for two vertex points in the real space. Our strategy now will be to first evaluate the functional integral over the fluctuating electrostatic potential field $\varphi(\mathbf{r})$ and then calculate the remaining integral over the auxiliary fields stemming from the Fourier representation of the delta functions. Therefore it follows that

$$G_1(\varphi_1, \varphi_2) = \int dk \exp(-ik_1\varphi_1) \int dk' \exp(-ik_2\varphi_2) \int \mathcal{D}[\varphi(\mathbf{r})] \exp\left(-\frac{1}{2} \int d\mathbf{r} d\mathbf{r}' \varphi(\mathbf{r}) G_0^{-1}(\mathbf{r}, \mathbf{r}') \varphi(\mathbf{r}') + i \int [t(\mathbf{r}) + \beta q e_0 \delta(\mathbf{r} - \mathbf{r}_0)] \varphi(\mathbf{r}) d^3\mathbf{r}\right), \quad (\text{E.3})$$

with the field $t(\mathbf{r})$ denoting

$$t(\mathbf{r}) = k_1 \rho_1(\mathbf{r}) + k_2 \rho_2(\mathbf{r}).$$

The above integral is a general Gaussian functional integral for the fluctuating potential $\varphi(\mathbf{r})$ and can be evaluated explicitly and exactly. The result is then an ordinary Gaussian integral over the variables k_1 and k_2 .

One has in fact

$$\delta(\varphi(\mathbf{r}_1) - \varphi_1)\delta(\varphi(\mathbf{r}_2) - \varphi_2) = \int dk_1 \exp\left(ik_1(\varphi(\mathbf{r}_1) - \varphi_1)\right) \int dk_2 \exp\left(ik_2(\varphi(\mathbf{r}_2) - \varphi_2)\right), \quad (\text{E.4})$$

after which one can derive

$$\begin{aligned} G_1(\varphi_1, \varphi_2) &= \frac{1}{\det G_0^{-1}(\mathbf{r}, \mathbf{r}')} \int dk_1 \exp(-ik_1\varphi_1) \int dk_2 \exp(-ik_2\varphi_2) \\ &\exp\left(-\frac{1}{2} \int d\mathbf{r}\mathbf{r}' [t(\mathbf{r}) + \beta qe_0\delta(\mathbf{r} - \mathbf{r}_0)] G_0(\mathbf{r}, \mathbf{r}') [t(\mathbf{r}') + \beta qe_0\delta(\mathbf{r}' - \mathbf{r}_0)]\right) \\ &= \frac{1}{\det G_0^{-1}(\mathbf{r}, \mathbf{r}')} \int_{-\infty}^{+\infty} \int_{-\infty}^{+\infty} dk_1 dk_2 \exp(-ik_1\varphi_1 - ik_2\varphi_2) \\ &\times \exp\left(-\frac{1}{2}k_1^2 G_0(\mathbf{r}_1, \mathbf{r}_1) - \frac{1}{2}k_2^2 G_0(\mathbf{r}_2, \mathbf{r}_2) - k_1 k_2 G_0(\mathbf{r}_1, \mathbf{r}_2)\right) \\ &\times \exp\left(-\frac{1}{2}\beta^2 q^2 e_0^2 G_0(\mathbf{r}_0, \mathbf{r}_0) - \frac{1}{2}\beta qe_0 [2k_1 G_0(\mathbf{r}_0, \mathbf{r}_1) + 2k_2 G_0(\mathbf{r}_0, \mathbf{r}_2)]\right). \quad (\text{E.5}) \end{aligned}$$

The fluctuating electrostatics potential propagator has thus been reduced to simple integrals in the variable $\mathbf{k} = (k_1, k_2)$.

The vacuum fluctuations term, $\det u_{DH}^{-1/2}(\mathbf{r}, \mathbf{r}')$, as well as the polyvalent ion bare self-interaction term $\exp(-\frac{1}{2}\beta^2 q^2 e_0^2 u_{DH}(\mathbf{r}_0, \mathbf{r}_0))$, will be neglected since they do not depend on the separation between the point-like macroions and thus make no contribution to the interactions between them. If the macroions had finite dimensions $\det u_{DH}^{-1/2}(\mathbf{r}, \mathbf{r}')$ would describe the thermal Casimir (vdW) interactions between them.

If one introduces a 2D wave-vector \mathbf{k} , together with the Einstein summation convention, this integral can be rewritten simply as

$$G_1(\varphi_1, \varphi_2) = \iint d^2\mathbf{k} \exp(-f(\mathbf{k})), \quad (\text{E.6})$$

where we introduced the function $f(\mathbf{k})$ as

$$f(\mathbf{k}) = k_j [i\varphi_j + \beta qe_0 u_{DH}(\mathbf{r}_0, \mathbf{r}_j)] + \frac{1}{2} k_j u_{DH}(\mathbf{r}_j, \mathbf{r}_l) k_l. \quad (\text{E.7})$$

Since this is a Gaussian integral, it can be evaluated explicitly as

$$\begin{aligned} G_1(\varphi_1, \varphi_2) &= \det u_{DH}^{-1/2}(\mathbf{r}, \mathbf{r}') \\ &\exp\left(\frac{1}{2} [i\varphi_i + \beta qe_0 u_{DH}(\mathbf{r}_0, \mathbf{r}_i)] u_{DH}^{-1}(\mathbf{r}_i, \mathbf{r}_j) [i\varphi_j + \beta qe_0 u_{DH}(\mathbf{r}_0, \mathbf{r}_j)]\right). \quad (\text{E.8}) \end{aligned}$$

The above expressions typically involve the Coulomb or the DH self-interaction $u_{DH}(\mathbf{r}, \mathbf{r})$, or indeed its inverse. This quantity is not unambiguously defined because the field representation does not describe the sizes of the charges in a consistent description. However, one usually assumes that the finite size can be approximately included as an ultraviolet cutoff in the Fourier space, or indeed by assuming that one has the Coulomb self-energy $u_{DH}(\mathbf{r}, \mathbf{r}) \sim 1/4\pi\epsilon\epsilon_0 a$, where a is the radius of the charge; to be consistent one needs to take $\kappa a \rightarrow 0$ in the DH expression, which gives its bare Coulomb limit.

Appendix F

Saddle-point and Gaussian fluctuations of volume integral \mathcal{F}

We now approximate the free energy $\tilde{\mathcal{F}}_1$ by its saddle point and Gaussian fluctuations around the saddle point. This leads to the well known expression

$$\tilde{\mathcal{F}}_1 = \int_V d\mathbf{r}_0 \exp\left(-\mathcal{S}(\mathbf{r}_0)\right) \simeq \frac{\exp\left(-\mathcal{S}(\mathbf{a})\right)}{\sqrt{\det(\partial^2\mathcal{S}(\mathbf{r}=\mathbf{a})/\partial\mathbf{r}\partial\mathbf{r})}}, \quad (\text{F.1})$$

where the most probable position of the polyvalent ion $\mathbf{r}_0 = \mathbf{a}$ corresponds to the equilibrium configuration of zero ‘‘force’’ defined by

$$\nabla\mathcal{S}(\mathbf{a}) = \mathbf{0}. \quad (\text{F.2})$$

It then follows straightforwardly that the determinant of the Hessian is

$$\det \frac{\partial^2\mathcal{S}(\mathbf{r}=\mathbf{a})}{\partial\mathbf{r}\partial\mathbf{r}} = \frac{\partial^2\mathcal{S}(\mathbf{r}=\mathbf{a})}{\partial x^2} \frac{\partial^2\mathcal{S}(\mathbf{r}=\mathbf{a})}{\partial y^2} \frac{\partial^2\mathcal{S}(\mathbf{r}=\mathbf{a})}{\partial z^2}, \quad (\text{F.3})$$

where at the saddle point

$$\begin{aligned} \mathcal{S}(\mathbf{a}) = & \frac{4qN(\text{pH} - \text{p}K) \ln 10 l_B}{2 + Nl_B \exp(-\kappa a)/a[1 + a/R \exp(-\kappa(R - a))]} \frac{\exp(-\frac{1}{2}\kappa R)}{R} \\ & + \frac{1}{2} q^2 l_B^2 \frac{((l_B/a) \exp(-\kappa a) + 2/N) 8 \exp(-\kappa R)/R^2 - 8l_B \exp(-2\kappa R)/R^3}{\frac{4}{N^2} + \frac{4}{N} \frac{l_B}{a} \exp(-\kappa a) + \frac{l_B^2}{a^2} \exp(-2\kappa a)[1 - \frac{a^2}{R^2} \exp(-2\kappa(R - a))]}, \end{aligned} \quad (\text{F.4})$$

while the Hessian gives

$$\begin{aligned} \frac{\partial^2\mathcal{S}(\mathbf{r}=\mathbf{a})}{\partial x^2} = \frac{\partial^2\mathcal{S}(\mathbf{r}=\mathbf{a})}{\partial y^2} = & \frac{qN(\text{pH} - \text{p}K) \ln 10 l_B \left(-16 \frac{\exp(-\frac{1}{2}\kappa R)}{R^3} - 8 \frac{\exp(-\frac{1}{2}\kappa R)}{R^2} \right)}{2 + Nl_B \frac{\exp(-\kappa a)}{a} [1 + \frac{a}{R} \exp(-\kappa(R - a))]} \\ & + \frac{1}{2} q^2 l_B^2 \frac{\left(\frac{l_B \exp(-\kappa a)}{a} + \frac{2}{N} \right) \left(-64 \frac{\exp(-\kappa R)}{R^4} - 32 \frac{\kappa \exp(-\kappa R)}{R^3} \right)}{\frac{4}{N^2} + \frac{4}{N} \frac{l_B}{a} \exp(-\kappa a) + \frac{l_B^2}{a^2} \exp(-2\kappa a)[1 - \frac{a^2}{R^2} \exp(-2\kappa(R - a))]} \\ & + \frac{1}{2} q^2 l_B^2 \frac{64l_B \frac{\exp(-2\kappa R)}{R^5} + 32l_B \kappa \frac{\exp(-2\kappa R)}{R^4}}{\frac{4}{N^2} + \frac{4}{N} \frac{l_B}{a} \exp(-\kappa a) + \frac{l_B^2}{a^2} \exp(-2\kappa a)[1 - \frac{a^2}{R^2} \exp(-2\kappa(R - a))]}; \end{aligned} \quad (\text{F.5})$$

Appendix F. Saddle-point and Gaussian fluctuations of volume integral \mathcal{F}

$$\begin{aligned} \frac{\partial^2 \mathcal{S}(\mathbf{r} = \mathbf{a})}{\partial z^2} &= \frac{qN(\text{pH} - \text{pK}) \ln 10 l_B \left(32 \frac{\exp(-\frac{1}{2}\kappa R)}{R^3} + 16\kappa \frac{\exp(-\frac{1}{2}\kappa R)}{R^2} + 4\kappa^2 \frac{\exp(-\frac{1}{2}\kappa R)}{R} \right)}{2 + Nl_B \frac{\exp(-\kappa a)}{a} \left[1 + \frac{a}{R} \exp(-\kappa(R-a)) \right]} \\ &+ \frac{1}{2} q^2 l_B^2 \frac{\left(\frac{l_B \exp(-\kappa a)}{a} + \frac{2}{N} \right) \left(192 \frac{\exp(-\kappa R)}{R^4} + 128 \frac{\kappa \exp(-\kappa R)}{R^3} + 32 \frac{\kappa^2 \exp(-\kappa R)}{R^2} \right) - 64 l_B \frac{\exp(-2\kappa R)}{R^5}}{\frac{4}{N^2} + \frac{4}{N} \frac{l_B}{a} \exp(-\kappa a) + \frac{l_B^2}{a^2} \exp(-2\kappa a) \left[1 - \frac{a^2}{R^2} \exp(-2\kappa(R-a)) \right]}. \end{aligned} \quad (\text{F.6})$$

This finally leads to the expression

$$-\ln \tilde{\mathcal{F}}_1(R) \simeq \mathcal{S}(\mathbf{r}_0 = \mathbf{a}) + \frac{1}{2} \ln \det \frac{\partial^2 \mathcal{S}(\mathbf{r} = \mathbf{a})}{\partial \mathbf{r} \partial \mathbf{r}}. \quad (\text{F.7})$$

Appendix G

Self energy of polyvalent ion

In Eq. (6.43), it is stated that the following form

$$W_{self} = q^2 \int \tilde{Q} d\tilde{Q} \frac{[J_0(Q\rho_0)]^2}{\tilde{p}}, \quad (\text{G.1})$$

corresponds exactly to the polyvalent ion self-energy $W_{self} = q^2/\kappa$. To prove that, we start from the expression for DH interaction energy of two flat plates in a 1:1 salt solution. In Q representation it is:

$$\int Q dQ J_0(Q\rho) \frac{\exp\left(-\sqrt{Q^2 + \kappa^2}z\right)}{\sqrt{Q^2 + \kappa^2}} = \frac{\exp\left(-\kappa\sqrt{\rho^2 + z^2}\right)}{\sqrt{\rho^2 + z^2}}. \quad (\text{G.2})$$

If one sets $z = 0$ one get identity:

$$\int Q dQ \frac{J_0(Q\rho)}{\sqrt{Q^2 + \kappa^2}} = \frac{\exp(-\kappa\rho)}{\rho}, \quad (\text{G.3})$$

which is going to be used further on in derivation. To continue, we use the identity from Ref. [142]:

$$J_0^2(x) = \frac{1}{\pi} \int_0^\pi J_0(2x \sin(Q)) dQ. \quad (\text{G.4})$$

With this two equalities, Eqs. (G.3) and (G.4), one can write:

$$\begin{aligned} \int Q dQ \frac{[J_0(Q\rho)]^2}{\sqrt{Q^2 + \kappa^2}} &= \\ \int_0^\pi dQ \int_0^\infty Q dQ \frac{J_0(2Q\rho \sin(Q))}{\sqrt{Q^2 + \kappa^2}} &= \frac{1}{\pi} \int_0^\pi dQ \frac{\exp(-2\kappa\rho \sin(Q))}{2\rho \sin(Q)} = F(\rho, \kappa). \end{aligned} \quad (\text{G.5})$$

Let's take now the derivative over κ :

$$\frac{\partial F}{\partial \kappa} = -\frac{1}{\pi} \int_0^\pi dQ \frac{2\rho \sin(Q) \exp(-2\kappa\rho \sin(Q))}{2\rho \sin(Q)} = -\frac{1}{\pi} \int_0^\pi dQ \exp(-2\kappa\rho \sin(Q)). \quad (\text{G.6})$$

Introducing a function

$$I_0(z) = \frac{1}{\pi} \int_0^\pi dQ \exp(-z \cos(Q)), \quad (\text{G.7})$$

Appendix G. Self energy of polyvalent ion

so that it becomes:

$$\frac{\partial F}{\partial \kappa} \sim I_0(2\kappa\rho). \quad (\text{G.8})$$

Since this expression corresponds to the self-energy of an isolated ion, with the bounding walls removed to infinity, it should not depend on its position and we can simply take $\rho \rightarrow 0$, so that one obtains:

$$F_{\rho \rightarrow 0} = \int_0^\kappa I_0(2\kappa\rho) d\kappa \sim \kappa, \quad (\text{G.9})$$

which is then the final expression for the self-energy of the ion.

One should note here that this convoluted route to the subtraction of the self-energy in Eq. (6.43) is basically due to the introduction of the Fourier–Bessel transform that assumes a delta function distribution for the ion charge in the z -direction. In the infinite space, on the other hand, it is clear that the Fourier transform would lead to exactly the same expression in the limit of a finite but small size of the ion.

Razširjeni povzetek

H.1 Uvod

Elektrostatične interakcije igrajo pomembno vlogo pri procesih v bioloških sistemih na molekularnem nivoju ter določajo obnašanje mehke snovi. Tako biološki sistemi kot mehka snov so tipično sestavljeni iz makromolekul kot so polimeri, koloidi, proteini, itd. Te makromolekule običajno pridobijo naboj, ko se nahajajo v polarni raztopini, kot je denimo voda. Do tega pride zahvaljujoč disociaciji kemijskih skupin na površinah makromolekul, ki sproščajo mobilne ione v raztopino. Druga možnost za pridobitev naboja je adsorpcija majhnih nabitih molekul ali ionov soli, ki se fizično ali kemijsko vežejo na površino makromolekul in jim s tem prinesejo efektivni površinski naboj. V raztopini soli je posamezna makromolekula obdana z oblakom nevtralizirajočih, nasprotno nabitih ionov, ki jih imenujemo *protiioni*, ter tudi z ioni enakega predznaka – *koioni*. Za razumevanje obnašanja makromolekul je tako potrebno razumeti predvsem obnašanje ionskih oblakov s katerim so obkrožene.

Teoretični opis takšnih večdelčnih Coulombskih sistemov se je pričel v prejšnjem stoletju, ko sta Louis Georges Gouy in David Leonard Chapman definirala *problem dvojne plasti*, ki se nanaša na porazdelitev protiionov blizu nabite ravne površine [11, 12]. Z nadaljevanjem Petra Debyeja in Ericha Hückla [13] je prišlo do razvoja znane DLVO teorije (Boris Derjaguin, Lev Landau, Evert Verwey, and Theodoor Overbeek) [15, 16], ki je uspešno opisala stabilnost koloidov s kombinacijo Poisson-Boltzmannovega elektrostatičnega odboja in van der Waalsovega privlaka. Temelječ na uporabi teorije povprečnega polja, ki zanemari ionske korelacije, pa teorije dvajsetega stoletja vseeno niso zmogle opisati močno koreliranih sistemov, kot je denimo makroion v raztopini polivalentne soli.

Simulacije in eksperimenti so pokazali, da lahko prisotnost polivalentnih protiionov privede do privlaka med enako nabitimi površinami [18, 19]. Slaven primer tega je denimo kondenzacija DNK [38, 39, 40]. Kot nenehen teoretični izziv so ti pojavi morali počakati na razvoj modernih teorij coulombskih tekočin, ki temelje na izpeljavi statistične vsote kot tudi funkcionalnega integrala fluktuirajočega elektrostatičnega polja [20]. Rudolf Podgornik in Boštjan Žekš sta pokazala, da pristop razvoja teorije polja v sedelni točki ustreza Poisson-Boltzmannovi enačbi [21]. To je utrla pot k posplošitvi teorij, ki obravnavajo več pojavov iz elektrostatike koloidov in hkrati podajo ustrezen teoretični opis eksotičnega privlaka med enako nabitimi delci. Teorije polja so pokazale, da v primeru velikih nabojev prevladujejo enodelčni prispevki, ki so poglavitni člen opisa v *limiti močne sklopitve* [24, 29, 77, 83, 84], medtem ko po drugi strani v *limiti šibke interakcije* prevlada teorija poprečnega polja. Ali Naji, Matej Kanduč in Rudolf Podgornik sta razvila ustrezen teoretični opis te dihotomije, ki je hkrati pokrila tudi asimetrične ionske raztopine s teorijo odetih ionov [10], in na ta način prispevala k fundamentalnemu razumevanju coulomb-

skih tekočin.

Kljub temu koraku so moderne teorije ostale omejene na ozek del parametrskega prostora, kjer se naboj na površini makromolekul obravnava kot stalen. Na ta način te teorije ne morejo opisati sistemov s fluktuirajočim nabojem, kot so na primer proteini. Proteini namreč izkazujejo nenavadno obnašanje, ki se ga ne da zaobjeti v znanih teoretičnih opisih. Iskanje ustrezne teorije, ki bi opisala ta zapleteni ples proteinov, je bila zato moja glavna motivacija pri nastanku pričujoče disertacije.

H.1.1 Proteini, regulacija naboja in interakcija Kirkwood-Shumakerja

Proteini so makromolekule, sestavljene iz aminokislin, ki svojo biološko funkcijo (kot so replikacija DNK, kataliza metabolnih reakcij, celično signaliziranje, imunski odziv, ipd.) najpogosteje opravljajo v kompaktni kvartarni strukturi. V tej strukturi, vódeni z elektrostatičnimi interakcijami, lahko tvorijo proteinske komplekse, kot so proteasom, DNK/RNK polimeraze, virusne kapside, ... Za razumevanje vseh teh pojavov je najbolj pomembno razumeti elektrostatiko, ki določa zapleteno obnašanje proteinov. To, kar proteine uvršča v posebno skupino eksotičnih delcev, katerih obnašanja se ne da opisati s standardnimi teorijami coulombskih tekočin, je njihova kompleksna struktura, ki vodi do spremenljivega naboja na njihovih površinah. Proteini so namreč amfoterične molekule zahvaljujoč aminokislinam iz katerih so sestavljeni. Vsaka aminokislina vsebuje poleg spremenljive stranske verige (ki določa vrsto aminokislina) tudi karboksilno skupino $-\text{COOH}$, ki se obnaša kot kislina (lahko donira proton raztopini), ter amino skupino $-\text{NH}_2$, ki se obnaša kot baza (lahko sprejme proton iz raztopine). Ko se protein nahaja v raztopini, naboj na njegovi površini fluktuirava z avoljo sledečih procesov:

- deprotonizacija karboksilne skupine na stranski verigi asparaginske in glutaminske kisline, $\text{RCOOH} \longrightarrow \text{RCOO}^- + \text{H}^+$;
- deprotonizacija hidroksilne skupine v fenilni skupini tirozina, $\text{ROH} \longrightarrow \text{RO}^- + \text{H}^+$;
- protonizacija amino skupine arginina in lizina, $\text{RNH}_2^+ \longrightarrow \text{RNH} + \text{H}^+$ in $\text{RNH}_3^+ \longrightarrow \text{RNH}_2 + \text{H}^+$;
- sekundarna amino skupina histidina lahko prav tako prispeva naboj, $\text{RNH}_2^+ \longrightarrow \text{RNH} + \text{H}^+$;
- končne skupine: deprotonacija karboksilne skupine, $\text{RCOOH} \longrightarrow \text{RCOO}^- + \text{H}^+$, in protonacija α -amino skupine, $\text{RNH}_2 + \text{H}^+ \longrightarrow \text{RNH}_3^+$;
- tudi cistein lahko prispeva k naboju proteina, saj je njegova stranska veriga tiol šibka kislina, vendar ga običajno ne upoštevamo, ker stranska veriga tvori disulfidne vezi.

Zaradi protonizacije in deprotonizacije je naboj proteina odvisen predvsem od pH vrednosti raztopine in je lahko pozitiven ali negativen. Vrednost pH pri kateri je

protein elektronevtralen se imenuje *izoelektrična točka*. Sprememba pogojev v raztopini tako privede do spremembe naboja na proteinu; ta pojav se imenuje *regulacija naboja*. Kljub temu, da je Linderström-Lang uvedel ta koncept že pred stotimi leti [89], moderne teorije ne upoštevajo regulacije naboja v svoji formulaciji in tako izvzemajo proteine iz svojega okvira obravnave. Na ta način eksotični elektrostatični pojavi, kot je privlak med elektronevtralnima proteinoma, ostanejo brez ustrezne razlage.

Pred petdesetimi leti sta Kirkwood in Shumaker prva prišla do tega pojava v okviru klasične teorije statistične mehanike na nivoju preprostega perturbacijskega razvoja [64, 65]. Brez upoštevanja regulacije naboja sta preučevala dva sferična proteina s predpostavko, da ima en protein ν_1 skupin intrinzičnega naboja e_i , drugi pa ν_2 skupin intrinzičnega naboja e_k . Tako je naboj na vsakem proteinu enak:

$$\begin{aligned} q_i^{(1)} &= e_i^{(1)} + e_0 x_i^{(1)}, \\ q_k^{(2)} &= e_k^{(2)} + e_0 x_k^{(2)}, \end{aligned} \quad (1)$$

in sicer lahko fluktuirata ter interagira elektrostatično kot

$$V = \sum_{i=1}^{\nu_1} \sum_{k=1}^{\nu_2} \frac{q_i^{(1)} q_k^{(2)}}{\epsilon R_{ik}^{(12)}}. \quad (2)$$

Perturbacijski razvoj da neničelni prispevek v točki ničelnega naboja proteinov ($\langle q^{(1)} \rangle = \langle q^{(2)} \rangle = 0$) v obliki:

$$W^{(11)}(R) = -\frac{\langle \Delta q^{(1)2} \rangle \langle \Delta q^{(2)2} \rangle}{2\epsilon^2 R^2 k_B T} \neq \frac{1}{R^6}. \quad (3)$$

Tako imenovana Kirkwood–Shumakerjeva (KS) interakcija ima drugačno obnašanje od van der Waalsove interakcije, ki je tipična za elektronevtralna telesa. Kirkwood–Shumakerjeva interakcija ni univerzalna in obstaja samo v sistemih s fluktuirajočim nabojem, skalira pa z nižjo obratno potenco razdalje, tako da je daljšega dosega od van der Waalsove interakcije.

Teorija Kirkwooda in Shumakerja je bila kasneje potrjena z eksperimenti in simulacijami, vendar je bilo fundamentalno razumevanje teh pojavov še vedno pomanjkljivo. Glavni cilj moje disertacije je predstaviti splošen teoretični okvir, v katerem je možno opisati pojave, ki nastopijo kot posledica regulacije naboja, in na ta način teoretično zajema vso zapleteno koreografijo, ki nam jo predstavljajo proteini plešoč po glasbi ionske raztopine v biološki snovi.

H.2 Interakcije površin reguliranega naboja v prisotnosti protiionov

Razumevanje pojava regulacije naboja je ključnega pomena za opis obnašanja proteinov. Kljub temu, da je ta tema področje raziskovanja že eno stoletje [59, 67, 68, 89, 93, 94, 95, 96, 97, 98, 99, 100], ostaja izziv njena vključitev v splošen teoretični okvir zajemajoč interakcijo med proteini pri različnih pogojih. Zato v delu začnem z najbolj preprostim modelom, ki ohranja najpomembnejše lastnosti regulacije naboja, in sicer s študijo interakcij posredovanih preko protiionov, ki se nahajajo med dvema

ravnima vzporednima površinama z enakomerno porazdelitvijo adsorbirajočih točk. Enovalentni protiioni se nahajajo v vodi in so posledica disociacije na površini plošč. Voda je opisana z dielektrično konstanto ϵ , medtem ko je prostor za ploščama opisan z dielektrično konstanto ϵ' , tako da sistem vsebuje dielektrični skok, ki je tipičen za biološke sisteme, kjer imamo običajno makromolekule z dielektrično konstanto $\epsilon' \sim 2-5$ in vodo z $\epsilon = 80$ pri sobni temperaturi. Obstoj dielektrične nehomogenosti lahko privede do sil med ionskimi slikami [31]. Problem bomo obravnavali v sistemu z dielektričnim skokom, pa tudi v primeru, ko sta dielektrični konstanti enaki, tako da bomo dobili določen občutek o vseh vrstah interakcij, ki lahko vplivajo na obnašanje sistema. Ideja je formulirati ustrezen teoretičen okvir, ki uporablja orodja iz teorije polja in s tem dovoljuje posplošitev na bolj komplicirane sisteme.

S formulacijo ustrezne statistične vsote kot funkcionalnega integrala elektrostatičnega potenciala smo dobili znano obliko, izpeljano za coulombske tekočine [21, 31], s prepoznavnim volumskim členom ter površinskim členom, ki potrebuje ustrezno posplošitev, da bi lahko opisal disociacijo na površini plošč. Do tega smo dospeli s predpostavko, da namesto linearne sklopitve površinskega naboja z elektrostatičnim potencialom mora biti le-ta nelinearna funkcija potenciala, oziroma ima obliko sledečega nastavka za površinski del:

$$i \oint \sigma_0 \varphi(\mathbf{r}) d^2 \mathbf{r} \longrightarrow \oint f(\varphi(\mathbf{r})) d^2 \mathbf{r}, \quad (4)$$

kjer je $f(\varphi(\mathbf{r}))$ splošna nelinearna funkcija lokalnega potenciala. Točna oblika površinske energije ni univerzalna, ampak je odvisna od uporabljenega modela za interakcijo med površino in ioni [117, 118]. Tukaj obravnavamo 'lattice-gas' model, ki sta ga v različnih kontekstih uvedla Fleck in Netz [119]. Naša površinska energija dobi naslednjo obliko:

$$f(\varphi(\mathbf{r})) = i\sigma_0 \varphi(\mathbf{r}) - k_B T \frac{|\sigma_0|}{e_0} \ln \left(1 + \exp \left(\beta \mu_S + i\beta e_0 \varphi(\mathbf{r}) \right) \right), \quad (5)$$

kjer je μ_S energija disociacije. V argumentu logaritma je moč prepoznati vsoto za sistem nenabitega osnovnega stanja ter nabitega stanja z efektivno energijo $\beta \mu_S + i\beta e_0 \varphi(\mathbf{r})$. V limiti $\beta \mu_S \rightarrow \infty$ so adsorpcijske točke povsem nedisociirane, površini sta nenabiti in ni prispevkov k površinski energiji. V nasprotni limiti $\beta \mu_S \rightarrow -\infty$ sta površini popolnoma disociirani in sistem se nahaja v režimu fiksnega naboja $f(\varphi(\mathbf{r})) = i\sigma_0 \varphi(\mathbf{r})$.

Vsota celotnega sistema je obravnavana v limiti šibke sklopitve, kjer smo na nivoju poprečnega polja dobili Poisson–Boltzmannovo enačbo z robnim pogojem, ki točno ustreza Ninham–Parsegianovemu modelu regulacije naboja [59]. Limita poprečnega polja da ravnovesno porazdelitev protiionov, ki ustreza minimumu celotne volumske in površinske vsote. Pri odmiku iz povprečnega polja smo izračunali prvi popravek v obliki Gaussovih fluktuacij in to je bil glavni izziv, saj smo pričakovali, da bo eksotična elektrostatika skrita v popravkih na več zankah. Zaradi neenakomerne porazdelitve protiionov v povprečnem polju, je bil to tudi zahteven matematični izziv. To je uspelo izračunati tako, da smo pridobljene popotne integrale obravnavali analogno Feynmanovemu propagatorju polja za harmonski oscilator s časovno odvisno frekvenco, in tako uspeli dobiti analitični in eksaktni prvi popravek k rezultatom povprečnega polja.

Izkaže se, da energija povprečnega polja privede do odboja med enako nabitimi površinami. Vendar je ta odboj odvisen od kemijske energije disociacije, tako

da lahko gre proti nič v primeru popolnoma adsorbiranih protiionov, ko površini postaneta elektronevtralni. V tem primeru privlak, ki se dobi kot prvi popravek, postane dominanten, tako da je celokupna interakcija privlačna. V primeru sistema s fiksnim nabojem je prvi popravek vedno subdominanten v primerjavi z rezultati v povprečnem polju. Na tem primeru vidimo, da ima regulacija naboja nezanemarljiv vpliv na odboj v povprečnem polju ter vpliva na privlak v prvem popravku. Poleg tega je izpeljana oblika fluktuacijskega privlaka splošen opis termalno-fluktuacijskih prispevkov, kjer sta van der Waalsov privlak in Kirkwood–Shumakerjeva interakcija neposredno vpeljana kot sklopljena prispevka, ki se lahko razklopita samo v primeru določene limite. Van der Waalsov privlak se tako dobi v limiti ničte koncentracije protiionov, medtem ko se Kirkwood–Shumakerjeva interakcija dobi v limiti ničtega dielektričnega skoka.

Izpeljana teorija omogoča predvsem posplošen okvir, v katerem je moč obravnavati širok spekter lastnosti coulombskih tekočin. Ena izmed novosti, ki je posledica nelinearne površinske energije, je neničelna kapacitivnost. Dosedanje moderne teorije coulombskih elektrolitov so obravnavale sisteme, kjer je kapacitivnost makromolekule enaka nič, kar je posledica približka fiksnega naboja. V našem primeru je površinska kapacitivnost odvisna od rešitve v povprečnem polju ter vpliva na rezultate fluktuacijskega privlaka. Zaradi tega so dobljeni rezultati predvsem različni od standardnega DLVO opisa, kjer van der Waalsov privlak nikoli ni bil odvisen od rešitve v približku povprečnega polja [66].

EkspONENT skaliranja fluktuacijskega tlaka kot funkcije razdalje med površinami ima približno vrednost okrog -3 v režimu, ki ustreza površini s fiksnim nabojem v raztopini protiionov; tam fluktuacijski tlak skalira točno po zakonu $\sim \log D \times D^{-3}$ [10]. Točna vrednost eksponenta skaliranja v primeru regulacije naboja zavisi od površinsko-interakcijskega parametra b . V prisotnosti dielektričnega skoka sta monopolni Kirkwood–Shumakerjev prispevek in dipolni van der Waalsov prispevek sklopljena skupaj v fluktuacijskem tlaku. Če je sistem dielektrično homogen, $\Delta \neq 0$, lahko določimo asimptotsko obliko skaliranja Kirkwood–Shumakerjevega prispevka. V limiti majhnih razdalj gre ta eksponent proti -1 , kot se pričakuje od Kirkwood–Shumakerjeve interakcije. Za večje razdalje gre eksponent proti večjim vrednostim, vendar ne pride do -3 , kot se zgodi v primeru sistema s fiksnim nabojem.

Da dobimo občutek o moči privlačnega prispevka, primerjamo izpeljan fluktuacijski tlak s standardnim van der Waalsovimi interakcijskim tlakom, $p_{vdW} = -H(\Delta)/12\pi D^3$ [66], kjer je $H(\Delta)$ Hamakerjev koeficient, za katerega vzamemo vrednost 4.3 zJ [125]. V primeru velike dielektrične nehomogenosti ($\Delta = 0.95$), razdalje med ploščami $D = 1 \text{ nm}$ ter površinskega naboja gostote $\sigma_0 = 0.5 \text{ e}_0/\text{nm}^2$, dobimo naslednje vrednosti za tlake: van der Waals $p_{vdW} = -1.1 \text{ bar}$, fluktuacijski tlak v primeru elektronevtralnih površin $p_{b=100} = -1.3 \text{ bar}$ ter fluktuacijski privlak v primeru maksimalne nabitosti površin $p_{b=0} = -0.8 \text{ bar}$. Kot je razvidno, so za izbrani nabor parametrov tlaki primerljivi z van der Waalsovo interakcijo.

Za zaključek je potrebno omeniti, da naša metodologija jasno pokaže monopolno naravo interakcije, ki nastane kot posledica regulacije naboja, in jo jasno razlikuje od van der Waalrove dipolne fluktuacijske interakcije. Izpeljana oblika fluktuacijske interakcije pokaže tudi, da te dve interakciji nista aditivni, ampak sta fundamentalno spojeni skupaj, tako da se lahko razklopita samo v ekstremnih limitah, ki sta bodisi primer ničelnega dielektričnega skoka, bodisi primer ničelne površinske kapacitivnosti. Bolj specifične napovedi, ki se nanašajo na disociabilne molekulske

skupine pri proteinih, so možne pri študiju modelov, ki vključujejo vpliv interventne soli v sistemih z regulacijo naboja. To bo tema naslednjih poglavij.

H.3 Interakcije točkastih makroionov reguliranega naboja v prisotnosti monovalentne soli

Sistem vzporednih ravnih površin v raztopini protiionov je služil kot dober model za postavitev ustreznega teoretičnega okvira za študiranje pojava regulacije naboja. Zdaj se bomo osredotočili na vpliv soli na ta pojav in tako zajeli tudi pogoje, ki so bolj podobni biološkim, kjer imamo ponavadi raztopine s tipično koncentracijo monovalentne soli od 0.1 M in več, kot je primer za fiziološke raztopine.

Obravnali smo model dveh titracijskih sferičnih makroionov v raztopini monovalentne soli. Naboj na površini ni konstanten, ampak je opisan z preprosto energijo disociacije, ki ustreza Nihnam–Parsegianovemu modelu, ki smo ga uvedli v prejšnjem poglavju, in sicer:

$$f_0(\varphi(\mathbf{r})) = i\sigma_0\varphi(\mathbf{r}) - \alpha k_B T \frac{\sigma_0}{e_0} \ln(1 + b \exp(i\beta e_0\varphi(\mathbf{r}))), \quad (6)$$

kjer α določa število disociabilnih mest, kemijska energija disociacije μ je vpeljana kot $\ln b = -(\text{pH} - \text{p}K) \ln 10 = \beta\mu_S$, kjer je $\text{p}K$ disociacijska konstanta. Tu je $\varphi(\mathbf{r})$ lokalni fluktuacijski potencial, ki ga je potrebno integrirati iz enačbe, da bi dobili končno površinsko vsoto. Poisson–Boltzmannov (PB) približek povprečnega polja se dobi tako, da prepoznamo $\varphi(\mathbf{r}) \rightarrow i\phi = i\phi_{\text{PB}}$ [126]. Celotna prosta energija disociacije sferičnega makroiona s polmerom a_0 je dovolj majhna, da lahko predpostavimo enakomeren elektrostatični potencial na površini, $\varphi(|\mathbf{r}| = a_0) = \varphi$, tako da lahko zapišemo

$$\begin{aligned} f(\varphi) &= \oint_S f_0(\varphi(\mathbf{r})) d^2\mathbf{r} \rightarrow \\ &\rightarrow iNe_0\varphi - \alpha k_B TN \ln(1 + b \exp(i\beta e_0\varphi)), \end{aligned} \quad (7)$$

kjer je N število adsorpcijskih mest, ki zadosti enačbo $\int dS\sigma_0 = Ne_0$, $\alpha > 1$ je koeficient asimetrije, ki določa širino intervala v katerem fluktuirajo efektivni naboj delca $e(\phi)$ kot funkcija elektrostatičnega potenciala povprečnega polja na njegovi površini, $\phi = \phi(a_0)$:

$$\begin{aligned} e(\phi = \phi(a_0)) &= \frac{\partial f(\phi)}{\partial \phi} \\ &= e_0 N \left(\left(\frac{\alpha}{2} - 1 \right) - \frac{\alpha}{2} \tanh \left(-\frac{1}{2} [\ln b - \beta e_0 \phi] \right) \right). \end{aligned} \quad (8)$$

Efektivni naboj makroiona tako fluktuirajo v intervalu $-Ne_0 < e < (\alpha - 1)Ne_0$, $\alpha > 1$. V primeru $\alpha = 2$ je interval v katerem naboj fluktuirajo simetričen $[-Ne_0, Ne_0]$. Podani izrazi za regulacijo naboja so ekvivalentni 'lattice-gas' modelu z variabilnim številom disociacijskih mest. Ti izrazi bodo uporabljeni v izpeljavi celotne statistične vsote. Poudariti je treba, da ta oblika preproste površinske energije temelji na približku majhnih makroionov, tako da površinski potencial ni funkcija kotnih spremenljivk, ampak velja $f(\varphi) = \oint_{|\mathbf{r}|=a_0} f_0(\varphi(\mathbf{r})) d^2\mathbf{r}$.

Ko fiksiramo fluktuacijski potencial na enem makroionu kot $\phi_1(a) = \varphi_1$ ter na drugem kot $\phi_2(a) = \varphi_2$, oba makroiona pa se nahajata v točkah z vektorjema \mathbf{r}_1 in \mathbf{r}_2 , lahko izpeljemo propagator polja v Debye–Hücklovi limiti, ki opiše dinamiko elektrostatičnega polja med enim in drugim makroionom. Z upoštevanjem površinskih prispevkov na eksaktni ravni lahko izpeljemo statistično vsoto kot funkcional vseh možnih vrednosti fluktuacijskega potenciala na makroionih φ_1 in φ_2 .

Tako smo izpeljali teorijo, ki temelji na dveh približkih: prvič, makroione obravnavamo kot točkaste (porazdelitev elektrostatičnega potenciala na površini je uniformna), in drugič, obdajajoča raztopina je obravnavana na Debye–Hücklovem nivoju (potencial v raztopini soli je dovolj majhen, da lahko Poisson–Boltzmannovo enačbo lineariziramo). Upoštevajoč različne vrednosti parametra asimetrije α smo obravnavali tri primere: simetrični sistem, sestavljen iz dveh identičnih makroionov z nabojem, ki fluktuirata v simetričnem intervalu; semi-simetričen sistem, pri katerem naboj fluktuirata v asimetričnem intervalu; ter asimetrični sistem, sestavljen iz dveh nasprotno nabitih makroionov.

Izkaže se, da regulacija naboja privede do privlaka med makroioni tako v simetričnem kot v semi-simetričnem sistemu, in sicer za vrednost pH raztopine, kjer makroiona dosežeta točko ničelnega naboja. Teorija je pokazala, da je ta privlak posledica asimetrične fluktuacije naboja v režimu nevtralizacije naboja. Privlak je opažen tudi v asimetričnem sistemu v primeru, ko je en makroion nabit, nabitost drugega pa izgine. Pokazali smo tudi, da je privlak posledica sklopitve fluktuacije naboja na enem ter celotnega naboja na drugem makroionu. Rezultati so dobljeni numerično z izračunom izpeljane particijske vsote. Z Gaussovimi približkom za binomski koeficient pri opisu disociacije na površini makroionov dobimo analitično interakcijsko prosto energijo kot vsoto dveh prispevkov. Prvi opisuje odboj med enako nabitimi makroioni in je odvisen od pH raztopine, tako da izgine v točki ničelnega naboja. Takrat postane dominanten drugi člen, ki podaja fluktuacijski privlak. Izkaže se, da ta privlačni člen v približni analitični obliki točno ustreza originalnemu Kirkwood–Shumakerjevemu rezultatu.

Parametri obdajajoče raztopine, kot sta pH ter koncentracija soli, tako igrajo pomembno vlogo v sistemih z reguliranim nabojem in pri interakcijah delujočih v teh sistemih. V vseh obravnavanih primerih je fluktuacijski privlak manjši v raztopinah z večjo koncentracijo monovalentne soli, zmanjšan pa je tudi odboj med enako nabitimi makroioni. To je skladno z učinkom senčenja. Večji privlak je opažen v sistemih z večjim številom adsorpcijskih mest, kar povzroča močnejše fluktuacije naboja.

Teorijo, izpeljano na tem modelu smo na to uporabili na sistemu makroionov, ki so bolj podobni proteinom. To smo naredili tako, da smo v površinski energiji disociacije upoštevali disociacijske konstante za nabite aminokisliline, ki prinesejo naboj proteinu: Z analizo dveh simetričnih sistemov, različnih v izbiri aminokislin,

	ASP	GLU	TYR	ARG	HIS	LYS	CYS
pK	3.71	4.15	10.10	12.10	6.04	10.67	8.14

Table H.1: Vrednosti pK aminokislinskih funkcionalnih skupin v razredčeni raztopini [57].

smo prišli do rezultata, ki nam pove, da privlak v točki ničelnega naboja ni odvisen

zgolj od števila adesorpcijskih mest, ampak tudi od kapacitete makroiona. Kakor sta pokazala Mikael Lund in Bo Jönsson [60], se kapaciteta makroiona lahko zapiše kot

$$\langle(\tilde{e} - \langle\tilde{e}\rangle)^2\rangle \sim \mathcal{C} = \frac{\partial\tilde{e}(\phi)}{\partial(\beta e_0\phi)} = -\frac{1}{\ln 10} \frac{\partial\tilde{e}(\phi)}{\partial\text{pH}}. \quad (9)$$

Če je sprememba predznaka naboja kot funkcija pH raztopine dovolj počasna, da se ustvari plato konstantnega naboja, to ustreza ničelni kapacitivnosti, ki ima za posledico, da privlak v točki ničelnega naboja izgine. Pojav, da je kapaciteta specifična za vsak protein ter da je privlak premo sorazmeren kapaciteti, je bil tako eksperimentalno opažen kot tudi potrjen s simulacijami [69]. Zdaj smo dobili tudi ustrezeni pionirski teoretični opis, na katerem lahko gradimo nadaljnje raziskovanje interakcij med proteini.

H.4 Interakcije točkastih makroionov reguliranega naboja v prisotnosti polivalentne soli

Sedaj se bomo osredotočili na problem interakcij, ki jih posredujejo polivalentni ioni. Eksperimenti so pokazali, da prisotnost polivalentnih protiionov privede do dodatnega privlaka, tako med enako nabitimi makromolekuli kot med makromolekulami reguliranega naboja v točki ničelnega naboja [133]. Kljub temu, da imajo v bioloških sistemih multivalentni ioni pomembno vlogo (denimo pri kondenzaciji semifleksibilnih biopolimerov [34, 35]), predstavlja ta problem poseben izziv, saj pred tem ni obstajal noben teoretičen opis, ki bi napovedal obnašanje sistema reguliranih nabojev v prisotnosti polivalentnih ionov.

Ob prisotnosti polivalentnih ionov v sistemu se šibka sklopitve zlomi, obstoj Kirkwood–Shumakerjeve interakcije pa postane dvomljiv. Vendar obstaja teorija, t.i. *teorija odetih ionov* [34, 35], ki temelji na asimetrični obravnavi različnih komponent sistema, ki jo bomo tu posplošili, tako da bo zajela tudi sisteme s spremenljivim nabojem. Bistvo teorije oblečenih ionov je uporaba Debye Hückel pristopa šibke sklopitve za opis monovalentne soli, medtem ko se za multivalentno sol uporabi pristop močne sklopitve. Na ta način dobimo odeto efektivno interakcijo med polivalentnimi ioni.

Za model smo izbrali dva majhna sferična makroiona v raztopini monovalentne soli ter polivalentne soli nizke koncentracije. Fluktuacija naboja na površini makroionov je opisana z enako površinsko prosto energijo kot v prejšnjem primeru, en. (7), ki je veljavna v približku točkastih makroionov. Analogno teoriji oblečenih ionov smo izpeljali ustrezno teorijo veljavno za pojave regulacije naboja. Prvi člen v tem virialnem razvoju ustreza direktni interakciji med titracijskima makroionoma v raztopini monovalentne soli, medtem ko je prvi popravek k temu prispevek polivalentnih ionov.

Izpeljana teorija pokaže, da prisotnost polivalentnih ionov privede do privlačnega prispevka v celotni prosti energiji. V primeru, ko so makroion in polivalentni ioni nasprotno nabiti, je ta privlak dovolj velik, da premaga odboj med enako nabitimi makroioni. To se zgodi, ker so nasprotno nabiti delci močno sklopljeni, tako da se znak takšnega sklopitvenega kompleksa spremeni. Ta fenomen je eksperimentalno opažen v primeru silikonskih delcev z reguliranim nabojem [133]. V nasprotnem primeru, ko so makroion in polivalentni ioni enako nabiti, ta privlačni prispevek

ni dovolj močan, da bi premagal odboj. Dominanten postane zgolj na velikih razdaljah, ko odboj oslabi ter postanejo asimetrične fluktuacije naboja na površini makroionov opazne. Eksperimenti so pokazali, da interakcije med delci reguliranega naboja, posredovane z multivalentnimi koioni, nimajo velikega vpliva na DLVO rezultate [106]. Najbolj pomemben rezultat naše teorije je opis interakcije v točki ničelnega naboja. Takrat odboj kot rezultat šibke sklopitve izgine, prvi popravek postane dominanten in prinese močan privlak med elektronevtralnimi makroioni. Izpeljana oblika proste energije nam pove, da je ta privlak posledica interakcije med ioni in induciranimi ioni. Tudi iz dobljenih rezultatov vidimo, da je ta vrsta interakcije precej močnejša od rezultata šibke sklopitve za Kirkwood–Shumakerjevo interakcijo. Na ta način smo dobili splošno obliko za opis Kirkwood–Shumakerjeve interakcije, posplošeno tako, da je veljavna tudi v režimu močne sklopitve, ter tako utemeljili pot za bolj podrobno raziskavo elektrostatičnih interakcij med proteini.

H.5 Interakcije površin reguliranega naboja v prisotnosti polivalentne soli

Za razliko od modela točkastih nabojev, je v tem poglavju tema našega raziskovanja interakcija med površinami, kjer titracijska mesta zavzemajo neskončno ploščo, tako da v termodinamski limiti dobimo končno porazdelitveno gostoto naboja na površini. Takšen model bo pomemben za sisteme, pri katerih je razdalja med nabitimi makroioni manjša od njihove velikosti. Končna velikost titracijskega makroiona bo privedla do dodatnih formalnih matematičnih težav, tako da bo naš cilj najti načine, kako jih premagati ter priti do razumevanja, kako prostorska porazdelitev fluktuirajočega naboja vpliva na skupno interakcijo takšnih površin v prisotnosti polivalentnih ionov.

Problem interakcij dvojnih plasti, posredovanih z multivalentnimi ioni, je bil dolgo časa izziv za teoretike, ustrezen teoretični opis pa sta prva podala Matej Kanduč in Rudolf Podgornik, leta 2010 za sistem s fiksnim nabojem, tako formulirajoč teorijo oblečenih ionov. Tukaj bomo razširili njuno teorijo tako, da bomo v naš okvir vključili pojav regulacije naboja. Ker v literaturi ne obstaja teoretični model za problem interakcije regulacijsko-nabitih delcev v prisotnosti multivalentnih ionov, smo začeli s preprostim modelom, ki privzame enakomerno porazdelitev adsorpcijskih mest na površinah ter predpostavi, da ni interakcije med sosednjimi titracijsko nabitimi delci na površini. Plošče so potopljene v raztopini monovalentnih in polivalentnih ionov. Cilj je dobiti posplošeno obliko za Kirkwood–Shumakerjevo interakcijo, ki jo lahko primerjamo z van der Waalsovo interakcijo.

Naša izpeljava teorije temelji na dekompoziciji particijske vsote na nivoju virialnega razvoja, analognega teoriji oblečenih ionov. En del privede do opisa proste energije med titracijskimi površinami v prisotnosti monovalentne soli na nivoju šibke sklopitve, medtem ko drugi člen ustreza prvemu popravku, ki je prispevek polivalentnih ionov, obravnavanih na nivoju močne sklopitve. Oba člena upoštevata točno formo površinske proste energije, ki ustreza regulaciji naboja, podobno kot v en. (5). Prvi prispevek smo definirali v obliki popotnega integrala v Fourier–Besselovem prostoru ter dobili obliko podobno Feynmanovemu vzbujanemu harmonskemu oscilatorju. To je bil zapleten del računa zaradi nehomegenih fluktuacij naboja na površinah, ki so prinesle dodatne matematične težave. Uporablja joč

metode iz teorije polja [124] smo dobili točno analitično obliko proste energije.

Vsota šibke sklopitve (ki opisuje sistem brez polivalentnih ionov v raztopini) se loči na dva člena: prvi opisuje odboj med enako nabitimi površinami in je odvisen od pH raztopine, medtem ko drugi opisuje privlak, ki postane dominanten v točki ničelnega naboja. Ta privlak predstavlja prepleteno van der Waalsovo in Kirkwood–Shumakerjevo interakcijo. Interakciji se lahko ločita v limiti dielektrično homogenega sistema, ko dobimo Kirkwood–Shumakerjevo interakcijo, ali pa v limiti fiksnega naboja, ko ostane van der Waalsova interakcija. Intenziteti obeh interakcij sta primerljivi.

Statistična vsota pri močni sklopitvi (ki opisuje prispevek polivalentnih ionov) nam je dala privlačen prispevek k prosti energiji. V odvisnosti od predznaka naboja na površinah je celotna interakcija lahko odbojna, če se polivalentni ioni obnašajo kot koioni, ali pa privlačna, če se polivalentni ioni obnašajo kot protiioni. V primeru koionov se lahko opazi privlak samo na velikih razdaljah, ko odboj oslabi zaradi senčenja ter asimetrične fluktuacije naboja imajo večji vpliv. V primeru protiionov je privlak močnejši za večje vrednosti naboja na površinah, pri večji koncentraciji polivalentne soli ter manjšemu senčenju.

Kadar površini dosežeta točko ničelnega naboja pride do privlaka. Rezultati so pokazali, da je ta privlak precej močnejši od privlaka v monovalentni soli. Razlog za to je, da v monovalentni soli privlak izhaja iz monopolarnih fluktuacij naboja. Tu polivalentni ioni prinesejo dodaten privlak, ki je posledica interakcije med ioni in induciranimi ioni, kjer polivalentni ioni močnejše inducirajo fluktuacije naboja na površinah. Te fluktuacije so nehomogeno razporejene na površinah, zaradi česar dobimo zapleteno obliko te interakcije.

Z izpeljano teorijo smo pokrili široko območje parametričnega prostora ter prispevali k bolj podrobnemu razumevanju problema dvojnih plasti, in s tem presegli standardni opis, ki temelji na približku fiksnega naboja na površinah. Naša teorija omogoča tudi razumevanje problema interakcije med proteini v močno koreliranih sistemih, ki so pogosti v bioloških pogojih.

H.6 Zaključek

Za zaključek moramo izpostaviti, da naše delo predstavlja razširitev stoletja dolge zgodovine teorij elektrostatičnih interakcij v fiziki koloidov. Coulombske tekočine, sestavljene iz makromolekul v ionski raztopini, predstavljajo pomemben večdelni problem, zahteven za analizo zaradi dolgega dosega elektrostatičnih interakcij. To je pustilo močan pečat pri razvoju znanstvenega področja, saj so teorije morale biti omejene na majhen del parametrskega prostora, da bi relevantni približki obdržali svojo veljavnost, s tem pa je bil celoten postopek pridobivanja novih spoznanj počasen in postopen. Z uvedbo orodij iz teorije polja smo naredili pomemben korak pri modernem razumevanju coulombskih tekočin. Kljub temu so tudi te moderne teorije ostale omejene na prostor parametrov, ki ustreza konstantnemu naboju na makromolekulah. Ta približek je seveda daleč od resničnosti, še posebej v svetu proteinov z disociabilnimi protoniranimi–deprotoniranimi aminokislinami. V takšnih sistemih pridejo do izraza učinki regulacije naboja s fluktuirajočim površinskim nabojem kot glavnim vodilom. Pričujoča disertacija je namenjena posplošitvi modernih teorij coulombskih elektrolitov z namenom razumevanja pojavov, ki nastanejo kot posledica regulacije naboja. Motivirani z izzivi iz fizike proteinov je v

disertaciji predstavljen teoretični okvir, v katerem smo obravnavali štiri probleme, ki se nanašajo na regulacijo naboja makromolekul v ionski raztopini. Seveda so nekateri približki še vedno prisotni, vendar predstavljene teorije zajemajo vse osnovne pojave, ki so prisotne med proteini ali pa katerimi drugimi objekti s spremenljivim nabojem.

Kljub temu, da je napredek razumevanja elektrostatičnih interakcij med proteini nezanemarljiv, je ostalo dovolj prostora za izboljšave in posplošitve. Kot prvo, veljavnost predstavljenih teoretičnih rezultatov je potrebno preveriti z računalniškimi simulacijami, kar je načrtovano v bližnji prihodnosti. Poleg tega so obravnavani makroioni opisani bodisi v limiti točkastih nabojev, zanemarjujoč prostorsko porazdelitev adsorpcijskih mest, bodisi z neskončnimi ravnimi površinami enakomerne porazdelitve adsorpcijskih mest, kjer so interakcije med njimi zanemarjene. Oba modela sta lahko še izboljšana in posplošena. Posebej zanimivo bi bilo videti, kako krpaste porazdelitve naboja vplivajo na regulacijo naboja. Lahko bi se šlo globlje v numeriko, kjer bi morali implementirati dobljene rezultate na primeru konkretnih proteinov. Kar se tiče nadaljnjega teoretičnega razvoja, bi bil naslednji korak v našem opisu vključitev multipolnih momentov ter polarizacijskih učinkov, kar bi prispevalo k boljšemu razumevanju osnovnih elektrostatičnih interakcij med proteini.

Bibliography

- [1] P. K. C. Holm and R. Podgornik, *Electrostatic Effects in Soft matter and Biophysics*, 3rd ed. (NATO Science Series, New York, 2000).
- [2] B. Honig and A. Nicholls, "Classical electrostatics in biology and chemistry", *Science* **268**, 1144 (1995).
- [3] P.-G. de Gennes, "Soft Matter", *Reviews of Modern Physics* **64**, 645 (1992).
- [4] R. Piazza, *Soft Matter: The Stuff that Dreams are Made of* (Springer, Berlin, 2011).
- [5] G. R. Strobl, *The Physics of Polymers*, Vol. 2 (Springer, Berlin, 1997).
- [6] E. Prohofsky, *Statistical Mechanics and stability of macromolecules: application to bond disruption, base pair separation, melting, and drug dissociation of the DNA double helix* (Cambridge University Press, 2005).
- [7] K. Kuwajima, Y. Goto, F. Hirata, M. Terazima and M. Kataoka, *Water and Biomolecules: Physical Chemistry of Life Phenomena* (Springer, Berlin, 2009).
- [8] O. Punkkinen, A. Naji, R. Podgornik, I. Vattulainen and P.-L. Hansen, "Ionic cloud distribution close to a charged surface in the presence of salt", *EPL (Europhysics Letters)* **82**, 48001 (2008).
- [9] G. C. Wong and L. Pollack, "Electrostatics of strongly charged biological polymers: ion-mediated interactions and self-organization in nucleic acids and proteins", *Annual Review of Physical Chemistry* **61**, 171 (2010).
- [10] A. Naji, M. Kanduč, J. Forsman and R. Podgornik, "Perspective: Coulomb fluids - Weak coupling, strong coupling in between and beyond", *Journal of Chemical Physics* **139**, 150901 (2013).
- [11] M. Gouy, "Sur la constitution de la charge électrique à la surface d'un électrolyte", *J. Phys. Theor. Appl.* **9**, 457 (1910).
- [12] D. L. Chapman, "A contribution to the theory of electrocapillarity", *The London, Edinburgh, and Dublin philosophical magazine and journal of science* **25**, 475 (1913).
- [13] P. Debye and E. Hückel, "De la théorie des électrolytes. i. abaissement du point de congélation et phénomènes associés", *Physikalische Zeitschrift* **24**, 185 (1923).

- [14] D. Andelman, "Electrostatic properties of membranes: The Poisson-Boltzmann theory", in *Handbook of Biological Physics: Structure and Dynamics of Membranes*, Vol. 1B, edited by R. Lipowsky and E. Sackmann (Elsevier Science B. V., Amsterdam, 1995).
- [15] B. Derjaguin and L. Landau, "Theory of the stability of strongly charged lyophobic sols and of the adhesion of strongly charged particles in solutions of electrolytes", *Acta physicochim. URSS* **14**, 633 (1941).
- [16] E. J. W. Verwey and J. T. G. Overbeek, "Theory of Stability of Lyophobic Colloids Elsevier", Amsterdam-New York **34** (1948).
- [17] T. Markovich, D. Andelman and R. Podgornik, "Charged Membranes: Poisson-Boltzmann theory, DLVO paradigm and beyond", in *Handbook of Lipid Membranes*, edited by C. Safynia and J. Raedler (Taylor and Francis, 2016).
- [18] L. Guldbrand, B. Jönsson, H. Wennerström and P. Linse, "Electrical double layer forces. A Monte Carlo study", *The Journal of Chemical Physics* **80**, 2221 (1984).
- [19] J. Marra, "Direct measurement of the interaction between phosphatidylglycerol bilayers in aqueous electrolyte solutions.", *Biophysical Journal* **50**, 815 (1986).
- [20] S. Edwards and A. Lenard, "Exact Statistical Mechanics of a One-Dimensional System with Coulomb Forces. II. The Method of Functional Integration", *Journal of Mathematical Physics* **3**, 778 (1962).
- [21] R. Podgornik and B. Žekš, "Inhomogeneous Coulomb fluid. A functional integral approach", *Journal of the Chemical Society, Faraday Transactions 2: Molecular and Chemical Physics* **84**, 611 (1988).
- [22] R. Podgornik, "An analytic treatment of the first-order correction to the Poisson-Boltzmann interaction free energy in the case of counterion-only Coulomb fluid", *Journal of Physics A: Mathematical and General* **23**, 275 (1990).
- [23] P. Attard, D. J. Mitchell and B. W. Ninham, "Beyond Poisson-Boltzmann: Images and correlations in the electric double layer. I. Counterions only", *The Journal of Chemical Physics* **88**, 4987 (1988).
- [24] A. G. Moreira and R. R. Netz, "Strong-coupling theory for counter-ion distributions", *EPL (Europhysics Letters)* **52**, 705 (2000).
- [25] A. G. Moreira and R. R. Netz, "Binding of similarly charged plates with counterions only", *Physical Review Letters* **87**, 078301 (2001).
- [26] A. Naji and R. R. Netz, "Attraction of like-charged macroions in the strong-coupling limit", *The European Physical Journal E* **13**, 43 (2004).
- [27] A. Naji, A. Arnold, C. Holm and R. R. Netz, "Attraction and unbinding of like-charged rods", *EPL (Europhysics Letters)* **67**, 130 (2004).

- [28] A. Naji, S. Jungblut, A. G. Moreira and R. R. Netz, "Electrostatic interactions in strongly coupled soft matter", *Physica A: Statistical Mechanics and its Applications* **352**, 131 (2005).
- [29] H. Boroudjerdi, Y.-W. Kim, A. Naji, R. R. Netz, X. Schlagberger and A. Serr, "Statics and dynamics of strongly charged soft matter", *Physics Reports* **416**, 129 (2005).
- [30] M. Kanduč, M. Trulsson, A. Naji, Y. Burak, J. Forsman and R. Podgornik, "Weak-and strong-coupling electrostatic interactions between asymmetrically charged planar surfaces", *Physical Review E* **78**, 061105 (2008).
- [31] M. Kanduč and R. Podgornik, "Electrostatic image effects for counterions between charged planar walls", *The European Physical Journal E* **23**, 265 (2007).
- [32] M. Kanduč, A. Naji, Y. Jho, P. A. Pincus and R. Podgornik, "The role of multipoles in counterion-mediated interactions between charged surfaces: strong and weak coupling", *Journal of Physics: Condensed Matter* **21**, 424103 (2009).
- [33] Y. Jho, M. Kanduč, A. Naji, R. Podgornik, M. Kim and P. A. Pincus, "Strong-coupling electrostatics in the presence of dielectric inhomogeneities", *Physical Review Letters* **101**, 188101 (2008).
- [34] M. Kanduč, A. Naji, J. Forsman and R. Podgornik, "Dressed counterions: Strong electrostatic coupling in the presence of salt", *The Journal of Chemical Physics* **132**, 124701 (2010).
- [35] M. Kanduč, A. Naji, J. Forsman and R. Podgornik, "Dressed counterions: Polyvalent and monovalent ions at charged dielectric interfaces", *Physical Review E* **84**, 011502 (2011).
- [36] M. Kanduč, A. Naji, J. Forsman and R. Podgornik, "Attraction between neutral dielectrics mediated by multivalent ions in an asymmetric ionic fluid", *The Journal of Chemical Physics* **137**, 174704 (2012).
- [37] I. Rouzina and V. A. Bloomfield, "Macroion Attraction Due to Electrostatic Correlation between Screening Counterions. 1. Mobile Surface-Adsorbed Ions and Diffuse Ion Cloud", *Journal of Physical Chemistry* **100**, 9977 (1996).
- [38] N. V. Hud and K. H. Downing, "Cryoelectron microscopy of λ phage DNA condensates in vitreous ice: the fine structure of DNA toroids", *Proceedings of the National Academy of Sciences* **98**, 14925 (2001).
- [39] G. E. Plum and V. A. Bloomfield, "Equilibrium dialysis study of binding of hexammine cobalt (III) to DNA", *Biopolymers* **27**, 1045 (1988).
- [40] A. Leforestier, A. Šiber, F. Livolant and R. Podgornik, "Protein-DNA interactions determine the shapes of DNA toroids condensed in virus capsids", *Biophysical Journal* **100**, 2209 (2011).
- [41] W. C. Poon and D. Andelman, *Soft condensed matter physics in molecular and cell biology* (CRC Press, 2006).

- [42] R. Piazza, "Protein interactions and association: an open challenge for colloid science", *Current Opinion in Colloid & Interface Science* **8**, 515 (2004).
- [43] A. V. Finkelstein and O. Ptitsyn, *Protein physics* (Academic Press, 2002).
- [44] O. College, "Constituent amino-acids can be analyzed to predict secondary, tertiary and quaternary protein structure, in this case hemoglobin containing heme units" (2013), https://upload.wikimedia.org/wikipedia/commons/2/26/225_Peptide_Bond-01.jpg.
- [45] L. Pauling and R. B. Corey, "The configuration of polypeptide chains in proteins", in *Fortschritte der Chemie Organischer Naturstoffe/Progress in the Chemistry of Organic Natural Products/Progrés dans la Chimie des Substances Organiques Naturelles* (Springer, 1954) pp. 180–239.
- [46] L. Pauling, R. B. Corey and H. R. Branson, "The structure of proteins: two hydrogen-bonded helical configurations of the polypeptide chain", *Proceedings of the National Academy of Sciences* **37**, 205 (1951).
- [47] D. Eisenberg, "The discovery of the α -helix and β -sheet, the principal structural features of proteins", *Proceedings of the National Academy of Sciences* **100**, 11207 (2003).
- [48] F. Sanger and H. Tuppy, "The amino-acid sequence in the phenylalanyl chain of insulin. 1. The identification of lower peptides from partial hydrolysates", *Biochemical Journal* **49**, 463 (1951).
- [49] I. M. Klotz, N. Langebman and D. Dahnall, "Quaternary structure of proteins", *Annual Review of Biochemistry* **39**, 25 (1970).
- [50] L. Holm and C. Sander, "Mapping the protein universe", *Science* **273**, 595 (1996).
- [51] D. Baker and A. Sali, "Protein structure prediction and structural genomics", *Science* **294**, 93 (2001).
- [52] J. Janin, R. P. Bahadur and P. Chakrabarti, "Protein–protein interaction and quaternary structure", *Quarterly Reviews of Biophysics* **41**, 133 (2008).
- [53] A. Griewel, "Examples of protein structures from PDB" (2011), https://upload.wikimedia.org/wikipedia/commons/2/24/Protein_structure_examples.png.
- [54] L. Pauling and R. B. Corey, "The structure of hair, muscle, and related proteins", *Proc Natl Acad Sci USA* **37**, 261 (1951).
- [55] Y. Mrabet, "Peptide bond formation" (2007), <https://upload.wikimedia.org/wikipedia/commons/archive/6/6d/2014072107571821Peptidformationball.svg>.
- [56] H. Boroudjerdi, Y.-W. Kim, A. Naji, R. R. Netz, X. Schlagberger and A. Serr, "Statics and dynamics of strongly charged soft matter", *Physics Reports* **416**, 129 (2005).

- [57] R. J. Nap, A. L. Božič, I. Szleifer and R. Podgornik, "The role of solution conditions in the bacteriophage PP7 capsid charge regulation", *Biophysical Journal* **107**, 1970 (2014).
- [58] A. L. Božič, A. Šiber and R. Podgornik, "How simple can a model of an empty viral capsid be? Charge distributions in viral capsids", *Journal of Biological Physics* **38**, 657 (2012).
- [59] B. W. Ninham and V. A. Parsegian, "Electrostatic potential between surfaces bearing ionizable groups in ionic equilibrium with physiologic saline solution", *Journal of Theoretical Biology* **31**, 405 (1971).
- [60] M. Lund and B. Jönsson, "On the charge regulation of proteins", *Biochemistry* **44**, 5722 (2005).
- [61] N. Boon and R. van Roij, "Charge regulation and ionic screening of patchy surfaces", *The Journal of Chemical Physics* **134**, 054706 (2011).
- [62] R. Netz, "Charge regulation of weak polyelectrolytes at low- and high-dielectric-constant substrates", *Journal of Physics: Condensed Matter* **15**, S239 (2002).
- [63] A. L. Božič and R. Podgornik, "Symmetry effects in electrostatic interactions between two arbitrarily charged spherical shells in the Debye-Hückel approximation", *The Journal of Chemical Physics* **138**, 074902 (2013).
- [64] J. G. Kirkwood and J. B. Shumaker, "Forces between protein molecules in solution arising from fluctuations in proton charge and configuration", *Proceedings of the National Academy of Sciences* **38**, 863 (1952).
- [65] J. G. Kirkwood and J. B. Shumaker, "The influence of dipole moment fluctuations on the dielectric increment of proteins in solution", *Proceedings of the National Academy of Sciences* **38**, 855 (1952).
- [66] V. A. Parsegian, *Van der Waals forces: A Handbook for Biologists, Chemists, Engineers, and Physicists* (Cambridge University Press, Cambridge, 2005).
- [67] A. Sadeghpour, I. Szilágyi and M. Borkovec, "Charging and aggregation of positively charged colloidal latex particles in presence of multivalent polycarboxylate anions", *Zeitschrift für Physikalische Chemie International journal of research in physical chemistry and chemical physics* **226**, 597 (2012).
- [68] F. J. M. Ruiz-Cabello, P. Maroni and M. Borkovec, "Direct measurements of forces between different charged colloidal particles and their prediction by the theory of Derjaguin, Landau, Verwey, and Overbeek (DLVO)", *The Journal of Chemical Physics* **138**, 234705 (2013).
- [69] M. Lund and B. Jönsson, "A mesoscopic model for protein-protein interactions in solution", *Biophysical Journal* **85**, 2940 (2003).
- [70] F. L. B. da Silva and B. Jönsson, "Polyelectrolyte-protein complexation driven by charge regulation", *Soft Matter* **5**, 2862 (2009).

- [71] F. L. B. da Silva, M. Lund, B. Jönsson and T. Åkesson, "On the complexation of proteins and polyelectrolytes", *The Journal of Physical Chemistry B* **110**, 4459 (2006).
- [72] J. Israelachvili, *Intermolecular and Surface Forces* (Academic Press, London, 1991).
- [73] D. Ben-Yaakov, D. Andelman, D. Harries and R. Podgornik, "Beyond standard Poisson–Boltzmann theory: ion-specific interactions in aqueous solutions", *Journal of Physics: Condensed Matter* **21**, 424106 (2009).
- [74] Y. Burak and D. Andelman, "Hydration interactions: Aqueous solvent effects in electric double layers", *Physical Review E* **62**, 5296 (2000).
- [75] M. Ghodrati, A. Naji, H. Komaie-Moghaddam and R. Podgornik, "Ion-mediated interactions between net-neutral slabs: Weak and strong disorder effects", *The Journal of Chemical Physics* **143**, 234701 (2015).
- [76] A. Naji, M. Kanduč, R. R. Netz and R. Podgornik, "Exotic Electrostatics: Unusual Features of Electrostatic Interactions between Macroions", in *Understanding Soft Condensed Matter via Modeling and Computations*, edited by W.-B. Hu and A.-C. Shi (World Scientific, Singapore, 2010).
- [77] A. Naji, S. Jungblut, A. G. Moreira and R. R. Netz, "Electrostatic interactions in strongly coupled soft matter", *Physica A: Statistical Mechanics and its Applications* **352**, 131 (2005).
- [78] D. Dean and R. Horgan, "Field theoretic derivation of the contact value theorem in planar geometries and its modification by the Casimir effect", *Physical Review E* **68**, 061106 (2003).
- [79] C. Fleck, R. R. Netz and H. H. von Grünberg, "Poisson–Boltzmann theory for membranes with mobile charged lipids and the pH-dependent interaction of a DNA molecule with a membrane", *Biophysical Journal* **82**, 76 (2002).
- [80] R. Podgornik, "Electrostatic correlation forces between surfaces with surface specific ionic interactions", *The Journal of Chemical Physics* **91**, 5840 (1989).
- [81] R. Podgornik and A. Vilfan, *Elektromagnetno polje* (DMFA-založništvo, Ljubljana, 2012).
- [82] B. Milić, *Maksvelova elektrodinamika* (Studentski trg, Beograd, 2002).
- [83] R. R. Netz, "Electrostatics of counter-ions at and between planar charged walls: From Poisson-Boltzmann to the strong-coupling theory", *The European Physical Journal E* **5**, 557 (2001).
- [84] A. G. Moreira and R. R. Netz, "Counterions at charge-modulated substrates", *EPL (Europhysics Letters)* **57**, 911 (2002).
- [85] A. Naji and R. Podgornik, "Quenched charge disorder and Coulomb interactions", *Physical Review E* **72**, 041402 (2005).

- [86] A. Naji, M. Ghodrat, H. Komaie-Moghaddam and R. Podgornik, "Asymmetric Coulomb fluids at randomly charged dielectric interfaces: Anti-fragility, overcharging and charge inversion", *The Journal of Chemical Physics* **141**, 174704 (2014).
- [87] M. Ghodrat, A. Naji, H. Komaie-Moghaddam and R. Podgornik, "Strong coupling electrostatics for randomly charged surfaces: antifragility and effective interactions", *Soft Matter* **11**, 3441 (2015).
- [88] M. Kanduč, *Macromolecular Interactions in the Limit of Weak and Strong Electrostatic Coupling*, Ph.D. thesis, Faculty of Physics, University of Ljubljana (2010).
- [89] K. Linderstrøm-Lang, "On the ionization of proteins", *CR Trav Lab Carlsberg* **15**, 1 (1924).
- [90] K. Linderstrøm-Lang, *Proteins and enzymes*, Vol. 6 (Stanford University Press, Stanford, 1952).
- [91] S. Englander, L. Mayne, Y. Bai and T. Sosnick, "Hydrogen exchange: The modern legacy of Linderstrøm-Lang", *Protein Science* **6**, 1101 (1997).
- [92] A. McLaren and K. Babcock, "Some characteristics of enzyme reactions at surfaces" (1959).
- [93] D. C. Prieve and E. Ruckenstein, "The surface potential of and double-layer interaction force between surfaces characterized by multiple ionizable groups", *Journal of Theoretical Biology* **56**, 205 (1976).
- [94] D. C. Prieve and E. Ruckenstein, "The double-layer interaction between dissimilar ionizable surfaces and its effect on the rate of deposition", *Journal of Colloid and Interface Science* **63**, 317 (1978).
- [95] S. L. Carnie and D. Y. Chan, "Interaction free energy between plates with charge regulation: a linearized model", *Journal of Colloid and Interface Science* **161**, 260 (1993).
- [96] D. Chan, T. W. Healy and L. R. White, "Electrical double layer interactions under regulation by surface ionization equilibria—dissimilar amphoteric surfaces", *Journal of the Chemical Society, Faraday Transactions 1: Physical Chemistry in Condensed Phases* **72**, 2844 (1976).
- [97] S. H. Behrens and M. Borkovec, "Electric double layer interaction of ionizable surfaces: Charge regulation for arbitrary potentials", *The Journal of Chemical Physics* **111**, 382 (1999).
- [98] F. J. Montes Ruiz-Cabello, G. Trefalt, P. Maroni and M. Borkovec, "Accurate Predictions of Forces in the Presence of Multivalent Ions by Poisson–Boltzmann Theory", *Langmuir* **30**, 4551 (2014).
- [99] G. Trefalt, F. J. M. Ruiz-Cabello and M. Borkovec, "Interaction Forces, Heteroaggregation, and Deposition Involving Charged Colloidal Particles", *The Journal of Physical Chemistry B* **118**, 6346 (2014).

- [100] R. Pericet-Camara, G. Papastavrou, S. H. Behrens and M. Borkovec, "Interaction between charged surfaces on the Poisson-Boltzmann level: The constant regulation approximation", *The Journal of Physical Chemistry B* **108**, 19467 (2004).
- [101] G. Trefalt, I. Szilagyi and M. Borkovec, "Poisson-Boltzmann description of interaction forces and aggregation rates involving charged colloidal particles in asymmetric electrolytes", *Journal of colloid and interface science* **406**, 111 (2013).
- [102] C. Labbez, B. Jonsson, M. Skarba and M. Borkovec, "Ion-ion correlation and charge reversal at titrating solid interfaces", *Langmuir* **25**, 7209 (2009).
- [103] M. Moazzami-Gudarzi, G. Trefalt, I. Szilagyi, P. Maroni and M. Borkovec, "Nanometer-ranged attraction induced by multivalent ions between similar and dissimilar surfaces probed using an atomic force microscope (AFM)", *Physical Chemistry Chemical Physics* **18**, 8739 (2016).
- [104] F. J. Montes Ruiz-Cabello, G. Trefalt, P. Maroni and M. Borkovec, "Accurate Predictions of Forces in the Presence of Multivalent Ions by Poisson-Boltzmann Theory", *Langmuir* **30**, 4551 (2014).
- [105] T. Cao, I. Szilagyi, T. Oncsik, M. Borkovec and G. Trefalt, "Aggregation of Colloidal Particles in the Presence of Multivalent Co-Ions: The Inverse Schulze-Hardy Rule", *Langmuir* **31**, 6610 (2015).
- [106] F. J. M. Ruiz-Cabello, M. Moazzami-Gudarzi, M. Elzbiaciak-Wodka, P. Maroni, C. Labbez, M. Borkovec and G. Trefalt, "Long-ranged and soft interactions between charged colloidal particles induced by multivalent coions", *Soft Matter* **11**, 1562 (2015).
- [107] M. Lund and B. Jönsson, "Charge regulation in biomolecular solution", *Quarterly Reviews of Biophysics* **46**, 265 (2013).
- [108] R. Podgornik and V. Parsegian, "An electrostatic-surface stability interpretation of the hydrophobic force inferred to occur between mica plates in solutions of soluble surfactants", *Chemical Physics* **154**, 477 (1991).
- [109] R. Podgornik and V. Parsegian, "Forces between CTAB-covered glass surfaces interpreted as an interaction-driven surface instability", *The Journal of Physical Chemistry* **99**, 9491 (1995).
- [110] D. Leckband and S. Sivasankar, "Forces controlling protein interactions: theory and experiment", *Colloids and Surfaces B: Biointerfaces* **14**, 83 (1999).
- [111] I. Borukhov, D. Andelman, R. Borrega, M. Cloitre, L. Leibler and H. Orland, "Polyelectrolyte titration: theory and experiment", *The Journal of Physical Chemistry B* **104**, 11027 (2000).
- [112] R. Kumar, B. G. Sumpter and S. M. Kilbey II, "Charge regulation and local dielectric function in planar polyelectrolyte brushes", *The Journal of Chemical Physics* **136**, 234901 (2012).

- [113] J. P. Mahalik, Y. Yang, C. Deodhar, J. F. Ankner, B. S. Lokitz, S. M. Kilbey, B. G. Sumpter and R. Kumar, "Monomer volume fraction profiles in pH responsive planar polyelectrolyte brushes", *Journal of Polymer Science Part B: Polymer Physics* (2016).
- [114] W. S. de Lint, P. M. Biesheuvel and H. Verweij, "Application of the charge regulation model to transport of ions through hydrophilic membranes: one-dimensional transport model for narrow pores (nanofiltration)", *Journal of Colloid and Interface Science* **251**, 131 (2002).
- [115] C.-Y. Leung, L. C. Palmer, S. Kewalramani, B. Qiao, S. I. Stupp, M. O. de la Cruz and M. J. Bedzyk, "Crystalline polymorphism induced by charge regulation in ionic membranes", *Proceedings of the National Academy of Sciences* **110**, 16309 (2013).
- [116] G. Pabst, N. Kučerka, M.-P. Nieh and J. Katsaras, *Liposomes, lipid bilayers and model membranes: from basic research to application* (CRC Press, 2014).
- [117] R. Podgornik, "Forces between surfaces with surface-specific interactions in a dilute electrolyte", *Chemical Physics Letters* **156**, 71 (1989).
- [118] T. Markovich, D. Andelman and R. Podgornik, "Surface tension of electrolyte solutions: A self-consistent theory", *EPL (Europhysics Letters)* **106**, 16002 (2014).
- [119] C. Fleck and R. Netz, "Surfaces with quenched and annealed disordered charge distributions", *The European Physical Journal E* **22**, 261 (2007).
- [120] I. Borukhov, D. Andelman and H. Orland, "Adsorption of large ions from an electrolyte solution: a modified Poisson–Boltzmann equation", *Electrochimica Acta* **46**, 221 (2000).
- [121] D. Ben-Yaakov, D. Andelman, R. Podgornik and D. Harries, "Ion-specific hydration effects: Extending the Poisson-Boltzmann theory", *Current Opinion in Colloid & Interface Science* **16**, 542 (2011).
- [122] D. Dean and R. Horgan, "Electrostatic fluctuations in soap films", *Physical Review E* **65**, 061603 (2002).
- [123] C. G. F. Steiner, *Handbook of Feynman Path Integrals* (Springer-Verlag, Berlin Heidelberg New York Tokio, 1998).
- [124] D. C. Khandekar and S. Lawande, "Feynman path integrals: some exact results and applications", *Physics Reports* **137**, 115 (1986).
- [125] R. Podgornik, R. H. French and V. A. Parsegian, "Nonadditivity in van der Waals interactions within multilayers", *The Journal of Chemical Physics* **124**, 044709 (2006).
- [126] N. Adžić and R. Podgornik, "Field-theoretic description of charge regulation interaction", *European Physical Journal E* **37**, 6 (2014).

- [127] H. Li and M. Kardar, "Fluctuation-induced forces between rough surfaces", *Physical Review Letters* **67**, 3275 (1991).
- [128] A. Maggs and R. Podgornik, "Electrostatic interactions in the presence of surface charge regulation: Exact results", *EPL (Europhysics Letters)* **108**, 68003 (2015).
- [129] I. Wolfram Research, "Mathematica Edition: Version 9.0" (2008).
- [130] A. Moreira and R. Netz, "Simulations of counterions at charged plates", *The European Physical Journal E* **8**, 33 (2002).
- [131] R. H. French, V. A. Parsegian, R. Podgornik, R. F. Rajter, A. Jagota, J. Luo, D. Asthagiri, M. K. Chaudhury, Y.-m. Chiang, S. Granick *et al.*, "Long-range interactions in nanoscale science", *Reviews of Modern Physics* **82**, 1887 (2010).
- [132] N. Adžić and R. Podgornik, "Charge regulation in ionic solutions: Thermal fluctuations and Kirkwood-Schumaker interactions", *Physical Review E* **91**, 022715 (2015).
- [133] V. Valmacco, M. Elzbieciak-Wodka, D. Herman, G. Trefalt, P. Maroni and M. Borkovec, "Forces between silica particles in the presence of multivalent cations", *Journal of Colloid and Interface Science* **472**, 108 (2016).
- [134] N. Adžić and R. Podgornik, "Titratable Macroions in Multivalent Electrolyte Solution? Strong Coupling Dressed IOn Approach", *Journal of Chemical Physics* **144**, 214901 (2016).
- [135] G. B. Arfken, H. J. Weber and F. E. Harris, *Mathematical methods for physicists: A comprehensive guide* (Academic press, 2011).
- [136] R. Podgornik, G. Cevc and B. Žekš, "Solvent structure effects in the macroscopic theory of van der Waals forces", *The Journal of Chemical Physics* **87**, 5957 (1987).
- [137] M. Moazzami Gudarzi, G. Trefalt, I. Szilagyi, P. Maroni and M. Borkovec, "Forces between Negatively Charged Interfaces in the Presence of Cationic Multivalent Oligoamines Measured with the Atomic Force Microscope", *The Journal of Physical Chemistry C* **119**, 15482 (2015).
- [138] G. Trefalt, S. H. Behrens and M. Borkovec, "Charge Regulation in the Electrical Double Layer: Ion Adsorption and Surface Interactions", *Langmuir* (2015).
- [139] T. P. Trefalt, Gregor and M. Borkovec, "Forces between Colloidal Particles in Aqueous Solutions Containing Monovalent and Multivalent Ions", *Current Opinion Colloid & Interface Science* (2016), in print.
- [140] D. Arzenšek, D. Kuzman and R. Podgornik, "Colloidal interactions between monoclonal antibodies in aqueous solutions", *Journal of colloid and interface science* **384**, 207 (2012).
- [141] D. Arzenšek, D. Kuzman and R. Podgornik, "Hofmeister Effects in Monoclonal Antibody Solution Interactions", *The Journal of Physical Chemistry B* **119**, 10375 (2015).

- [142] M. Abramowitz and I. A. Stegun, *Handbook of Mathematical Functions* (Dover, New York, 1972).

List of publications

0. Nataša Adžić and Rudolf Podgornik, *Kirkwood-Shumaker interactions and general thermal fluctuation forces*, <http://arxiv.org/pdf/1401.5252.pdf>
1. Nataša Adžić and Rudolf Podgornik, *Field-theoretic description of charge regulation interaction*, *The European Physical Journal E* **37**, 49 (2014).
2. Nataša Adžić and Rudolf Podgornik, *Charge regulation in ionic solutions: Thermal fluctuations and Kirkwood- Shumaker interactions*, *Physical Review E* **91**, 022715 (2015).
3. Nataša Adžić and Rudolf Podgornik, *Titrateable Macroions in Multivalent Electrolyte Solution: Strong Coupling Dressed Ion Approach*, *Journal of Chemical Physics*, **144**, 214901 (2016).

Izjava o avtorstvu in objavi elektronske oblike

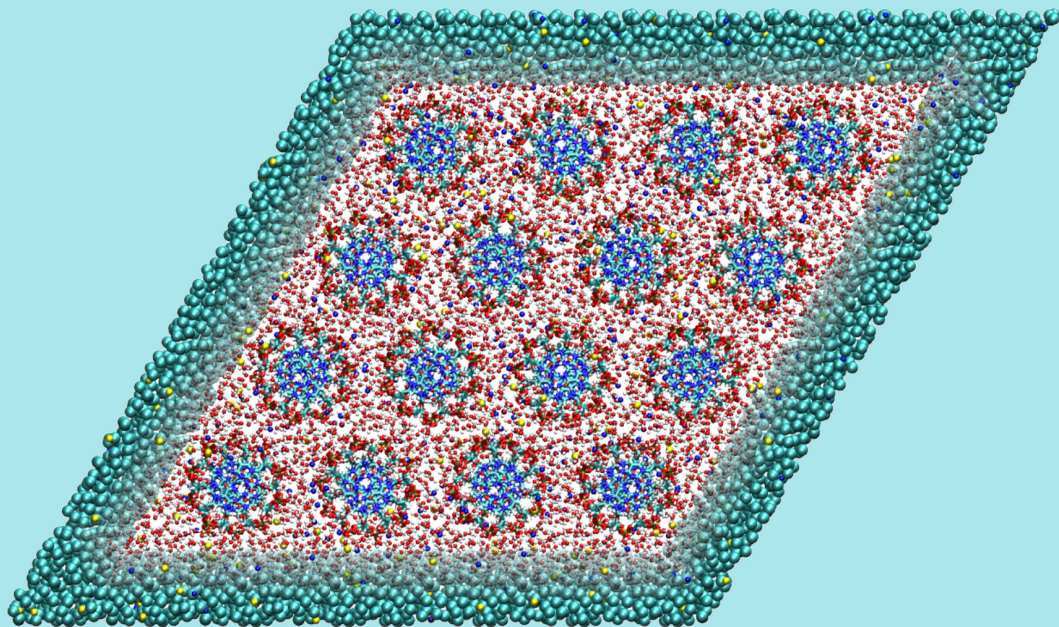
Izjavljam:

- da sem doktorsko disertacijo z naslovom *Raznolikost in fenomenologija elektrostatičnih interakcij v fiziki proteinov* izdelala kot rezultat lastnega raziskovalnega dela pod mentorstvom prof. dr. Rudolfa Podgornika,
- da je elektronska oblika dela identična s tiskano obliko in
- da Fakulteti za matematiko in fiziko Univerze v Ljubljani dovoljujem objavo elektronske oblike svojega dela na spletnih straneh Repozitorija Univerze v Ljubljani.

Ljubljana, dne
20. 06. 2016

Podpis:
Nataša Adžić

CECAM and IUPAP workshop on
**High density DNA arrays:
models, theories and
multiscale simulations**



Book of abstracts

Ljubljana, Slovenia

July 24 2019 – July 26 2019

CECAM and IUPAP workshop on
**High density DNA arrays:
Models, theories and multiscale
simulations**

Book of abstracts

National Institute of Chemistry, Ljubljana, Slovenia

July 24 2019 – July 26 2019



Contents

General Information	7
Description	13
Schedule	15
Abstracts – invited lectures	19
Modeling high density DNA arrays: Mission accomplished! (<i>Aleksei Aksimentiev</i>)	20
Lyotropic cholesteric phases of DNA and its assemblies (<i>Jonathan Doye</i>)	21
Super resolution microscopy of DNA packaging in mammalian cell nuclei (<i>Christoph Cremer</i>)	22
Open boundary molecular dynamics of star-polymer melt and DNA in salt solution (<i>Jurij Sablić</i>)	24
Multiscale simulations of DNA aggregation by multivalent ions (<i>Alexander Lyubartsev, Tiedong Sun, Alexander Mirzoev, Vishal Minhas, Nikolay Korolev and Lars Nordenskiöld</i>)	26
Nucleosome conformational variability in interphase nuclei and in solution explored by cryo-electron microscopy and tomography of vitreous sections (<i>Mikhail Eltsov, Diana Grew, Françoise Livolant, Amélie Leforestier</i>) .	27
Polymer globules in bulk and in confinement (<i>Stanard Mbebe Pachong, Jan Smrek, Kurt Kremer</i>)	29
Toward controlled self-assembly of peptides (<i>Achille Giacometti</i>)	30
DNA without DNA: Watson-Crick selectivity controls the self-assembly of mononucleotides (<i>Tommaso Fraccia, Marco Todisco, Giuliano Zanchetta, Greg Smith, Noel Clark, Tommaso Bellini</i>)	31

Spontaneous domain formation in spherically-confined elastic filaments (<i>Tine Curk, James D. Farrell, Jure Dobnikar, Rudi Podgornik</i>)	32
How to model DNA translocation through nanopores – A multiscale simulational exploration (<i>Christian Holm</i>)	33
Effect of knots during viral DNA packaging and ejection (<i>Cristian Micheletti</i>)	34
Density-nematic coupling in isotropic linear polymers: acoustic and osmotic birefringence (<i>Aleksandar Popadić, Daniel Svenšek, Rudolf Podgornik, and Matej Praprotnik</i>)	35
Homology recognition without proteins [DNA sequence-structure relationship, helical coherence, and a universal homology recognition mechanism-theory vs experiments] (<i>A.A. Kornyshev, D.J.(O') Lee, S.Leikin, A.A. Wynveen</i>)	36
From chromosome territories to ring polymers: Physical properties of untangled polymer melts (<i>Angelo Rosa</i>)	38
“Genetics” in two dimensions: DNA base pairing in thin surface films (<i>Matjaž Ličen, Lucija Čoga, Stefano Maseiro, Lea Spindler, Irena Drevenšek-Olenik</i>)	39
Atomistic MD simulations as a tool to elucidate mechanical properties of DNA/RNA systems (<i>Franči Merzel</i>)	42
DNA-based dendrimers: From a single molecule to the dense solution description (<i>N. Adžić, C. Jochum, E. Stiakakis, G. Kahl, C. N. Likos</i>)	43
Free energy landscapes for dendrimer-like DNAs via neural networks (<i>Florian Buchner, Clemens Jochum, Gerhard Kahl, Andreas Singraber, Christoph Dellago</i>)	45
Abstracts – contributed lectures	47
Analysis structures and forces defining chromatin condensation (<i>Nikolay Korolev, Wahyu Surya, Sook Yi Wong, Qinming Chen Alexander P. Lyubartsev, John van Noort, Lars Nordenskiöld</i>)	48
Genetic outbreak from the endosome: A molecular perspective on gene therapy (<i>Bart Bruininks</i>)	49
Multiscale simulations of double-stranded DNA with sequence-dependent mechanical and conformational properties (<i>Salvatore Assenza</i>)	50
Dynamics and organization of cyclic polymers melt in a confinement (<i>S.M. Pachong, J. Smrek, K. Kremer</i>)	51

DNA-based dendrimers: From a single molecule to the dense solution description

N. Adžić¹, C. Jochum², E. Stiakakis³, G. Kahl², C. N. Likos¹

¹Faculty of Physics, University of Vienna, Boltzmanngasse 5, A-1090 Vienna, Austria

²Institute for Theoretical Physics, TU Wien, Wiedner Hauptstraße 8-10, A-1040 Vienna, Austria

³Institute of Complex Systems 3, Forschungszentrum Jülich, Leo-Brandt-Straße, D-52425

Jülich, Germany

e-mail: natasa.adzic@univie.ac.at

We present a joint theoretical-experimental study of a novel class of macromolecules, the so-called DNA-based dendrimers. They have recently been synthesized from the enzymatic ligation of Y-shaped DNA unit, a three-armed structure consisting of double-stranded DNA (ds-DNA), formed via hybridization of three single-stranded DNA chains (ss-DNA), each of which has partially complementary sequences to the other two [1]. In order to describe such dendrimers of various generations we have employed two independent models: a bead-spring model and the oxDNA model. In the bead-spring model, base-pairs of a single DL-DNA molecule are modeled by charged monomers, whose interactions are chosen to mimic the equilibrium properties of DNA correctly. On the other hand, the oxDNA model allows us to take a closer look into the DNA structure, treating DNA as a string of rigid nucleotides which interact through potentials that depend on the position and orientation of the nucleotides. We have performed Molecular Dynamics Simulations and we have also employed dynamic/static light scattering in order to determine equilibrium properties and conformational characteristics of all-DNA dendrimers as well as the behavior of their solutions. We have investigated their behavior in ionic solution, paying particular attention on their salt-responsiveness. Our computational and experimental results reveal that the DL-DNA are rigid objects with low internal monomer concentration, regular voids in their interior, with high percentage of absorbed counterions, and that show high resistance to stimuli-responsiveness [2]. These properties shape the behaviour of their solutions. Namely, both experimental as well as computational results show anomalous structure factor of dense DL-DNA solutions, as it had been predicted theoretically in Ref [3]. In this way we have found the object which was a missing puzzle in understanding the full phase diagram of star polymer solutions.

[1] Y. Li, Y. Tseng, and D. Luo, *Nat. Mater.* **3**, 38, (2004).

[2] C. Jochum, N. Adžić, E. Stiakakis, T. L. Derrien, D. Luo, G. Kahl, and C. N. Likos, *Nanoscale*, **11**, 1604 (2019).

SCALING EXPONENT OF COMPACT POLYMER CONFORMATIONS IN NON HOMOGENEOUS MEDIA

Dušana Lekić^{1,*}, Sunčica Elezović Hadžić², Nataša Adžić³

¹University of Banja Luka, Faculty of Natural Sciences, Mladena Stojanovića 2,
Banja Luka, Republic of Srpska

²University of Belgrade, Faculty of Physics, Studentski trg 12,
Beograd, Serbia

³Department of Theoretical Physics, J. Štefan Institute, Jamova cesta 39,
Ljubljana, Slovenia

Abstract: We studied compact conformations of a ring polymer adsorbed on the non homogeneous (e. g. porous) substrates. Substrates are represented by the generalization of modified rectangular (MR) lattice – a hierarchically constructed family of fractal lattices embedded in 2d space and parameterized with an integer $p > 1$. Analyzing the exact set of recursive relations for arbitrary value of p , we established an asymptotic form of a number of conformations. As a correction to the leading exponential factor we obtained the stretched exponential factor with the exponent $\sigma = 1/2$ on each member of the fractal family. Although it is believed that the critical exponent σ on fractal lattices is determined not only by the fractal dimension of the underlying lattice but also by other lattice parameters, here we found that σ had the same value on different fractals with the same fractal dimension ($d_f = 2$).

Keywords: non-homogeneous media, fractal, polymer, scaling functions, critical exponents.

1. INTRODUCTION

Polymer is a large molecule made up of covalently bonded units called monomers. As solid material, a synthetic polymer can exist in various forms: from ordinary thermoplastics used in everyday life to some highly advanced polymer matrix composites used in marine and aerospace applications. Nature also prefers polymers since all living beings are comprised of polymers such as structural or functional proteins whose performance is directed and controlled by other well known polymers: DNA and RNA.

The conformational properties of a single polymer are best learned when the polymer is immersed in a solvent. Then, due to the thermal agitation, polymer continuously changes its shape and acquires different conformations. Depending on the quality of the solvent and /or temperature, there are three qualitatively different regimes. In good solvent (or high temperature), the regime polymer is in an extended state. Lowering the solvent quality or temperature, at the so called Θ - condition, a polymer undergoes collapse transition from expanded to com-

compact state. In the bad solvent regime (or low temperature) when polymer is in compact state, it occupies compact, globular conformations in order to minimize contacts with the solvent. Statistics of linear polymer conformations in all three regimes are well described by a suitable kind of random walks defined on a lattice [1]. In good solvent regime, when conformations are of the random coil type, self-avoiding random walks are applicable, a concept originally introduced in polymer physics by Montroll [2]. Self avoiding random walks (SAWs) are random walks that never visit some lattice site more than once, i.e. they do not intersect themselves, a property that mimics the self-excluded volume in real polymers. Compact conformations are best represented by Hamiltonian walks (HWs) which are SAWs that visit each lattice site and therefore maximally occupy the lattice. The compact state of a polymer is a principal state in the biological world due to the fact that the functional proteins under normal conditions fold into the unique compact conformation, or to the fact that chromatin in eukaryotic cells is compactly packed into the nucleus.

In this article we study conformations of a ring polymer that are compact and fractal in charac-

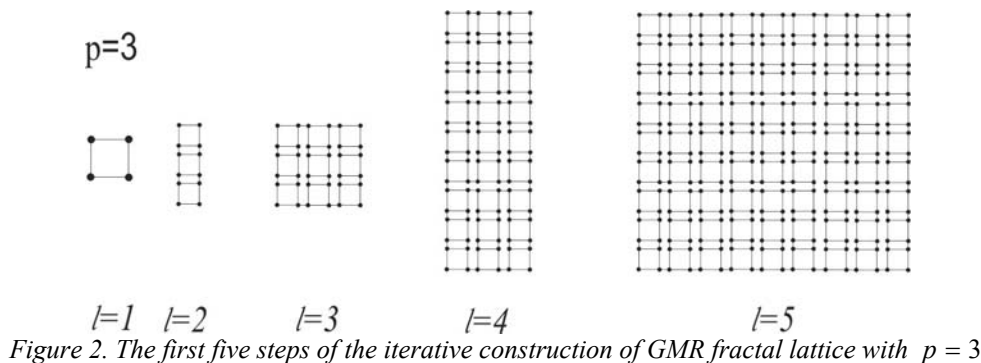
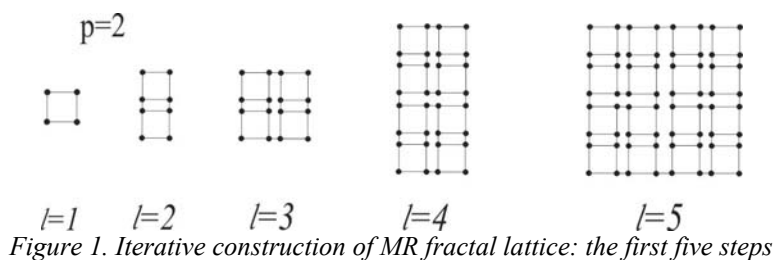
* Corresponding author: dusamar@netscape.net

ter, which is directly applicable to chromatin organization in the nucleus as stated in [3–6]. These kinds of conformations are generated by the Hamiltonian closed walks (cycles) on fractal lattices, where each walk can be viewed as space-filling fractal curve. Utilizing self-similarity of fractal lattices, through the exact set of recurrence equations, we determine how the number of HWs (Z) grows with the number of lattice sites (N) when $N \rightarrow \infty$ (asymptotic law).

2. MODIFIED RECTANGULAR LATTICE AND ITS GENERALIZATION

Modified rectangular (MR) lattice and its generalization (GMR) are fractal lattices embedded in 2d space [7,8]. Each fractal of GMR family is parameterized with an integer p , $2 \leq p \leq \infty$. The case $p = 2$ corresponds to MR lattice. Construction of fractals is

iterative, step by step, as illustrated in Figure 1 and Figure 2. For an arbitrary p , the first four steps of construction are: 1st step – graph of four points in the form of the unit square is constructed; 2nd step – p unit squares are connected in the form of rectangle; 3rd step – p rectangles, as the one obtained in the previous step, are connected in the form of a $p \times p$ square; 4th step – p squares from the previous step are connected in the form of a rectangle. Fractal is obtained after infinitely many steps in which we alternatively generate rectangular and square shapes. The structure obtained in the l^{th} step of the construction is called the l^{th} order generator, and is denoted by G_l . For a given p generator $G_l(p)$ comprises $N_l = 4 \cdot p^{l-1}$ lattice sites, and each fractal lattice obtained when $l \rightarrow \infty$ has fractal dimension $d_f = 2$, independently of p .



3. RECURSIVE ENUMERATION OF WALKS AND ASYMPTOTICS

In order to enumerate all Hamiltonian cycles on $G_{l+1}(p)$, in Figure 3 we schematically represent all cycles on the coarse grained $G_{l+1}(p)$ – generator of order $l+1$ (square or rectangle) that consists of p generators of order l (rectangles or squares) whose internal structure is not shown. It turns out that for any p there is only one coarse grained cycle. This cycle on $G_{l+1}(p)$ consists of p steps (parts), each one through one of the $G_l(p)$. Steps are denoted

by B if they consist of one brunch that enters and leaves $G_l(p)$ through vertices of $G_l(p)$ belonging to different $G_{l-1}(p)$. Actually, step B represents all Hamiltonian walks that enter and leave generator through mentioned vertices, and whose number on $G_l(p)$ is denoted by B_l . Similarly, steps are denoted by D if they consist of two brunches, each of them entering and leaving $G_l(p)$ through vertices of $G_l(p)$ belonging to the same $G_{l-1}(p)$. Step D represents all walks of that type whose number on $G_l(p)$ is denoted by D_l . We can see in Figure 3 that

there are two B steps and $p - 2$ steps D , so that the overall number of Hamiltonian cycles on $G_{l+1}(p)$ can be expressed as :

$$Z_{l+1} = B_l^2 D_l^{p-2} . \quad (1)$$

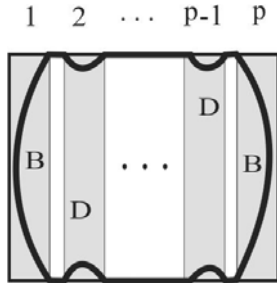


Figure 3. Schematic representation of all Hamiltonian cycles on $G_{l+1}(p)$. Grey rectangles represent $G_l(p)$.

Due to the self-similarity of fractal lattices the numbers of walks of B and D types can be obtained recursively, but in order to achieve this, the other two types of walks, denoted by A and E , are needed. Schematic representation of walks of type A , B and E are given in Figure 4, and that of walk D is given in Figure 5. Recurrence equations are:

$$A_{l+1} = B_l D_l^{p-1} , \quad (2)$$

$$B_{l+1} = A_l^p , \quad (3)$$

$$D_{l+1} = p D_l^{p-1} E_l + (p-1) B_l^2 D_l^{p-2} , \quad (4)$$

$$E_{l+1} = D_l^p . \quad (5)$$

This system of non-linear difference equations should be supplemented with the initial conditions – the numbers of walks on the unit square: $A_1 = B_1 = D_1 = E_1 = 1$.

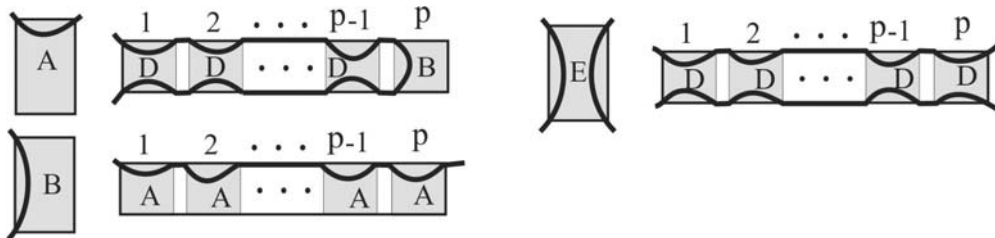


Figure 4. Graphic representation of A , B and E type of walks together with schematic derivation of the corresponding recurrence relations

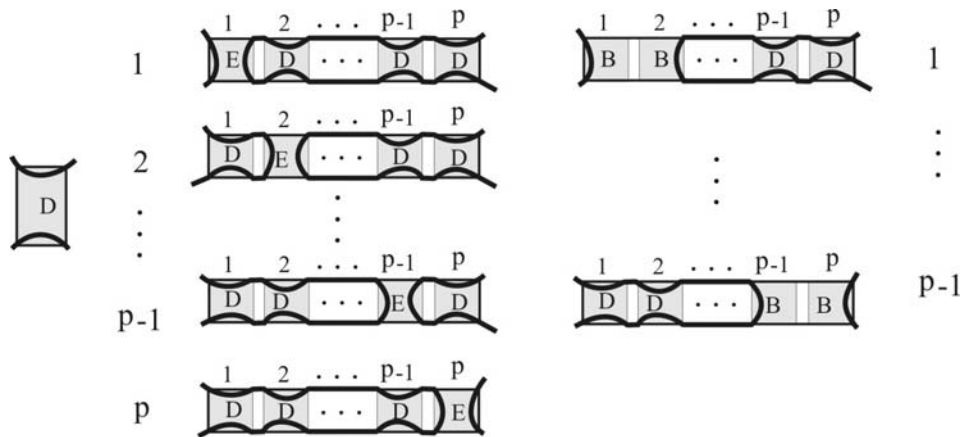


Figure 5. Schematic representation of D type of walks and illustration of obtaining recurrence relation

The numerical iteration shows that variables A_l , B_l , D_l and E_l grow very fast with each iteration l , so that we rescale them dividing A_l , B_l and E_l by D_l , and obtain new, rescaled variables defined as: $x_l = A_l / D_l$, $y_l = B_l / D_l$ and $z_l = E_l / D_l$. Recurrence equations for rescaled variables, that follow from equations (2), (3) and (5) are:

$$x_{l+1} = \frac{y_l}{(p-1)y_l^2 + pz_l} , \quad (6)$$

$$y_{l+1} = \frac{x_l^p}{(p-1)y_l^2 + pz_l} , \quad (7)$$

$$z_{l+1} = \frac{1}{(p-1)y_l^2 + pz_l} , \quad (8)$$

while equation (4) turns to

$$D_{l+1} = D_l^p [(p-1)y_l^2 + pz_l] . \quad (9)$$

By numerical iteration we obtain that $x_l, y_l \rightarrow 0$ for large l , while $z_l \rightarrow const$ whose value depends on the parity of l . With these facts,

combining equations (6) and (7) for $l \gg 1$ it follows that $y_l \approx \text{const } y_{l-2}^p$, meaning that

$$y_l \approx \begin{cases} C_1 \lambda_e^{p^{\frac{l}{2}}}, & \text{for even } l \\ C_2 \lambda_o^{p^{\frac{l-1}{2}}}, & \text{for odd } l. \end{cases} \quad (10)$$

From equation (9) for $l \gg 1$ we have $D_{l+1} \sim \text{const } D_l^p$ so that variable D asymptotically grows as $D_l \sim \text{const } \omega_1^{p^l}$, where ω_1 can be obtained numerically as $\ln \omega_1 = \lim_{l \rightarrow \infty} \frac{\ln D_l}{p^l}$ for each value of p . In rescaled variables relation (1) becomes $Z_{l+1} = y_l^2 D_l^p$, from which, together with the asymptotic given by (10), asymptotic for D_l and relation for the number of lattice sites $N_l = 4 \cdot p^{l-1}$, it is derived that the number of

Hamiltonian cycles on GMR lattices for arbitrary p asymptotically behaves as

$$Z_l \sim \begin{cases} \text{const } \omega^{N_l} \mu_e^{N_l^\sigma}, & \text{for even } l \\ \text{const } \omega^{N_l} \mu_o^{N_l^\sigma}, & \text{for odd } l, \end{cases} \quad (11)$$

where the connectivity constant $\omega = \omega_1^{\frac{p}{4}}$ and constant μ in the stretched exponential factor depend on p , but μ also depends on the parity of l for given p .

We obtained that $\mu_e = (\lambda_o)^{\frac{1}{\sqrt{p}}}$ while $\mu_o = \lambda_e$. Exponent σ in the stretched exponential factor is equal to 1/2 for all p . Values of ω , λ_e and λ_o as functions of p are given in Table 1 for $2 \leq p \leq 10$, and graphical presentations of ω , μ_o and μ_e are given in Figures 6 and 7.

Table 1. Values of parameters ω , λ_e and λ_o appearing in scaling form (10) for $2 \leq p \leq 10$

p	2	3	4	5	6	7	8	9	10
ω	1.1687	1.1474	1.1293	1.1151	1.1039	1.0948	1.0872	1.0809	1.0755
λ_e	0.4621	0.5537	0.6141	0.6574	0.6903	0.7164	0.7377	0.7555	0.7706
λ_o	0.1660	0.1154	0.08999	0.07430	0.06352	0.05561	0.04953	0.04469	0.04075

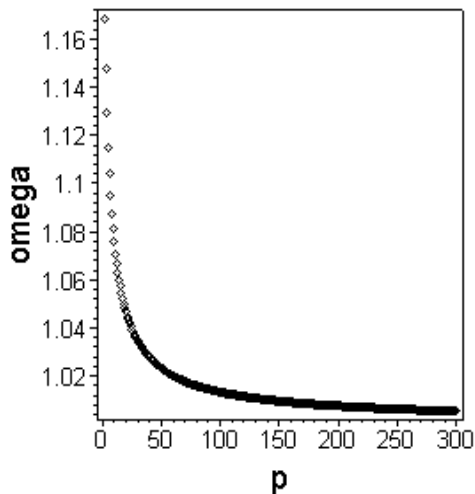


Figure 6. Connectivity constant ω as a function of p .

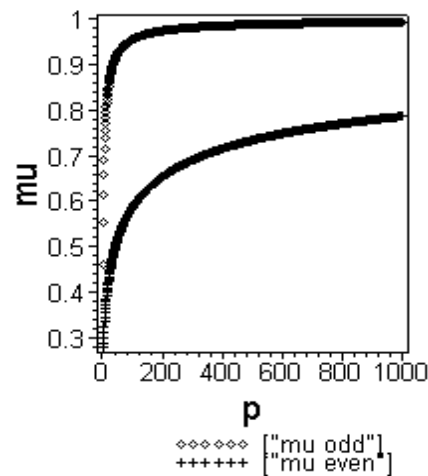


Figure 7. Constant λ for even and odd values of l as a function of p .

4. DISCUSSION OF THE RESULTS

In this paper we established an asymptotic form given by the equation (11) for the number of Hamiltonian cycles on GMR fractal lattices. As a correction to the leading exponential factor we obtained the stretched exponential factor with $\sigma = 1/2$ on the whole fractal family. It is well known that the bases

ω and μ in the scaling form (11) depend on lattice details, but it is expected that σ on homogeneous lattices depends only on lattice dimension due to its origin in surface correction [10,11]. Contrary to homogeneous lattices, as pointed out in [12-14], σ on fractal lattices should be of non-universal character, meaning that it should depend not only on the

fractal dimension but on other lattice parameters too. Here we found the same value of σ on the whole family of similar, but slightly different lattices, with the same fractal dimension. Although lattice dependent on fractals, we see that σ is less sensitive on lattice details than ω and μ . Furthermore, it follows from Figure 7 that the connectivity constant ω slightly decreases with p , although for all p lattices have the same coordination number (three). Due to the high anisotropy of horizontal and vertical directions for each p , by varying p we obtained two branches for the base μ in the stretched exponential factor (for even and odd values of l) as depicted in Figure 7. In the end, we can say that this is an instructive example of a study of how topological properties of lattices influence scaling parameters of Hamiltonian walks.

5. ACKNOWLEDGMENT

This work has been supported by the Project No. OI 171015 funded by the Serbian Ministry of Science and Technological Development.

6. REFERENCES

- [1] C. Vanderzande, *Lattice models of polymers*, Cambridge University press, Cambridge 1998, 1–10.
- [2] E. W. Montroll, *Markoff chains and excluded volume effect in polymer chains*, J. Chem. Phys., Vol.18 (1950) 734–743.
- [3] A. Y. Grosberg, S. K. Nechaev, E. I. Shakhnovich, *The role of topological constraints in*

the kinetics of collapse of macromolecules, J. Phys., Vol. 49 (1988) 2095–2100.

[4] J. Smrek, A. Y. Grosberg, *A novel family of space-filling curves in their relation to chromosome conformation in eukaryotes*, Physica A, Vol. 392 (2013) 6375–6388.

[5] J. D. Halverson, J. Smrek, K. Kremer, A. Y. Grosberg, *From a melt of rings to chromosome territories: the role of topological constraints in genome folding*, Rep. Prog. Phys., Vol. 77 (2014) 022601 (24pp).

[6] L. A. Mirny, *The fractal globule as a model of chromatin architecture in the cell*, Chromosome Res., Vol. 19 (2011) 37–51.

[7] D. Dhar, *Lattices of effectively nonintegral dimensionality*, J. Math. Phys., Vol.18-4 (1977) 577–585.

[8] D. Dhar, *Self-avoiding random walks: Some exactly soluble cases*, J. Math. Phys., Vol.19-1 (1978) 5–11.

[9] D. Dhar, J. Vannimenus, *The collapse transition of linear polymers on fractal lattices*, J. Phys. A: Math. Gen. 20 (1987) 199–213.

[10] A. L. Owczarek, T. Prellberg, R. Brak, *New scaling form for the collapsed polymer phase*, Phys. Rev. Lett., Vol. 70-7 (1993) 951–953.

[11] A. L. Owczarek, *Scaling in the collapsed polymer phase: exact results*, J. Phys. A: Math. Gen. 26 (1993) L647–L653.

[12] J. Stajić, S. Elezović-Hadžić, *Hamiltonian walks on Sierpinski and n-simplex fractals*, J. Phys. A: Math. Gen., 38 (2005) 5677–5695.

[13] S. Elezović-Hadžić, D. Marčetić, S. Maletić, *Scaling of Hamiltonian walks on fractal lattices*, Phys. Rev. E., 76 (2007) 011107(17).

[14] D. Lekić, S. Elezović-Hadžić, *A model of compact polymers on a family of three-dimensional fractal lattices*, J.Stat.Mech. (2010) P02021 (27pp).



ЕКСПОНЕНТ СКАЛИРАЊА КОМПАКТНИХ ПОЛИМЕРНИХ КОНФОРМАЦИЈА У НЕХОМОГЕНИМ СРЕДИНАМА

Сажетак: Проучавали смо компактне конформације прстенастих полимера адсорбованих на нехомогене (нпр. порозне) супстрате. Супстрати су представљени генерализацијом модификоване правоугаоне (МП) решетке – хијерархијски конструисаном фамилијом фракталних решетки смјештених у дводимензионални простор и параметрисаних са цијелим бројем p , $p > 1$. Анализом егзактног система рекурентних релација за произвољну вриједност p , успоставили смо асимптотски облик функције скалирања укупног броја конформација. Као корекцију на водећи експоненцијални фактор добили смо проширени експоненцијални фактор са експонентом $\sigma = 1/2$ на сваком фракталу разматране фамилије. Иако се сматра да критични експонент σ на фракталним решеткама не одређује само фрактална димензија решетке већ и њени остали параметри, овдје смо добили да σ има исту вриједност на различитим фракталним решеткама исте фракталне димензије ($d = 2$).

Кључне ријечи: нехомогене средине, фрактал, полимер, функције скалирања, критични експоненти.





SUMMERSOLSTICE 2014
International Conference On
Discrete Models Of Complex Systems

22-25 June 2014, Institute Jozef Stefan, Ljubljana, Slovenia

B O O K
O F
A B S T R A C T S

Edited by

Bosiljka Tadić & Milovan Šuvakov

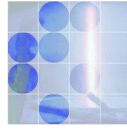
©Department of Theoretical Physics, Jozef Stefan Institute, Slovenia; June 2014

Bstar© 2013 ☆

Follow post-conference updates at the Web page: <http://www-f1.ijs.si/~tadic/Workshops/Solstice14/>

Discrete Models of Complex Systems
SUMMERSOLSTICE 2014

6th Edition



June 23—25, 2014, Institute Jožef Stefan, Ljubljana, Slovenia

BOOK OF ABSTRACTS

©Department of Theoretical Physics, Jožef Stefan Institute, Ljubljana, June 2014

Program Committee

Franco Bagnoli	University of Florence, Italy
Marian Boguna	University of Barcelona, Spain
Zdzislaw Burda	Jegallonian University, Krakow, Poland
Bruno N Di Stefano	Nuptek Systems Ltd, Toronto, Canada
Nazim Fates	INRIA Nancy - Grand Est, France
Rolf Hoffmann	Technical University of Darmstadt, Germany
Andrzej Krawiecki	Warsaw University of Technology, Poland
Anna T. Lawniczak	University of Guelph, Canada
Danuta Makowiec	University of Gdansk, Poland
Marija Mitrović	University of Helsinki, Finland
Andrea Rapisarda	University of Catania, Italy
Raul Rechtman	Universidad Nacional Autonoma de Mexico, Mexico
Jose Mendes	University of Aveiro, Portugal
Bosiljka Tadić	Jozef Stefan Institute, Slovenia
Pieter Van der Weeën	Ghent University, Belgium

Local Organizers

Bosiljka Tadić (chair), Milovan Šuvakov, Nataša Adžić, Nevenka Hauschild (secretary)
Theoretical Physics Department, Jožef Stefan Institute, Ljubljana, Slovenia
CONTACT: Phone: +38614773767; FAX: +38614773724; E-mail: bosiljka.tadic@ijs.si;

Webpage: <http://www-fl.ijs.si/~tadic/Workshops/Solstice14/>

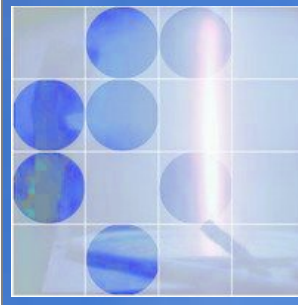
Supported

In part by ARRS Agency for Research of the Republic of Slovenia, the Program P1-0044
and by The Jožef Stefan Institute through the Colloquium program.

SUMMERSOLSTICE 2014

International Conference on Discrete Models of Complex Systems

22--25 June 2014, Institute Jozef Stefan, Ljubljana, Slovenia



Search >

[Home](#) | [Organization](#) | [Call for papers](#) | [Speakers](#) | [Program](#) | [Registration](#) | [Abstracts](#) | [Updates](#) | [Travel](#)

6th Conference *Discrete Models of Complex Systems*

Program for Monday, 23rd June 2014

Monday 23. June 2014

Chair: Geoff Rodgers, Brunel University

TIME	Speaker	Title
09:00-09:30	Stefan Thurner Medical University Vienna	Entropies for Complex Systems
09:30-10:00	Milan Rajkovic Institute Vinca-Belgrade	Quantifying self-organization and complexity with a wavelet machine?
10:00-10:30	COFFEE BREAK	
10:30-11:00	Andrea Rapisarda University of Catania	Micro and Macro Benefits of Random Investments in Financial Markets
11:00-11:30	Jelena Grujic Imperial College London	Multi-strategy game as a complex system
11:30-12:00	Raul Rechtman UNAM Mexico	Topological bifurcations in a model of a society of reasonable contrarians
12:00-13:00	Lunch Break	

Monday 23. June 2014

Chair: Franco Bagnoli, University of Florence

TIME	Speaker	Title
13:00-13:30	Andrea Guazzini University of Florence	Sociophysics of Human Virtual Dynamics
13:30-14:00	Jiri Fiser Purkinje University	ETOS- domain specific language for discrete simulation
14:00-14:30	Anna Carbone Politecnico di Torino	Detrending Moving Average Algorithm: a Non-Random Walk through Complex Systems Science
14:30-15:00	Alexander Povolotsky BLTP, Dubna	Interacting particle systems: Integrability vs. universality
15:00-15:30	COFFEE BREAK	

Monday 23. June 2014

Chair: Matjaz Perc, University of Maribor

TIME	Speaker	Title
15:30-16:00	Alvaro Corral Barcelona University	Zipf's law and a scaling law, in texts and in music
16:00-16:30	Maria Letizia Bertotti Free University of Bozen	Correlation between economic inequality and mobility in kinetic models for social sciences
16:30-17:00	JiriSkvara J. E. Purkinje University	Stock Price Dynamics: Application of Simple Fluids Models and Percolation
17:00-17:30	Harbir Lamba George Mason University	Endogenous Dynamics in Financial and Economic Systems
17:00-19:00	Free time	

6th Conference *Discrete Models of Complex Systems*

Program for Tuesday, 24th June 2014

Tuesday 24. June 2014

Chair: Andrea Rapisarda, University of Catania

TIME	Speaker	Title
09:00-09:30	Matjaz Perc University of Maribor	Bargaining with discrete strategies
09:30-10:00	Marija Mitrovic Intitute of Physics Belgrade	Agent-Based Modeling and Social Structure in Bloggers' Dynamics
10:00-10:30	COFFEE BREAK	
10:30-11:00	Bruno Di Stefano Nuptek Systems, Toronto	Biomimicri As A Method For Developing Cognitive Agents
11:00-11:30	Anna T. Lawniczak University of Guelph	Model Of A Population Of Autonomous Simple Cognitive Agents And Their Performance In Various Environments
11:30-12:00	Rolf Hoffmann Tech. University Darmstadt	Ordering Colors into Strings by Agents
12:00-13:00	Lunch Break	

Tuesday 24. June 2014

Chair: Stefan Thurner, Medical University Vienna

TIME	Speaker	Title
13:00-14:00	Roderick Melnik WLU Waterloo, Canada	Interacting Scales and Coupled Phenomena in Nature and Models (<i>IJS Colloquium</i>)
14:00-14:30	Anton Grigoryev Saratov Technical University	DNA Sequencing by Discrete Dynamics DNA Elongation Monitoring
14:30-15:00	Luca Tubiana Jozef Stefan Institute	A simple one-dimensional model for composite polymer knots
15:00-15:30	COFFEE BREAK	

Tuesday 24. June 2014

Chair: Andrzej Krawiecki, Warsaw University Technol.

TIME	Speaker	Title
15:30-16:00	Jian Yuan, Tsinghua University Beijing	Understanding the Large Scale Urban Vehicular Mobility by Discrete Models
16:00-16:30	Pieter Van der Weeën Ghent University	Influence of the grid resolution on output accuracy and parameter sensitivity
16:30-17:00	Artem Badasyan University of Nova Gorica	Spin-based description of water in models of biological macromolecules
17:00-17:30	Natasa Adzic Jozef Stefan Institute	Field theoretic description of charge-regulation interaction
17:30-19:30	Short Excursion: <i>Ljubljana Castle, Guided tour</i>	
20:00-22:00	Conference Dinner	

6th Conference *Discrete Models of Complex Systems*

Program for Wednesday, 25th June 2014

Wednesday 25. June 2014

Chair: Rolf Hoffmann, Technical University Darmstadt

TIME	Speaker	Title
09:00-09:30	Jose F.F. Mendes University of Aveiro	Structural properties of complex networks
09:30-10:00	Geoff J. Rodgers Brunel University London	Network growth model with intrinsic vertex fitness
10:00-10:30	COFFEE BREAK	
10:30-11:00	Veronika Stoka Jozef Stefan Institute	A Structural and Functional Network as a Tool to Analyze Complex Biological Systems
11:00-11:30	Franco Bagnoli University of Florence	A self-organized method for risk perception in epidemic spreading on multiplex networks
11:30-12:00	Andrzej Krawiecki Warsaw Technology Univ	Dynamical Phase Transition in the Ising model on Scale-Free Networks
12:00-13:00	Lunch Break	

Wednesday 25. June 2014

Chair: Bosiljka Tadic, Jozef Stefan Institute

TIME	Speaker	Title
13:00-13:30	Joaquin Marro University of Granada	Non-equilibrium Phase Transitions in the Brain
13:30-14:00	Zeynep Kaya, Cognitive Neurosci. SISSA	Adding New Neurons on the Tail of a Binomial
14:00-14:30	Maximilian Sadilek Medical University of Vienna	From Wilson-Cowan to Kuramoto: Multiplex Formulation of Neural Activity
14:30-15:00	Zoran Levnajic University Novo Mesto	Reconstructing network structure from dynamical signals
15:00-15:30	COFFEE BREAK	

Wednesday 25. June 2014

Chair: Anna T. Lawniczak, University of Guelph

TIME	Speaker	Title
15:30-16:00	Benedikt Fuchs Medical University of Vienna	Behavioral and Network Origins of Wealth Inequality: Insights from a Virtual World
16:00-16:30	An Zeng University of Fribourg	Enhancing network functionalities by manipulating complex networks
16:30-17:00	Gamaliel Percino Medical University of Vienna	Complexity and the evolution of music-production networks
17:00-17:30	Bosiljka Tadic, Milovan Suvakov Jozef Stefan Institute	Triggering Mechanisms in Emotion Dynamics: From Brain Activity to Collective Social Behavior
17:30-17:40	Conference Closing	

Field theoretic description of charge-regulation interaction

Nataša Adžić¹, Rudolf Podgornik²

¹ Department of Theoretical Physics, Jožef Stefan Institute, Ljubljana, Slovenia, natasa.adzic@ijs.si

² Department of Theoretical Physics, Jožef Stefan Institute, and Department of Physics, Faculty of Mathematics and Physics, University of Ljubljana, 1000 Ljubljana, Slovenia, rudolf.podgornik@fmf.uni-lj.si

In order to find the exact form of the electrostatic interaction between two proteins with dissociable charge groups in aqueous solution, we have studied a model system composed of two macroscopic surfaces with charge dissociation sites immersed in a counterion-only ionic solution [1]. We introduced a surface free energy corresponding to a simple model of charge regulation. Charge regulation is an old concept referring to the case, where the effective charge on a macroion, e.g. protein surface, responds to the local solution conditions, such as local pH, local electrostatic potential, salt concentration, dielectric constant variation and the presence of other charged groups. While in nanoscale interactions one often assumes constancy of surface macroion charge [2], in fact the charge state of the dissociable groups on the macroion surface always depends strongly on the acid-base equilibrium that defines the fraction of acidic (basic) groups that are dissociated and requires to be consistently included in any theoretical formulation. Due to it, we derived a theory, starting from the field-theoretic representation of the grand canonical partition function. It is evaluated within the mean field approximation giving the Poisson-Boltzmann theory with the Ninham-Parsegian boundary condition [3]. Gaussian fluctuations around the mean-field are then analyzed in the lowest order correction that we calculate *analytically* and *exactly*, using the path integral representation for the partition function of a harmonic oscillator with time-dependent frequency. Our general result gives attractive, long-ranged, fluctuation interaction which depends on the pH of the solution. The obtained attraction can overcome mean field repulsion when the surfaces reach their point of zero charge (PZC). Taking the proper limits, our result reduces to the zero-frequency van der Waals term, but also gives the correct Kirkwood-Shumaker result [4]-[5], which opens up the possibility to investigate the Kirkwood-Shumaker interaction in more general contexts where their original derivation fails.

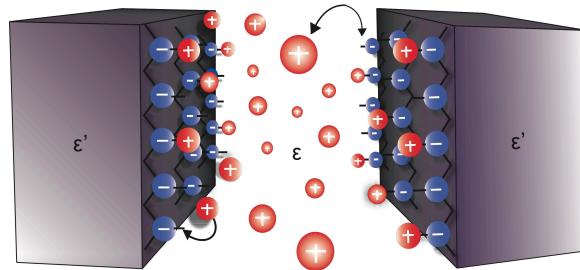


Figure 1: Graphical representation of the model: two charged planar surfaces with charge dissociation sites distributed uniformly along the surfaces and with counterions between the surfaces. The counterions originate from the charge dissociation of the dissociable groups (AC) through the reaction $AC \leftrightarrow A^- + C^+$.

This work was supported by program P1-0055 of the Research Agency of the Republic of Slovenia.

References

- [1] N. Adžić and R. Podgornik, Eur. Phys. J. E (2014) submitted.
- [2] A. Naji, M. Kanduč, J. Forsman, and R. Podgornik, J. Chem. Phys. **139** 150901 (2013).
- [3] B.W. Ninham and V.A. Parsegian, J. Theor. Biol. **31** 405 (1973).
- [4] J. Kirkwood and J.B. Shumaker, Proc. Natl. Acad. Sci. USA **38** 855 (1952).
- [5] J. Kirkwood and J.B. Shumaker, Proc. Natl. Acad. Sci. USA **38** 863 (1952).

XIX Symposium on
Condensed Matter Physics
SFKM 2015

Book of Abstracts



Phenomenology Of Charge-Regulation Interaction In The Protein World

Nataša Adžić^a and Rudolf Podgornik^b

^aJožef Stefan Institute, Ljubljana, Slovenia

^bJožef Stefan Institute, Ljubljana, Slovenia, Faculty of Mathematics and Physics, University of Ljubljana, Slovenia

Abstract. In the world of proteins one can find exotic electrostatic phenomena such as long-ranged attraction between two electro-neutral proteins in an aqueous solution, stemming from thermal charge fluctuations of dissociable charge groups on their surface, known as the Kirkwood-Schumaker (KS) interaction [1]. We present here an extension of KS theory, formulating it in a field-theoretical framework. Our model takes two small spherical macro-ions with dissociable charge groups, which are immersed in a monovalent salt solution. Fluctuating charge on a macro-ion's surface is regulated by local variables such as pH, salt concentration and local electrostatic potential. Charge regulation is described with the proper free energy function [2] for each of the macro-ions, while the coupling between the charges is evaluated at the approximate Debye-Hückel level. Strong attraction between like-charged particles is found close to the point of zero charge, specifically due to asymmetric and anticorrelated charge fluctuations of the macroion charges. The general theory is then implemented for a system of two protein-like macro-ions with known amino acid composition, generalizing the form and magnitude of the Kirkwood-Schumaker interaction. Results show that the strength of protein electrostatic interactions depends on the rate of change of the charge of the macro-ion with respect to the solution pH, i.e. the molecular capacitance of the macro-ion, which is protein specific [3, 4].

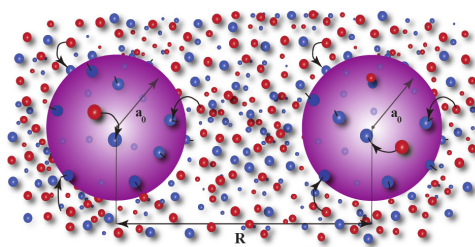


FIGURE 1. Two charge-regulated macro-ions, immersed in a solution composed of monovalent salt ions that can be exchanged with the surface sites.

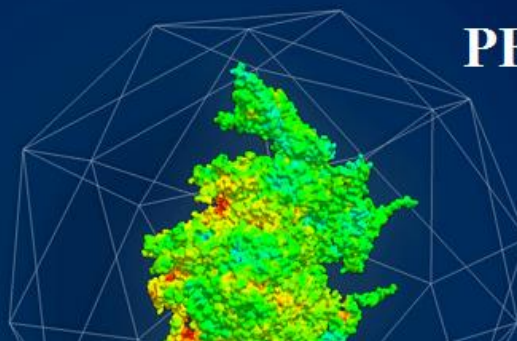
REFERENCES

1. J. Kirkwood, J.B. Shumaker *Proc. Natl. Acad. Sci. USA* **38** 855 (1952).
2. N. Adžić, R. Podgornik *Eur. Phys. J. E* **37** 49 (2014).
3. M. Lund, B. Jönsson *Biochemistry* **44** 5722-5727 (2005).
4. N. Adžić, R. Podgornik *Phys. Rev. E* **91** 022715 (2015).

Protein
Electrostatics
Berlin 2016

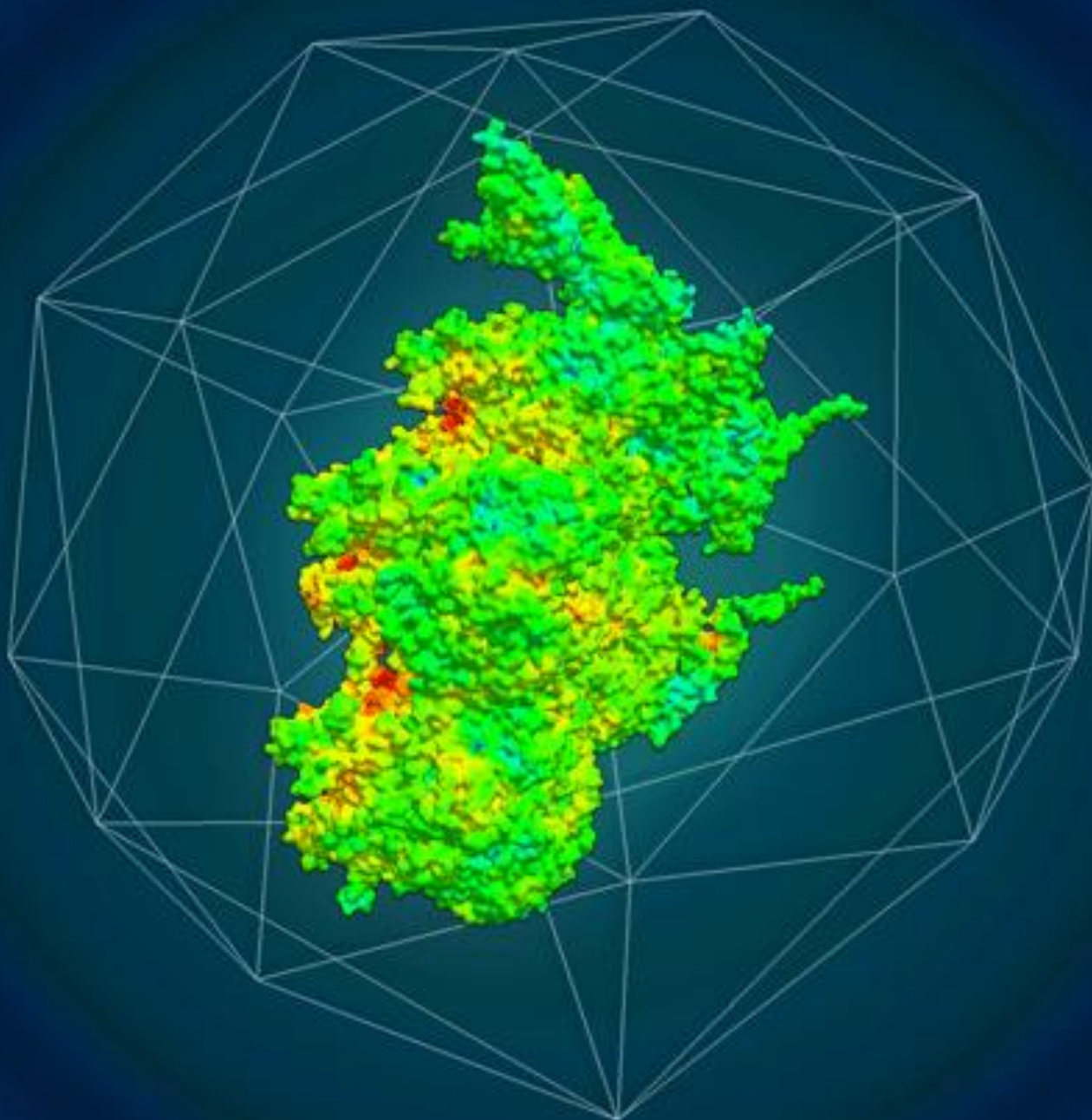
Tuesday, July 19th – Thursday July 21th 2016

PEB 2016



BOOK OF ABSTRACTS

POSTER PRESENTATIONS



Titrateable Macroions in Multivalent Electrolyte Solutions

Nataša Adžić^a, Rudolf Podgornik^{a, b}

^a*Jožef Stefan Institute, Ljubljana, Slovenia*

^b*Faculty of Mathematics and Physics, University of Ljubljana, Slovenia*

Email: natasa.adzic@ijs.si

In the world of proteins one can find exotic electrostatic phenomena such as long-ranged attraction between two electro-neutral protein particles in an aqueous solution, stemming from thermal charge fluctuations of dissociable charge groups on their surface. It was first observed by Kirkwood and Schumaker, half a century ago, who described it in the framework of statistical mechanical perturbation theory and showed that this interaction scales different from standard van der Waals interaction. Recently we have formulated a theory of fluctuation interaction between macroions subject to charge regulation and showed how the Kirkwood-Schumaker (KS) interaction follows directly from charge regulation, thereby generalizing the KS perturbation approach. Nevertheless, it has been a challenge to broaden a theory to be valid in the regimes where the original KS results fails, which is the case in strongly coupled electrolyte solutions. The experiments showed that the presence of multivalent ions can even enlarge this type of attraction between electro-neutral proteins.

Here we present a theoretical description of the effect of polyvalent ions on the interaction between titrateable macro-ions. The model system consists of two point-like macro-ions with dissociable sites, immersed in an asymmetric ionic mixture of monovalent and polyvalent salts. We formulate a dressed ion strong coupling theory, based on the decomposition of the asymmetric ionic mixture into a weakly electrostatically coupled monovalent salt, and into polyvalent ions that are strongly electrostatically coupled to the titrateable macro-ions. The charge of the macroions is not considered as fixed, but is allowed to respond to local bathing solution parameters (electrostatic potential, pH of the solution, salt concentration) through a simple charge regulation model. The approach presented, yielding an effective polyvalent-ion mediated interaction between charge-regulated macro-ions at various solution conditions, and describes the strong coupling equivalent of the Kirkwood-Schumaker interaction.

[← BACK](#)

Flagship Workshop

Computational biophysics on your desktop: is that possible?

September 3, 2018 - September 6, 2018

University of Trento - Dipartimento di Lettere e Filosofia - via Tommaso Gar, 14 - Trento, Italy

Description	Participants	Program	Abstracts (poster & talk)
-------------	--------------	---------	-----------------------------

Austria

Natasia Adzic (Faculty of Physics, University of Vienna) - Speaker

Emanuele Locatelli (Technical University of Vienna) - Speaker

British Indian Ocean Territory

Apratim Chatterji (Indian Institute of Science Education and Research, Pune)

Canada

Mikko Karttunen (Dept. of Mathematics and Computer Science, Eindhoven University of Technology) - Speaker

Czech Republic

Tomas Drsata (University of Chemistry and Technology Prague)

Filip Lankas (University of Chemistry and Technology Prague) - Speaker

Denmark

Matteo Tiberti (Danish Cancer Society Research Center) - Speaker

France

Ralf Everaers (École Normale Supérieure de Lyon) - Speaker

Germany

Robin Cortes-Huerto (Max Planck Institute for Polymer Research)

Roberto Covino (Frankfurt Institute for Advanced Studies) - Speaker

Christoph Globisch (University of Konstanz) - Speaker

Kurt Kremer (Max Planck Institute for Polymer Research) - Speaker

Tobias Lemke (University of Konstanz)

Roberto Menichetti (Max Planck Institute for Polymer Research)

Claudio Perego (Max Planck Institute for Polymer Research, Mainz) - Speaker

Giovanni Settanni (Johannes Gutenberg University Mainz) - Speaker

Jakob Steuer (University of Konstanz)

Greece

Doros Theodorou (National Technical University of Athens) - Speaker

Iran

Azadeh Ebrahim-Habibi (Tehran University of Medical Sciences)

Israel

Dennis C. Rapaport (Bar-Ilan University) - Speaker

Italy

Gianfranco Abrusci (University of Trento)

Irene Adroher-Benítez (Scuola Internazionale Superiore di Studi Avanzati)

Giovanni Bussi (Scuola Internazionale Superiore di Studi Avanzati) - Speaker

Giovanni Ciccotti (University "La Sapienza") - Speaker

Pietro Faccioli (Physics Department of Trento University)

Gianluca Lattanzi Lattanzi (University of Trento) - Organiser

Diego Liberati (National Research Council of Italy @ Polytechnic University)

Simone Melchionna (ISC - Consiglio Nazionale Delle Ricerche) - Speaker

Giuseppe Milano (Dept. Of Organic Materials Science, Yamagata University) - Speaker

Simone Orioli (University of Trento and Trento Institute for Fundamental Physics and Applications)

Raffaello Potestio (University of Trento - Physics Dept.) - Organiser

Angelo Rosa (Scuola Internazionale Superiore di Studi Avanzati (SISSA)) - Organiser

Lorenzo Rovigatti (Dipartimento di Fisica, Sapienza Università di Roma) - Speaker

Giovanni Spagnolli (Centre for Integrative Biology - University of Trento)

Guido Tiana (University of Milan, Italy) - Speaker

Antonio Trovato (Università degli Studi di Padova) - Speaker

Michele Turelli (Department of Physics, University of Trento)

Netherlands

Paulo Telles De Souza (Univ. Groningen (The Netherlands)) - Speaker

Norway

Sigbjørn Bore (University of Oslo)

Michele Cascella (University of Oslo) - Speaker

Pakistan

Muhammad Ahsan (National University of Sciences & Technology)

Slovenia

Matej Praprotnik (National Institute of Chemistry) - Speaker

Spain

Ivan Coluzza (Center for Cooperative Research In Biomaterials) - Speaker

Switzerland

Luciano Abriata (EPFL) - Speaker

John Maddocks (Swiss Federal Institute of Technology Lausanne (EPFL)) - Speaker

United Kingdom

Sarah Harris (University of Leeds) - Speaker

Oliver Henrich (University of Strathclyde, Glasgow)

Agnes Noy (IRB,MMB,UB) - Speaker

United States

Ron Elber (Univ of Texas at Austin) - Speaker

← BACK

Flagship Workshop

Computational biophysics on your desktop: is that possible?

September 3, 2018 - September 6, 2018

University of Trento - Dipartimento di Lettere e Filosofia - via Tommaso Gar, 14 - Trento, Italy

Description	Participants	Program	Abstracts (poster & talk)
-------------	--------------	---------	-----------------------------

All listed times are in Europe/Zurich - GMT+01:00

Monday September 3rd 2018 - Day 1

Convert to my time

Time set by organisers

Session 1 - Aula A001

- 09:00 to 09:10 - Registration
- 09:10 to 09:50 - Ralf Everaers - TBA
- 09:50 to 10:30 - Paulo Telles de Souza - The future prospects of the MARTINI Force Field
- 10:30 to 11:00 - Lunch
- 11:00 to 11:40 - DOROS THEODOROU - Interfacial Properties of Polymer Melts: Atomistic and Mesoscopic Simulations
- 11:40 to 12:20 - Simone Melchionna - Multiscale biofluidics: from molecular transport to physiological flows

Lunch Break

Session 2 - Aula A001

- 14:00 to 14:40 - Giovanni Bussi - RNA structure and dynamics using models at different resolution and experimental data
- 14:40 to 15:20 - Ron Elber - Why does RNA fold?
- 15:20 to 15:50 - Lunch
- 15:50 to 16:30 - Guido Tiana - Data-driven coarse-grained models of biomolecules
- 16:30 to 17:10 - John Maddocks - Coarse-grain modelling of DNA on the desktop: the cgDNA family of models
- 17:10 to 17:30 - Emanuele Locatelli - Condensation and Demixing in Solutions of DNA Nanostars and Their Mixtures: a mean-field approach

Tuesday September 4th 2018 - Day 2

Roundtable - Aula A001

- 09:00 to 09:40 - Giovanni Ciccotti - Molecular Dynamics: Where From, Where To
- 09:40 to 12:00 - Coffee break

Lunch Break

- 12:00 to 14:00 -

Session 3 - Aula A001

- 14:00 to 14:40 - Kurt KREMER - TBA
- 14:40 to 15:20 - Giovanni Settanni - Nano-bio interfaces investigated using molecular dynamics simulations
- 15:20 to 15:50 - Lunch
- 15:50 to 16:30 - Matej Praprotnik - Open Boundary Molecular Dynamics of DNA
- 16:30 to 17:10 - Agnes Noy - The role of DNA dynamics on genome function & how to model it
- 17:10 to 17:30 - Luciano Abriata - Prospect for immersive, interactive, integrative molecular modeling using commodity software and hardware

Forsterbräu Trento

- 19:30 to 22:30 -

Wednesday September 5th 2018 - Day 3

Session 4 - Aula A001

- 09:00 to 09:40 - Lorenzo Rovigatti - The importance of softness and deformability, from DNA origami to microgels
- 09:40 to 10:20 - Mikko Karttunen - Simulating cell division on a desktop
- 10:20 to 10:50 - Lunch
- 10:50 to 11:30 - Sarah Harris - Mind the Gap: Bridging between atomistic models and the continuum limit with Fluctuating Finite Element Analysis
- 11:30 to 11:50 - Christoph Globisch - Multiscale simulation study of penta peptide aggregation: From atomistic details to a mechanistic interpretation.
- 11:50 to 12:10 - Filip Lankas - Coarse-graining of nucleic acids: atomic to rigid base and beyond

Lunch Break

Session 5 - Aula A001

- 14:00 to 14:40 - Giuseppe Milano - Multi-scale Modelling of Soft Matter: hybrid particle field models
- 14:40 to 15:20 - Michele Cascella - Hybrid Particle-Field Model for Peptide Chains
- 15:20 to 15:50 - Lunch
- 15:50 to 16:30 - Dennis C. Rapaport - Desktop supercomputing: Dynamics of virus self-assembly and packaging with GPU-based MD
- 16:30 to 17:10 - Roberto Covino - Machine learning assisted enhanced sampling and interpretation of molecular dynamics simulations
- 17:10 to 17:30 - Claudio Perego - Study Complex-Lasso Protein Folding via the Elastic Folder Model

Thursday September 6th 2018 - Day 4

Session 6 - Aula A001

- 09:00 to 09:20 - Natasa Adzic - Structure and stimuli-responsiveness of all DNA dendrimers
- 09:20 to 10:00 - Antonio Trovato - Correlation between self-entanglement and amino acid sequences in proteins
- 10:00 to 10:30 - Lunch
- 10:30 to 11:10 - Ivan Coluzza - Identification of protein functional regions
- 11:10 to 11:50 - Matteo Tiberti - Efficient tools for the study of protein mutations: Double Force Scanning and MutateX
- 11:50 to 12:00 - Closing Word

← BACK

The 9th International Conference on
Multiscale Materials Modeling

Oct. 28 - Nov. 2, 2018

Osaka International Convention Center

Abstract Book

<http://mmm2018.jp>



2018



(P1-51)

Multi-scale modeling of DNA-dendrimers in electrolyte solutions

*Natasa Adzic¹, Clemens Jochum², Gerhard Kahl², Christos Likos¹

1. Faculty of Physics, University of Vienna, 2. Institute for Theoretical Physics, Vienna University of Technology

We have studied a novel class of macromolecules, the so-called DNA-based dendrimers. They have recently been synthesized from the enzymatic ligation of Y-shaped DNA building blocks. In order to describe such dendrimers of various generations we have performed MD simulations employing two independent models: a bead-spring model and the oxDNA model. The former one models each base-pair of double-stranded DNA as a single charged monomer and the interactions and interaction parameters in the model have been carefully chosen to mimic the structural properties of a single DNA chain. The system was immersed in water, which was modeled as a uniform dielectric and counterions were introduced in the system to preserve electroneutrality. Furthermore, we added salt, treating it explicitly, in order to investigate its influence on conformational characteristics of a single dendrimer molecule. On the other hand, the oxDNA model allowed us to take a closer look into the DNA structure, treating DNA as a string of rigid nucleotides which interact through potentials that depend on the position and orientation of the nucleotides. Equilibrium properties of a single dendrimer-like DNA molecule from the first to the sixth generations obtained from these two models have been investigated and the obtained simulation results have also been compared to the experiments. We have found an excellent agreement between the theoretical and experimental results, which has encouraged us to use the introduced models for theoretical analysis of novel self-assembled structures, such as cluster crystals in the bulk. The study of these charged dendrimer-systems is an important field of research in the area of soft matter due to their potential role in various interdisciplinary applications, ranging from molecular cages and carriers for drug and gene delivery in a living organism to the development of dendrimer-based ultra-thin films in the area of nanotechnology.

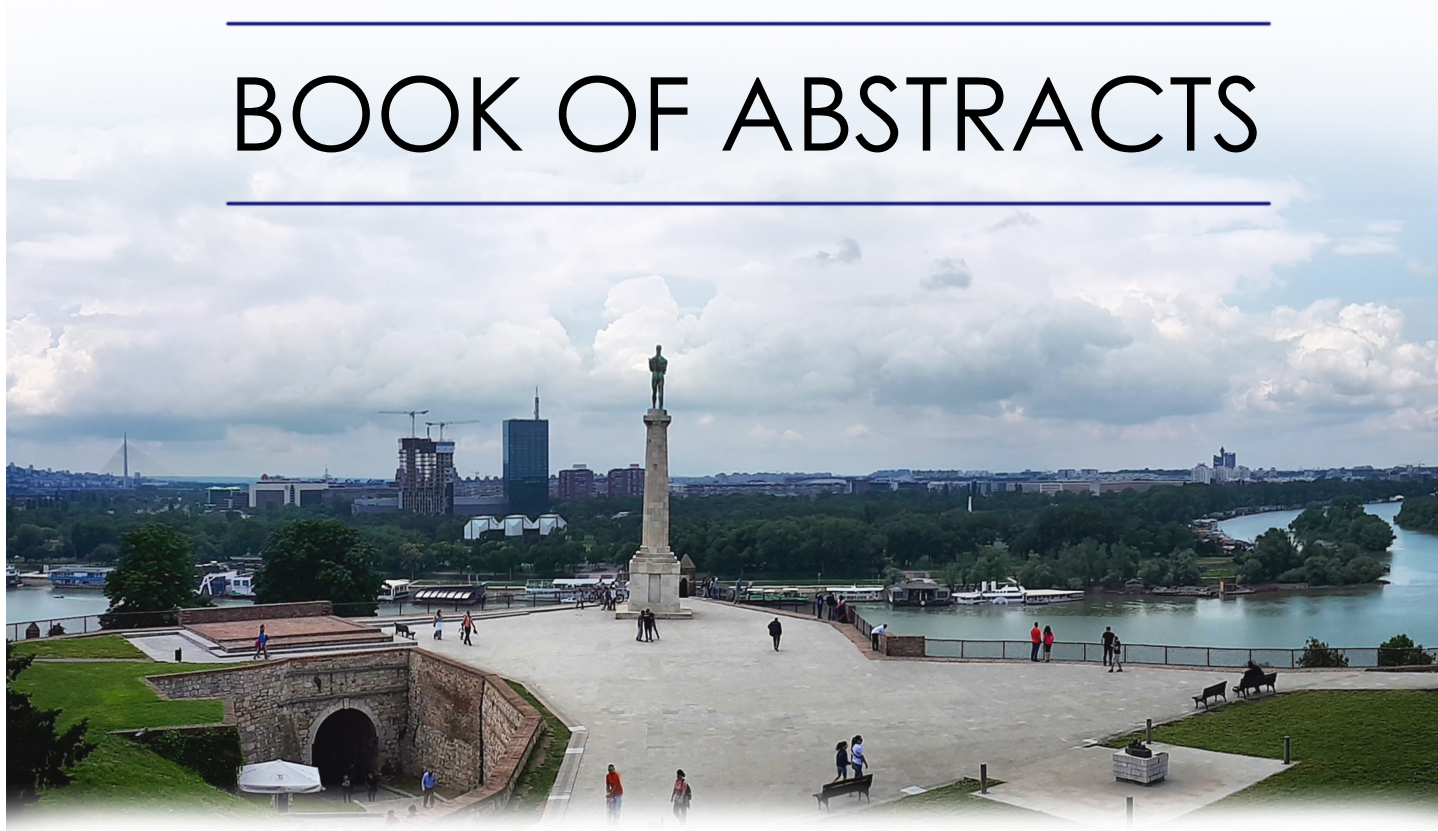
7-11th October 2019
Belgrade, Serbia



<http://www.sfkm.ac.rs/>

The 20th Symposium on Condensed Matter Physics

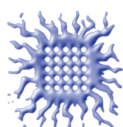
BOOK OF ABSTRACTS



University of Belgrade,
Faculty of Physics



Institute of Physics Belgrade



Vinca Institute
of Nuclear Sciences



Serbian Academy
of Sciences and Arts



Ministry of Education, Science and
Technological Development,
Republic of Serbia

DNA-Based Dendrimers: Novel Macromolecules With Peculiar Characteristics

Nataša Adžić^a, Clemens Jochum^b, Emmanuel Stiakakis^c, Gerhard Kahl^b
and Christos Likos^a

^aFaculty of Physics, University of Vienna, Austria

^bInstitute for Theoretical Physics, TU Wien, Vienna, Austria

^cInstitute of Complex Systems 3, Forschungszentrum Jülich, Germany

Abstract. We present a joint theoretical-experimental study of a novel class of macromolecules, the so-called dendrimer-like DNAs (DL-DNAs). They have recently been synthesized from the enzymatic ligation of Y-shaped DNA unit, a three-armed structure consisting of double-stranded DNA (ds-DNA), formed via hybridization of three single-stranded DNA chains (ss-DNA), each of which has partially complementary sequences to the other two [1]. To describe such dendrimers of various generations we have employed a bead-spring model, in which base-pairs of a single DL-DNA molecule are modeled by charged monomers, whose interactions are chosen to mimic the equilibrium properties of DNA correctly. We have performed Molecular Dynamics Simulations and we have also employed dynamic/static light scattering in order to determine equilibrium properties and conformational characteristics of all-DNA dendrimers as well as the behavior of their solutions. We have investigated their behavior in ionic solution, paying particular attention on their salt-responsiveness. Our computational and experimental results reveal that the DL-DNAs are rigid objects with low internal monomer concentration, regular voids in their interior, with high percentage of absorbed counterions, and that show high resistance to stimuli-responsiveness [2]. These properties shape the behaviour of their solutions. Namely, both experimental as well as computational results show anomalous structure factor of dense DL-DNA solutions, as it had been predicted theoretically in Ref [3]. In this way we have found the object which was a missing puzzle in understanding the full phase diagram of star polymer solutions.

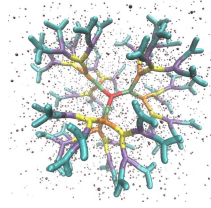


FIGURE 1. 6th generation of the dendrimer composed of Y-shaped DNA building blocks.

REFERENCES

1. Li, Y., Tseng, Y. and Luo, D., *Nat. Mater.* **3**, 38-42 (2004).
2. Jochum, C., Adžić, N., Stiakakis, E., Derrien, T.L., Luo, D., Kahl, G., and Likos, C.N., *Nanoscale* **11**, 1604-1617 (2019).
3. Watzlawek, M., Lowen, H., and Likos, C.N., *J. Phys.: Condens. Matter* **10**, 8189-8205 (1998).

Protein Electrostatics Berlin 2016

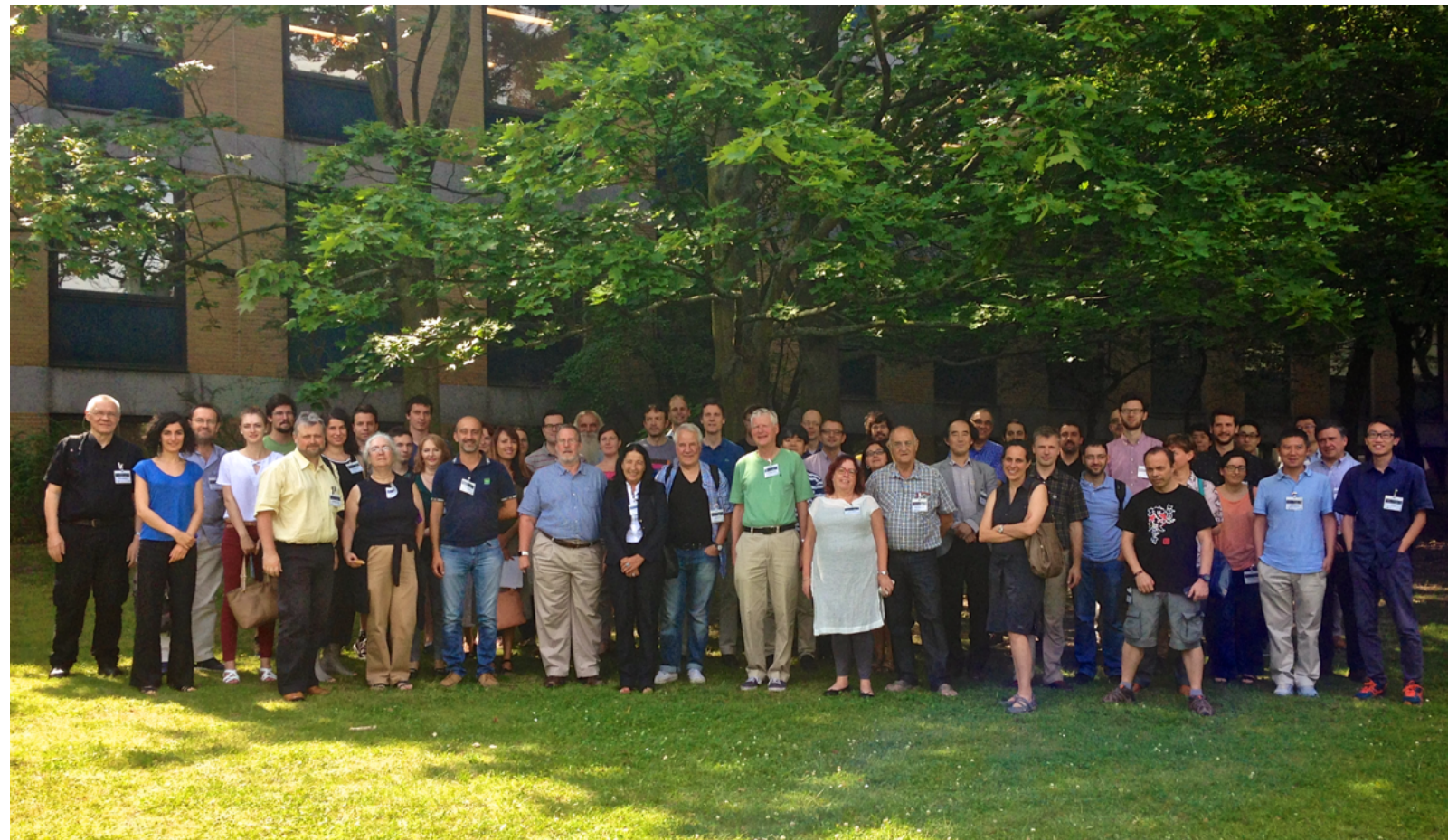
Tuesday, 19 July to Thursday, 21 July 2016

[home](#) [important dates and info](#) [Committees](#) [program](#) [venue](#) [Conference fee](#) [Registration](#) [abstract sample](#) [Photos](#)

[Supporters](#) [Financial support](#) [housing](#) [conference dinner](#) [Letter of invitation](#) [contact](#) [Poster Presentations](#) [Photos](#)

[Introduction](#)

Group photo



Poster Prize winners

Martin Culka (The University of Bayreuth, Germany) 1st prize
Nataša Adžić (Jozef Stefan Institute, Slovenia) 1st prize
Alexander Schlaich (Free University of Berlin, Germany) 1st prize



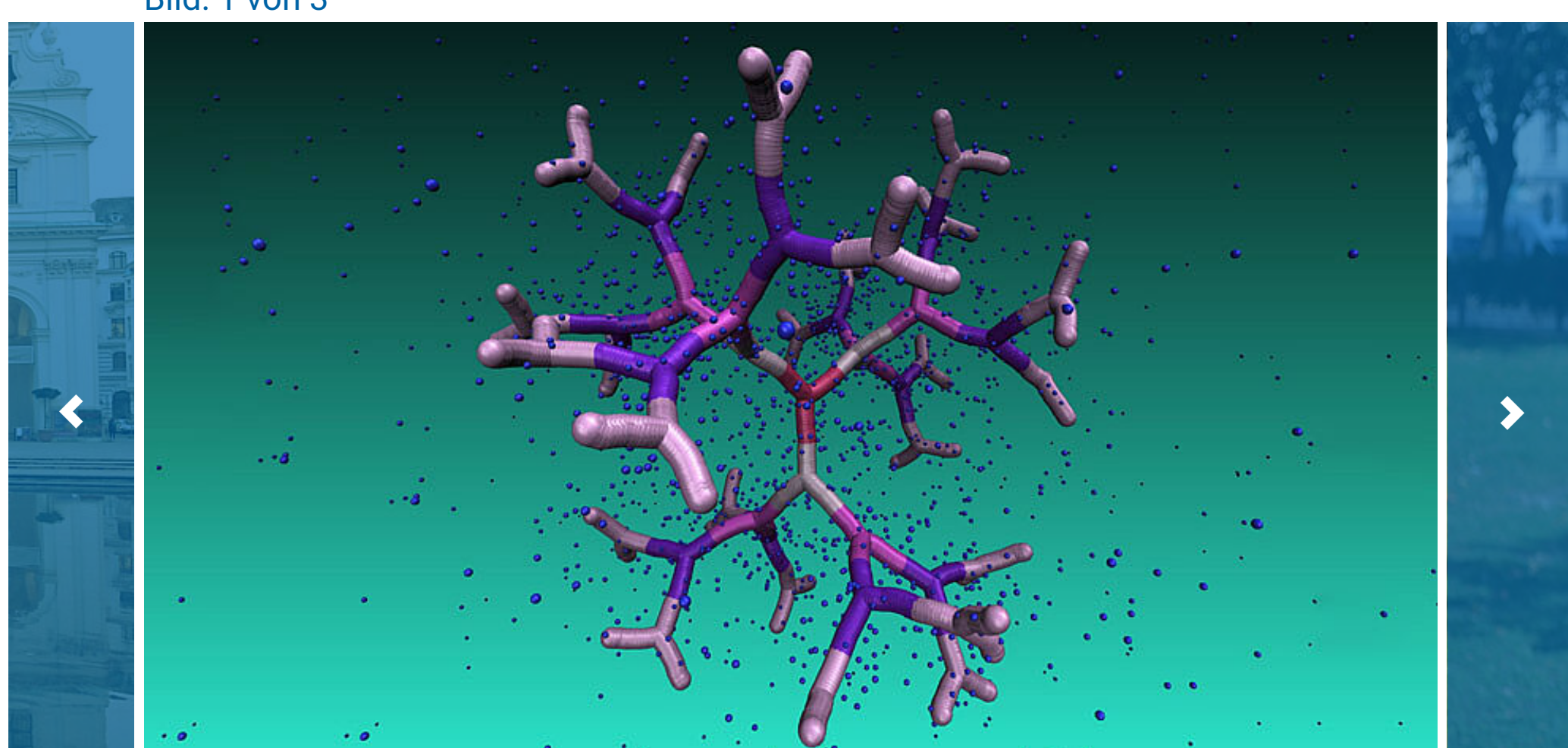
supported by
ERNST-REUTER-GESELLSCHAFT
der Freunde, Förderer & Ehemaligen
DER FREIEN UNIVERSITÄT BERLIN E.V.



Nanocages in the lab and in the computer: how DNA-based dendrimers transport nanoparticles

18. Oktober 2018

Bild: 1 von 3



DNA-based dendrimer of the fifth generation immersed in a counterion solution. Regular voids in the interior of this novel macromolecule can be employed as nano-carriers (© Nataša Adžić).

How to create nanocages, i.e., robust and stable objects with regular voids and tunable properties? Short segments of DNA molecules are perfect candidates for the controllable design of novel complex structures. Physicists from the University of Vienna, the Technical University of Vienna, the Forschungszentrum Jülich in Germany and Cornell University in the U.S.A., investigated methodologies to synthesize DNA-based dendrimers in the lab and to predict their behavior using detailed computer simulations. Their results are published in the high-impact journal *Nanoscale*.

Nanocages are highly interesting molecular constructs, from the point of view of both fundamental science and possible applications. The cavities of these nanometer-sized objects can be employed as carriers of smaller molecules, which is of critical importance in medicine for drug or gene delivery in living organisms. This idea brought together researchers from various interdisciplinary fields who have been investigating dendrimers as promising candidates for creating such nano-carriers. Their tree-like architecture and step-wise growth with repeating self-similar units results in dendrimers containing cavities, hollow objects with controllable design. Nevertheless, decades of research have showed that vast number of different dendrimer types experience back-folding of outer branches with growing dendrimer generations, giving rise to a higher density of constituents in the molecule's interior. The effect of back-folding is enhanced upon addition of salt in the solution, whereby flexible dendrimers undergo significant shrinking, becoming compact objects with no hollow spaces in their interior.

The team of collaborators consisted of Nataša Adžić and Christos Likos (University of Vienna), Clemens Jochum and Gerhard Kahl (TU Vienna), Emmanuel Stiakakis (Jülich) as well as Thomas Derrien and Dan Luo (Cornell). The researchers found a way to create dendrimers rigid enough to prevent back-folding of outer arms even in the case of high branching generations, preserving regular voids in their interior. Moreover, their novel macromolecules are characterized by remarkable resistance to added salt: they showed that the morphology and conformational characteristics of these systems stay unaffected even upon addition of salt even at high concentration. The nanocages they created, in the lab and studied computationally are DNA-based dendrimers, or so-called, dendrimer-like DNAs (DL-DNA). The building block they are composed of is a Y-shaped double-stranded DNA unit, a three-armed structure consisting of double-stranded DNA (ds-DNA), formed via hybridization of three single-stranded DNA chains (ss-DNA), each of which has partially complementary sequences to the other two. Each arm is made up of 13 base pairs and a single-stranded sticky end with four nucleobases which acts as a glue. While a single Y-DNA corresponds to the first dendrimer generation, the attachment of further Y-DNA elements yields DL-DNA of higher generations. The resulting dendrimer is a charged and hollow-containing macromolecular assembly with tree-like architecture. Due to the rigidity of dsDNA, the branches of DL-DNA are stiff so that the whole molecule is rigid. Since DNA is charged, the electrostatic repulsion enhances the rigidity of the molecule.

DL-DNA molecules have been assembled in the laboratory by the Jülich and Cornell partners with remarkable control and sub-nanometer precision through programmable sticky-end cohesions. Their step-wise growth is highly controllable, unidirectional and non-reversible. This property is of high importance, as it has been shown that DNA-based dendrimers have been envisioned to play a promising role in developing nanoscale-barcodes, DNA-based vaccine technologies, as well as a structural probes involving multiplexed molecular sensing processes. Sizes, shapes as well as additional conformational details invisible to the experimentalists, such as the size of voids and the degree of branches back-folding, have been analyzed by computer simulations in Vienna. To describe the complex structure of DNA units, the group used a simple monomer-resolved model with interactions carefully chosen to mimic the equilibrium properties of DNA in physiological solution. The excellent agreement obtained between experiments and simulations for the dendrimer characteristics validates the theoretical models employed and paves the way for further investigation of the nanocages' properties and their applications as functional and smart nanocarriers and as building blocks for engineering biocompatible artificial materials.

The research is supported by the Austrian Science Fund (FWF) under Grant number I 2866-N36 and by the Deutsche Forschungsgemeinschaft (DFG) under Grant number STI 664/3-1.

Original publication in "Nanoscale":

Clemens Jochum, Nataša Adžić, Emmanuel Stiakakis, Thomas L. Derrien, Dan Luo, Gerhard Kahl, and Christos N. Likos: Structure and stimuli-responsiveness of all-DNA dendrimers: theory and experiment, *Nanoscale* (2018).

<https://pubs.rsc.org/en/content/articlelanding/2018/nr/c8nr05814h/unauth>
#divAbstractDOI: 10.1039/C8NR05814H

Wissenschaftlicher Kontakt

Univ.-Prof. Dipl.-Ing. Dr. Christos N. Likos

Fakultät für Physik
Universität Wien
1090 - Wien, Sensengasse 8/15
+43-1-4277-732 30
christos.likos@univie.ac.at

Rückfragehinweis

Dr. Christiane Maria Losert-Valiente Kroon

Fakultät für Physik
Universität Wien
1090 - Wien, Boltzmannngasse 5
+43-664-60277-725 68
christiane.losert@univie.ac.at

Stephan Brodicky

Pressebüro der Universität Wien
Universität Wien
1010 - Wien, Universitätsring 1
+43-1-4277-175 41
+43-664-60277-175 41
stephan.brodicky@univie.ac.at

Downloads:

Dendrimer (© Nataša Adžić) DG5_01.png	Download Dateigröße: 361,86 KB
Nataša Adžić (© privat) DSC_0955_01.JPG	Download Dateigröße: 3,7 MB
Nataša Adžić and Clemens Jochum (© Clemens Jochum) Foto_Karlsplatz_01.jpg	Download Dateigröße: 1,59 MB

teilen tweet

Zur Liste

Rubriken

- Aktuelle Pressemeldungen
- Foto-Service
- Presseverteiler
- Team
- Zahlen & Fakten
- Press Service

Download-Service

Dateien als ZIP-Archiv herunterladen

Wissenschaftlicher Kontakt

Univ.-Prof. Dipl.-Ing. Dr. Christos N. Likos

Fakultät für Physik
Universität Wien
1090 - Wien, Sensengasse 8/15
+43-1-4277-732 30
christos.likos@univie.ac.at

Rückfragehinweis

Dr. Christiane Maria Losert-Valiente Kroon

Fakultät für Physik
Universität Wien
1090 - Wien, Boltzmannngasse 5
+43-664-60277-725 68
christiane.losert@univie.ac.at

Stephan Brodicky

Pressebüro der Universität Wien
Universität Wien
1010 - Wien, Universitätsring 1
+43-1-4277-175 41
+43-664-60277-175 41
stephan.brodicky@univie.ac.at

Informationen für ...

Studieninteressierte	Studierende	Alumni	Weiterbildung
Bewerber*innen	Mitarbeiter*innen (Login)	Forschende	Lehrende
Besucher*innen (Führungen)	Sportinteressierte	Presse	Wissenschaftsinteressierte

Meistgesuchte Services ...

Studieren an der Universität Wien	u:find Vorlesungs-/ Personensuche	u:space	Bibliothek
Moodle (E-Learning)	COVID-19 Informationen	Fakultäten & Zentren	Webmail
Intranet für Mitarbeiter*innen	Kontakt & Services von A-Z		

Robuste Nanokäfige aus DNA

Nanokäfige sind winzige Strukturen, in denen man etwa Medikamente zu ihrem Wirkort bringen könnte. Forscher haben nun Nanokäfige aus kurzen DNA-Abschnitten hergestellt, die sich im Gegensatz zu anderen ähnlichen Strukturen als sehr robust erwiesen.

Als vielversprechende Kandidaten für die Herstellung von Nanokäfigen gelten sogenannte [Dendrimere](#). Das sind chemische Verbindungen, die sich wie ein Baum verästeln. Mit ihrer baumartigen Struktur und einem schrittweisen Wachstum mit sich wiederholenden, selbstähnlichen Einheiten können diese Moleküle die gewünschten Hohlräume bilden.

Die Studie

"Structure and stimuli-responsiveness of all-DNA dendrimers: theory and experiment "

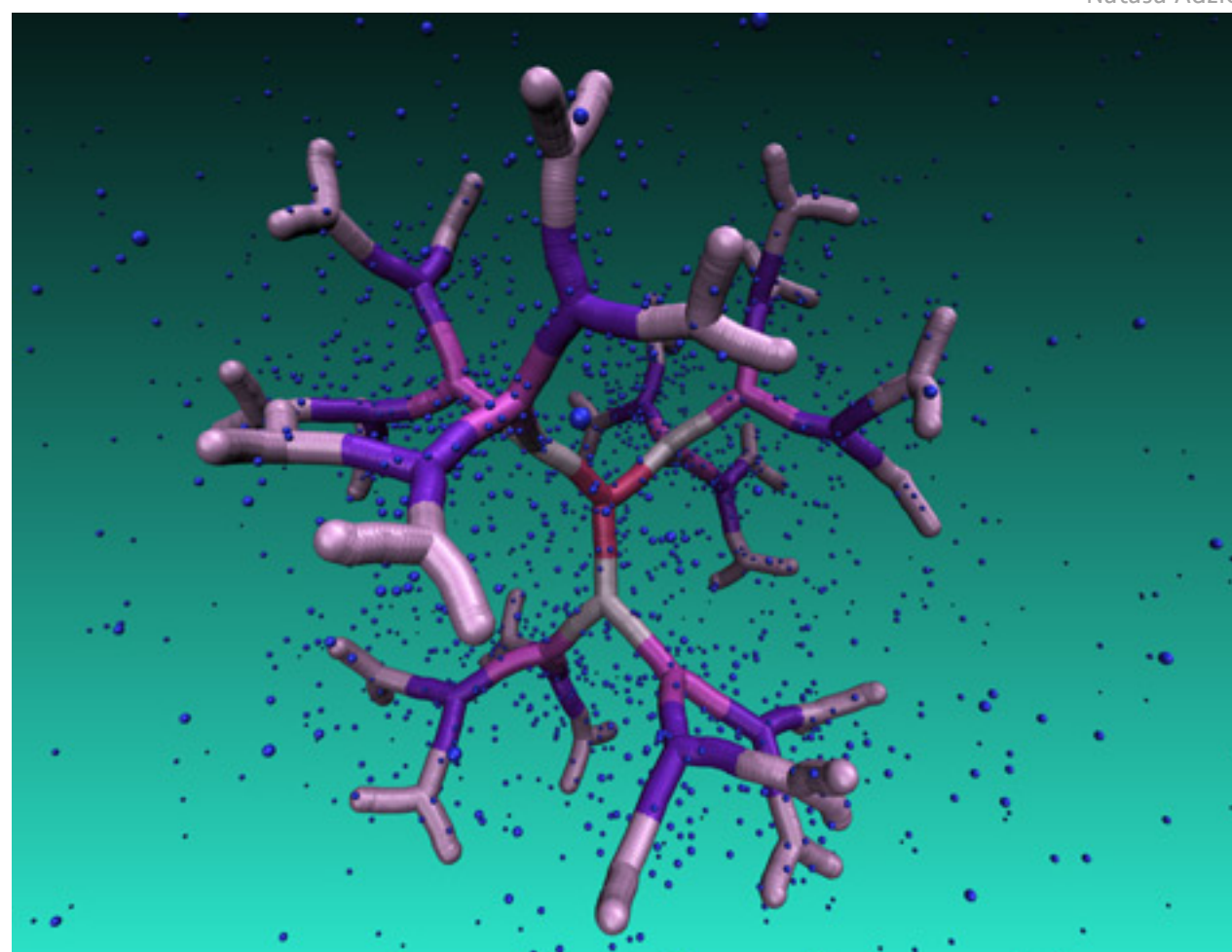
(pubs.rsc.org/en/content/articlelanding/2018/c3/nr51432g zurück zur Startseite) dazu, dass der Hohlraum im Inneren kleiner wurde bzw. ganz verschwand.

Speziell in salzigen Lösungen verstärkte sich dieser Effekt, was etwa ihren Einsatz als Medikamenten-Transporter im Blut erschweren bzw. unmöglich machen würde, erklärt [Christos Likos](#) vom Fachbereich Computergestützte Physik der Universität Wien.

Hohe Steifigkeit

Likos und seine Kollegin [Nataša Adžić](#) haben gemeinsam mit Wissenschaftlern der Technischen Universität (TU) Wien, des Forschungszentrums Jülich (Deutschland) und der Cornell University (USA) einen Weg gefunden, starre Dendrimere zu erzeugen, deren Äste sich auch bei starker Verzweigung nicht zurückfalten. Selbst in Lösungen mit hoher Salzkonzentration blieben die Nanokäfige stabil.

Nataša Adžić



DNA-basiertes Dendrimer, eingetaucht in eine Gegenionenlösung

Aufgebaut sind diese Dendrimere aus dreiarmligen doppelsträngigen DNA-Abschnitten, die einem Ypsilon ähneln. Jeder Arm besteht aus 13 Basenpaaren und hat an seinem Ende einen DNA-Einzelstrang mit vier Basen. Dieser Einzelstrang wirkt als Klebeende, über den sich die einzelnen Y-Bausteine miteinander verbinden. Die relativ starren doppelsträngigen DNA-Elemente verleihen dem gesamten Molekül eine hohe Steifigkeit.

Während die Partner in Deutschland und USA die neuen Dendrimere im Labor in hohem Maße kontrollierbar schrittweise wachsen lassen können, haben die Wiener Forscher die Moleküle in Computersimulationen analysiert. Zwischen Experiment und Simulation gab es dabei nach Angaben der Wissenschaftler eine ausgezeichnete Übereinstimmung, was die verwendeten theoretischen Modelle bestätigte.

Neben der Anwendung als Medikamenten-Transporter könnten solche DNA-Dendrimere auch als biokompatible künstliche Materialien eingesetzt werden. Likos nannte etwa eine künstliche Haut oder Beschichtungen als mögliche Anwendungen, da DNA-basierte Materialien ohne Probleme im Körper verwendet werden könnten.

science.ORF.at/APA

Mehr zum Thema

- [Forscher entwickeln Nano-Krebstherapie](#)
- [Was die Eierschale so besonders macht](#)
- [Forscher entwickeln schwebende Nano-Uhr](#)

18.10.2018 [Mail an die Redaktion](#) [ausdrucken](#) [Seitenanfang](#) ▲

You are here: ▶ [University of Vienna](#) ▶ [Faculty of Physics](#) ▶ [Computational and Soft Matter Physics](#) ▶ [News/Highlights](#) ▶ [Details News](#)

New State of Matter: Crystalline and Flowing at the Same Time

09.12.2021

More than 20 years ago, researchers predicted that with sufficiently high density certain particles of matter would form a new state of matter that features the properties of both crystalline solids and flowing liquids. Scientists from Forschungszentrum Jülich, the University of Siegen, and the University of Vienna have now succeeded in creating this state in a laboratory. Their experimental concept opens up the possibility for further development and could pave the way for further discoveries in the world of complex states of matter.

Through their research efforts, the team was able to finally disprove an intuitive assumption that in order for two particles of matter to merge and form larger units (i.e. aggregates or clusters), they must be attracted to each other. As early as the turn of the century, a team of soft matter physicists headed by Christos Likos of the University of Vienna predicted on the basis of theoretical considerations that this does not necessarily have to be the case. They suggested that purely repulsive particles could also form clusters, provided they are fully overlapping and that their repulsion fulfils certain mathematical criteria.

Since then, further theoretical and computational work has demonstrated that if compressed under external pressure, such clusters develop crystalline order in a way similar to conventional materials such as copper and aluminium. Put simply, a crystalline order signifies a periodic lattice structure in which all particles have fixed positions. In contrast to metals, however, the particles that form cluster crystals are highly mobile and continuously jump from one lattice site to the next. This gives these solids properties that are similar to liquids. Each particle will at some point be found at each lattice site.

Particles with pom-pom-like structure

It proved difficult to produce particles that had the necessary characteristics for the detection of cluster crystals. However, Emmanuel Stiakakis from Forschungszentrum Jülich and his colleagues have now succeeded in achieving this aim in close collaboration with theoreticians from Vienna and polymer chemists from Siegen. The researchers were able to produce hybrid particles with a pom-pom-like structure. The core of these particles is comprised of organic polymers to which DNA molecules are attached and which stick out in all directions like the threads of a pom-pom. This structure enables the molecules to be pushed far inside each other and thus to be sufficiently compressed. At the same time, the combination of an electrostatic repulsion of naturally charged DNA components and a weak interaction of polymers at the centre of the constructs ensures the necessary overall interaction.

"DNA is particularly well suited for our intentions, as it can be assembled relatively easily in the desired shape and size due to the Watson–Crick base pairing mechanism. In combination with polymer cores, the shape and repulsion of the hybrid particles can be fine-tuned and different variations can be produced relatively quickly," explains Stiakakis, who conducts research at Forschungszentrum Jülich's Institute of Biological Information Processing. The physicist with a PhD in the field of physical chemistry has long been using these helix molecules to investigate aspects of self-assembling soft matter.

"After extensive efforts and by applying numerous experimental methods, including biochemical synthesis and characterization as well as X-ray scattering and light scattering, we have now been able to bring a more than 20-year search for cluster crystals to a successful conclusion," says a delighted Likos. The theoretical physicist at the University of Vienna's Faculty of Physics now anticipates the discovery of further complex states of matter, which will be formed by the new macromolecular aggregates.

Original publication:

E. Stiakakis et al.; Self assembling cluster crystals from DNA based dendritic nanostructures; Nat. comm. 9 December 2021

DOI: [10.1038/s41467-021-27412-3](https://doi.org/10.1038/s41467-021-27412-3)

Wissenschaftlicher Kontakt

Univ.-Prof. Dipl.-Ing. Dr. Christos N. Likos

Fakultät für Physik
Universität Wien
1090 - Wien, Kolingasse 14-16
+43-1-4277-732 30
christos.likos@univie.ac.at

Rückfragehinweis

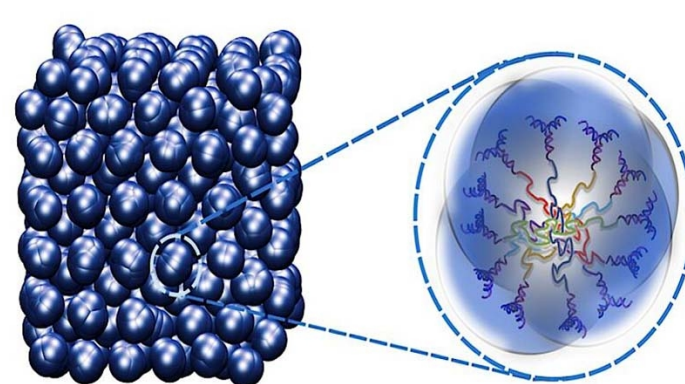
Mag. Alexandra Frey

Pressebüro und stv. Pressesprecherin
Universität Wien
1010 - Wien, Universitätsring 1
+43-1-4277-175 33
+43-664-60277-175 33
alexandra.frey@univie.ac.at

> see [press report \(English\)](#)

> see [press report \(Deutsch\)](#)

◀ [Back](#)



Cluster crystals consist of a core of organic polymers surrounded by DNA molecules (right). Pressed together (left), they exhibit properties of crystals and liquids at the same time. (© Natasa Adzic, University of Vienna)

Contact

Kolingasse 14-16
1090 Wien
T: +43-1-4277-73201



Important links

Faculty of Physics ▶	E-CAM ▶	Collidense ▶	NANOTRANS ▶
ViCoM ▶	CMS ▶		

Most searched-for services ...

Studying at the University of Vienna ▶	u:find Course / Staff search ▶	Webmail ▶	Intranet for employees ▶
u:space ▶	Library ▶	Moodle (e-learning) ▶	Faculties & centres ▶
Contact & services from A to Z ▶			